University of Southampton

Faculty of Engineering and Physical Sciences

School of Chemistry

Structural Studies into π···π Interactions and their Cooperativity Effect on the Spin Crossover Behaviour of a Novel Series of Naphthalimide Compounds

By

Ningjin Zhang, BSc MSc

Thesis for the degree of Doctor of Philosophy

August 2020

University of Southampton

Abstract

The crystal engineering of metal-organic materials is an active area of research in the field of materials science with a wide variety of diverse functions, properties, and promising applications. Prominent work has been pioneered over the last few decades in crystal engineering where structure directing components have been systematically built into molecular building blocks. However, this has not been fully exploited, particularly in the field of magnetically switchable materials. The numerous interesting properties of spin crossover (SCO) active systems, combined with the current trend to develop molecular electronics and machines has resulted in a dramatic increase in the exploration compounds exhibiting this phenomenon.

Modifying the solid-state interactions between metal complexes is essential for controlling the nature of the SCO event. One approach to achieve this is to use supramolecular chemistry to assemble complexes into high ordered arrays through non-covalent supramolecular interactions. Hydrogen bonding is typically the main tool used to control the formation of networks in crystal engineering due to its reproducible, well defined, and directional properties. Previous work has investigated the effect that hydrogen bonding and halogen bonding has on the cooperative nature of the SCO event, which proposed that other supramolecular interactions can also alter the nature of this cooperativity. The focus of this work is on utilising $\pi\cdots\pi$ interactions to systematically modify the SCO transition.

The use of $\pi\cdots\pi$ stacking interactions has been become prevalent since the discovery that the electron density within the π systems defines the strength of the interaction. The established order of stability in the interaction of two π systems is π-deficient$\cdots\pi$-deficient > π-deficient$\cdots\pi$-rich > π-rich$\cdots\pi$-rich. A key aim of this project is to exploit $\pi\cdots\pi$ stacking interactions for the engineering of magnetically switchable metal-organic supramolecular networks.

Naphthalimide-based functional groups were identified as the target for this project because of: a) their inherent ability to induce SCO in Fe(II); b) the long range ordering achieved through π-stacking and c) the interesting photophysical properties of the 1,8-naphthalimide moiety. The electron deficient 1,8-naphthalimide systems have not only been utilised as ligand scaffolds for metal complexes, but also investigated as non-coordinating anions to incorporate this structure directing group into the lattice.

While systematically varying the nature of substituents on naphthalimide backbone, we will use quantum crystallography methods to develop an understanding of how subtle changes in electron withdrawing/donating substituents influence the nature of interactions, and accordingly how $\pi\cdots\pi$ interactions influence magnetic properties. The calculation of the intermolecular interaction energies has resulted in an array of information which provides insights, that we wish to develop into detailed structure function relationship, thereby increasing control over the behaviour of magnetic materials.

Table of Contents

Table of Tables

Table of Figures

List of Accompanying Materials

The NMR, MS, and crystal structure information are included in the appendix and ESI.

The electron appendix organised by chapter 5 includes:

Crystallographic Information Files (.cif) for all the crystal structure reported in the thesis;

Hirshfeld Surfaces analysis and related data;

Interaction energy calculation output files from PIXEL and Crystal Explorer;

The output files calculated by Mopro.

https://doi.org/10.5258/SOTON/D1596

Research Thesis: Declaration of Authorship

Print name:	Ningjin Zhang

Title of thesis:	Structural Studies into π···π Interactions and their Cooperativity Effect on the Spin Crossover Behaviour of a Novel Series of Naphthalimide Compounds

I declare that this thesis and the work presented in it are my own and has been generated by me as the result of my own original research.

I confirm that:

1. This work was done wholly or mainly while in candidature for a research degree at this University;
2. Where any part of this thesis has previously been submitted for a degree or any other qualification at this University or any other institution, this has been clearly stated;
3. Where I have consulted the published work of others, this is always clearly attributed;
4. Where I have quoted from the work of others, the source is always given. With the exception of such quotations, this thesis is entirely my own work;
5. I have acknowledged all main sources of help;
6. Where the thesis is based on work done by myself jointly with others, I have made clear exactly what was done by others and what I have contributed myself;
7. Parts of this work have been published as seen:
    a) J. A. Kitchen, N. Zhang, A. B. Carter, A. J. Fitzpatrick and G. G. Morgan, *Journal of Coordination Chemistry*, "Structural and magnetic properties of dinuclear Cu(II) complexes featuring triazolyl-naphthalimide ligands", 2016, **69**, 2024-2037.
    b) A. B. Carter, N. Zhang, I. A. Kühne, T. D. Keene, A. K. Powell and J. A. Kitchen, *ChemistrySelect*, "Layered Ln(III) Complexes from a Sulfonate-Based 1,8-Naphthalimide: Structures, Magnetism and Photophysics", 2019, **4**, 1850-1856.

Signature:		Date:	17/08/20

Acknowledgements

Thanks for the funding from Chinese Scholar Council (CSC) and University of Southampton Doctoral College.

Thanks for the grant from European Crystallographic Association that allowed me to attend the Erice International School of Crystallography 52nd Course in Quantum Crystallography.

Thanks my supervisor Dr. Jonathan Kitchen (Massey University of New Zealand) for his support and guidance of my work and progression. Particularly, he overcame the time and distance difficulties to supervise my work continually and remotely after moving to New Zealand from 2nd year of my PhD.

I'd like to thank my supervisor Prof. Simon Coles (University of Southampton) for his support and guidance of my work throughout my PhD. Since Dr. Kitchen moved to New Zealand, Simon welcomed me into the fantastic research group and really warm NCS family. I really appreciate all the opportunities he gave me to attend conferences, workshops, and summer schools.

Thanks for the support from my co-supervisor Prof. Steve Goldup and countless hours entertaining me in the lab with his research group members (Mike, Peggy, Andrew, Amenda, Mat, Shu, Poom).

I'd like to thank the kindness and support from all the fellows of National Crystallography Service (NCS) team, Drs. Peter Horton, Graham Tizzard, Laura McCormick, Wim Klooster, James Orton, Rob Bannister, and Mr. Chris Holes, as well as the PhD students in Prof. Simon Coles research group, Eleanor, Wilma, Joe, and Anna. They not only taught me the crystallographic knowledge, but also gave me a lot of meaningful advices in life. The time I spent with them is the best period of my PhD that I would never forget in my life.

Thanks for my board game team, Graham, Peter, and Steve. We had great fun playing Terraforming Mars online. It helped me a lot being depressed with writing during the COVID-19 lockdown. I am also looking forward to their visiting China in the near future.

Thanks my fellow PhD in Dr. Jonathan Kitchen research group, Blue and Rob for their friendships and encouragement, particularly Blue for his boundless encouragement and proofreading help in the last stages of my project. I am looking forward to seeing Blue next year in China.

Thanks for the friendship and encouragement from my friend Maria, Sue, and Sarah. It's shame that I couldn't spend a lot of time with them before leaving UK due to the COVID-19. But we will manage to visit each other in the future.

And of course, I'd like to thank all of family my Mum, Dad and husband, who continually encourage and support me. Their belief and love kept me moving on.

Definitions and Abbreviations

3D	Three dimensional
BCP	Bond critical point
CCDC	Cambridge Crystallographic Data Centre
CCP	Cage critical point
CIF	Crystallographic Information Framework
CP	Critical Point
DFT	Density Functional Theory
ESP	Electrostatic Potential
HS	High Spin
IAM	Independent Atom Model
IUPAC	International Union of Pure and Applied Chemistry
LS	Low Spin
MS	mass spectrometry
MM	The multipole model
NCI	Non-covalent Interaction
NMR	nuclear magnetic resonance spectroscopy
PIXEL	A program for semi-classical density sums interaction energy calculations
RCP	Ring Critical Point
QTAIM	Quantum Theory of Atoms in Molecules
SCO	Spin Crossover
SCXD	single crystal X-ray diffraction
Δoct	Octahedral splitting parameter

Chapter 1 Introduction

1.1 Thesis Outline

This work is organised in 6 chapters. The first chapter gives an introduction to the phenomenon of spin crossover and a brief review of naphthalimide-based compounds, including the importance of analysing π···π interactions of potential SCO ligands using quantum crystallography. The second chapter reports a number of naphthalimide-based anions with electron withdrawing/donating groups which were introduced into mononuclear Fe(II) bis-picolylamine complexes. The third section moves to a study of dinuclear spin crossover compounds with a series of naphthalimide-based anions. The fourth section discusses using naphthalimide as a secondary motif to design new potential spin crossover ligands. In the chapter following this, a selection of naphthalimide ligands were chosen for electron density studies and quantum crystallographic calculations in order to probe the relationship between π interaction and SCO behaviour. Finally, the last chapter concludes the work and outlines plans for future studies.

1.2 The Spin Crossover (SCO) phenomenon

1.2.1 Introduction to Spin Crossover (SCO)

Spin crossover (SCO) complexes are d^4-d^7 transition metal containing complexes that are able to transition between the high spin (HS) and low spin (LS) electronic states in response to external stimuli, such as temperature, pressure, irradiation by light or application of a magnetic field.[1-5] The SCO phenomenon can be harnessed for potential use in material science, medical application and biology fields due to its bistability, particularly in Fe(II) compounds which adopt either HS or LS associated with paramagnetic and diamagnetic states. The first spin crossover (SCO) active compound was characterised by Cambi and Szego in 1931.[6] However, this unusual magnetic behaviour was not explained until König and Madeja's 1963 paper,[7] where they reported the thermally induced transition between HS and LS and this explanation is still widely accepted today.

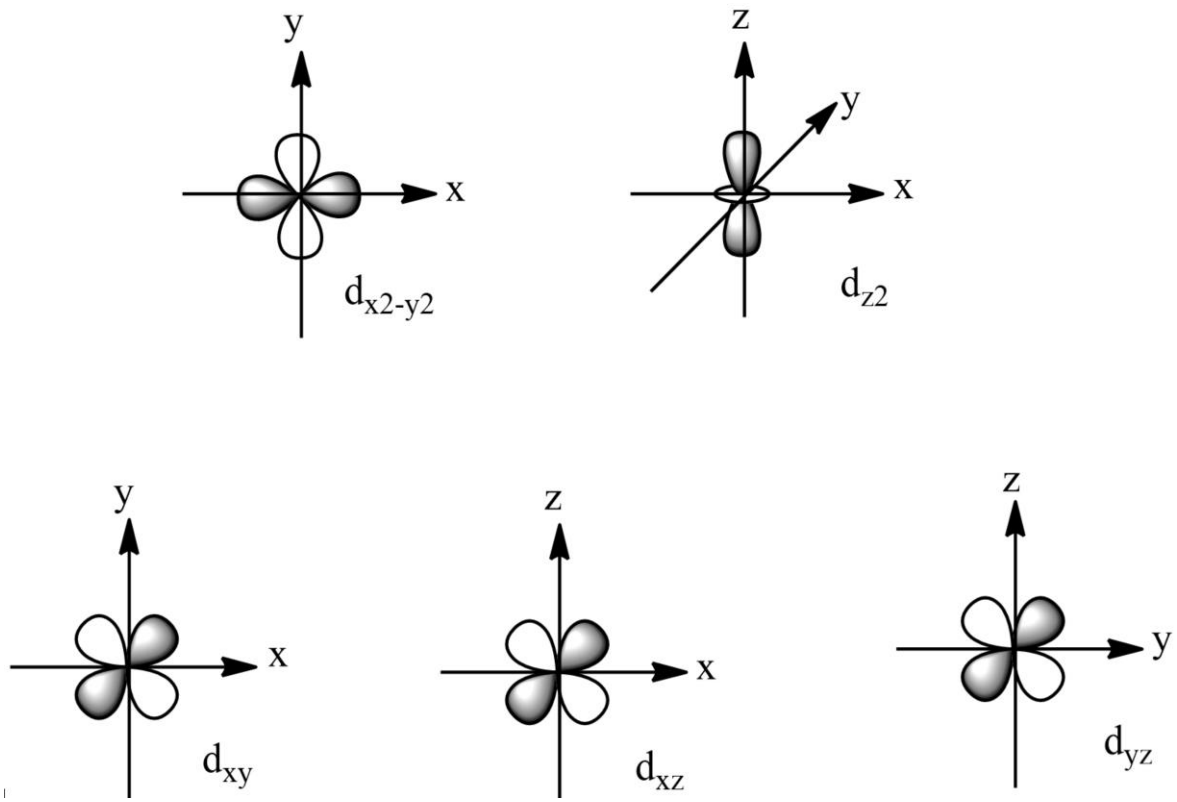

Figure 1-1 The shape and orientation of the orbitals[8]

It is helpful to explain this phenomenon using crystal field theory. When a d^4-d^7 metal centre experiences a perfectly octahedral coordination geometry, the five 3d orbitals would split to different subsets t_{2g} and e_g (Figure 1-1). In an octahedral field, d_{x2-y2} and d_{z2} become anti-bonding ligand orbitals and move to the higher e_g energy level, as they are directly orientated towards the ligands with a repulsive interaction. In contrast, d_{xy}, d_{xz} and d_{yz} orbitals, which point between the ligands, become non-bonding in a lower energy level termed t_{2g} (Figure 1-2). The energy difference between these two subsets, t_{2g} and e_g, is referred to as the splitting energy Δ_o. According to the publication by Madeja and König,[7] the splitting energy changes by altering the strength of metal-ligands bonds. They reported a systematic study on $[Fe^{(II)}(Phen)_2X_2]$(Phen=Phenanthroline) systems ($X=Cl^-$, Br^-, I^-, N_3^-, OCN^-, HCO_2^-) and detected the magnetic changes of the metal centre by altering the coordinated anion X^-. In addition, many other influencing factors also have been reported, especially the number, nature and exact position of the ligands, or the solvation of complexes.[9]

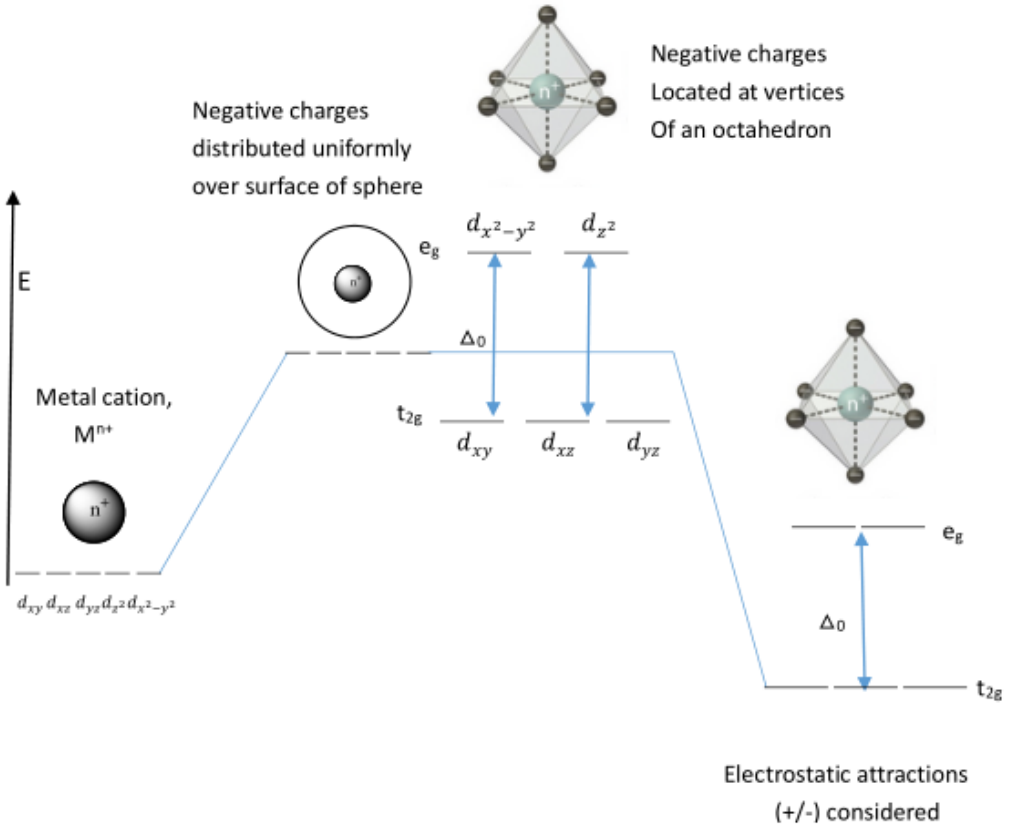

Figure 1-2 When ligands approach the metal ion, the five orbitals split into two groups with different energies: the $d_{x^2-y^2}$ and d_{z^2} orbitals increase in energy as e_g, while the d_{xy}, d_{xz} and d_{yz} orbitals decrease in energy as t_{2g}. The difference in energy between the two new levels is the splitting energy, Δo, figures adapted from Madeja, K. *et al*.[8]

Fe(II), a d^6 metal, is one of the most studied transition metal ions involved with SCO active complexes. To predict the transition between two spin configurations, in addition to the splitting energy, the pairing energy also needs to be considered. The pairing energy, P, is defined as the energy required to overcome electron-electron repulsion.[8, 10-11] In the HS configuration, splitting energy is less than P, the 3d orbitals are filled following Hund's rule with 4 unpaired electrons, resulting in a paramagnetic form. Conversely, LS has the minimum unpaired electrons 0, giving a diamagnetic state due to having a higher splitting energy than P (Figure 1-3). Typically, 4d and 5d metals only form LS complexes, with a much higher splitting energy than 3d metals and therefore the SCO phenomenon is only commonly observed in 3d transition metals.[9]

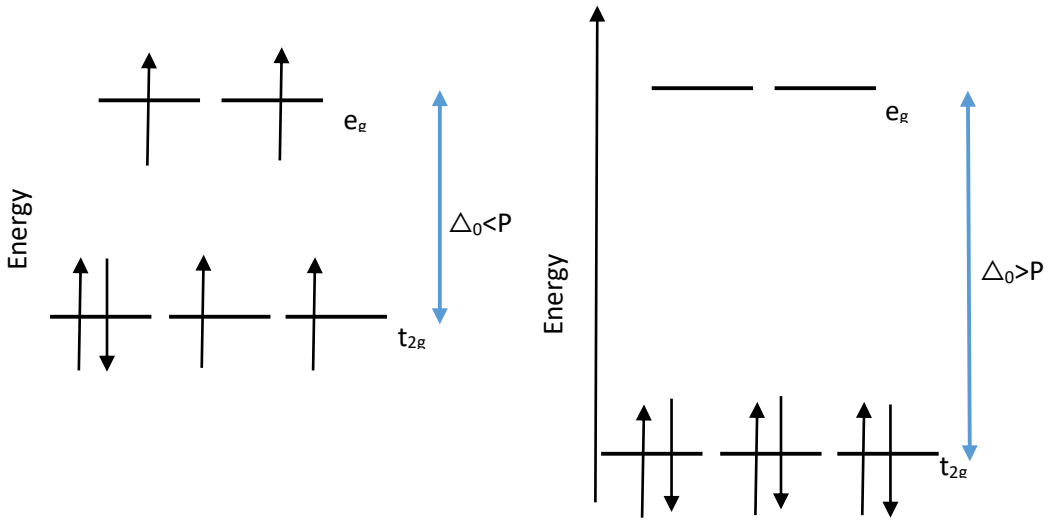

Figure 1-3 The two possible electronic states for a d^6 metal ion, such as iron(II)

1.2.2 Measuring Spin Crossover

Various factors induce the SCO phenomenon, however varying the temperature is the most easily achieved and commonly applied approach to induce SCO. Therefore, a spin transition is often observed when measuring the magnetic susceptibility of SCO active complexes across a range of temperatures. The magnetic susceptibility $\chi(T)$ is determined by the temperature dependent contributions χ_{HS} and χ_{LS} and is calculated thus $\chi(T)= \gamma_{HS}\,\chi_{HS}+ \chi_{LS}\,\gamma_{IS,}$ where γ_{HS} is the mole fraction of HS state and χ_{HS} and χ_{LS} are the known susceptibilities of pure HS and LS states respectively.[9]

Typical plots are then represented on a graph where the fraction of complex molecules in the high spin state, γ_{HS}, is plotted on the y axis and the temperature, T, on the x axis. These graphs can be used to determine the temperature where an inflection point, $T_{1/2}$, occurs (Figure 1-4).[1]

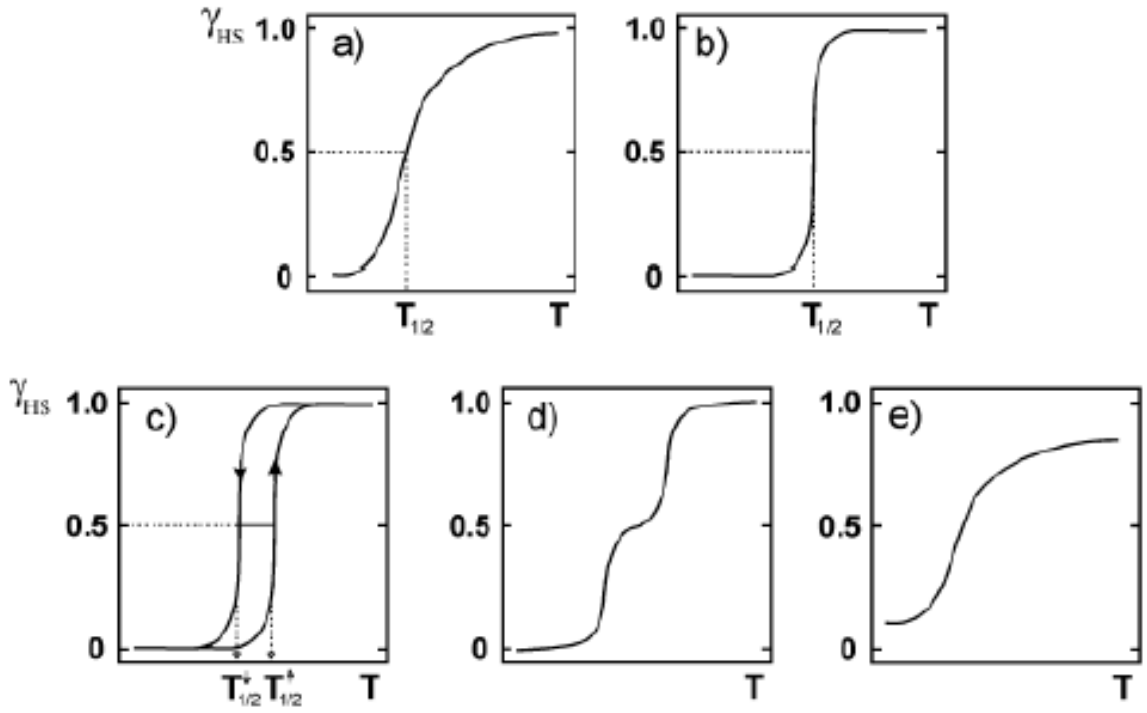

Figure 1-4 Graphical representation of the types of spin transition curves[1] (HS fraction (γ_{HS}) vs temperature (T), where γ_{HS} ($T_{1/2}$)=0.5): a) Gradual; b) Abrupt; c) Hysteresis; d) Stepwise; e) Incomplete, figures adapted from Halcrow, M. A.[12]

a) Gradual transition occurs when metal centres undergo a spin state change from LS to HS with an increasing temperature.

b) Abrupt transition change from LS to HS during a very narrow temperature range. This is usually caused by cooperativity with neighbouring metal centres, where the transition is propagated through links to neighbouring metals.

c) The transition curves shown here exhibit thermal hysteresis, where the cooperativity between metal centres causes similar systems in the LS and HS simultaneously. However, the forward and reverse transition do not occur at the same temperature, resulting in molecular bistability. This results from an even stronger cooperativity than the interactions in Figure 4b.

d) A stepwise transition gives two $T_{1/2}$, which often occurs in dinuclear or multinuclear systems due to the different metal environments.

e) Incomplete transition occurs when the residual HS or LS metal centres exist at either end of a transition.

For most practical applications, hysteresis or abrupt transitions are desired. This requires cooperativity, which can be achieved through interactions causing changes to be propagated throughout a sample. Work has been conducted investigating the effect of hydrogen[13-14] and

halogen bonding[15], however $\pi\cdots\pi$ interactions may provide a promising starting point for new investigations.

1.2.3 Characterisation of SCO behaviour

1.2.3.1 Magnetic Susceptibility Measurements

As discussed previously, magnetic susceptibility measured as a function of temperature χ(T) is the primary technique for characterisation of spin crossover potential samples. There are a number of methods used for magneto-chemical studies. The Evans NMR[16] method is typically applied in solution studies. For solid materials studies a Foner type magnetometer or SQUID (Superconducting Quantum Interference Device), are typically used to collect susceptibility data. As SQUID has much better performance in terms of sensitivity and accuracy, it is the primary technique used in modern laboratories. These measurements are also enhanced by running at liquid helium temperatures and using various extra external perturbations such as high magnetic field, light irradiation and hydrostatic pressure.

Alternatively, instead of a plot of γ_{HS} (T) as shown in Figure 1-4, the spin transition curve is also commonly expressed as variable temperature magnetic susceptibility measurements χ(T) vs T, especially in some cases where quantities of χ_{HS} and χ_{LS} are not accessible or accurately detectable. The χ(T) value of a compound pertains to the effective magnetic moment, which is proportional to the number of unpaired electrons in the complex (Equation 1-1).

(1) $$\mu_{so} = \sqrt{n(n+2)} \approx \mu_{eff}$$

(2) $$\mu_{eff} = \sqrt{\frac{3k\chi_m T}{N{\mu_B}^2}} \approx 2.38\sqrt{\chi_m T}$$

(3) $$\chi_m T \approx \frac{n(n+2)}{(2.83)^2}$$

Equation 1-1 Where n = number of unpaired electrons; k = Boltzmann's constant (1.381 x10^{-16} erg K-1); N = Avogadro's constant (6.022 x1023 mol^{-1}) ; μB = the Bohr magneton (9.274 x10^{-21} erg G^{-1}).

The paramagnetic HS state (n=4) is expected to exhibit a $\chi_m T \approx 3.00\ cm^3 mol^{-1}\ K$, which can be distinguished from the diamagnetic LS state (n=0) with $\chi_m T \approx 0\ cm^3 mol^{-1}\ K$. Notably, in the HS state, observed $\chi_m T$ values are often higher due to spin-orbit coupling, which are found in the range of $\chi_m T \approx 3.3$ to $3.6\ cm^3 mol^{-1}\ K$.[17] A typical χ(T) vs T plot is presented in Figure 1-5.

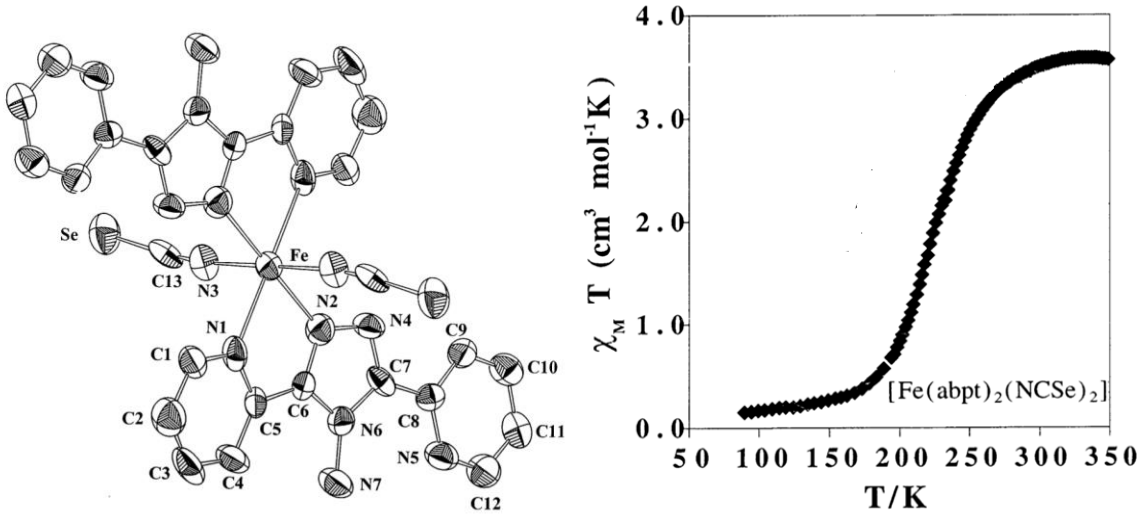

Figure 1-5 The $[Fe(abpt)_2(NCSe)_2]$ (abpt= 4-amino-3,5-bis(pyridin-2-yl)-1,2,4-triazole) molecule is shown on the left; *A variable temperature magnetic susceptibility curve* of χ(T) vs T for a bulk sample of $[Fe(abpt)_2(NCSe)_2]$ consisting of well-shaped single crystals is shown on the right. Figures adapted from Moliner, N. *et al*. [18]

1.2.3.2 X-ray Structural Studies

Single crystal X-ray diffraction, with data collected systematically over a range of temperatures, or at either side of transition temperature, is a common and accurate method used to determine the differences in bond lengths and structural distortion between LS and HS states. Higher repulsion occurs due to the occupied anti-bonding e_g^* orbitals in HS states, which results in increased ligand to metal bond lengths. When comparing the HS state to the LS state, longer Fe-N bond lengths (normally 2.1 – 2.3 Å) and *cis*<(N-Fe-N) distorted from ideal 90° are expected. With empty e_g^* orbitals in the Fe(II) LS state, shorter Fe-N bond lengths (normally 1.8 – 2.0 Å) and a more ideal octahedral geometry is observed, which is a result of stronger metal-ligand bonding. There are two key parameters used to measure the deviation of a coordination configuration from an ideal octahedral geometry, Σ and θ (Figure 1-6).[10] An ideal six-coordinated octahedral complex exhibits $\Sigma = \theta = 0$. Notably, low spin complexes usually give substantially lower distortion indices. Equation 1-2 shows how Σ and θ are calculated.

(1) $$\Sigma = \sum_{i=1}^{12} |90 - \alpha_i|$$

(2) $$\theta = \sum_{j=1}^{24} |60 - \theta_j|$$

Equation 1-2 Distortion indices Σ (1) and θ (2). Where α_i are the twelve cis-N-Fe-N angles about the coordinated iron centre and θ_j are the 24 unique N-Fe-N angles measured on the projection of two triangular faces of octahedron along their common pseudo-three fold axis.[10]

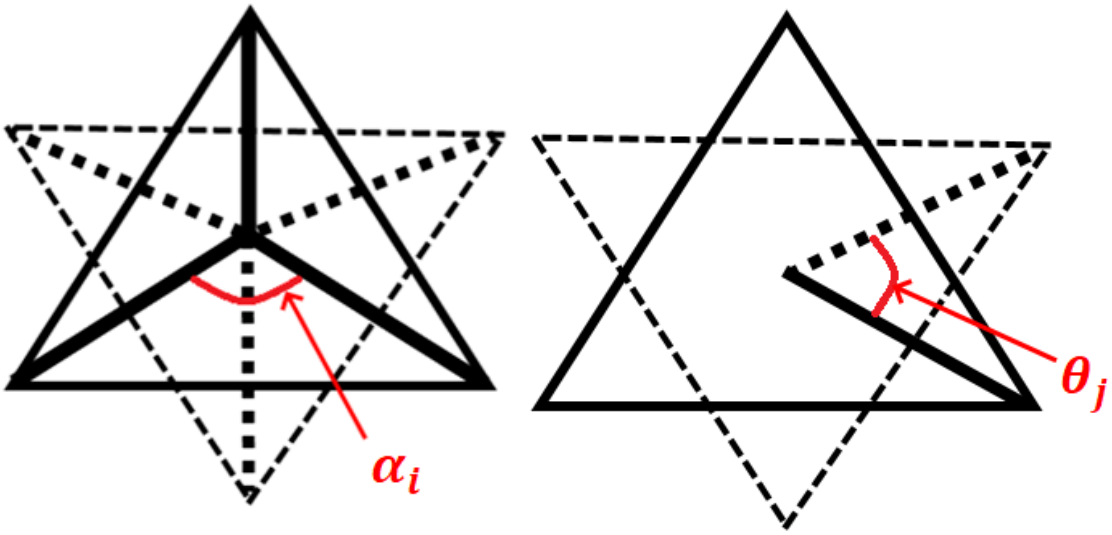

Figure 1-6 Definition of the angles used to calculate distortion indices Σ and θ for six-coordinated complexes. Figures reproduced from Halcrow, M. A. *et al*.[10]

1.2.3.3 ^{57}Fe Mössbauer Spectroscopy

Another well-known technique used for the characterisation of SCO compounds of iron at various temperatures is ^{57}Fe Mössbauer spectroscopy. There are two important parameters derived from ^{57}Fe Mössbauer spectroscopy, the isomer shift δ and the electric quadrupole splitting energy ΔE_Q. The isomer shift, δ, is proportional to the electron density at the nucleus and hence is directly influenced by the *s*-electron population and indirectly influenced by *d*-electron population, therefore it gives information particularly on oxidation state. The electric quadrupole splitting energy, ΔE_Q, is higher in the HS state due to the occupied anti-bonding orbitals e_g^* with a distorted configuration, while in the diamagnetic LS state a more spherical arrangement of d-electrons gives a smaller ΔE_Q.[19-20] [Fe(adpt)(DAPP)$_2$](ClO$_4$)$_2$ was be used as an example of observing this Mössbauer measurement in order to distinguish spin state (Figure 1-7).[20] This study was carried out in the range of 80 K to 293 K in both cooling and warming modes respectively. Selected temperature data is shown in Figure 7. In the cooling mode, HS was observed at 211 K and began to disappear, giving LS when cooled to 185 K. The spectrum below 170 K was characterised as LS in both modes, however, in the warming mode the spectrum at 185 K was found to be HS, which is different to the one observed in cooling mode, thus demonstrating the occurrence of hysteresis.

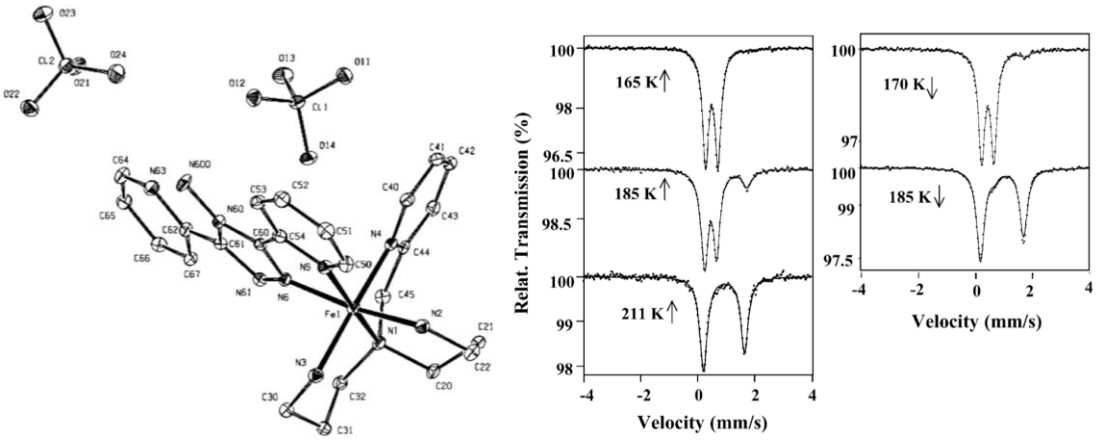

(a) (b)

Figure 1-7 (a) Structure of [Fe(**adpt**)(DAPP)$_2$](ClO$_4$)$_2$; (b) ^{57}Fe Mössbauer spectra of [Fe(**adpt**)(DAPP)$_2$](ClO$_4$)$_2$ recorded in the cooling and warming modes. The solid lines represent fitted curves. Figures adapted from Matouzenko, G. S. *et al*. [20]

Notably, ^{57}Fe Mössbauer spectroscopy is a unique method for characterising the nature of two step transitions in dinuclear iron complexes.

1.2.3.4 Other characterisation methods

In addition to the three principle techniques introduced above, there are a number of other methods that can also be applied to monitor spin transition. For instance, a convenient and quick way to detect the transition is by observing the colour changing at different temperatures. As the charge transfer bands are displaced to lower frequency upon as the system changes from a HS to a LS state the the visible colour of the system often becomes more intense. Electron Paramagnetic Resonance (EPR) spectroscopy has been employed frequently in Fe(III) and Co(II) SCO research, and gives sufficiently well fitted spectra in both HS and LS states;[1] Infrared or Raman spectroscopy can also be used to probe spin state by detecting the frequency of an appropriate metal-ligand vibration, and is widely applied for Fe(II)N$_6$ coordinated systems with NCS^- or $NCSe^-$ ligands;[1] Extended X-ray Absorption Fine Structure (EXAFS) measurements also provide a complementary tool, using synchrotron radiation, to determinate structural details for SCO compounds which cannot be characterised by X-ray diffraction.[1]

1.2.4 Perturbation of the SCO system

Of the different SCO behaviours, abrupt, stepwise and hysteresis spin transitions are the most studied. In the solid state, such spin transitions are mainly affected by cooperativity, where an individual metal centre undergoes a spin transition which propagates throughout the bulk sample due to lattice properties.[1, 9] To this extent, the spin change in response to an external stimulus

(temperature, pressure, etc.) is associated with the degree of cooperativity. The degree of cooperativity between metal centres plays a major role in determining the nature of the spin transition. This occurs as the interactions between complexes with a bulk of sample allow spin events to be propagated throughout the solid, the degree of coopretivitiy is determined by the lattice properties. Relatively weak cooperative interactions mostly lead to gradual transitions, which are commonly observed. Strong cooperative interactions generally induce an abrupt transition, whilst the exact reasons for the occurrence of hysteresis loops have not been clearly defined. There are two primary candidates to explain hysteresis in transition curves: hysteresis associated with a spin transition is usually accompanied by a structural phase change with an associated energy, or intramolecular changes occurring with a transition affect the neighbouring molecules through highly cooperative interactions between them. The variety of manifestations suggest that the appearance of a hysteresis transition may result from particularly high cooperativity.[1, 9-10, 21]

Through a careful understanding of the factors involved in controlling the nature of a SCO transition, one can develop strategies to control the desired behaviour: 1) Linkage of spin centres via covalent bonding in polynuclear complexes or coordination polymers; [9] 2) Incorporation of hydrogen bonding or halogen bonding interactions from anions or solvent molecules;[10] 3) Incorporation of π···π interactions throughout the lattice from aromatic moieties in the ligand structure.[21-22] Importantly, for a more detailed study of spin transition behavior it is necessary to determine the molecular structure and the structural differences in both the HS and LS spin states.

1.2.4.1 Anion Effects

The variation of the anions associated with a cationic Fe(II) SCO system have been studied.[23-24] One investigation of the $[Fe(2\text{-pic})_3]^{2+}\cdot X_2$ (2-pic=2-picolylamine; X= I, Br, Cl) system (Figure 1-8), demonstrated that one complex with a series of anions could dramatically alter the nature of SCO transition, even to the extent that SCO is no longer observed. For this system, the iodide compound did not present any SCO phenomenon, as the value of μ_{eff} is nearly constant. However, the chloride compound showed as an abrupt spin transition, with $T_{1/2}$=100 K, giving the best performance in completion and abruptness of spin transition among these three anions.

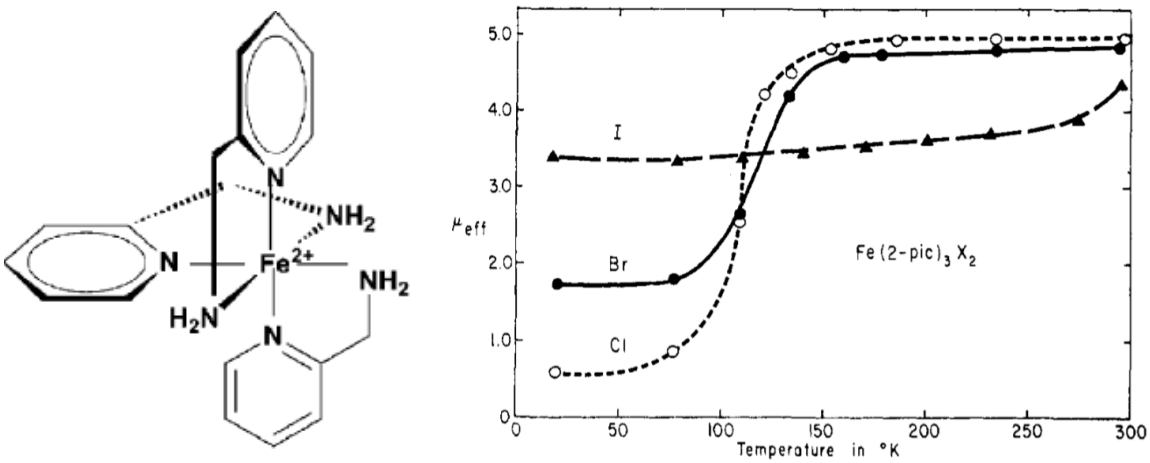

Figure 1-8 $[Fe(2\text{-pic})_3]^{2+}$ is shown on the left; A plot of the magnetic moment μ_{eff} vs T plot for bulk samples of $[Fe(2\text{-pic})_3]^{2+}$ consisting of well-shaped single crystals is shown on the right. Figures adapted from Renovitch, G. A.*et al*. [23]

In addition to this study, other non-coordinated functional anions were also introduced into SCO systems. Xin-Yi Wang[25] investigated introducing various organosulfonate anions into the $[Fe(2\text{-pic})_3]^{2+}$ SCO system (Figure 1-9). Three SCO compounds $[Fe(2\text{-pic})_3]\cdot X_2$ (X = m-ABS^-, **1**; A = *p*-ABS^-, **2**; A = OTf^-, **3**, where *m*-HABS = *m*-aminobenzenesulfonic acid, *p*-HABS = paminobenzenesulfonic acid and HOTf = trifluoromethanesulfonic acid) were prepared and characterised structurally and magnetically. This variation of the anions resulted in a displacement of the transition temperature, and also caused a fundamental change in the nature of the transition. Compound **1** underwent an abrupt spin transition with $T_{1/2}\downarrow$ = 100 K and $T_{1/2}\uparrow$ = 103 K; compound **2** exhibited a gradual transition curve at $T_{1/2}\uparrow$ = 218 K; compound **3** presented significantly different SCO properties to compound **1** and **2**, with an abrupt spin transition associated with a 10 K hysteresis loop at $T_{1/2}\downarrow$ = 333 K and $T_{1/2}\downarrow$ = 343 K. Notably, compounds **1** and **2** are in the meridional (mer-) configuration, while compound **3** represented the first structurally characterised *fac*-$[Fe(2\text{-pic})_3]^{2+}$ (facial configuration) motif showing SCO property. The meridional and facial configurations are illustrated in Figure1-10.

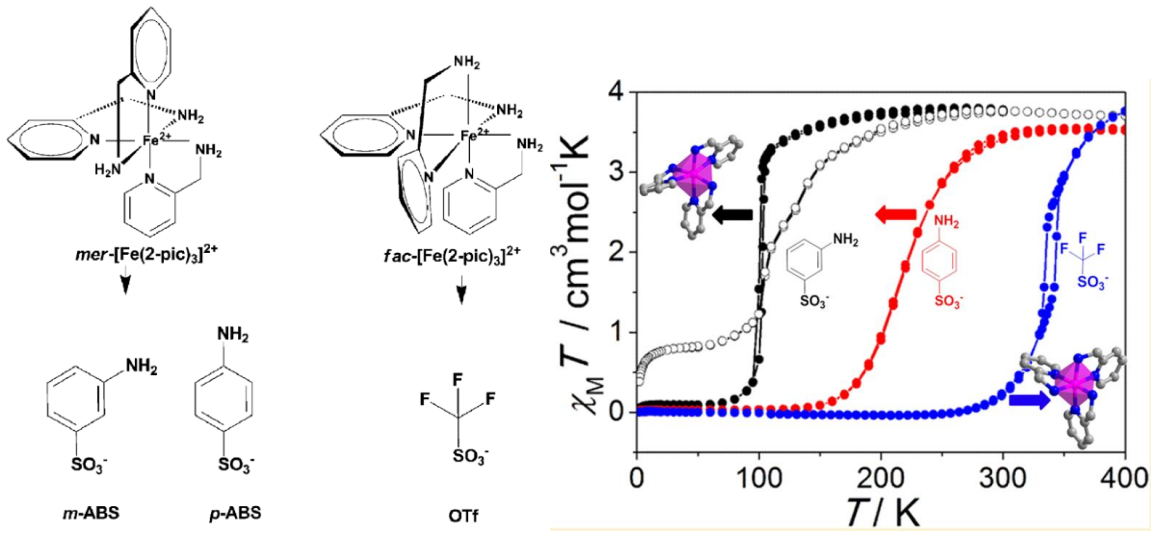

Figure 1-9 A series of anions with $[Fe(2\text{-pic})_3]^{2+}$ structures are shown on the left; Variable temperature magnetic susceptibility curves χ(T) vs T plot for bulk samples of $[Fe(2\text{-pic})_3]^{2+}$ consisting of well-shaped single crystals is shown on the right. Figures adapted from Zhao, X. H. *et al*. [25]

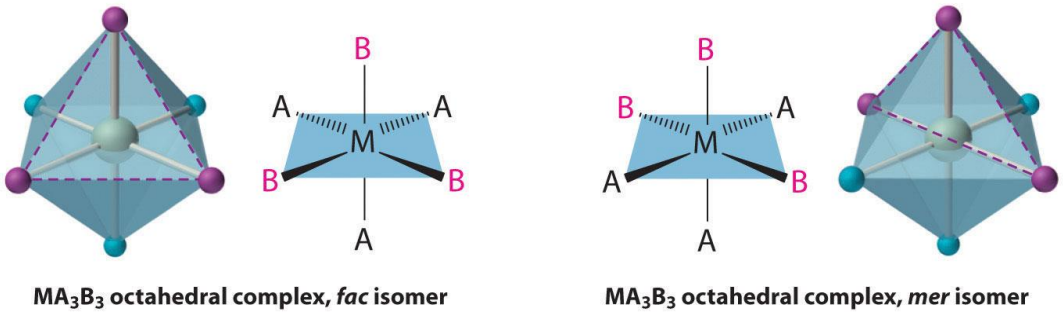

Figure 1-10 Illustration of facial and meridional configurations in octahedral complex. Figures adapted from House, J. E. *et al*. [11]

1.2.4.2 Hydrogen Bonding Effect

Non-covalent contacts, especially hydrogen bonding, have played an interesting role in producing cooperative spin transition.[1] Previous studies investigated the relationship between the strength of hydrogen bonding and spin crossover complex behaviour.[13, 26] A series of [Fe(L)(NCX)]·Solv complexes were produced, where X = S, Solv = tetrahydrofuran (THD) (**1a**); X = S , Solv = methanol (MeOH) and 0.5 pyrazine (PYZ) (**1b**); X = S, Solv =butanone (MEK) (**1c**); X = S, Solv = N'N-dimethylforamide (DMF) (**1d**); X = Se, Solv = N,N'-dimethylformamide (1**d**'); X = S, Solv = dimethyl sulfoxide (DMSO) (**1e**); X = S, Solv = 0.5 MeOH and 0.5 MEK) (**1f**). A scheme of the H_2L ligand is represented in Figure 1-11.

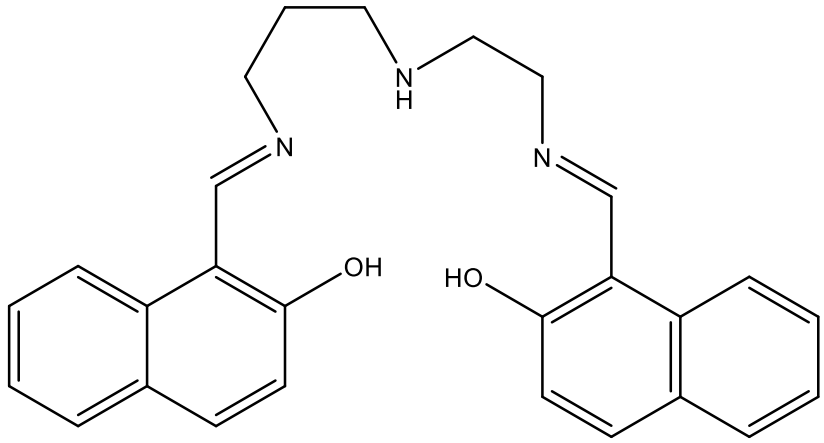

Figure 1-11 Schematic representation of the H_2L ligand

All the complexes were crystallographically characterised. The complexes form similar three-dimensional frameworks through C-H···O and π-based interactions. The essential packing of the framework comprises a centrosymmetric dimer of two adjacent [Fe(**L**)(NCX)] molecules *via* a C-H···π non-covalent interaction between the CH group of the naphthalene ring and the phenolic oxygen atom. An offset π···π stacking provides further stabilization between two dimers. In the same layers, adjacent molecules are connected by weak C-H···π and C-H···S non-covalent contacts. **1a** is selected as an example to demonstrate this intermolecular interaction in Figure 1-12. A detailed view of the hydrogen bonding of the all the complexes is shown in Figure 1-13 and bond length information is shown in Table1-1.

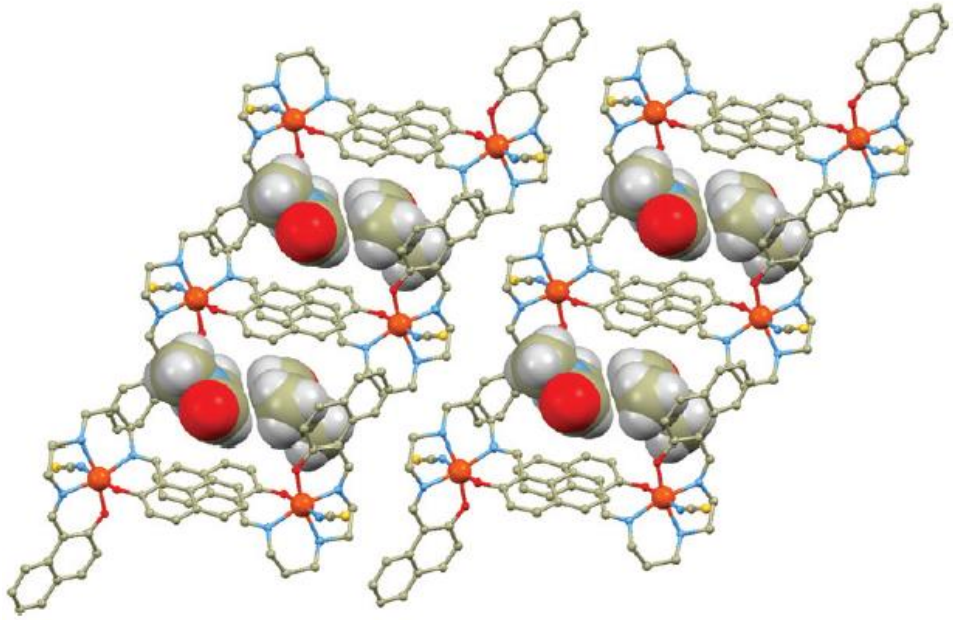

(a)

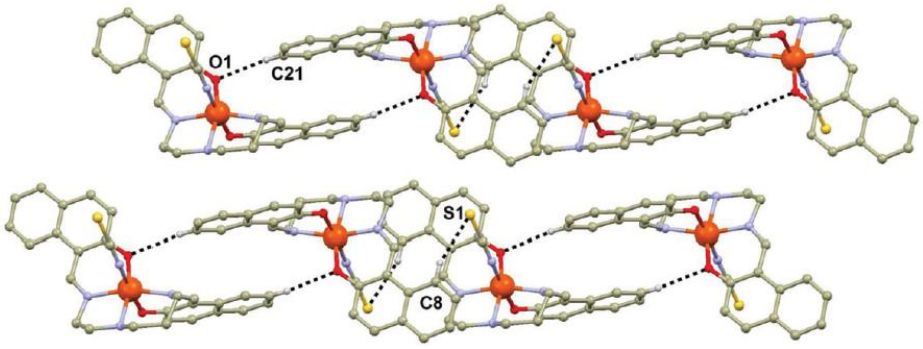

(b)

Figure 1-12 (a) Perspective view of fragments of the crystal structure of complex **1a**, with the guest molecules highlighted in space-fill representation; (b) parts of the crystal structures of complex **1a**, showing non-covalent contacts (black dashed lines). Selected hydrogens were omitted for clarify, apart from those involved in the non-covalent contacts.[13]

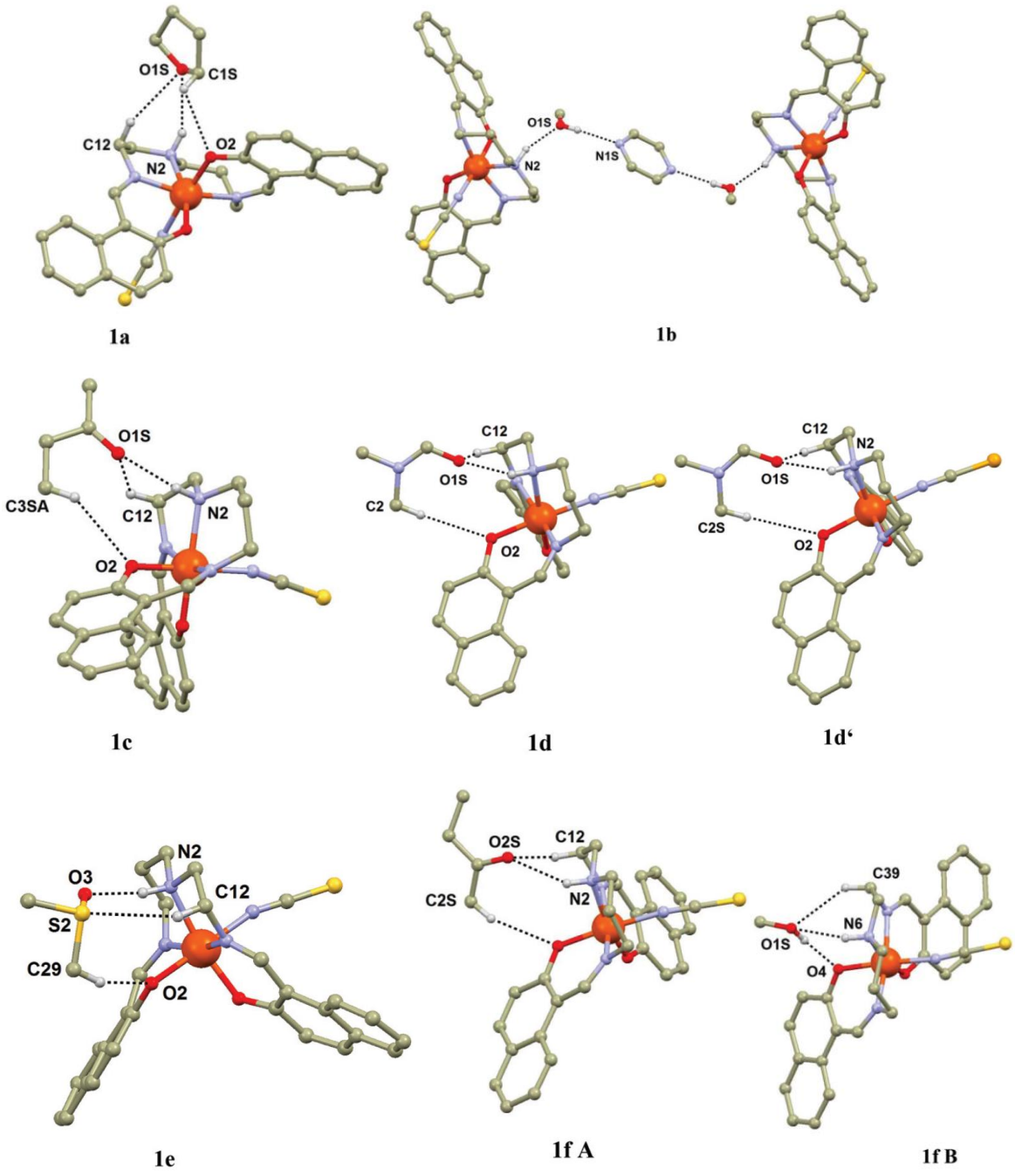

Figure 1-13 Perspective view of hydrogen bonding of the Solv molecule with [Fe(L)(NCX)] in **1a**-**1f**. Most hydrogen atoms are omitted for clarity, except for those involved in hydrogen bonding and non-covalent contacts (black dashed lines).[13]

Table 1-1 Bond lengths (in Å) in the vicinity of the iron atom and selected structural parameters for **1a-1f**. The average values calculated from two bond lengths: N_{am} represents amine nitrogen atoms, N_{NCX} represents nitrogen atoms from the NCX group and N_{im} represents imino nitrogen atoms. The N···O (donor-acceptor) hydrogen bond distances in **1a**-**1f** and critical temperature of the SCO transition ($T_{1/2}$). All data were collected at 100 K except for 1d and **1d'**.[13]

	Fe-N_{am} (Å)	Fe-N_{NCX} ((Å))	Fe-N_{im} (Å)	Fe-O (Å)	D(N···O)/ Å	$T_{1/2}$/K
1a	2.2137(14)	2.0849(15)	2.082	1.939	3.295(2)	HS
1b	2.209(2)	2.085(2)	2.080	1.945	3.110(3)	HS
1c	2.1937(14)	2.0908(16)	2.069	1.942	2.988(8)	84
1d 298 K	2.008(3)	2.086(3)	2.068	1.941	2.941(2)	232↓ 235↑
1d 150 K	2.0087 (16)	1.9447(17)	1.925	1.884	2.944(4)	
1d' 308 K	2.173 (3)	2.096(4)	2.064	1.935	2.935(5)	244
1d' 150 K	2.003 (4)	1.942(4)	1.927	1.884	2.921(6)	
1e	2.185 (2)	2.077(2)	2.077	1.940	3.004(3)	127↓ 138↑
1f Fe1	2.218 (3)	2.094(3)	2.080	1.940	3.272(4)	HS
1f Fe2	2.210 (3)	2.088(2)	2.078	1.944	3.154(4)	

The presence of hydrogen bonds between guest solvent(s) and the complex plays an important role in magnetic behaviour. The donor-acceptor (D-A) distances of N-H-O hydrogen bonds are summarised in Table1-1. These results found that SCO only occurred in compounds with an N···O distance shorter than *ca.* 3.0 Å. 1a, 1b, and 1f with longer N···O distances remain HS over the investigated temperature range. Comparison of 1c and 1f (MEK) provides a good example to illustrate the relationship between strength of hydrogen bonding and magnetic properties, as both of them have MEK guest molecules. Compound 1f is pure HS with d(N···O) = 3.154(4) Å, while 1c showed an abrupt SCO with a significantly shorter d(N···O) = 2.988(8) Å. The associated magnetic properties are shown in Figure 1-14.

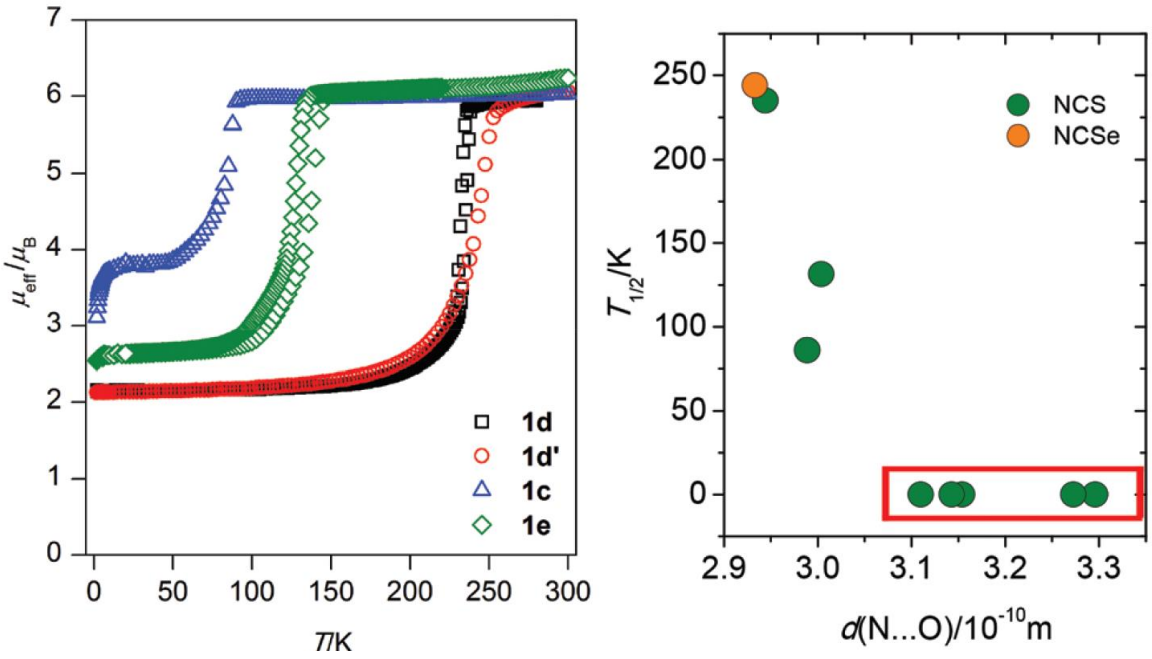

Figure 1-14 Temperature dependence of effective magnetic moment for compounds **1c, 1d, 1d'** and **1e** (left). Plot of possible $T_{1/2}$ vs d(N···O).[13]

1.2.4.3 π···π Interactions Effects

π-π stacking interactions within crystal structures have become a common feature of SCO compounds, since SCO complexes often contain aromatic or N-heterocyclic moieties.[27] A study by Real *et al*[28] containing three related π-stacking complexes of $[Fe(NCS)_2L_2]$ showed that SCO cooperativity increased along this order in the series:

L = btz (gradual) < L = phen (abrupt, no hysteresis) < L = dppz (abrupt, 40 K hysteresis loop)

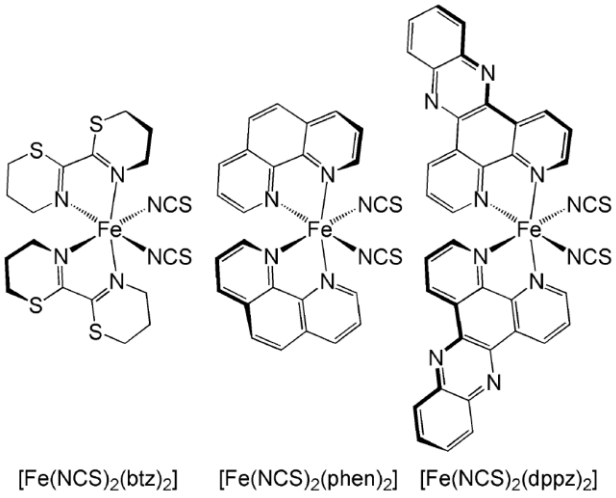

Figure 1-15 Molecular structures of the $[Fe(NCS)_2L_2]$ complexes

All the ligands exhibit similar face-to-face overlap π- π stacking with neighbouring molecules in the crystal structure. It is remarkable that the strength of inter-ligand π- π interactions are associated

with cooperativity in their SCO complexes. However, it is not clear how the π-stacking controls the cooperativity of the systems. Further studies are clearly needed to investigate this phenomenon.

1.2.5 Applications of SCO active materials

Ever since the development of telecommunication and the internet, the necessity for size reduction of components used in component devices has considerably increased. The molecular scale is increasingly being considered as an approach to achieve the miniaturization of components. Silicon-based components as a conventional technology in electronic devices have been manipulated to smaller and smaller scales. However, as the nanometer approaches, the fabrication and manipulation of miniaturised devices faces significant challenges. Nowadays, molecular-based derivatives are being considered due to their prospects in sensitivity and selectivity levels. As spin crossover (SCO) active materials have a spin transition between high spin (HS) and low spin (LS) electronic configurations under external perturbations, there is potential to apply these compounds in uses such as molecular switches, data storage, display devices and non-linear optics.

1.2.6 Fe(III) vs Fe(II)

The spin transition of Fe(II) between LS and HS states changes from diamagnetic (0 unpaired electrons) to paramagnetic (4 unpaired electrons) and has the largest change in magnetic susceptibility, giving an easily detectable result in magnetic studies. Unfortunately, Fe(II) is often air sensitive and oxidised during the synthesis process once complexes have been formed. It requires careful consideration of the working procedure and storage environment to prevent oxidation. Fe(III) complexes are more stable than Fe(II) and therefore have less constraints on the working environment, however, the LS state still retains some magnetic behaviour (1 unpaired electron). Despite the same difference of unpaired electrons (4) between LS and HS for both Fe(II) and Fe(III), the non-magnetic state of LS Fe(II) results in an easier to detect change in working devices. Therefore, Fe(II) is chosen as the main SCO system used in this research project.

1.3 Introduction to 1,8-Naphthalimide based Derivatives

The properties of 1,8-naphthalimide derivatives have been put to use in many fields of chemistry and materials science as potential fluorescent sensors[29-32], DNA binders[33] and probes[34-35], anti-cancer treatment[36], electrochromic switches[37], energy storage devices[38-39] and cellular imaging agents[3, 40]. Furthermore, 1,8-naphthalimide units have been utilised as secondary building units (SBUs) through strong $\pi\cdots\pi$ stacking for metal-organic networks. There are three main types of $\pi\cdots\pi$ stacking interactions in naphthalimide systems[22, 27, 41-45] (Figure 1-16). Many interesting packing arrangements can be formed by their strong aromatic interactions dictating different conformations in the solid structure.

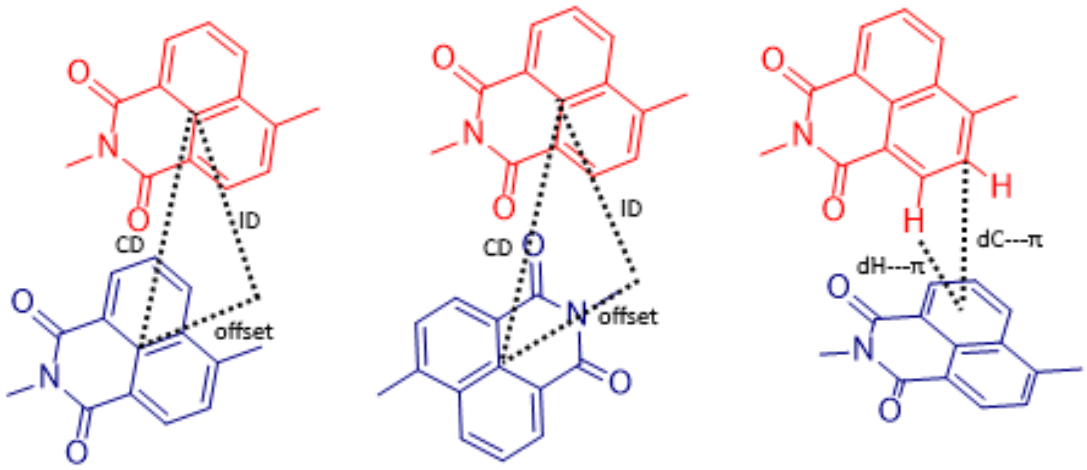

(a) (b) (c)

Figure 1-16 Different interaction types between naphthalimide moieties. (a) parallel translated head to head (π-stacking). (b) parallel translated head to tail (π-stacking). (c) edge-to-face (herringbone) dimers. Geometric parameters are shown: CD = distance between the naphthalimide core centre, ID = interplanar distance, and offset. Figure adapted from F. Grepioni *et al.*[41]

A variety of functional binding sites (such as triazoles, dopamine, pyridine and other coordinating groups) can be tethered to the 1,8-naphthalimide unit following highly modular synthetic methods (Figure 1-16). These supramolecular synthons can be developed and evaluated for their ability to extend the structure through $\pi\cdots\pi$ based and other non-covalent interactions. Another attraction of 1,8-naphthalimide ligands is that their electronic properties can be readily manipulated through substituents in the 4-position (Figure 1-17). These interactions can be influenced through small and iterative modification, particularly electron donating and withdrawing modifications. In addition, 1,8-naphthalimide ligands also have further potential in

the development of more complicated linked naphthalimide systems (e.g. Trögers' base linked systems)[46-51] (Figure 1-18). Therefore, there is a wide range of applications and properties that make naphthalimide based ligands ideal for the generation of multifunctional architectures.

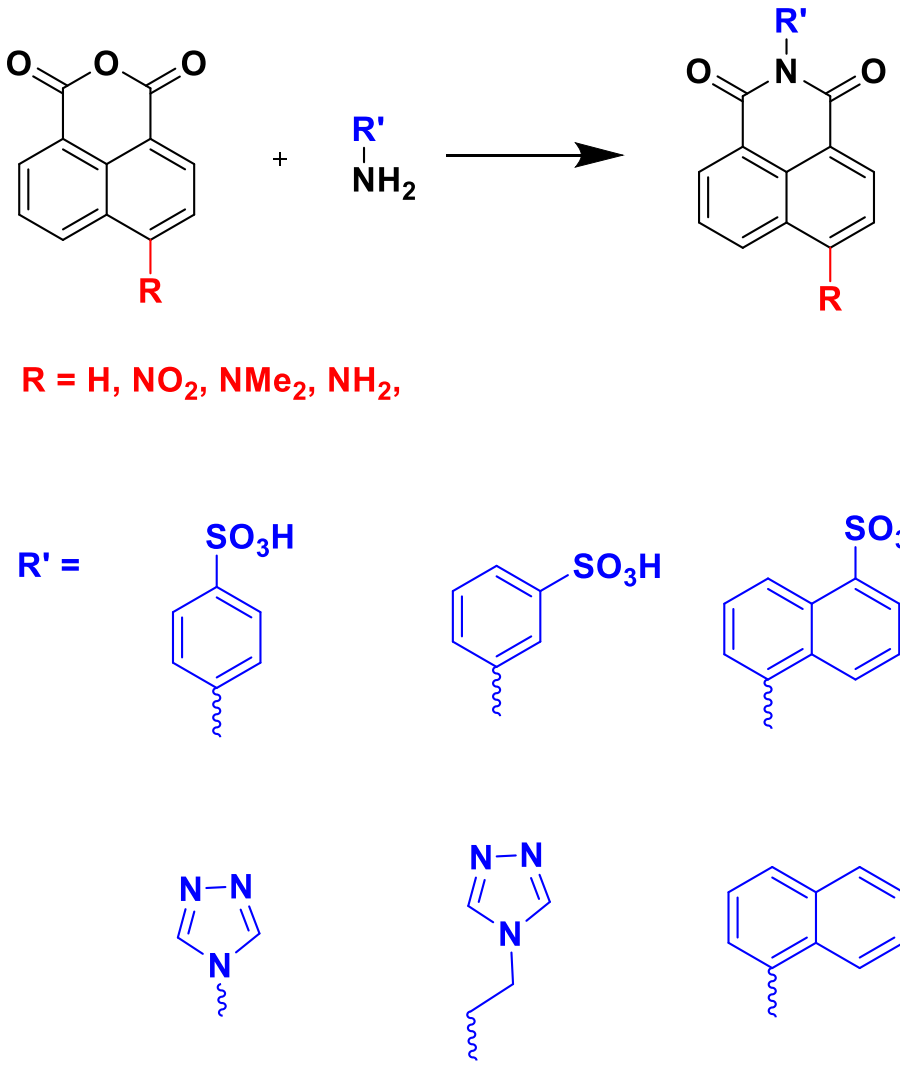

Figure 1-17 Selected 1,8-naphthalimide compounds structures used in this thesis

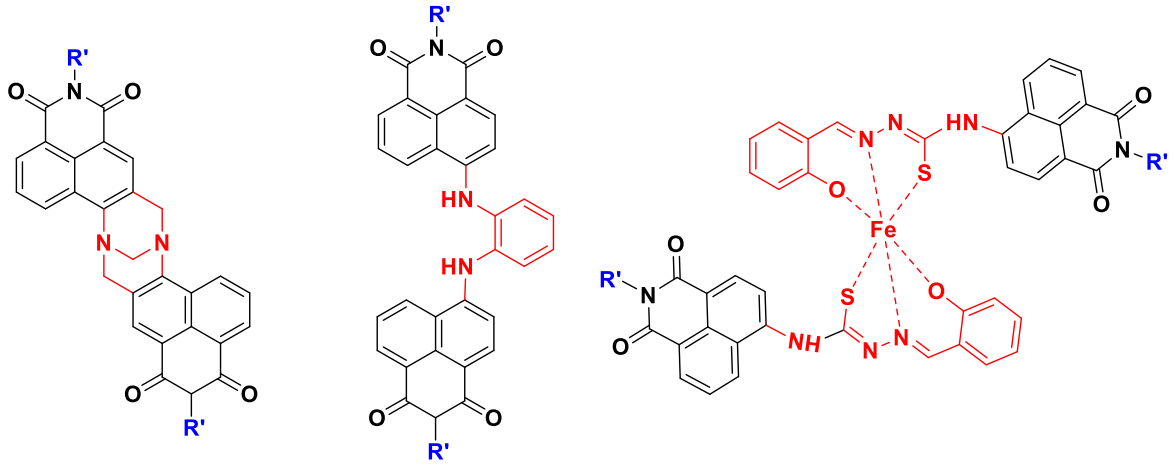

Figure 1-18 Bridged/linked naphthalimide systems

As the interest in complexes containing *N*-substituted-1,8-naphthalimides has covered many areas, the number of structures of metal complexes with *N*-substituted-1,8-naphthalimide ligands in the Cambridge Structural Database (CSD) is of the order of 300, and still growing. In this field, the Reger[2, 26, 31, 52] group has played a main role in investigating metal naphthalimides complexes, and studying the structural aspects of these resulting complexes. Some classic complexes containing s, p, d, f group metals are introduced in the following section respectively. These examples highlight the structure directing ability of the naphthalimide moiety.

1.3.1 S-Block 1,8-Naphthalimide Containing Complexes

To date, only a limited amount of work has investigated naphthalimide containing S-block complexes.[37, 39, 53-54] In 2012, the first potassium complexes were produced from enantiopure amino acid based 1,8-naphthalimide ligands.[54] The resulting "MOF-type" compounds were structurally characterised, with strong $\pi\cdots\pi$ stacking interactions arising from the naphthalimide architectures.

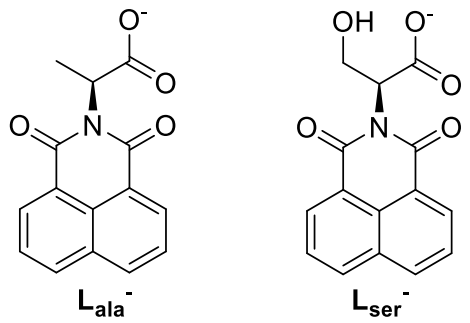

Figure 1-19 Structure of the first ligands used to prepare s-group 1,8-naphthalimide complexes

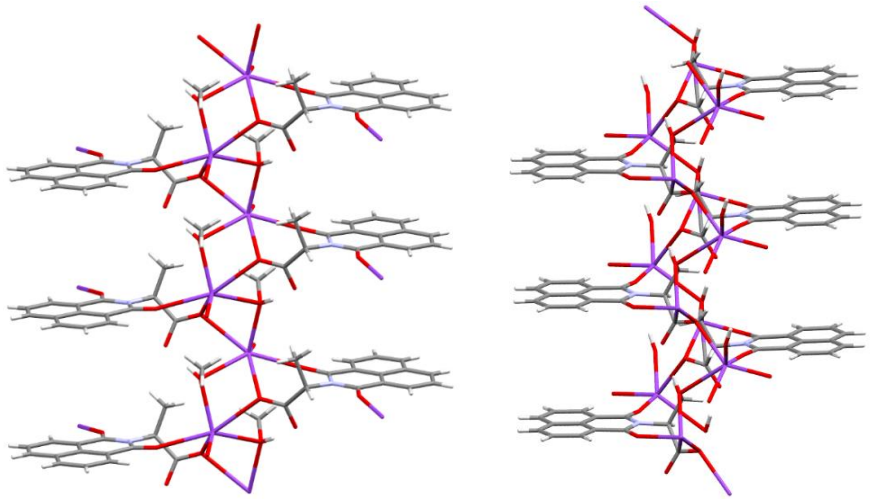

(a) (b)

Figure 1-20 (a) The chain of K(L_{ala}) complex through K-O-K-O atoms; (b) packing interaction along the *a* axis of K(L_{ser}).

Two complexes K(L_{ala}) and K(L_{ser}) are shown in Figure 19. In the K(L_{ala}) complex, the molecules form a chain through K-O-K-O atoms (Figure1-20 (a)). For each chain, four neighbouring helical rods are linked by the naphthalimide carbonyls generating coordination "squares". In these interactions, the perpendicular distance between the planes of the naphthalimide rings is 3.45 Å, which is consistent with a typical π-stacking interaction (Figure1-21 (a)). A similar chain is found in K(L_{ser}) which is also formed by K-O-K-O atoms (Figure 1-20(b)). A remarkable three-dimensional supramolecular structure is generated by $\pi\cdots\pi$ stacking interactions forming a "zipperlike" structure along the a axis (Figure1- 21(b)) and extended sheets along the c axis (Figure 1-21 (c)) with the average distance between the parallel naphthalimide rings being 3.30 Å.

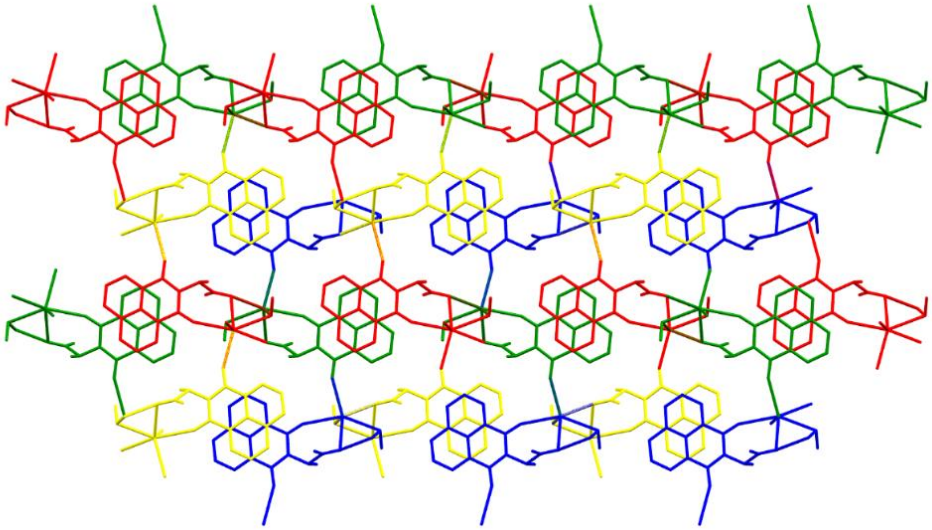

(a)

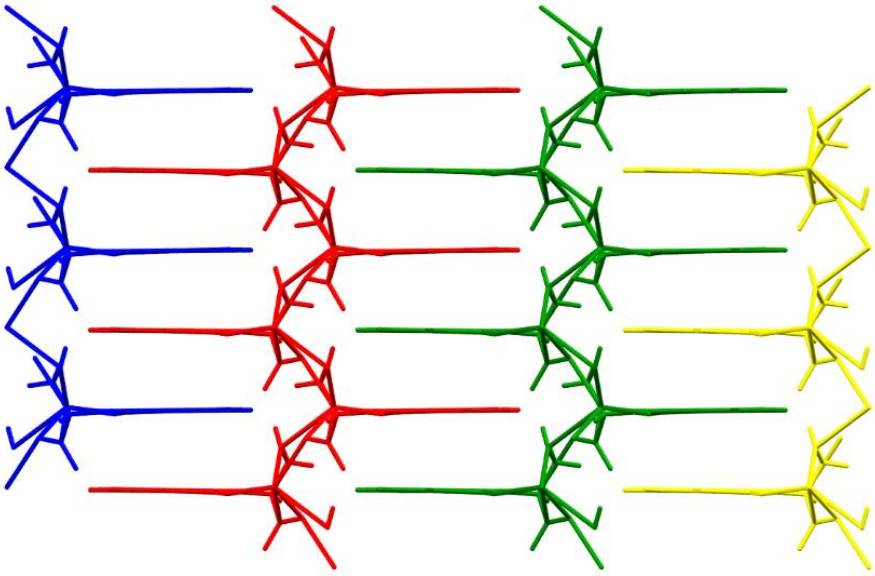

(b)

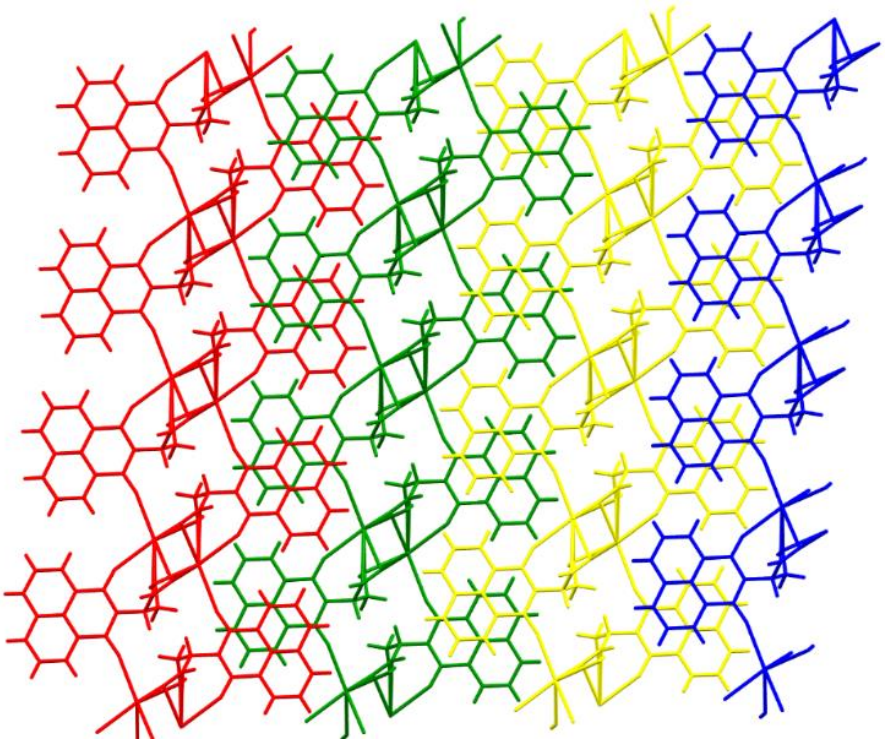

(C)

Figure 1-21 (a) Packing interactions along the *a* axis of K(L_{ala}); (b) packing interactions along the *a* axis of K(L_{ser}); (c) Packing interactions along the *c* axis of K(L_{ser}).

1.3.2 P-Block 1,8-Naphthalimide Containing Complexes

The first P-block complexes were designed using sulfur-based 1,8-naphthalimide ligands and arsenic(III) by 2005.[55] In the last decade, carboxylic acid based napththalimide ligands have been the primary choice for developing P-block complexes. Among these, two typical ligands are chosen to introduce the interaction with the naphthalimide π-system (Figure1-22).[56]

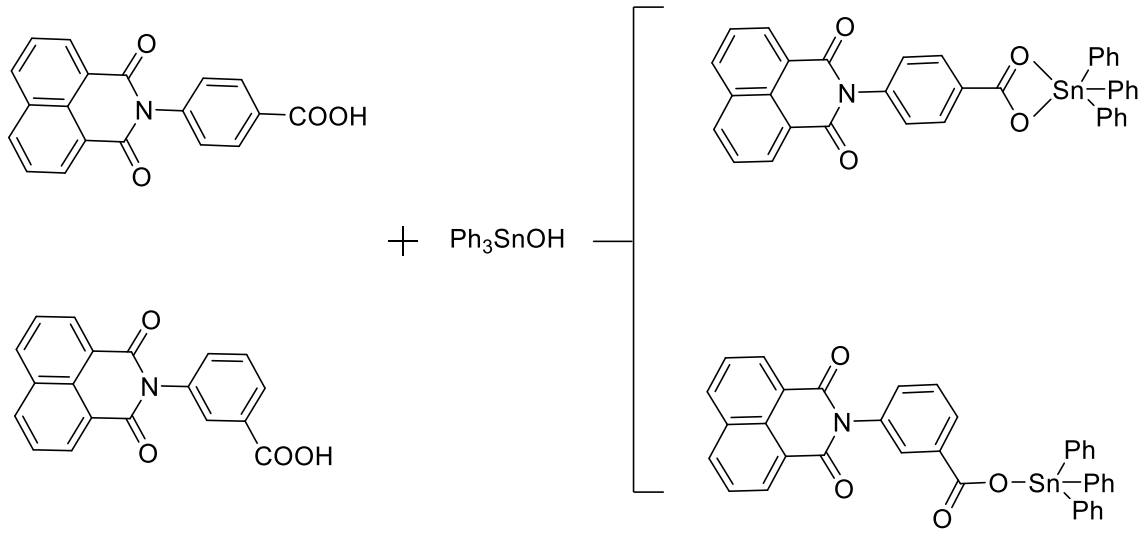

Figure 1-22 Synthesis of complexes **1** and **2**

The complexes were synthesised from a mixture of ligand and triphenyltin hydroxide in refluxing toluene. The colourless crystals were obtained from slow evaporation of the solvent. In Figure 1-23, $\pi\cdots\pi$ offset stacking interactions exist in neighbouring naphthalimide rings with distances of 3.53 Å. Additionally, adjacent molecules form a chain through a non-classical C-H hydrogen bond from the naphthalimide oxygen, with geometry C-H···O=2.409 Å, bond angle ∠(C-H···O=175.76°. Similar offset $\pi\cdots\pi$ effects dominate the packing interactions between the neighbouring naphthalimide rings with a distance of 3.727 Å. Adjacent molecules are also linked by a non-classical hydrogen bond to a naphthalimide oxygen (C-H···O=2.498 Å, bond angle ∠(C-H···O=128.70°) forming a 1D chain.

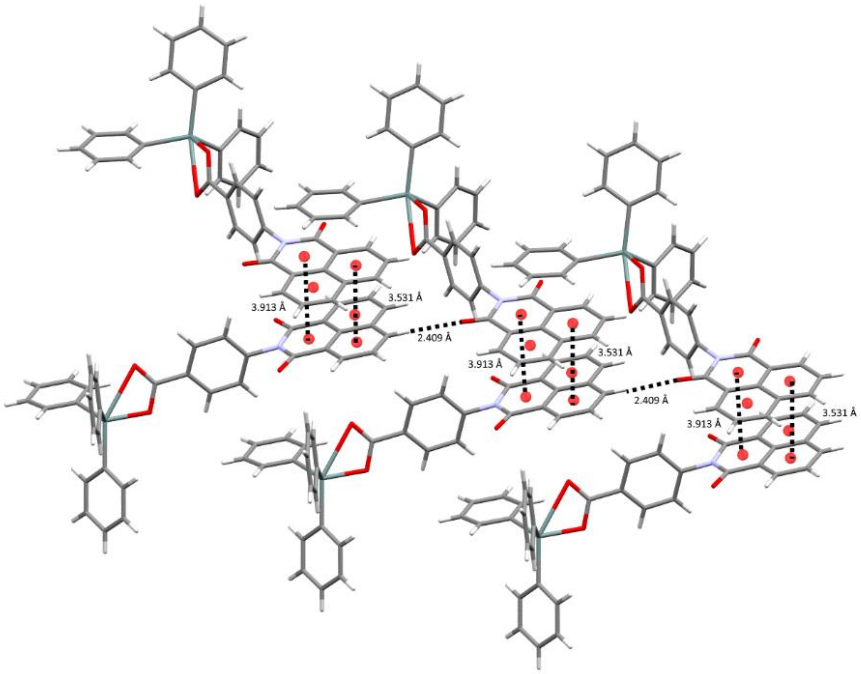

(a)

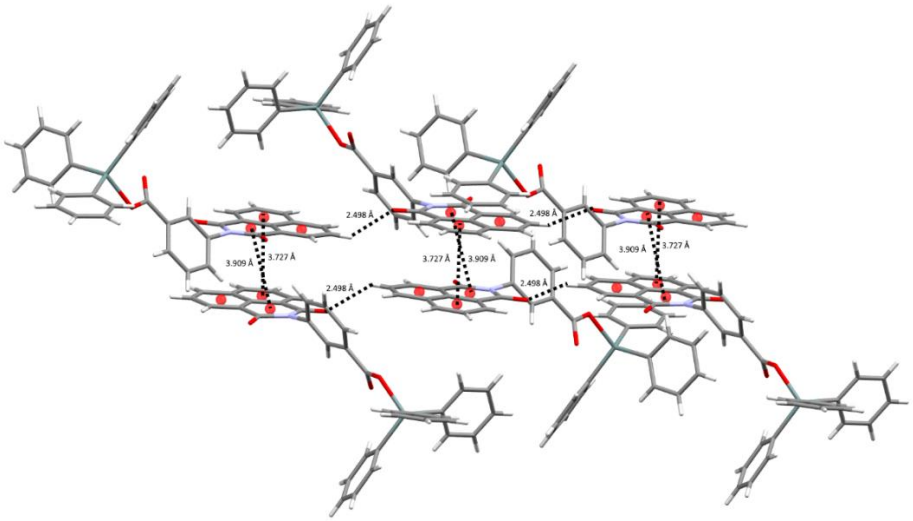

(b)

Figure 1-23 1D chain structure of complexes **1** (a) and **2** (b).

1.3.3 D-Block 1,8-Naphthalimide Containing Complexes

At the time of writing 203 metal complexes containing d-group metals have been structurally characterised, typically with first row d-group metals. Over the last decade Reger and co-workers have prepared a series of Cu(II) complexes using a carboxylate containing 1,8-naphthalimide ligands. These representative ligands were part of a series where the length of the link between the carboxylate donor group and the 1,8-naphthalimide ring was altered. *N*-(2-Ethanoic acid)-1,8-naphthalimide (**HL_{C1}**), *N*-(3-Prpanioic acid)-1,8-naphthalimide (**HL_{C2}**), and *N*-(4-Butanoic acid)-1,8-naphthalimide (**HL_{C3}**) were synthesized by reacting the amino acids with 1,8-naphthalic anhydride in DMF (Figure 1-24).[52] **HL_{C3}**, **HL_{C3}**, and **HL_{C3}** all produced crystals with $Cu_2(O_2CCH_3)_4(H_2O)_2$ through the layering method. Firstly, each DCM solution containing drops of pyridine of **HL_{C3}**, **HL_{C3}**, and **HL_{C3}** were layered on pure methanol, then the methanol solution of $Cu_2(O_2CCH_3)_4(H_2O)_2$ was added as third layer. After a few days, single crystals of $[Cu_2(\mathbf{L_{c1}})_4(py)_4].2(CH_2Cl_2)$ (**1**)[26], $[Cu_2(\mathbf{L_{c2}})_4(py)_2].2(CH_2Cl_2)$ (**2**)[26], and $[Cu_2(\mathbf{L_{c3}})_4(py)_2].2(CH_2Cl_2)$ (**3**)[2] were obtained.

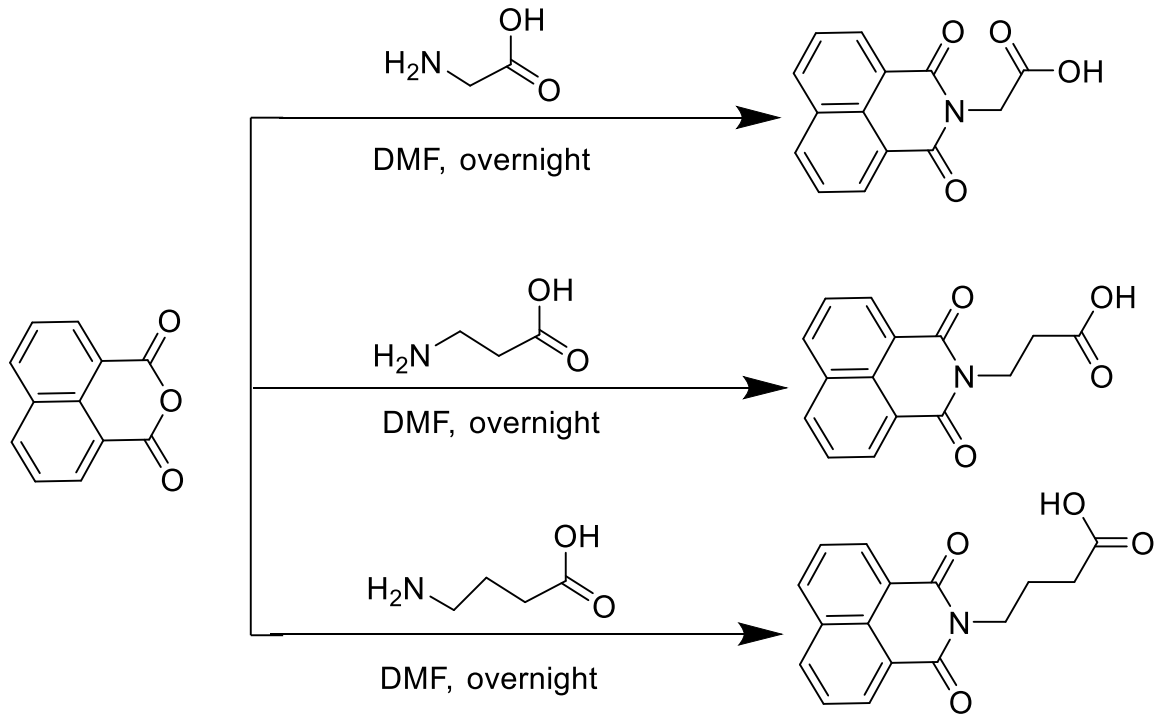

Figure 1-24 Synthesis of **HL_{C1}**, **HL_{C2}**, and **HL_{C3}**

From their molecular structures, Reger found that the modification of the length of the chain between carboxylic group and naphthalimide ring influenced the structure of their complexes. In $[Cu_2(\mathbf{L_{c1}})_4(py)_4].2(CH_2Cl_2)$, a centrosymmetric copper dimer formed through linking between two equivalent copper(II) irons and two ligands (Figure 25 *a*). However, in $[Cu_2(\mathbf{L_{c2}})_4(py)_2].2(CH_2Cl_2)$ (**2**) and $[Cu_2(\mathbf{L_{c3}})_4(py)_2].2(CH_2Cl_2)$ **(3)**, a similar "paddlewheel" motif was observed, where four carboxylic groups from four separate ligands bridge the two copper(II) atoms (Figure 25 *b&c*). Compared to $[Cu_2(\mathbf{L_{c2}})_4(py)_2].2(CH_2Cl_2)$ (**2**), the extra CH_2 within the alkyl chain in

$[Cu_2(\mathbf{L_{c3}})_4(py)_2].2(CH_2Cl_2)$ **(3)** provided enough space for two naphthalimide groups to arrange themselves on top of each other.

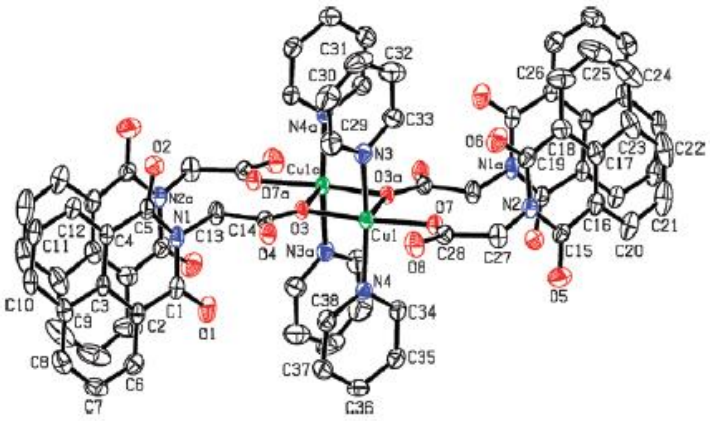

(a)

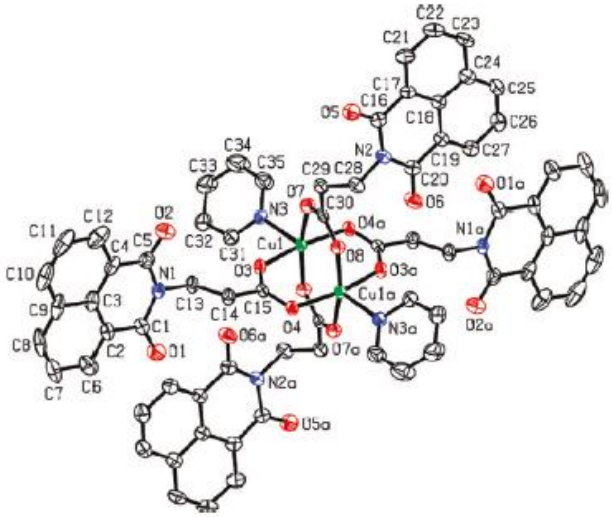

(b)

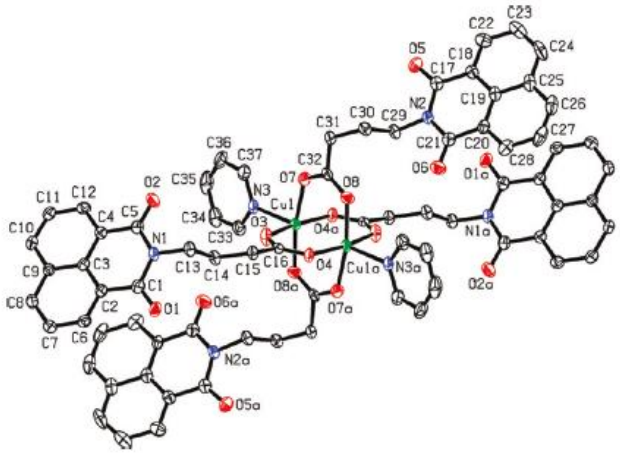

(c)

Figure 1-25 Molecular structure of (a) $[Cu_2(L_{c1})_4(py)_4].2(CH_2Cl_2)$ (1); (b) $[Cu_2(L_{c2})_4(py)_2].2(CH_2Cl_2)$ (2); (c)and $[Cu_2(L_{c3})_4(py)_2].2(CH_2Cl_2)$ (3)

The packing interactions are dominated by $\pi\cdots\pi$ stacking between neighbouring naphthalimide moieties (Figure 26). In the chain structure of **(1)** and **(3)**, each naphthalimide participated in $\pi\cdots\pi$

stacking, forming a long chain through linking with neighbouring naphthalimide moieties. However, in the chain structure of **(2)**, only two of the naphthalimide moieties exhibited $\pi\cdots\pi$ stacking between the adjacent molecules. This is caused by the intramolecular $\pi\cdots\pi$ stacking of the arms to orient the naphthalimide rings in **(1)** and **(3)**. In addition to this, **(3)** provides more flexibility and so can accommodate a neighbouring naphthalimide ring being inserted into the middle of two naphthalimide rings by $\pi\cdots\pi$ stacking.

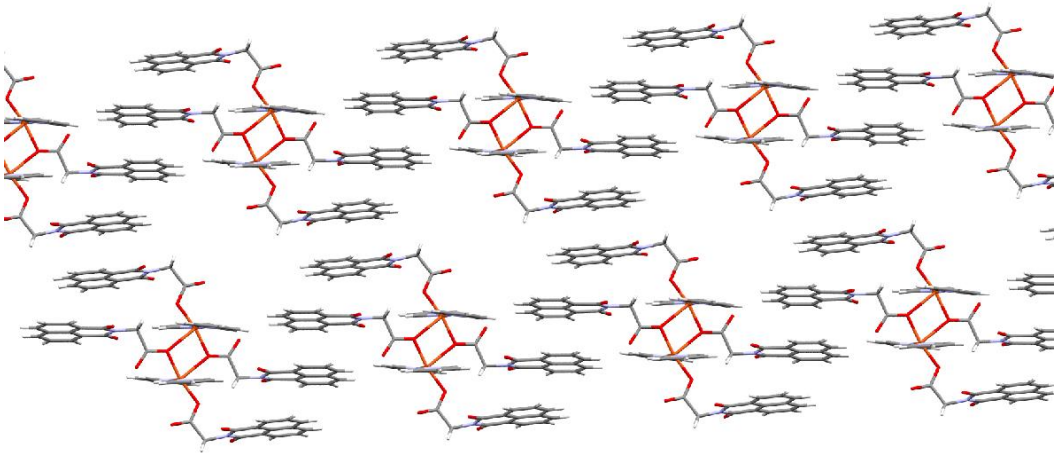

(a)

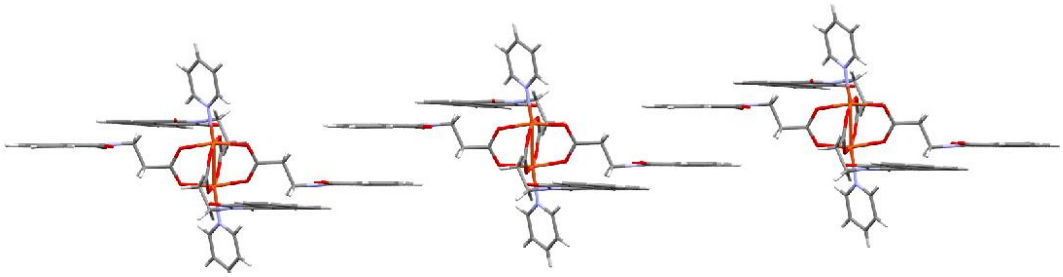

(b)

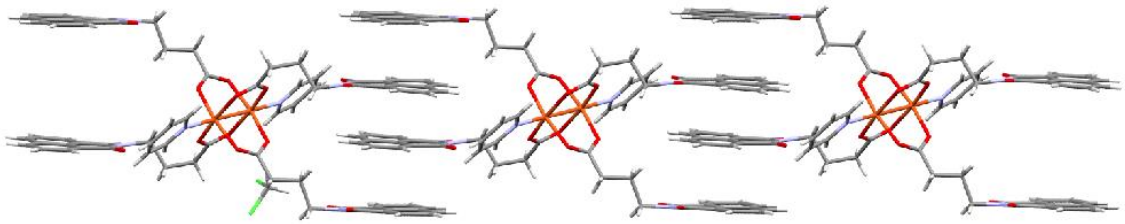

Figure 1-26 Packing interaction along the chains in (a) $[Cu_2(\mathbf{L_{c1}})_4(py)_4].2(CH_2Cl_2)$ (**1**); (b) $[Cu_2(\mathbf{L_{c2}})_4(py)_2].2(CH_2Cl_2)$ (**2**); (c)and $[Cu_2(\mathbf{L_{c3}})_4(py)_2].2(CH_2Cl_2)$ (**3**)

1.3.4 F-Block 1,8-Naphthalimide Containing Complexes

Recently, researchers have begun to consider f-block complexes using naphthalimide based ligands[32, 34, 57]. New structurally characterised lanthanide complexes utilising the photo physical properties of 1,8-naphthalimide were obtained in 2015 by Yan *et al*[57], where they achieved white-light emission. The simple synthesis (Figure 26) relied upon diffusing a methanolic solution of **HL** and triethylamine into an aqueous solution of $LnCl_3 \cdot 6H_2O$ with the ratio 3:1, colourless crystals of complex **1** and **2** were obtained after two weeks.

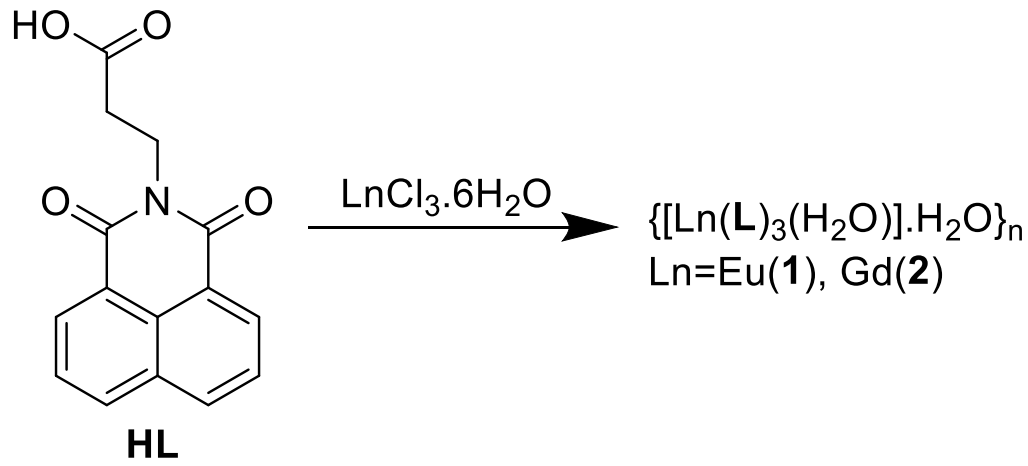

Figure 1-27 Synthesis of complexes **1** and **2**

A 1D chain using the carboxylic acid as a bridging ligand between two metal centres, Eu-O-Eu-O, was formed. This unit is also connected to the six neighbouring naphthalimide moieties via head-to-tail $\pi\cdots\pi$ stacking interactions with a distance of 3.632 Å, leading to a three-dimensional framework Figure 1-28. As shown in Figure 1-29, the complexes exhibited blue-green emission based on the ligand with bands in the range of 375-600 nm. Compared to **2,** the emission intensity of complex **1** decreased in the range of 400-550 nm, where the maximum emission band showed a blue-shift from approximately 470 to 450 nm. In addition, complex **1** also exhibited narrow emissions at 590, 620 and 690 nm, resulting in the appearance of white light to the eye as the intensity was far greater than the ligand under UV irradiation.

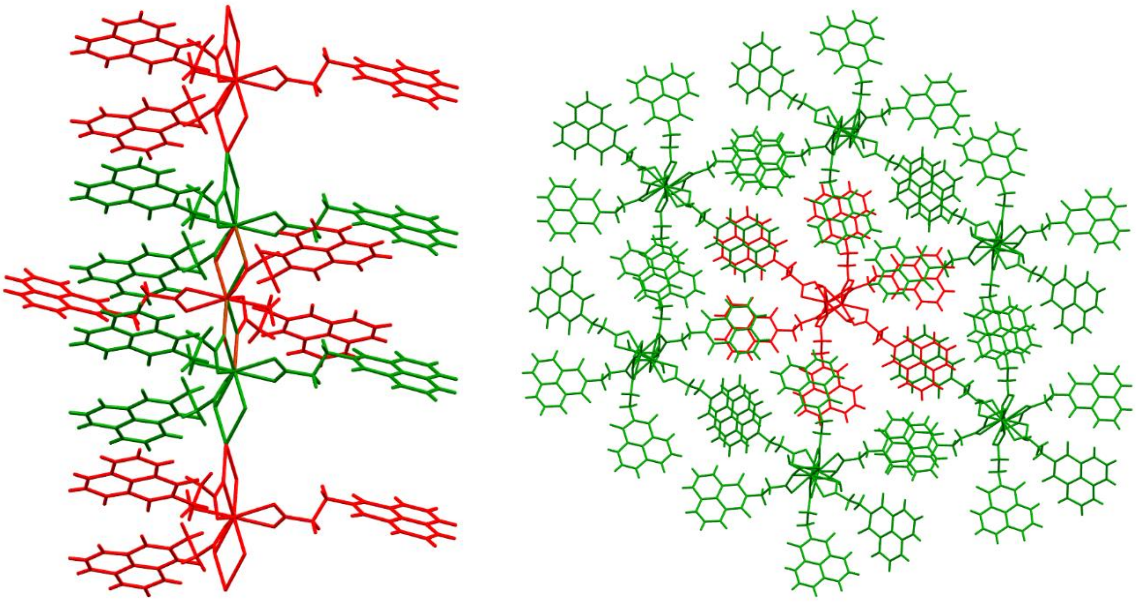

(a) (b)

Figure 1-28 (a) 1D chain of complex **1** through Eu-O-Eu-O atoms; (b) 3D structure of complex **1** along the [1 0 0] direction.

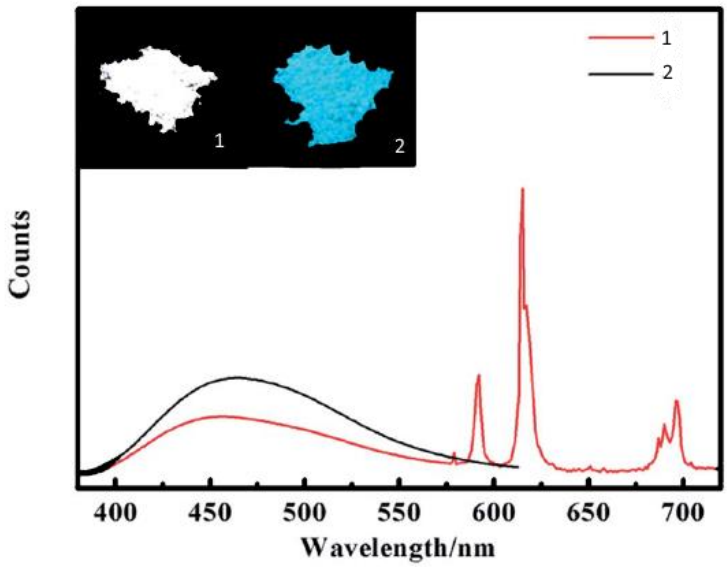

Figure 1-29 Emission spectra of complexes **1** and **2** in solid state

1.4 High Resolution Crystallography Studies

As discussed in previous sections, spin crossover (SCO) studies revealed that non-covalent interactions play an important role in enhancing cooperativity of solid-state SCO materials, including hydrogen bonds, halogen bonds, and π interactions. In particular, the relationship between π interactions (such as π-π stacking, C-H···π, N-H···π, C=O···π, anion-π, and cation-π) and spin crossover phenomenon is yet to be fully understood.

Standard X-ray diffraction methods (0.8 Å resolution) readily provide the atomic coordinates and hence molecular structures, which enables a geometric analysis associated with molecular bond lengths, angles, and conformation. However, further information concerning non-covalent bonds and associated energies cannot be obtained from standard resolution X-ray diffraction experiments.[58-62] Considerably higher resolution X-ray diffraction data, to at least 0.5 Å, needs to be collected to investigate intermolecular interactions in more detail. Such measurements enable more precise nuclear positions to be determined as the scattering power of valence electrons decreases rapidly from low resolution to high resolution. Accurate atomic nuclear positions from high resolution experiments are combined with valence electron information derived from multipole refinement to give the charge distribution between molecules and thus greater insight into the differences between related systems.[63-69] Moreover, a topological analysis of the electron density distribution can aid in the identification and classification of hydrogen bonds and π interactions.

A series of electron donating and electron withdrawing naphthalimide derivatives were combined with 1,2,4-triazole ligands known to induce SCO in Fe(II) to generate new ligands with SCO potential. Their π-deficient character has been exploited giving systems where the extension of structure arises through π-based contacts and weak non-covalent interactions. High resolution crystallography can be used to explore π deficiency in this system and how these non-covalent interactions potentially affect the relevant SCO behaviour.

1.4.1 Non-Covalent Interactions

Non-covalent interactions (NCI) are very important in both supramolecular chemistry and crystal engineering to aid and direct the assembly and packing of molecules and also to stabilise the molecular construct.[70-71] Therefore, they can influence and control the formation of the solid state in chemical systems. Compared to the energy of covalent bonds (400 kJ mol^{-1}), NCIs are generally much weaker, with energies in the range 1-15 kJ mol^{-1}.[72] Typical types of NCIs include electrostatic interactions, hydrogen and halogen bonds, van der Waals forces and π···π interactions.[73-76] Of these, π···π interactions and weak hydrogen bonds will particularly be investigated in section 5.5.

1.4.1.1 π···π interactions

π···π interactions can be found in systems containing aromatic rings. Aromatic rings contain conjugated π-systems, such as benzene rings, which exhibit a positively charged σ-framework and a negatively charged π-cloud above and below the plane of the ring, as shown in Figure 1-30.

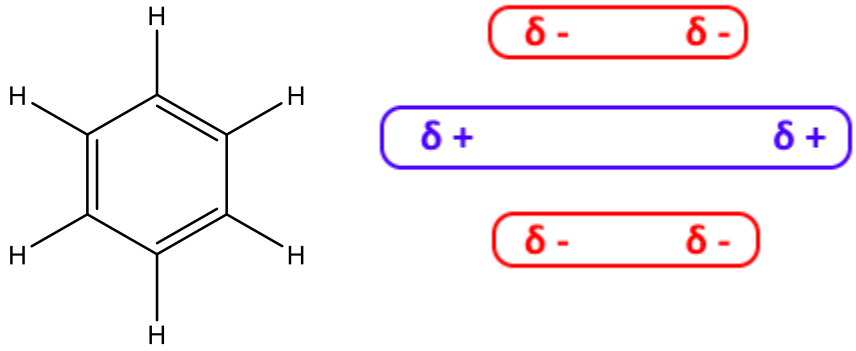

Figure 1-30 Schemes for describing the electrostatistic view of aromatic interactions.

Attractive interactions between aromatic rings can occur with positive cations or partial charge (dipoles) and the electron cloud, or other effects through π-orbitals.In Figure 1-31, there are three main ways of π···π stacking in aromatic rings: T-shape edge-to-face, parallel stacks, and parallel displaced (slipped) stacks.[77-81]

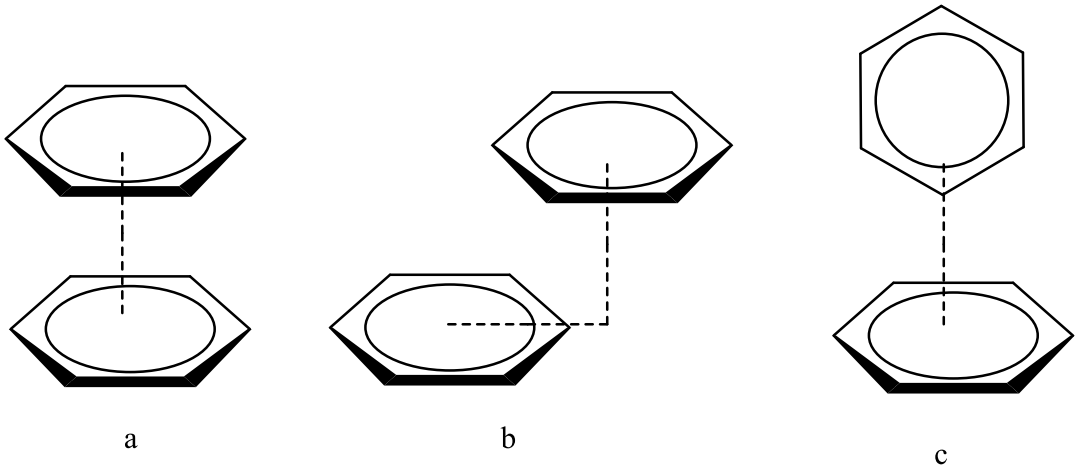

Figure 1-31 Three main stacking arrangements of benzene ring, a: parallel face to face stacked; b: slipped face-to-face stacked; c: edge-to-face.

In 1990, Hunter and Saunders[82] proposed a simple physical model to illustrate the favourable π···π interactions, as shown in Figure 1-32. They noted that direct face-to-face contact is the least favoured due to the electrostatic repulsion between overlapping π-electrons clouds. Slipped and

edge-to-face configurations minimise the π-electrons repulsion, which allows an interaction between the negative π-cloud of one ring and the positive σ-framework of another.

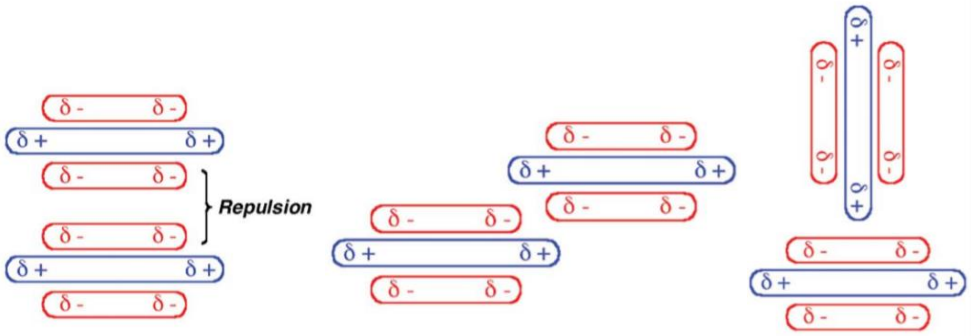

Figure 1-32 Simple electrostatic scheme for three main stacking arrangements of aromatic rings, a: parallel face to face stacked; b: slipped face-to-face stacked; c: edge-to-face.

1.4.1.2 Hydrogen bonds

In 2011 the International Union of Pure and Applied Chemistry (IUPAC) put forward a definition of hydrogen bonds: "an attractive interaction between a hydrogen atom from a molecule or a molecular fragment X-H in which X is more electronegative than H, and an atom or a group of atoms in the same or different molecule, in which there is evidence of bond formation".[83] This definition illustrates that hydrogen bonds are an attractive interaction between a partially positive hydrogen atom and an electronegative atom. Hydrogen bonds generally are depicted as D-H···A, where D denotes a hydrogen bond donor and A denotes a hydrogen bond acceptor. Typical hydrogen bonds acceptors include O, N, S, F, Cl, Br, which contain a sterically accessible concentration of charge leading to relative electronegativity.[83-84] The hydrogen bond donor, D, is more electronegative than the hydrogen atom to which it is bonded, generating a slightly polar D-H bond. Recently, weak organic hydrogen bonds such as C-H···A have become increasingly important in crystal engineering. They share the same principle features as traditional hydrogen bonds however, due to the lesser electronegativity of the C atom C-H bonds, are less polar and result in less rigid and longer hydrogen bonds.[70, 85]

In hydrogen bonds, D···A distances, D-H···A angles, and interaction strength are important parameters for classification. Generally, strong hydrogen bond interaction energies are in the range 60-120 kJ mol^{-1}, with D···A distances of 2.2-2.5 Å and D-H···A angles of 175-180°; moderate hydrogen bond interaction energies are in range 15-60 kJ mol^{-1}, with D···A distances of 2.5-3.2 Å and D-H···A angles of 130-180°; weak hydrogen bond interaction energies are up to 15 kJ mol^{-1}, with D···A distances up to 4 Å and D···A angles of 90-150°. These parameters are guidelines to classify hydrogen bonds, however experimental hydrogen bonds may not adhere to these values exactly.[86]

1.4.2 Single Crystal X-ray diffraction

Crystallography is the study of molecular and crystalline structure and aims to determine the location of atoms with respect to each other and deduce how they interact.[65] Crystals are highly ordered structures and contain a vast number of identical chemical units in a regular periodic arrangement in all three dimensions. A complete structure can be described as a one chemical unit, which is repeated by translation symmetry. These repeated units are defined as lattice points. The translation symmetry is defined by the lattice. Any translation from one lattice point to another can be represented as a vector with certain length and direction. For any two lattice points which can be constructed by putting together multiples of shortest three non-coplanar vectors between pairs of adjacent lattice points. These three basic vector lengths are defined *a*, *b* and *c*, and the three angles α, β, and γ. These three vectors make a parallelepiped defined as the unit cell, which is the regular repeating pattern of a crystal structure. The unit cell is the smallest possible parallelepiped representing the full symmetry of the repeat unit. The unit cells must comply with one of the seven crystal systems – triclinic, monoclinic, orthorhombic, tetragonal, rhombohedral, hexagonal and cubic.

Unit cells with one lattice point are referred to as primitive (P), however, it is convenient to choose a unit cell with more than one lattice point for some crystal structures with specific symmetry. Those which comprise more than one lattice point are called centred. I, F and A/B/C are used to symbolise body centred, all-face centred, and one-face centred lattices, respectively. The different possible combinations of lattice symmetry with primitive and centred cells are referred to as the 14 Bravais lattices. Individual molecules have proper (1-, 2-, 3-, 4-, 6-fold) and improper rotations which combine a rotation and an inversion centre ($\bar{1}$, $\bar{2}$/m, $\bar{3}$, $\bar{4}$, $\bar{6}$-fold) leading to 32 unique point groups in crystal system. Within a crystal structure, these are accompanied by movements in space which are known as glide planes and screw axes. The total of these symmetry operations and 14 Bravais lattices leads to a total of 230 possible space groups.

The molecules are built up into a crystal which interacts with a beam of some type and resulting in diffraction of the beam. Diffraction is the bending of waves when they meet a slit or obstacle of comparable size to their wavelength. The diffraction caused by an individual atom is too weak to detect, however, the regular array of repeating molecules in the crystal results in magnification of this effect, allowing for measurement of the diffraction. Atomic radii are ≈0.3 – 3.0 Å, which is roughly comparable to the wavelength of hard X-rays (1-2 Å). Atoms can therefore cause diffraction of X-rays, which interact with the valence electrons. This thesis will mainly focus on crystal structure elucidation based on X-ray diffraction.

1.4.2.1 Bragg's Law

The diffraction pattern from a crystal is observed where constructive interference of the scattered waves occurs. The geometry conditions under which diffraction is detected were determined by William and Lawrence Bragg and are described by Bragg's Law[87], Equation 1-3.

$$2d_{hkl}Sin\theta = n\lambda$$

Equation 1-3 Bragg's Law

θ is the Bragg angle (incidence angle), λ is the wavelength of the X-rays, d_{hkl} is the plane spacing, and the n is the additional path length the wave must travel. Here, n must be a whole integer as it passes through the crystal lattice resulting in constructive interference; it is generally treated as 1, as multiples of wavelength can be taken into account by the Miller indices *h*, *k*, *l* of a particular reflection. The illustration of geometric criteria for this equation are shown in Figure 1-33.

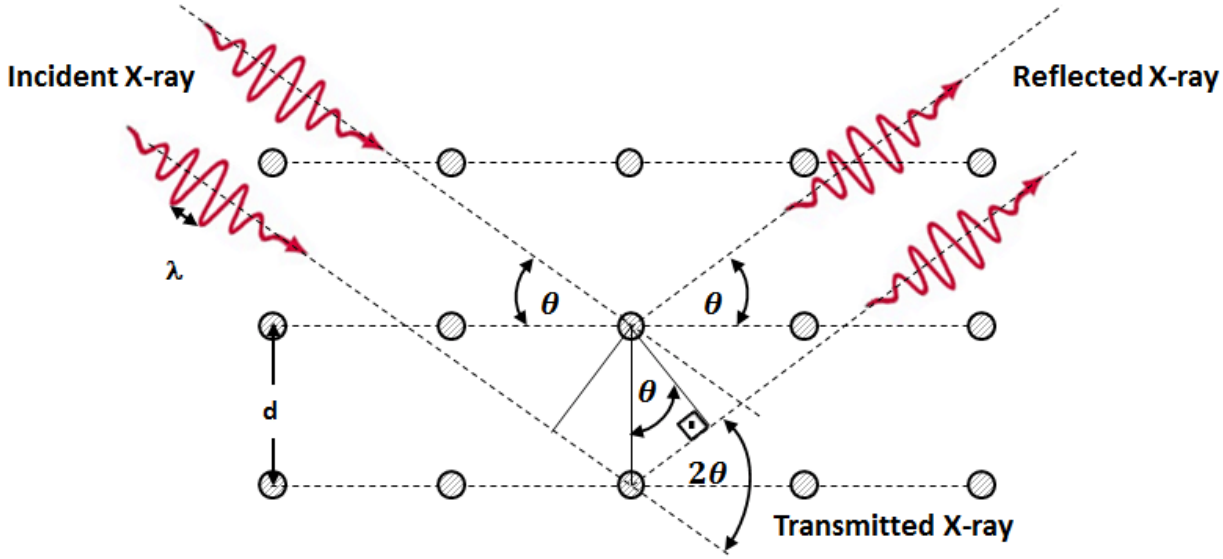

Figure 1-33 Bragg's Law: the geometric principle for the observed diffraction with crystal lattice

The observed diffraction pattern is a lattice formed of spots with defined positions and relevant intensities on a 2D detector. The diffraction pattern reveals the symmetry elements present in the crystal structure. This lattice has a reciprocal relationship to the crystal structure. Geometry of the reciprocal lattice provides information about the distances in the crystal, or real lattice, and the intensities of the observed reflections relate to electron density, from which the location of atoms can be determined.

1.4.2.2 Structure Factors and Electron Density

Each reflection in a crystal diffraction pattern is related to two numerical values: the amplitude ($|F|$) and the phase φ. $[F]^2$ is proportional to the intensity, which can be obtained from the diffraction experiment. However, the phase φ cannot be measured, it needs to be approximated

from different techniques and cannot be obtained directly, this is known as phase problem. Each reflection for indices *h*, *k*, *l* has a structure factor calculated from amplitude and phase (Equation 1-4)

$$F_{(hkl)} = |F_{hkl}| \bullet \exp[(i\varphi_{(hkl)}]$$

Equation 1-4 Structure factor from amplitude and phase of wave

Structure factor with the summation of all the reflections is shown in Equation 1-5,

$$F_{(hkl)} = \sum_{j=1}^{N} f_j \, |F_{hkl}| \bullet \exp\left[2\pi i(hx_j + ky_j + lz_j)\right]$$

Equation 1-5 Structure factor equation, where f_j represents the effect of atomic scattering.

The structure factor is related to electron density via a forward Fourier transformation (Equation 1-6)

$$F(hkl) = \int_{cell} \rho(xyz) \bullet \exp[2\pi i\left(hx_j + ky_j + lz_j\right)] \, dV$$

Equation 1-6 Structure factor equation in relation to electron density

The electron density (ED) is derived from a reverse Fourier transform of the diffraction pattern, shown in Equation 1-7.

$$\rho(xyz) = \frac{1}{V} \sum_{h,k,l} |F(hkl)| \cdot \exp[\mathrm{i}\varphi(\mathrm{hkl})] \cdot \exp[-2\pi i(hx + ky + lz)]$$

Equation 1-7 Electron density equation with separated phase and amplitude components of F(hkl).

Currently, standard resolution crystallographic studies use the Independent Atom Model (IAM) to calculate structure factors and this has been implemented in many software packages.[88] This approach relies on an assumption that the atomic electrons are localized around the nuclei position and free of orbitals.[88] This model assumes that atomic scattering is spherical, resulting in the spherical-atom approximation. In the IAM, six anisotropic displacement parameters (ADPs) and three positional parameters (x, y, and z) can be optimised for each atom by least-squares refinement.[89] Hydrogen atoms are however typically described by three positional parameters and single isotropic displacement parameter. Therefore, the IAM is an effective approximation used in crystal structure determination where core scattering is dominant, which is especially the case for heavy atoms. However, there are still many limitations for IAM, as it does not allow for the accurate description of electron density distribution in covalent and non-covalent bonds. This problem can be overcome by the application of Quantum Mechanical calculations.

1.4.3 Theoretical Quantum Mechanical Studies

1.4.3.1 Theory of Theoretical studies

Quantum mechanical computational chemistry methods can be used to obtain electron density. These ultimately trace back to the Schrodinger equation.[89] A multinuclear, multielectron system of the Schrödinger equation is generalised as Equation 1-8.

$$\hat{\mathrm{H}}\psi = E\psi$$

Equation 1-8 Schrödinger equation

Here $\hat{\mathrm{H}}$ is the Hamiltonian operator, which is a differential operator described in atomic units as Equation 1-9

Equation 1-9 $$\hat{\mathrm{H}} = \frac{1}{2}\sum_{i=1}^{N}\nabla_i^2 - \frac{1}{2}\sum_{A=1}^{M}\frac{1}{M_A}\nabla_A^2 - \sum_{i=1}^{N}\sum_{A=1}^{M}\frac{Z_A}{r_{iA}} + \sum_{i=1}^{N}\sum_{j>i}^{N}\frac{1}{r_{ij}} + \sum_{A=1}^{M}\sum_{B>A}^{M}\frac{Z_A Z_B}{R_{AB}}$$

$$\text{Where } \nabla^2 = \frac{\partial^2}{\partial x_q^2} + \frac{\partial^2}{\partial y_q^2} + \frac{\partial^2}{\partial z_q^2}$$

The first two terms describe the kinetic and nuclei energy of electrons with M and N representing nuclei and electrons respectively. M_A is the ratio of mass of nucleus A to the mass of an electron, Z is the nuclear charge, r_{iA}, r_{ij}, and R_{AB} mean the distance between two subscript electrons, respectively.

Unfortunately, the limitations of the Schrödinger equation mean that we are only able to solve it for the case of the hydrogen atom, rather than any multi-electron system; even a hydrogen molecule or helium atom is unfeasible.[90-91] Hence, essential approximations must be used to produce a multi-electronic Schrödinger equation. One widely applied assumption is the Born-Oppenheimer approximation. In this system, nuclei are assumed to move much 'slower' than the speed of electrons. Therefore, the positions of nuclei are fixed and only the electronic motion is considered, as described in Equation 1-10.

Equation 1-10 $$\hat{\mathrm{H}}_{elec}\psi_{elec} = E_{elec}\psi_{elec}$$

Based on this assumption, the Schrödinger equation can be simplified from Equation 9 by considering kinetic energy as zero and nuclei-nuclei repulsion as merely constant,[92] shown as Equation 1-11.

Equation 1-11 $$\hat{\mathrm{H}}_{elec} = -\frac{1}{2}\sum_{i=1}^{N}\nabla_i^2 - \sum_{i=1}^{N}\sum_{A=1}^{M}\frac{Z_A}{r_{iA}} + \sum_{A=1}^{N}\sum_{j>i}^{N}\frac{1}{r_{ij}}$$

The Hartree-Fock approximation states that electrons move independently. Individual electrons are assumed to move in an average field of all the other electrons referred to as a 'self-consistent

field' (SCF).[91] Hence, these individual electrons are confined to each eigenfunction, which is called the Slater determinant.

Due to the Pauli exclusion principle, the total wavefunction for the system must be antisymmetric under the interchange of electron coordination as follows:

Equation 1-12 $\psi(x_1, x_2, \cdots, x_i, \cdots, x_j, \cdots x_N,) = -\psi(x_1, x_2, \cdots, x_i, \cdots, x_j, \cdots x_N,)$

Here, x_i includes both coordination position and spin.

Therefore, the Slater determinant wavefunction described in Equation 1-13 is also antisymmetric.

Equation 1-13 $$\psi = \begin{vmatrix} \chi_1(1) & \chi_2(1) & \cdots & \chi_n(1) \\ \chi_1(2) & \chi_2(2) & \cdots & \chi_n(2) \\ \vdots & \vdots & \vdots & \vdots \\ \chi_1(N) & \chi_2(N) & \ldots & \chi_n(N) \end{vmatrix}$$

Where χ_i refers to spin and spatial coordination of electron i.

The Hartree-Fock approximation derives a set of differential equations which are the Hartree-Fock equations. An additional common assumption is the Linear Combination of Atomic Orbitals (LCAOs) approximation, used to make the Hartree-Fock equation numerical.[93] It is assumed that the wavefunction of polyelectronic systems are expressed as linear combinations of all the one-electron wavefunctions. Similarly, the molecular wavefunction is a linear sum of a set of atomic wavefunctions.[61] The prescribed wavefunctions are known as basis functions, ϕ. Linear Combination of Atomic Orbitals (LCAOs) are described in Equation 9, where c refers to molecular orbitals coefficients.

Equation 1-14 $$\psi_i = \sum_\mu c_{\mu i}\phi_\mu$$

1.4.3.2 Density Function Theory (DFT)

Computational quantum mechanical modelling methods using the principles discussed above are referred to as *ab-initio* methods. Another popular method for calculating charge density distributions is Density Function Theory (DFT) provided by Hohebery and Kohn.[91, 94] In DFT the sum of exchange and correlation energies of the ground-state system can be described by only the electron density. In the Kohn-Sham formalism, the ground-state energy, E, is written as a sum of the external potential, $V_{ext}(\mathbf{r})$, the kinetic energy, E_{KE}, the statistic energy, E_H, and the exchange and correction energy, E_{XC}. They include the local density approximation with the same density $\rho(\mathbf{r})$ seen in Equation 1-15.[91-92]

Equation 1-15 $$E[\rho(r)] = \int V_{ext}(\boldsymbol{r})\rho(\boldsymbol{r})d\boldsymbol{r} + E_{KE}[\rho(\boldsymbol{r})] + E_H[\rho(r)] + E_{XC}[\rho(\boldsymbol{r})]$$

1.4.4 Charge Density Analysis

Charge density is deriving an actual electron distribution around nuclei, in bonds, from experimental single crystal data analysis. It can only be performed established on high resolution data (at least 0.5 Å) due to the deconvolution of thermal effects and nuclear positions. This requires a more detailed experiment covering a much higher proportion of reciprocal space. The development of laboratory diffractometers with higher data collection speeds and more powerful capability makes this type of data collection more accessible. Good quality and well-diffracting crystals are measured under low temperature to acquire a suitable dataset for charge density analysis.

1.4.4.1 The multipole model (MM)

Chemical bonds cause the atoms involved to become non-spherical, resulting in the generation of other properties, such as dipole moment and electrostatic moments. Considering its limitations, it is not sufficient to use an IAM in covalently bonded structures if these properties are to be investigated, instead the multipole model has been successfully developed by Hansen and Coppens[89, 93, 95-96] and is most widely used to model atomic non-sphericity.

The multipole model was built upon the IAM model, however the electron density (ρ(**r**)) is split into three terms.

$$\rho(r) = \rho_{core}(r) + P_v k^3 \rho_{valence}(\kappa r) + \sum_{l=0}^{lmax} k'^3 R_l(\kappa' r) \sum_{m=0}^{+l} P_{lm} d_{lm\pm} \pm (\nu, \varphi)$$

Equation 1-16 Hansen-Coppens Formalism[93]

The ($\rho_{core}(r)$) term represents the spherical core electron density, the ($\rho_{valence}$) term accounts for spherical valence electron density with a contraction term (κ) in the valence shell, the remaining terms describe the deformation valence density, including radial expansion and contraction (κ') of the valence shell and normalized spherical harmonics $d_{lm\pm}$.

1.4.4.2 Quantum Theory of Atoms in Molecules (QTAIM)

The key method of Bader[97-98] to interpret the interactions between atoms is based on the topology of electron density. The Quantum Theory of Atoms in Molecules (QTAIM) provides possibilities to partition electron density in various ways to define the character of bonds and atomic domains (or basins). In QTAIM chemical bonding and the structure of chemical system is based on the topological of the electron density. The character of bonds are defined by the electron density and Laplacian density. The electron density can be partitioned in various ways to define atomic basins related to individual atoms in the molecule. These topological properties can

be best explored by analysing its gradient vector field (Figure 1-34). The gradient equation is as follows.[95]

Equation 1-17 $$\nabla\rho(\boldsymbol{r}) = i\frac{\delta\rho}{\delta x} + j\frac{\delta\rho}{\delta y} + k\frac{\delta\rho}{\delta z}$$

In this model, trajectories or gradient paths are defined by the paths that follow the largest increase in electron density, which is always normal to the electron density contour lines, $\rho(\mathbf{r})$. It means the gradient paths of $\nabla\rho(\boldsymbol{r})$ must originate from a minima or saddle point (minimum in at least one direction) and terminate at a maxima or saddle point (again maximum in at least one direction) as follows (Figure 1-34). The boundaries of atomic basins are described as zero flux surfaces. In this interatomic surface, **n(r)** refers to a vector which is perpendicular to the surface as shown (Figure 1-35). Since each atomic domain is separated from others by the interaction surfaces, the volume of the atomic basins and the topological charge of the atom based on the electron density integration of the volume can be defined by the interaction surfaces as well. Additionally, zero flux surfaces do not only appear at the boundaries of atoms, but also occur inside basins on the atom itself.

Equation 1-18 $$\nabla\rho(\boldsymbol{r}) \cdot \boldsymbol{n}(\boldsymbol{r}) = 0$$

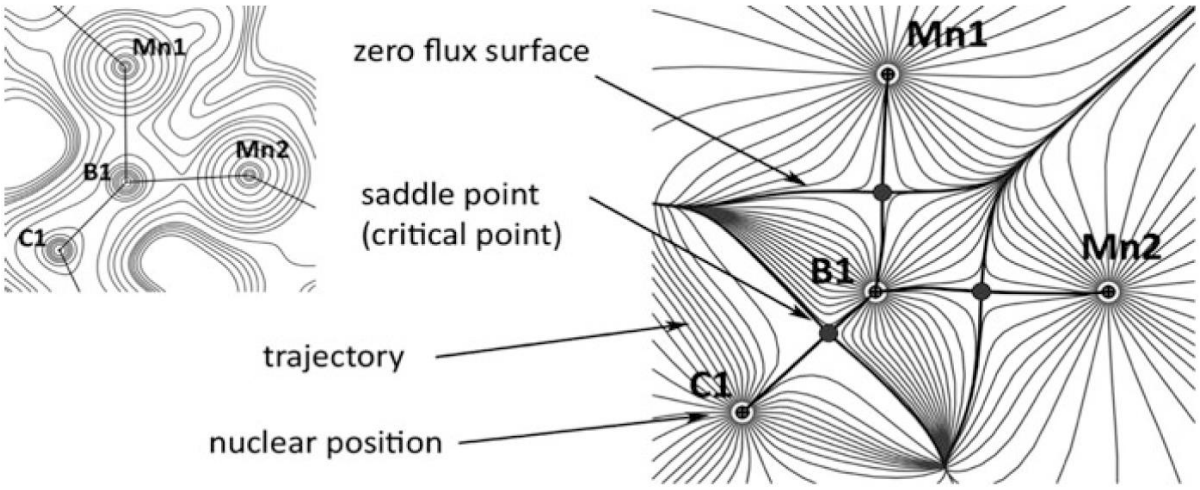

(a) (b)

Figure 1-34 (a) Electron density distribution in Mn_2B plane of $^7_2$(μ-BtBu)]; (b) the associated with the trajectories of the gradient field.[63]

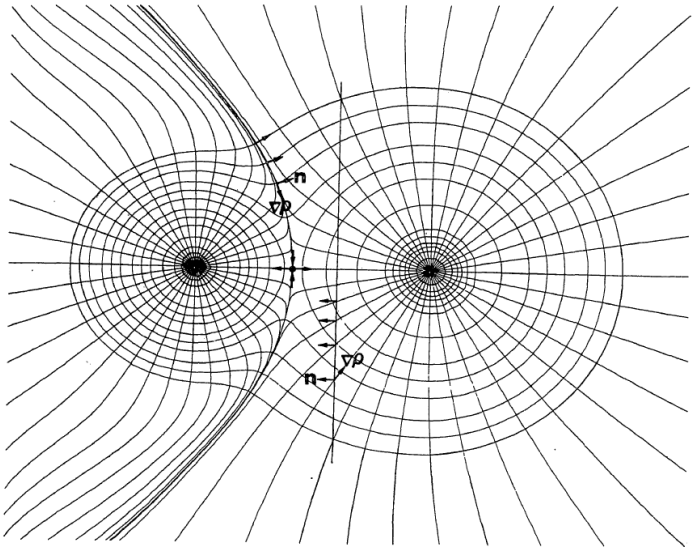

Figure 1-35 The trajectories of the gradient field of the charge density superimposed on charge density contours for the NaCl. Zero flux surfaces in the gradient vectors forming the boundaries of atomic basins illustrated for the interatomic surface whose intersection with this plane is given by the two atoms.[95]

1.4.4.3 Evaluation of modelled electron density distribution

Deformation density, allows diagnostic methods to evaluate how well the diffraction data fits the aspherical models, and these main models are summarised as follows.[89, 99]

1.4.4.3.1 Residual density

The residual density is generated from the difference between the observed and calculated electron density calculated through a Fourier summation[96] (Equation 1-19)

Equation 1-19 $$\Delta\rho(r) = \frac{1}{V}\sum_{h,k,l}(F^0 - F^1)e^{-2\pi i\varphi^1}e^{-2\pi i(hx+ky+lz)}$$

Here, for each reflection *hkl*, F^0 is the observed structure factor modulus (amplitude), and F^1 and φ^1 are the structure factor modulus and phase calculated by the given model. Due to the different refinement models used, the resulting residual density will exhibit different features. The less electron residual the better the model adopted. Figure 1-36 shows residual density maps of $S(N^tBu)_3$ calculated by IAM refinement and MM refinement.

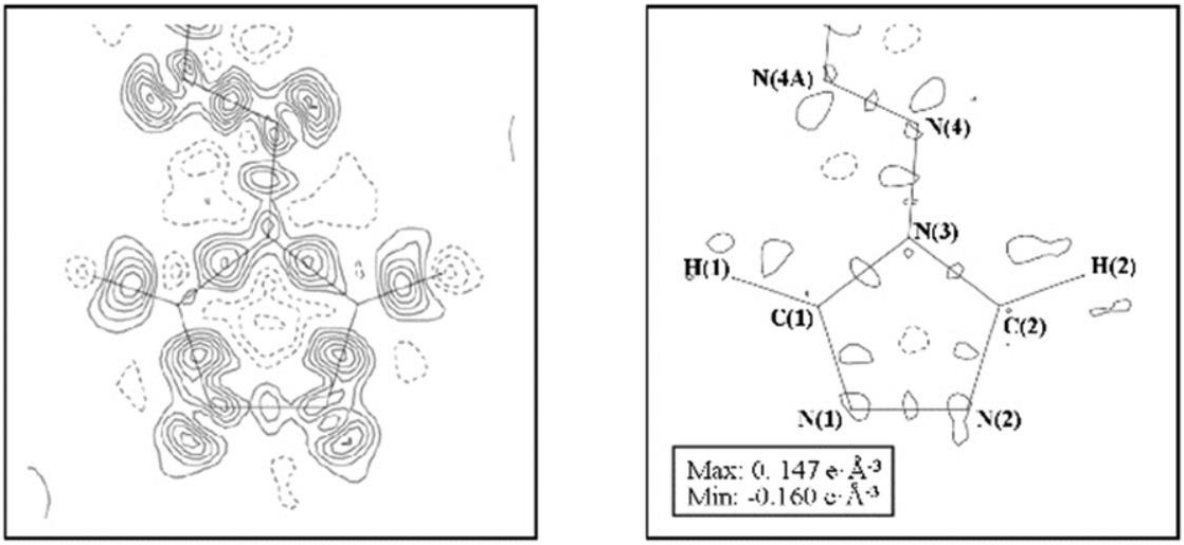

Figure 1-36 Residual density map of 1,2,4 triazole molecule after (a) IAM refinement and MM (b) refinement. Solid lines refer to positive residual density, dashed lines represents negative residual density. The contour spacing is 0.1 e $Å^{-3}$.[100]

In terms of the limitations of spherical approximations, IAM fails to accurately determine the electron density distribution in chemical bonds. This results in residual density maxima on the bonds in the IAM model. The electron density contained in a bond can be modelled by MM, leading to a better adapted structural model. This is the reason why MM gives a flat residual map also with featureless bonding area.

1.4.4.3.2 X-N deformation density

Similar to the Fourier summation in Equation 1-19, F_0 is the observed modulus of the structure factor, while F1 and $\varphi 1$ are calculated with IAM using thermal and positional parameters obtained from neutron calculated values or from a neutron structure.[89] Neutrons are scattered by nuclei and not electrons of atoms and therefore positional parameters are much more precise and closer to reality. Due to the high accuracy of neutron data, the X-N deformation density map should mostly return the aspherical electron density distribution.

1.4.4.3.3 X-X deformation density

This method also uses the same calculation from Equation 1-19, however, F^1 and φ^1 are calculated from IAM only with high resolution data (typically at least above 0.7 Å).[89] As before, F^0 is the observed modulus of the structure factor from X-ray. As the valence electrons only diffract to low angle and do not scatter at high angle, this gives rise to the main features of the valence electron density. This density map should be generated from high standard quality crystal data.

1.4.4.3.4 Static deformation density

Static deformation density is calculated from the difference of electron density between the MM and IAM as follows.[101] The static deformation density ($\Delta\rho_{static}(\boldsymbol{r})$) (Equation 1-20) shows the difference between the thermally averaged multipole model (MM) ($\rho_{MM}(\boldsymbol{r})$) and the average spherical density from the IAM ($\rho_{IAM}(\boldsymbol{r})$). The electron density arising from this method is mainly located in bond areas and should be quite similar to the X-X deformation density as shown in Figure 1-37 (a hydrogen oxalate anion in L-histidinium hydrogenoxalate)

Equation 1-20 $$\Delta\rho_{static}(\boldsymbol{r})) = \rho_{MM}(\boldsymbol{r}) - \rho_{IAM}(\boldsymbol{r})$$

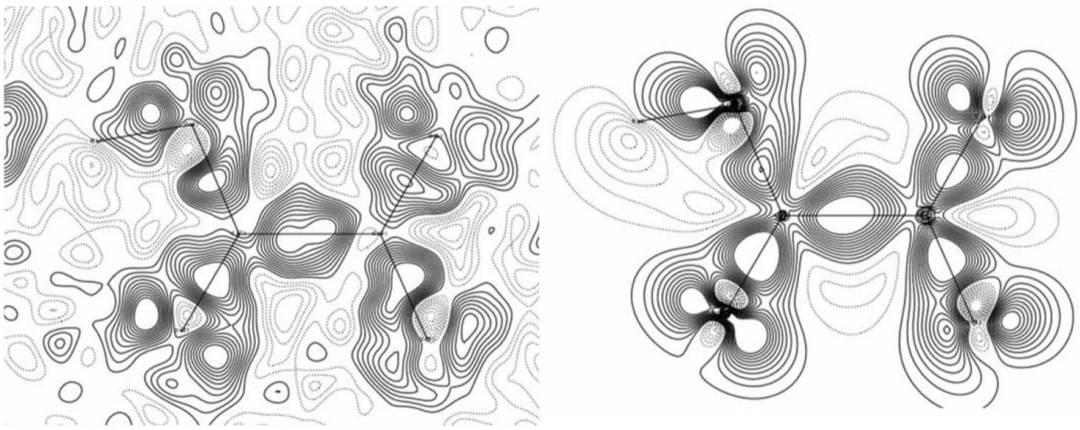

(a) (b)

Figure 1-37 (a) Residual density map after MM refinement; (b) Static deformation electron density map. Contours are 0.05 Å^{-3}. Solid and dotted lines represent positive and negative electron density contours respectively.[89]

1.4.4.4 Charge Density Properties Analysis

Crystallographic topology is the combination of geometric topology and structural crystallography concepts. It aims to analyse the energy density of atoms and intermolecular interaction properties.[102]

1.4.4.4.1 Bond Path (BP) and Critical Point (CP)

Two atomic nuclei are linked by a pair of their corresponding gradient paths forming a interaction line of locally maximal electron density which is defined as a bond path (BP).[101] A bond critical point (CP) is generated at the cross between the interaction line and the associated interatomic surface (Figure 1-38). CPs are the key features used to characterise and evaluate the nature and electron density distribution of a bond.

Equation 1-21

$$H(\boldsymbol{r}) = \begin{pmatrix} \frac{\delta^2\rho(\boldsymbol{r})}{\delta x^2} & \frac{\delta^2\rho(\boldsymbol{r})}{\delta x\delta y} & \frac{\delta^2\rho(\boldsymbol{r})}{\delta x\delta z} \\ \frac{\delta^2\rho(\boldsymbol{r})}{\delta y\delta y} & \frac{\delta^2\rho(\boldsymbol{r})}{\delta y^2} & \frac{\delta^2\rho(\boldsymbol{r})}{\delta y\delta z} \\ \frac{\delta^2\rho(\boldsymbol{r})}{\delta z\delta x} & \frac{\delta^2\rho(\boldsymbol{r})}{\delta z\delta y} & \frac{\delta^2\rho(\boldsymbol{r})}{\delta z^2} \end{pmatrix}$$

The identification of CPs is based on the 3 X 3 Hessian matrix of the electron density. The Hessian matrix (Equation 19) is generalized by the second derivatives of ρ(r) and diagonalised to provide three eigenvalues λ_1, λ_2, λ_3. These eigenvalues each correspond to an eigenvector, which represents an axis and coincides with the principal axis of curvature. The number of non-zero eigenvalues of a critical point defines the *rank* (ω), the sum of the signs of eigenvalues associated with the CPs defines the signature (σ). The classifications of the CPs are determined by the rank and signature as the Table 3 shows. There are four types of critical points.[101]

(3, -3) Nuclear attractor: three negative curvatures, ρ(r) is the local maxima i.e. an atomic nucleus.

(3, -1) Bond critical point: two negative curvatures and one positive curvature, which means ρ(r) is at a maximum along two directional axes and minimum along the third axis. This is typically the type of CP characterising a covalent bond.

(3, +1) Ring critical point: two positive curvatures and one negative curvature, which means ρ(r) is at a minimum along two directional axes and a maximum along the third axis.

(3, -3) Cage critical point: three positive curvatures, ρ(r) is the local minimum.

In an isolated molecule, the total number of critical points should obey the Poincaré-Hopf relationship:

Equation 1-22

$$N_{ccp} - N_{RCP} + N_{BCP} - N_{NA} = 1$$

Here, N means the number of associated critical points.

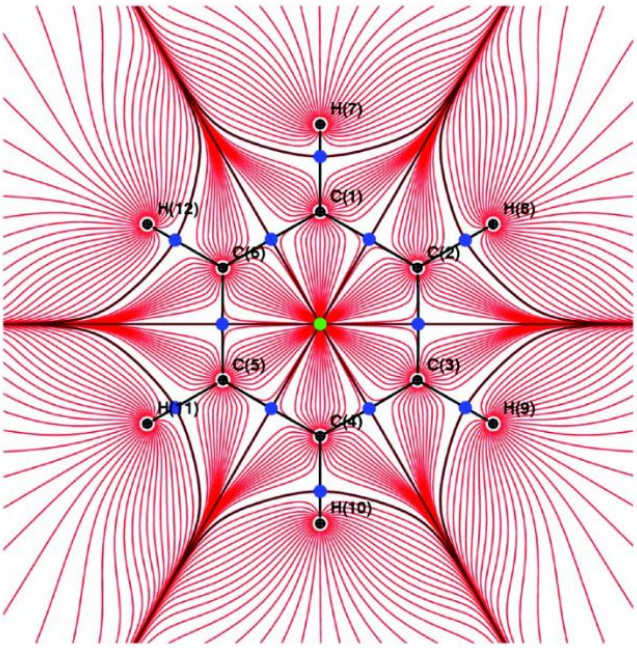

Figure 1-38 Gradient field map of benzene ring. Red lines show gradient paths for each atomic basin, Black lines represent bond paths, blue and green spheres refer to bond and ring critical points.[89]

Table 1-2 Critical points categories and signs of each type of CP

Critical point	Abbrevation	Extrema type	λ_1	λ_2	λ_3	Classification (ω, σ)
Neclear attractor	NA	Maximum	-	-	-	(3, -3)
Bond critical point	BCP	Saddle point	-	-	+	(3, -1)
Ring critical point	RCP	Saddle point	-	+	+	(3, +1)
Cage critical point	CCP	Minimum	+	+	+	(3, +3)

1.4.4.4.2 The Laplacian of electron density

The Laplacian is calculated from second-order derivatives and plays an important role in detecting small fluctuations in the electron density distribution.[89] The scalar field as described in Equation 1-23 is based on the Hessian matrix described in section 1.4.3.4.1.

Equation 1-23 $$\nabla^2\rho(r) = \frac{\delta^2\rho(r)}{\delta x^2} + \frac{\delta^2\rho(r)}{\delta y^2} + \frac{\delta^2\rho(r)}{\delta z^2} = \lambda_1 + \lambda_2 + \lambda_3$$

Where $\nabla^2\rho(r)$>0 represents charge depletion and $\nabla^2\rho(r)$<0 means charge concentration. $\nabla^2\rho(r)$<0 is referred to as the Valence Shell Charge Concentration (VSCC), which is associated with covalent bonds at BCPs. Covalent bonds are therefore an accumulation of electron density with VSCCs, known as 'open-shell' or 'shared' interactions. Conversely, there are 'closed shell' interactions in ionic bonds or non-covalent bonds, where $\nabla^2\rho_{BCP}(r)$>0.[89] The Laplacian of electron density offers an essential way to characterise the type of bond.

1.4.4.4.3 Local Energy Density

It is possible to estimate energy properties from $\rho(r_{BCP})$ and $\nabla^2\rho(\boldsymbol{r}_{BCP})$ values at critical points. According to the Espinosa-Molins-Lecomte (EML)[103] approach combined with the formula of Abramov[104], the local kinetic energy density, $G(\boldsymbol{r}_{BCP})$, the local electrostatic potential energy, $V(\boldsymbol{r}_{BCP})$, and the total energy density $H(\boldsymbol{r}_{BCP})$, can be calculated as shown below (Equation 1-24 to Equation 1-26)

$$G(\boldsymbol{r}_{BCP}) = \left(\frac{3}{10}\right)(3\pi^2)^{\frac{2}{3}}\rho(\boldsymbol{r}_{BCP})^{\frac{5}{3}} + (\frac{1}{6})\nabla^2\rho(\boldsymbol{r}_{BCP})$$

Equation 1-24 Calculation of the local kinetic energy density. $\rho(\boldsymbol{r}_{BCP})$ is shown in atomic units.

$$V(\boldsymbol{r}_{BCP}) = \left(\frac{\hbar^2}{4m}\right)\nabla^2\rho(\boldsymbol{r}_{BCP}) - 2G(\boldsymbol{r}_{BCP})$$

Equation 1-25 Calculation of the local electrostatic potential energy. $\rho(\boldsymbol{r}_{BCP})$ is shown in atomic units.

$$H(\boldsymbol{r}_{BCP}) = G(\boldsymbol{r}_{BCP}) - V(\boldsymbol{r}_{BCP})$$

Equation 1-26 Calculation of the total electron density

The values of these three quantities are part of the criteria used to estimate energy strength for interactions. Notably, the ratio of $V(\boldsymbol{r}_{BCP})/G(\boldsymbol{r}_{BCP})$ indicates stability of interaction regarding a local concentration of charge, where $V(\boldsymbol{r}_{BCP})/G(\boldsymbol{r}_{BCP})$ > 1 denotes an intermediate closed-shell interaction and $V(\boldsymbol{r}_{BCP})/G(\boldsymbol{r}_{BCP})$ < 1 denotes an electrostatic interaction.

1.5 Aims

Therefore this thesis sets out to address the following aims:

1. Systematically design and modify a series of electron withdrawing/donating naphthalimide-based functional groups as the target for this project. These electron deficient 1,8-naphthalimide systems are then not only introduced into potential SCO

complexes as non-coordinating anions, but also utilised as ligand scaffolds for metal complexes.

2. Initially, use standard resolution X-ray crystallography to characterise the compounds and then investigate their magnetic properties in order to begin to analyse the effect of altering chemical substituents on both the crystal structures and magnetic properties.
3. In order to analyse the relationship between π interactions and magnetic properties, in this ligand system in particular, a deeper and more extensive analysis of intermolecular interactions and associated energies needs to be conducted using high resolution X-ray crystallography and quantum crystallographic methods.
4. Electron density distribution analysis will be conducted to analyse the effects of different substituents on π···π interactions and hydrogen bonds strength in the system. Particularly, to understand how the π-stacking controls the cooperativity of the systems.

Chapter 2 Bis-picolylamine Fe(II) complexes and naphthalimide functional anions system

2.1 Study of pyridyl-based mononuclear Fe(II) complexes with simple anions

Six-coordinated iron(II) complexes with an Fe-N_6 coordination sphere were chosen for this project as they exhibit the greatest structural differences between low spin and high spin states.[10] A large number of pyridyl-based ligands have been the subject of considerable interest in forming octahedral Fe(II) complexes which have the potential to show spin crossover phenomenon. Considering the need for high throughput with synthetically challenging organic anions, picolylamine and bis-piclylamine ligands were chosen as their cationic metal complexes do not require arduous organic preparation.

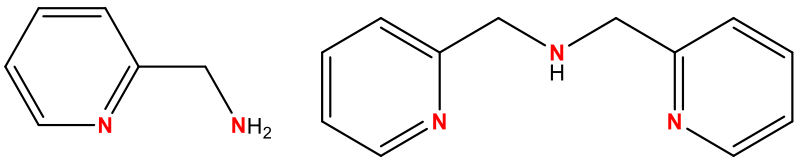

Figure 2-1 Structure of 2-picolylamine and bis-picolylamine with nitrogen binding sites highlighted in red

Figure 2-1 presents their structures, illustrating how the nitrogen donor could be held in close proximity to a coordinated Fe(II) centre. The binding modes are presented in Figure 2-2.

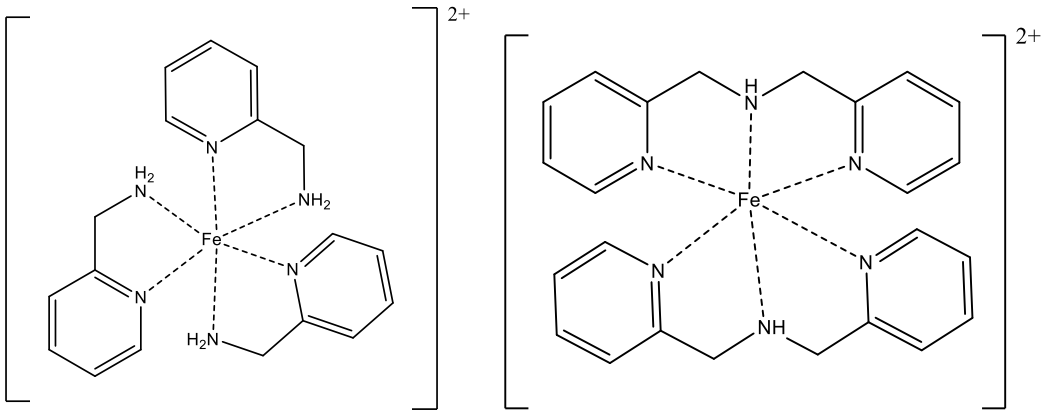

Figure 2-2 Structure of N_6 coordinated Fe(II) complexes

There are 21 relevant Fe(II) complexes with the proposed ligands listed in the CSD, details of the solvents and anions can be found in (Table2-1). As this table demonstrates, successful investigations have been made with tris-(2-picolylamine) Fe(II) complexes. Through the production of complexes with different solvents and anions it is possible to analyse the relationship with magnetic behaviour. In particular, a [Fe(**2-pic**)$_3$(m-ABS)$_2$]·CH_3OH, [Fe(**2-pic**)$_3$(p-ABS)$_2$], and [Fe(**2-pic**)$_3$(OTf)$_2$] study demonstrated that replacing anions is a very promising method to adjust the structure and therefore improve the SCO properties. However, there has been limited investigation into the magnetic properties of Fe(II) bis-picolylamine complexes, therefore full magnetic analysis of these complexes would be interesting.

Table 2-1 Summary of information on the crystallographically characterised Fe(II) complexes with **2-pic** and **bpa**.

complex	Anion	Solvent	Collected T (K)	Fe-N(pyridyl) (Å)	Fe-N(amine) (Å)	Σ[°]	Spin state	$T_{1/2}$(K)	Ref.
[Fe(**2-pic**)$_3$ Cl_2]•2H_2O	Cl^-	water	300	1.986	2.026	49.58	LS	N/A	[105]
[Fe(**2-pic**)$_3$ Cl_2]•H_2O	Cl^-	water	150	1.965	2.009	50.37	SCO (hysteresis)	204↓ 295↑	[106-107]
[Fe(**2-pic**)$_3Cl_2$]•CH_3OH	Cl^-	methanol	300	2.210	2.186	94.6	SCO	150	[106-107]
Fe(**2-pic**)$_3Cl_2$]•CH_3CH_2OH	Cl^-	ethanol	292	2.194	2.168	100.6	SCO (2 steps)	118	[107]
[Fe(**2-pic**)$_3Cl_3$]•CH_2CHCH_3OH	Cl^-	allyl alcohol	200	2.201	2.174	100.7	SCO	124	[107]
[Fe(**2-pic**)$_3Cl_3$] •$(CH_3)_2CHOH$	Cl^-	2-propanol	200	2.216	2.182	100.5	SCO	147	[107]
[Fe(**2-pic**)$_3Cl_2$] •$CH_3CH_2CH_2OH$	Cl^-	1-propanol	200	2.211	2.184	103.7	HS	N/A	[107]
[Fe(**2-pic**)$_3Cl_2$] •$(CH_3)_3CHOH$	Cl^-	*tert*-butyl alcohol	200	2.230	2.182	111.3	HS	N/A	[107]
				2.208	2.182	98.9			
[Fe(**2-pic**)$_3I_2$]	I^-	N/A	300	2.051	2.076	62	HS	N/A	[108]

Complex	Anion	Solvent	Collected T (K)	Fe-N(pyridyl) (Å)	Fe-N(amine) (Å)	Σ[°]	Spin state	$T_{1/2}$(K)	Ref.
[Fe(**2-pic**)$_3$ Br_2]]•CH_3CH_2OH	Br^-	ethanol	215	2.202	2.186	100.59	SCO hysteresis)	123	[109]
[Fe(**2-pic**)$_3$$I_2$]•$CH_2Cl_2$	Cl^-	dichloromethane	100	2.202	2.164	97.69	NR	N/A	[110]
[Fe(**2-pic**)$_3$(m-ABS)$_2$]]•CH_3OH	Cl^-	methanol	120	2.197	2.173	91.57	SCO (hysteresis)	100↓ 103↑	[111]
[Fe(**2-pic**)$_3$(p-ABS)$_2$]	Cl^-	N/A	120	1.989	2.018	52.71	SCO	218	[111]
[Fe(**2-pic**)$_3$(OTf)$_2$]	Cl^-	N/A	120	1.972	2.024	51.19	SCO (hysteresis)	333↓ 343↑	[111]
[Fe(**2-pic**)$_3$$Cl_2$]•$(EtOH)_{0.744}$(2-PrOH)$_{0.256}$	Cl^-	Mixed ethanol & 2-propanol	160	1.997	2.022	59.86	SCO	122	[112]
[Fe(**bpa**)$_2$ Cl_2]•$2H_2O$	ClO_4^-	N/A	200	1.978	1.997	78.17	NR	NR	[113]
				1.978	1.991	76.59			
[Fe(**bpa**)$_2$ (BF_4]$_2$]	BF_4^-	N/A	300	1.968	2.057	81.55	LS	N/A	[114]
[Fe(**bpa**)$_2$ Br_2]•MeOH	Br^-	methanol	183	1.994	2.031	72.4	LS	N/A	[115]

Complex	Anion	Solvent	Collected T (K)	Fe-N(pyridyl) (Å)	Fe-N(amine) (Å)	Σ[°]	Spin state	$T_{1/2}$(K)	Ref.
[Fe(**bpa**)$_2$ Cl_2]•MeCN	Cl^-	acetonitrile	150	1.984	2.020	69.76	NR	NR	[116]
[Fe(**bpa**)$_2$ Cl_2]•CH_2Cl_2	Cl^-	dichloromethane	183	1.987	2.031	65.88	NR	NR	[117]
[Fe(**bpa**)$_2$ $(CF_3SO_3]_2$]•MeCN	CF_3SO_3	acetonitrile	100	1.976	2.009	72.87	NR	NR	[111]
				1.980	2.009	73.49			

Notes: 1. NR= Not reported

2. $\Sigma = \sum_{i=1}^{12} |90 - \alpha_i|$

3. Fe-N is average bond length

2.2 Introducion of Sulfonated Naphthalimide Anions into Mononuclear Complexes Systems

Non-coordinating 1,8-naphthalimide anionic groups can be introduced into mononuclear complex systems. These anionic systems act as secondary building units (SBUs) giving the potential for "directed assembly" of the solid state. The initial focus of this work was on developing a family of sulfonated naphthalimide anions. This anion family is shown in Figure 2-3 and includes the unsubstituted naphthalimide systems (A1, A6, A9 A12), which have previously been reported.[118]

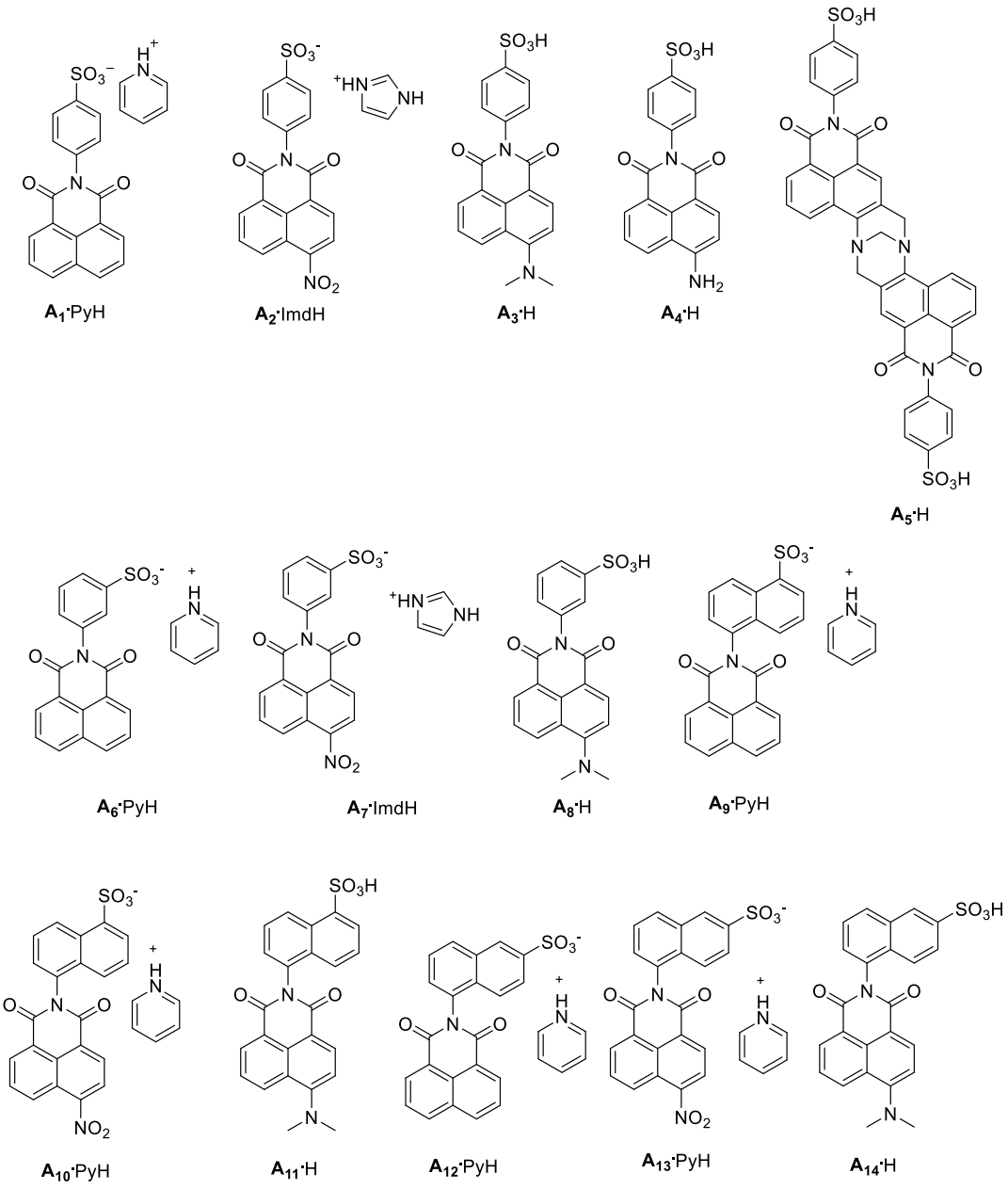

Figure 2-3 Structures of naphthalimide anions systems

Building upon this published work, substitution at the naphthalimide 4-position was undertaken with the goal of altering the crystal engineering packing/ordering properties through incorporation of additional structure directing groups (SDGs). The withdrawing/donating groups NO_2, NMe_2, and NH_2 were used to potentially alter the π-based interactions involving the naphthalimide ring. The most structurally interesting and complex system was the Trögers' base system of **A$_5$**·2H, where two sulfonated-naphthalimides are linked together and which has not been used previously as an anion with targeted structure properties. The Trögers' base system can provide further rigid properties in connected 3D coordination polymers, and potentially result in porous structures. This series of anion systems was produced in order to investigate the ability of anions to influence structure and magnetism properties of Fe(II) complexes.

In this thesis work, a series of π-based naphthalimide anions were initially introduced into $[Fe(2\text{-}pic)_2]^{2+}$ complexes. Unfortunately, due to the large steric effect of the naphthalimide anions, the limited available space only allowed two 2-picolylamine ligands to be coordinated to the Fe(II), the other sites were occupied with H_2O and this results in a HS configuration as shown in Figure 2-4. So the investigation of functional anions effects on Fe(II) complexes studies moved to the tridentate bis-picolylamine system. Detailed studies were then carried out to understand how π-interactions influence the crystal structure and how this in turn modifies the magnetic behaviour.

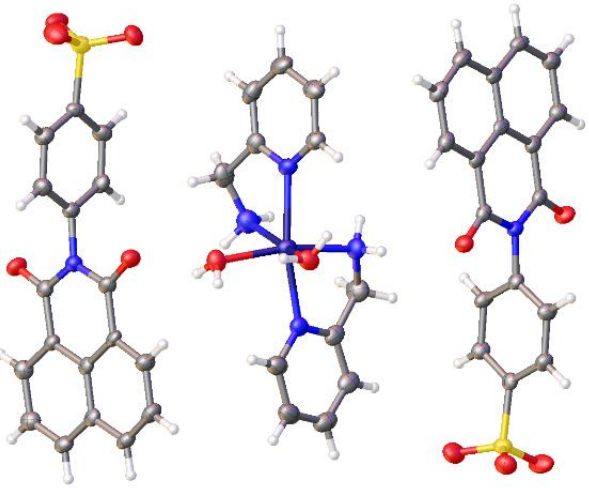

Figure 2-4 Crystal structure of $[Fe(2\text{-}Pic)_2(H_2O)_2]\cdot(\mathbf{A_1})_2$

2.3 Design of Sulfonated Naphthalimide Anion Systems

The synthesis of the H-substituted naphthalimide anions (**A1**, **A6**, **A9**, **A12**) followed a previously established method.[118] Full characterisation data are provided in experimental section 2.8.

2.3.1 Synthesis of Ar(4-SO_3)-Nap-H·PyH (A_1·PyH)

The Ar(4-SO_3-)Nap-H·PyH (**A_1**·PyH) (Figure 2-5) was synthesised following the established reaction between 4-sulfanilic acid and 1,8-naphthalic anhydride in refluxing pyridine for 2 hours. After cooling to room temperature, the pyridine was removed by vacuum. This resulted in a pale orange solid which was washed with diethyl ether, to give the product as the pyridinium salt.

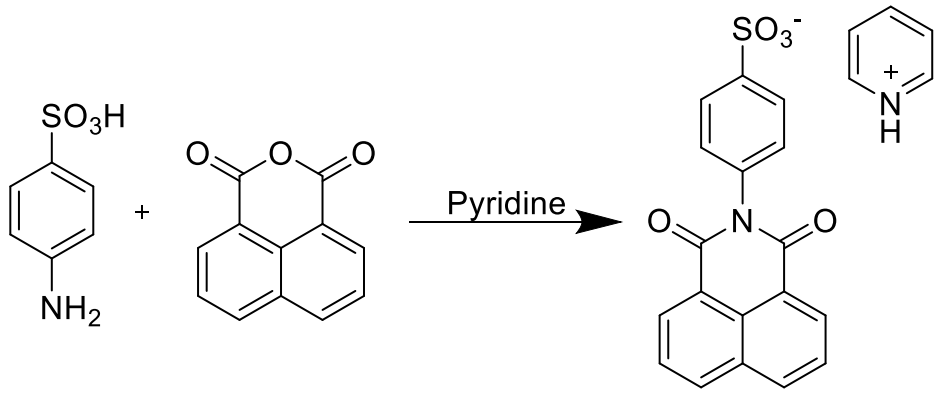

Figure 2-5 Synthesis of Ar(4-SO_3)-Nap-H·PyH (**A_1**-PyH)

2.3.2 Synthesis of Ar(4-SO_3)-Nap-NO_2·ImdH (A_2·ImdH)

The Ar(4-SO_3-)Nap-NO_2·ImdH (**A_2**·ImdH) (Figure 2-6) was synthesised by refluxing 4-sulfanilic acid and 4-NO_2-naphthalic anhydride, and a large excess of imidazole in chloroform for 6 hours. After cooling to room temperature, the chloroform was removed by vacuum and distilled water was added to the orange solid. The mixture was sonicated and then filtered and washed with ice-cold ethanol, to give the pure imidazolium product.

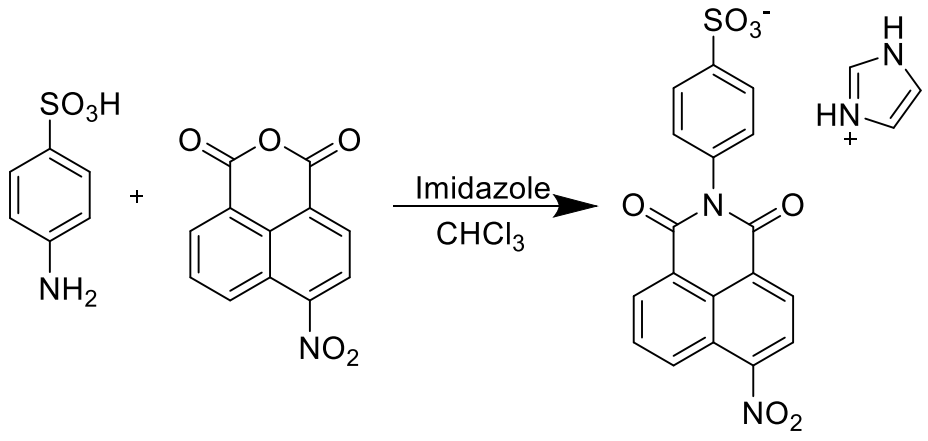

Figure 2-6 Synthesis of Ar(4-SO_3)-Nap-NO_2·ImdH (**A_2**·ImdH)

2.3.3 Synthesis of Ar(4-SO_3)-Nap-$N(Me)_2$·H (**A_3**·H)

The Ar(4-SO_3-)Nap-$N(Me)_2$·ImdH (**A_3**·ImdH) (Figure 2-7) was synthesised by refluxing 4-sulfanilic acid and 4-$N(Me)_2$-naphthalic anhydride, and a large excess of imidazole in chloroform for 6 hours. After cooling to room temperature, the chloroform was removed by vacuum. The resulting imidazolium crude product was dissolved in a small amount of deionised water and diluted hydrochloride acid was added until the pH of the solution approached 7. This resulted in a bright yellow solid which was washed with cold ethanol to give the pure protonated compound (**A_3**·H).

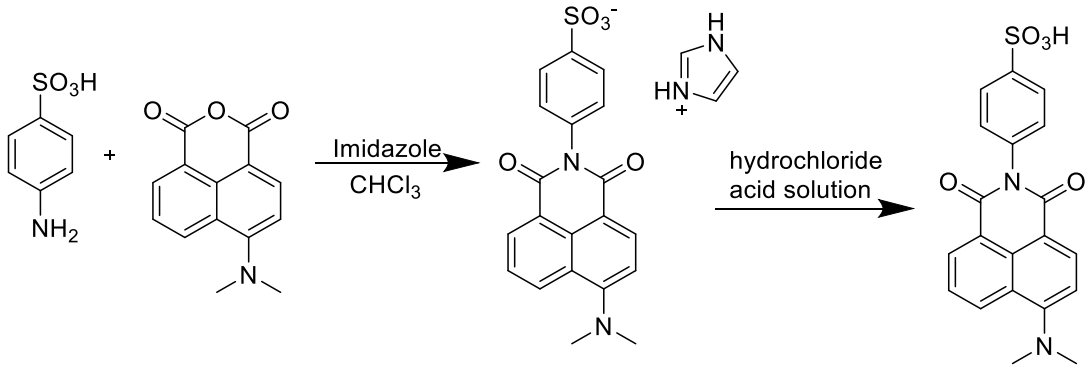

Figure 2-7 Synthesis of Ar(4-SO_3)-Nap-$N(Me)_2$·H (**A_3**·H)

2.3.4 Synthesis of Ar(4-SO_3)-Nap-NH_2·H (**A_4**·H)

The Ar-(4-SO_3)-nap-NH_2·H (**A_4**·H) (Figure 2-8) was synthesised by refluxing Ar-(4-SO_3)-nap-NO_2·ImdH (**A_2**·ImdH) in methanol with a 10% palladium on carbon catalyst under hydrogen atmosphere for 12 hours. This resulted in a suspension which was dissolved with an equal amount of methanol and then filtered through celite. The resulting bright orange solid was collected by vacuum filtration.

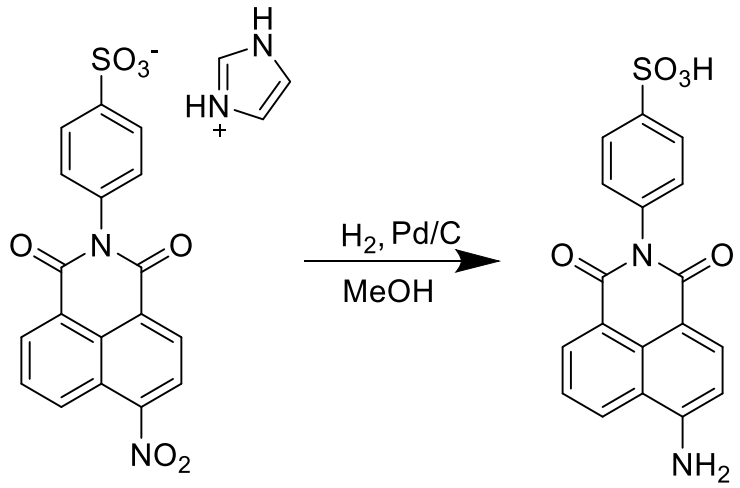

Figure 2-8 Synthesis of Ar(4-SO_3)-Nap-NH_2·H (**A_4**·H)

2.3.5 Synthesis of Ar(4-SO_3)-Nap-Tröger's base·2H (A_5·2H)

A_4·H was next converted into the Ar(4-SO_3)-nap-Tröger's base·2H (**A_5**·2H), by stirring with 1.5 equiv. paraformaldehyde in neat trifluoroacetic acid under an N_2 atmosphere for 24 hours at room temperature (Figure 2-9). The solvent was removed by vacuum and the solid was suspended in ethanol and filtered through celite. The filtrate was evaporated in vacuum resulting in a yellow solid. Mass spectrometry analysis and single crystal X-ray structural analysis confirmed successful formation of the Tröger's base.

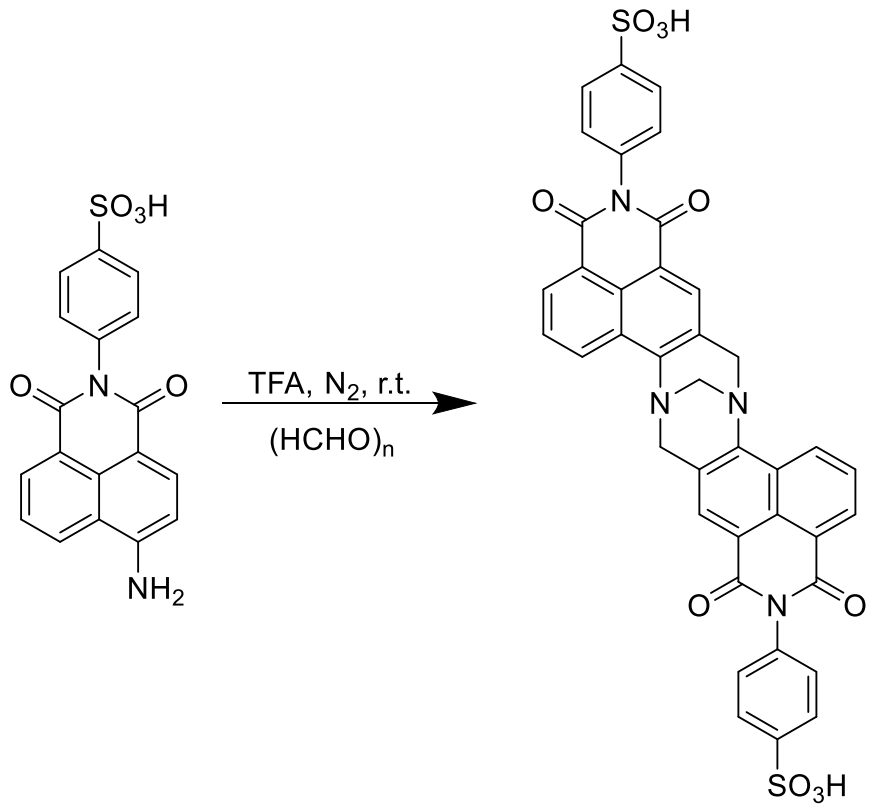

Figure 2-9 Synthesis of Ar(4-SO_3)-Tröger's base·2H (**A_5**·2H)

2.3.6 Synthesis of Ar(3-SO_3)-Nap-H·PyH (A_6·PyH)

The Ar(4-SO_3-)Nap-H·PyH (**A_6**·PyH) (Figure 2-10) was synthesised by refluxing 3-sulfanilic acid and 1,8-naphthalic anhydride in for 2 hours. After cooling to room temperature, the pyridine was removed by vacuum. This resulted in a pale orange solid which was washed with distilled water and diethyl ether respectively, to give the product as the pyridinium salt.

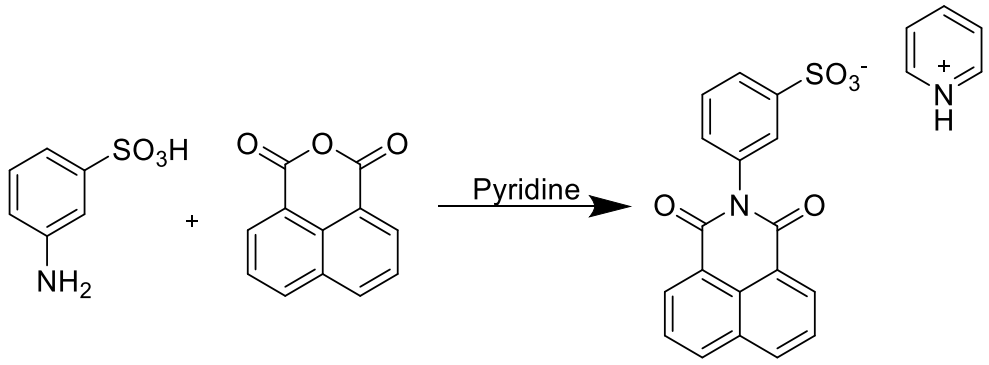

Figure 2-10 Synthesis of Ar(3-SO_3)-Nap-H·PyH (**A_6**·PyH)

2.3.7 Synthesis of Ar(3-SO_3)-Nap-NO_2·ImdH (**A_7**·ImdH)

The Ar(4-SO_3-)-nap-NO_2·ImdH (**A_7**·ImdH) (Figure 2-11) was synthesised by reaction of 3-sulfanilic acid and 4-NO_2-naphthalic anhydride, and a large excess of imidazole in a refluxing chloroform for 6 hours. After cooling to room temperature, the chloroform was removed by vacuum. This resulted in a light orange solid which was washed with distilled water and diethyl ether, to give the pure product.

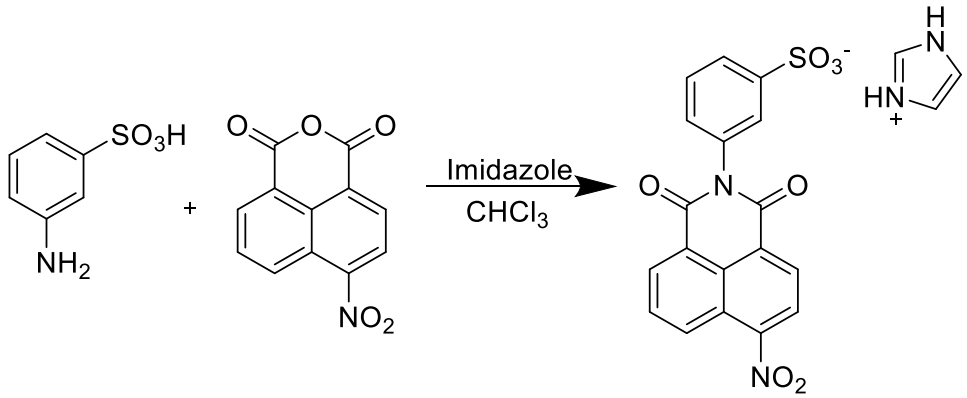

Figure 2-11 Synthesis of Ar(3-SO_3)-Nap-NO_2·ImdH(**A_7**·ImdH)

2.3.8 Synthesis of Ar(3-SO_3)-Nap-$N(Me)_2$·H (**A_8**·H)

The Ar(3-SO_3-)Nap-$N(Me)_2$·ImdH (**A_8**·PyH) (Figure 2-12) was synthesised by refluxing 3-sulfanilic acid and 4-$N(Me)_2$-naphthalic anhydride, and a large excess of imidazole in chloroform for 6 hours. After cooling to room temperature, the chloroform was removed by vacuum. The resulting imidazolium crude product was dissolved in a small amount of deionised water and dilute hydrochloride acid was added until the solution had a pH of 7. This resulted in a bright yellow solid which was washed with cold ethanol to give the pure protonated compound (**A_8**·H).

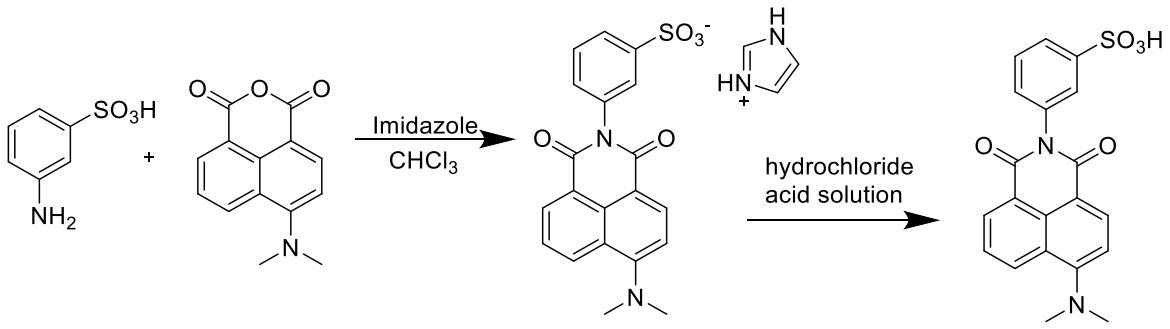

Figure 2-12 Synthesis of Ar(3-SO_3)-Nap-N(Me)$_2$·H (**A$_8$**·H)

2.3.9 Synthesis of 5-Naph(1-SO_3)-Nap-H·PyH (**A$_9$**·PyH)

The 5-Naph(1-SO_3)-nap-H·PyH (**A$_9$**·PyH) (Figure 2-13) was synthesised by reaction of 5-amino-1-naphthalenesulfonic acid with 1,8-naphthalic anhydride in refluxing pyridine for 2 hours. After cooling to room temperature, the pyridine was removed by vacuum. This resulted in a light purple solid which was washed with diethyl ether to give the pure product as a pyridinium salt.

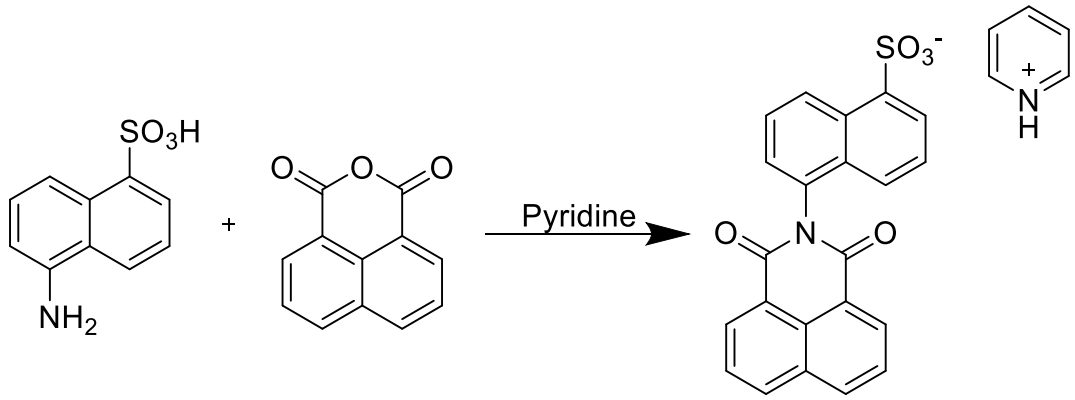

Figure 2-13 Synthesis of the anionic 5-Naph(1-SO_3)-Nap-H·PyH (**A$_{10}$**·PyH)

2.3.10 Synthesis of 5-Naph(1-SO_3)-Nap-NO_2·PyH (**A$_{10}$**·PyH)

The 5-Naph(1-SO_3)-nap-NO_2·PyH (**A$_{10}$**·PyH) (Figure 2-14) was synthesised by reaction of 5-amino-1-naphthalenesulfonic acid with 4-NO_2-naphthalic anhydride in refluxing pyridine for 2 hours. After cooling to room temperature, the pyridine was removed by vacuum. This resulted in a pale orange solid which was washed with diethyl ether, to give the product as the pyridinium salt.

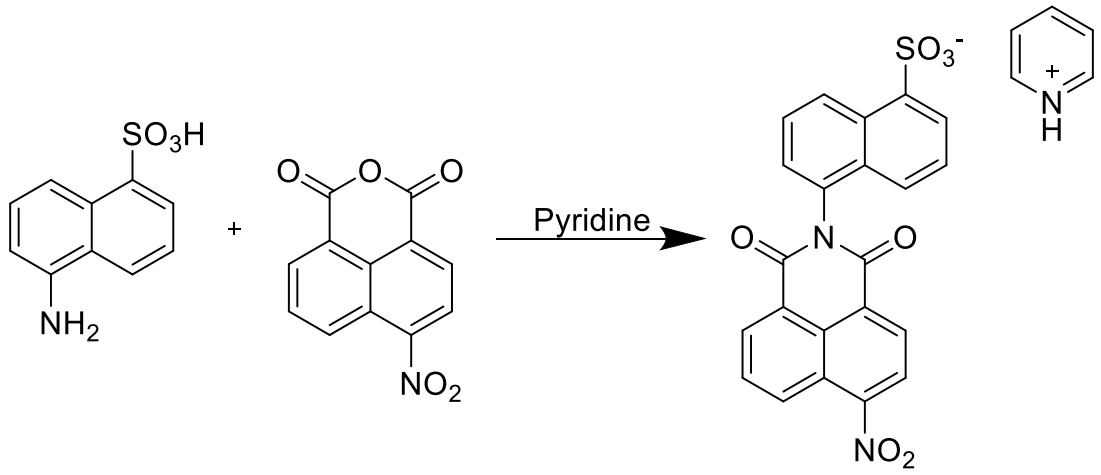

Figure 2-14 Synthesis of the anionic 5-Naph(1-SO_3)-Nap-H·PyH (**A_{11}**·PyH)

2.3.11 Synthesis of 5-Naph(1-SO_3)-Nap-N(Me)$_2$·H (**A_{11}**·H)

The 5-Naph(1-SO_3)-Nap-N(Me)$_2$·ImdH (**A_{11}**·ImdH) (Figure 2-15) was synthesised by refluxing 5-amino-1-naphthalenesulfonic acid and 4-N(Me)$_2$-naphthalic anhydride, and a large excess of imidazole in deionised water for 6 hours. After cooling to room temperature the resulting imidazolium crude product was dissolved in a small amount of deionised water and dilute hydrochloride acid was added until the solution had a pH of 7 . This resulted in a bright yellow solid which was washed with cold ethanol to give the pure protonated compound (**A_{11}**·H).

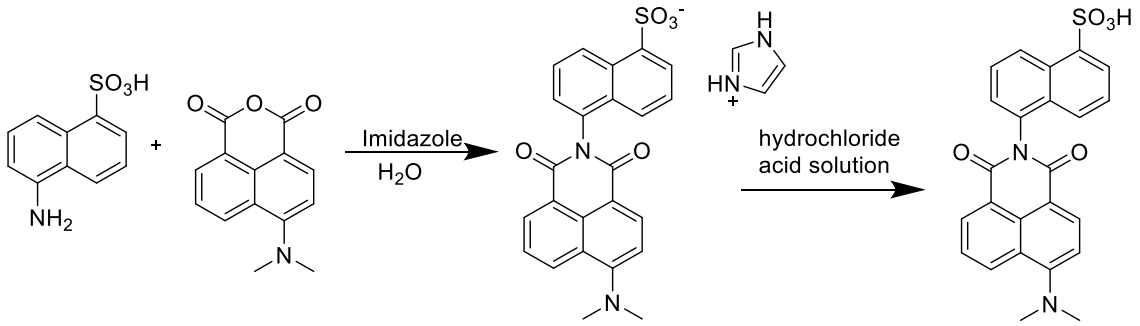

Figure 2-15 Synthesis of 5-Naph(1-SO_3)-Nap-N(Me)$_2$·H (**A_{11}**·H)

2.3.12 Synthesis of 5-Naph(2-SO_3)-Nap-H·PyH (**A_{12}**·PyH)

The 5-Naph(2-SO_3)-Nap-H·PyH (**A_{12}**·PyH) (Figure 2-16) was synthesised by reaction of 5-amino-2-naphthalenesulfonic acid with 1,8-naphthalic anhydride in refluxing pyridine for 2 hours. After cooling to room temperature, the pyridine was removed by vacuum. This resulted in a light purple solid which was washed with diethyl ether to give the pure product as a pyridinium salt.

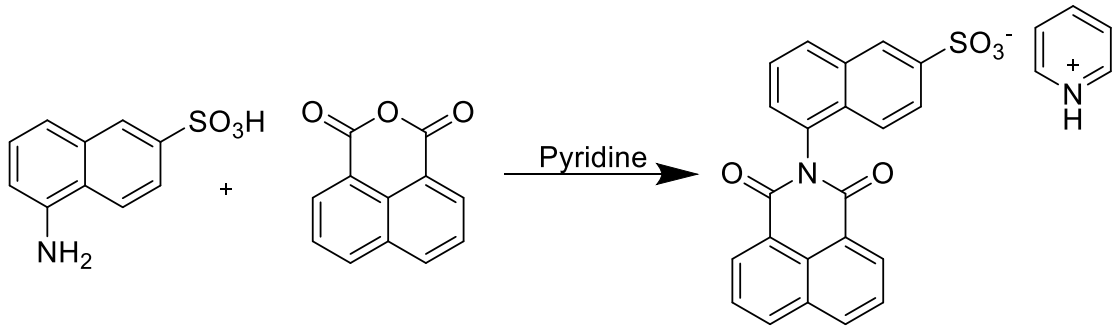

Figure 2-16 Synthesis of 5-Naph(2-SO_3)-Nap-H·PyH (**A_{12}**·PyH)

2.3.13 Synthesis of 5-Naph(2-SO_3)-Nap-NO_2·PyH (**A_{13}**·PyH)

The 5-Naph(2-SO_3)-Nap-NO_2·PyH (**A_{13}**·PyH) (Figure 2-17) was synthesised by reaction of 5-amino-2-naphthalenesulfonic acid with 4-NO_2-naphthalic anhydride in refluxing pyridine for 2 hours. After cooling to room temperature, the pyridine was removed by vacuum. This resulted in a pale orange solid which was washed with diethyl ether, to give the product as the pyridinium salt.

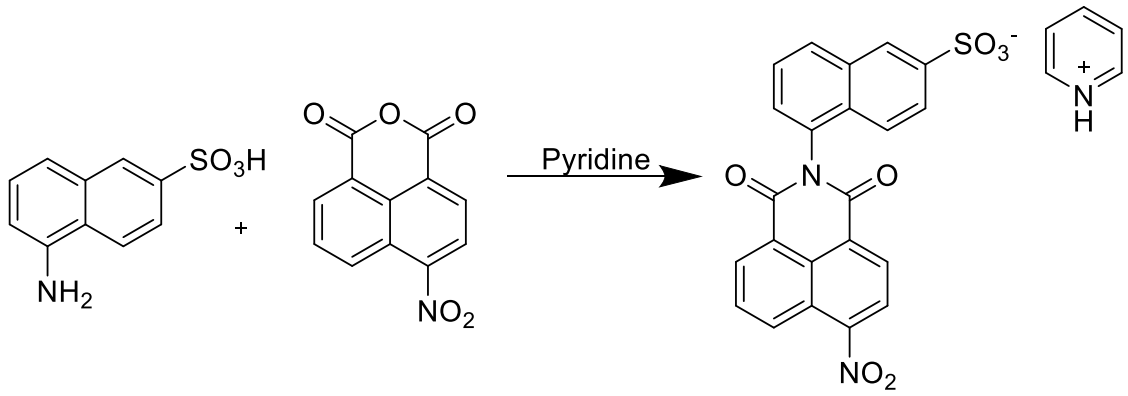

Figure 2-17 Synthesis of 5-Naph(2-SO_3)-Nap-NO_2·PyH (**A_{13}**·PyH)

2.3.14 Synthesis of 5-Naph(2-SO_3)-Nap-$N(Me)_2$·H (**A_{14}**·H)

The 5-Naph(2-SO_3)-Nap-$N(Me)_2$·ImdH (**A_{14}**·ImdH) (Figure 2-18) was synthesised by refluxing 5-amino-2-naphthalenesulfonic acid and 4-$N(Me)_2$-naphthalic anhydride, and a large excess of imidazole in deionised water for 6 hours. After cooling to room temperature the resulting imidazolium crude product was dissolved in a small amount of deionised water and dilute hydrochloride acid was added until the solution had a pH of 7. This resulted in a bright yellow solid which was washed with cold ethanol to give the pure protonated compound (**A_{14}**·H).

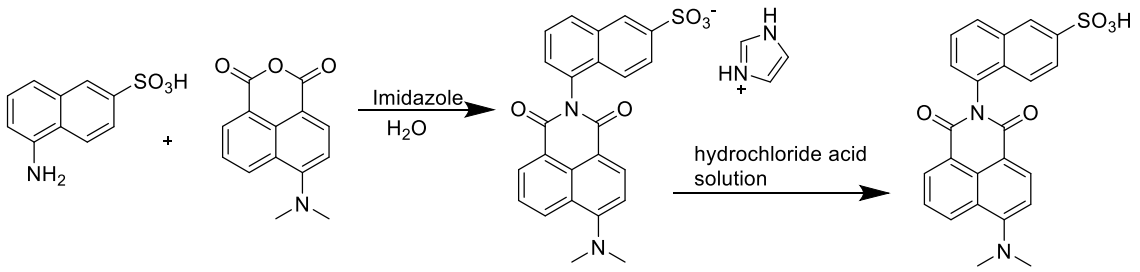

Figure 2-18 Synthesis of 5-Naph(2-SO3)-Nap-N(Me)$_2$·H (**A$_{14}$**)

2.4 Synthetic Routes to Fe(bpa)$_2$(A$_X$) Complexes, where X=1, 2, 3, 5, 6, 8, 9, 11, 12, 13, 14

2.4.1 Preparation of [Fe(bpa)$_2$(BF$_4$)$_2$] complex

The [Fe(bpa)$_2$(BF$_4$)$_2$] was prepared by Fe(BF$_4$)$_2$ and bis-pycolylamine (**bpa**) in methanol solvent with an addition of an excess ratio (Fe:**bpa**=1:2.5).[116] The reaction was stirred at 50 °C for 30 minutes to give the [Fe(bpa)$_2$(BF$_4$)$_2$] complex as a red precipitate. The resulting complex was filtered and washed with methanol.

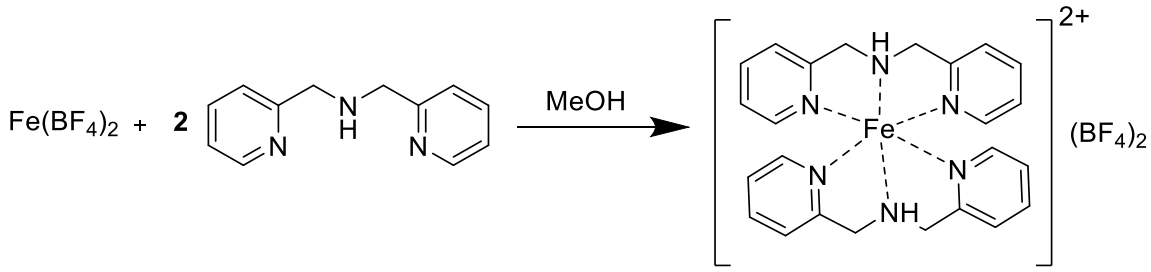

Figure 2-19 Synthetic route of [Fe(**bpa**)$_2$(BF$_4$)$_2$] complex

2.4.2 General Procedure for the Synthesis of [Fe(bpa)$_2$(A$_X$)$_2$], where X= 1,2,6,9,12,14

The [Fe(**bpa**)$_2$(BF$_4$)$_2$] complex as prepared in section 2.3.1 (0.025 mmol) was suspended in methanol (5 mL) then added to a methanol solution (5 ml) of 2 equivalents 1,8-naphthalimide (**A$_1$**, **A$_2$**, **A$_6$**, **A$_9$**, **A$_{12}$**, **A$_{14}$**). The dark red solution was heated to 50 °C and stirred at for 30 min, before being cooled to room temperature. The resulting solutions were subjected to vapour diffusion of diethyl or slow evaporation of the methanol.

2.4.3 Procedure for the Synthesis of [Fe(bpa)$_2$(A$_3$)$_2$] (3)

To a suspension of 1,8-naphthalimide **A$_3$** (0.05 mmol) in water (2 ml), 1.5 equivalents bis-picolylamine was added resulting in a transparent solution. 0.5 equivalents of Fe(BF$_4$)$_2$·6H$_2$O in

water (1 ml) was added and the solution was stirred for 2 minutes. Acetone was added to the orange-red suspension until the solid dissolved (approximately 10 mL) becoming transparent. The resulting solution was left to slowly evaporate.

2.4.4 Procedure for the Synthesis of [Fe(bpa)$_2$(A$_5$)] (4)

To the Tröger base compound **A$_5$** (0.025 mmol) in methanol (5 ml) and DMF (3 ml), 1.5 equivalents of bis-picolylamine was added forming a transparent solution. 1 Equivalent $Fe(BF_4)_2{\cdot}6H_2O$ in methanol solution (5 ml) then was added in and stirred for 2 min, the resulting solution was left to slowly evaporate.

2.4.5 General Procedure for the Synthesis of [Fe(bpa)$_2$(A$_x$)$_2$] Where X=8, 11, 13)

To a solution of 1, 8-Naphthalimide compound (**A$_8$**, **A$_{11}$**, **A$_{13}$**, **A$_{14}$**) (0.05 mmol) in a methanol (5 ml), 1.5 equivalents bis-picolylamine was added forming a transparent solution. 1 equivalent of $Fe(BF_4)_2{\cdot}6H_2O$ in methanol (5 ml) was added and the resulting solution was stirred for 2 min and filtered. The orange-red filtrate was subjected to vapour diffusion of diethyl or slow evaporation of the methanol.

2.5 Crystallographic characterisation of complexes [Fe(bpa)$_2$](A$_x$)

2.5.1 Crystallographic analysis of [Fe(bpa)$_2$](A$_1$)$_2$·CH$_3$OH (1)

Vapour diffusion of diethyl ether into a methanolic solution of [Fe(**bpa**)$_2$](**A$_1$**)$_2$ resulted in red plate-like crystals of [Fe(**bpa**)$_2$] (**A$_1$**)$_2$·CH_3OH that crystallised in the monoclinic space group *P*2$_1$/*c*. The asymmetric unit contained half of one [Fe(**bpa**)$_2$]$^{2+}$ complex cation, one **A$_1$** anion, and one interstitial methanol molecule, with the remainder of the complex cation generated by an inversion centre (Figure 2-20a). The complete [Fe(**bpa**)$_2$]$^{2+}$ is shown in Figure2-20b. The Fe(II) is coordinated to two tridentate bis-picolyl (**A$_1$**) amine ligands, giving an overall N_6 coordination sphere with Fe-N bond lengths and angles consistent with a low-spin configuration (table 2-2). The Fe(II) centre adopts a distorted octahedral geometry with a distortion parameter (Σ) of 73.96° which is consistent with a LS electronic structure and other previously reported Fe(**bpa**)$_2$ systems.[116]

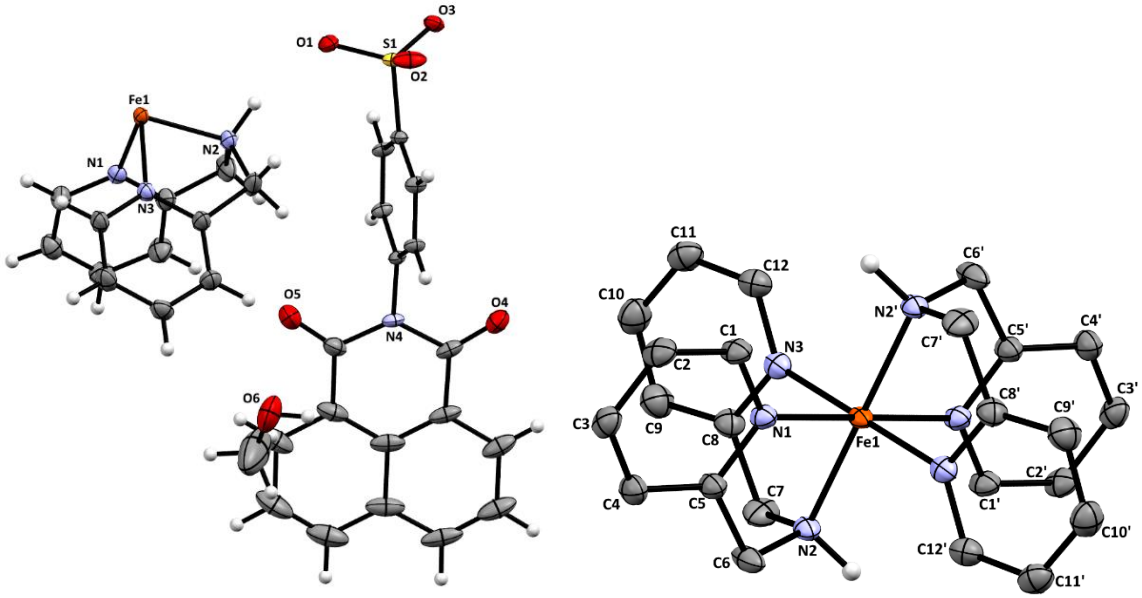

(a) (b)

Figure 2-20 (a) Asymmetric unit of the crystal structure of **1** with ellipsoids at 50% probability level; (b) configuration of the $[Fe(bpa)_2]^{2+}$ fragment, all C-bound H atoms are omitted for clarity.

As previously observed for complexes containing 1,8-naphthalimide-based anions, π-based interactions were found to be present throughout the structure. The first of these is a weak head-to-tail $\pi\cdots\pi$ stacking between a naphthalene group and an imide ring on a symmetry equivalent molecule [centroid···centroid = 4.022 Å] (Figure 2-21). The second is an anion···π interaction between oxygen atom O2 (of the electron rich SO_3^- group) of one anion and an electron deficient imide ring [O2···centroid = 2.979 Å] (Figure 2-21) of another. In addition to these desired π-interactions, two hydrogen bonding interactions are also observed involving the remaining oxygen atoms of the SO_3^- group; one from an amine NH of the bis-picolylamine ligand [N···O = 3.0111(5) Å, and ∠(N-H···O = 164(10)°], and the other from the OH group of the methanol solvate molecule [O6···O3 = 2.759(2) Å, and ∠(O6···O3 = 173(9)°] (Figure 2-22). When investigating the long-range ordering in $[Fe(\mathbf{L_1})_2]\cdot(\mathbf{A_1})_2\cdot 2CH_3OH$, these four supramolecular interactions give rise to extended layers throughout the structure (Figure 2-23) where neighbouring complex molecules are linked together through the aforementioned H-bonding and π-based interactions.

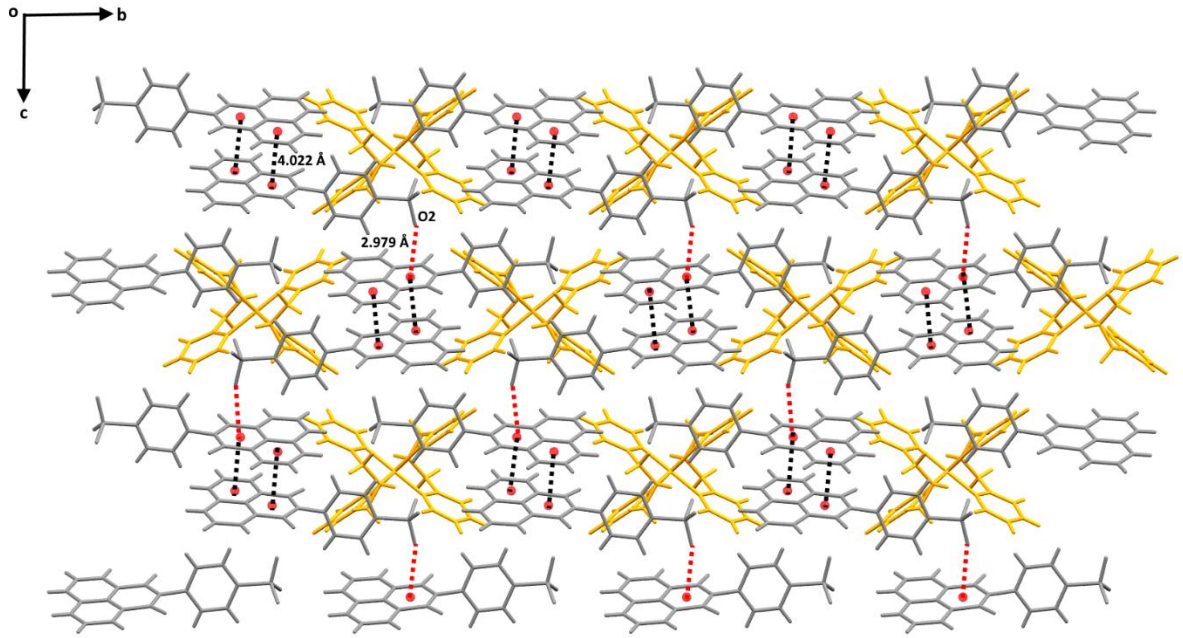

Figure 2-21 Packing interaction of **1** showing $\pi\cdots\pi$ stacking view along the *a* axis. Naphthalimide molecules are presented in grey, $[Fe(\mathbf{bpa})_2]^{2+}$ molecules are presented in yellow, solvent molecules are omitted for clarity.

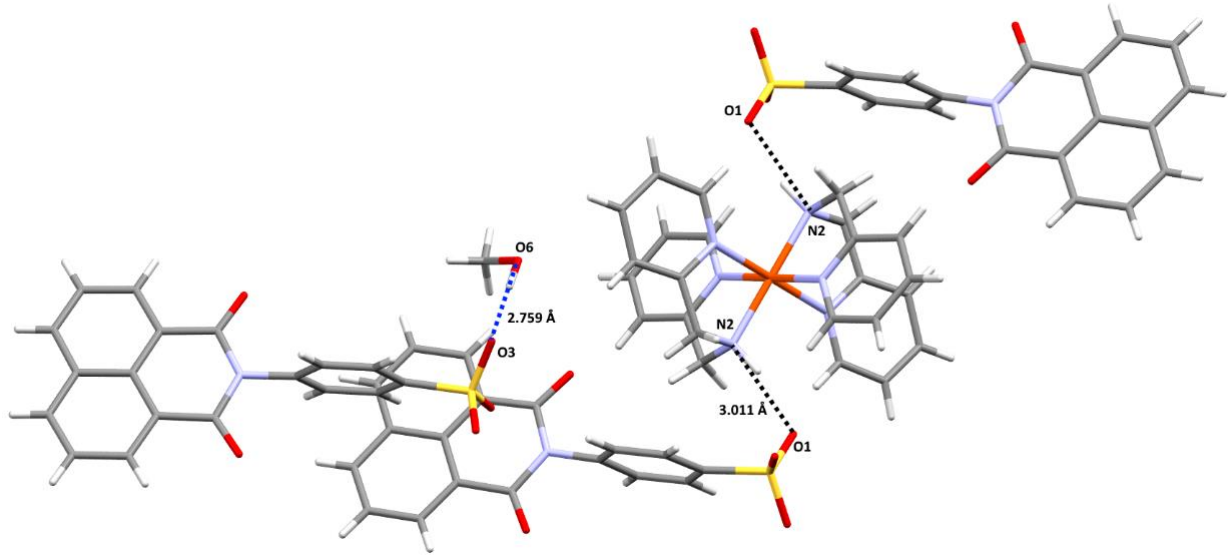

Figure 2-22 View of hydrogen-bonding interactions in **1**

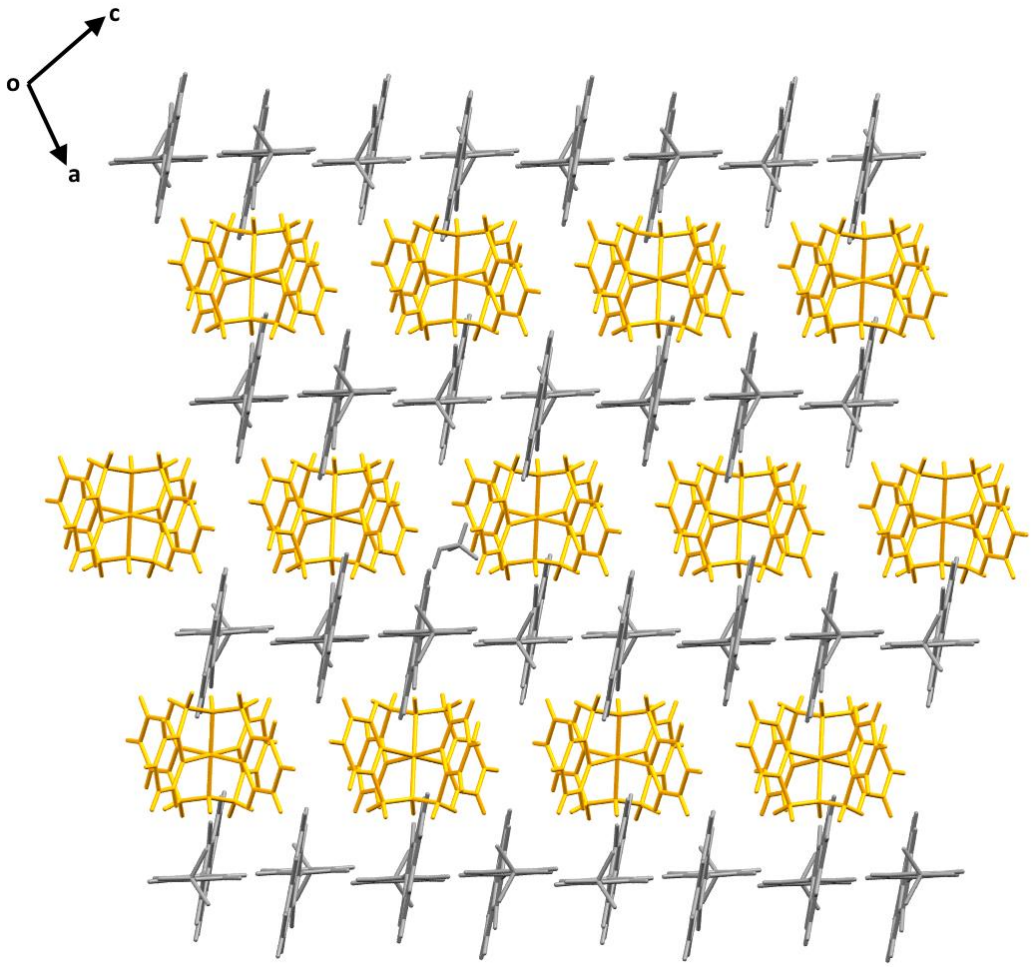

Figure 2-23 Packing interaction of **1** showing $\pi\cdots\pi$ stacking view along the *b* axis. Naphthalimide molecules are presented in grey, $[Fe(\mathbf{bpa})_2]^{2+}$ molecules are presented in yellow, solvent molecules are omitted for clarity.

2.5.2 Crystallographic Analysis of $[Fe(bpa)_2](A_2)_2{\cdot}CH_3OH$ (2)

Vapour diffusion of diethyl ether into a methanolic solution of complex **2** resulted in red plate-like crystals of $[Fe(\mathbf{bpa})_2](\mathbf{A_2})_2{\cdot}CH_3OH$ that crystallised in the triclinic space group $P\bar{1}$. The complete $[Fe(\mathbf{bpa})_2]^{2+}$ is shown in Figure2-24b. The Fe(II) centre in the $[Fe(\mathbf{bpa})_2]^{2+}$ complex cation again adopts the expected N_6 distorted octahedral coordination geometry with bond lengths, angles and distortion parameter consistent with LS Fe(II) (table 2-2). The $\mathbf{A_2}$ anion in this system now contains the electron withdrawing nitro group which in this complex is disordered over two sites (relative occupancies of 0.75 and 0.25).

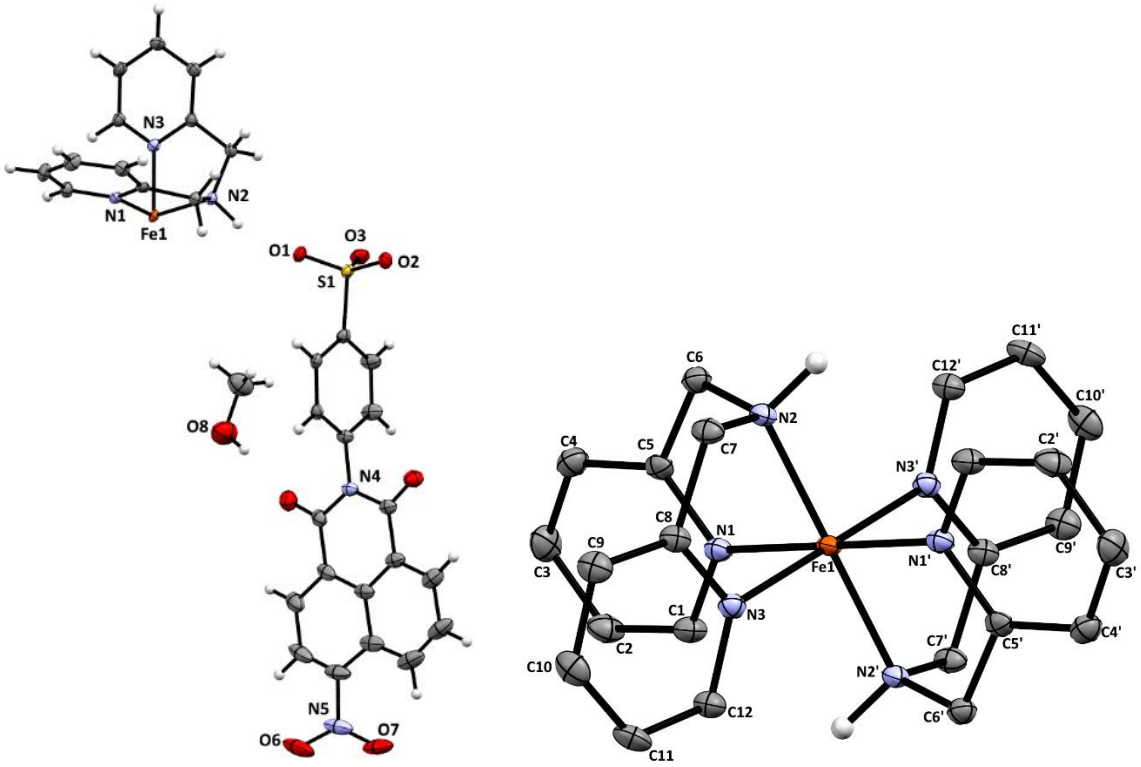

(a) (b)

Figure 2-24 (a) Molecular structure of **2** with ellipsoids at 50% probability level; (b) configuration of the $[Fe(bpa)_2]^{2+}$ fragment, all C-bound H atoms are omitted for clarity.

As π-based packing interactions are vital to this work, any disruption to the planar nature of the anion must be considered. In this structure the NO_2 functional group is twisted by 39° from the mean plane of the naphthalimide ring. Despite this additional bulk, as with **1**, π-based interactions were important for driving the long-range ordering. Off-set head-to-tail $\pi\cdots\pi$ stacking is clearly observed between the naphthalene rings of symmetry equivalent anions [centroid⋯centroid = 3.693 Å] and $SO_3\cdots\pi$ interaction between the anion and the electron deficient imide ring [O3⋯centroid = 3.306 Å] (Figure 2-25).

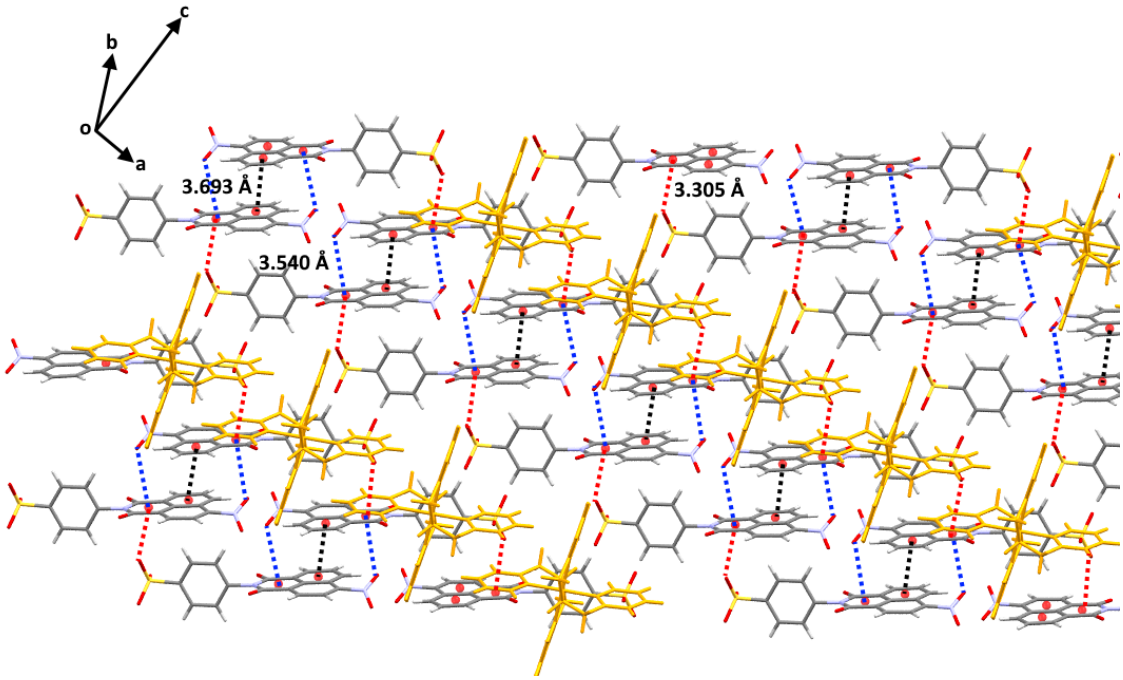

Figure 2-25 Packing interaction of **2** with $\pi\cdots\pi$ interaction. $[Fe(\mathbf{bpa})_2]^{2+}$ molecules are presented in yellow, solvent molecules are omitted for clarity.

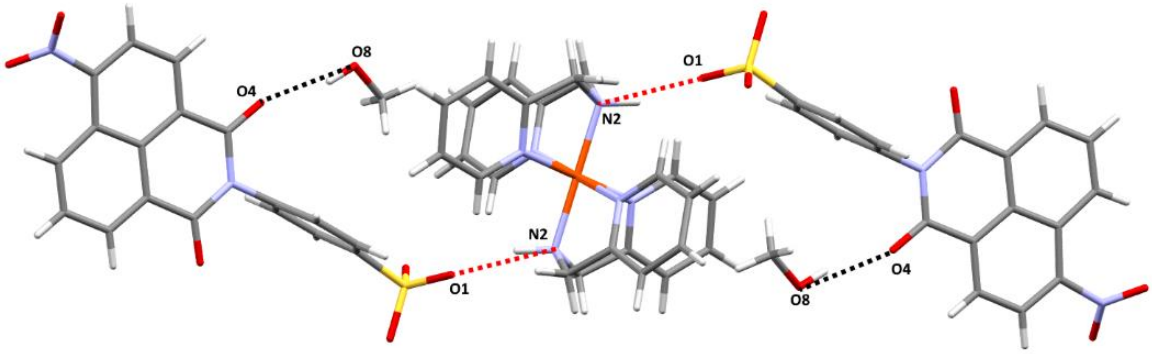

Figure 2-26 View of hydrogen-bonding interactions in **2.**

In this system the $\pi\cdots\pi$ stacking is stronger than previously observed for **2**, one potential reason for this is an additional weak interaction from an oxygen of the NO_2 group and the imide ring [O7···centroid = 3.354 Å] providing further stabilisation. In addition to this there are two hydrogen bonds present, the first between the amine NH of the bis-picolylamine ligand [N2···O1 = 2.867(2) Å, and ∠(N-H···O) = 161(12)°], and the other from the OH group of the methanol solvate molecule to an oxygen atom on the sulfonate moiety [O4···O8 = 2.840(3) Å, and ∠(O-H···O) = 167(9)°] (Figure 2-26). The overall effect is a long-range structure similar to that observed for the complex containing an unsubstituted naphthalimide anion where distinct layers of the metal complex can be observed (Figure 2-27).

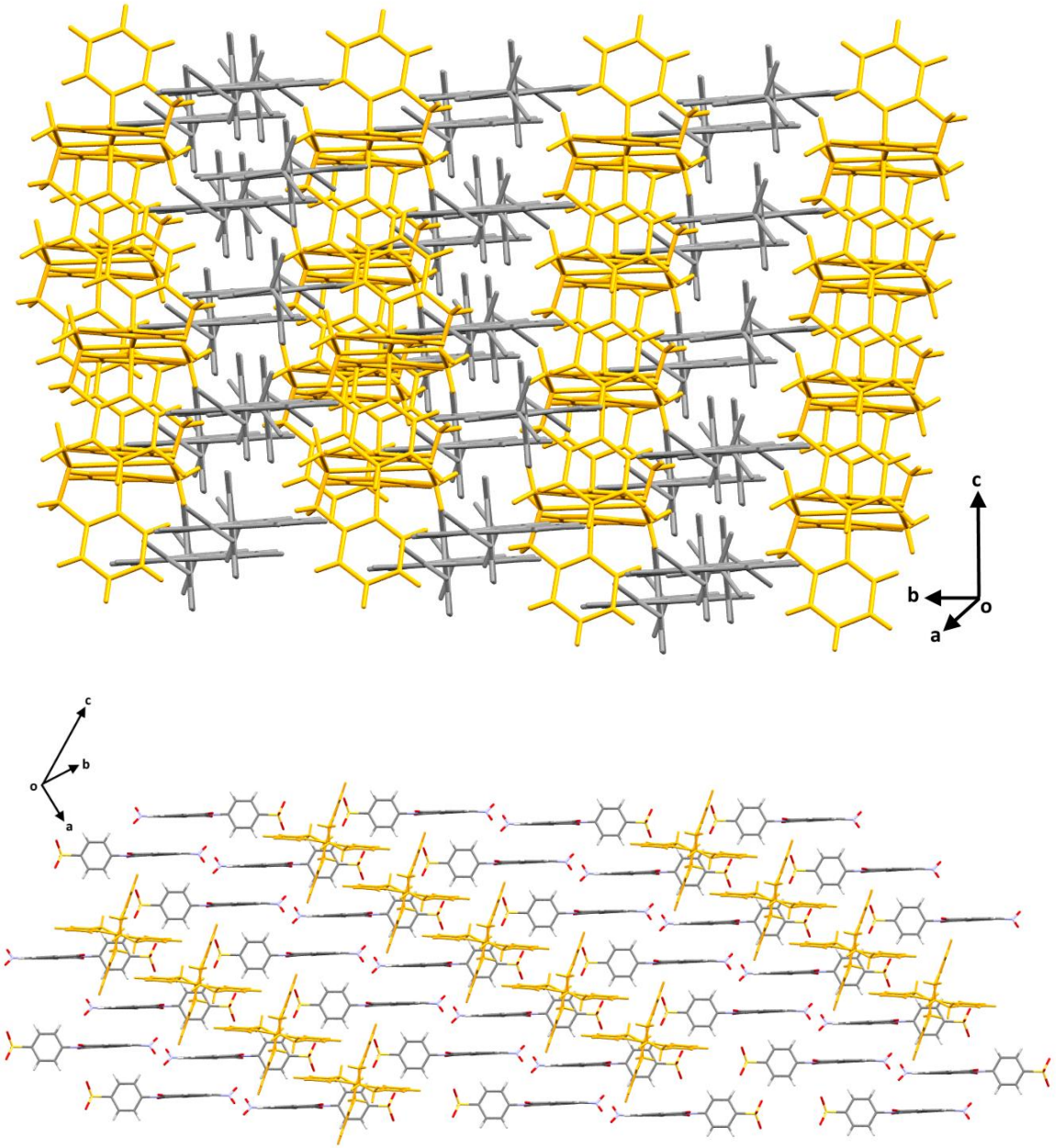

Figure 2-27 Packing interaction of **2**. Naphthalimide molecules are presented in grey, $[Fe(\mathbf{bpa})_2]^{2+}$ molecules are presented in yellow, solvent molecules are omitted for clarity.

2.5.3 Crystallographic analysis of $[Fe(bpa)_2](A_3)_2\cdot(CH_3)_2CO$ (3)

Red block-like single crystals of $[Fe(\mathbf{bpa})_2](\mathbf{A_3})_2\cdot(CH_3)_2CO$ were grown by slow evaporation of a solution of **3** in a water:acetone (4:1) solvent mixture and crystallised in the triclinic space group $P\bar{1}$ with half of one complex cation in the asymmetric unit. The complete $[Fe(\mathbf{bpa})_2]^{2+}$ is shown in Figure 2-28. The Fe(II) centre again adopted a distorted octahedral N_6 coordination geometry (Σ = 70.74°) with bond lengths and angles consistent with LS Fe(II) (Table2-2).

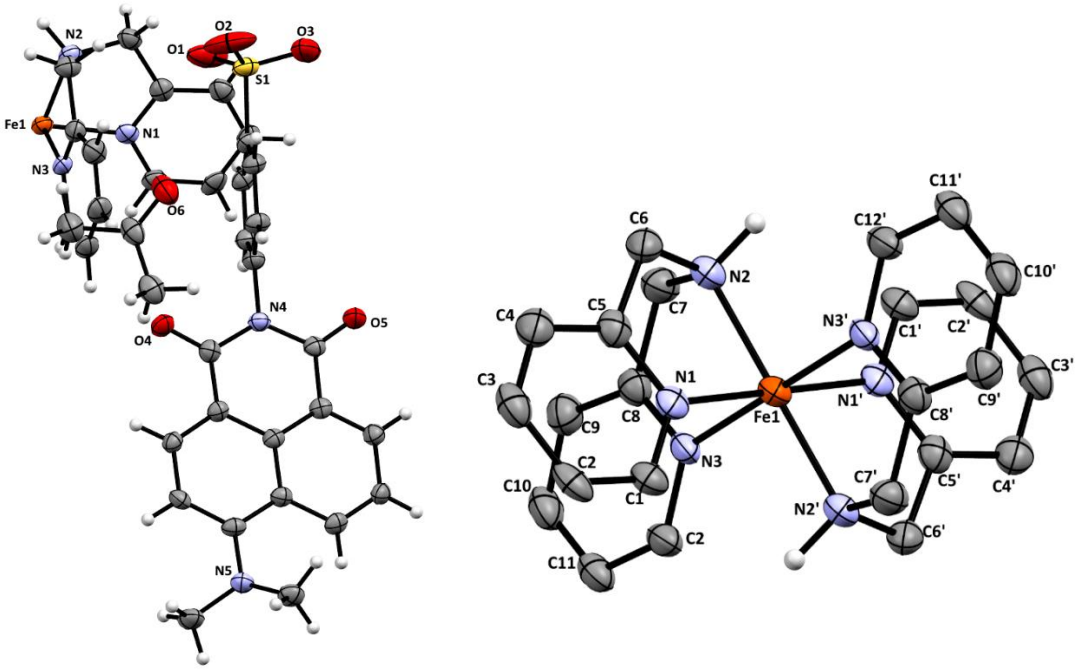

(a) (b)

Figure 2-28 (a) Asymmetric molecular structure of **3** with ellipsoids at 50% probability level.(b) Right: configuration of the $[Fe(\mathbf{bpa})_2]^{2+}$ fragment, all C-bound H atoms are omitted for clarity.

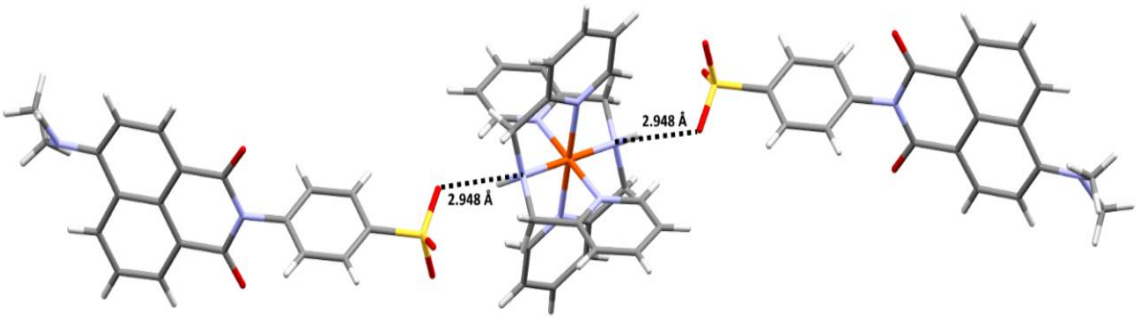

Figure 2-29 View of hydrogen-bonding interactions in **3**.

In this system the mean plane of the dimethyl amine substituent is twisted by 43° from the mean plane of the naphthalimide ring. Like **1** and **2**, the long-range ordering in **3** also involved hydrogen-bonding interactions between NH from bis-picolylamine group and neighbouring oxygen atoms from the sulfanilic group [N2···O2 = 2.984(5) Å, bond angle ∠(N-H···O = 152(6)°)]. (Figure 2-29). Similar to the crystal packing of complexes **1** and **2**, in complex **3** π-based interactions dominated the long-range ordering, where head-to-tail π stacking formed layers between two naphthalimide units [centroid···centroid = 3.616 Å] (Figure 2-30). Apart from the classic π-based interactions observed in the naphthalimide anion, π-stacking is also observed between two aromatic rings from neighbouring bis-picolylamine ligands [centroid···centroid = 3.663 Å] (Figure 2-31).

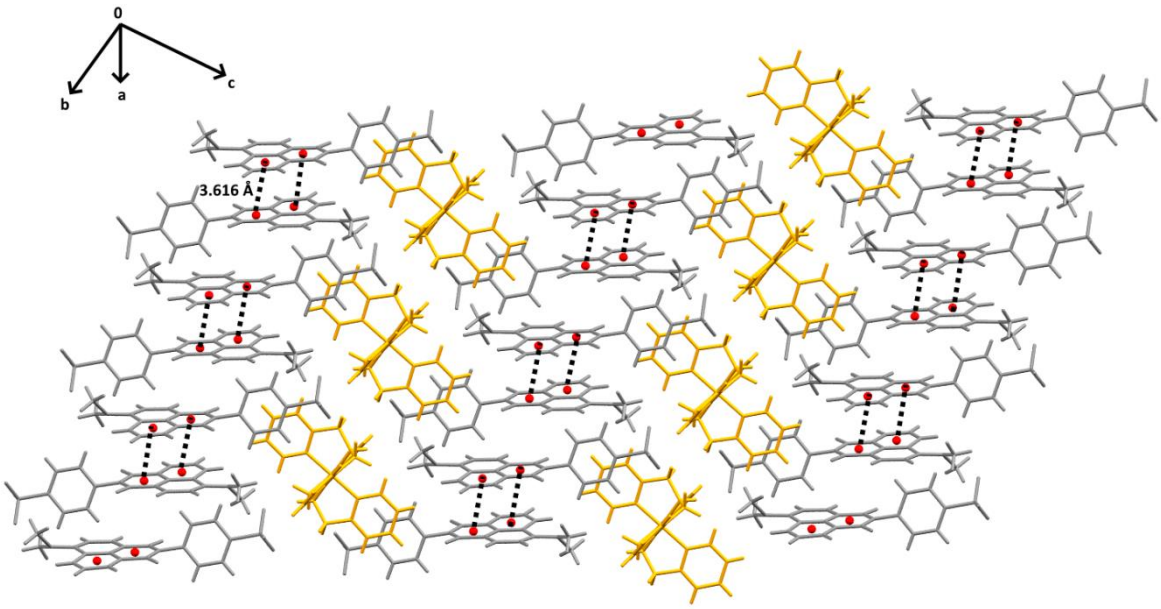

Figure 2-30 $\pi\cdots\pi$ stacking interaction between naphthalimides of **3.** Naphthalimide molecules are presented in grey, $[Fe(\mathbf{bpa})_2]^{2+}$ molecules are presented in yellow, solvent molecules are omitted for clarity.

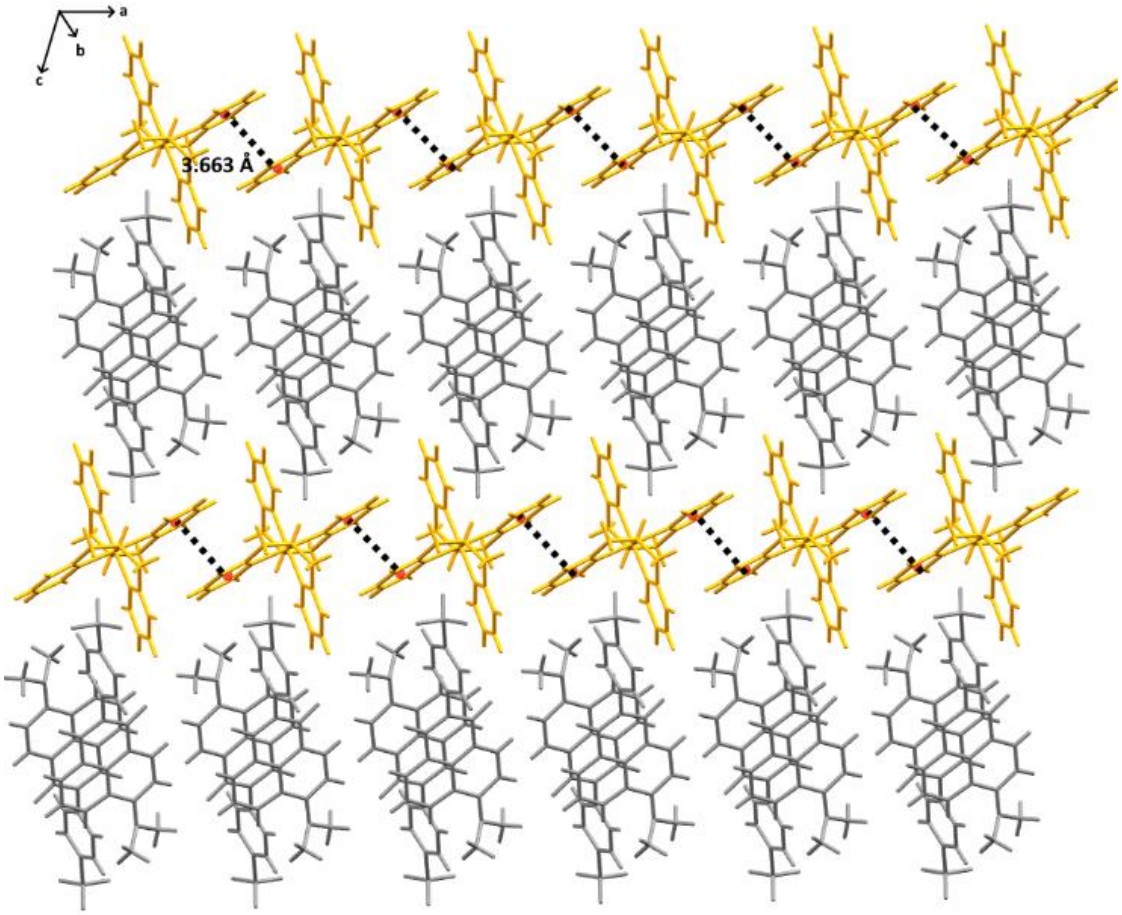

Figure 2-31 $\pi\cdots\pi$ stacking interaction between bis-picolylamine of **3.** Naphthalimide molecules are presented in grey, $[Fe(\mathbf{bpa})_2]^{2+}$ molecules are presented in yellow, solvent molecules are omitted for clarity.

2.5.4 Crystallographic analysis of [Fe(bpa)$_2$](A$_5$)·DMF (4)

Small orange-red plate-like single crystals of [Fe(**bpa**)$_2$](**A$_5$**)·DMF were grown by slow evaporation of a solution of compound **4** in a DMF:methanol (1:9) solvent mixture. They crystallised in the triclinic space group $P\bar{1}$ with the asymmetric unit containing two half [Fe(**bpa**)$_2$]$^{2+}$ cations (each consisting of the Fe(II) metal centre and one ligand). The solvent mask routine in Olex2 was required to mask electron density from severely disordered solvents (Figure 2-32). The two Fe(II) centres are both N6 distorted octahedral (Σ_{Fe1} = 75.05)°, Σ_{Fe1} = 93.40°) with bond lengths and angles consistent with LS Fe(II).

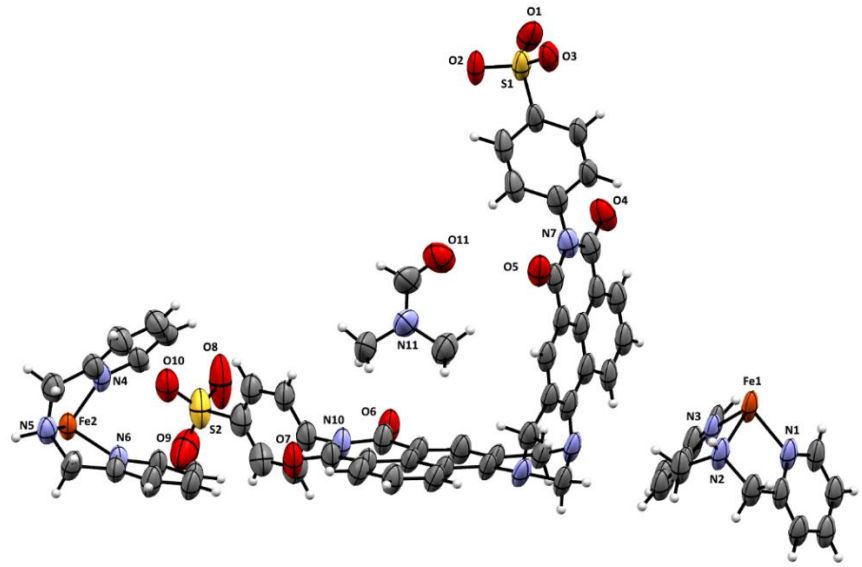

(a)

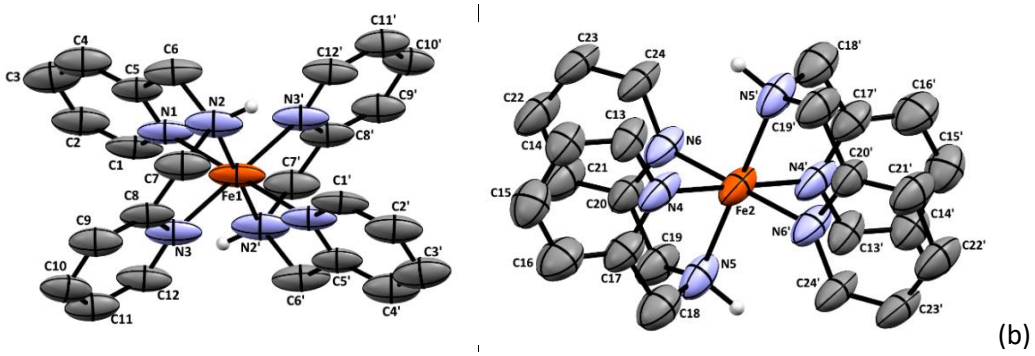

(b)

Figure 2-32 (a) Asymmetric unit of the crystal structure of **4** with ellipsoids at 50% probability level; (b) configuration of two [Fe(bpa)2]2+ fragments, all C-bound H atoms are omitted for clarity.

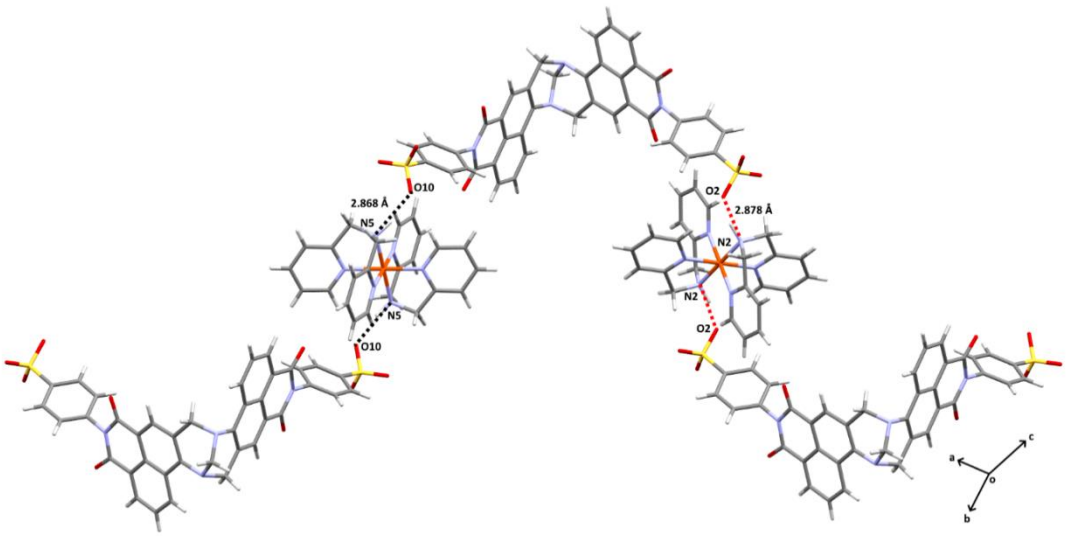

Figure 2-33 View of hydrogen-bonding interactions in **4**. Hydrogen bonds involving O10 are shown as black dotted lines, while those involving O2 are shown as red dotted lines.

The Tröger's-base anions and Fe(II) complex cations were connected through hydrogen bonding interactions between NH from the bis-picolylamine group and neighbouring SO_3^- oxygen atoms [N5···O10 = 2.868(6) Å, bond angle ∠(N5-H···O10 = 148.18(11)° and N2···O2 = 2.878(7) Å, bond angle ∠(N2-H···O2 = 148.46(16)°)] (Figure 2-33). The inclusion of the fused "V-shaped" Tröger's base anion imparts a significant structure directing effect. This is particularly noticeable when viewing the H-bonding interactions between the NH of the picolylamine and the SO_3^- oxygen atoms where a zig-zag chain propagates through the crystal lattice (Figure 2-34). Neighbouring chains interact through non-classical CH hydrogen bonding between pyridyl CH groups and SO_3^- groups [C31···O4 = 3.132(7) Å, bond angle ∠(C-H···O = 147(9)°)], and π-stacking between pyridyl rings and the naphthalimide groups on neighbouring chains [centroid1···centroid2 = 3.695 Å; centroid4···centroid5 = 3.634 Å], resulting in off-set chains [centroid2···centroid3 = 3.832 Å] (Figures 2-34 & 35). The overall long-range ordering in this molecule shows an obvious structure directing influence brought about by the Tröger's base moiety.

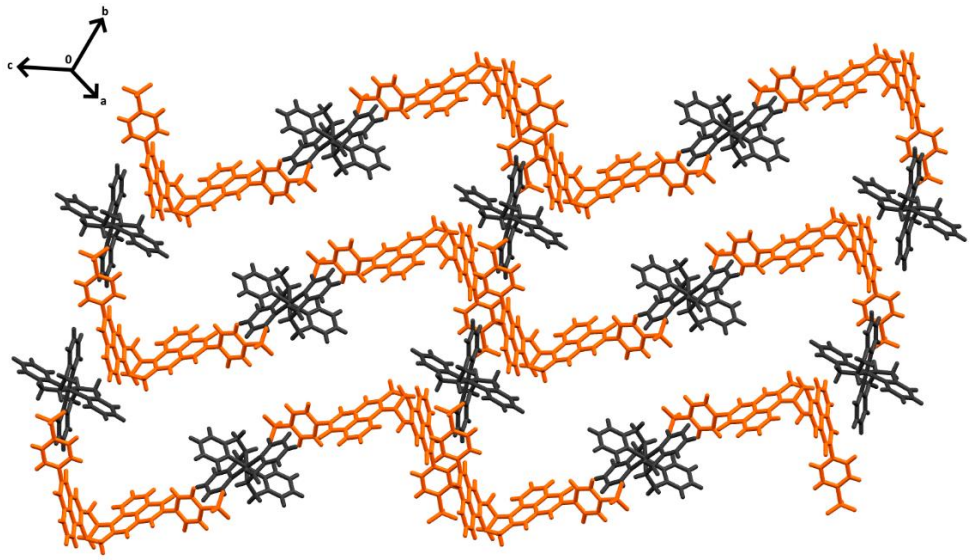

Figure 2-34 Packing interaction network of **4**. Tröger's-base molecules are presented in orange, $[Fe(\mathbf{bpa})_2]^{2+}$ molecules are presented in grey, solvent molecules are omitted for clarity.

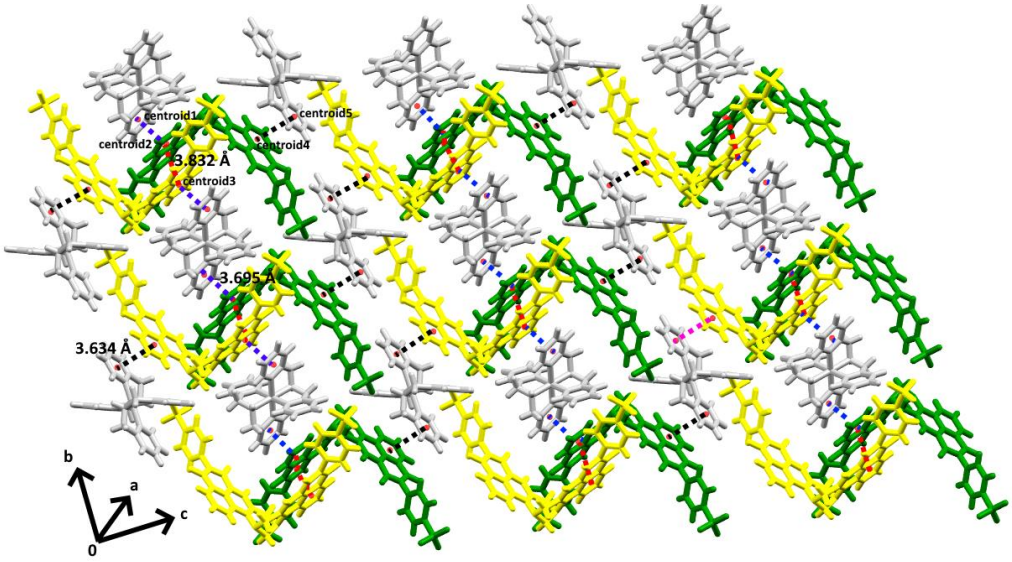

Figure 2-35 $\pi\cdots\pi$ stacking interaction between bis-picolylamine of **4.** Tröger's-base molecules are presented in yellow and green, $[Fe(\mathbf{bpa})_2]^{2+}$ molecules are presented in grey, solvent molecules are omitted for clarity

2.5.5 Crystallographic analysis of $[Fe(bpa)_2](A_6)_2{\cdot}CH_3OH$ (5)

Vapour diffusion of diethyl ether into the methanolic reaction solution resulted in dark orange plate-like crystals of $[Fe(\mathbf{bpa})_2](\mathbf{A_6})_2{\cdot}CH_3OH$ that crystallised in the triclinic space group $P\bar{1}$. The Fe(II) centre in the $[Fe(\mathbf{bpa})_2]^{2+}$ complex cation again adopted an octahedral coordination geometry with bond lengths, angles and distortion parameter (Σ = 76.04°) consistent with LS Fe(II) (table 2-2). The $\mathbf{A_6}$ anion in this system has been selected because it contains the SO_3^- anionic group at the meta position of the phenyl ring in order to investigate how this subtle change can

alter the crystal engineering of the system. The naphthalimide ring of **A_6** is disordered over two sites with relative occupancies of 0.56 and 0.44. Only one methanol molecule was modelled and the solvent mask routine in Olex2 was required to remove the rest severely disordered methanol molecules (Figure 2-36).

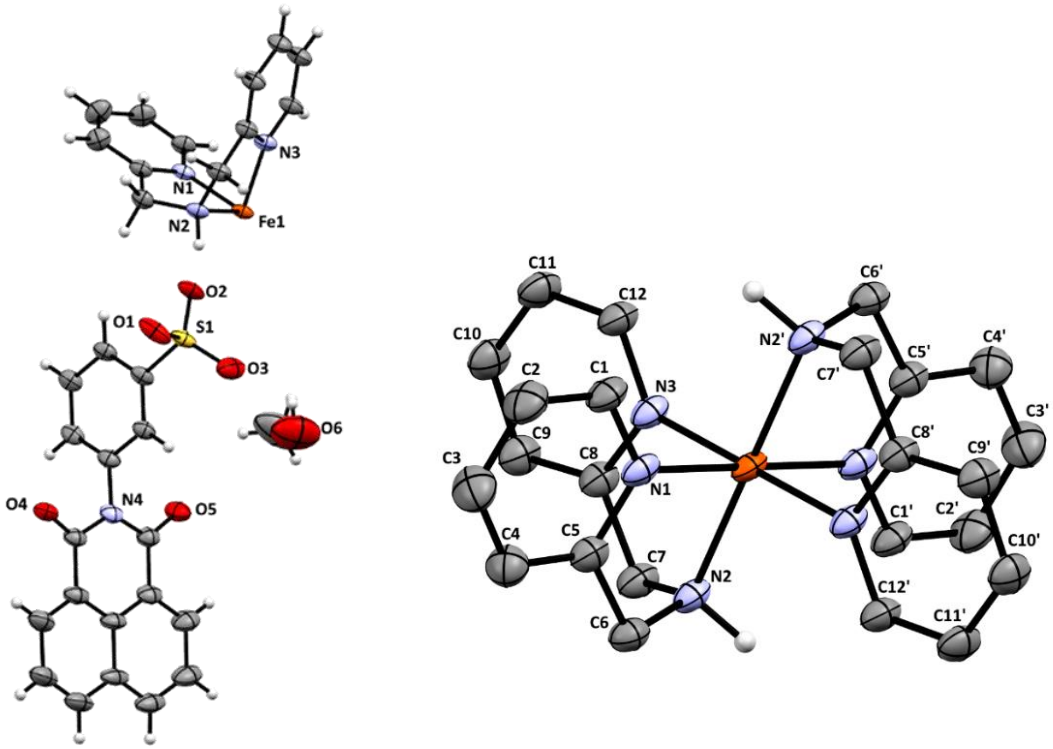

(a) (b)

Figure 2-36 (a) Asymmetric unit of the crystal structure of 5 with ellipsoids at 50% probability level; (b) configuration of the $[Fe(bpa)_2]^{2+}$ fragment, all C-bound H atoms are omitted for clarity.

As in the previous structures discussed in this chapter, the formation of layers within the crystals was driven by classic head-to-tail π-π stacking interactions between the naphthalene rings on neighbouring **A_5** molecules [centroid⋯centroid 3.644 Å], as well as strong anion⋯π interactions [SO_3⋯centroid 3.024 Å] between the sulfonate substituent and the imide ring on a neighbouring molecule (Figure 2-37). Hydrogen bonding interactions are similar to the previous structures where an interaction is observed between the NH from bis-picolylamine group to the neighbouring sulfonate group [N2⋯O2=2.841(3) Å, bond angle ∠(N2-H⋯O2=152(7)°]. Additionally, there is a hydrogen bond between the OH group of the methanol solvate to a sulfonate oxygen atom [O6⋯O3 = 2.811(7) Å, and ∠(O6-H⋯O3) = 133(13)°] (Figure 2-38).

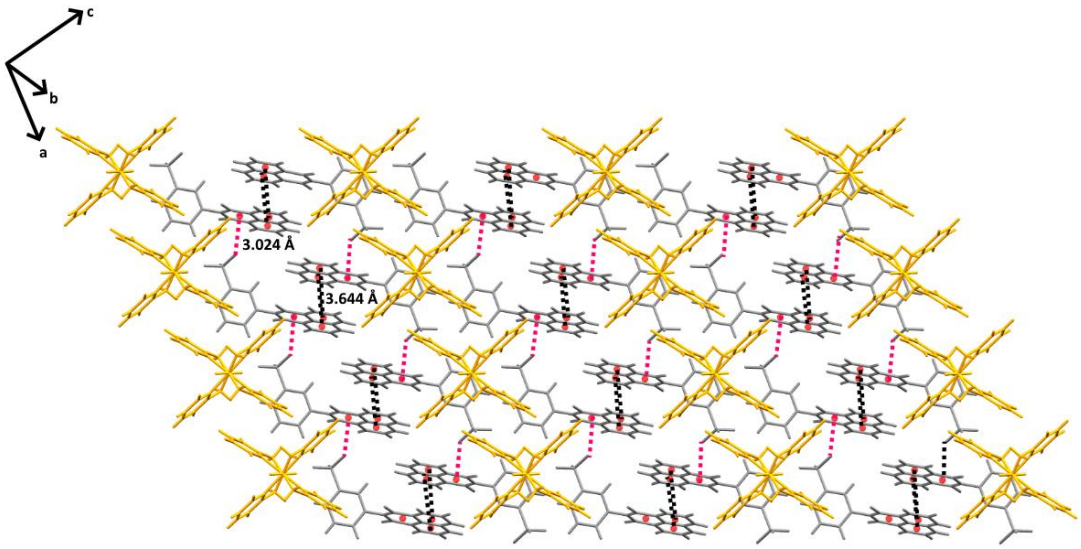

Figure 2-37 Packing interaction of **5** showing $\pi\cdots\pi$ stacking (pink dashed lines from sulfonate to neighbouring naphthalimide ring which is 3.024 Å; black dashed line is between alternate naphthalimide rings which is 3.644 Å). Naphthalimide molecules are presented in grey, [Fe(**bpa**)$_2$]$^{2+}$ molecules are presented in yellow, solvent molecules are omitted for clarity.

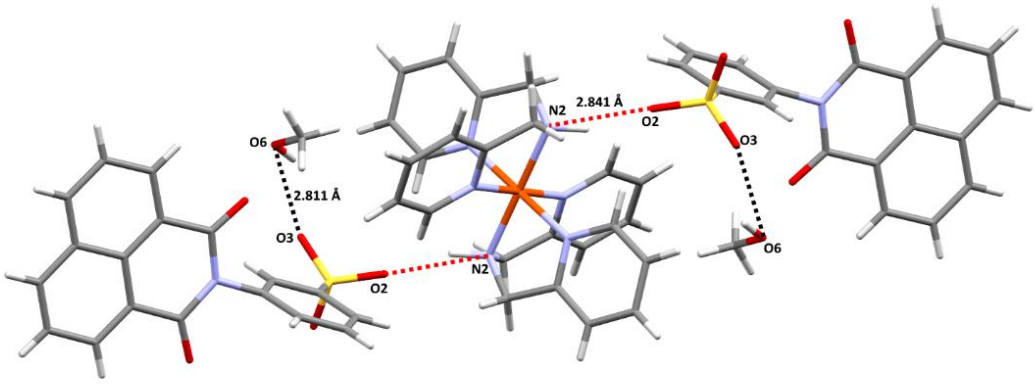

Figure 2-38 View of hydrogen-bonding interactions in **5**

2.5.6 Crystallographic analysis of [Fe(bpa)$_2$](A$_8$)$_2$ (6)

Dark red plate-like single crystals of [Fe(**bpa**)$_2$](**A$_8$**)$_2$ (**6**) were grown by slow evaporation of a methanol solution of **6** and crystallised in the triclinic space group $P\bar{1}$ with the unit cell containing one formula unit of **6** (Figure 2-39). The dimethyl amino functional group in **A$_8$** is disordered over two sites of equal occupancy. The solvent mask routine in Olex2 was required to mask the contribution from a severely disordered methanol molecule. The Fe(II) centre in the [Fe(**bpa**)$_2$]$^{2+}$ complex cation again adopted an octahedral coordination geometry with bond lengths, angles and distortion parameter (Σ = 68.36°) consistent with LS Fe(II) (table 2-2).

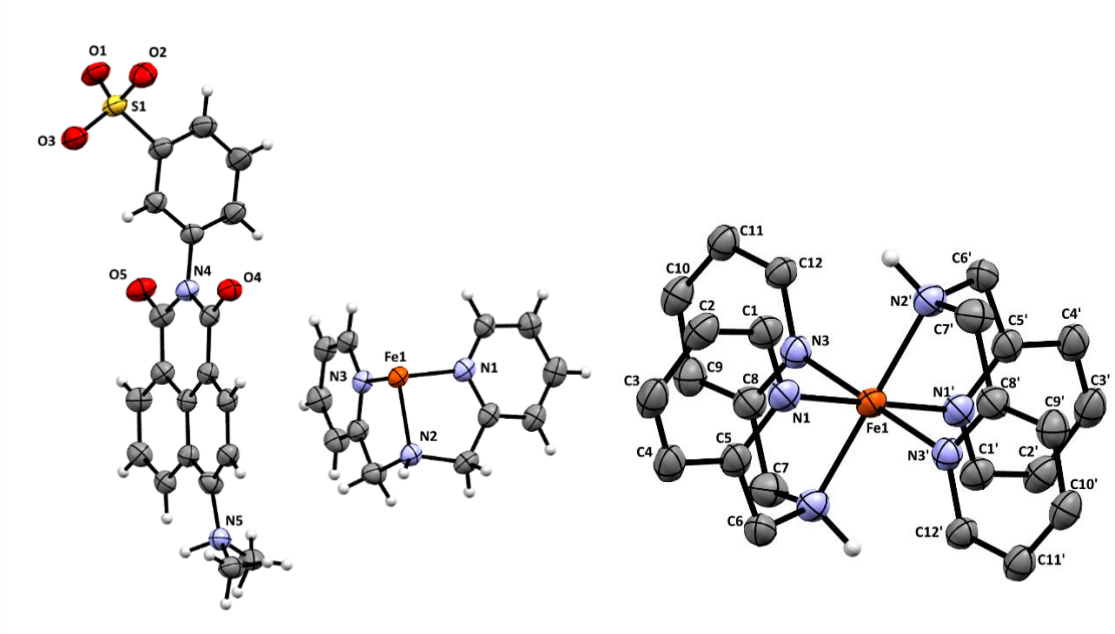

(a) (b)

Figure 2-39 (a) Asymmetric unit of the crystal structure of **6** with ellipsoids at 50% probability level; (b) Right: configuration of the [Fe(bpa)2]2+ fragment, all C-bound H atoms are omitted for clarity.

Hydrogen bonding patterns similar to those seen in the previous structure were observed, with an interaction between the NH from bis-picolylamine group to the neighbouring sulfonate [N2···O1 = 2.888(3) Å, bond angle ∠(N2-H···O1 = 161(8)°] (Figure 2-40). In this structure the $N(Me)_2$ functional group was twisted by 38° from the mean plane of the naphthalimide ring. The π-stacking interactions occur not only between pairs of naphthalene rings but also between the sulfonate phenyl rings and naphthalene rings. This results in head-to-tail π-stacking interactions between the alternated naphthalene rings [centroid−centroid 3.649 Å] and also π-stacking interactions involving neighbouring sulfonate phenyl rings [centroid−centroid 3.865 Å] along the vertical dimension. Additionally, there is also π-stacking interaction between naphthalene rings and the pyridinyl rings in the complex [centroid···centroid 3.599 Å] (Figure 2-41).

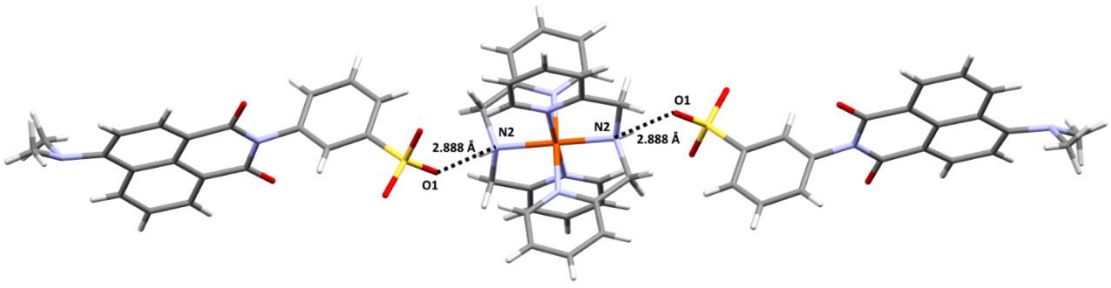

Figure 2-40 View of hydrogen-bonding interactions in **6**

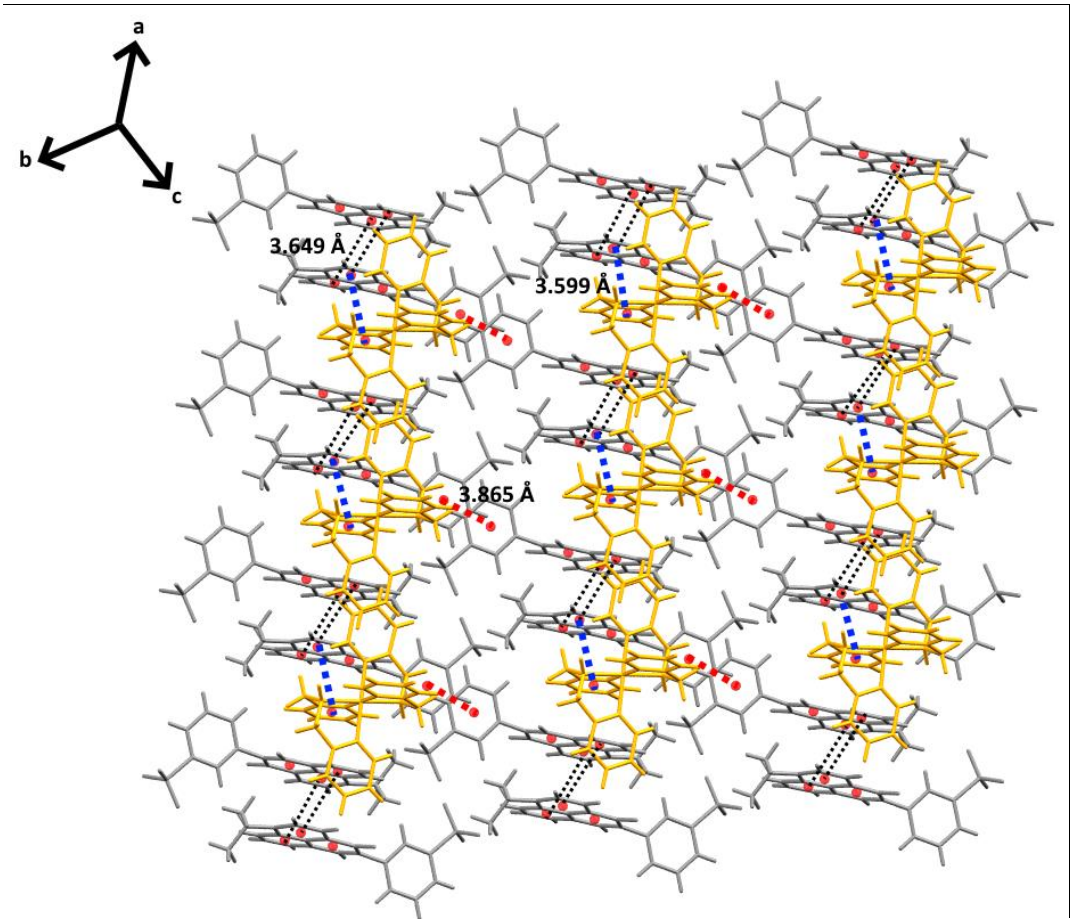

Figure 2-41 Packing interaction of **6** showing $\pi\cdots\pi$ stacking (black dashed line is 3.649 Å; Blue dashed line is 3.599 Å; red dashed line is 3.865 Å). Naphthalimide molecules are presented in grey, $[Fe(\mathbf{bpa})_2]^{2+}$ molecules are presented in yellow, solvent molecules are omitted for clarity.

2.5.7 Crystallographic analysis of $[Fe(bpa)_2](A_9)_2\cdot 5CH_3OH$ (7)

Vapour diffusion of diethyl ether into the methanolic reaction solution resulted in large, dark red plate-like crystals of $[Fe(\mathbf{bpa})_2](\mathbf{A_9})_2\cdot 5CH_3OH$ that crystallised in the triclinic space group $P\bar{1}$ (Figure 2-42). The Fe(II) centre in the $[Fe(\mathbf{bpa})_2]^{2+}$ complex cation again adopted an octahedral coordination geometry with bond lengths, angles and distortion parameter (Σ = 72.58°) consistent with LS Fe(II) (table 2-2). Interestingly, in this complex the Fe(II) is not situated on a centre of inversion, as the picolyl NH groups are in a *cis* arrangement. The $\mathbf{A_{10}}$ anion in this system now contains a naphthalene moiety instead of a phenyl ring, which increases the ability of the anion to participate in π-stacking, as well as moving the position of the SO_3^- group further from the naphthalimide ring.

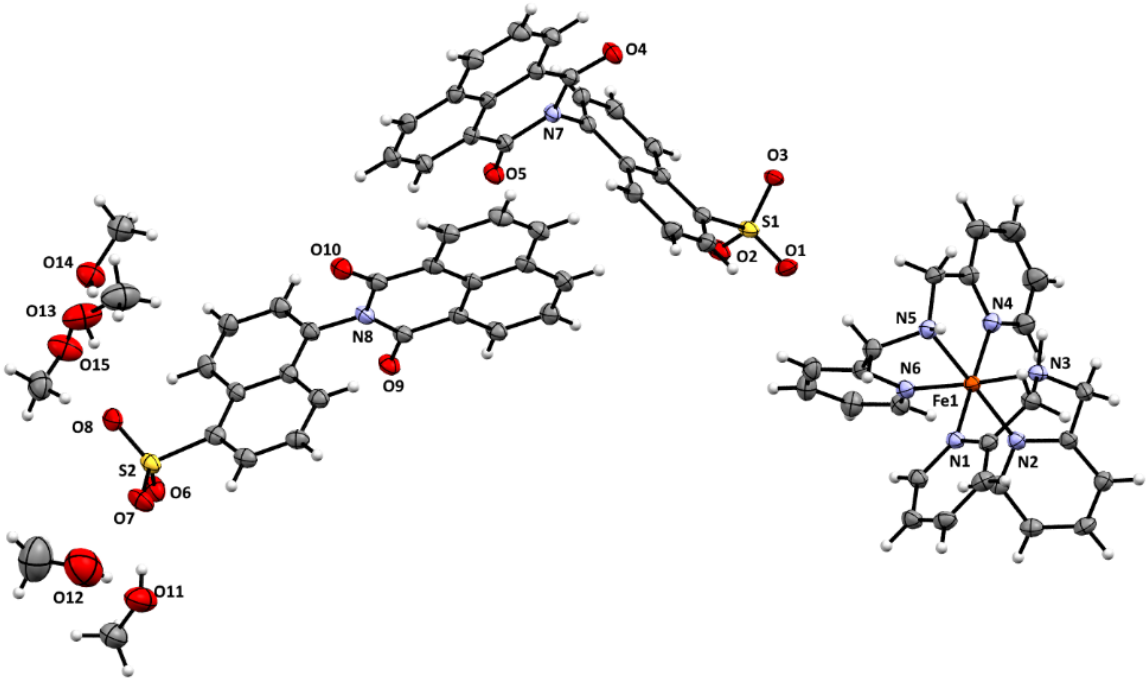

Figure 2-42 Asymmetric unit of the crystal structure of **7** with ellipsoids at 50% probability level.

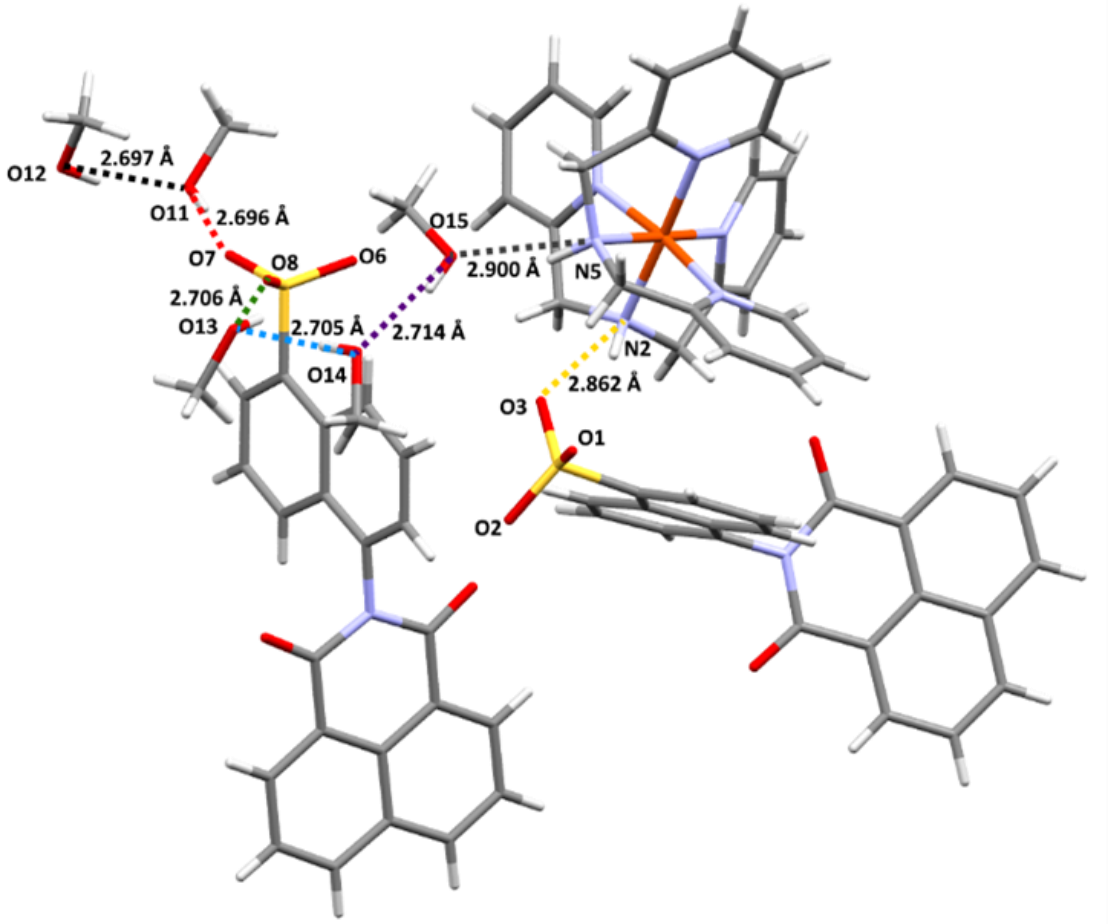

Figure 2-43 View of hydrogen-bonding interactions in **7.**

Unlike in the majority of the previous structures, the methanol solvate molecules play an important role in long-range ordering, as they form a bridge between the naphthalimide anions

and the $[Fe(\mathbf{bpa})_2]^{2+}$ complex cations. The cation is involved in two hydrogen bonding interactions, one from each of the two NH groups from the bis-picolylamine ligands. One is a direct hydrogen bond with a neighbouring oxygen atom from a sulfonate group [N2···O3 = 2.862(3) Å, bond angle ∠(N-H···O = 146.98(9)°]. The other is to the oxygen atom acceptor of a methanol solvate [N5···O15 = 2.900(3) Å and ∠(N-H···O) = 154.38(6)°], this OH group then acts as a donor to a second neighbouring methanol oxygen [O11···O12 = 2.697(6) Å and ∠(OH···O) = 164.30(11)°; O15···O14 = 2.714(3) Å; ∠(OH···O) = 162.96(7)°; O14···O13 = 2.705(3) Å and ∠(OH···O) = 164.30(7)°], which itself acts as a donor to the sulfonate oxygen [O8···O13 = 2.706(3) Å and ∠(OH···O) = 147.79(6)°] (Figure 2-43). Head-to-tail π-based interactions are also observed between two neighbouring naphthalimide rings [centroid···centroid = 3.624 Å]. Additionally, head-to-head π-based interactions to the opposite faces of the naphthalimides [centroid···centroid = 3.668 Å] result in short π-stacks of four naphthalimides throughout the structure (Figure 2-44).

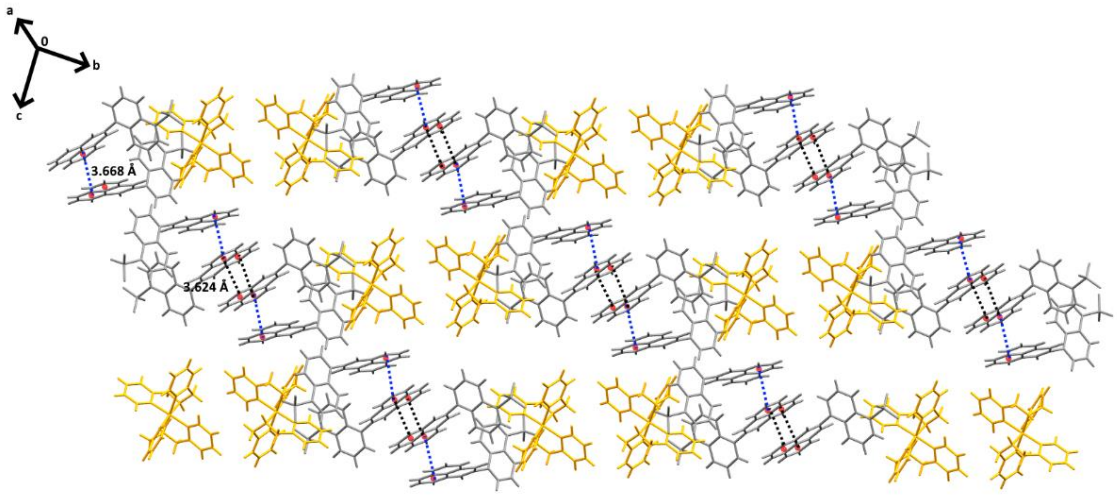

Figure 2-44 Packing interaction of **7** showing $\pi\cdots\pi$ stacking (black dashed line is 3.624 Å; Blue dashed line is 3.668 Å). Naphthalimide molecules are presented in grey, $[Fe(\mathbf{bpa})_2]^{2+}$ molecules are presented in yellow, solvent molecules are omitted for clarity

2.5.8 Crystallographic analysis of $[Fe(bpa)_2](A_{11})_2{\cdot}H_2O{\cdot}CH_3OH$ (8)

Red plate-like single crystals of $[Fe(\mathbf{bpa})_2](\mathbf{A_{11}})_2{\cdot}H_2O{\cdot}CH_3OH$ were grown by slow evaporation of a solution of **8** in a methanol:water (1:1) solvent mixture and crystallised in the triclinic space group $P\bar{1}$ with the unit cell containing one $[Fe(\mathbf{bpa})_2](\mathbf{A_{11}}){\cdot}H_2O{\cdot}CH_3OH$ formula unit (Figure 2-45). The asymmetric unit contained one anion and half of the $[Fe(\mathbf{bpa})_2]^{2+}$ cation with the other half generated by a centre of inversion situated on the Fe(II). Again the Fe(II) centre in the $[Fe(\mathbf{bpa})_2]^{2+}$ complex cation again adopts an octahedral coordination geometry with bond lengths, angles and distortion parameter (Σ=94.8°) consistent with LS Fe(II) (table 2-2).

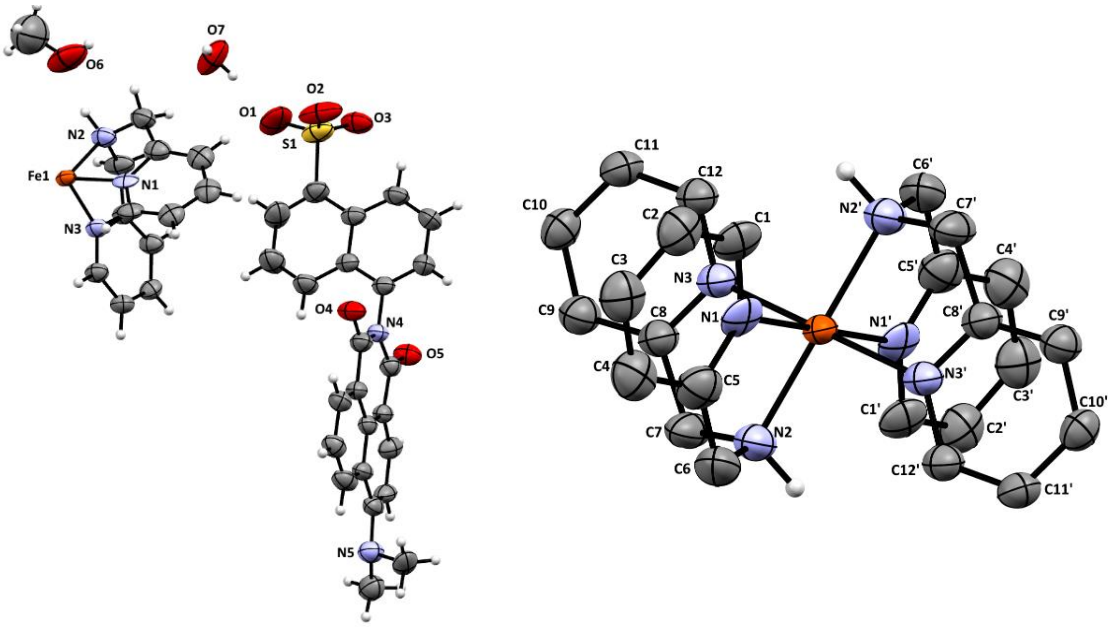

(a) (b)

Figure 2-45 (a) Asymmetric unit of the crystal structure of **8** with ellipsoids at 50% probability level. (b) Configuration of the $[Fe(\mathbf{bpa})_2]^{2+}$ fragment, all C-bound H atoms are omitted for clarity.

Methanol and water play crucial roles in the hydrogen bonding observed in the long-range ordering of this compound. Specifically, the naphthalimide anions are arranged into dimers through hydrogen bonding between two methanol molecules and two naphthalimide anions [O2···O7 = 2.940(8) Å, ∠(O-H···O = 105(11)°; O1···O7 = 2.664(12) Å, ∠(O-H···O = 168(12)°]. These dimers are then connected to the Fe^{II} complex through hydrogen bonding interactions between the interstitial water [N2···O6 = 2.881(6) Å, ∠(N-H···O=160(9)°; O2···O6 = 2.709(9) Å, ∠(OH···O=126(10)°] (Figure 2-46). In this structure the $N(Me)_2$ functional group was twisted by 42° from the mean plane of the naphthalimide ring however, the anions still participate in off-set head-to-tail $\pi\cdots\pi$ stacking between the naphthalene rings of symmetry equivalent anions [centroid−centroid = 3.618 Å] (Figure 2-47). In addition to the standard $\pi\cdots\pi$ stacking interaction, there is another edge-to-face π-based interaction from the CH of the naphthalene sulfonate ring to a neighbouring naphthalimide ring [CH···centroid = 2.913 Å] (Figure 2-47). The overall effect is a long-range packing driven by both hydrogen bonding and π stacking that results in cation-anion-cation layering and large spacing between complex molecules.

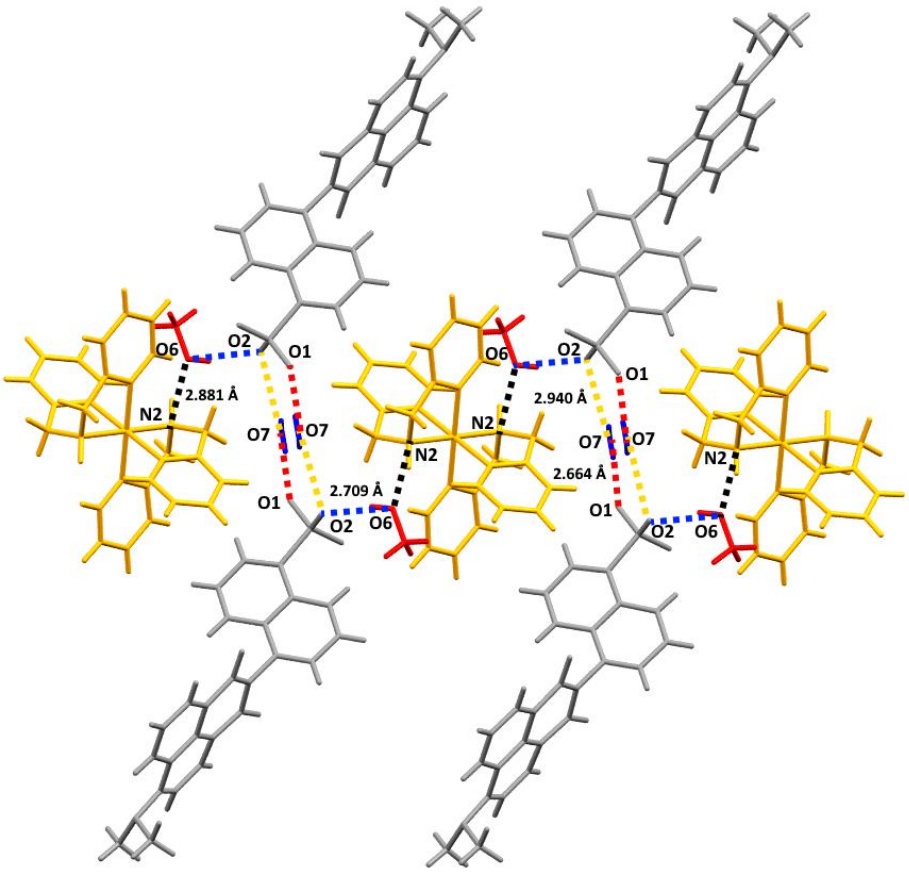

Figure 2-46 View of hydrogen-bonding interactions in **8**

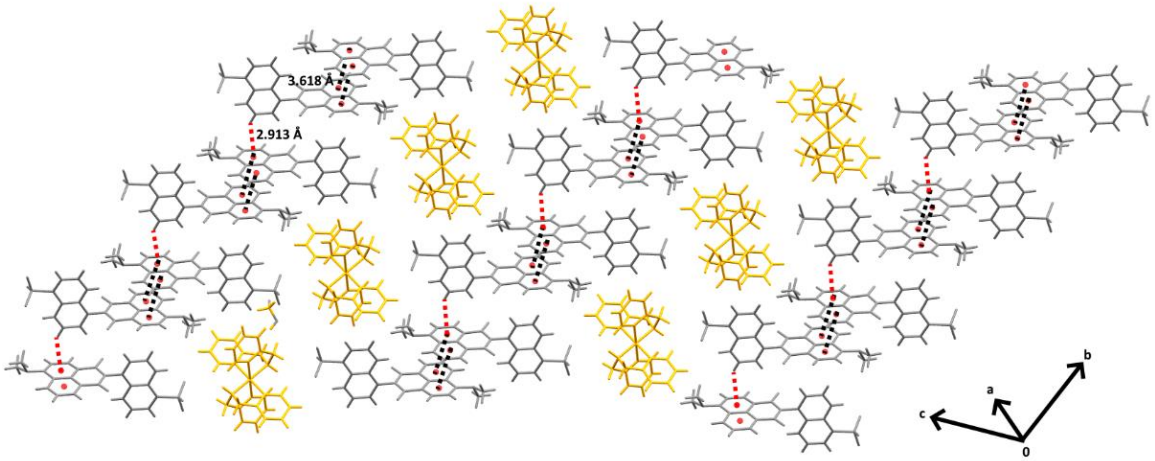

Figure 2-47 Packing interaction of **8** showing $\pi\cdots\pi$ stacking. Naphthalimide molecules are presented in grey, [Fe(**bpa**)$_2$]$^{2+}$ molecules are presented in yellow, solvent molecules are omitted for clarity.

2.5.9 Crystallographic analysis of [Fe(bpa)$_2$](A$_{12}$)$_2$·0.66H$_2$O (9)

Vapour diffusion of diethyl ether into the methanolic reaction solution of **9** resulted in red plate-like crystals of [Fe(**bpa**)$_2$](**A$_{12}$**)$_2$·0.66H$_2$O that crystallised in the monoclinic space group *P*2/*c* with the asymmetric unit containing one [Fe(**bpa**)$_2$]$^{2+}$ cation, however two crystallographically

independent $[Fe(\mathbf{bpa})_2]^{2+}$ cations are present (each as one half with the other half generated by a 2-fold axes operation forming the cis NH_2 group) (Figure 2-48).

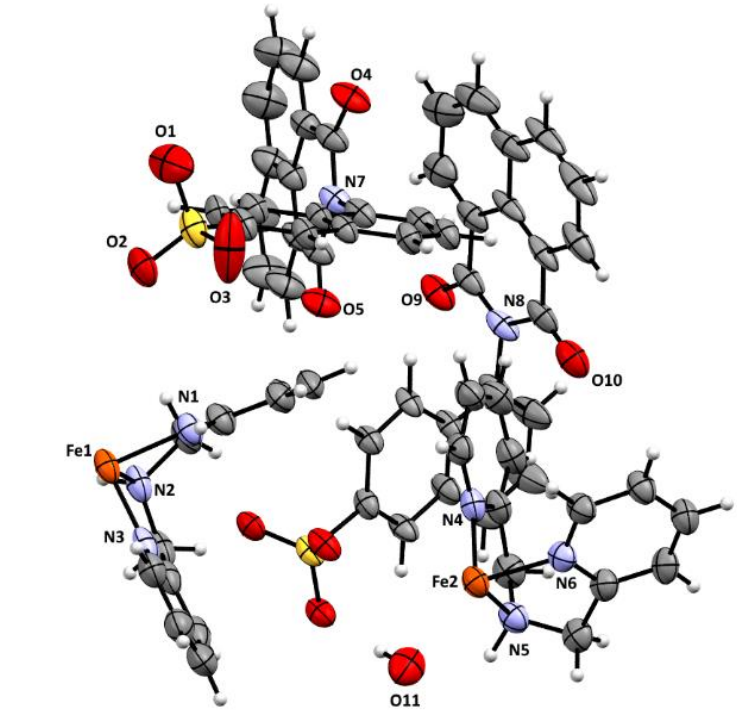

(a)

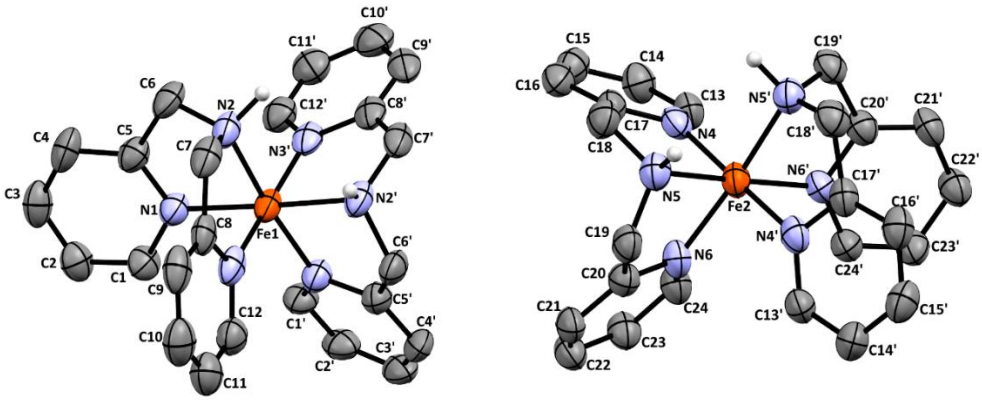

(b)

Figure 2-48 (a) Asymmetric unit of the crystal structure of **9** with ellipsoids at 50% probability level; (b) configuration of the $[Fe(\mathbf{bpa})_2]^{2+}$ fragment, all C-bound H atoms are omitted for clarity.

The Fe(II) centres in the $[Fe(\mathbf{bpa})_2]^{2+}$ complex cations again adopted octahedral coordination geometries with bond lengths, angles and distortion parameters (Σ = 70.01° and 79.64°) consistent with LS Fe(II) (table 2-2). There is disorder of the -SO_3 groups in both of the unique A9 anions. In one, the SO_3 group is positionally disordered over two sites, with relative occupancies of 0.66 and 0.34. In the second, the -SO_3 oxygen atoms are rotationally disordered and have been

modelled over two sites with relative occupancies of 0.77 and 0.23. The structure also contained a partial occupancy water (0.66 occupancy) as well as other 3 methanol solvates that could not be refined and were removed using the solvent mask routine in Olex2.

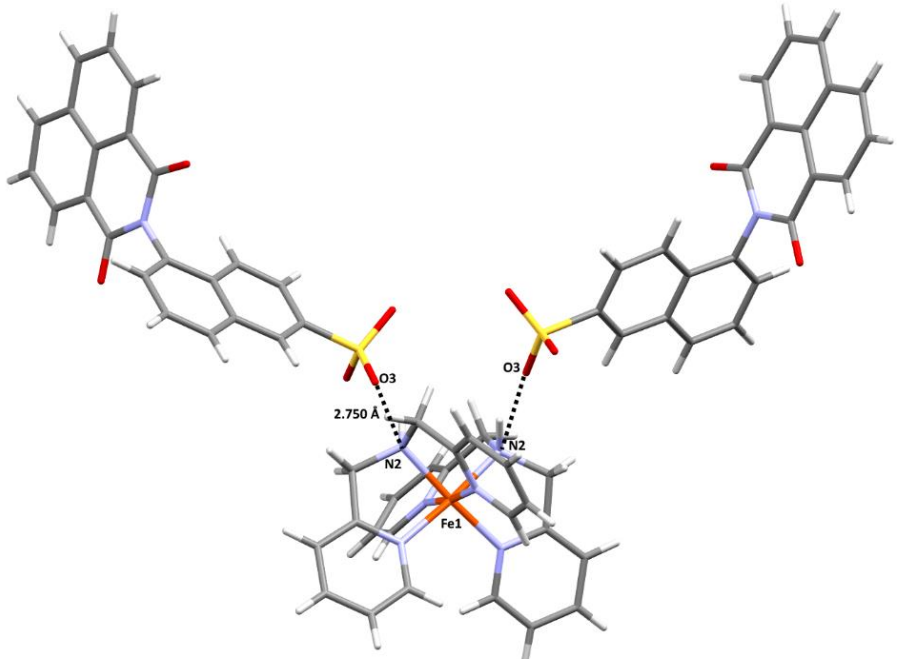

Figure 2-49 View of hydrogen-bonding interactions in Fe1 centre complexes of **9.**

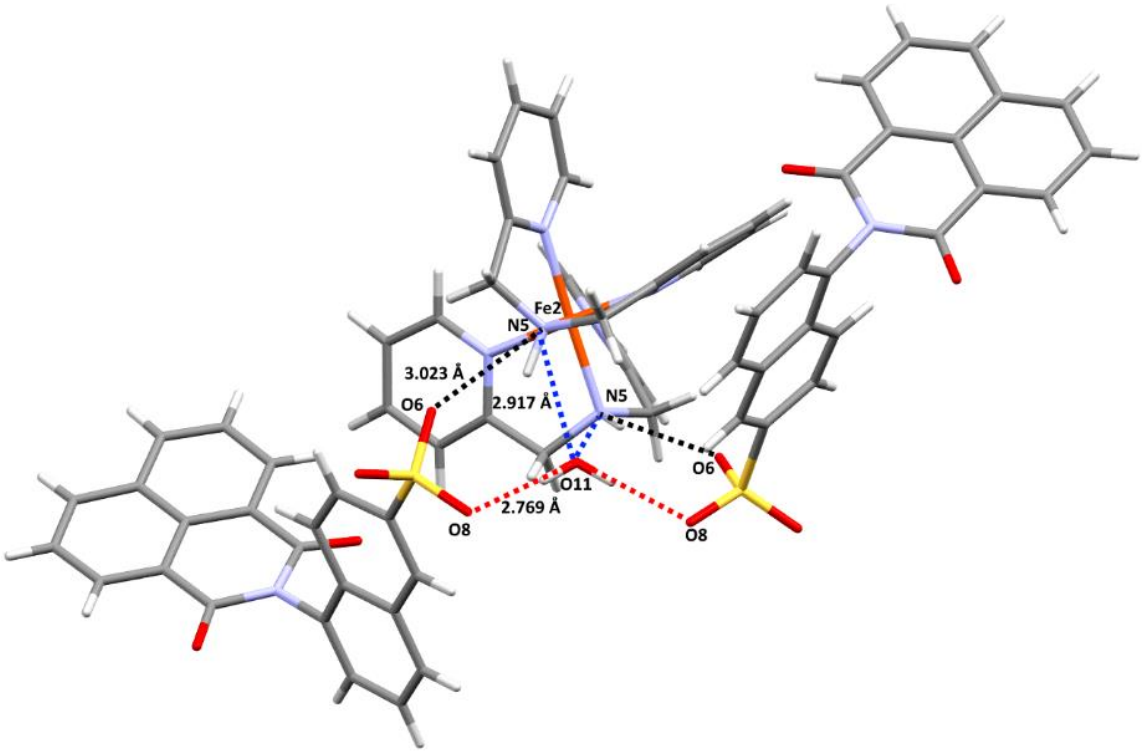

Figure 2-50 View of hydrogen-bonding interactions in Fe2 centre complexes of **9.**

Hydrogen bonding plays an important role in the long-range ordering in **9** where the two crystallographically independent Fe(II) complex cations have very different H-bonding interactions with the naphthalimide anions. In Fe1 the picolyl NH group from bis-picolylamine directly interacts with SO_3 groups on naphthalimide molecules [N2···O3 = 2.750(7) Å, ∠(N-H···O) = 156(11)°] (Figure 2-49) whereas the Fe2 complex has both a direct hydrogen bonding with a SO_3 group [N5···O6 = 3.023(8) Å, ∠(N-H···O = 134(7)°] as well as an interaction with the interstitial water that then bridges the complex cation and the naphthalimide anion [N5···O11 = 2.917(8) Å, ∠(N-H···O = 131(12)°]. This water also bridges two naphthalimide anions via the SO_3^- groups [O11···O8 = 2.769(7) Å, ∠(O-H···O = 174(5)°] (Figure 2-50). In addition to these hydrogen bonding interactions, a number of π-based interactions exist in this structure. The typical head-to-tail π stacking between the adjacent naphthalimide rings is again present [centroid···centroid = 3.531 Å (black dashed line) and centroid···centroid = 3.743 Å (blue dashed line) in Figure2-51] results in π-stacked columns of naphthalimides throughout the structure. Edge-to-face π-based interactions from the CH of a naphthalimide ring to the sulfonate-substituted naphthalene ring [CH···centroid = 3.127 Å (red dashed line)] in Figure 2-51 further link together the $\mathbf{A_9}$ anions. The overall result of these interactions is a layered naphthalimide-based structure.

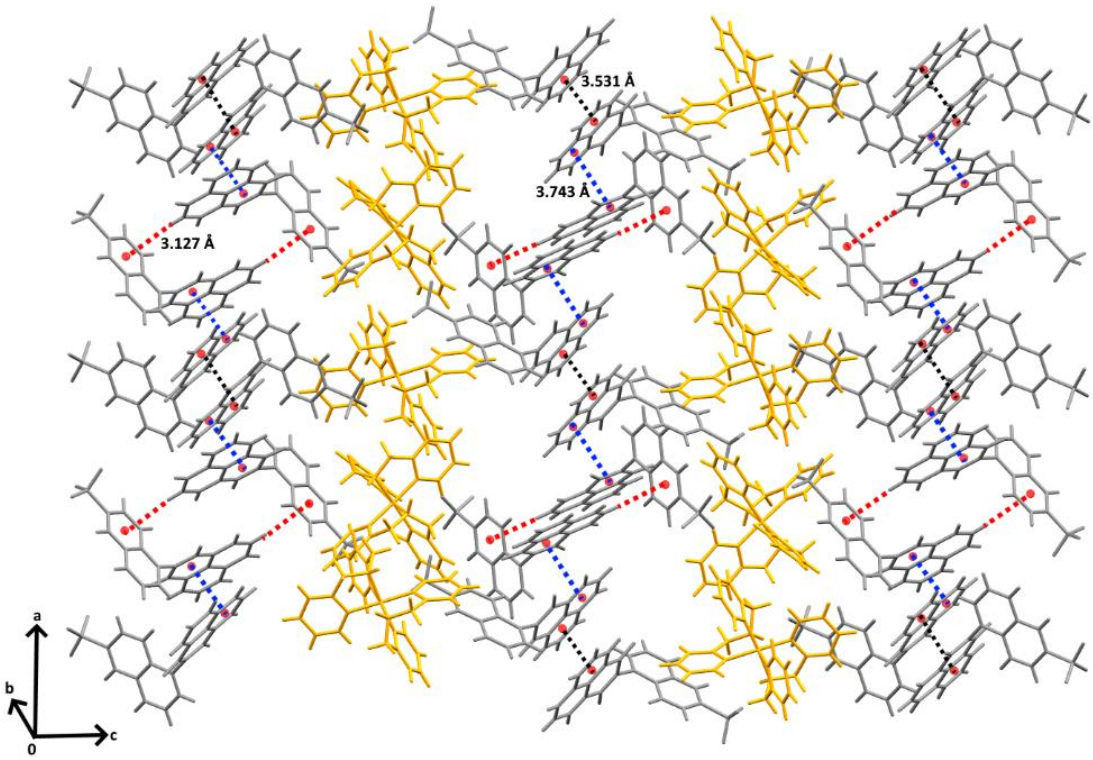

Figure 2-51 Packing interaction of **9** showing $\pi\cdots\pi$ stacking (black dashed line is 3.531 Å; Blue dashed line is 3.743 Å; red dashed line is 3.127 Å;). Naphthalimide molecules are presented in grey, $[Fe(\mathbf{bpa})_2]^{2+}$ molecules are presented in yellow, solvent molecules are omitted for clarity.

2.5.10 Crystallographic analysis of $[Fe(bpa)_2](A_{13})_2 \cdot H_2O \cdot CH_3OH$ (10)

Vapour diffusion of diethyl ether into the methanolic reaction solution resulted in red plate-like crystals of $[Fe(\mathbf{bpa})_2](\mathbf{A_{13}})_2 \cdot H_2O \cdot CH_3OH$ that crystallised in the triclinic space group $P\bar{1}$ with the asymmetric unit containing half of one complex cation, one anion and a water molecule and a methanol solvate (Figure 2-52). The Fe(II) centres in the $[Fe(\mathbf{bpa})_2]^{2+}$ complex cations again adopted octahedral coordination geometries with bond lengths, angles and distortion parameters (Σ = 59.46°) consistent with LS Fe(II) (table 2-2). The NO_2 naphthalimide substituent was disordered over two sites with relative occupancies of 0.65 and 0.35 with the major component displaying a 16° twist out of the mean plan of the naphthalimide (the minor component has a twist of 24°).

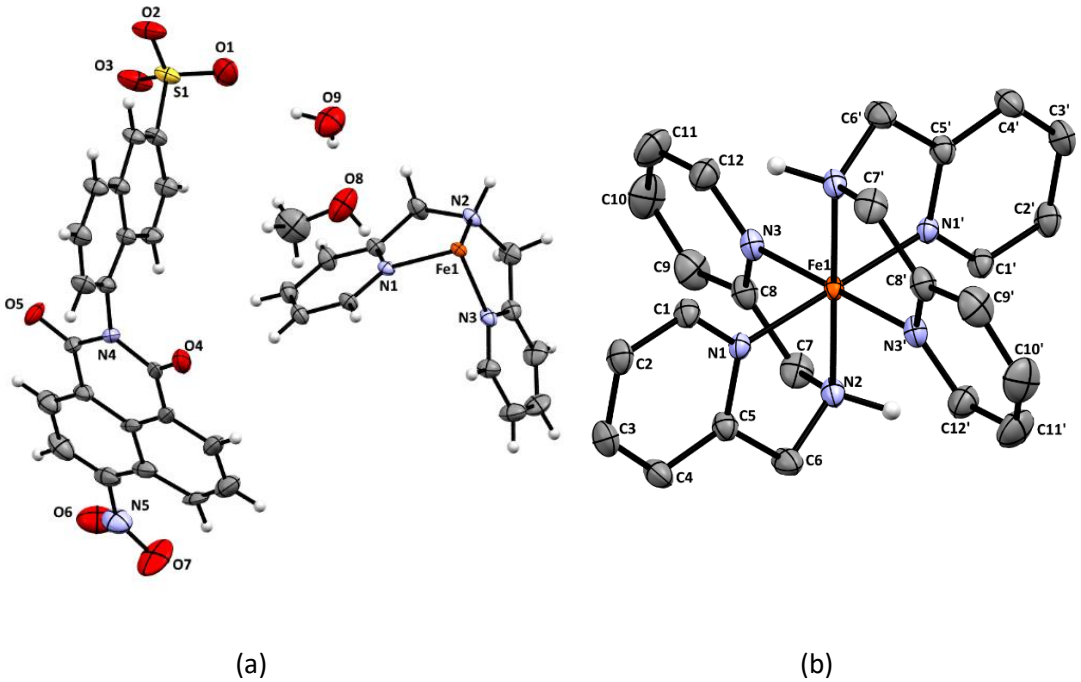

(a) (b)

Figure 2-52 (a) Asymmetric unit of the crystal structure of **10** with ellipsoids at 50% probability level. (b) Configuration of the $[Fe(\mathbf{bpa})_2]^{2+}$ fragment, all C-bound H atoms are omitted for clarity

In this complex, the hydrogen-bonding interactions from NH group of bis-picolylamine and the SO_3 group of naphthalimide are weaker than in previous complexes [O1···N2 = 3.089(4) Å ∠(N-H···O) = 151(7)°] (green dashed line in Figure 2-53). Continuous H-bonded chains were facilitated by the interstitial water and methanol molecules through hydrogen bonding to naphthalimide SO_3^- groups, which resulted in layers of the naphthalimide anions [O9···O1 = 2.843(5) Å, ∠(O-H···O) = 165(7)°(black dashed line); O8···O2 = 2.890(5) Å, ∠(O-H···O) = 163(9)°(blue dashed line); and O9···O8 = 2.802(5) Å, ∠(O-H···O) = 175(6)°(red dashed line) Figure 2-54]. Head-to-tail π-based interactions were also observed in this structure [centroid···centroid=3.692 Å (black dashed line) (Figure 2-54)] giving rise to the typical naphthalimide π-stacks as seen previously in this chapter.

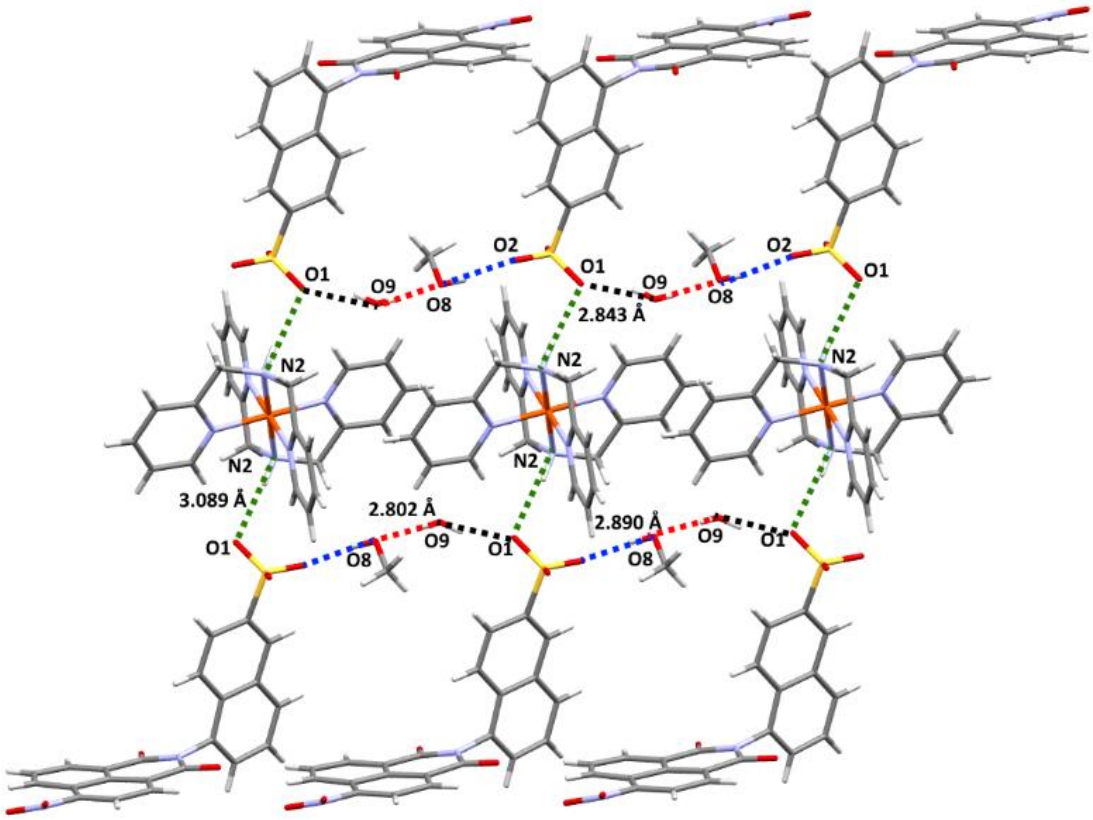

Figure 2-53 View of hydrogen-bonding interactions in **10.**

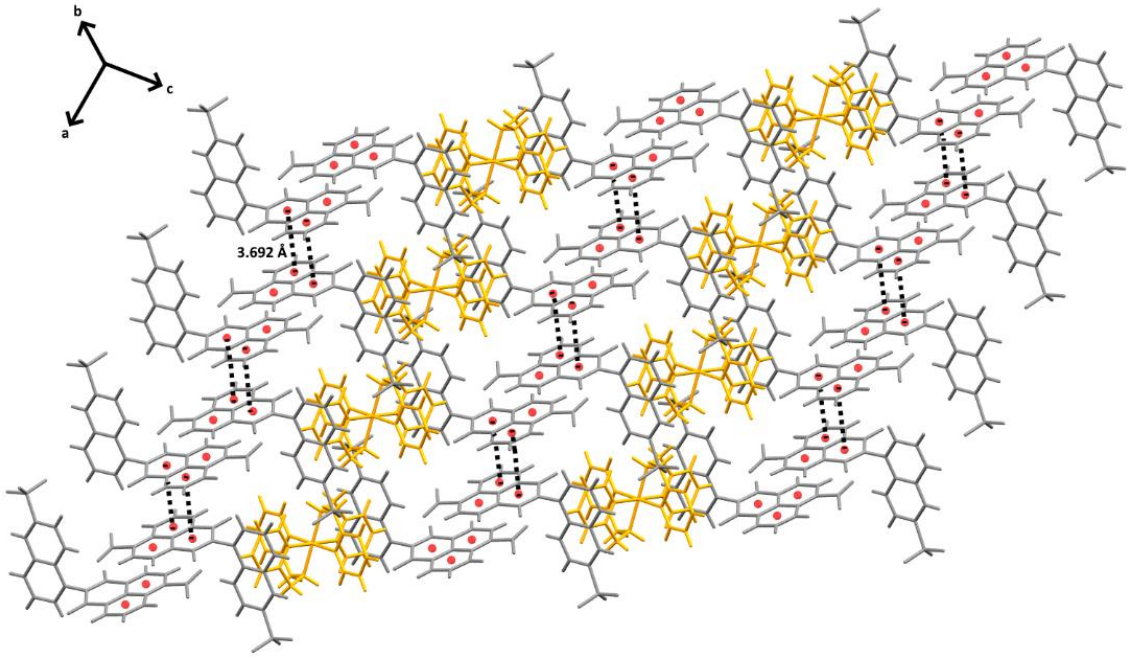

Figure 2-54 Packing interaction of **10** showing $\pi\cdots\pi$ stacking. Naphthalimide molecules are presented in grey, $[Fe(\mathbf{bpa})_2]^{2+}$ molecules are presented in yellow, solvent molecules are omitted for clarity.

2.5.11 Crystallographic analysis of $[Fe(bpa)_2]\cdot(A_{14})_2\cdot H_2O$ (11)

Red plate-like single crystals of $[Fe(\mathbf{bpa})_2](\mathbf{A_{14}})\cdot H_2O$ were grown by slow evaporation of a methanol solution and crystallised in the triclinic space group $P\bar{1}$ with the unit cell containing one complex molecule. The asymmetric unit contained half of one complex cation with the other half generated by a centre of inversion situated on the Fe(II) and an interstitial water molecule (Figure 2-55). Again, the Fe(II) centre in the $[Fe(\mathbf{bpa})_2]^{2+}$ complex cation adopted an octahedral coordination geometry with bond lengths, angles and distortion parameter (Σ = 61.58°) consistent with LS Fe(II) (table 2-2).

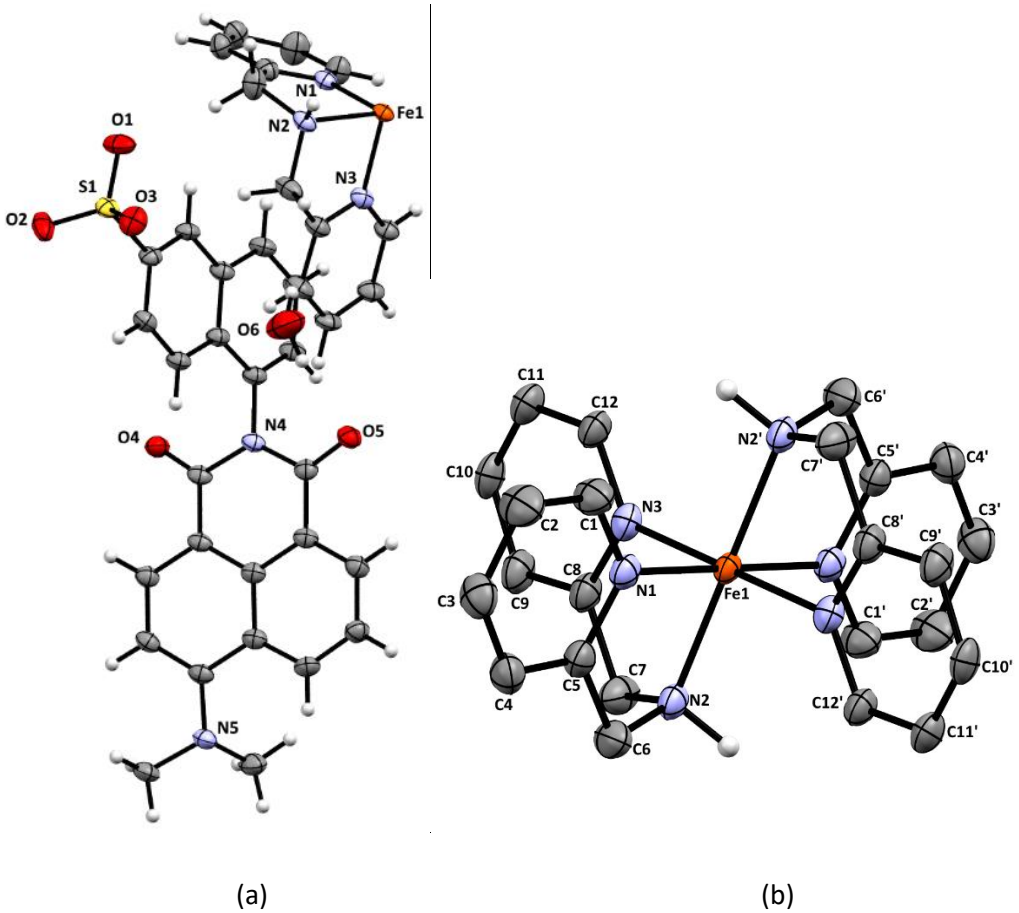

(a) (b)

Figure 2-55 (a) Asymmetric unit of the crystal structure of **11** with ellipsoids at 50% probability level; (b) configuration of the $[Fe(\mathbf{bpa})_2]^{2+}$ fragment, all C-bound H atoms are omitted for clarity.

As observed in the previous structures, hydrogen bonding interactions occur between the NH from the bis-picolylamine group to the neighbouring sulfonate group [N2···O3=2.857(3) Å, bond angle ∠(N2-H···O2=153(5)°]. Additionally, there is a hydrogen bond between the OH group of the lattice water to an oxygen atom on the sulfonate moiety [O6···O1 = 2.782(3) Å, and ∠(O6-H···O3) = 174(6)°] (Figure 2-56). In this structure, the -$N(Me)_2$ functional group was twisted by 38° from the mean plane of the naphthalimide ring. The formation of layers in compound 11 is driven by

off-set head-to-tail $\pi\cdots\pi$ stacking between the naphthalene rings of symmetry equivalent anions [centroid···centroid = 3.792 Å] as well as the edge-to-face π-based interaction from the CH of the naphthalene sulfonate ring to a neighbouring naphthalimide ring [CH···centroid = 2.994 Å] (Figure 2-56). There are also π-stacking interactions between naphthalene and pyridinyl rings [centroid···centroid 3.887 Å] (Figure 2-57). The overall effect is a long-range packing driven by both hydrogen-bonding and π stacking that results in cation-anion-cation layering and large spacing between complex molecules.

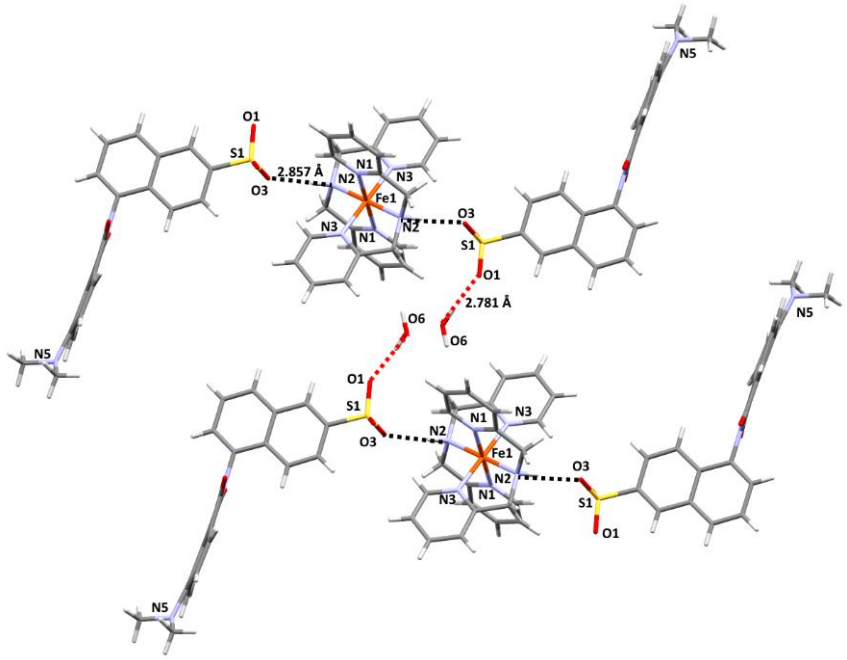

Figure 2-56 View of hydrogen-bonding interactions in **11.**

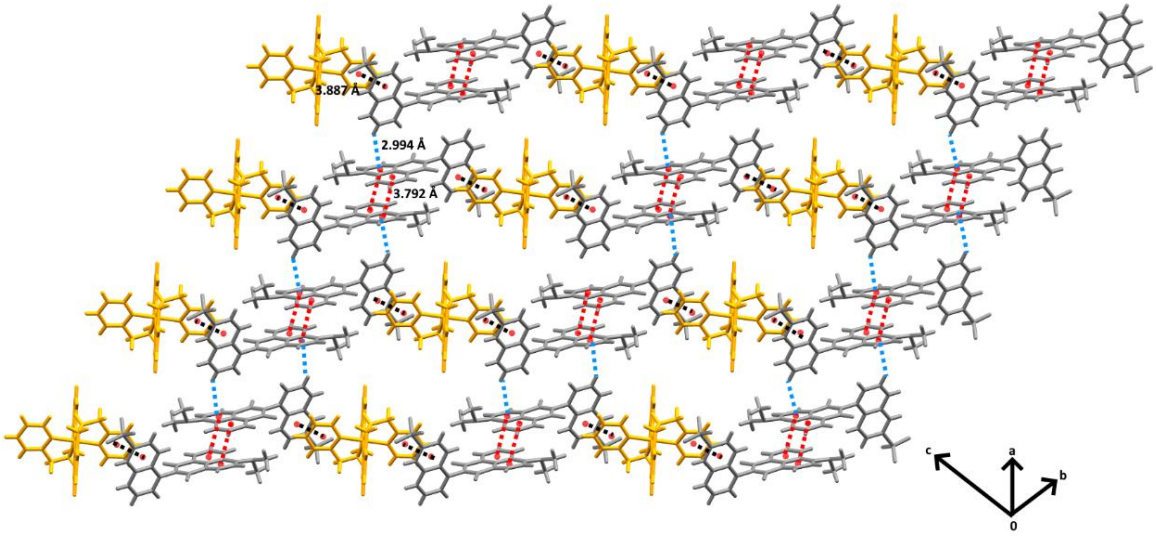

Figure 2-57 Packing interaction of **11** showing $\pi\cdots\pi$ stacking. Naphthalimide molecules are presented in grey, $[Fe(\mathbf{bpa})_2]^{2+}$ molecules are presented in orange, solvent molecules are omitted for clarity

Table 2-2 Summary of information on the crystallographically characterised[[Fe(**bpa**)$_2$]·(A$_x$)·Solvent. All the crystals were collected at 100 K.

Complex	Mean Fe-N(pyridyl) (Å)	Mean Fe-N(amino) (Å)	Σ[°]	Configuration
[Fe(**bpa**)$_2$](**A$_1$**)$_2$·CH$_3$OH (**1**)	1.999	2.036	73.96	*trans*-meridional
[Fe(**bpa**)$_2$](**A$_2$**)$_2$·CH$_3$OH(**2**)	1.986	2.029	71.72	*trans*- meridional
Fe(**bpa**)$_2$](**A$_3$**)$_2$·(CH$_3$)$_2$CO(**3**)	1.990	2.008	70.74	*trans*- meridional
[Fe(**bpa**)$_2$](**A$_5$**)·DMF(**4**)	1.991	2.042	75.05	*trans*- meridional
	2.000	2.024	93.4	
[Fe(**bpa**)$_2$](**A$_6$**)$_2$·CH$_3$OH(**5**)	1.990	2.024	76.04	*trans*- meridional
[Fe(**bpa**)$_2$](**A$_8$**)$_2$(**6**)	1.989	2.043	68.36	*trans*- meridional
[Fe(**bpa**)$_2$](**A$_9$**)$_2$·5CH$_3$OH(**7**)	1.977	2.012	72.58	*cis*-facial
[Fe(**bpa**)$_2$](**A$_{11}$**)·H$_2$O·CH$_3$OH(**8**)	2.195	2.039	94.8	*trans*- meridional
[Fe(**bpa**)$_2$](**A$_{12}$**)$_2$·0.66H$_2$O(**9**)	1.963	2.012	70.01	*cis*-facial
	1.967	2.009	79.64	
[Fe(**bpa**)$_2$](**A$_{13}$**)$_2$·H$_2$O·CH$_3$OH(**10**)	1.978	2.033	59.46	*trans*- meridional
[Fe(**bpa**)$_2$](**A$_{14}$**)·H$_2$O(**11**)	1.984	2.022	61.58	*trans*- meridional

For complexes **1**-**11**, the majority are observed in trans-meridional configuration as also with the systems reported with simple inorganic anions.[116] In Ar(4-SO_3)-nap-Tröger's base complex (**4**), there are two independent Fe(II) centres with slightly different bond lengths and angles. Remarkably, 5-Naph(1-SO_3)-nap-NO_2 and 5-Naph(2-SO_3)-Nap-H anions exhibit *cis*-facial configuration in [Fe(**bpa**)$_2$](**A$_x$**)$_2$ systems and these are the first *cis*-facial structures (**7** and **10**) confirmed in Fe(II) bis-picolylamine complexes.

2.6 Magnetism Results Discussion

Given the LS spin nature of the complexes determined from single crystal XRD experiments at 100 K, variable temperature magnetic susceptibility measurements were attempted on crystalline samples of complexes of **1**-**11**. Unfortunately complexes 4-11 showed no magnetic signal at the attempted sample centring temperatures (100 K, 200 K and 300 K), which meant the sample position could not be determined. This indicated that the sample was Fe(II) LS with 0 unpaired electrons, and therefore diamagnetic, as such no data was collected. ^{1}H NMR was collected on solutions of dissolved crystals in DMSO-D6 and no paramagnetic shift was observed, for further supporting information see ESI.

Complexes **1**-**3** were successfully centred and magnetic susceptibility measurements were collected at temperatures between 50 to 400 K under an applied field of 1,000 Oe (0.1 T) for **1** and **3**, and 10,000 Oe (1 T) for **2**.

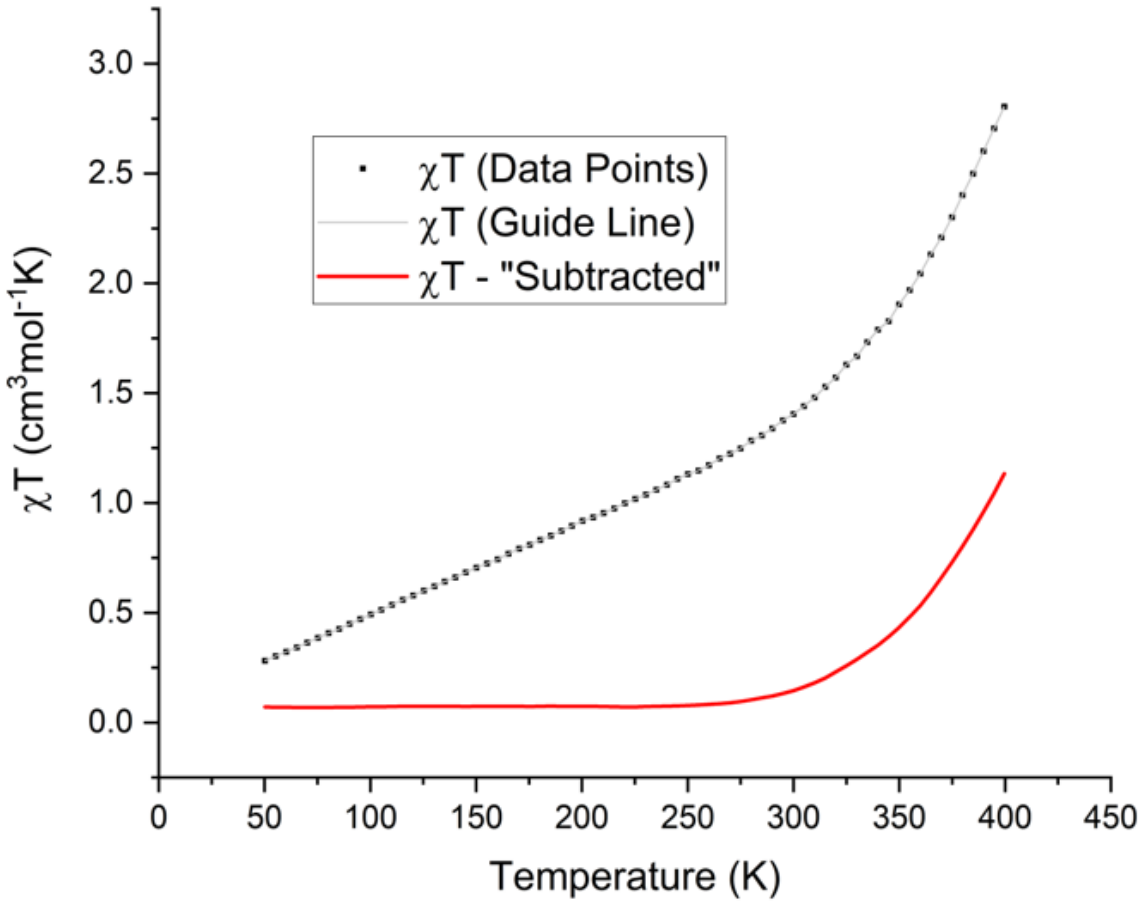

Figure 2-58 Plot of $\chi_M T$ vs. T for complex **1**

Complex **1** exhibits some evidence of an incomplete spin crossover event with a dramatic increase in the gradient occurring around 300 K (figure 2-58). However, it is linear in nature between 50 K and 275 K, which could be a paramagnetic impurity in this sample (a linear response in the magnetic susceptibility across different temperatures). This is not unusual given that air sensitive Fe(II) systems can oxidise to magnetite or hematite, both of which are Curie magnets across the entire temperature range measured. In an attempt to observe the SCO event more clearly a crude approximation was made. Applying the gradient of the linear region between 50 K and 250 K, the value contributed from the paramagnetic impurity was removed across all temperature ranges. To calculate the "subtracted" values, the following formula was used:

$$\chi T_{subtracted} = \chi T - 0.004202T$$

This gives a low temperature χT value of approximately 0.06 $cm^3mol^{-1}K$ which undergoes a spin transition beginning at 275 K, resulting in a max value of 1.13 $cm^3mol^{-1}K$ at 400 K which is the limit of the experiment. Although this value is below the value for HS Fe(II), 3.00 $cm^3mol^{-1}K$, the shape of the graph indicates that the transition would continue if measurements were available above 400 K. In addition to this, as air sensitive Fe(II) compounds have likely been oxidised to give an unknown quality sample, the mass used in calculating the χT per mol is unreliable.

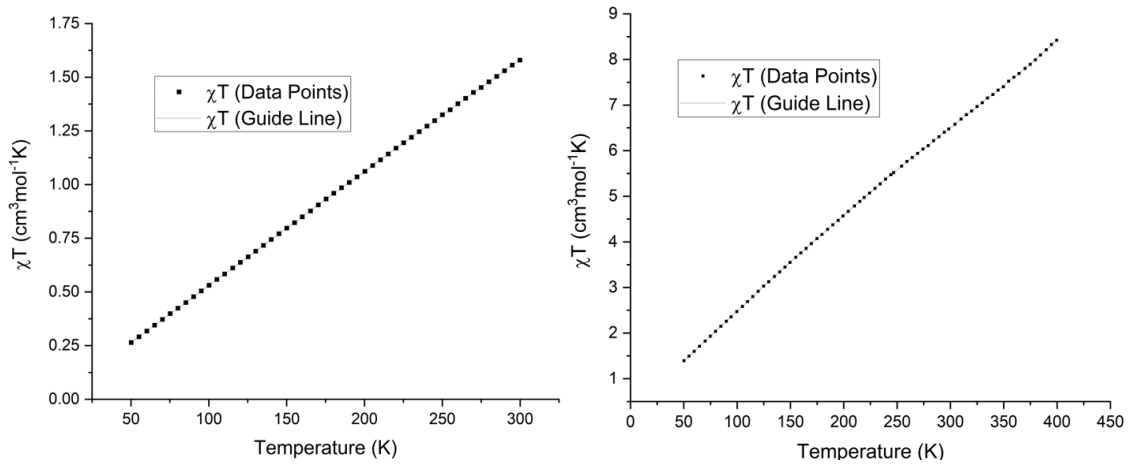

Figure 2-59 Plots of $\chi_M T$ vs. T for complexes **2** and **3**

The other two datasets were collected on samples **2** and **3** (figure 2-59). Unfortunately these appear to have a linear response in χT across the temperature range measured, indicating the overwhelming presence of a paramagnetic impurity.

2.7 Conclusion

A family of different substituted sulfonate 1,8-naphthalimide anions have been synthesised, characterised and subsequently used in the formation of Fe(II) bis-picolylamine complexes. The naphthalimide anions provide additional properties to extend the crystal structure through their π-based interactions as well as weak hydrogen bonds. A structural analysis displayed layered packing *via* the naphthalimide moieties where it was confirmed that naphthalimide anions play an integral part in the structure and ordering of the system.

From magnetism data, the Ar(4-SO_3)-Nap-H (**A_1**) anion influenced the magnetic property in [Fe(**bpa**)$_2$]$^{2+}$ complexes, which indicated that introducing structure-directing agents into coordination complexes has potential to enhance the cooperativity. Complex **1** appeared to show an SCO event starting at 275 K. The data indicated the presence of some paramagnetic impurity, most likely an iron oxide species such as magnetite or hematite which are both Curie magnets below 400 K. The magnetic data collected for complexes **2** and **3** appear to follow the Curie law across the entire temperature range, given the large magnetic susceptibility value expected from some iron oxide species a small amount of impurity may overwhelm any SCO signal, particularly when the prepared samples contained less than 10 mg of complex.

The remaining magnetic data suggests that most of [Fe(**bpa**)$_2$]$^{2+}$ systems are in LS configuration across the measurable temperature range (50 K – 400 K) and do not feature any desired spin transition. This is supported by NMR and single crystal X-ray studies indicating the LS state at the temperatures measured. This work indicated the potential of the sulfonate anion to modify SCO systems. Due to the interesting magnetic properties observed in the Ar(4-SO_3)-Nap (**A_1**) anion, it

was chosen for further investigation in Chapter 3, but utilising a different SCO active cationic complex.

2.8 Experimental

NMR spectra were recorded on a Bruker DPX400 NMR spectrometer at 300 K. Chemical shifts are reported in parts per million and referenced to the residual solvent peak ($(CD_3)_2SO$: ^1H δ 2.50 ppm, ^{13}C δ 39.52 ppm). Standard conventions indicating multiplicity were used: m = multiplet, t = triplet, d = doublet, s = singlet. Mass spectrometry samples were analysed using a MaXis (Bruker Daltonics, Bremen, Germany) mass spectrometer equipped with a Time of Flight (TOF) analyser. Samples were introduced to the mass spectrometer via a Dionex Ultimate 3000 autosampler and uHPLC pump [Gradient 20% acetonitrile (0.2% formic acid) to 100% acetonitrile (0.2% formic acid) in five minutes at 0.6 mL min. Column: Acquity UPLC BEH C18 (Waters) 1.7 micron 50 x 2.1mm]. Single-crystal X-ray diffraction data was either collected at 100 K on a Rigaku AFC12 goniometer equipped with an enhanced sensitivity (HG) Saturn 724+ detector mounted at the window of an FR-E+ Superbright Mo-Kα rotating anode generator (λ = 0.71075 Å) with HF or VHF varimax optics, or a Rigaku 007 HF diffractometer equipped with an enhanced sensitivity Saturn 944+ detector with a Cu-Kα rotating anode generator (λ = 1.5418 Å) with HF varimax optics. Unit cell parameters were refined against all data and an empirical absorption correction applied in either CrystalClear or CrysalisPro. All structures were solved by direct methods using SHELXS-2013[119] and refined on F_O^2 by SHELXL-2013 using Olex2.[120]

2.8.1 Synthesis of Ar(4-SO_3)-Nap-H·PyH (A_1·PyH)

4-sulfanilic acid (0.350 g, 2 mmol) was combined with 1,8-naphthalic anhydride (0.400 g, 2 mmol) in refluxing pyridine (5 ml) for 6 hours. After cooling to room temperature, the pyridine was removed by vacuum. The resulting off-white powder was filtered and washed with diethyl either (30 mL) until the pyridine was removed. Mass Spec. (HR, ESI+) *m/z*: 354.0431 [$\mathbf{A_1}$-H + H]$^+$, ^1H NMR (400 MHz, DMSO-d_6) δ 9.00 – 8.92 (m, 2H), 8.62 (ddt, 1H), 8.52 – 8.47 (m, 4H), 8.09 (dd, 2H), 7.89 (dd, *J* = 8.1, 7.4 Hz, 2H), 7.83 – 7.75 (m, 2H), 7.42 – 7.34 (m, 2H). ^{13}C NMR (101 MHz, DMSO-d_6) δ 164.14, 148.43, 146.71, 142.77, 136.65, 134.98, 131.89, 131.24, 129.03, 128.26, 127.68, 126.68, 122.95.

2.8.2 Synthesis of Ar(4-SO_3)-Nap-NO_2·ImdH (A_2·ImdH)

4-sulfanilic acid (0.350 g, 2 mmol) was combined 4-NO_2-naphthalic anhydride (0.486 g, 2 mmol), and a large excess of imidazole (1.360 g 20 mmol) in chloroform (10 ml) and refluxed for 6 hours.

After cooling to room temperature, the solvent was removed in vacuum and distilled water (5 mL) was added to the orange solid. The mixture was sonicated for 10 minutes in an ice cold sonicator and then filtered and washed with ice-cold ethanol (2x 10 mL) resulting in a pale orange solid. Mass Spec. (HR, ESI+) *m/z*: 399.0278 [**A$_2$**-H + H]$^+$; ^{1}H NMR (400 MHz, DMSO-d_6) δ 9.06 (s, 1H), 8.77 (d, *J* = 8.8 Hz, 1H), 8.69 – 8.56 (m, 3H), 8.14 (dd, *J* = 8.7, 7.3 Hz, 1H), 7.75 (d, *J* = 8.4 Hz, 2H), 7.69 (s, 2H), 7.37 (d, *J* = 8.4 Hz, 2H). ^{13}C NMR (101 MHz, DMSO-d_6) δ 163.70, 162.89, 149.75, 148.82, 136.02, 134.88, 132.21, 130.60, 130.11, 129.33, 129.28, 128.81, 127.72, 126.70, 124.71, 123.83, 123.34, 119.83.

2.8.3 Synthesis of Ar(4-SO$_3$)-Nap-N(Me)$_2$·H (A$_3$·H)

A 4-sulfanilic acid (0.350 g, 2 mmol) was combined 4-N(Me)$_2$-naphthalic anhydride (0.482 g, 2 mmol), and a large excess of imidazole (1.360 g, 20 mmol) in chloroform (10 ml) and refluxed for 6 hours. After cooling to room temperature, the solvent was removed in vacuum and distilled water (5 mL) was added to the orange solid. 1 M hydrochloric acid was then added dropwise to the resulting solution until the pH reached 7. The mixture was filtered and washed with cold ethanol (2x 10 mL) resulting in a bright yellow solid. Mass Spec. (HR, ESI-) *m/z*: 395.0709 [**A$_3$**]$^-$, ^{1}H NMR (400 MHz, DMSO-d_6) δ 8.57 (dd, *J* = 8.5, 1.2 Hz, 1H), 8.47 (dd, *J* = 7.3, 1.2 Hz, 1H), 8.36 (d, *J* = 8.3 Hz, 1H), 7.79 (dd, *J* = 8.5, 7.2 Hz, 1H), 7.76 – 7.70 (m, 2H), 7.32 – 7.27 (m, 2H), 7.26 (d, *J* = 8.4 Hz, 1H), 3.12 (s, 6H). ^{13}C NMR (101 MHz, DMSO) δ 164.35, 163.69, 157.16, 148.36, 136.78, 132.83, 132.20, 131.17, 130.60, 128.99, 126.56, 125.52, 124.83, 123.25, 114.17, 113.51, 44.90.

2.8.4 Synthesis of Ar(4-SO$_3$)-Nap-NH$_2$·H (A$_4$·H)

Ar-(4-SO$_3$)-Nap-NO$_2$ (190 mg 0.4 mmol) was suspended in methanol with a 10% palladium on carbon catalyst (50 mg) under hydrogen atmosphere in ethanol (20 ml) for 12 hours. This resulted in a suspension that had methanol (500 ml) added, then was filtered through celite. Removal of solvent in vacuum gave a red solid. Mass Spec. (HR, ESI-) *m/z*: 367.0387 [**A$_4$**]$^-$, ^{1}H NMR (400 MHz, DMSO-d_6) δ 8.68 (s, 1H), 8.65 (dd, *J* = 8.4, 1.2 Hz, 1H), 8.44 (dd, *J* = 7.3, 1.2 Hz, 1H), 8.20 (d, *J* = 8.4 Hz, 1H), 7.76 – 7.69 (m, 2H), 7.68 (dd, *J* = 8.4, 7.3 Hz, 1H), 7.50 (s, 2H), 7.30 – 7.22 (d, 2H), 6.89 (d, *J* = 8.4 Hz, 1H). ^{13}C NMR (101 MHz, DMSO-d_6) δ 164.51, 163.64, 153.19, 147.92, 137.20, 134.54, 131.72, 130.66, 130.01, 129.05, 126.53, 124.56, 122.60, 119.87, 108.61, 108.21.

2.8.5 Synthesis of Ar(4-SO$_3$)-Nap-Tröger's base·2H (A$_5$·2H)

A$_4$ (92 mg, 0.25 mmol) and paraformaldehyde (15 mg, 0.5 mmol) were stirred in neat TFA (2 ml) for 12 hours at room temperature under a nitrogen atmosphere. Ethanol (500 ml) was added to

the suspension before the mixture was filtered through celite. Removal of solvent in vacuum gave a yellow solid. HRMS (ESI-): 771.0860. The crude compound (10 mg) was dissolved in DMF (2 ml). This bright yellow solution that was subjected to vapour diffusion of diethyl ether. After three days, this resulted in yellow-orange block crystals. Mass Spec. (HR, ESI-): 385.0385 $[\mathbf{A_5}]^{2-}$.

Crystal Data for $C_{41}H_{31}N_5O_{10.5}S_2$ (*M* =825.83 g/mol): triclinic, space group $P\bar{1}$ (no. 2), *a* = 9.3292(5) Å, *b* = 18.3198(7) Å, *c* = 18.4859(8) Å, α = 70.885(4)°, β= 84.102(4)°, γ = 76.035(4)°, V = 2896.0(2) Å^3, *Z* = 2, T = 100(2) K, μ(Mo Kα) = 0.138 mm^{-1}, *Dcalc* = 0.947 g/cm^3, 56034 reflections measured (3.846° ≤ 2Θ ≤ 54.968°), 12786 unique (R_{int} = 0.0413, R_{sigma} = 0.0373) which were used in all calculations. The final R_1 was 0.0916 (I > 2σ(I)) and wR_2 was 0.3032 (all data).

2.8.6 Synthesis of Ar(3-SO$_3$)-Nap-H·PyH (A$_6$·PyH)

3-sulfanilic acid (0.350 g, 2 mmol) was combined with 1,8-naphthalic anhydride (0.400 g, 2 mmol) in refluxing pyridine (5 ml) for 6 hours. After cooling to room temperature, the pyridine was removed by vacuum. The resulting off-white powder was filtered and washed with diethyl either (30 mL) until the pyridine was removed. Mass Spec. (HR, ESI+): 354.0430 $[\mathbf{A_6}\text{-H} + \text{H}]^+$; ^{1}H NMR (400 MHz, DMSO-d_6) δ 8.99 – 8.87 (m, 2H), 8.58 (tt, *J* = 7.8, 1.6 Hz, 1H), 8.53 – 8.48 (m, 4H), 8.09 – 8.03 (m, 2H), 7.91 (t, *J* = 1.7 Hz, 2H), 7.70 (dt, *J* = 7.7, 1.4 Hz, 1H), 7.62 (t, *J* = 1.8 Hz, 1H), 7.49 (t, *J* = 7.7 Hz, 1H), 7.35 (ddd, *J* = 7.8, 2.1, 1.1 Hz, 1H). ^{13}C NMR (101 MHz, DMSO) δ 164.19, 149.56, 146.25, 143.11, 135.91, 134.88, 131.92, 131.17, 129.75, 128.77, 128.35, 127.68, 127.52, 126.77, 125.94, 123.14.

2.8.7 Synthesis of Ar(3-SO$_3$)-Nap-NO$_2$·ImdH (A$_7$ ·ImdH)

3-sulfanilic acid (0.350 g, 2 mmol) was combined with 4-NO_2-naphthalic anhydride (0.486 g, 2 mmol), and a large excess of imidazole (1.360 g 20 mmol) in chloroform (10 ml) and refluxed for 6 hours. After cooling to room temperature, the solvent was removed in vacuum and distilled water (5 mL) was added to the orange solid. The mixture was sonicated for 10 minutes in an ice cold sonicator and then filtered and washed with ice-cold ethanol (2x 10 mL) resulting in a pale orange solid. Mass Spec. (HR, ESI+): 399.0276 $[\mathbf{A_7}\text{-H} + \text{H}]^+$; ^{1}H NMR (400 MHz, DMSO-d_6) δ 9.07 (t, *J* = 1.3 Hz, 1H), 8.75 (dd, *J* = 8.7, 1.1 Hz, 1H), 8.64 (dd, *J* = 7.3, 1.1 Hz, 1H), 8.60 (dd, *J* = 16.3, 8.0 Hz, 2H), 8.12 (dd, *J* = 8.7, 7.3 Hz, 1H), 7.72 (dt, *J* = 7.7, 1.3 Hz, 1H), 7.70 – 7.65 (m, 3H), 7.51 (t, *J* = 7.8 Hz, 1H), 7.37 (ddd, *J* = 7.8, 2.1, 1.2 Hz, 1H). ^{13}C NMR (101 MHz, DMSO) δ 163.73, 162.93, 149.68, 149.63, 135.44, 134.86, 132.09, 130.57, 129.98, 129.57, 129.31, 129.24, 128.82, 127.87, 126.70, 126.17, 124.71, 123.95, 123.33, 119.82.

2.8.8 Synthesis of Ar(3-SO_3)-Nap-$N(Me)_2$·H (A_8·H)

3-sulfanilic acid (0.350 g, 2 mmol) was combined with 4-$N(Me)_2$-naphthalic anhydride (0.482 g, 2 mmol), and a large excess of imidazole (1.360 g, 20 mmol) in chloroform (10 ml) and refluxed for 6 hours. After cooling to room temperature, the solvent was removed in vacuum and distilled water (5 mL) was added to the orange solid. 1 M hydrochloric acid was then added dropwise to the resulting solution until the pH reached 7. The mixture was filtered and washed with cold ethanol (2x 10 mL) resulting in a bright yellow solid. Mass Spec. (HR, ESI+): 397.0855 [**A_8**-H + H]$^+$; ^{1}H NMR (400 MHz, DMSO-d_6) δ 8.55 (dd, *J* = 8.5, 1.2 Hz, 1H), 8.45 (dd, *J* = 7.3, 1.1 Hz, 1H), 8.33 (d, *J* = 8.3 Hz, 1H), 7.77 (dd, *J* = 8.5, 7.3 Hz, 1H), 7.68 (dt, *J* = 7.7, 1.4 Hz, 1H), 7.55 (t, *J* = 1.8 Hz, 1H), 7.48 (t, *J* = 7.8 Hz, 1H), 7.29 (ddd, *J* = 7.8, 2.2, 1.2 Hz, 1H), 7.24 (d, *J* = 8.3 Hz, 1H), 3.11 (s, 6H). ^{13}C NMR (101 MHz, DMSO) δ 164.36, 163.69, 157.03, 149.36, 136.12, 132.76, 132.09, 131.11, 130.56, 129.87, 128.74, 126.78, 125.78, 125.53, 124.82, 123.28, 114.28, 113.56, 44.90.

2.8.9 Synthesis of 5-Naph(1-SO_3)-Nap-H·PyH (A_9·PyH)

5-amino-1-naphthalenesulfanilic acid (0.446 g, 2 mmol) was combined with 1,8-naphthalic anhydride (0.400 g, 2 mmol) in refluxing pyridine (5 ml) for 6 hours. After cooling to room temperature, the pyridine was removed by vacuum. The resulting off-white powder was filtered and washed with diethyl either (30 mL) until the pyridine was removed. Mass Spec. (HR, ESI+): 404.0587 [**A_9**-H + H]$^+$; ^{1}H NMR (400 MHz, DMSO-d_6) δ 9.03 (dt, *J* = 8.4, 1.2 Hz, 1H), 8.92 (dt, *J* = 5.2, 1.6 Hz, 2H), 8.61 – 8.53 (m, 5H), 8.06 – 7.99 (m, 3H), 7.95 (dd, *J* = 8.3, 7.3 Hz, 2H), 7.80 (dt, *J* = 8.5, 1.2 Hz, 1H), 7.72 – 7.59 (m, 2H), 7.39 (dd, *J* = 8.5, 7.1 Hz, 1H). ^{13}C NMR (101 MHz, DMSO-d_6) δ 164.44, 146.09, 144.93, 143.22, 135.12, 133.26, 132.07, 131.14, 130.40, 129.04, 128.73, 127.77, 127.46, 127.19, 126.00, 125.80, 125.08, 124.41, 123.11.

2.8.10 Synthesis of 5-Naph(1-SO_3)-Nap-NO_2·PyH (A_{10}·PyH)

5-amino-2-naphthalenesulfanilic acid (0.446 g, 2 mmol) was combined with 4-NO_2-naphthalic anhydride (0.486 g, 2 mmol) in pyridine for 6 hours. After cooling to room temperature, the pyridine was removed by vacuum. The resulting off-white powder was filtered and washed with diethyl either (30 mL) until the pyridine was removed. Mass Spec. (HR, ESI-): 447.0296 [**A_{10}**]$^-$; ^{1}H NMR (400 MHz, DMSO-d_6) δ 9.04 (dt, *J* = 8.2, 1.4 Hz, 1H), 8.97 – 8.92 (m, 2H), 8.80 (dd, *J* = 8.7, 1.1 Hz, 1H), 8.72 – 8.56 (m, 4H), 8.16 (dd, *J* = 8.7, 7.3 Hz, 1H), 8.11 – 8.05 (m, 2H), 8.01 (dd, *J* = 7.1, 1.2 Hz, 1H), 7.92 (d, *J* = 8.4 Hz, 1H), 7.72 – 7.61 (m, 2H), 7.39 (dd, *J* = 8.5, 7.1 Hz, 1H). ^{13}C NMR (101 MHz, DMSO-d_6) δ 163.99, 163.20, 149.89, 146.68, 144.90, 142.78, 132.76, 132.32, 131.08, 130.61,

130.39, 130.22, 129.79, 129.40, 129.27, 127.85, 127.66, 127.09, 126.00, 125.78, 125.16, 124.66, 124.62, 123.97, 123.43.

2.8.11 Synthesis of 5-Naph(1-SO_3)-Nap-$N(Me)_2$·H (A_{11}·H)

5-amino-1-naphthalenesulfanilic acid (0.446 g, 2 mmol) was combined with 4-NO_2-naphthalic anhydride (0.486 g, 2 mmol), and imidazole (0.1360 g 2 mmol) in distilled water (10 ml) and refluxed for 6 hours. After cooling to room temperature, diluted hydrochloride acid solution was added to the resulting imidazolium initial product until the pH approached 7. This resulted in a bright yellow solid which was washed with cold ethanol to give the pure protonated compound with high yield. Mass Spec. (HR, ESI+): 447.1011 [$\mathbf{A_{11}}$-H + H]$^+$; ^{1}H NMR (400 MHz, DMSO-d_6) δ 9.01 (d, *J* = 8.6 Hz, 1H), 8.62 (d, *J* = 8.5 Hz, 1H), 8.51 (d, *J* = 7.2 Hz, 1H), 8.39 (d, *J* = 8.3 Hz, 1H), 8.00 (d, *J* = 7.0 Hz, 1H), 7.83 (t, *J* = 7.9 Hz, 1H), 7.72 – 7.62 (m, 2H), 7.56 (d, *J* = 7.1 Hz, 1H), 7.39 (t, *J* = 7.7 Hz, 1H), 7.29 (d, *J* = 8.3 Hz, 1H), 3.15 (s, 6H). ^{13}C NMR (101 MHz, DMSO-d_6) δ 164.63, 163.94, 157.39, 144.94, 133.49, 133.01, 132.40, 131.34, 131.15, 130.95, 130.39, 128.86, 127.19, 125.94, 125.77, 125.56, 125.00, 124.93, 124.27, 123.26, 114.08, 113.53, 44.91.

2.8.12 Synthesis of 5-Naph(2-SO_3)-Nap-H·PyH (A_{12}·PyH)

5-amino-2-naphthalenesulfanilic acid (0.446 g, 2 mmol) was combined with 1,8-naphthalic anhydride (0.400 g, 2 mmol) in refluxing pyridine (5 ml) for 2 hours. After cooling to room temperature, the pyridine was removed by vacuum. The resulting off-white powder was filtered and washed with diethyl either (30 mL) until the pyridine was removed. Mass Spec. (HR, ESI+): 404.0589 [$\mathbf{A_{12}}$-H + H]$^+$; ^{1}H NMR (400 MHz, DMSO-d_6) δ 8.92 (dd, *J* = 6.4, 1.5 Hz, 2H), 8.60 – 8.51 (m, 5H), 8.30 (d, *J* = 1.6 Hz, 1H), 8.15 (dt, *J* = 7.9, 1.2 Hz, 1H), 8.04 (t, *J* = 8.0, 7.4 Hz, 2H), 7.94 (dd, *J* = 8.2, 7.3 Hz, 2H), 7.77 (d, *J* = 8.8 Hz, 1H), 7.72 – 7.62 (m, 3H). ^{13}C NMR (101 MHz, DMSO-d_6) δ 164.37, 146.33, 146.13, 143.17, 135.14, 133.53, 133.30, 132.06, 131.44, 130.41, 129.92, 128.71, 128.05, 127.78, 127.47, 126.68, 125.42, 124.89, 123.08, 122.90.

2.8.13 Synthesis of 5-Naph(2-SO_3)-Nap-NO_2·PyH (A_{13}·PyH)

5-amino-2-naphthalenesulfanilic acid (0.446 g, 2 mmol) was combined with 4-NO_2-naphthalic anhydride (0.486 g, 2 mmol) in pyridine and refluxed for 6 hours. After cooling to room temperature, the pyridine was removed by vacuum. The resulting off-white powder was filtered and washed with diethyl either (30 mL) until the pyridine was removed. Mass Spec. (HR, ESI-): 447.0297 [$\mathbf{A_{13}}$]$^-$; ^{1}H NMR (400 MHz, DMSO-d_6) δ 8.95 – 8.91 (m, 2H), 8.81 (dd, *J* = 8.8, 1.1 Hz, 1H), 8.70 – 8.61 (m, 3H), 8.57 (tt, *J* = 7.9, 1.6 Hz, 1H), 8.30 (d, *J* = 1.6 Hz, 1H), 8.17 (ddd, *J* = 7.3, 5.5, 3.2

Hz, 2H), 8.08 – 8.02 (m, 2H), 7.90 (d, *J* = 8.8 Hz, 1H), 7.73 – 7.64 (m, 3H). ^{13}C NMR (101 MHz, DMSO-d_6) δ 163.93, 163.13, 149.90, 146.46, 146.23, 143.12, 133.54, 132.80, 132.34, 130.62, 130.35, 130.24, 130.17, 129.78, 129.43, 127.95, 127.83, 127.51, 126.66, 125.38, 124.86, 124.68, 123.95, 123.44, 123.07.

2.8.14 Synthesis of 5-Naph(2-SO_3)-Nap-N(Me)$_2$·H (A_{14}·H)

5-amino-1-naphthalenesulfanilic acid (0.446 g, 2 mmol) was combined with 4-NO_2-naphthalic anhydride (0.486 g, 2 mmol), and imidazole (0.1360 g 2 mmol) in distilled water (10 ml) and refluxed for for 6 hours. After cooling to room temperature, diluted hydrochloride acid solution was added to the resulting imidazolium initial product solution until pH approach 7. This resulted in a bright yellow solid which was washed with cold ethanol to give the pure protonated compound with high yield. Mass Spec. (HR, ESI+): 447.1013 ([**A_{14}**-H + H]$^+$; ^{1}H NMR (400 MHz, DMSO-d_6) δ 8.63 (d, *J* = 8.5 Hz, 1H), 8.51 (d, *J* = 7.2 Hz, 1H), 8.39 (d, *J* = 8.3 Hz, 1H), 8.29 (s, 1H), 8.14 (d, *J* = 8.2 Hz, 1H), 7.83 (t, *J* = 7.9 Hz, 1H), 7.76 – 7.50 (m, 4H), 7.29 (d, *J* = 8.3 Hz, 1H), 3.15 (s, 6H). ^{13}C NMR (101 MHz, DMSO-d_6) δ 164.56, 163.88, 157.43, 146.34, 133.56, 133.53, 133.03, 132.43, 131.36, 130.96, 130.43, 129.76, 128.07, 126.65, 125.57, 125.41, 124.94, 124.90, 123.24, 122.78, 113.53, 44.92.

2.8.15 Synthesis of [Fe(bpa)$_2$(BF_4)$_2$] complex

A solution of Fe(BF_4)$_2$·6$H_2$0 (101 mg, 0.3 mmol) in ethanol (5 mL) was added to a stirred solution bis-picolylamine (81 mg, 0.75 mmol) in ethanol (5 mL) and heated to 50 ˚C for 30 minutes. After cooling to room temperature, the red solid [Fe(**bpa**)$_2$](BF_4)$_2$] was precipitated from the brown red solution (150 mg, 0.27 mmol, 90 %).

2.8.16 Synthesis of [Fe(bpa)$_2$](A_1)$_2$·CH_3OH (1)

A solution of Fe(**bpa**)$_2$(BF_4)$_2$] complex (18.43 mg, 0.025 mmol) in methanol (5 mL) was added to a stirred suspension of A_1 (21.6 mg, 0.05 mmol) in methanol (5 mL) and heated to 50 ˚C for 30 minutes. The resulting solution was cooled to room temperature. Red single crystals of [Fe(**bpa**)$_2$](**A_1**)$_2$·CH_3OH (**1**) were crystallised from methanol by slow evaporation. A suitable crystal was selected and collected at 100 K.

Crystal Data for $C_{124}H_{108}N_{16}O_{24}S_4Fe_2$ (*M* =2446.20 g/mol): monoclinic, space group $P2_1/n$ (no. 14), *a* = 11.2103(3) Å, *b* = 14.7235(3) Å, *c* = 17.8602(4) Å, β = 107.395(2)°, V = 2813.09(12) Å^3, Z = 1, T = 100(2) K, μ(Mo Kα) = 0.416 mm^{-1}, *Dcalc* = 1.444 g/cm^3, 22076 reflections measured (4.706° ≤

2Θ ≤ 57.398°), 7223 unique (R_{int} = 0.0164, R_{sigma} = 0.0191) which were used in all calculations. The final R_1 was 0.0445 (I > 2σ(I)) and wR_2 was 0.1178 (all data).

2.8.17 Synthesis of [Fe(bpa)$_2$](A$_2$)$_2$·CH$_3$OH (2)

A solution of Fe(**bpa**)$_2$(BF$_4$)$_2$] complex (18.43 mg, 0.025 mmol) in methanol (5 mL) was added to a stirred suspension **A$_2$** (23.3 mg, 0.05 mmol) in methanol (5 mL) and heated to 50 ˚C for 30 minutes. The resulting solution was filtered and cooled to room temperature. Red single crystals of [Fe(**bpa)**$_2$](**A$_2$**)$_2$·CH$_3$OH (**2**) were crystallised from vapour diffusion of diethyl ether into the resulting reaction. A suitable crystal was selected and collected at 100 K.

Crystal Data for $C_{62}H_{52}FeN_{10}O_{16}S_2$ (*M* =1313.10 g/mol): triclinic, space group $P\bar{1}$ (no. 2), *a* = 8.4691(4) Å, *b* = 10.9865(5) Å, *c* = 17.2843(9) Å, α = 72.563(5)°, β = 79.889(4)°, γ = 68.649(4)°, V = 1425.02(13) Å^3, Z = 1, T = 100(2) K, μ(Mo Kα) = 0.422 mm^{-1}, *Dcalc* = 1.530 g/cm^3, 19898 reflections measured (5.906° ≤ 2Θ ≤ 57.396°), 6769 unique (R_{int} = 0.0382, R_{sigma} = 0.0427) which were used in all calculations. The final R_1 was 0.0468 (I > 2σ(I)) and wR_2 was 0.1110 (all data).

2.8.18 Synthesis of [Fe(bpa)$_2$](A$_3$)$_2$·(CH$_3$)$_2$CO (3)

To a suspension of Ar(4-SO$_3$)-Nap-N(Me)$_2$ **A$_3$** (23.2 mg, 0.05 mmol) in distilled water(2 ml) was added bis-picolylamine (30 mg, 0.15 mmol) forming a transparent solution. Fe(BF$_4$)$_2$·6H$_2$O (8.4 mg, 0.025 mmol) in distilled water solution (1 ml) then was added, the resulting orange-red suspension was added acetone (10 ml) until becoming transparent. Red single crystals of [Fe(**bpa**)$_2$](**A$_3$**)$_2$·(CH$_3$)$_2$CO (**3a**) were crystallised from the reaction solution by slow evaporation. A suitable crystal was selected and collected at 100 K.

Crystal Data for $C_{70}H_{68}FeN_{10}O_{12}S_2$ (*M* =1361.31 g/mol): triclinic, space group $P\bar{1}$ (no. 2), *a* = 8.6396(7) Å, *b* = 9.5036(6) Å, *c* = 20.1911(14) Å, α = 92.693(5)°, β = 95.523(6)°, γ = 96.876(6)°, V = 1635.4(2) Å^3, Z = 1, T = 100.00(10) K, μ(MoKα) = 0.366 mm^{-1}, *Dcalc* = 1.382 g/cm^3, 14585 reflections measured (4.06° ≤ 2Θ ≤ 50.056°), 5763 unique (R_{int} = 0.0700, R_{sigma} = 0.0941) which were used in all calculations. The final R_1 was 0.0764 (I > 2σ(I)) and wR_2 was 0.2197 (all data).

2.8.19 Synthesis of [Fe(bpa)$_2$](A$_5$)·DMF (4)

To a solution of Tröger base coumpound **A$_5$** (20 mg, 0.025 mmol) in a methanol (5 ml) and DMF (3 ml) bis-picolylamine (30 mg, 0.15 mmol) was added forming a transparent solution. A methanolic solution of Fe(BF$_4$)$_2$·6H$_2$O (8.4 mg, 0.025 mmol in 5 mL) was added in and stirred for 2 min. Red

single crystals of [Fe(**bpa**)$_2$](**A$_5$**)·DMF (**4**) were crystallised from the reaction solution by slow evaporation. A suitable crystal was selected and collected at 100 K.

Crystal Data for $C_{66}H_{49}N_{11}O_{13}S_2Fe$ (*M* =1327.33 g/mol): triclinic, space group $P\bar{1}$ (no. 2), *a* = 12.5603(8) Å, *b* = 14.1964(7) Å, *c* = 23.5545(12) Å, α = 73.807(5)°, β = 77.945(5)°, γ = 68.824(5)°, V = 3733.5(4) Å^3, Z = 2, T = 100.00(10) K, μ(Cu Kα) = 2.669 mm^{-1}, *Dcalc* = 1.181 g/cm^3, 48394 reflections measured (7.098° ≤ 2θ ≤ 133.192°), 12969 unique (R_{int} = 0.1286, R_{sigma} = 0.1173) which were used in all calculations. The final R_1 was 0.0926 (I > 2σ(I)) and wR_2 was 0.2640 (all data).

2.8.20 Synthesis of [Fe(bpa)$_2$](A$_6$)$_2$·CH$_3$OH (5)

A solution of Fe(**bpa**)$_2$(BF$_4$)$_2$] complex (18.43 mg, 0.025 mmol) in methanol (5 mL) was added to a stirred suspension A$_6$ (21.6 mg, 0.05 mmol) in methanol (5 mL) and heated to 50 ˚C for 30 minutes. The resulting solution was cooling to room temperature. Red single crystals of [Fe(**bpa)**$_2$](**A$_6$**)$_2$·CH$_3$OH (**5**) were crystallised from methanol by slow evaporation. A suitable crystal was selected and collected at 100 K.

Crystal Data for $C_{64}H_{58}FeN_8O_{10}S_2$ (*M* =1219.15 g/mol): triclinic, space group $P\bar{1}$ (no. 2), *a* = 8.4078(4) Å, *b* = 11.2222(5) Å, *c* = 15.5918(7) Å, α = 84.554(4)°, β = 89.406(4)°, γ = 71.275(4)°, V = 1386.68(11) Å^3, Z = 1, T = 100.00(10) K, μ(CuKα) = 3.473 mm^{-1}, *Dcalc* = 1.460 g/cm^3, 24428 reflections measured (8.358° ≤ 2Θ ≤ 140.312°), 5161 unique (R_{int} = 0.0660, R_{sigma} = 0.0439) which were used in all calculations. The final R_1 was 0.0634 (I > 2σ(I)) and wR_2 was 0.1810 (all data).

2.8.21 Synthesis of [Fe(bpa)$_2$](A$_8$)$_2$ (6)

To a suspension of Ar(3-SO$_3$)-Nap-N(Me)$_2$ **A$_8$** (23.2 mg, 0.05 mmol) in methanol (5 ml) bis-picolylamine (30 mg, 0.15 mmol) was added forming a transparent solution. Fe(BF$_4$)$_2$·6H$_2$O (8.4 mg, 0.025 mmol) in methanol (5 ml) then was added in to the solution. Red single crystals of [Fe(**bpa**)$_2$](**A$_8$**)$_2$ (**6**) were crystallised from the reaction solution by slow evaporation. A suitable crystal was selected and collected at 100 K.

Crystal Data for $C_{64}H_{58}FeN_8O_{10}S_2$ (*M* =1219.15 g/mol): triclinic, space group $P\bar{1}$ (no. 2), *a* = 8.4078(4) Å, *b* = 11.2222(5) Å, *c* = 15.5918(7) Å, α = 84.554(4)°, β = 89.406(4)°, γ = 71.275(4)°, V = 1386.68(11) Å^3, Z = 1, T = 100.00(10) K, μ(CuKα) = 3.473 mm^{-1}, *Dcalc* = 1.460 g/cm^3, 24428 reflections measured (8.358° ≤ 2Θ ≤ 140.312°), 5161 unique (R_{int} = 0.0660, R_{sigma} = 0.0439) which were used in all calculations. The final R_1 was 0.0634 (I > 2σ(I)) and wR_2 was 0.1810 (all data).

2.8.22 Synthesis of [Fe(bpa)$_2$](A$_9$)$_2$·5CH$_3$OH (7)

A solution of Fe(**bpa**)$_2$(BF$_4$)$_2$] complex (18.43 mg, 0.025 mmol) in methanol (5 mL) was added to a stirred suspension **A$_9$** (24.1 mg, 0.05 mmol) in methanol (5 mL) and heated to 50 ˚C for 30 minutes. The resulting solution was filtered and cooled to room temperature. Red single crystals of [Fe(**bpa)**$_2$](**A$_9$**)$_2$·5CH$_3$OH (**7**) were crystallised from vapour diffusion of diethyl ether into the resulting reaction solution. A suitable crystal was selected and collected at 100 K.

Crystal Data for $C_{73}H_{70}FeN_8O_{15}S_2$ (*M* =1419.34 g/mol): triclinic, space group $P\bar{1}$ (no. 2), *a* = 11.86110(10) Å, *b* = 13.9723(2) Å, *c* = 20.4738(2) Å, α = 95.451(1)°, β = 105.032(1)°, γ = 95.614(1)°, V = 3235.56(6) Å^3, Z = 2, *T* = 100.01(10) K, μ(CuKα) = 3.121 mm^{-1}, *Dcalc* = 1.457 g/cm^3, 65944 reflections measured (6.406° ≤ 2Θ ≤ 140.624°), 12196 unique (R_{int} = 0.0425, R_{sigma} = 0.0283) which were used in all calculations. The final R_1 was 0.0486 (I > 2σ(I)) and wR_2 was 0.1389 (all data).

2.8.23 Synthesis of [Fe(bpa)$_2$](A$_{11}$)$_2$·H$_2$O·CH$_3$OH (8)

5-Naph(1-SO$_3$)-Nap-N(Me)$_2$ **A$_{11}$** (25.7 mg, 0.05 mmol) in methanol suspension (5 ml) was added with bis-picolylamine (30 mg, 0.15 mmol) forming a transparent solution. Fe(BF$_4$)$_2$·6H$_2$O (8.4 mg, 0.025 mmol) in methanol (5 ml) then was added, the resulting orange-red suspension was added acetone (10 ml) until becoming transparent. Red single crystals of [Fe(**bpa**)$_2$](**A$_{11}$**)$_2$·H$_2$O·CH$_3$OH (**8**) were crystallised from the reaction solution by slow evaporation. A suitable crystal was selected and collected at 100 K.

Crystal Data for $C_{37}H_{35}Fe_{0.5}N_5O_{6.5}S$ (*M* =713.68 g/mol): triclinic, space group $P\bar{1}$ (no. 2), *a* = 8.1701(4) Å, *b* = 9.5689(4) Å, *c* = 21.1592(8) Å, α = 100.522(3)°, β = 94.786(3)°, γ = 95.227(3)°, V = 1611.14(12) Å^3, Z = 2, T = 99.99(13) K, μ(MoKα) = 0.377 mm^{-1}, *Dcalc* = 1.471 g/cm^3, 30561 reflections measured (3.936° ≤ 2Θ ≤ 50.054°), 5697 unique (R_{int} = 0.0554, R_{sigma} = 0.0387) which were used in all calculations. The final R_1 was 0.0707 (I > 2σ(I)) and wR_2 was 0.2015 (all data).

2.8.24 Synthesis of [Fe(bpa)$_2$](A$_{12}$)$_2$·0.66H$_2$O (9)

A solution of Fe(**bpa**)$_2$(BF$_4$)$_2$] complex (18.43 mg, 0.025 mmol) in methanol (5 mL) was added to a stirred suspension **A$_{12}$** (24.1 mg, 0.05 mmol) in methanol (5 mL) and heated to 50 ˚C for 30 minutes. The resulting solution was filtered and cooled to room temperature. Red single crystals of [Fe(**bpa)**$_2$](**A$_{12}$**)$_2$·5CH$_3$OH (**9**) were crystallised from vapour diffusion of diethyl ether into the resulting reaction solution. A suitable crystal was selected and collected at 100 K.

Crystal Data for $C_{68}H_{50.6625}FeN_8O_{10.33}S_2$ (*M* =2530.15 g/mol): monoclinic, space group P2/c (no. 13), *a* = 16.3311(3) Å, *b* = 9.27470(10) Å, *c* = 41.2768(7) Å, β = 90.571(2)°, V = 6251.72(17) Å^3, *Z* = 4, T = 100(2) K, μ(Cu Kα) = 3.110 mm^{-1}, D*calc* = 1.344 g/cm^3, 64309 reflections measured (6.868° ≤ 2Θ ≤ 133.158°), 11039 unique (R_{int} = 0.0694, R_{sigma} = 0.0483) which were used in all calculations. The final R_1 was 0.0815 (I > 2σ(I)) and wR_2 was 0.2147 (all data).

2.8.25 Synthesis of [Fe(bpa)$_2$](A$_{13}$)$_2$·H$_2$O·CH$_3$OH (10)

A solution of Fe(**bpa**)$_2$(BF$_4$)$_2$] complex (18.43 mg, 0.025 mmol) in methanol (5 mL) was added to a stirred suspension **A$_{13}$** (26.4 mg, 0.05 mmol) in methanol (5 mL) and heated to 50 ˚C for 30 minutes. The resulting solution was filtered and cooled to room temperature. Red single crystals of [Fe(**bpa**)$_2$](**A$_{13}$**)$_2$·H$_2$O·CH$_3$OH (**10**) were crystallised from methanol by slow evaporation. A suitable crystal was selected and collected at 100 K.

Crystal Data for $C_{70}H_{60}FeN_{10}O_{18}S_2$ (*M* =1449.25 g/mol): triclinic, space group $P\bar{1}$ (no. 2), *a* = 8.9362(2) Å, *b* = 9.2403(3) Å, *c* = 19.5603(4) Å, α = 81.641(2)°, β = 85.433(2)°, γ = 78.225(2)°, V = 1562.29(7) Å^3, Z = 1, T = 100(2) K, μ(Mo Kα) = 0.395 mm^{-1}, D*calc* = 1.540 g/cm^3, 39510 reflections measured (4.662° ≤ 2Θ ≤ 52.746°), 6394 unique (R_{int} = 0.0331, R_{sigma} = 0.0223) which were used in all calculations. The final R_1 was 0.0672 (I > 2σ(I)) and wR_2 was 0.1735 (all data).

2.8.26 Synthesis of [Fe(bpa)$_2$](A$_{14}$)$_2$·H$_2$O (11)

5-Naph(2-SO$_3$)-Nap-N(Me)$_2$ **A$_{14}$** (25.7 mg, 0.05 mmol) in methanol suspension (5 ml) was added with bis-picolylamine (30 mg, 0.15 mmol) forming a transparent solution.Fe(BF$_4$)$_2$·6H$_2$O (8.4 mg, 0.025 mmol) in methanol (5 ml) then was added, the resulting orange-red suspension was added acetone (10 ml) until becoming transparent. Red single crystals of [Fe(**bpa**)$_2$](**A$_{11}$**)$_2$·H$_2$O·CH$_3$OH (**8**) were crystallised from the reaction solution by slow evaporation. A suitable crystal was selected and collected at 100 K.

Crystal Data for $C_{72}H_{64}FeN_{10}O_{12}S_2$ (*M* =1381.30 g/mol): triclinic, space group $P\bar{1}$ (no. 2), *a* = 8.8437(2) Å, *b* = 9.0638(2) Å, *c* = 19.7303(3) Å, α = 92.303(2)°, β = 90.8270(10)°, γ = 95.388(2)°, V = 1573.01(6) Å^3, Z = 1, T = 100(1) K, μ(Cu Kα) = 3.168 mm^{-1}, D*calc* = 1.458 g/cm^3, 26790 reflections measured (4.482° ≤ 2Θ ≤ 140.738°), 5839 unique (R_{int} = 0.0761, R_{sigma} = 0.0595) which were used in all calculations. The final R_1 was 0.0572 (I > 2σ(I)) and wR_2 was 0.1729 (all data).

Chapter 3 The Introduction of Naphthalimide Anion Systems into 1,2,4-Triazole Based Dinuclear Complexes

3.1 Dinuclear Complexes of the Bis-terdentate 1,2,4-triazole Ligands (PMRT)

Compounds containing a 1,2,4-triazole have been prevalent for many years in a number of research areas, such as anti-fungals, intermediates in organic transformations and coordination chemistry, due to their variety of chemical and biological properties.[121] There has been a huge amount of work to functionalise 1,2,4-triazole of 4 positions, and the primarily work to functionalise 2,5 positions and complexes has been investigated in Brooker's research group.[122] According to this work the introduction of substituents at the carbon positions of the 1,2,4-triazole ring allows for preparation and control over complexes. Investigations on PMRT systems have produced a significant number of dinuclear Fe(II) complexes (Figure 3-1).[122-123] These PMRT ligand containing Fe(II) complexes exhibit SCO properties and further demonstrate the tunability of the systems through the ligands substituents. A large variety of different SCO properties have been observed through changing the substitution patterns on these ligands. A brief summary of their use in SCO complexes is provided in Table 3-1.

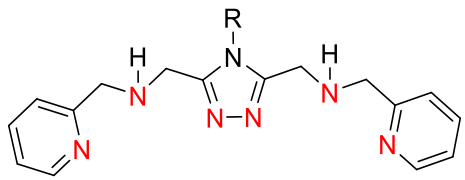

PMRT

Figure 3-1 General structure of the PMRT ligand family with the coordinating nitrogen atoms highlighted in red

Table 3-1 Tabulated data available on current PMRT iron(II) systems for easy comparison. *Squeeze (PLATON)[124] applied.

Structure of Ligand	Complex Tested for SCO	Crystal Structure Determined	SCO Properties	Year and Reference
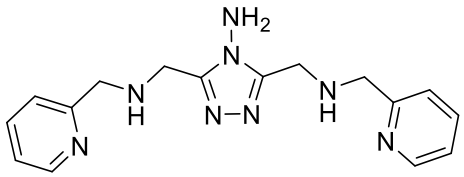 **PMAT**	$[Fe_2(PMAT)_2](BF_4)_4 \cdot DMF$	At 123 and 298 K $[Fe_2(PMAT)_2](BF_4)_4 \cdot DMF$	Abrupt half spin transition between [HS-HS] and [HS-LS] with a $T_{1/2}$ = 224 K	2011[125]
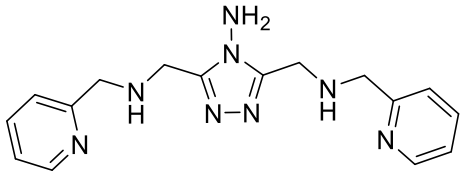 **PMAT**	N/A	At 90 and 293 K $[Fe2(PMAT)_2]Cl_4 \cdot 2MeOH \cdot H_2O$	N/A	2011[125]
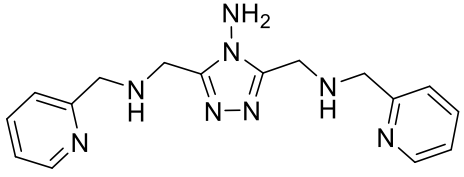 **PMAT**	$[Fe_2(PMAT)_2](PF_6)_4$	No	Gradual partial SCO mixture of [HS-LS] and [HS-HS]to [HS-HS]	2011[125]

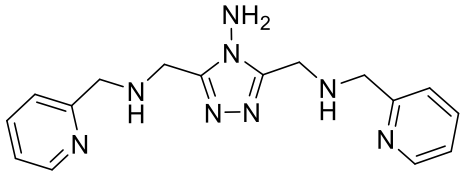 **PMAT**	$[Fe_2(PMAT)_2](SbF_6)_4 \cdot 2H_2O$	No	Gradual partial SCO mixture of [HS-LS] and [HS-HS] to [HS-HS]	2011[125]
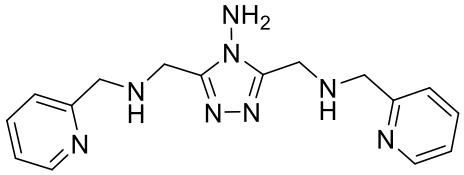 **PMAT**	$[Fe_2(PMAT)_2](CF_3SO_3)_4 \cdot H_2O$	No	Gradual partial SCO from [HS-LS] to a mixture of [HS-LS] and [HS-HS] at $T_{1/2} \approx 180$ K	2011[125]
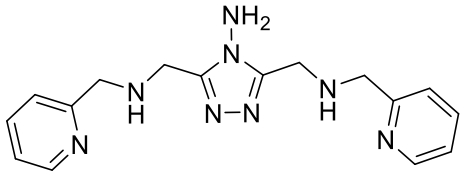 **PMAT**	$[Fe_2(PMAT)_2](CF_3SO_3)_4 \cdot 3/4IPA \cdot H_2O$	At 90 K $[Fe_2(PMAT)_2](CF_3SO_3)_4 \cdot 3/4IPA \cdot H_2O$	[HS-HS] at 90 K	2011[125]

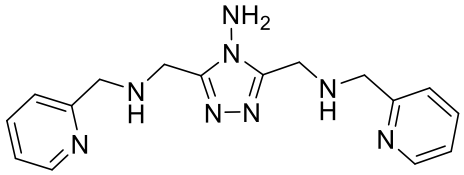 **PMAT**	$[Fe_2(PMAT)_2](B(PhF)_4)_4 \cdot 1/2MeCN$	No	approximately [LS-HS] at all temperatures, with an onset of gradual SCO with $T_{1/2}$ > 300 K.	2011[125]
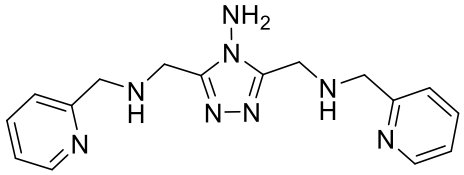 **PMAT**	$[Fe_2(PMAT)_2](C_{16}H_{33}SO_3)_4 \cdot 1/2MeCN$	No	approximately [LS-HS] at all temperatures, with an onset of gradual SCO with $T_{1/2}$ > 300 K.	2011[125]
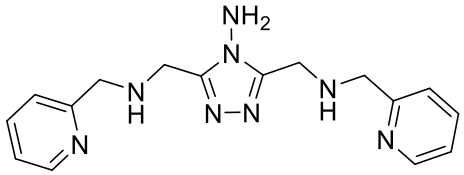 **PMAT**	$[Fe_2(PMAT)_2](C_{16}H_{33}SO_3)_4 \cdot 1.6MeOH \cdot 0.4 H_2O$	At 90 K $[Fe_2(PMAT)_2](C_{16}H_{33}SO_3)_4 \cdot 1.6MeOH \cdot 0.4H_2O$	[HS-HS] at 90 K	2011[125]

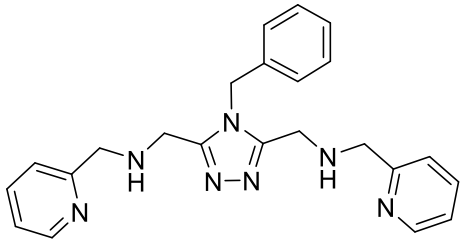 **PMBzT**	$[Fe_2(PMBzT)_2](BF_4)_4$	At 89 K $[Fe_2(PMBzT)_2](BF_4)_4 \cdot CH_3CN$	Gradual half SCO between [HS-HS] and [HS-LS] with a $T_{1/2}$ = 147 K	2013[121]
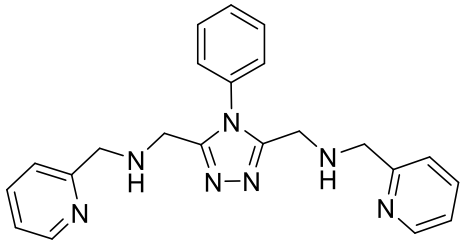 **PMPhT**	$[Fe_2(PMPhT)_2](BF_4)_4$	No	Gradual half SCO between [HS-HS] and [HS-LS] with a $T_{1/2}$ = 187 K	2013[121]
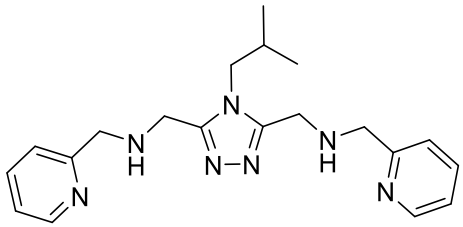 **PMibT**	$[Fe_2(PMibT)_2](BF_4)_4 \cdot 3H_2O$	No	Gradual half SCO between [HS-HS] and [HS-LS] with a $T_{1/2}$ = 234 K	2013[121]

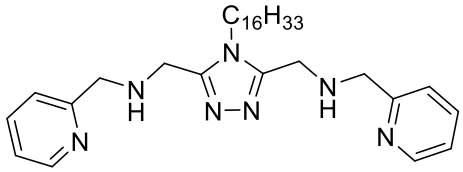 **$PMC_{16}T$**	$[Fe2(PMC_{16}T)_2](BF_4)_4$	No	Gradual half SCO between [HS-HS] and [HS-LS] with a $T_{1/2}$ = 224 K	2013[121]
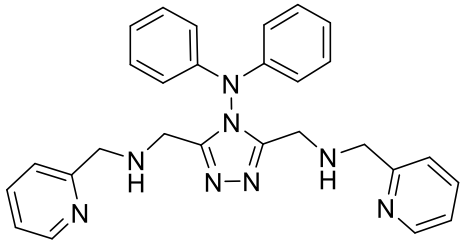 **$PM^{Ph}AT$**	$[Fe_2(PM^{Ph}AT)_2](BF_4)_4$	At 91 K $[Fe_2(PM^{Ph}AT)_2](BF_4)_4 \cdot$solvents*	[HS-HS] across all temperatures down to 4 K	2013[121]
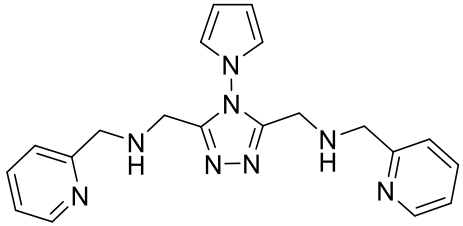 **PMPT**	$[Fe_2(PMPT)_2](BF_4)_4 \cdot H_2O$	At 90 K $[Fe_2(PMPT)_2](BF_4)_4 \cdot 4DMF$	[HS-HS] across all temperatures down to 4 K	2013[121]

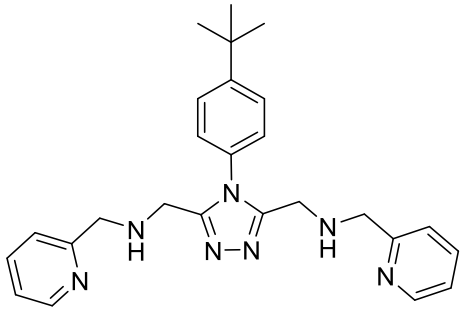 **PMPh^{tBu}T**	$[Fe_2(PMPh^{tBu}T)_2](BF_4)_4 \cdot 3.5H_2O$	At 90 K $[Fe_2(PMPh^{tBu}T)_2](BF_4)_4 \cdot 3CH_3CN \cdot 0.5(C_4H_{10}O)$	Scan rate dependent thermal hysteresis between the [HS-HS] and [HS-LS] state	2013[121]
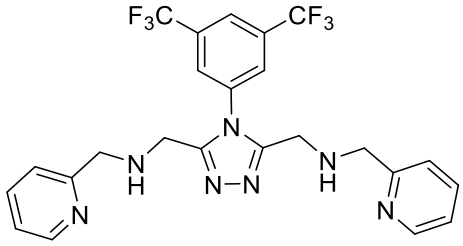 **PM^{CF3}PhT**	$[Fe_2(PM^{CF3}PhT)_2](BF_4)_4 \cdot H_2O \cdot DMF$	No	Gradual half SCO between [HS-HS] and [HS-LS] with a T1/2 = 133 K	2013[121]

From Table 3-1, it can be seen that only two spin state configurations of the two metal centres have been observed to date, the [HS-HS] and [HS-LS], with no observations of a [LS]-[LS] complex. $[Fe_2(PMAT)_2](BF_4)_4$·DMF can be seen below to exhibit these observed spin states of the two metal centres (Figure 3-2). An abrupt half spin transition occurs between [HS-HS] and [HS-LS] with a $T_{1/2}$ = 224 K. Upon further cooling to a temperature of 2 K, the spin transition still remains as [HS-LS]. This complex has also been subjected to other extreme conditions and there is no evidence of a fully diamagnetic [LS-LS] configuration even under high pressure (1 GPa, approximately 10,000x atmospheric).

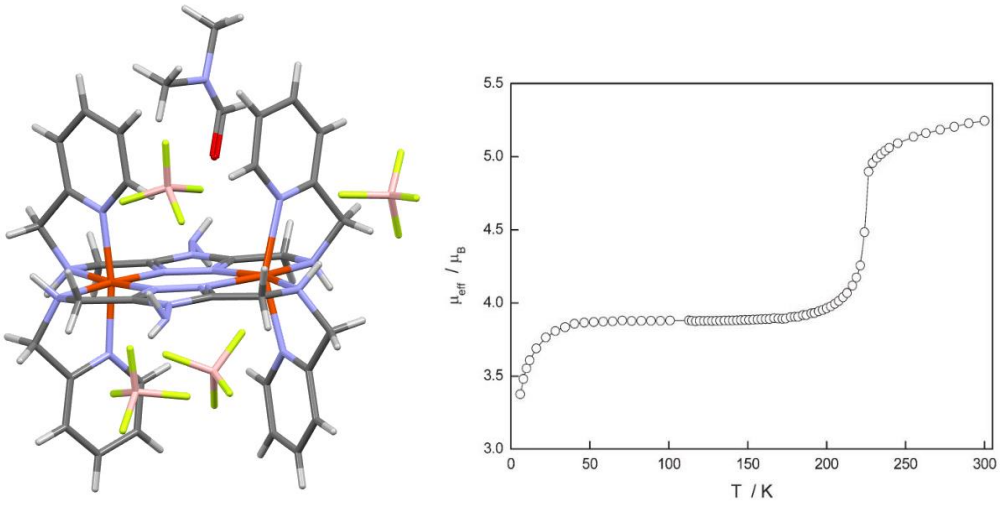

(a) (b)

Figure 3-2 (a) Crystal structure of $[Fe_2(PMAT)_2](BF_4)_4$·DMF; (b) Effective magnetic moment μ_{eff} Vs. temperature (K) for $[Fe_2(PMAT)_2](BF_4)_4$·DMF crsytals. Figure adapted from Brooker, S. *et al.*[125]

This behaviour is confirmed again with a half SCO between [HS-HS] and [HS-LS]in the crystal structure of $[Fe_2(PMBzT)_2](BF_4)_4$. This crystal structure was determined at 89 K with acetonitrile solvent included as $[Fe_2(PMBzT)_2](BF_4)_4$·CH_3CN. The magnetic data shows a gradual spin transition with a $T_{1/2}$ = 187 K. The bond lengths and cis <N-Fe-N angles for both $[Fe_2(PMAT)_2](BF_4)_4$·DMF and $[Fe_2(PMBzT)_2](BF_4)_4$·CH_3CN are presented in Table 3-2 below.

Considering the synthesis procedure, crystal accessibility and SCO properties, $[Fe_2(PMAT)_2](BF_4)_4$·DMF and $[Fe_2(PMBzT)_2](BF_4)_4$·CH_3CN were chosen to continue experiments to introduce a naphthalimide anion into the system.

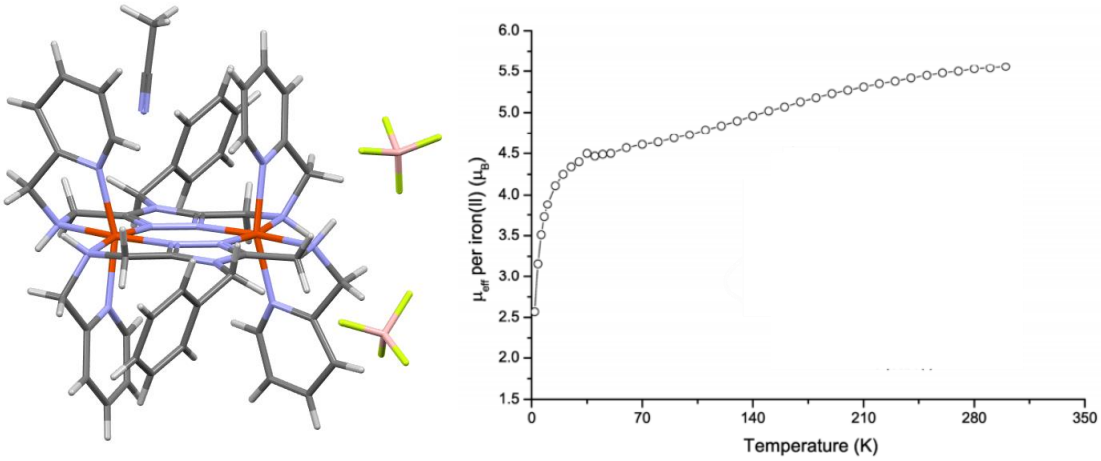

(a) (b)

Figure 3-3 (a) Crystal structure of $[Fe_2(\mathbf{PMBzT})_2](BF_4)_4{\cdot}CH_3CN$; (b) Effective magnetic moment μ_{eff} vs. temperature (K) for $[Fe_2(\mathbf{PMBzT})_2](BF_4)_4$ crystals. Figure adapted from Brooker, S. *et al.*[121]

Table 3-2 Comparison of selected bond distances (Å) and angles (°) for $[Fe_2(\mathbf{PMAT})_2](BF_4)_4{\cdot}DMF$[125] and $[Fe_2(\mathbf{PMBzT})_2](BF_4)_4{\cdot}CH_3CN$[121]

	$[Fe_2(\mathbf{PMAT})_2](BF_4)_4{\cdot}DMF$[125]		$[Fe_2(\mathbf{PMBzT})_2](BF_4)_4{\cdot}CH_3CN$[121]
Collected T	123 K [HS-LS]	298 K [HS-HS]	89 K
Fe_N_{pyr} [Å]	Fe(HS) 2.159(4), 2.155(4) Fe(LS) 1.934(3), 1.986(4)	2.148(2),2.147(5)	2.056(6), 2.058(6)
Fe_N_{NH} [Å]	Fe(HS) 2.319(4), 2.312(4) Fe(LS) 2.066(4), 2.071(4)	2.289(5), 2.303(5)	2.159(7), 2.173(5)
Fe_N_{triaz} [Å]	Fe(HS) 2.136(3), 2.131(3) Fe(LS) 1.946(3), 1.934(3)	2.123(4), 2.116(4)	2.020(4), 2.032(5)
average Fe-N [Å]	Fe(HS) 2.202 Fe(LS) 1.989	2.188	2.083
Cis<N-Fe-N [°] range	Fe(HS) 75.1(2)-121.7(2) Fe(LS) 81.8(2)-101.1(2)	75.9(2)-115.9(2)	78.0(3)−111.0(2)
Σ [°]	Fe(HS) 133.1 Fe(LS) 64.9	117.5	99.4

3.2 Synthesis of Complexes of $[Fe_2(PMAT)_2](A_x)\cdot$Solvent and $[Fe_2(PMBzT)_2](A_x)\cdot$Solvent, Where x=1, 2, 5

The general routes to **PMAT** and **PMBzT** ligands, as well as their complexes $[Fe_2(\mathbf{PMAT})_2](BF_4)_4$ and $[Fe_2(PMBzT)_2](BF_4)_4$ followed those published by Brooker.[122]

3.2.1 Synthetic Routes for Ligand PMAT

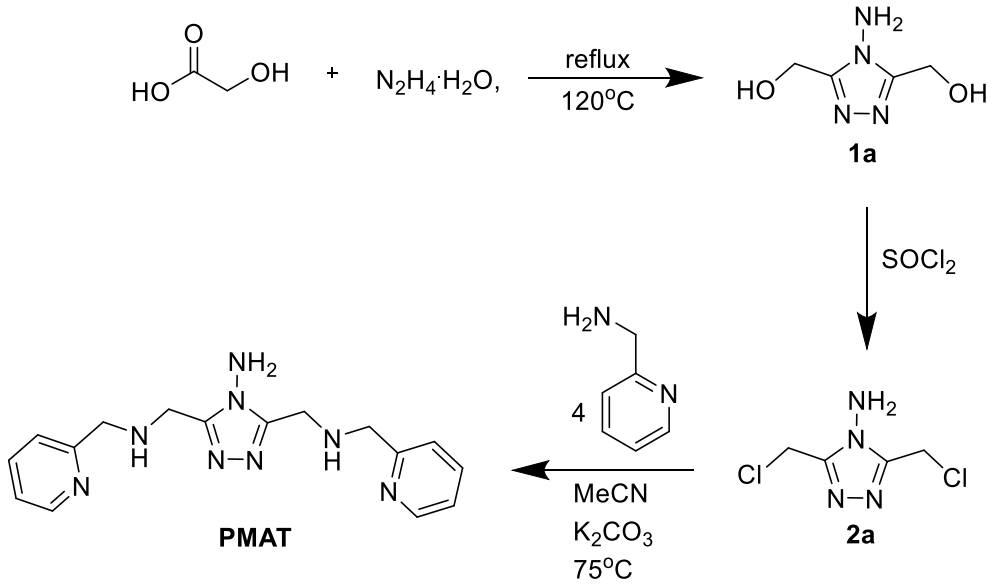

Figure 3-4 Synthetic routes for ligand **PMAT**.

Hydrazine monohydrate was added dropwise at 0 °C to a large excess of 70% aqueous glycolic acid. The resulting solution was heated at 120 °C and refluxed overnight. The excess hydrazine was removed by vacuum to give pure product **1a**. **1a** was dissolved in an excess of thionyl chloride at room temperature stirring for 12 h. The crude product **2a** was obtained as a yellowish solid after removal of excess of thionyl chloride in vacuum. The final step is the reaction of **2a** with an excess of 2-aminomethylpyridine (4 equiv) and K_2CO_3 (6 equiv) in acetonitrile at 75 °C for 7 h to give the **PMAT** product. The crude ligand was purified by further complexation.

3.2.2 Synthetic Routes for the PMBzT ligand

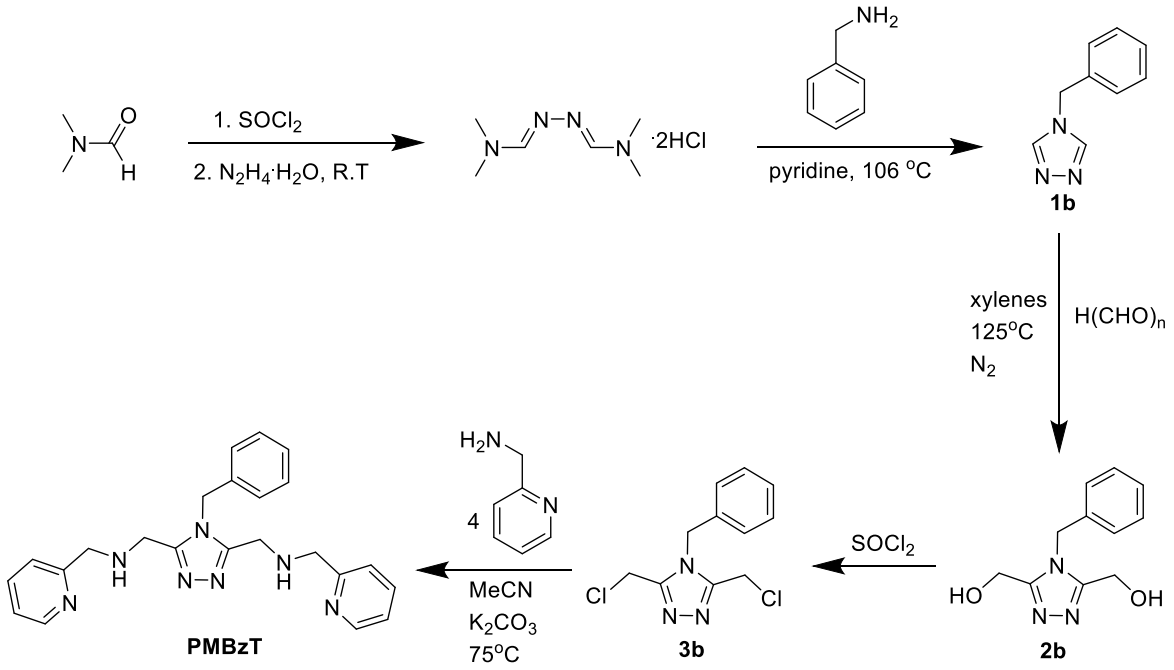

Figure 3-5 Synthetic routes for ligand **PMBzT**.

Thionyl chloride ($SOCl_2$) was added with stirring to a large access of DMF at 5 °C, which was stirred at 5 °C for 4 h and then hydrazine hydrate (0.25 equiv) slowly added into it. After addition, the mixture was stirred at room temperature for 48 h and the white **DMAZ** precipitate (N,N-dimethyl formamide amine dihydrochloride) was collected by filtration and washed with DMF and Et_2O.

DMAZ was used in a slight excess (1.5 equiv) over refluxing benzylamine (1 equiv) at 106 °C for 24 h. On cooling to room temperature, a colourless crystalline solid formed. The pyridine was removed in vacuum, the trace amounts with toluene to give an orange-yellow oily solid. This was taken up in methanol to give a clear yellow solution. The methanol was removed in vacuum and the oily solid then taken up in DCM to give a clear yellow solution. This solution was washed with water, $NaHCO_3$ (sat. aq.) and NaCl (sat. aq.) before drying over $MgSO_4$ and removing the solvent. The pure product **1b** was recrystallised from toluene. **1b** then was heated to 115 °C in xylenes under nitrogen, and 10 equiv of paraformaldehyde was added. Once the entire portion of paraformaldehyde was added the temperature was raised to 125 °C and another 10 equiv of paraformaldehyde added, and heating continued overnight. The resulting solution was filtered and the excess xylenes removed in vacuum. The oily product was then dissolved in ethanol and filtered. The oily compound **2b** was obtained by vacuum filtration.

2b was dissolved in an excess of thionyl chloride at room temperature stirring for 12 h. The crude product **2a** was obtained as a yellowish solid after removal of excess of thionyl chloride in vacuum. The final step is the reaction of **3b** with an excess of 2-aminomethylpyridine (4 equiv)

and K_2CO_3 (6 equiv) in acetonitrile at 75 °C for 7 h to give a product **PMBzT**. The crude ligand was purified by further complexation.

3.2.3 General Procedure for Complexes $[Fe_2(PMAT)_2](BF_4)_4$ and $[Fe_2(PMBzT)_2](BF_4)_4$

A solution of $Fe(BF_4)_2{\cdot}6H_2O$ (675 mg, 0.2 mmol) in methanol (10 ml) was added dropwise to a stirring solution of **PMAT** or **PMBzT** ligand (0.1 mmol) in methanol (5 ml) for 30 min. After cooling down, the precipitate was filtered off and washed with methanol.

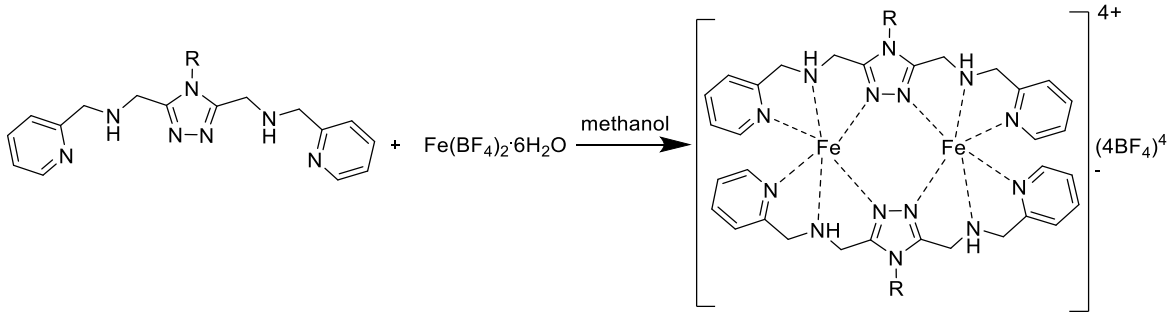

3.2.4 General Procedure for Complexes of $[Fe_2(PMAT)_2](A_x){\cdot}$Solvent and $[Fe_2(PMBzT)_2](A_x){\cdot}$Solvent, Where x=1, 2, 5

The $[Fe_2(PMAT)_2](BF_4)_4$ and $[Fe_2(PMBzT)_2](BF_4)_4$ complexes as prepared in section 3.2.3 (0.025 mmol) were suspended in a solvent mixture of methanol:acetonitrile (1:1) (10 mL) then added to a solvent mixture of methanol:acetonitrile (1:1) solution (10 ml) of $\mathbf{A_1}{\cdot}$PyH (4 equiv), $\mathbf{A_2}{\cdot}$ImdH(4 equiv), or $\mathbf{A_5}{\cdot}$2H (2 equiv). The resulting solution was stirred for 15 min. The resulting solutions were subjected to slow evaporation. Full experimental for all the complexes will be discussed in Chapter 3.7.

3.3 Crystallographic Characterisation of Complexes $[Fe_2(PMAT)_2](A_x)_4{\cdot}$Solvent, X=1, 2

3.3.1 Crystallographic Analysis of $[Fe_2(PMAT)_2](A_1)_4{\cdot}$MeOH (12)

Pale yellow plate-like single crystals of $[Fe_2(\mathbf{PMAT})_2](\mathbf{A_1})_4{\cdot}$MeOH (**12**) were grown by slow evaporation of a solution of $[Fe_2(\mathbf{PMAT})_2](\mathbf{A_1})_4$ in a MeCN:MeOH (1:1) mixture and crystallised in the triclinic space group $P\bar{1}$. The asymmetric unit is made up of one half of the complex cation $[Fe(\mathbf{PMAT})]^{2+}$, two A_1 anions, and a methanol molecule as shown in Figure3-6a. The complete $[Fe_2(\mathbf{PMAT})_2]^{4+}$ fragment is shown in Figure3-6b. The Fe(II) centre adopted a distorted octahedral N_6 coordination geometry (Σ = 79.4°) with bond lengths and angles detailed in table 3-3.

Compared to $[Fe_2(\mathbf{PMAT})_2](BF_4)_4 \cdot DMF$ (table 3-2), this complex appears to feature a LS-HS configuration in Fe(II). Further details on the magnetic properties of this system are provided in Chapter 3.4.

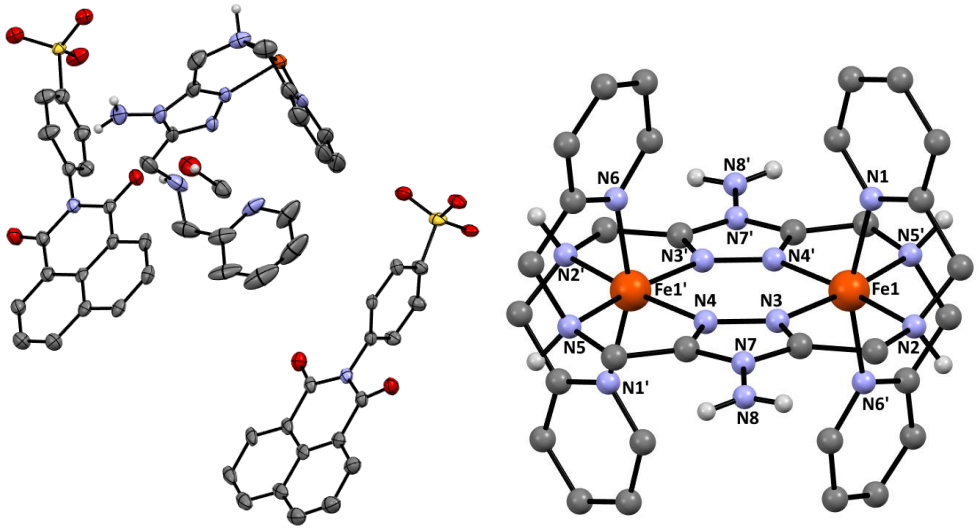

(a) (b)

Figure 3-6 (a) Asymmetric unit of the crystal structure of **12** with ellipsoids at 50% probability level; (b) Configuration of the $[Fe_2(PMAT)_2]^{4+}$ fragment, all C-bound H atoms are omitted for clarity.

The coordination arrangement is as seen in $[Fe_2(\mathbf{PMAT})_2](BF_4)_4 \cdot DMF$ in Chapter 3.1, where coordinated NH groups and triazole rings occupy the equatorial positions and coordinated pyridine rings are situated at the apical sites. The non-coordinated naphthalimide anions interact with adjacent coordinated NH groups and the non-coordinated NH_2 group of **PMAT** complexes through hydrogen bonding to an oxygen atom of a SO_3^- group [N8···O1 = 2.765 (3) Å, and ∠(N-H···O) = 146.52(6)°; N8···O1 = 2.937 (5) Å, and ∠(N-H···O) = 147.01(8)°] (Figure 3-7). The oxygen of a methanol solvate in turn forms a hydrogen bond to the SO_3^- groups of the anions [O11···O7 = 2.990 (4) Å, and ∠(O-H···O) = 157.77(5)°] (Figure 3-7). In addition to this, there are also weak hydrogen bonds from the CH groups of the benzene rings to the SO_3^- group [C21···O7 = 3.001 (5) Å, and ∠(C-H···O) = 124.48°] (Figure 3-7).

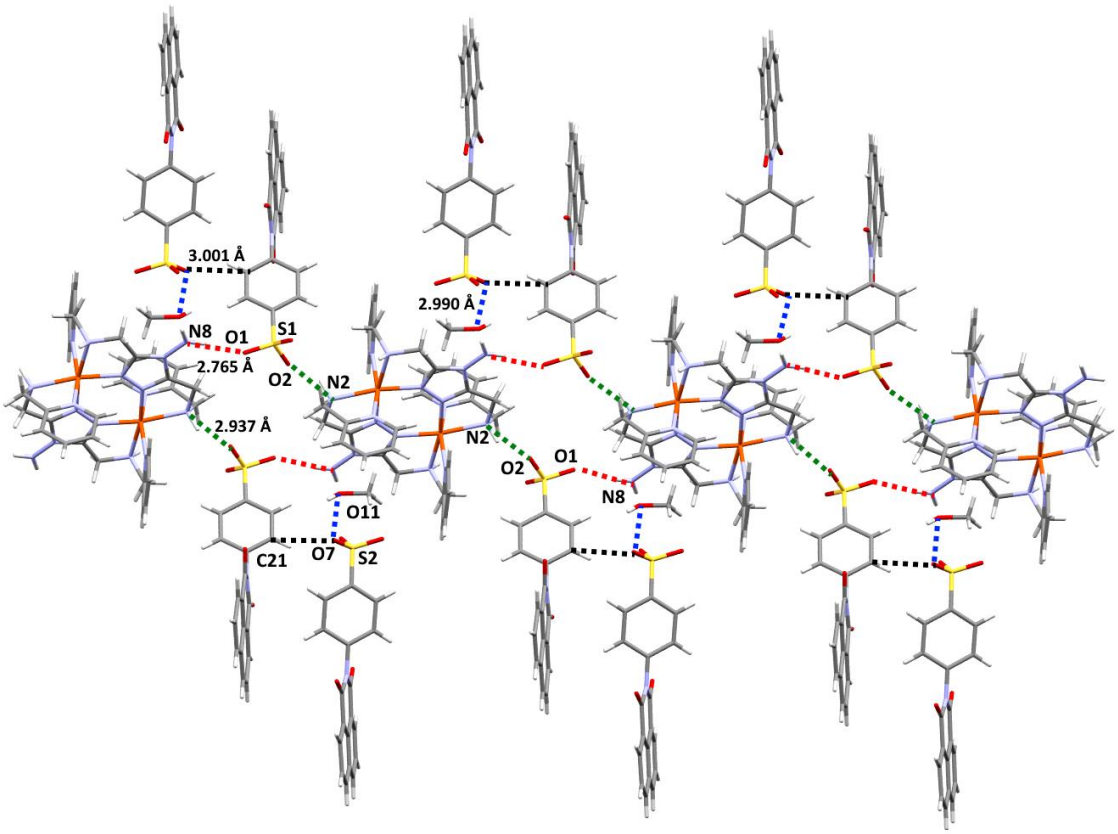

Figure 3-7 View of hydrogen-bonding interactions in **12**

The naphthalimide anions are linked *via* π···π interactions. The head-to-tail π-stacking layers [centroid···centroid = 3.711 Å, in red dashed lines] are linked to neighbouring head-to-tail π-stacking layers [centroid···centroid = 3.524 Å, in blue dashed lines] via head-to-head π-stacking layers [centroid···centroid = 3.614 Å, in black dashed lines] (Figure 3-8). The overall result is an efficiently layer-packed array of interacting complexes (Figure 3-9).

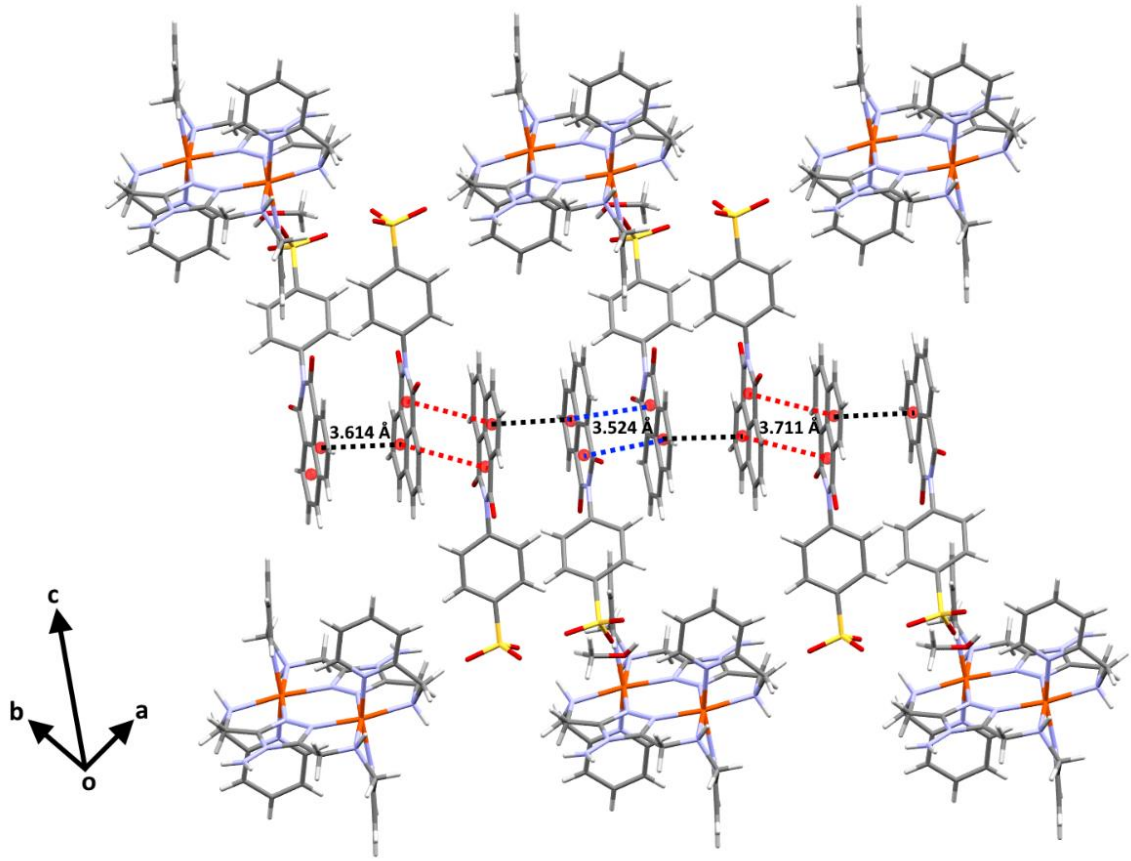

Figure 3-8 Packing interaction of **12** showing $\pi\cdots\pi$ stacking.

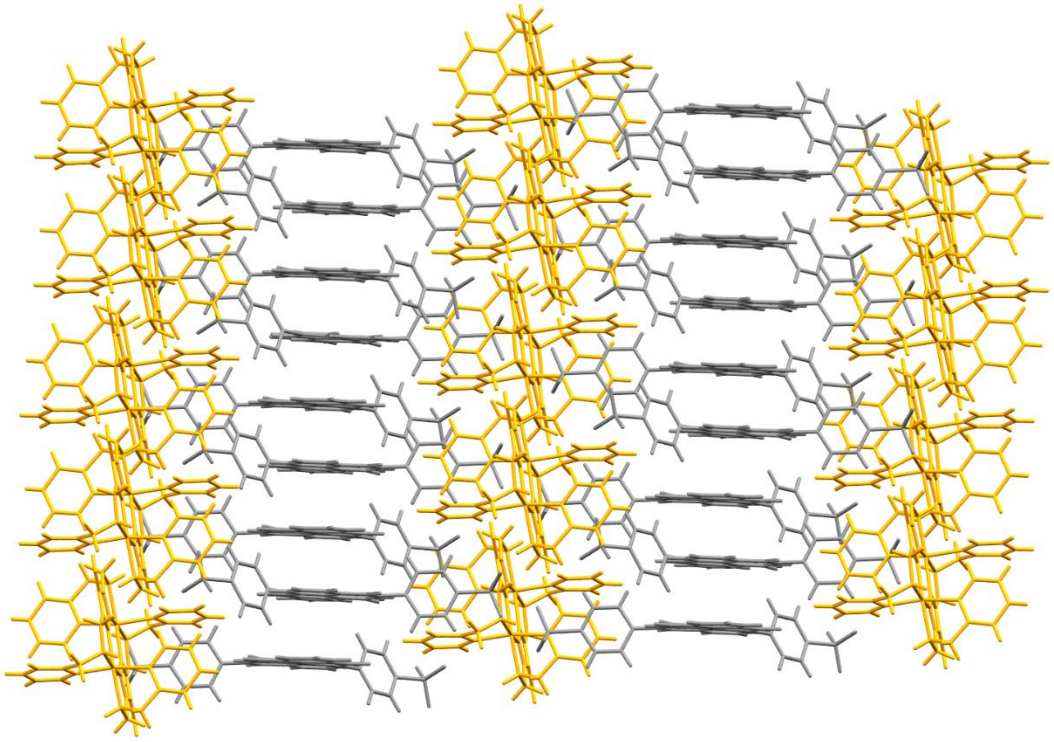

Figure 3-9 Packing interaction of **12**. Naphthalimide molecules are presented in grey, $[Fe_2(\mathbf{PMAT})_2]^{4+}$ molecules are presented in yellow, solvent molecules are omitted for clarity.

3.3.2 Crystallographic Analysis of $[Fe_2(PMAT)_2](A_2)_4$ (13)

Pale yellow plate-like single crystals of $[Fe_2(\mathbf{PMAT})_2](\mathbf{A_1})_4$ (**13**) were grown by slow evaporation of a solution of $[Fe_2(\mathbf{PMAT})_2](\mathbf{A_2})_4$ in a MeCN:MeOH (1:1) mixture and crystallised in the triclinic space group $P\bar{1}$.

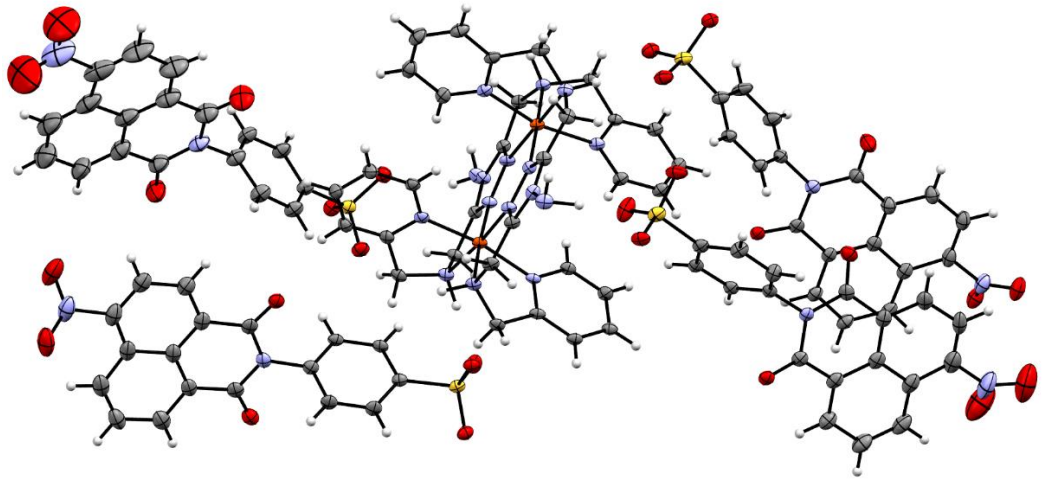

(a)

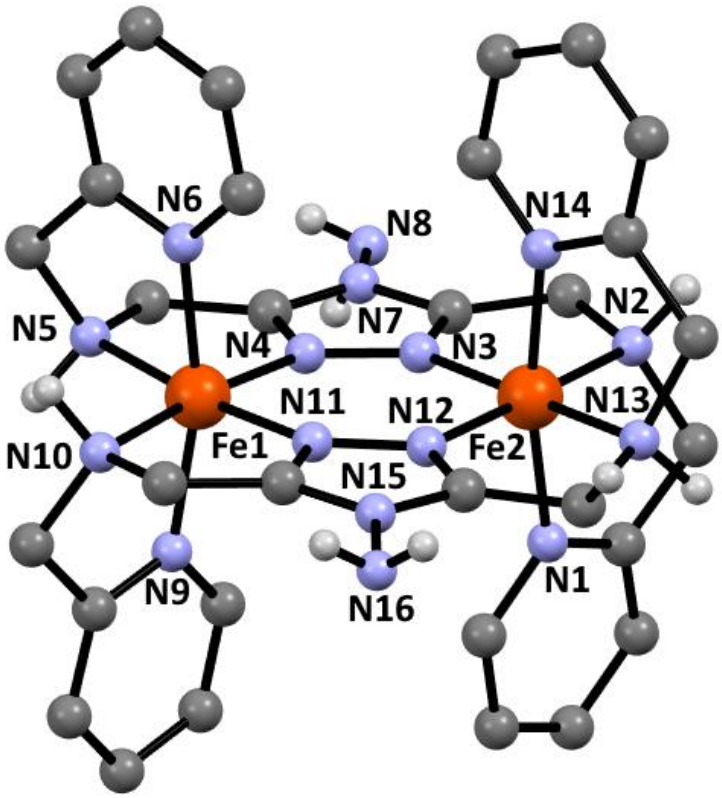

(b)

Figure 3-10 (a) Asymmetric unit of the crystal structure of **13** with ellipsoids at 50% probability level; (b) configuration of the $[Fe_2(PMAT)_2]^{4+}$ fragment, all C-bound H atoms are omitted for clarity.

The asymmetric unit is made up of one $[Fe(\mathbf{PMAT})_2]^{4+}$ cation and four sulfonate naphthalimide anions (Figure 3-10a). The solvent mask routine was used to squeeze 9 acetonitrile molecules and 10 methanol molecules, which cannot be modelled, from the unit cell. The two Fe(II) centres have similar octahedral geometry with two coordinated pyridyl nitrogen atoms, two coordinated triazole nitrogen atoms and two bonded NH groups (Figure 3-10b). The values of Σ are ΣFe1= 64.99° and ΣFe2= 74.92°, the bonds lengths are 1.897-2.052 Å and 1.941-2.020 Å respectively, which are consistent with the LS-LS configuration as shown in Table 3-3. The bound NH groups and triazoles are in a planar arrangement and the coordinated pyridyl rings are again at the apical sites.

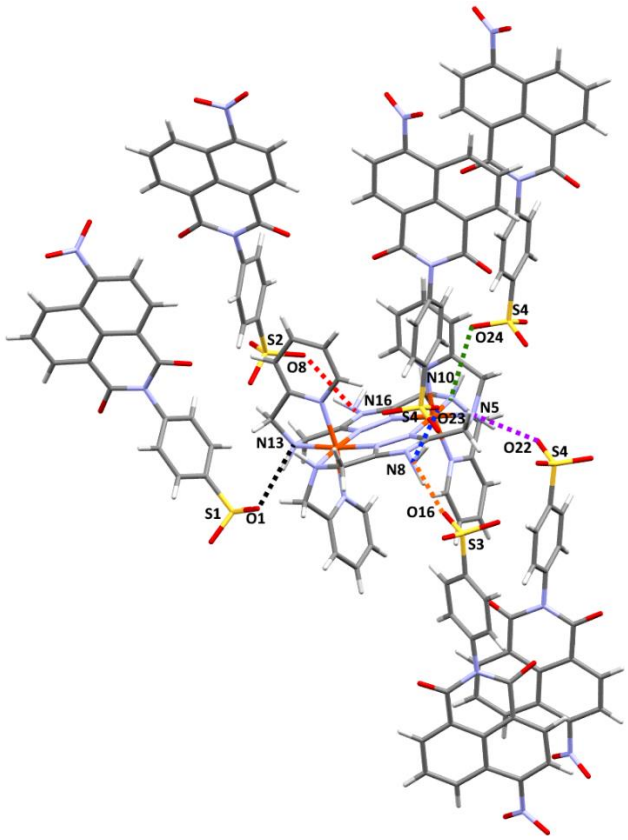

(a)

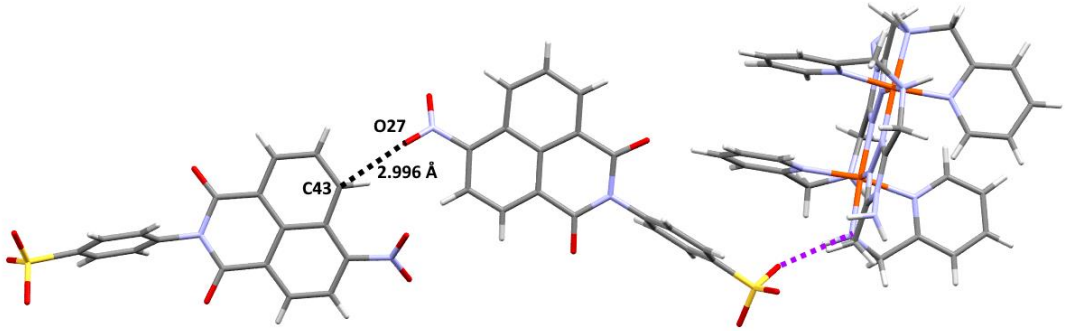

(b)

Figure 3-11 View of hydrogen-bonding interactions in **13**

The strong hydrogen bonds exist in this complex, involving the SO_3 groups from naphthalimide anions and coordinated NH groups from the $[Fe(\mathbf{PMAT})_2]^{2+}$ cation [N13···O1 = 2.867 (3) Å, and ∠(N-H···O) = 174.18(10)° in black dashed line; N5···O22 = 2.907 (5) Å, and ∠(N-H···O) = 164.09(9)° in purple dashed line; N10···O24 = 2.907 (5) Å, and ∠(N-H···O) = 149.12(6)° in green dashed line] (Figure 3-11a). The non-coordinated NH_2 groups from the $[Fe(\mathbf{PMAT})_2]^{2+}$ cation also exhibit some N-H···O interactions with the SO_3 of the naphthalimide anions [N16···O8 = 2.897 (5) Å and ∠(N-H···O) = 149.62(5)° in red dashed line; N8···O23 = 2.907 (5) Å and ∠(N-H···O) = 153.03(9)° in blue dashed line; N8···O16 = 2.907 (6) Å and ∠(N-H···O) = 126.82(9)° in orange dashed line] (Figure 3-11a). In additional to these, a non-classic hydrogen bond was also observed from the NO_2 group of the naphthalimide anion to an adjacent CH group of another naphthalimide anion [C43···O27 = 2.996 (5) Å, and ∠(N-H···O) = 120.38(9)°] (Figure 3-11b).

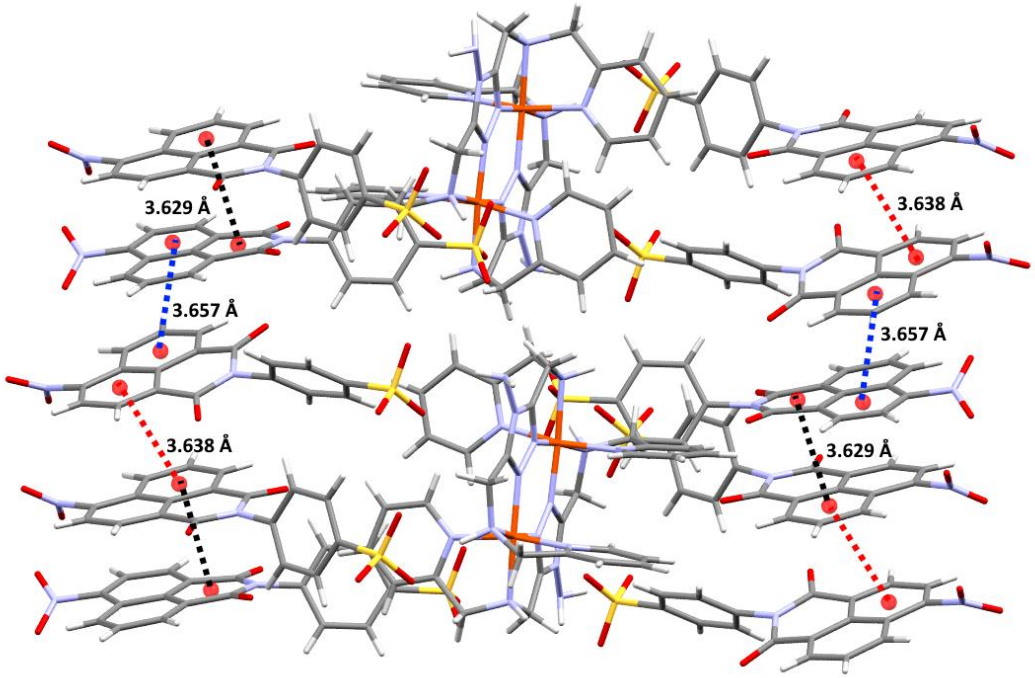

Figure 3-12 Packing interaction of **13** showing $\pi\cdots\pi$ stacking.

There are also strong π···π head-to-head interactions between the alternating naphthalene rings [centroid−centroid 3.657 Å (in blue dashed line) and centroid−centroid 3.638 Å (in red dashed line)] and π-stacking interactions involving neighbouring imide rings [centroid−centroid 3.629 Å (in black dashed line)] (Figure 3-12). Overall the interactions in this complex cause the formation of layers (Figure 3-13).

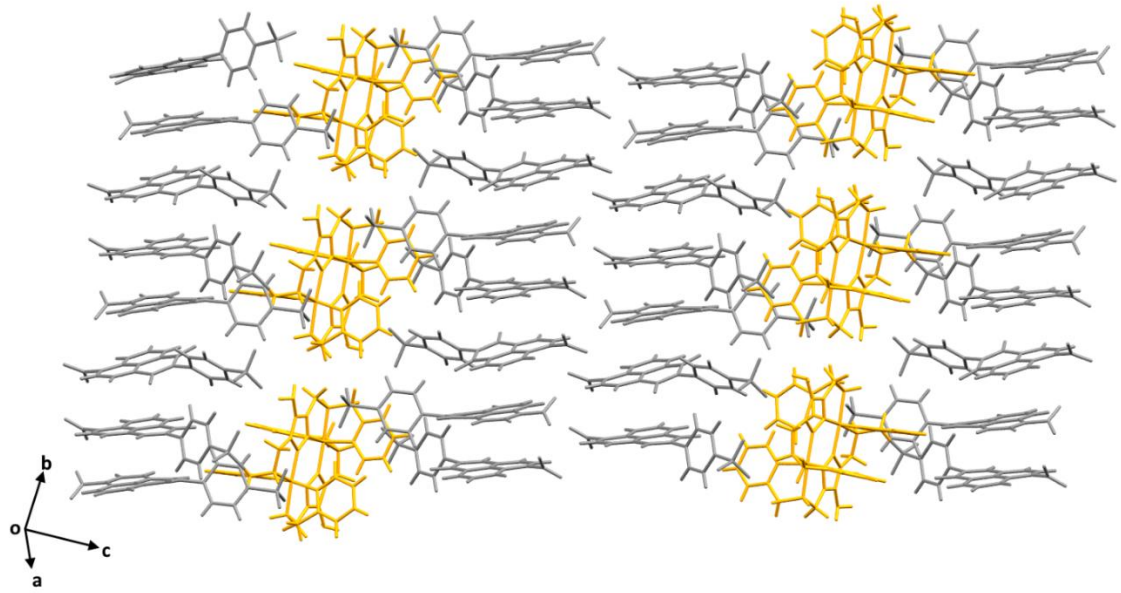

Figure 3-13 Packing interaction of **13**. Naphthalimide molecules are presented in grey, $[Fe_2(\mathbf{PMAT})_2]^{4+}$ molecules are presented in yellow, solvent molecules are omitted for clarity.

Table 3-3 Comparison of Selected Bond Distances (Å), Angles (°), and other data for $[Fe_2(\mathbf{PMAT})_2](BF_4)_4 \cdot DMF$[125], $[Fe_2(\mathbf{PMAT})_2](A_1)_4$ (**12**) and $[Fe_2(\mathbf{PMAT})_2](A_2)_4$ (**13**).

	$[Fe_2(\mathbf{PMAT})_2](BF_4)_4 \cdot DMF$[125]	$[Fe_2(\mathbf{PMAT})_2](A_1)_4$ (**12**)	$[Fe_2(\mathbf{PMAT})_2](A_2)_4$ (**13**)
Collected T /K	123	100	100
Fe_N_{pyr} [Å]	Fe(HS) 2.159(4), 2.155(4)	2.052(7), 2.053(7)	Fe1: 1.989(5), 1.974(5)
	Fe(LS) 1.934(3), 1.986(4)		Fe2: 1.989(5), 2.009(5)
Fe_N_{NH} [Å]	Fe(HS) 2.319(4), 2.312(4)	2.190(7), 2.188(7)	Fe1: 2.052(4), 2.047(5)
	Fe(LS) 2.066(4), 2.071(4)		Fe2: 2.076(5), 2.080(4)
Fe_N_{triaz} [Å]	Fe(HS) 2.136(3), 2.131(3)	2.022(6), 2.032(6)	Fe1: 1.897(5), 1.912(4)
	Fe(LS) 1.946(3), 1.934(3)		Fe2: 1.950(4), 1.941(5)
average Fe-N [Å]	Fe(HS) 2.202	2.090	Fe1: 1.979
	Fe(LS) 1.989		Fe2: 2.008
Cis<N-Fe-N [°] range	Fe(HS) 75.1-121.7	77.9-100.9	Fe1: 81.36-102.97
	Fe(LS) 81.8-101.1		Fe2: 80.16-106.39
Σ [°]	Fe(HS) 133.1	79.4	Fe1: 64.99
	Fe(LS) 64.9		Fe2: 74.92

From the data presented in Table 3-3, the Σ value and angles of complex **12** are consistent with the the HS-LS configuration of $[Fe_2(PMAT)_2](BF_4)_4 \cdot DMF$. However, it may be possible that due to the influences of solvent, the bond lengths observed are between those of HS and LS. Remarkably, all the bond lengths, angles and Σ values of complex **13** indicate that it is likely to be the LS-LS configuration, which is the first LS-LS structure in this system. More detailed magnetism data will be discussed in Chapter 3.4.

3.4 Results and Discussion of $[Fe_2(PMAT)_2](A_1)_4$ (12) and $[Fe_2(PMAT)_2](A_2)_4$ (13)

Given the LS-LS spin nature of the complex of **13** determined from single crystal XRD experiments at 100 K, variable temperature magnetic susceptibility measurements were attempted on this crystalline sample. Complex **13** showed no magnetic signal at the attempted sample centring temperatures (200 K, 300 K, and 100 K), which meant the sample position could not be determined. This indicated that the sample was fully Fe(II) LS with 0 unpaired electrons at these temperatures, and therefore diamagnetic, as such no data was collected.

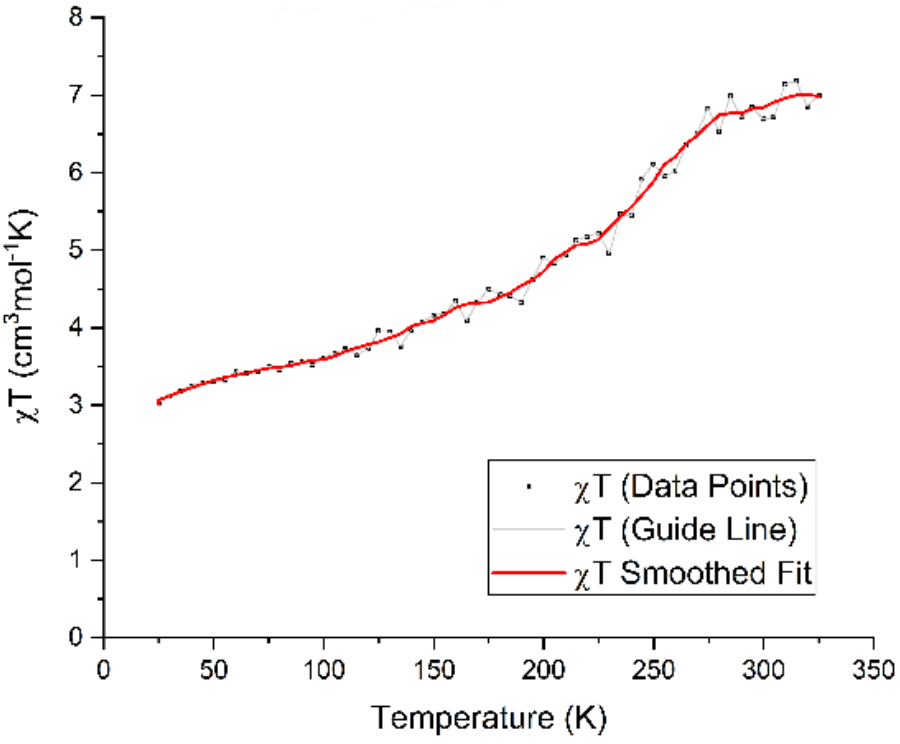

Figure 3-14 Plot of $\chi_M T$ vs. T for complex **12**

Complex **12** was successfully centred and magnetic susceptibility measurements were collected at temperatures between 25 to 350 K under an applied field of 1,000 Oe (0.1 T). Its behaviour,

displayed in Figure 3-14 shows a gradual SCO phenomenon which is different to the abrupt SCO in $[Fe_2(\mathbf{PMAT})_2](BF_4)_4 \cdot DMF$.

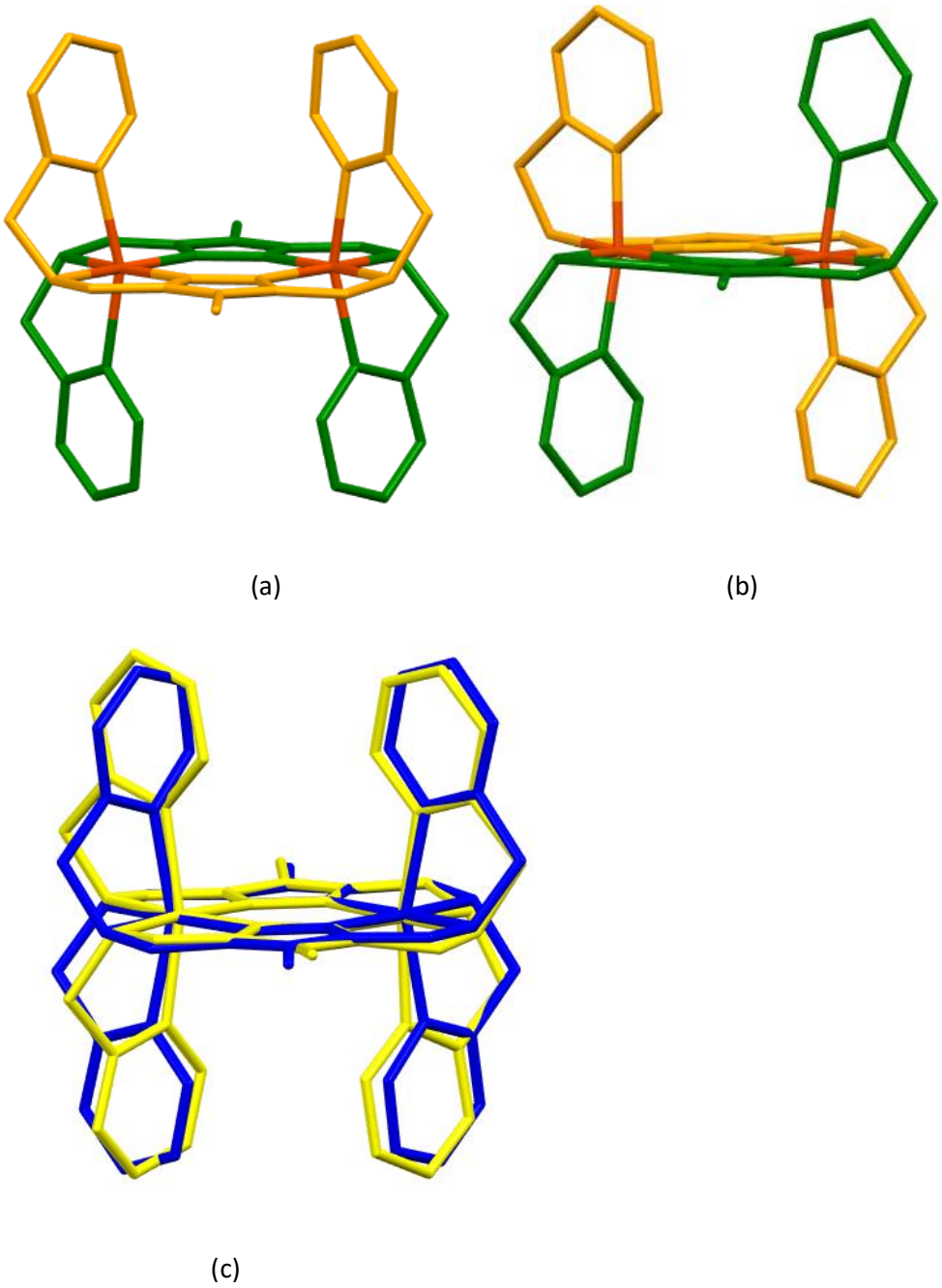

(a) (b)

(c)

Figure 3-15 (a) $[Fe_2(\mathbf{PMAT})_2]^{4+}$ structure of complex **12**. (b) $[Fe_2(\mathbf{PMAT})_2]^{4+}$ structure of complex **13**; different **PMAT** ligands are present in yellow and green respectively. (c) Overlapped structures of complexes **12** (blue) and **13** (yellow) . All the anions, solvents and hydrogens were omitted for clarity.

As there were no previously reported LS-LS complexes for this system, structural comparisons are made in Figure 3-15. The **PMAT** ligands are bound in a cis-configuration for complex **12**, in addition to this the pyridyl rings on the same side as the plane of each other are inserted at

86.83°, which is also similar to $[Fe_2(\mathbf{PMAT})_2](BF_4)_4 \cdot DMF$. However, in complex **13** a trans-configuration of the ligands was observed. This is the first trans-configuration in this system and it results in the pyridyl rings being parallel to each other. It is possible that this trans-configuration may play an important in role the observed LS-LS spin state.

3.5 Crystallographic Characterisation of Complexes $[Fe_2(PMBzT)_2](A_x)_{2/4} \cdot$Solvent, X=1, 2, 4

3.5.1 Crystallographic Analysis of $[Fe_2(PMBzT)_2](A_1)_4 \cdot$MeCN (14)

Pale yellow plate-like single crystals of $[Fe_2(\mathbf{PMBzT})_2](\mathbf{A_1})_4$ (**14**) were grown by slow evaporation of a solution of $[Fe_2(\mathbf{PMBzT})_2](\mathbf{A_1})_4$ in a MeCN:MeOH (1:1) mixture and crystallised in the triclinic space group $P\bar{1}$.

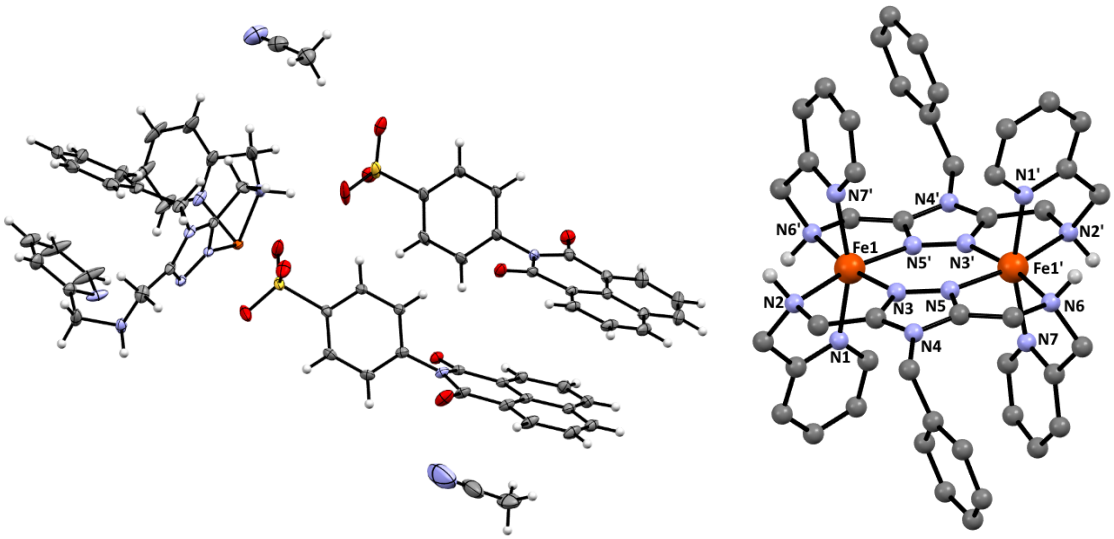

(a) (b)

Figure 3-16 (a) Asymmetric unit of the crystal structure of **14** with ellipsoids at 50% probability level; (b) configuration of the $[Fe_2(\mathbf{PMBzT})_2]^{4+}$ fragment, all C-bound H atoms are omitted for clarity.

Half of the complex cation $[Fe(\mathbf{PMAT})]^{2+}$, two A_1 anions and two acetonitrile molecules are present in the asymmetric unit as shown in Figure3-16a. The complete $[Fe_2(\mathbf{PMAT})_2]^{4+}$ fragment is shown in Figure3-16b. The octahedral Fe(II) centre is coordinated in the same fashion to two pyridyl rings and to two triazoles and NH groups in the same equatorial plane with Σ=98.1°. Compared to $[Fe_2(\mathbf{PMBzT})_2](BF_4)_4 \cdot CH_3CN$ (table 3-2), this complex appears to feature a LS-HS configuration in Fe(II). Further magnetism characterisation is provided in Chapter 3.6.

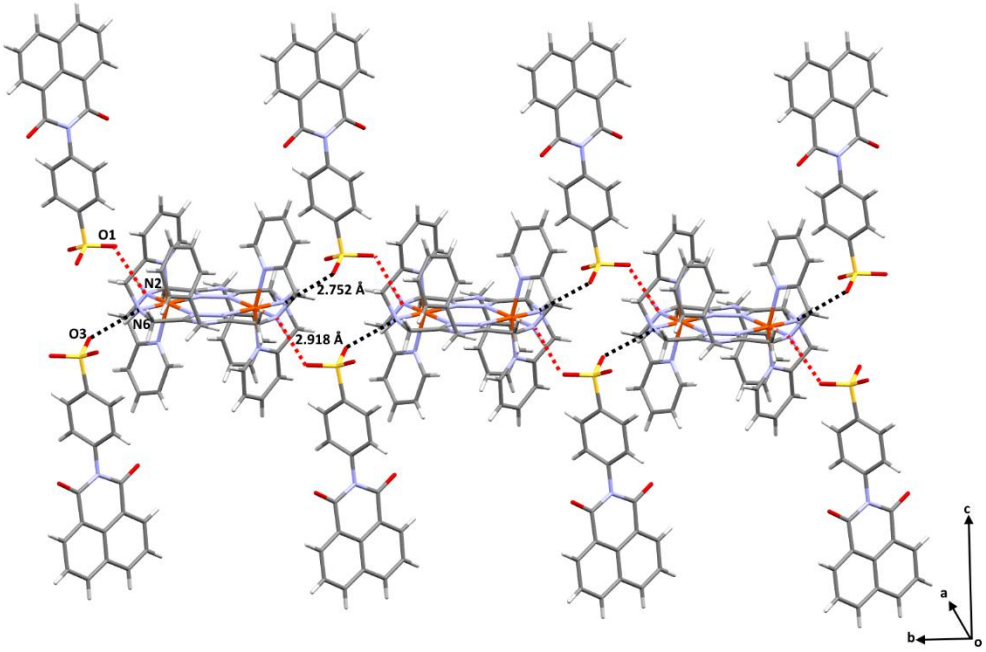

Figure 3-17 View of 1D chain hydrogen-bonding interactions along b axis in **14**.

A 1D chain was driven by strong hydrogen bonds formed between the SO_3 groups of naphthalimide anions and the coordinated nitrogen atoms of NH groups [N2···O1 = 2.752 (5) Å, and ∠(N-H···O) = 171.36(8)° in red dashed line; N6···O3 = 2.918 (5) Å, and ∠(N-H···O) = 161.83(11)° in black dashed line] (Figure 3-17).

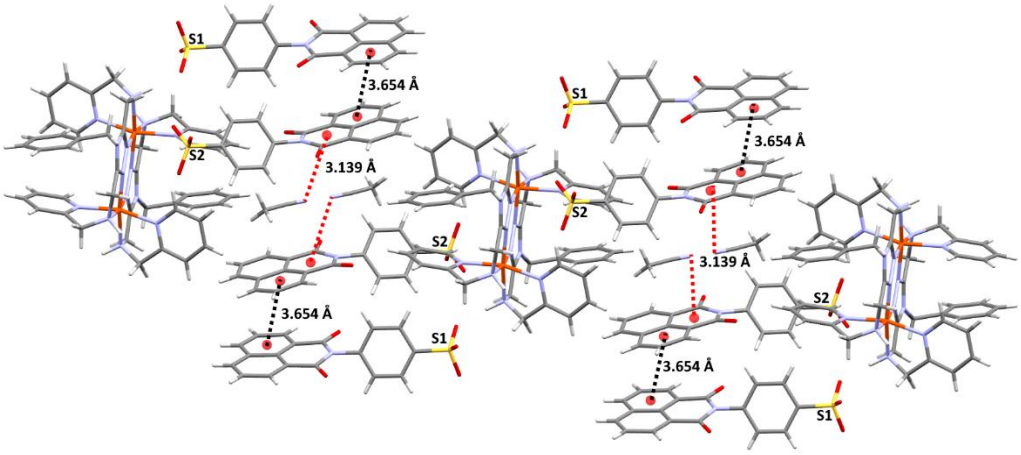

Figure 3-18 Packing interaction of **14** showing $\pi\cdots\pi$ stacking.

Due to the acetonitrile molecules, N···π interactions were observed in this structure where the nitrogen atom interacts with the adjacent imide ring [N···centroid = 3.139 Å in red dashed line] (Figure 3-18). The naphthalimide anions are also offset head-to-head self-complementary π··π interactions linking a neighbouring naphthalimide anion [centroid···centroid = 3.654 Å in black dashed line] (Figure 3-18). These interactions are propagated throughout the structure resulting in the aforementioned layers (Figure 3-19)

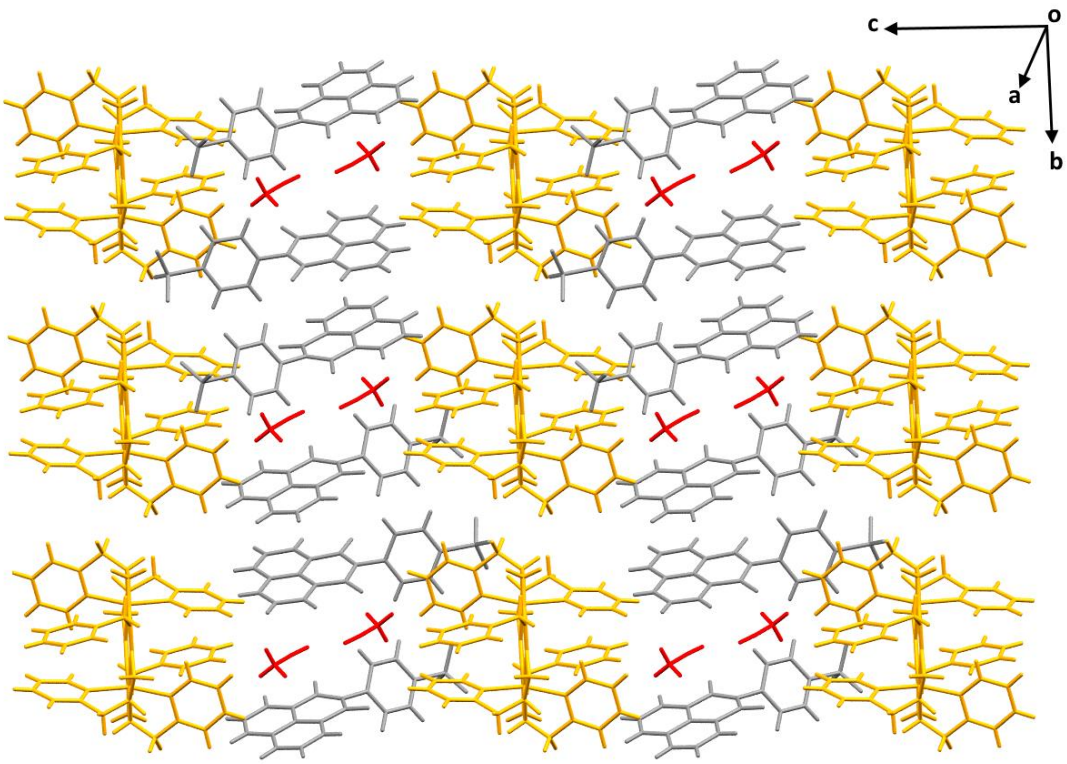

Figure 3-19 Packing interaction of **14**. Naphthalimide molecules are present in grey, $[Fe_2(\mathbf{PMBzT})_2]^{4+}$ molecules are present in yellow, acetonitrile solvent molecules are present in red.

3.5.2 Crystallographic Analysis of $[Fe_2(PMBzT)_2](A_2)_4$ (15)

Pale yellow plate-like single crystals of $[Fe_2(\mathbf{PMBzT})_2](\mathbf{A_2})_4$ (**15**) were grown by slow evaporation of a solution of $[Fe_2(\mathbf{PMBzT})_2](\mathbf{A_2})_4$ in a MeCN:MeOH (1:1) mixture and crystallised in the triclinic space group $P\bar{1}$.

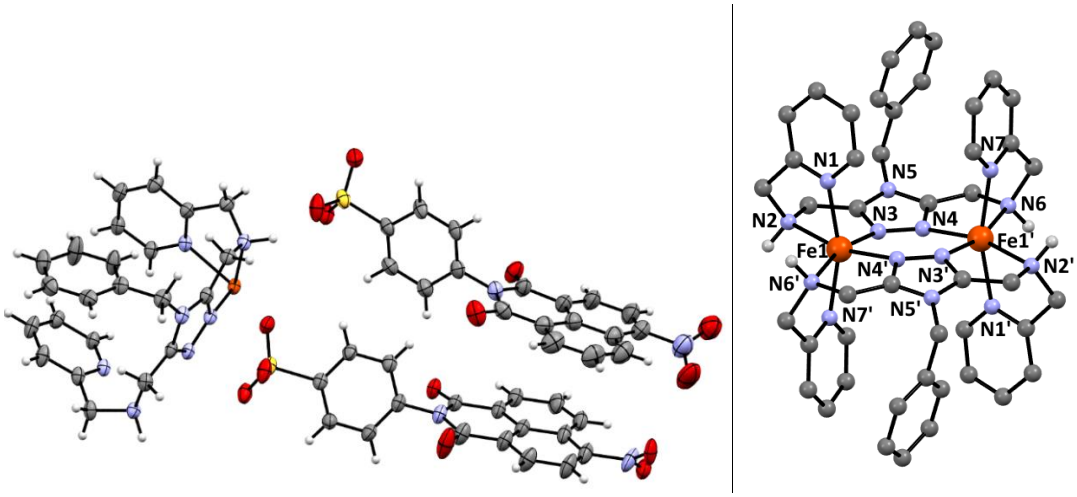

Figure 3-20 (a) Asymmetric unit of the crystal structure of **15** with ellipsoids at 50% probability level; (b) configuration of the $[Fe_2(\mathbf{PMBzT})_2]^{4+}$ fragment, all C-bound H atoms are omitted for clarity.

The **A_2** anion in this system contains the electron withdrawing nitro group which in this complex is disordered over two sites (relative occupancies of 0.5 and 0.5) and the solvent mask routine in Olex2 was required to remove two severely disordered methanol and two acetonitrile molecules in the unit cell (Figure 3-20). The Fe(II) centres are N6 distorted octahedral (Σ_{Fe1} = 114.7°) with bond lengths and angles consistent with HS Fe(II) configuration (Table 3-4).

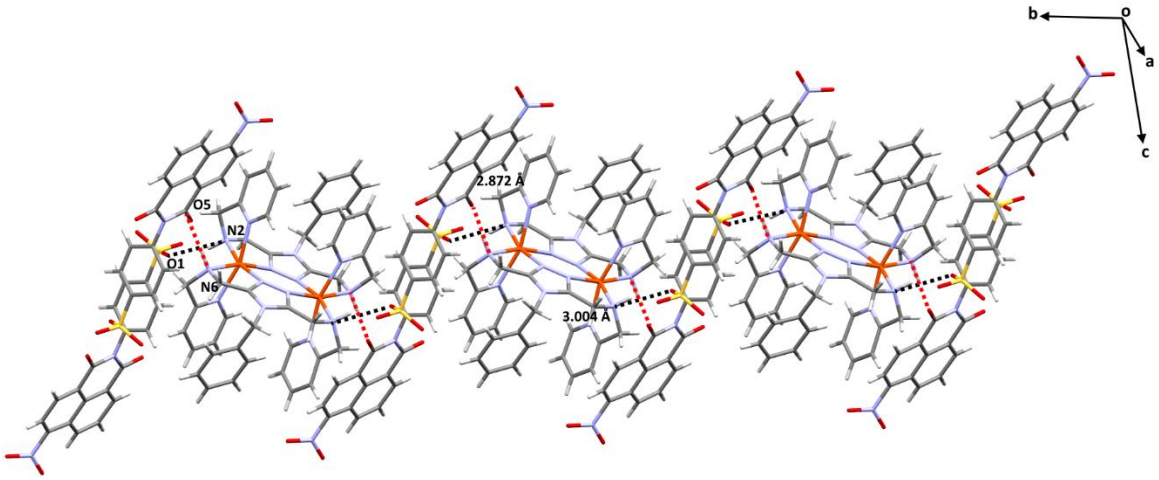

Figure 3-21 View of 1D chain hydrogen-bonding interactions along b axis in **15**.

Along the b axis, not only the SO_3 groups, but also the O atoms from the imide play important roles in forming a hydrogen bonded chain. The N-H···O hydrogen bonds occur between coordinated NH groups and the adjacent naphthalimide anions [N2···O1 = 3.004 (5) Å, and ∠(N-H···O) = 144.00(5)° in black dashed line; N6···O3 = 2.872 (5) Å, and ∠(N-H···O) = 164.83(11)° in red dashed line] (Figure 3-21).

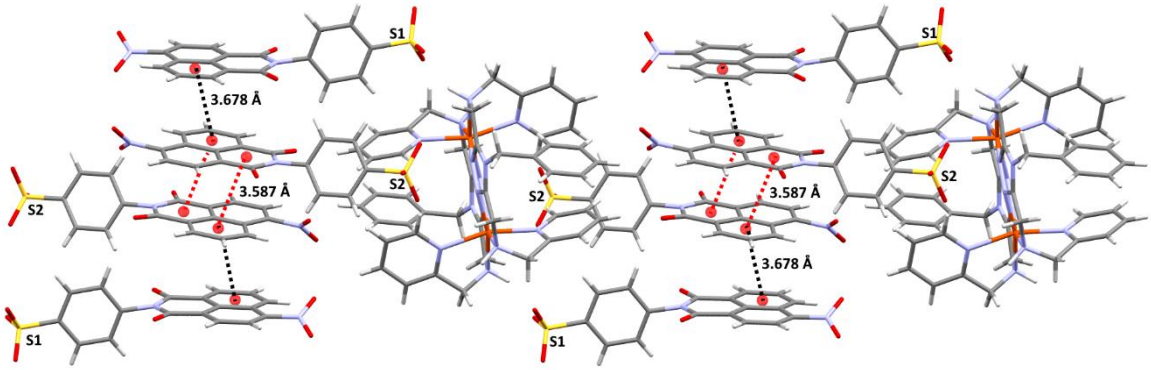

Figure 3-22 Packing interaction of **15** showing $\pi\cdots\pi$ stacking.

Once again, π···π interactions are seen to play a key role in the packing of the molecules. There are four naphthalimide anions π-stacked between two neighbouring $[Fe_2(\mathbf{PMBzT})_2]^{4+}$ molecules. The head-to-head π···π interactions form pairs of naphthalimide anions [centroid···centroid = 3.678 Å in black dashed line], which are then linked through head-to-tail π-stacking to the

adjacent naphthalimide anions [centroid···centroid = 3.678 Å in black dashed line] (Figure 3-22). Overall, the layers of complexes are separated by the sheet of naphthalimide anions (Figure 3-23).

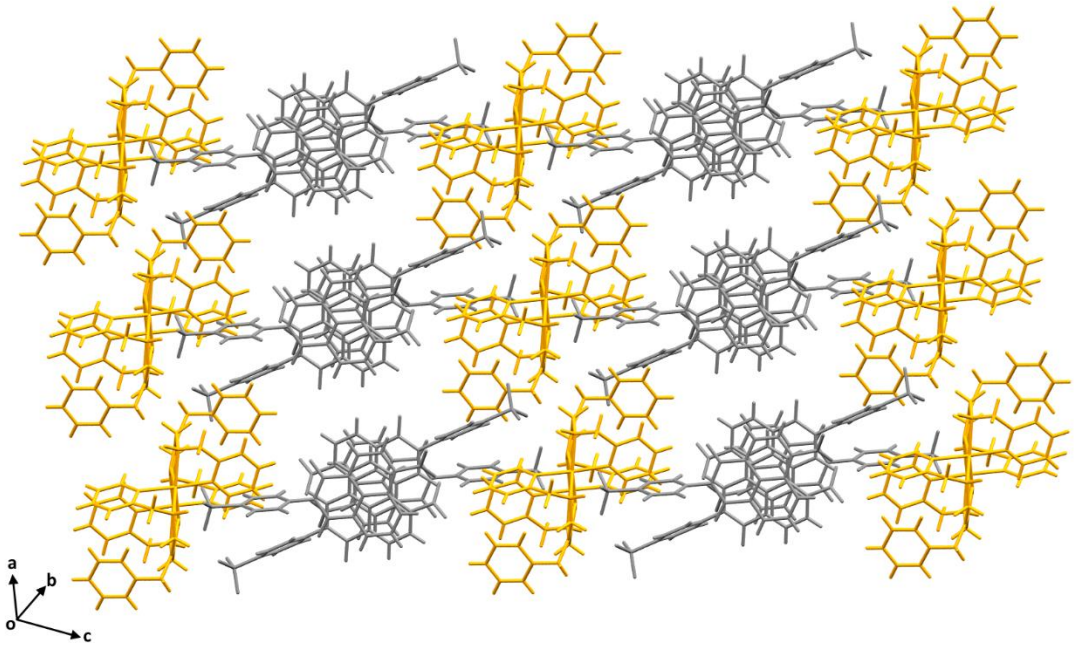

Figure 3-23 Packing interaction of **15**. Naphthalimide molecules are in grey, $[Fe_2(\mathbf{PMBzT})_2]^{4+}$ molecules are in yellow.

3.5.3 Crystallographic Analysis of $[Fe_2(PMBzT)_2](A_5)_2 \cdot MeCN$ (16)

Small orange-yellow plate-like single crystals of $[Fe_2(\mathbf{PMBzT})_2](\mathbf{A_5})_2 \cdot$MeCN were grown by slow evaporation of a solution of compound $[Fe_2(\mathbf{PMBzT})_2](\mathbf{A_5})_2$ in a MeCN:H_2O (1:1) solvent mixture. They crystallised in the triclinic space group $P\bar{1}$ with the asymmetric unit containing one $[Fe_2(\mathbf{PMBzT})_2]^{4+}$ cation, two sulfonated naphthalimide anions and an acetonitrile solvent molecule (Figure 3-24). The solvent mask routine in Olex2 was required to mask electron density from seven acetonitrile and seven water disordered solvents.

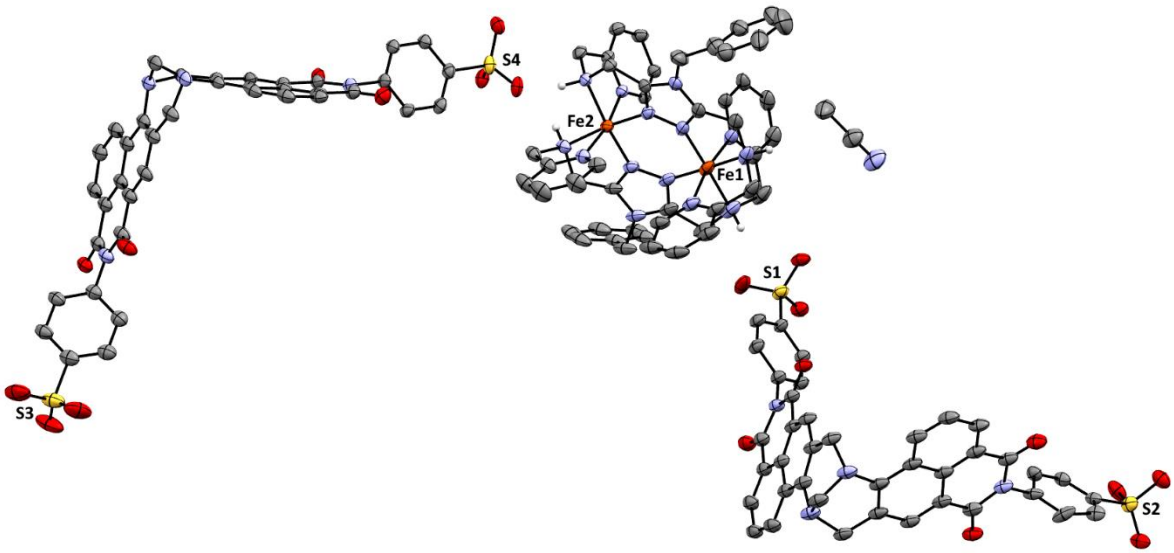

Figure 3-24 Asymmetric unit of the crystal structure of **16** with ellipsoids at 50% probability level all C-bound H atoms are omitted for clarity.

The sulfanilic unit (S3) is disordered over two sites with relative occupancies of 0.56 and 0.44 and in the second (S4) the -SO_3 oxygen atoms are rotationally disordered and have been modelled over two sites with relative occupancies of 0.77 and 0.23. The two Fe(II) centres are both N6 distorted octahedral (Σ_{Fe1} = 79.86°, Σ_{Fe2} = 66.87°) with bond lengths and angles consistent with LS-LS Fe(II) (Table 3-4).

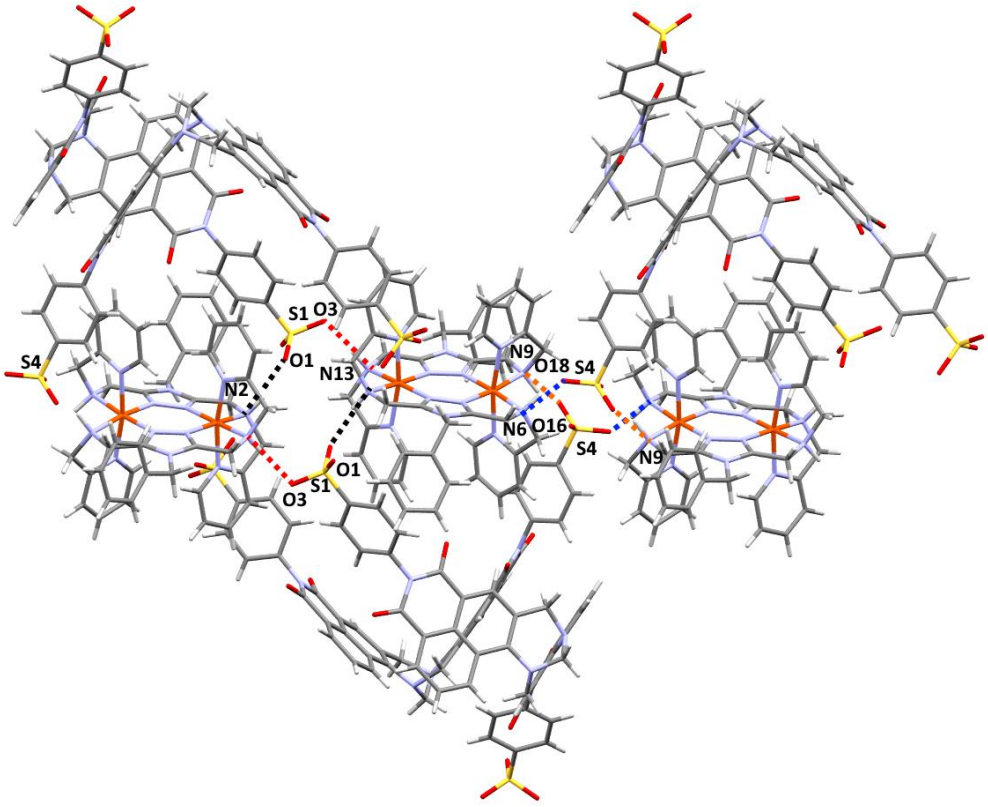

Figure 3-25 View of hydrogen-bonding interactions along b axis in **16**.

The adjacent $[Fe_2(\mathbf{PMBzT})_2]^{4+}$ moieties are linked through hydrogen bonds between two independent sulfonated naphthalimide anions. The N-H···O hydrogen bonds occur between SO_3 groups of the naphthalimide anions and the coordinated NH group of the complex [N2···O1 = 2.901 (5) Å, and ∠(N-H···O) = 164.44° in black dashed line; N13···O3 = 2.819 (6) Å, and ∠(N-H···O) = 166.31(12)° in red dashed line; N6···O18 = 2.867 (4) Å, and ∠(N-H···O) = 135.91(9)° in blue dashed line; N9···O6 = 3.058 (5) Å, and ∠(N-H···O) = 169.46(9)° in orange dashed line] (Figure 3-25).

The sheets of naphthalimide anions were dominated by different types of π···π interactions. Strong face-to-back π···π interactions between imide rings and an adjacent naphthalene rings from another Ar(4-SO_3)-nap-Tröger's base anion exists [centroid···centroid = 3.614 Å in red dashed line; centroid···centroid = 3.558 Å in purple dashed line] (Figure 3-26). In addition to this, back-to-back π···π interactions also exist between neighbouring equivalent Ar(4-SO_3)-nap-Tröger's base anions [centroid···centroid = 3.630 Å in black dashed line; centroid···centroid = 3.622 Å in blue dashed line] (Figure 3-26). Overall, these interactions give a layer packing where the Ar(4-SO_3)-nap-Tröger's base anions layers are separated by $[Fe_2(\mathbf{PMBzT})_2]^{4+}$ layers (Figure 3-27).

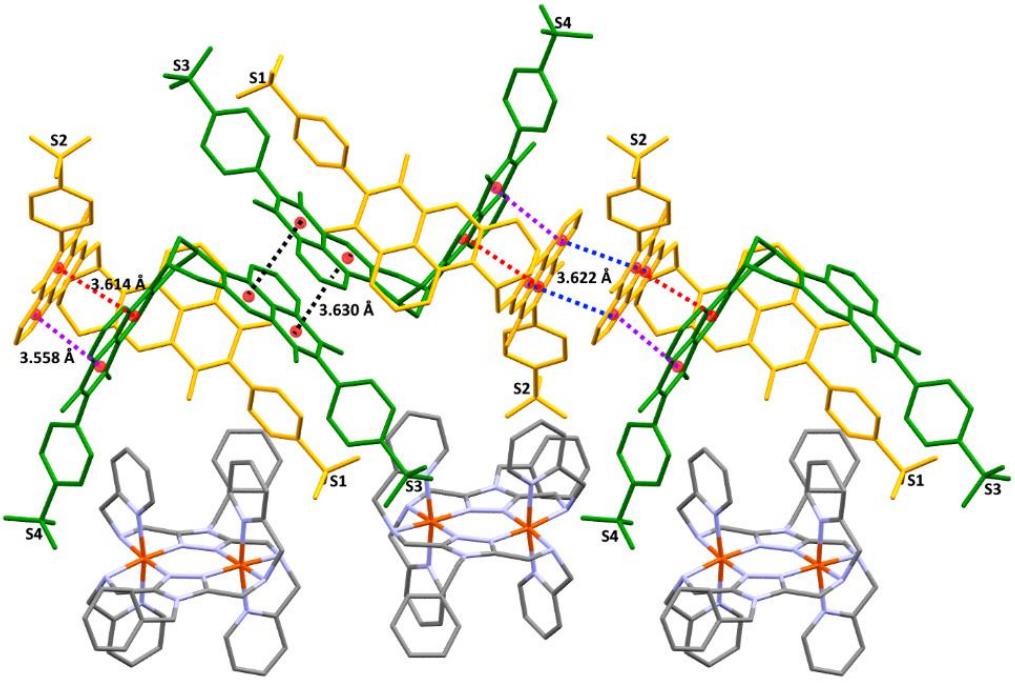

Figure 3-26 Packing interaction of **16** showing $\pi\cdots\pi$ stacking. Ar(4-SO_3)-nap-Tröger's base anions are present in yellow and green; the same colour indicates equivalent molecules.

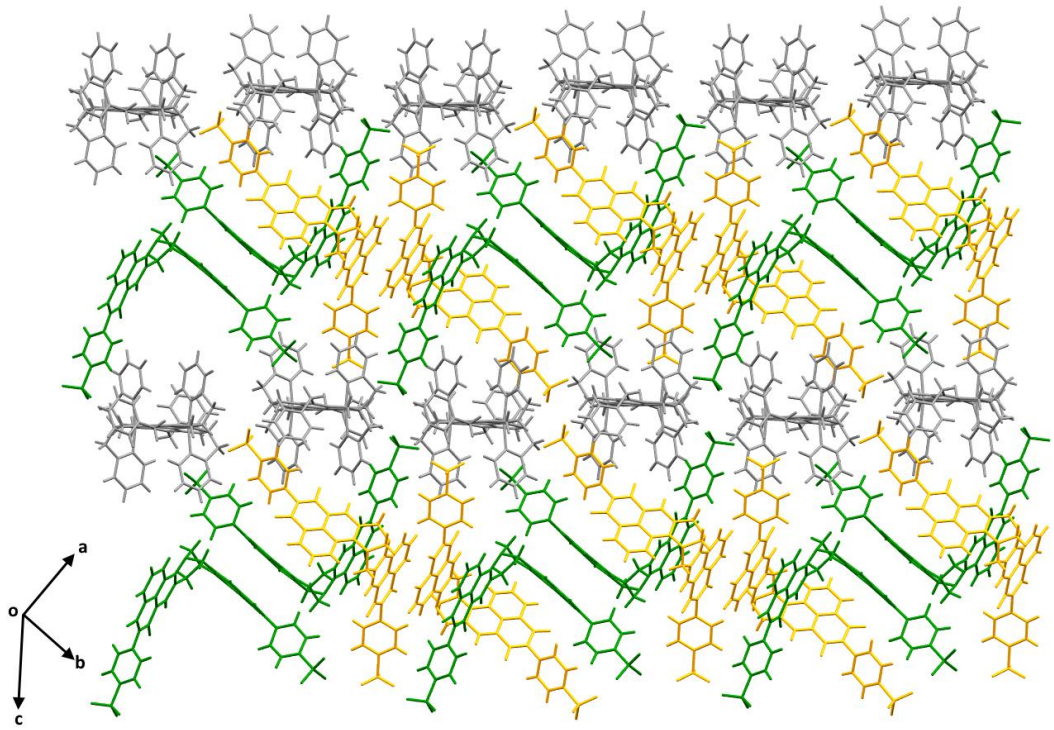

Figure 3-27 Packing interaction of **16**. Ar(4-SO_3)-nap-Tröger's base anions molecules are in green and yellow, $[Fe_2(\mathbf{PMBzT})_2]^{4+}$ molecules are in grey and the same colour indicates equivalent molecules.

From Table 3-4, $[Fe_2(\mathbf{PMBzT})_2](\mathbf{A_1})_4\cdot$MeCN (**14**) displays HS-LS configuration which is similar to $[Fe_2(\mathbf{PMBzT})_2](BF_4)_4\cdot$MeCN. $[Fe_2(\mathbf{PMBzT})_2](\mathbf{A_2})_4$ (**15**) exhibits a HS-HS configuration and its bonds lengths and Σ value are longer than observed in $[Fe_2(\mathbf{PMBzT})_2](BF_4)_4\cdot$MeCN, which indicates that the NO_2-substituted naphthalimide anion has changed the spin state of the complex. Remarkably, all the bonds lengths, angles and Σ values of complex $[Fe_2(\mathbf{PMAT})_2](\mathbf{A_5})_2\cdot$MeCN (**16**) indicate that it is likely to be the LS-LS configuration, which is the first LS-LS structure in this system. More detailed magnetism data will be discussed in Chapter 3.6.

Table 3-4 Comparison of selected bond distances (Å) and angles (°) for $[Fe_2(\mathbf{PMBzT})_2](BF_4)_4\cdot MeCN$[121], $[Fe_2(\mathbf{PMBzT})_2](\mathbf{A_1})_4\cdot MeCN$ (**14**), $[Fe_2(\mathbf{PMAT})_2](\mathbf{A_2})_4$ (**15**), and $[Fe_2(\mathbf{PMAT})_2](\mathbf{A_5})_2\cdot MeCN$ (**16**). * Cannot distinguish because spin is between two states and therefore may have a partial SCO.

	$[Fe_2(\mathbf{PMBzT})_2](BF_4)_4\cdot MeCN$[121]	$[Fe_2(\mathbf{PMBzT})_2](\mathbf{A_1})_4\cdot MeCN$ (**14**)	$[Fe_2(\mathbf{PMBzT})_2](\mathbf{A_2})_4$ (**15**)	$[Fe_2(\mathbf{PMAT})_2](\mathbf{A_5})_2\cdot MeCN$ (**16**)
Collected T	89 K	100 K	100 K	100 K
Fe_N_{pyr} [Å]	2.056(6), 2.058(6)	2.058(2), 2.070(3)	2.186(3), 2.126(3)	Fe1: 1.997(4), 1.977(4) Fe2: 1.977(4), 1.998(5)
Fe_N_{NH} [Å]	2.159(7), 2.173(5)	2.144(3), 2.164(2)	2.264(3), 2.277(3)	Fe1: 2.026(4), 2.059(4) Fe2: 2.049(5), 2.036(6)
Fe_N_{triaz} [Å]	2.020(4), 2.032(5)	2.017(2), 2.0273(19)	2.109(3), 2.126(3)	Fe1: 1.909(4), 1.911(5) Fe2: 1.892(6), 1.916(5)
average Fe-N [Å]	2.083	2.080	2.181	Fe1: 1.980 Fe2: 1.978
Cis<N-Fe-N [°] range	78.0−111.0	79-111.76	75.2-115.58	Fe1: 81.07-103.56 Fe2: 80.09-103.3
Σ [°]	99.4	98.1	114.7	Fe1: 69.86 Fe2: 66.87
Spin state	HS-LS*	HS-LS*	HS-HS	LS-LS

3.6 Results and Discussion of $[Fe_2(PMBzT)_2](A_1)_4\cdot MeCN$ (14), $[Fe_2(PMBzT)_2](A_2)_4$ (15) and $[Fe_2(PMAT)_2](A_5)_2\cdot MeCN$ (16)

Given the LS spin nature of the complex of **16** determined from single crystal XRD experiments at 100 K, variable temperature magnetic susceptibility measurements were attempted on this crystalline sample. Complex **16** showed no magnetic signal at the attempted sample centring temperatures (200 K, 300 K, and 100 K), which meant the sample position could not be

determined. This indicated that the sample was fully Fe(II) LS with 0 unpaired electrons at these temperatures, and therefore diamagnetic and as such no data was collected.

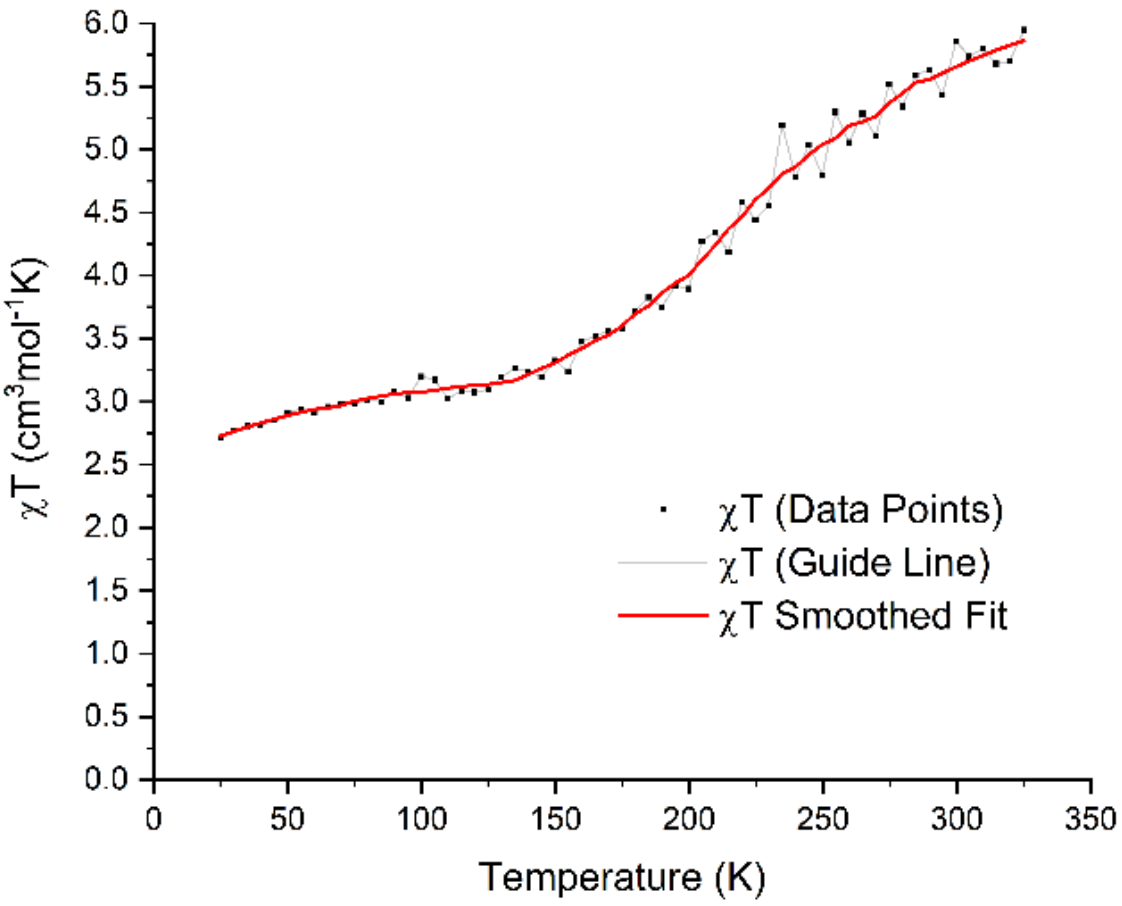

Figure 3-28 Plot of $\chi_M T$ vs. T for complex **14**

Complexes **14** and **15** were successfully centred and magnetic susceptibility measurements were collected at temperatures between 25 and 350 K under an applied field of 1,000 Oe (0.1 T). From Figure 3-28, complex **14** can be seen to display a half gradual SCO phenomena from 150 K, whilst this begins at a higher temperature than the SCO event in $[Fe_2(\mathbf{PMBzT})_2](BF_4)_4$. The T1/2 cannot be accurately determined as the crossover appears to be ongoing at the maximum measured temperature of 350 K. From figure 3-29, complex **15** exhibits a constant HS-HS state.

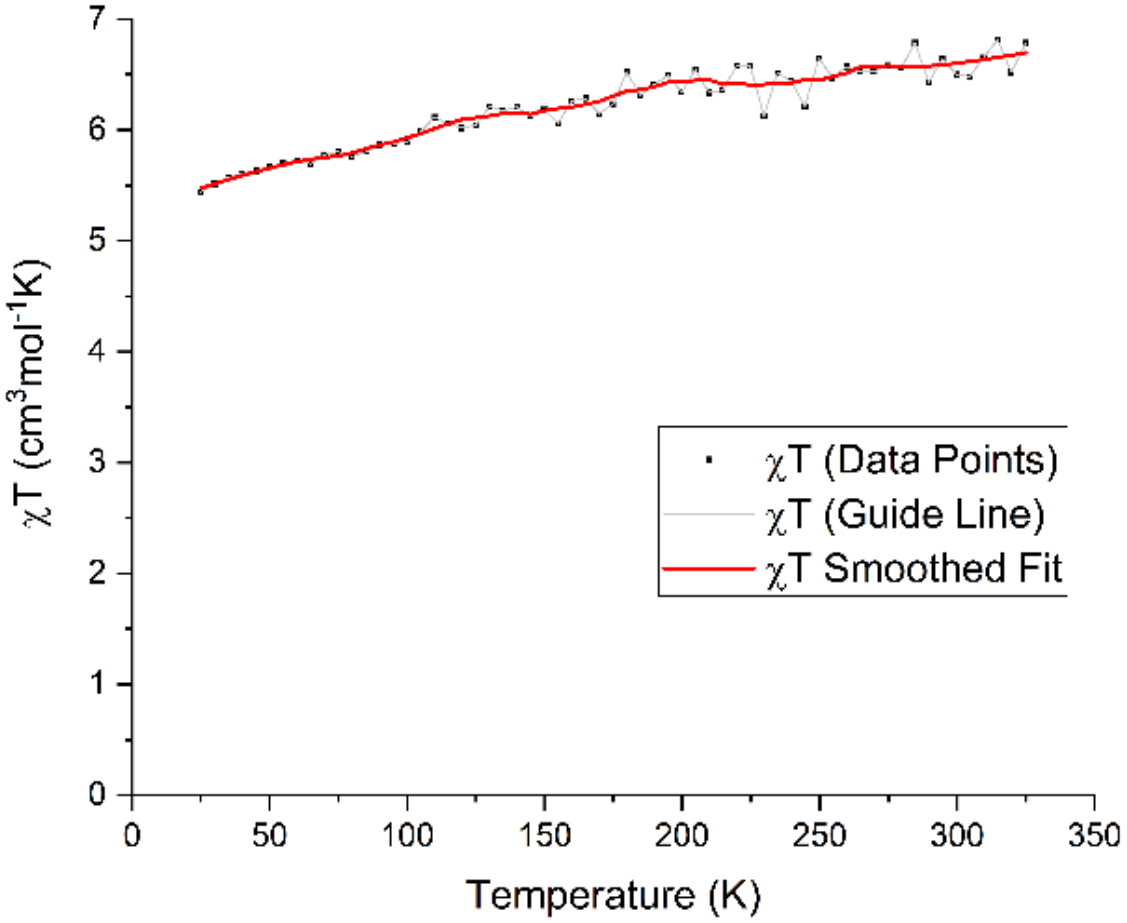

Figure 3-29 Plot of $\chi_M T$ vs. T for complex **15**

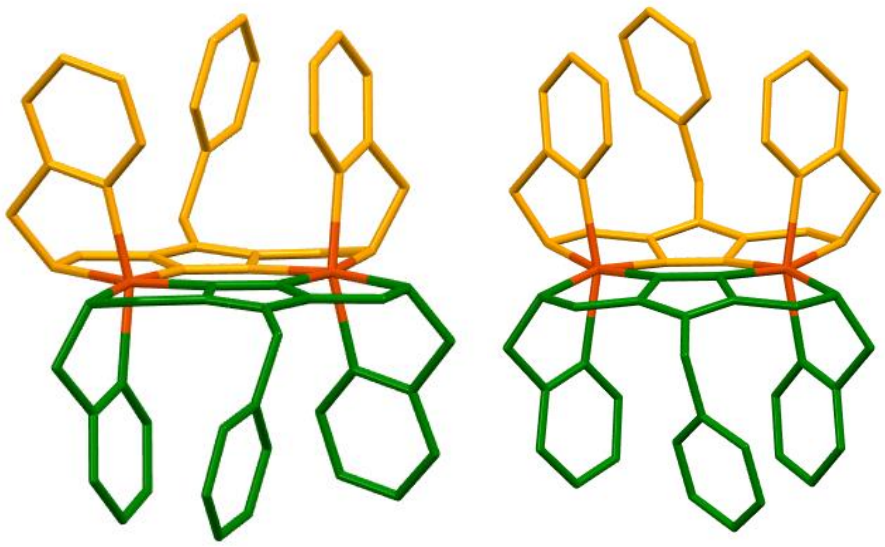

(a) (b)

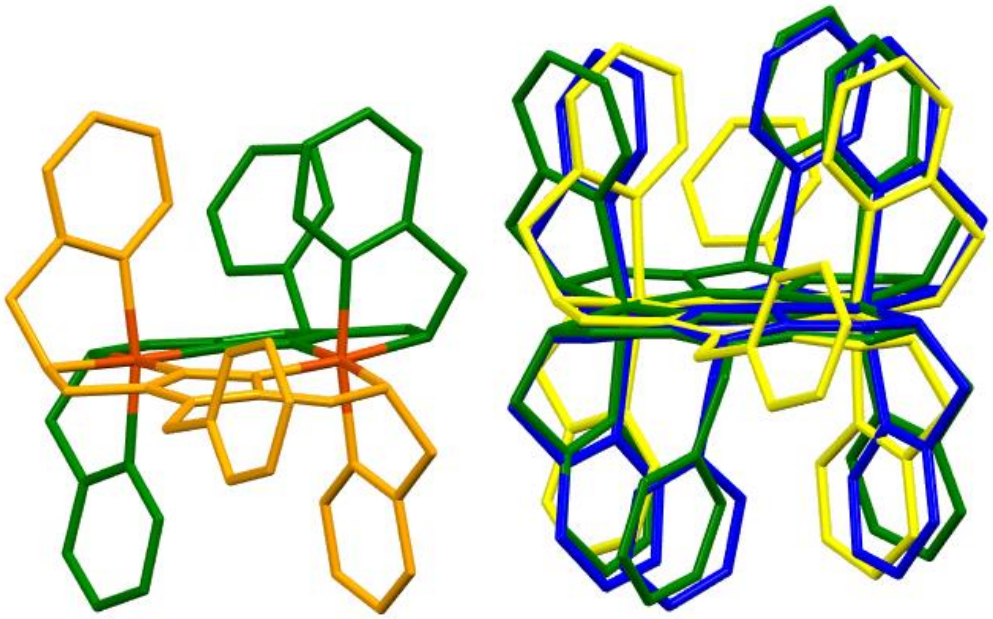

(c) (d)

Figure 3-30 (a) $[Fe_2(\mathbf{PMBzT})_2]^{4+}$ structure of complex **14**; (b) $[Fe_2(\mathbf{PMBzT})_2]^{4+}$ structure of complex **15**; (c) (b) $[Fe_2(\mathbf{PMBzT})_2]^{4+}$ structure of complex **16;** different **PMAT** ligands are present in yellow and green respectively. (c) Overlapped structures of complexes **14, 15**, and **16**; complex **14** is in green, complex **15** is in blue, and complex **16** is in yellow. All the anions, solvents and hydrogens are omitted for clarity.

As there were no previously reported LS-LS complexes for this system, structural comparisons are made in Figure 3-30. **PMBzT** ligands are bonded in a cis-configuration for complex **14** and **15**, while complex **16** features a trans-configuration of the ligands. In complexes **14** and **15**, the pyridyl rings on the same side of the complex and the planes of the pyridyl rings are inserted at 88.02° and 83.78° respectively, which is similar to $[Fe_2(\mathbf{PMBzT})_2](BF_4)_4{\cdot}CH_3CN$. Conversely, in complex **13** the pyridyl rings are parallel to each other. Both the parallel nature of the pyridyl rings and the trans configuration of the ligand are consistent with a LS-LS configuration for complex **13**. This further reinforces the idea that the trans-configuration is essential for achieving the LS-LS spin state.

3.7 Experimental

3.7.1 Synthesis of of $[Fe_2(PMAT)_2](A_1)_4{\cdot}MeOH$ (12)

A solution of the $Fe_2(\mathbf{PMAT})_2(BF_4)_2]$ complex (34.8 mg, ≈0.025 mmol) in a mixture solvent of methanol:acetonitrile (1:1) (10 mL) was added to a stirred suspension of $\mathbf{A_1}$ (43.2 mg, ≈0.1 mmol) in a solvent mixture of methanol:acetonitrile (1:1) (10 mL) and stirred for 15 min. Red single

crystals of $[Fe_2(\mathbf{PMAT})_2](\mathbf{A_1})_4 \cdot MeOH$ (**12**) were crystallised from the reaction solution by slow evaporation. A suitable crystal was selected and collected at 100 K.

Crystal Data for $C_{53}H_{44}FeN_{10}O_{11}S_2$ (M =1135.51 g/mol): triclinic, space group $P\bar{1}$ (no. 2), a = 10.9689(3) Å, b = 12.0883(3) Å, c = 22.0093(4) Å, α = 75.835(2)°, β = 86.454(2)°, γ = 73.906(2)°, V = 2718.65(12) Å^3, Z = 2, T = 100.01(10) K, μ(Cu Kα) = 3.281 mm^{-1}, D$calc$ = 1.387 g/cm^3, 51498 reflections measured (7.836° ≤ 2Θ ≤ 140.666°), 10129 unique (R_{int} = 0.0351, R_{sigma} = 0.0219) which were used in all calculations. The final R_1 was 0.0531 (I > 2σ(I)) and wR_2 was 0.1433 (all data).

3.7.2 Synthesis of of $Fe_2(PMAT)_2](A_2)_4$ (13)

A solution of the $Fe_2(\mathbf{PMAT})_2(BF_4)_2]$ complex (34.8 mg, ≈0.025 mmol) in a mixture solvent of methanol:acetonitrile (1:1) (10 mL) was added to a stirred suspension of $\mathbf{A_2}$ (46.6 mg, ≈0.1 mmol) in a solvent mixture of methanol:acetonitrile (1:1) (10 mL) and stirred for 15 min. Red single crystals of $[Fe_2(\mathbf{PMAT})_2](\mathbf{A_1})_4$ (**13**) were crystallised from the reaction solution by slow evaporation. A suitable crystal was selected and collected at 100 K.

Crystal Data for $C_{104}H_{76}Fe_2N_{24}O_{28}S_4$ (M =2351.82 g/mol): triclinic, space group $P\bar{1}$ (no. 2), a = 11.1788(3) Å, b = 19.2268(9) Å, c = 30.0855(13) Å, α = 106.525(4)°, β = 90.498(3)°, γ = 98.919(3)°, V = 6114.8(4) Å^3, Z = 2, T = 100.00(10) K, μ(Cu Kα) = 3.206 mm^{-1}, D$calc$ = 1.277 g/cm^3, 101619 reflections measured (4.86° ≤ 2Θ ≤ 133.196°), 21449 unique (R_{int} = 0.1332, R_{sigma} = 0.1039) which were used in all calculations. The final R_1 was 0.0914 (I > 2σ(I)) and wR_2 was 0.2431 (all data).

3.7.3 Synthesis of of $[Fe_2(PMBzT)_2](A_1)_4 \cdot MeCN$ (14)

A solution of the $Fe_2(\mathbf{PMBzT})_2(BF_4)_2]$ complex (38.6 mg, ≈0.025 mmol) in a solvent mixture of methanol:acetonitrile (1:1) (10 mL) was added to a stirred suspension of A_2 (43.2 mg, ≈0.1 mmol) in a solvent mixture of methanol:acetonitrile (1:1) (10 mL) and stirred for 15 min. Red single crystals of $[Fe_2(\mathbf{PMBzT})_2](\mathbf{A_1})_4$ (**14**) were crystallised from the reaction solution by slow evaporation. A suitable crystal was selected and collected at 100 K.

Crystal Data for $C_{126}H_{102}Fe_2N_{22}O_{20}S_4$ (M =2484.23 g/mol): triclinic, space group $P\bar{1}$ (no. 2), a = 11.8637(2) Å, b = 12.3709(3) Å, c = 19.5210(5) Å, α = 87.155(2)°, β = 87.576(2)°, γ = 78.282(2)°, V = 2800.31(11) Å^3, Z = 1, T = 100(2) K, μ(Mo Kα) = 0.418 mm^{-1}, D$calc$ = 1.473 g/cm^3, 71410 reflections measured (4.024° ≤ 2Θ ≤ 64.598°), 16288 unique (R_{int} = 0.0325, R_{sigma} = 0.0326) which were used in all calculations. The final R_1 was 0.0653 (I > 2σ(I)) and wR_2 was 0.1706 (all data).

3.7.4 Synthesis of of $[Fe_2(PMBzT)_2](A_2)_4$ (15)

A solution of the $Fe_2(\mathbf{PMBzT})_2(BF_4)_2]$ complex (38.6 mg, ≈0.025 mmol) in a solvent mixture of methanol:acetonitrile (1:1) (10 mL) was added to a stirred suspension of $\mathbf{A_2}$ (46.6 mg, ≈0.1 mmol) in a solvent mixture of methanol:acetonitrile (1:1) (10 mL) and stirred for 15 min. Red single crystals of $[Fe_2(\mathbf{PMBzT})_2](\mathbf{A_2})_4$ (**15**) were crystallised from the reaction solution by slow evaporation. A suitable crystal was selected and collected at 100 K.

Crystal Data for $C_{128}Fe_2H_{114}N_{28}O_{32}S_4$ (*M* =2796.41 g/mol): triclinic, space group $P\bar{1}$ (no. 2), *a* = 11.7521(3) Å, *b* = 14.0281(3) Å, *c* = 19.4654(3) Å, α = 94.428(2)°, β = 96.013(2)°, γ = 97.583(2)°, V = 3149.98(12) Å^3, Z = 1, T = 99.9(9) K, μ(Cu Kα) = 3.239 mm^{-1}, D*calc* = 1.474 g/cm^3, 56229 reflections measured (6.384° ≤ 2Θ ≤ 136.486°), 11454 unique (R_{int} = 0.0800, R_{sigma} = 0.0580) which were used in all calculations. The final R_1 was 0.0777 (I > 2σ(I)) and wR_2 was 0.2144 (all data).

3.7.5 Synthesis of of $[Fe_2(PMBzT)_2](A_5)_2 \cdot MeCN$ (16)

A solution of the $Fe_2(\mathbf{PMBzT})_2(BF_4)_2]$ complex (19.3 mg, ≈0.0125 mmol) in a solvent mixture of methanol:acetonitrile (1:1) (12 mL) was added to a stirred suspension of $\mathbf{A_2}$ (19.3 mg, ≈0.025 mmol) in a solvent mixture of methanol:acetonitrile (1:1) (12 mL) and stirred for 15 min. Red single crystals of $[Fe_2(\mathbf{PMBzT})_2](\mathbf{A_2})_2$ (**15**) were crystallised from the reaction solution by slow evaporation. A suitable crystal was selected and collected at 100 K.

Crystal Data for $C_{126}H_{97}Fe_2N_{23}O_{20}S_4$ (*M* =2493.20 g/mol): triclinic, space group $P\bar{1}$ (no. 2), *a* = 17.8838(3) Å, *b* = 18.7156(2) Å, *c* = 23.2334(3) Å, α = 112.2890(10)°, β = 101.2300(10)°, γ = 100.3390(10)°, V = 6777.03(17) Å^3, Z = 2, T = 100.01(10) K, μ(Cu Kα) = 2.872 mm^{-1}, D*calc* = 1.222 g/cm^3, 127048 reflections measured (5.204° ≤ 2Θ ≤ 140.762°), 25327 unique (R_{int} = 0.0628, R_{sigma} = 0.0463) which were used in all calculations. The final R_1 was 0.0909 (I > 2σ(I)) and wR_2 was 0.2985 (all data).

Chapter 4 1,2,4-Triazole Based Naphthalimide Complexes

4.1 Introduction to N-substituted-1,2,4-triazole Based Ligands

As already discussed, materials exhibiting the SCO phenomenon have been prevalent in an increasing number of studies, due to their versatile properties in the fields of material science, crystal engineering, and supramolecular chemistry. Most of these materials incorporate multidentate nitrogen donors from heterocyclic systems.[126-127] One particularly good heterocycle for generating SCO active compounds is the 1,2,4-triazole ring. The field strength is often appropriate for SCO in Fe(II) and the N^1 and N^2 atoms are in the correct orientation to efficiently bridge transition metal ions, giving the possibility of multi-nuclear SCO active complexes.[60, 128-130] (Figure 4-1). Additionally, functionalisation at the N^4 position affords synthetic modularity to fine tune the ligand filed strength, as well as introduce additional properties to the system (e.g. additional coordination sites, structure-directing groups, materials formation substituents such as long alkyl chains).[131-133] Substituents at the carbon positions of the 1,2,4-triazole ring can be included to provide chelate pockets and allow control over metal nuclearity[133] (as shown in the chapter 3 PMRT-based ligands), however this study investigates 1,2,4-triazole systems without substitution at the carbon positions.

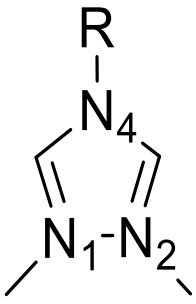

Figure 4-1 Schematic representation of 4-susbtituted 1,2,4-triazole

Mononuclear 1,2,4-triazole-metal complexes (with no carbon substituents) are rare, however, N^1, N^2-bridging of multiple first row transition metal centres is frequently observed (576 multi-nuclear and polymeric complexes in the CSD vs 46 mononuclear). The bridge can adopt different geometries depending on the properties of the metal and the ligands. As the two bridged metal ions are brought into close proximity, ~400 pm (Figure 4-2),[128-129] double or triple bridges are easily formed reducing the electrostatic repulsion of the two metals. However, for N^4-substituted-1,2,4-triazole (unsubstituted at the 3 and 5 positions) metal complexes, triple N^1,N^2-bridging is the

preferred geometry due to the strain-free binding of this configuration.[127, 134] N1, N2-triazole bridged metal ion complexes contain a trigonal axis with 90° coordination angles (N-M-N) around metal centre and 125° for the M-N-N angles. This results in a triple bridge formation without appreciable strains, as the M-N-N angles are very close to the exocyclic free donor electron pair of a regular five-membered ring (126°).[128-129]

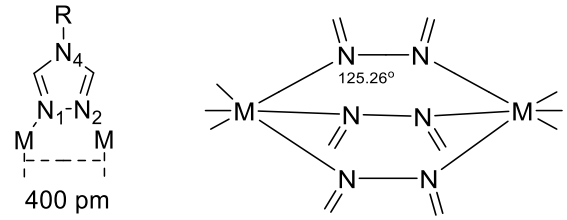

Figure 4-2 Geometry of triple bonding mode

4.1.1 Review of 1,2,4-triazole containing complexes

The Iron(II) triazolate (trz) family is by far the most striking compound the occurrence of SCO. Interest in this family of ligands arose when Martin *et al.*[135] used 4-aminotriazole (NH_2trz) as a ligand, successfully producing SCO active Fe_xCo_{1-x}(4,4'-bis-1,2,4-triazole)$_2$($NCS)_2$]·H_2O mixed crystal compounds. Interest in polymeric 1,2,4-triazole systems has steadily grown since 1995 when Lavrenova *et al.*[136] used 4-aminotriazole (NH_2trz) as a ligand to produce a series of SCO active Fe(II) complexes with the formula Fe(4atrz)$_3A_2$ (where A= ClO_4 and NO_3).

However, the structures of these polymeric compounds were not confirmed until the first single crystal diffraction data was obtained by Guionneau *et al.* in 2011.[137] In this study the polymer structure of Fe(NH_2trz)$_3$($NO_3)_2$.2H_2O was published, The tiny needle single crystal was grown by the slow diffusion layering method between a solution of Fe$(NO)_3$ and a solution of NH_2trz. As the crystal was unstable above room temperature, only the LS crystal structure was obtained (Figure 4-3a). This compound exhibited a thermal spin transition with a wide thermal hysteresis near room temperature as shown in Figure 4-3b.

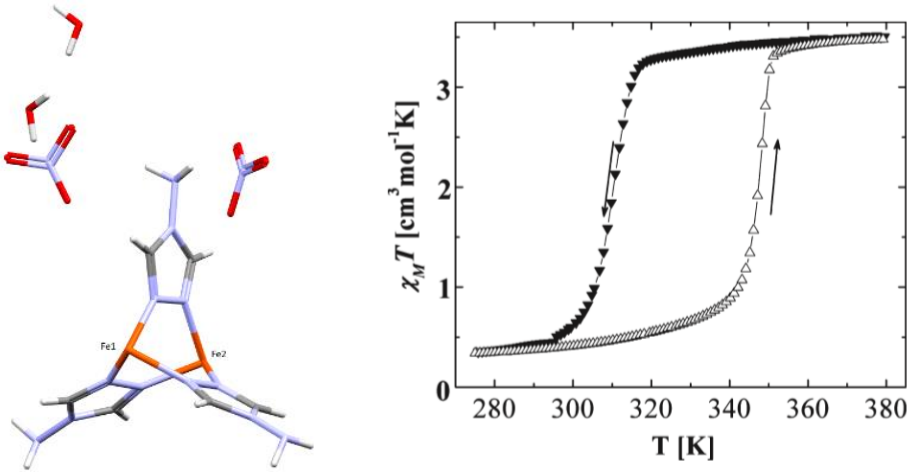

(a) (b)

Figure 4-3 (a) Asymmetric unit cell of in single crystal of $Fe(NH_2trz)_3(NO_3)_2.2H_2O$ at 120 K; (b) $\chi_M T$ versus T plot for $Fe(NH_2trz)_3(NO_3)_2$ over temperature range 274-380 K. Figure adapted from Guionneau *et al.*[137]

The two iron(II) centres were bridged with three μ_2-triazole ligands with an M⋯M distance of 3.655 Å. Among the average Fe-N distances the typical bond lengths of Fe(II) in the LS state were observed at <Fe1-N>=1.95 Å and <Fe2-N>=1.99 Å. In addition, the low distortion of the coordination spheres (ΣFe1=15(1)° and ΣFe2=11(1)°) results in a geometry around Fe close to perfect octahedral. The average angle of Fe-N-N is around 125°, close to the exocyclic free donor electron pair angle of a regular five-membered ring (126°), indicating only weak strain in this structure. Therefore, all of the triple-bridged iron centres are aligned along the a-direction and form a 1-D coordination polymer (Figure 4-4). The crystal packing interactions are dominated by strong hydrogen bonding involving the NH_2 where two adjacent chains are strongly H-bonded through NO_3 anions, at distances ranging from 2.901 Å to 3.033 Å (Figure 22)

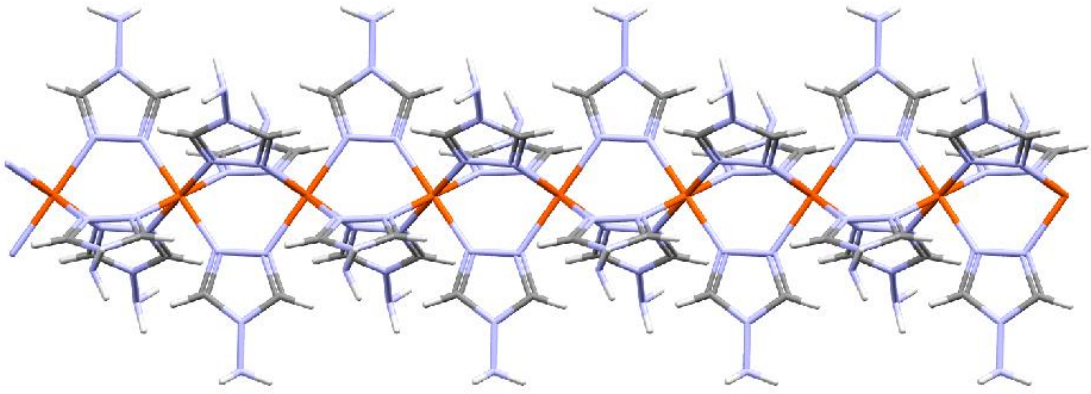

Figure 4-4 View of 1-D chains along a direction in the structure of $Fe(NH_2trz)_3 \cdot 2H_2O$

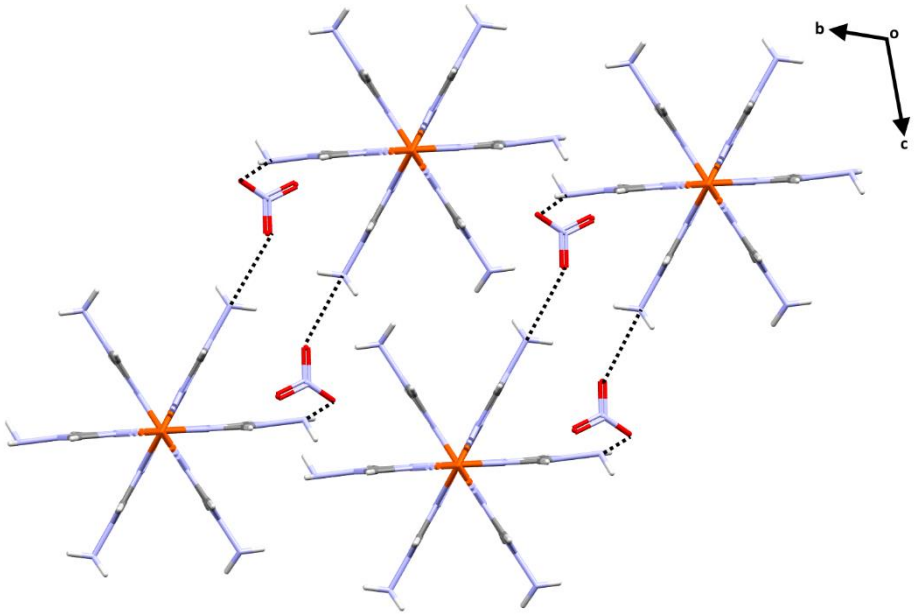

Figure 4-5 Inter chain interaction in the structure of $Fe(NH_2trz)_3 \cdot 2H_2O$ along *a* axis.

In this chapter, the naphthalimide group is introduced into such 1,2,4-triazole systems, with the aim of acting as secondary building units through π-based interactions. In addition to this, there is scope to expand upon the field of fluorescent SCO complexes[138-139] by the potentially fluorescent naphthalimide moiety into these systems, however, this lies beyond the remit of this work.

A series of new ligands were generated that feature both an unsubstituted 1,2,4-triazole ring and a 1,8-naphthalimide system, thereby providing both nitrogen-based coordination sites and structure directing through π-based interactions. The inclusion of strong π-based interactions has potential to allow hysteresis to be enhanced in these interesting polymeric triply bridged systems.

4.2 Triazole Based 1,8-Naphthalimide Ligand Design

The design paradigms follow on from chapter 2, only herein coordinating nitrogen-containing heterocycles are introduced into the naphthalimides, rather than non-coordinating anionic groups. Initially the focus was on developing a family of ligands where the triazole was directly attached to the 1,8-naphthalimide ring. This built on published results from our previous work[140] where interesting Cu(II) complexes were prepared. The ligand family is shown in Figure 4-6 and contained the unsubstituted naphthalimide system, which acted as a control. Further substitution at the naphthalimide 4-position was undertaken with the goal of altering the crystal engineering properties of the ligands through incorporation of additional structure directing groups. NO_2 in **L_2** was incorporated as an H-bond acceptor, as well as allowing for $NO_2 \cdots NO_2$ interactions – it also functioned as an electron withdrawing group to potentially alter the naphthalimide ring pi-based

interactions. NH_2 in **L_3** was incorporated as an H-bond donor as well as an electron donating group to give a highly fluorescent naphthalimide and potentially alter pi-based interactions. NMe_2 in **L_4** was added as a non-Hydrogen bonding electron donating group. The most interesting and complex system was the Trögers' base system of **L_5** where two triazole-naphthalimides were linked together, potentially allowing for more rigidly connected 3D coordination polymer formation (and potential porous structures).[141-144] Full experimental characterisation will be discussed in Chapter 4.7.

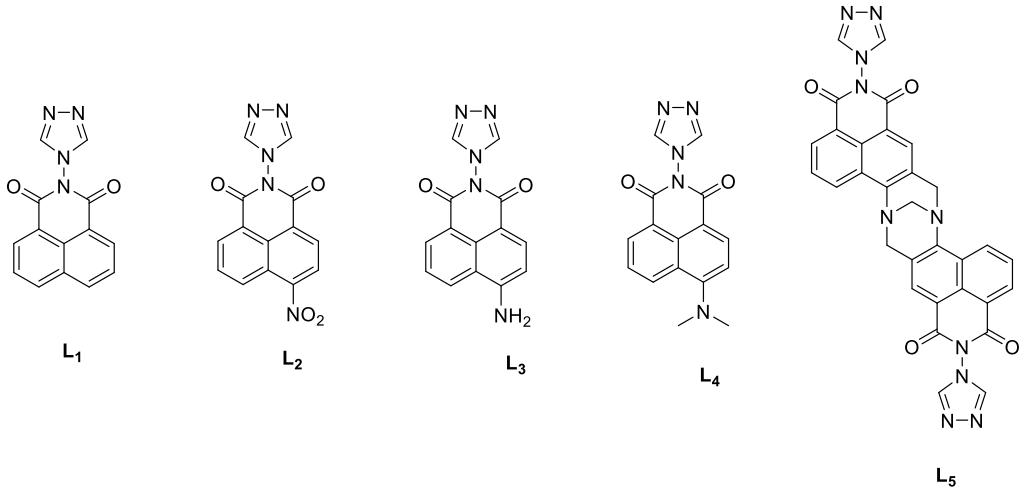

Figure 4-6 Structures of 1,2,4-triazole naphthalimide ligands family

Here, the synthesis of each ligand is presented along with a detailed structural analysis, which was carried out on the ligands in order to assess what influence the naphthalimide substituents had on the system before coordination studies were attempted.

4.2.1 Synthesis and Crystallographic Analysis of 4-(1,2,4trz)-Nap-H (L_1)

The 4-(1,2,4tz)-Nap-H ligand (Figure 4-7) was synthesised by reacting 1, 8-naphthalic anhydride and 4-amino-4H-1,2,4-triazole in a 1:1 ratio in DMF at 160 ^oC under N_2. After cooling down, the reaction was added to water resulting in white precipitate. The solid was isolated by filtration and washed with ice cold water before being dried in the oven.

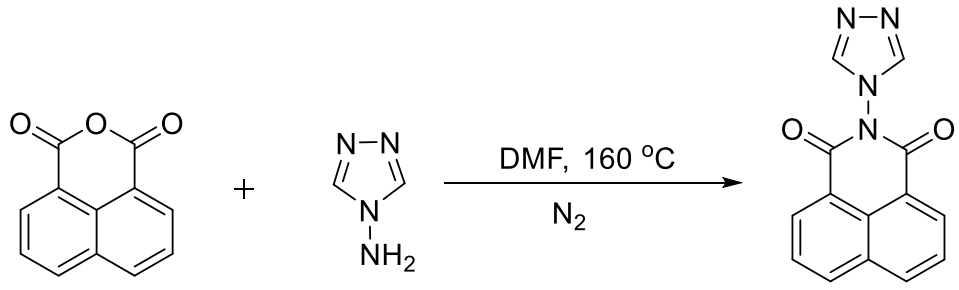

Figure 4-7 Synthesis of 4-(1,2,4trz)-Nap-NO_2 (**L_1**)

Small colourless plate-like single crystals of **L$_1$** were grown from slow evaporation of a DMF solution and the low temperature (100K) molecular structure determined. **L$_1$** crystallised in the *P*2$_1$/*c* monoclinic space group and contained one complete molecule in the asymmetric unit (Figure 4-8a). The triazole ring and naphthalimide moiety planes bisect at an angle of 79°. The packing interactions of **L$_1$** were dominated by $\pi\cdots\pi$ stacking between neighbouring molecules, where the naphthalimides are arranged in a head-to-head configuration through offset $\pi\cdots\pi$ stacking (centroid⋯centroid= 3.556 Å) of the naphthalene ring (Figure 4-8b).

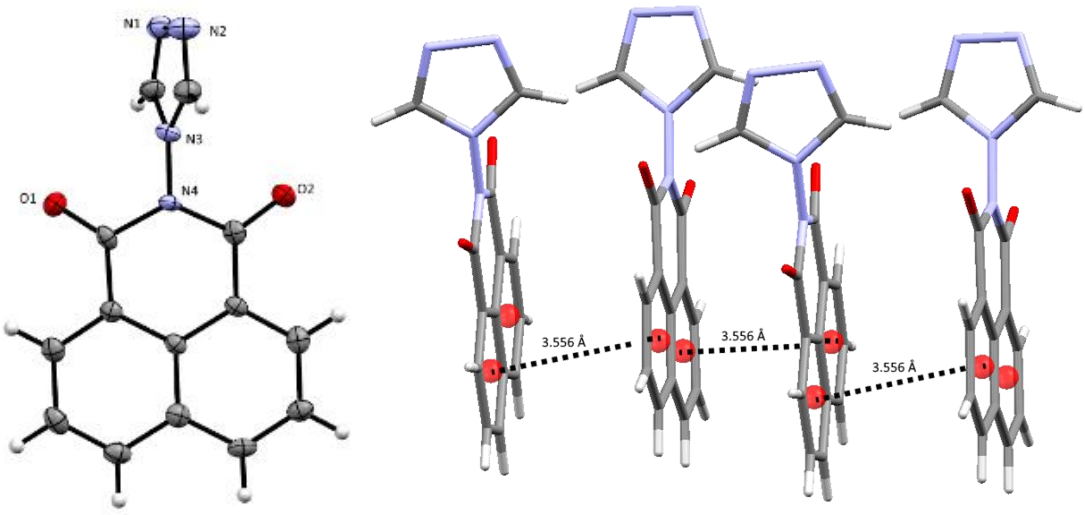

(a) (b)

Figure 4-8 (a) Molecular structure of L1 with ellipsoids at 50% probability level. (b) Packing of L1 showing π⋯π stacking between molecules.

Additionally, weaker non-classical hydrogen bonds (C-H⋯O and C-H⋯N) are present in the solid-state packing (Figure 4-9a), which are C5⋯N4 = 3.265(3)Å, and ∠(C5-H⋯N4) = 127.7(6)° in black dashed line; C7⋯N3 = 3.608(3)Å, and ∠(C7-H⋯N3) = 155.84(9)° in red dashed line; C13⋯O2 = 3.187(2)Å, and ∠(C13-H⋯O2) = 145.96(7)° in yellow dashed line; C14⋯O2 = 3.160(2)Å, and ∠(C14-H⋯O2) = 126.15(7)° in purple dashed line. The alternating stacks were also linked to the neighbouring molecules through neighbouring carbonyl oxygen atoms (Figure 4-9b). The result of these interactions is a 1D π-stacked chain of **L$_1$** molecules running along the crystallographic c-axis.

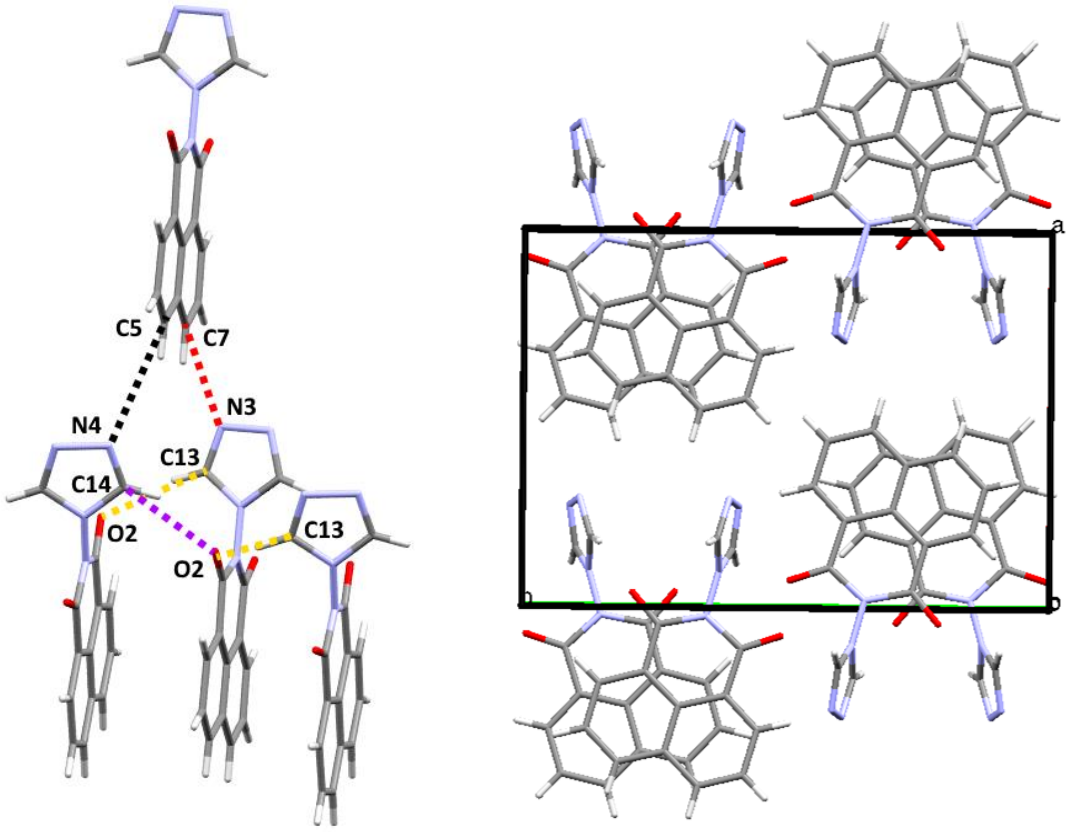

(a) (b)

Figure 4-9 (a) View of hydrogen-bonding interactions in **L_1**. Weak non-classical hydrogen bonds are shown in dashed line (b) Packing of **L_1** showing π-stacked chains in the crystallographic c direction.

4.2.2 Synthesis and Crystallographic Analysis of 4-(1,2,4trz)-Nap-NO_2 (L_2)

The 4-(1,2,4tz)-nap-NO_2 ligand (Figure 4-10) was synthesised by reacting 4-nitro-1,8-naphthalic anhydride with a 2-fold excess of 4-amino-4H-1,2,4-triazole, and a large excess of imidazole in refluxing chloroform for 6 hours. After cooling to room temperature, the chloroform was removed in vacuum. This resulted in a light orange solid which was washed with distilled water and ethanol, to give the pure product.

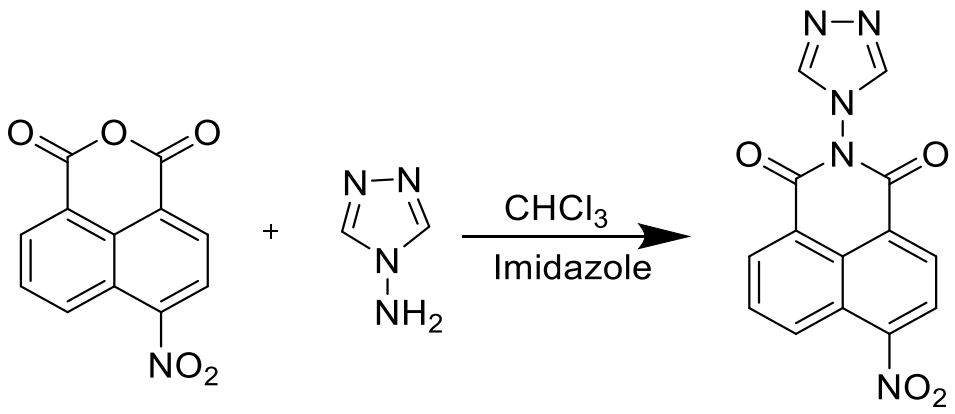

Figure 4-10 Synthesis of 4-(1,2,4trz)-Nap-NO_2 (**L_2**)

Small colourless plate-like single crystals of **L_2** were obtained by slow evaporation from a solvent mixture of methanol and acetonitrile (1:1) and the low temperature (100K) molecular structure determined. **L_2** crystallised in the *P*2_1/*c* monoclinic space group and contained one complete molecule in the asymmetric unit (Figure 4-11a). The triazole ring and naphthalimide moiety planes bisect at an angle of 78.2°. The packing interactions are dominated by $\pi\cdots\pi$ stacking between neighbouring molecules (Figure 4-11b), where the naphthalimide units are arranged in a head-to-tail configuration through $\pi\cdots\pi$ stacking of naphthalene rings [centroid⋯centroid=3.763 Å] and self-complimentary $NO_2\cdots\pi$ interactions between the nitro substituent on one molecule and the imide ring on a neighbouring molecule [O⋯centroid=2.959 Å] (Figure 4-11 (b).

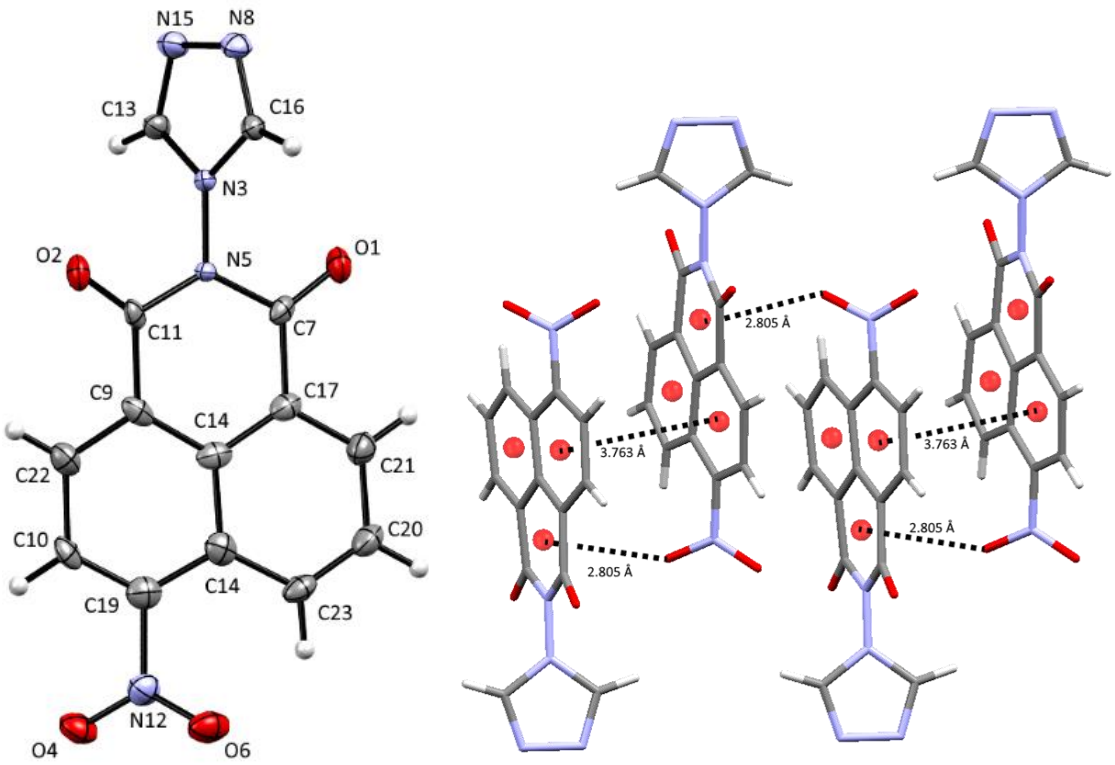

(a) (b)

Figure 4-11 (a) Molecular structure of **L_2** with ellipsoids at 50% probability level. (b) Packing of **L_2** showing $\pi\cdots\pi$ stacking between molecules.

These π···π interactions give rise to a 1D π-stacked chain of **L_2** molecules running along the crystallographic a-axis (Figure 4-12a). The alternating stacks are then linked to the neighbouring molecules through the triazole group CH moiety hydrogen bonding to the neighbouring carbonyl oxygen atom (Figure 4-12a). Unlike the π-based packing interactions in **L_1**, the structure of **L_2** does not show offset head-to-head $\pi\cdots\pi$ stacking (Figure 4-12b), instead a head-to-tail stacking is observed due to the favourable self-complimentary $NO_2\cdots\pi$ interactions which are absent in **L_1**.

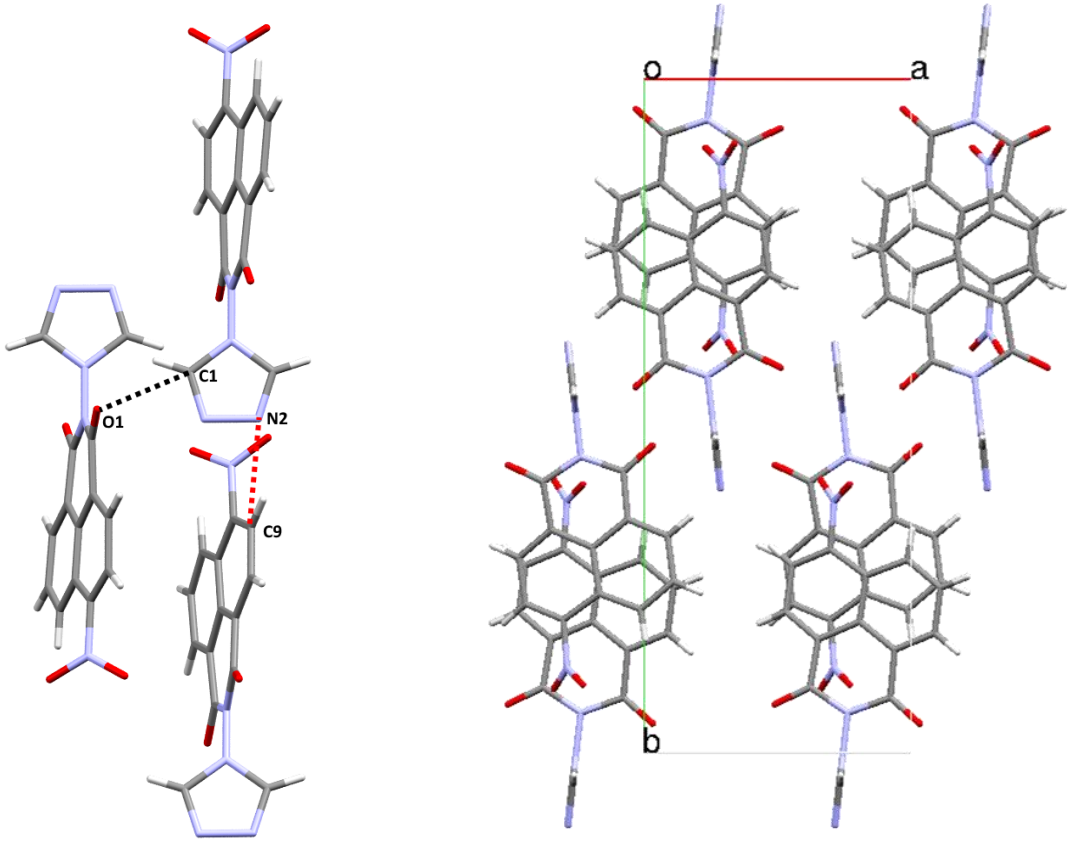

(a) (b)

Figure 4-12 (a) View of hydrogen-bonding interactions in L3.Weak non-classical hydrogen bonds are shown in dashed line.

4.2.3 Synthesis and Crystallographic Analysis of 4-(1,2,4trz)-Nap-NH_2 (L_3)

The 4-(1,2,4tz)-nap-NH_2 (**L_3**) ligand (Figure 4-13) was synthesised by reducing 4-(1,2,4tz)-nap-NO_2 (**L_2**) with a palladium on carbon (10%) catalyst under a hydrogen atmosphere for 12 hours. This resulted in a suspension which was dissolved with a large amount of acetone and then filtered through celite. The solvent was remove in vacuum resulting in a red solid.

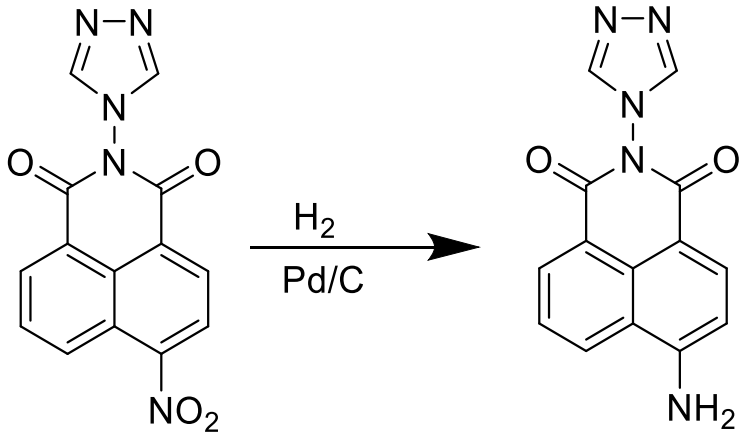

Figure 4-13 Synthesis of 4-(1,2,4tz)-Nap-NH_2 (**L_3**)

Small yellow plate-like single crystals of **L_3** were obtained by slow evaporation from a DMF solution and the low temperature (100K) molecular structure determined. **L_3** crystallised in the orthorhombic space group *Pna2₁* and contain one complete molecule in the asymmetric unit (Figure 4-14a).

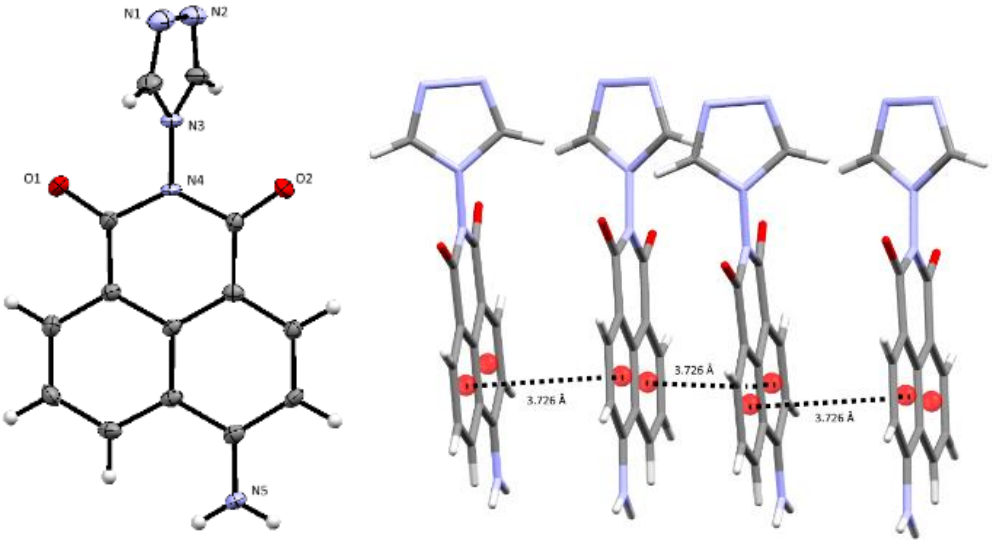

(a) (b)

Figure 4-14 (a) Molecular structure of **L_3** with ellipsoids at 50% probability level. (b) Packing of **L_3** showing π···π stacking between molecules.

The triazole ring and naphthalimide moiety planes bisect at an angle of 70.7°. The packing interactions are dominated by *π*···*π* stacking between neighbouring molecules (Figure 4-14b), where the naphthalimide groups are arranged in a head-to-head configuration through offset *π*···*π* stacking of naphthalene rings [centroid···centroid=3.726 Å]. The result of these *π*-based interactions is a 1D *π*-stacked chain of **L_3** molecules running along the crystallographic *a*-axis

(Figure 4-15a). Apart from the π interactions, NH hydrogen bonding from the naphthalimide NH_2 groups are also present (Figure 4-15b). These alternating stacks are then linked to neighbouring stacks through NH···O and NH···N hydrogen bonding N5···O1 = 3.060(3) Å, and ∠(N5-H···O1) = 148.13(9)° and N5···N1 = 3.220(3) Å, and ∠(N5-H···N1) = 164.10(6)°).

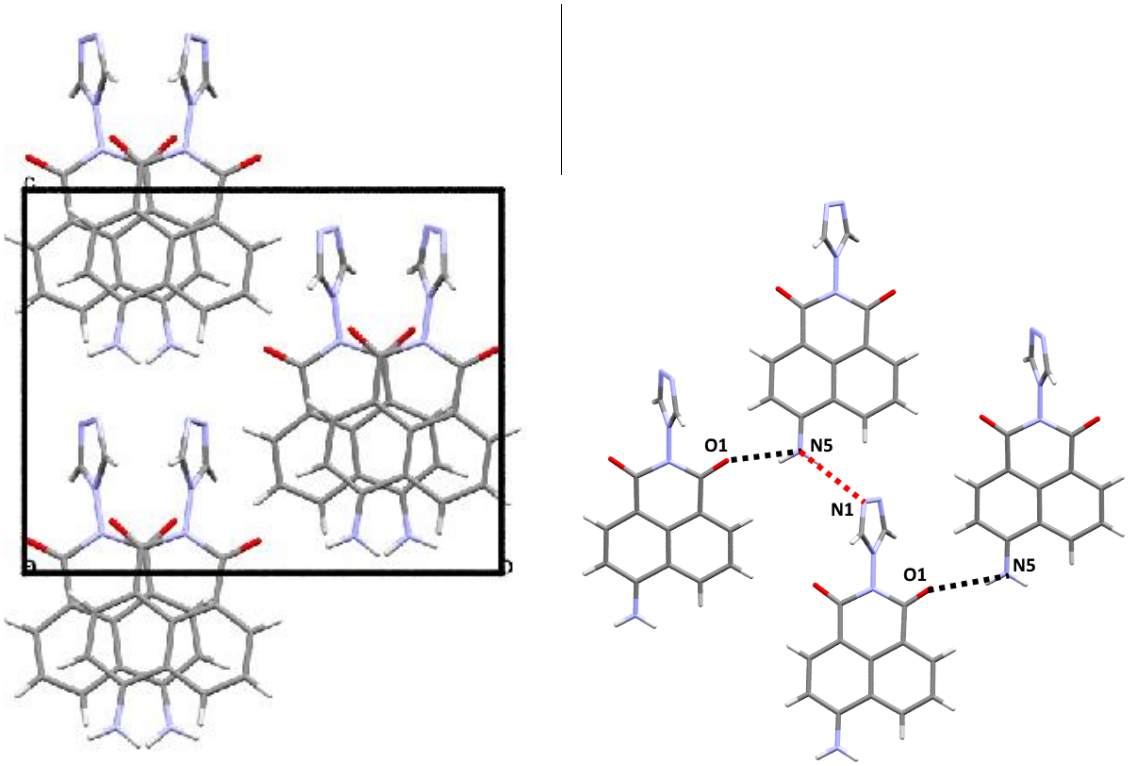

(a) (b)

Figure 4-15 (a) Packing of **L_3** showing π-stacked chains along the crystallographic a direction. Weak non-classical hydrogen bonds are shown in dashed line. (b) View of NH-based hydrogen-bonding interactions in **L_3**.

4.2.4 Synthesis and Crystallographic Analysis of 4-(1,2,4trz)-Nap-N(Me)$_2$ (L_4)

The 4-(dimethylamino)-1, 8-naphthalic anhydride was prepared from the reaction between 4-bromo-1, 8-naphthalic anhydride and dimethylamine following published procedures.[145] This was then added to three equivalents of 4-amino-4*H*-1,2,4-triazole in DMF under an N_2 atmosphere and refluxed for eight hours. After cooling, an orange solid was precipitated using water. The solid was isolated by filtration and washed with ice cold water before being dried in the oven.

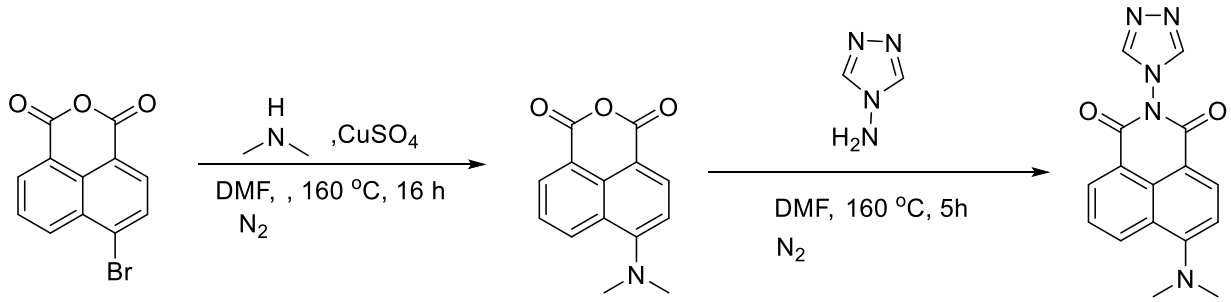

Figure 4-16 Synthesis of 4-(1,2,4trz)-Nap-NMe_2 (**L_4**)

Small orange crystals of **L_4** were obtained from slow evaporation of a DMF solution and the low temperature (100 K) X-ray structure was determined. **L_4** crystallized in the monoclinic space group *P*21/*c* with one molecule in the asymmetric unit (Figure 4-17a). The triazole ring and naphthalimide moiety planes bisect at an angle of 81°. The packing interactions are also dominated through $\pi\cdots\pi$ stacking where the naphthalimide units are arranged in a head-to-head configuration [centroid⋯centroid=3.601 Å] (Figure 4-17b), along with weaker non-classical CH hydrogen bonding from the triazole CH groups (Figure 4-18a). The result of these π-based interactions is a 1D π-stacked chain of **L_2** molecules running in the crystallographic c-axis (Figure 4-18b).

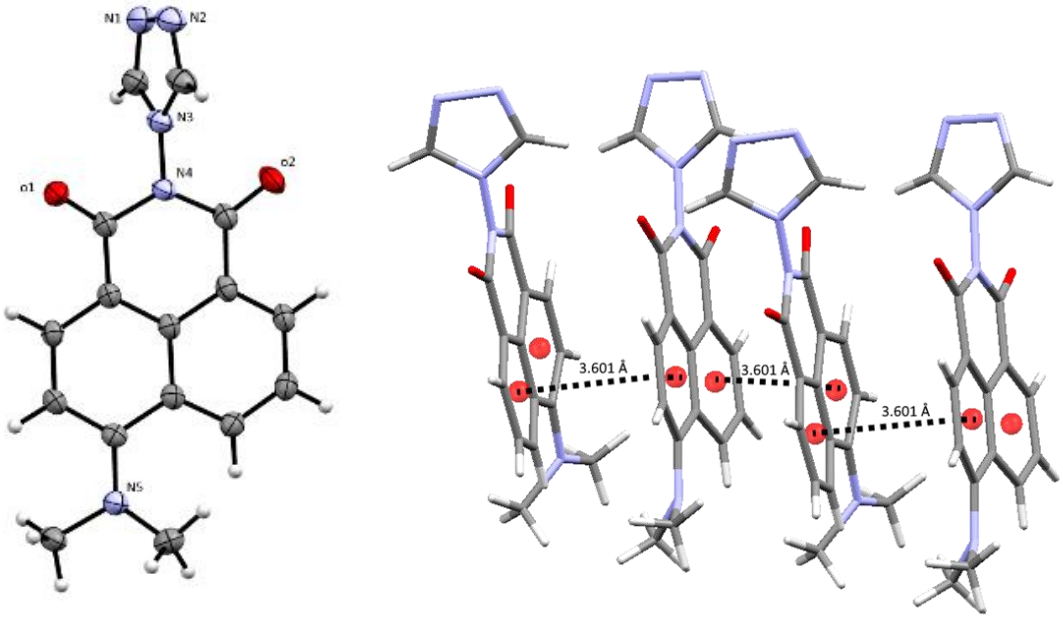

(a) (b)

Figure 4-17 (a) Molecular structure of **L_4** with ellipsoids at 50% probability level. (b) Packing of **L_4** showing π⋯π stacking between molecules.

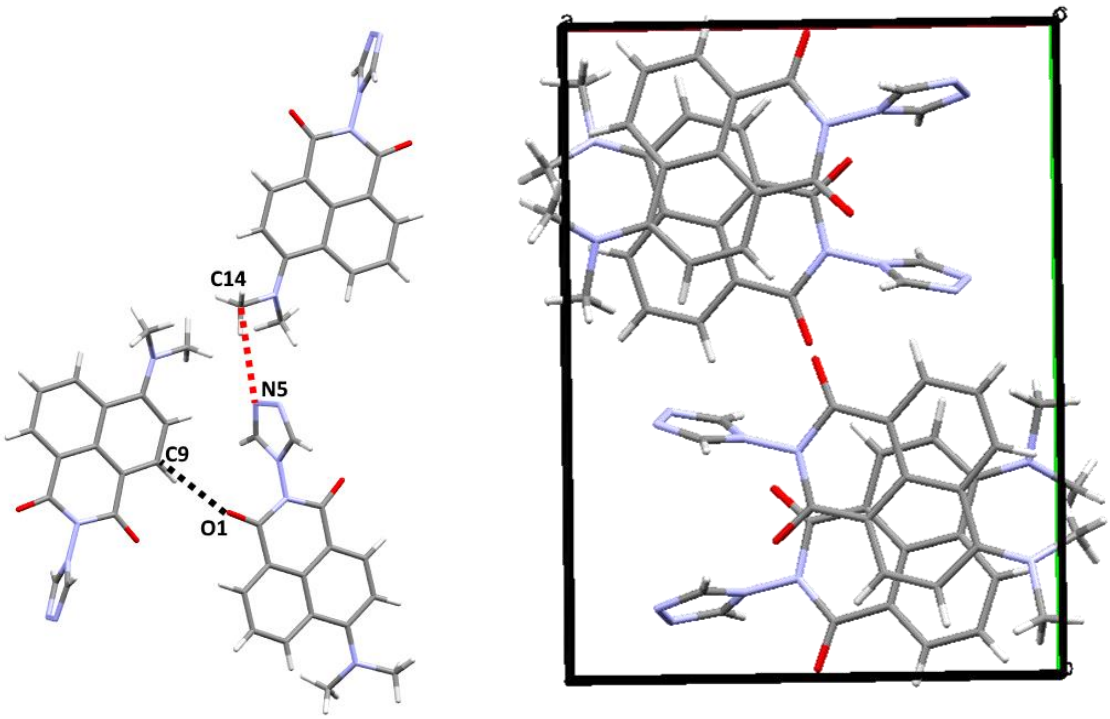

(a) (b)

Figure 4-18 (a) View of hydrogen-bonding interactions in **L_4**. Weak non-classical hydrogen bonds are shown in dashed line. (b) Packing of **L_4** showing π-stacked chains in the direction of the crystallographic *c* axis.

4.2.5 Synthesis and Crystallographic Analysis of 4-(1,2,4trz)-Nap-Tröger's base (L_5)

L_4 was then converted into the 4-(1,2,4tz)-Nap-Tröger's base **L_5**, by stirring with 1.7 equiv. of paraformaldehyde in neat trifluoroacetic acid under an N_2 atmosphere for 24 hours at room temperature (Figure 4-19). The solvent was removed in vacuum and the solid was suspended in ethanol and filtered through celite. The filtrate was evaporated in vacuum resulting in a yellow solid. Mass spec and crystal structure analysis confirmed successful formative of the Tröger's base.

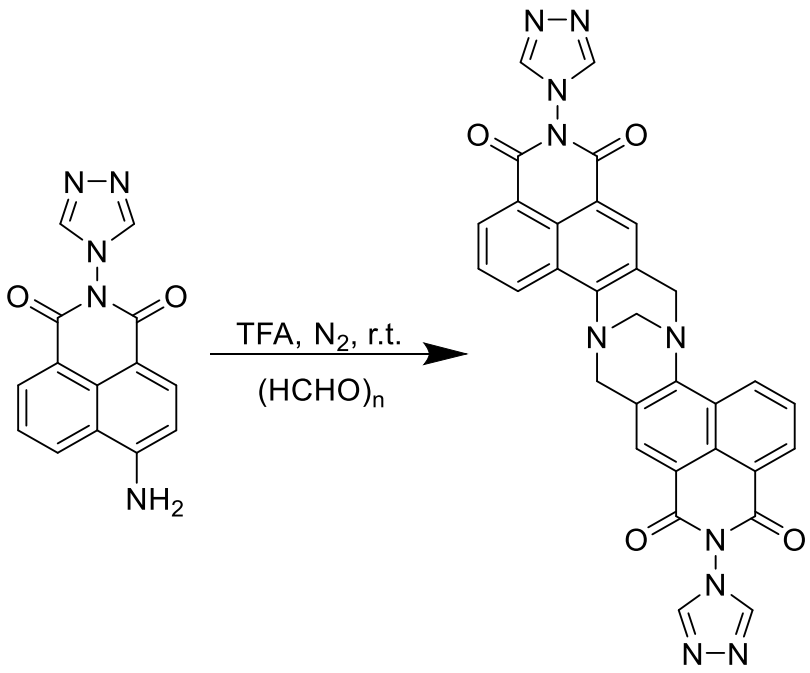

Figure 4-19 Synthesis of 4-(1, 2, 4trz)-Nap-Tröger's base(**L5**)

ligand crystallized in the monoclinic crystal system in the centrosymmetric space group $P2_1/c$. The crystal structure of **L5** shows that the methano-1,5-diazocine ring places the two naphthalimides at 63.68° to each other (Figure 4-20) which is not consistent with the 90° in "typical" Tröger's base compounds.[142]

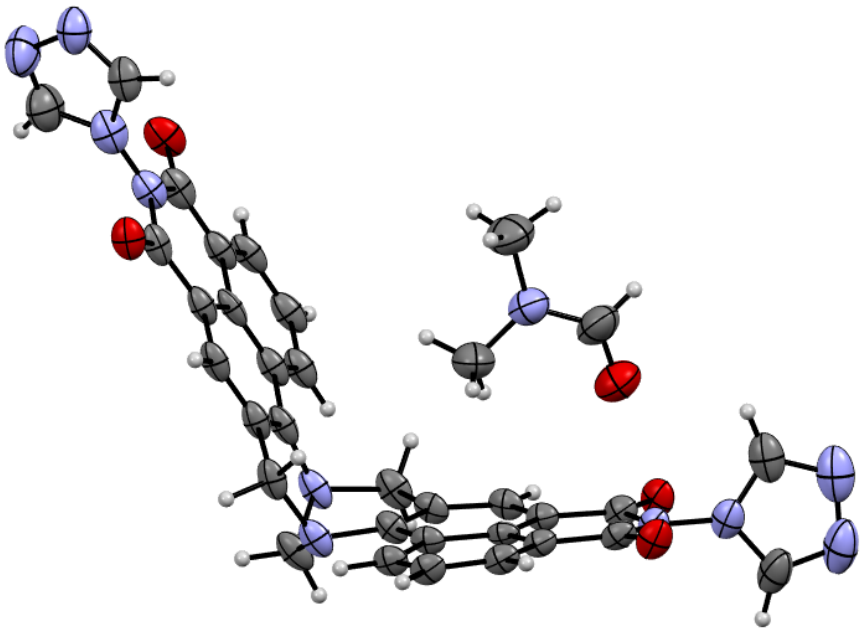

Figure 4-20 Molecular structure of **L5**·DMF with ellipsoids at 50% probability level

The yellow block-like single crystals were crystallised from slow evaporation of DMF solvent. The Along *a* axis, the molecules pack in pairs due to head-to-tail π···π stacking interactions between the naphthalimide moieties of two neighbouring molecules [centroid−centroid 3.549 Å]. Among

these two parallel packing molecules, hydrogen bonding can also be observed between the CH of triazole ring and oxygen atom of the neighbouring naphthalimide rings with [C2···O1=3.150(3) Å, bond angle ∠(C2-H···O1= 157.82(8)°] (Figure 4-21b).

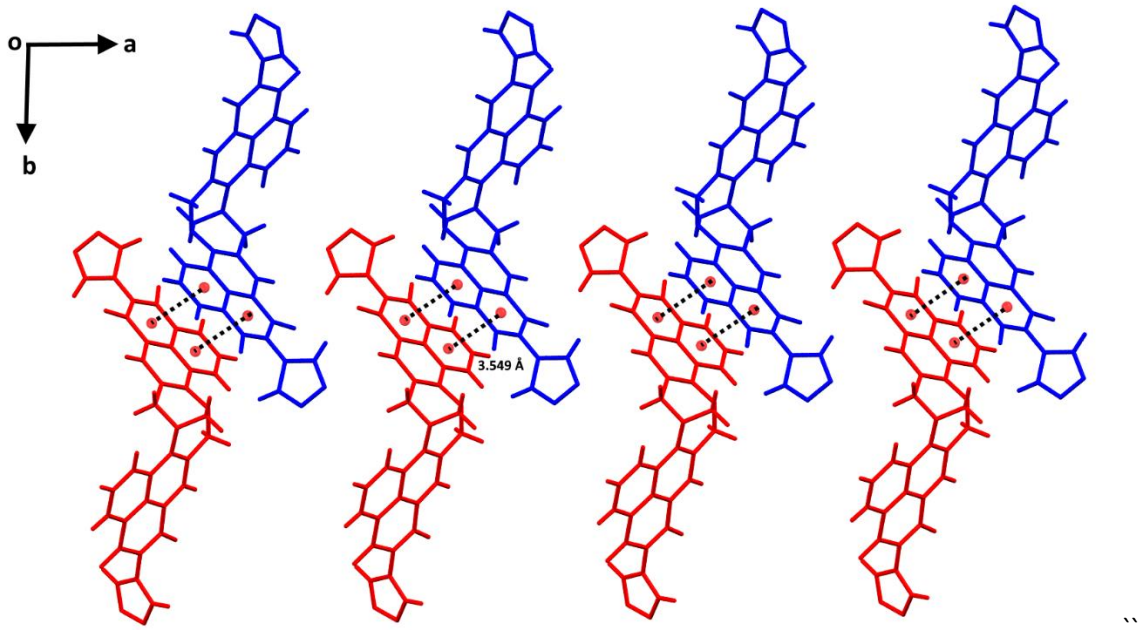

(a)

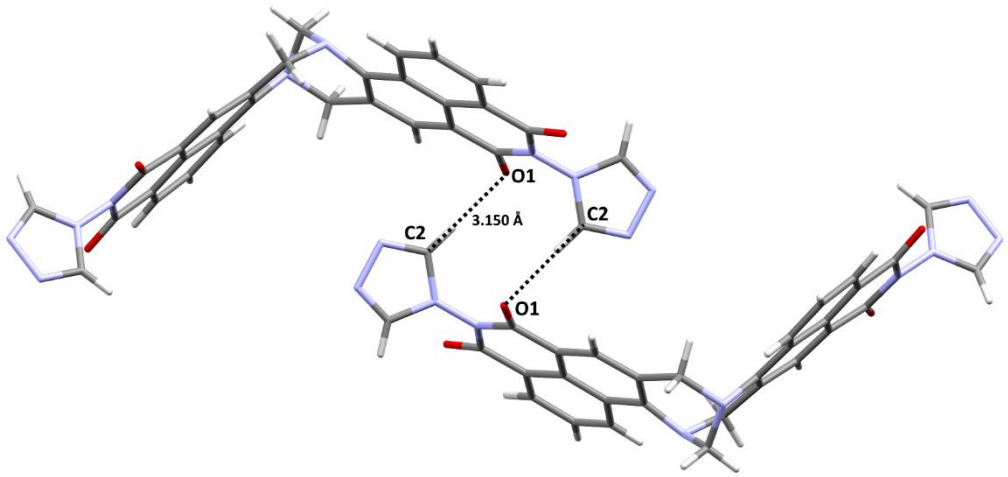

(b)

Figure 4-21 (a) Packing of $\mathbf{L_5}$ showing π-stacking in the crystallographic *a* direction. (b) Hydrogen bonding between head-to tail stacked packing shown as a dashed line.

Along the *c* axis, the packing interactions are organised by $\pi\cdots\pi$ interactions between neighbouring molecules where the naphthalimide units are arranged in a head-to-head configuration by $\pi\cdots\pi$ stacking of naphthalene rings [centroid⋯centroid=3.763 Å] and non-classical hydrogen bonding through a DMF molecule held in the neighbouring packing molecules [C31⋯O2=3.016(9) Å, bond angle ∠(C31-H⋯O2= 123.51(12)°] (Figure 4-22b).

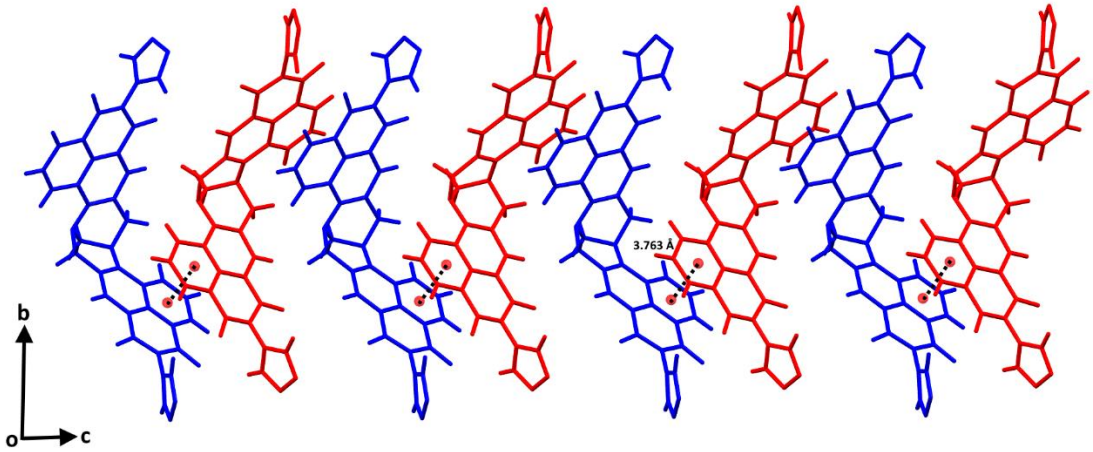

(a)

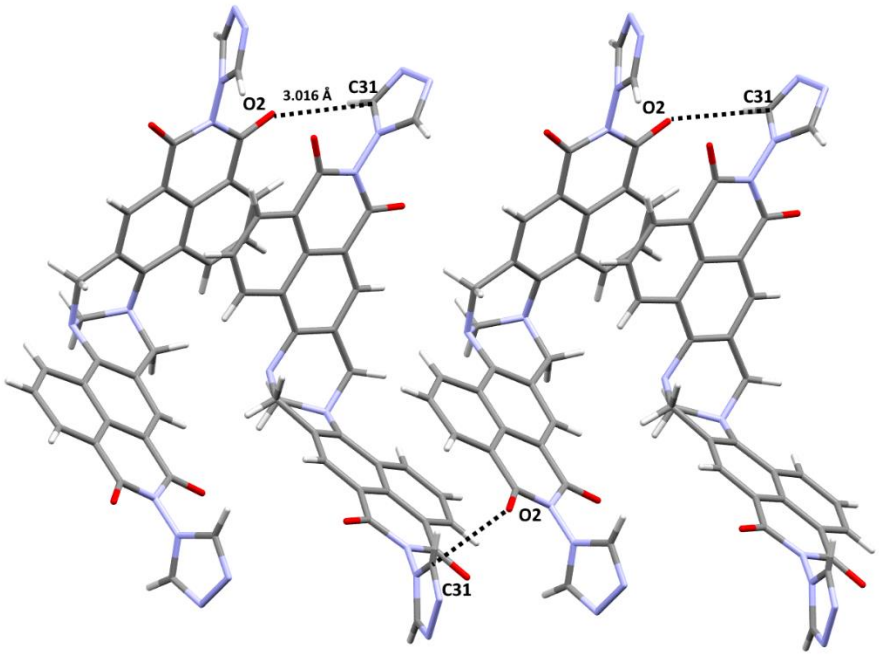

(b)

Figure 4-22 (a) Packing of $\mathbf{L_5}$ showing π-stacking in the crystallographic *a* direction. (b) Hydrogen bonding between neighbouring molecules shown as a dashed line.

4.2.6 Structural comparisons of L_1 – L_5

From the detailed structural analysis of **L_1** – **L_5**, it is clear that the naphthalimide substituents have a role to play in the packing interactions, however the naphthalimide…naphthalimide π-stacking interactions are always present and the substituent has a slight effect (see table 4-1), most likely through a combination of steric and electronic effects. Given such strong and interesting crystal packing and crystal engineering potential of these triazole-naphthalimide conjugates, an investigation of their complexes was then carried out.

Table 4-1 Comparison of π-stacking interactions in 1,2,4-triazole based naphthalimide ligands family

Ligands	Substituent	π-stacking type of naphthalimide moieties	Centroid-Centroid distance / Å
L_1	H	Head-to-Head	3.556
L_2	NO_2	Head-to-Tail	π···π 3.763 NO_2···π 2.805
L_3	NH_2	Head-to-Head	3.726
L_4	$N(Me)_2$	Head-to-Head	3.601
L_5	Tröger's base	Head-to-Head & Head-to-Tail	3.763 & 3.549

4.3 Complex Synthesis and Characterisation

After preparing this family of ligands, the coordination properties of these new ligands were investigated with Fe^{2+} and Co^{2+} metal salts (despite Fe(II) being the focus of this thesis, Co(II) is also SCO active and the lack of Fe(II) crystals, see below, meant Co(II) was investigated as well). A key goal was to obtain single crystals suitable for diffraction studies in order not only to determine the coordination modes of the 1,2,4-triazole based ligands, but also how the crystal packing is influenced by the presence of the naphthalimide moiety. Many attempts to prepare crystals were carried out [initially using Fe(II) and then using Co(II)] for all ligands, a range of Fe(II) and Co(II) salts, and a range of solvents. Frustratingly, despite many hundreds of reactions being set up, crystals were only ever obtained for complexes with **L_1** (the unsubstituted ligand). The lack of structural characterisation of **L_2** – **L_5** meant drawing any conclusions between ligand types was

impossible, but did indicate that the substituents play a role, albeit a negative one, in crystallising the complexes (under the conditions attempted herein). Nevertheless, some interesting multinuclear complexes of L_1 were obtained and their detailed structural analysis is highlighted in the following sections.

4.3.1 Complexation between L_1 and $Co(BF_4)_2$ (C_1)

L_1 and $Co(BF_4)_2$ were dissolved in DMF in sealed scintillation vials and then heated to 135 °C overnight. Small, block-like orange crystals were grown from slow evaporation over a few weeks, and the low temperature (100 K) molecular structure was determined.

$[Co_2(L_1)_3(DMF)_4(H_2O)_2](BF_4)_4 \cdot 4DMF \cdot H_2O$ (**C_1**) crystallized in the triclinic space group $P\bar{1}$. The asymmetric unit (Figure 4-23a) shows, two cobalt centres triply bridged by three 4-(1,2,4tz)-nap-H units (through the N^1 and N^2 donor atoms), four coordinated DMF molecules, two coordinated water molecules, four interstitial DMF solvates, one interstitial water, and four BF_4 counter anions. The result is a triple bridge dinuclear complex where the two cobalt ions are connected by three μ_2-**L_1** ligands at a distance of around 3.838 Å, with the remainder of the coordination sphere consisting of DMF and water molecules to give an overall N_3O_3 coordination sphere. The cobalt ions display slightly distorted octahedral geometry, with sigma values for Co1 and Co2 of 24.58° and 19.02° respectively. The Co-N-N angles range from 122.63° to 126.84°, which are close to the exocyclic free donor electronic pair angles of five membered rings with very little strain.

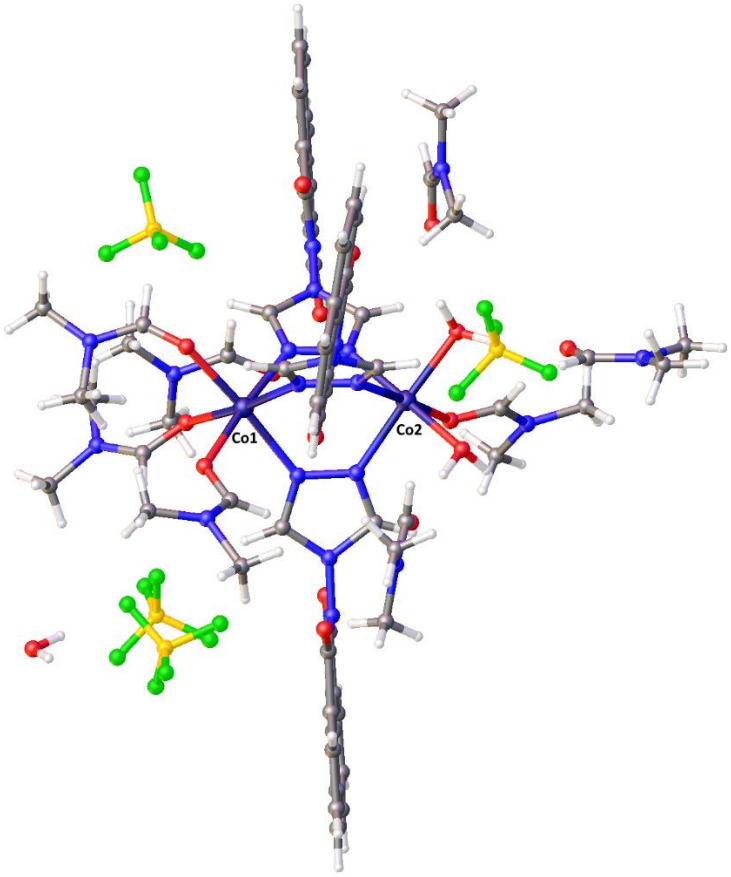

(a)

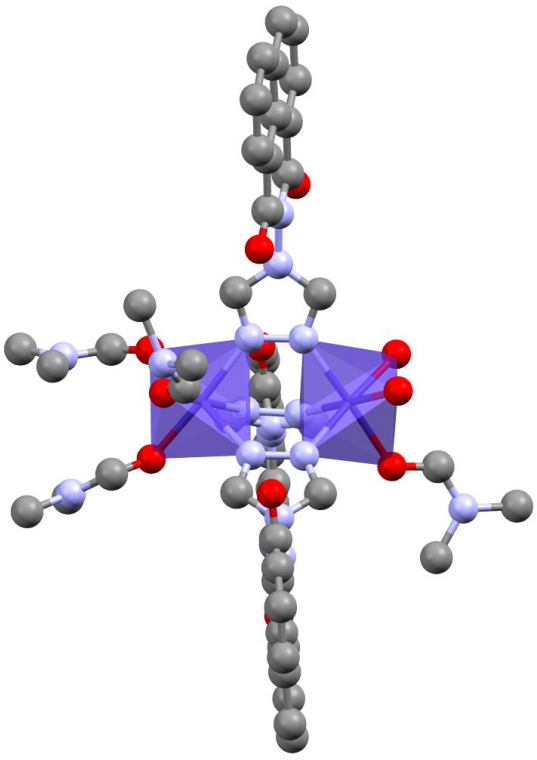

(b)

Figure 4-23 (a) Asymmetric unit of **C_1**. (b) Polyhedral structure of **C_1**, with anions, solvents and hydrogen atoms omitted for clarify.

The packing interactions in **C_1** are interesting and the naphthalimide is clearly showing its ability to act as a pi-based second building unit (SBU). The nature of the complex (*i.e.* three ligands bridging the Co(II) centres) results in three naphthalimides oriented at ~120°, ideally positioned to extend the structure through pi-stacking SBUs. Each of these naphthalimides is involved in a head-to-tail, offset face-to-face pi-stacking interaction [$\pi\cdots\pi$ stacking interactions between neighbouring complex molecules with centroid⋯centroid = 3.719 Å and centroid⋯centroid = 3.572 Å (Figure 4-25)]. These result in π-stacked 2D-sheets of complexes extending in the direction of the crystallographic a and c axes. These sheets are linked to sheets above and below through hydrogen bonding and anion⋯π interactions. There exist two weak hydrogen bonds through a DMF molecule involving the coordinated water and the naphthalimide moiety from a neighbouring complex, O7⋯O13 = 2.714(3) Å, bond angle ∠(O7-H⋯O13 = 157.44(8)°), and C56⋯O1 = 3.071(2) Å, bond angle ∠(C56-H⋯O1 = 119.16(9)°).(Figure 4-24). Additionally, the adjacent molecule is also connected to the interstitial DMF solvate by weak hydrogen bonding. There also exists an anion⋯π interaction between the BF_4 and the adjacent naphthalimide ring, with a distance of anion⋯π = 2.997 Å. (Figure 4-24). The interactions are self-complementary, giving a total of three interactions between two neighbouring naphthalimide moieties and this extends them into two directional chains, thus forming a network.

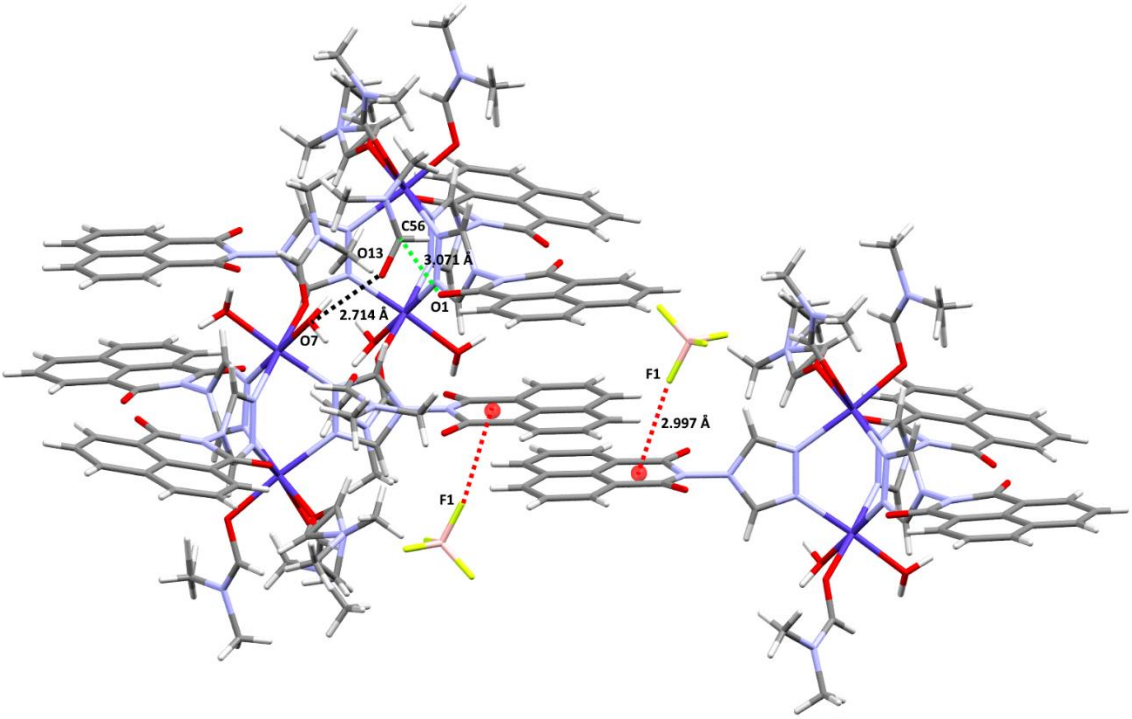

Figure 4-24 View of hydrogen-bonding and anion⋯π interactions in **C_1**.

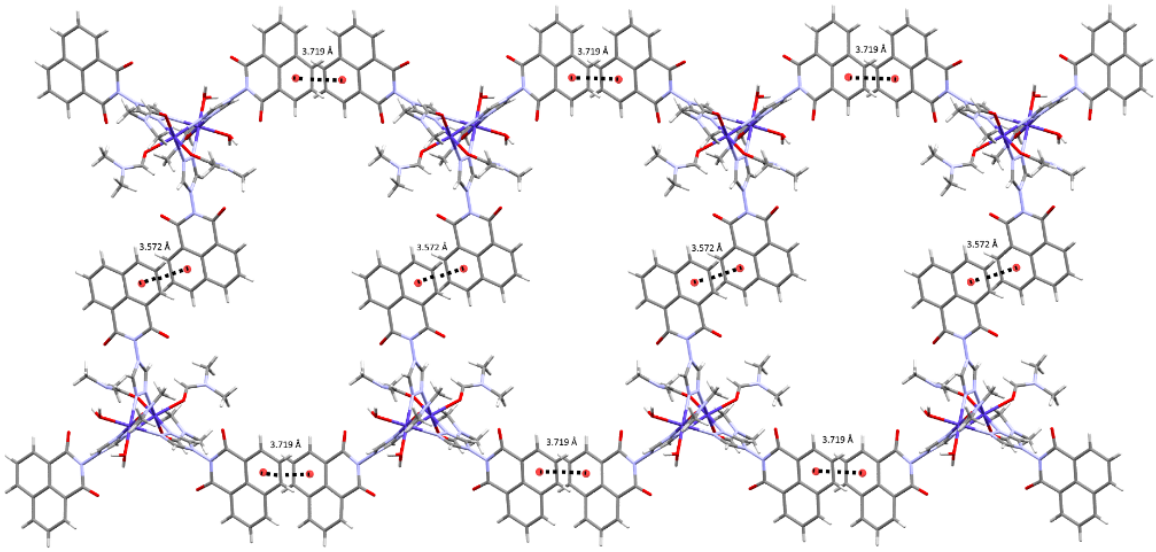

Figure 4-25 Packing interaction of **C_1** showing π···π stacking between molecules.

4.3.2 Complexation between L_1 and $Co(NO_3)_2$ (C_2)

Changing the counter anion from BF_4 to NO_3 allows the influence of the anion on the supramolecular arrangement to be determined. This is particularly desirable given the interplay between the anion and naphthalimide π-system that was previously observed. L1 and $Co(NO_3)_2$ were dissolved in DMF in sealed scintillation vials and then heated to 135 °C for 24 hours. Small block-like orange crystals were grown from slow evaporation over several weeks and the low temperature (100 K) crystal structure determined.

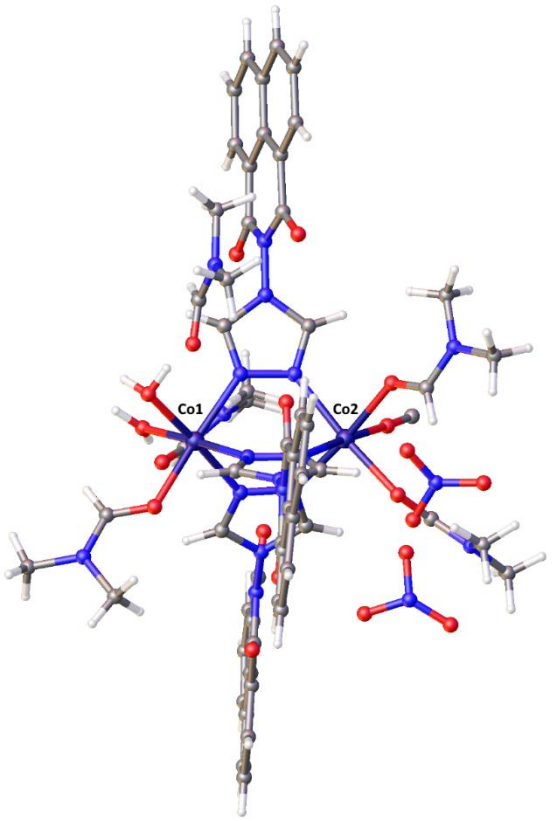

(a)

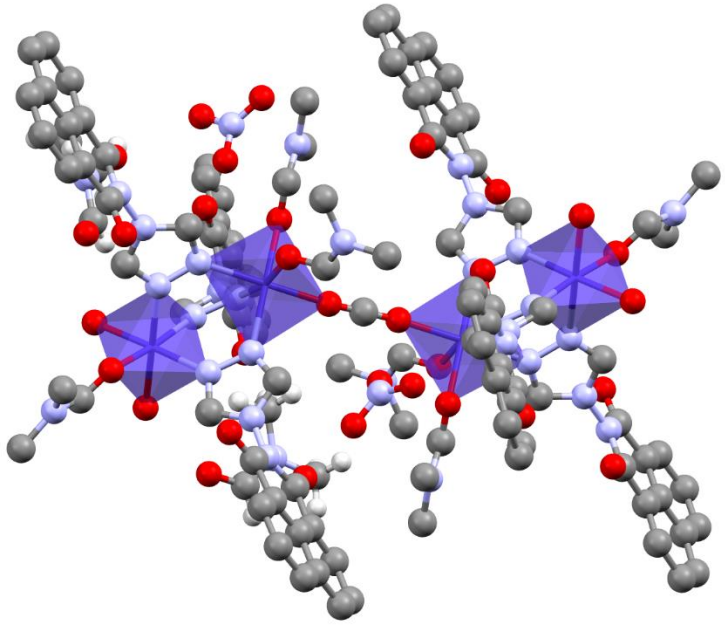

(b)

Figure 4-26 (a) Asymmetric unit of **C_2**. (b) Polyhedral whole molecular structure of **C_2**, with anions, solvents and hydrogen atoms omitted for clarify.

This resulted in an unexpected and highly novel structure of $[Co_2(\mathbf{L_1})_2(DMF)_3(H_2O)_2(\mu_2\text{-}HCO_2)Co_2(\mathbf{L_1})_2(DMF)_3(H_2O)_2](NO_3)_7.4DMF$ (**C_2**), where two asymmetric units consisting of $[Co_2(L_1)_2(DMF)_3(H_2O)_2{\cdot}(NO_3)_4]$ are connected by one freely rotating HCO_2 forming a large

symmetrical, tetranuclear Co(II) molecule. The origin of the HCO_2 is likely from DMF decomposition[146-147] and such trapping of HCO_2 has been observed in MOFs[148], however it is much rarer to observe this in discrete complexes. Unfortunately, only a small number of crystals were obtained and further analysis could not be conducted. $(\mathbf{C_2})_2 \cdot HCO_2$ crystallised in the triclinic space group $P\bar{1}$ and contained half of one molecule in the asymmetric unit with the other half generated by a centre of inversion (carbon is freely rotating, average position is what makes it look linear.). The coordination geometry around Co(II) is similar to $\mathbf{C_1}$, which reveals the degree of Σ to be Co1 Σ = 27.35° and Co2 Σ =17.91°. These values are consistent with a slightly distorted octahedral geometry (Figure 4-26).

The packing interactions in $\mathbf{C_2}$ also involve the naphthalimide π stacking system (Figure 4-27). The units are packed in to 1-D chains through face to face $\pi\cdots\pi$ stacking between neighbouring naphthalimide moieties [centroid⋯centroid = 3.421 Å]. These chains are then linked to neighbouring chains through another $\pi\cdots\pi$ stacking between two molecular naphthalimide moieties [centroid⋯centroid = 3.550 Å].

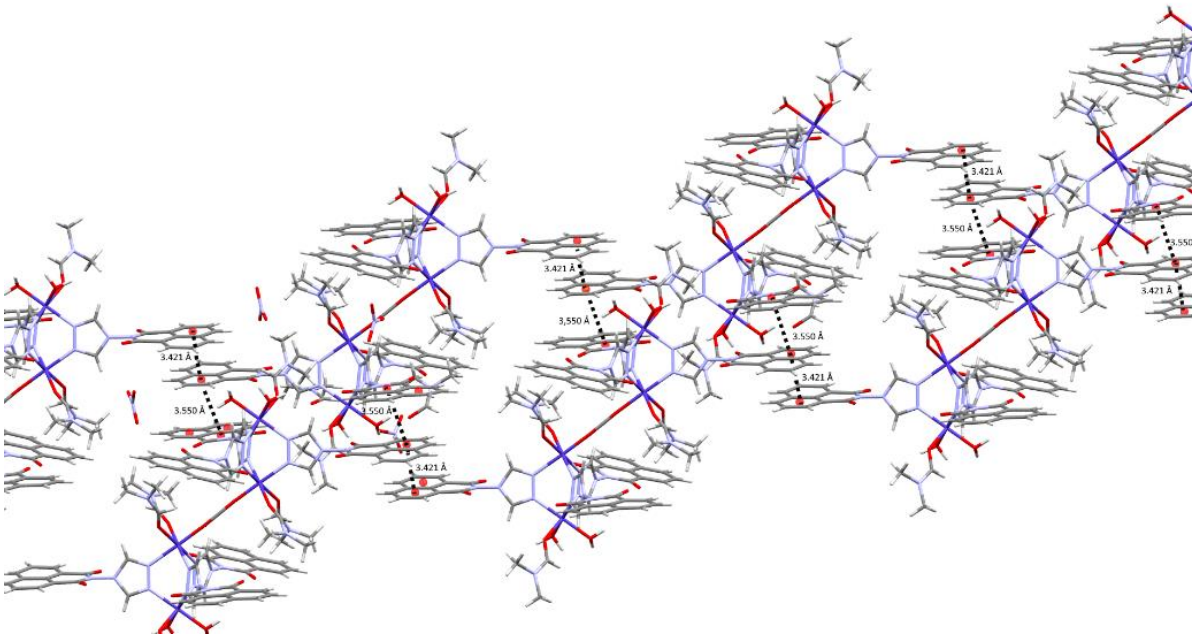

Figure 4-27 Long range order of $\mathbf{C_2}$ showing $\pi\cdots\pi$ stacking between molecules.

4.3.3 Complexation between L_1 and $Fe(II)(ClO_4)_2$ in MeOH (C_3)

$\mathbf{L_1}$ and $Fe(II)(ClO_4)_2$ (ratio 6 : 1) were reacted by stirring in methanol at 60 °C for 3 hours. After cooling to room temperature, the clear yellow solution was subjected to vapour diffusion of diethyl ether. After 3 days, yellow block-like crystals were obtained and the low temperature (100 K) crystal structure was determined. $[Fe(\mathbf{L_1})_6](ClO_4)_3$ ($\mathbf{C_3}$) crystallised in the trigonal space group, $P\bar{3}$ and contained one-sixth of the complex molecule and half of one ClO_4 anion in the asymmetric

unit (Figure 4-28a). The crystal structure revealed that the Fe(II) complex had been oxidised to Fe(III) during the reaction.

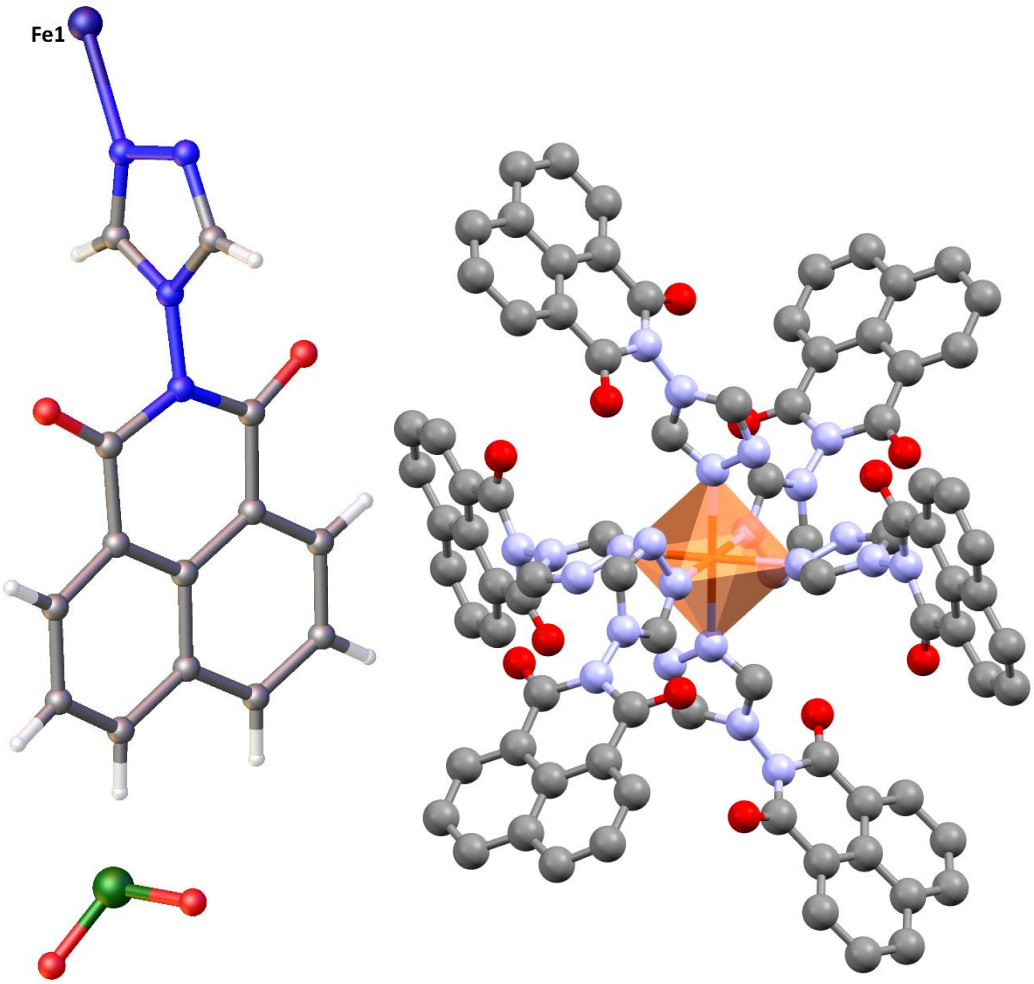

(a) (b)

Figure 4-28 (a) Asymmetric unit of **C_3**. (b) Polyhedral whole molecular structure of **C_3**, with anions and hydrogen atoms omitted for clarity.

Interestingly, the triazole was not observed to bridge through N^1 and N^2, instead only N^1 binding was observed. The mononuclear complex consists of one Fe(III) centre coordinated to six nitrogen atoms from six different triazole rings. The Fe(III) metal centre has a distorted octahedral geometry with a Σ value of 40.56 (Figure 4-28b). Packing interactions in **C_3** are heavily dominated by $\pi\cdots\pi$ stacking interactions involving the naphthalimide groups. There are six offset face to face $\pi\cdots\pi$ stacks surrounding one **C_3** complex and each naphthalimide moiety forms a $\pi\cdots\pi$ interaction with a neighbouring naphthalimide ring of a different molecule [centroid⋯centroid = 3.925 Å – the high symmetry means on one interaction is present, but repeated six times per complex]. The result is a large 3D network constructed of these π interactions (Figure 4-29).

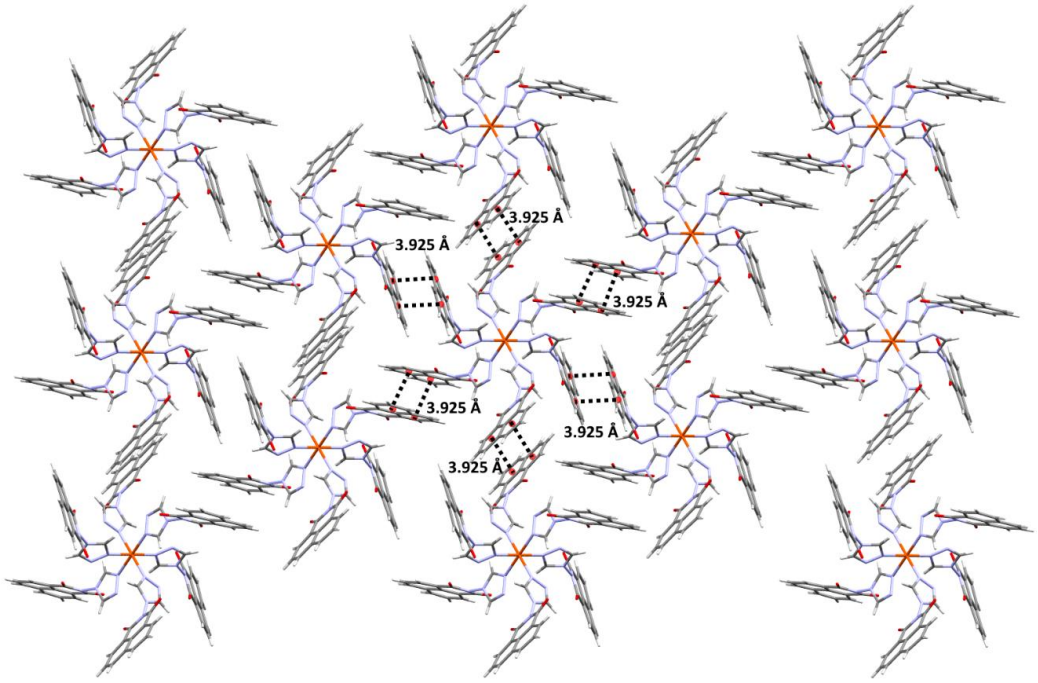

Figure 4-29 Packing interaction of C_3 showing π···π stacking between molecules

This structure is very similar to a result published in 2019 from a collaboration between the Triki and Boukheddaden groups.[149] Their complex was synthesised from a Fe(II) salt and **L₁** with 1,1,3,3-tetracyano-2-thiomethylpropenide anion (tcnsme) and included acetonitrile solvent molecules in the crystal structure, giving a formula $[Fe(\mathbf{L_1})_6(tcnsme)_2]\cdot 4CH_3CN$. The coordination of this complex is similar to **C_3**, where the Fe(II) metal centre is surrounded by six ligands (Figure 4-30). $[Fe(\mathbf{L_1})_6(tcnsme)_2]\cdot 4CH_3CN$ exhibits a gradual SCO with $T_{1/2}$ = 114 K (Figure 4-31).

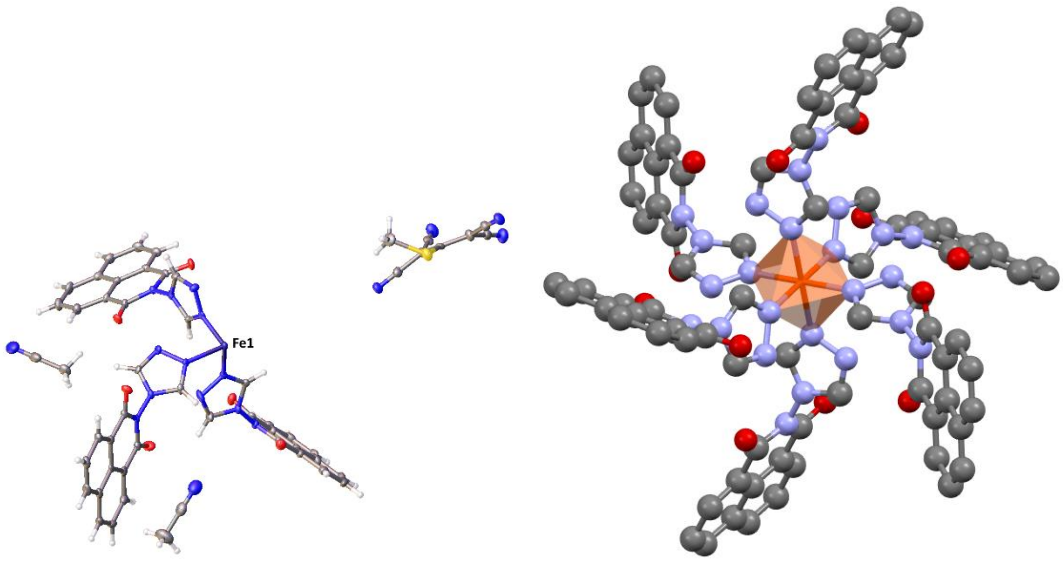

Figure 4-30 (a) Asymmetric unit of $[Fe(\mathbf{L_1})_6(tcnsme)_2]\cdot 2CH_3CN$. (b) Polyhedral whole molecular structure of $[Fe(\mathbf{L_1})_6(tcnsme)_2]$, with anions and hydrogen atoms omitted for clarity. Figure adapted from Triki and Boukheddaden groups.[149]

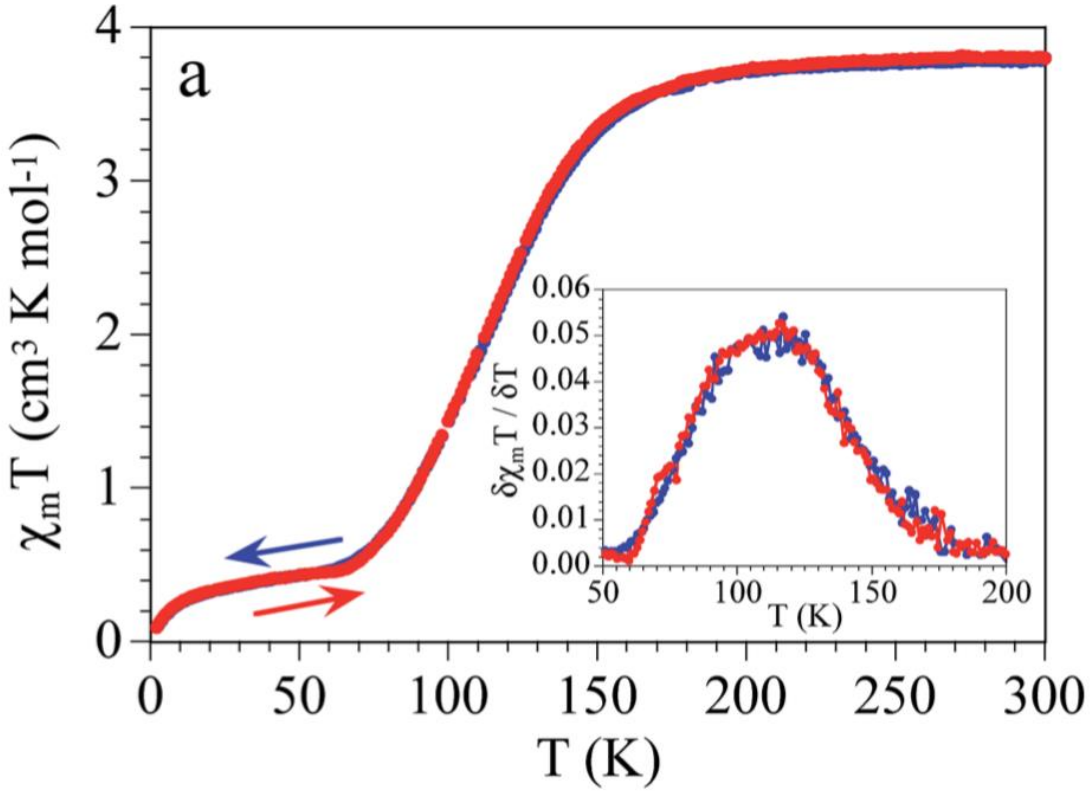

Figure 4-31 . $\chi_M T$ versus T plot for [Fe(**L₁**)$_6$(tcnsme)$_2$]·4CH$_3$CN over temperature range 2-300 K. Figure adapted from Triki and Boukheddaden groups.[149]

In the [Fe(**L₁**)$_6$(tcnsme)$_2$] packing arrangement, there are a number of π···π interactions in all directions of the octahedral geometry, as observed in **C₃** (Figure 4-32). Only one π-stacking interaction along the naphthalimide moiety was observed where the centroid···centroid distance = 3.717 Å. Crystallographic details, Fe–N distances (˚A), distortion parameters (°) between [Fe(**L₁**)$_6$](ClO$_4$)$_3$ (**C₃**) and [Fe(**L₁**)$_6$(tcnsme)$_2$] are shown in Table 4-2, however these comparissions are of limited use given the differences between Fe(II) and Fe(III).

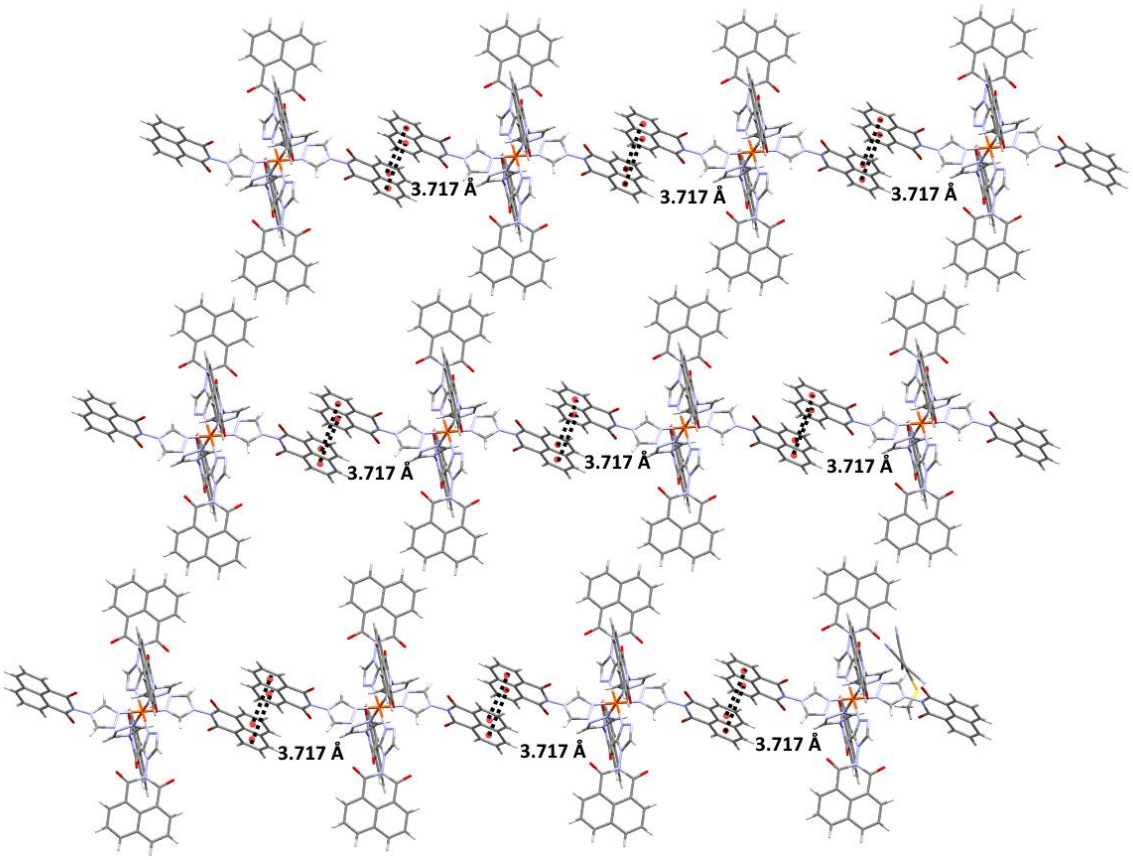

Figure 4-32 Packing interaction of $[Fe(\mathbf{L_1})_6(tcnsme)_2]$ showing π···π stacking between molecules

Table 4-2 Fe–N distances (˚A), distortion parameters (°) between $[Fe(\mathbf{L_1})_6(tcnsme)_2]$ [149] and $[Fe(\mathbf{L_1})_6](ClO_4)_3$ ($\mathbf{C_3}$).

	$[Fe(\mathbf{L_1})_6(tcnsme)_2]$ – Fe(II) [149]		$\mathbf{C_3}$ $[Fe(\mathbf{L_1})_6](ClO_4)_3$ -Fe(III)
	100 K	296 K	100 K
Space group	$P2_1/c$	$P2_1/c$	$P\bar{3}$
Fe1-N / Å	1.999 (4) 1.993 (4) 1.994 (4)	2.200 (4) 2.190 (4) 2.176 (4)	2.174 (1)
Σ (°)	16.8	17.3	40.56

4.3.4 Complexation between L_1 and $Fe(II)(ClO_4)_2$ in MeCN and DMF solvent mixture (C_4)

With methanol giving a mononuclear system, the same ligand and metal salt were reacted in a different solvent to see if polynuclear systems could be obtained. When $\mathbf{L_1}$ and $Fe(II)(ClO_4)_2$ were reacted in MeCN with a minimum volume of DMF and refluxed at 60 °C for 3 hours, small block-

like yellow crystals were grown from vapour diffusion of diethyl ether over a few days and the low temperature (100 K) crystal structure was determined.

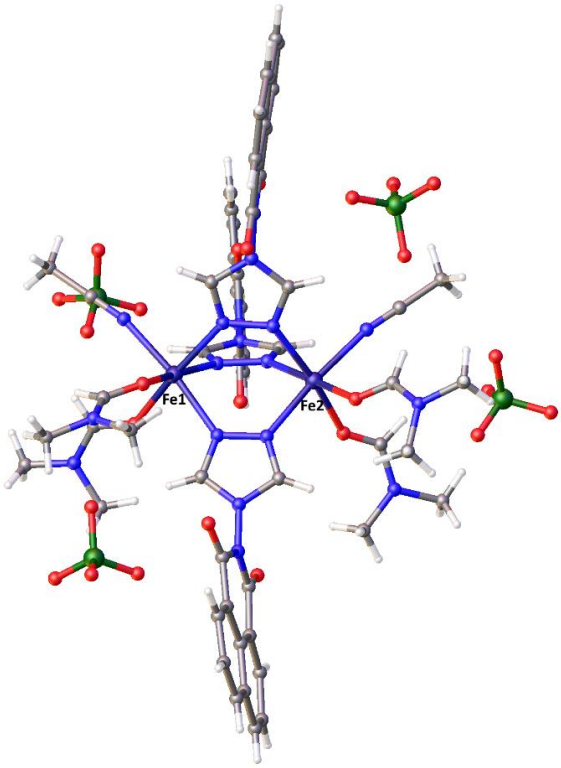

(a)

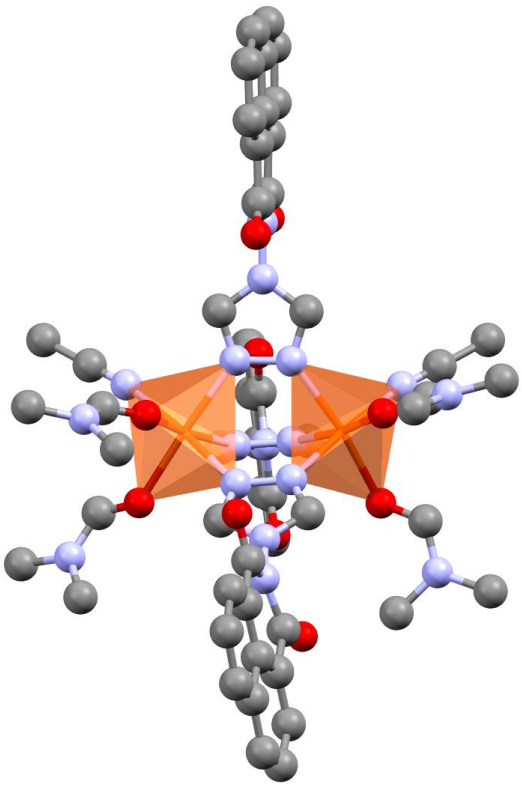

(b)

Figure 4-33 (a) Asymmetric unit of **C4**. (b) Polyhedral structure of **C4**, with solvents and hydrogen atoms omitted for clarity.

$[Fe_2(\mathbf{L_1})_3(DMF)_4(MeCN)_2](ClO_4)_4$ (**C_4**) crystallised in the triclinic space group $P\bar{1}$. The asymmetric unit shows two iron(II) centres triply bridged by three 4-(1,2,4tz)-nap-H units through N^1 and N^2 donor atoms (Figure 4-33), four coordinated DMF molecules, two coordinated acetonitrile molecules and four ClO_4 counter anions. Each iron(II) centre has a distorted octahedral geometry with Σ values of 35.6 and 40.5 for Fe1 and Fe2 respectively. The Fe-N bond lengths are 2.147 (2)-2.209(3) Å and Fe-O are 2.052 (3)-2.091(3) Å respectively, which are consistent with the HS configuration. Among these bridges, Fe-N-N angles range from 123.77° to 126.50°, which is close to the exocyclic free donor electronic pair angles of a five membered ring with little strain.

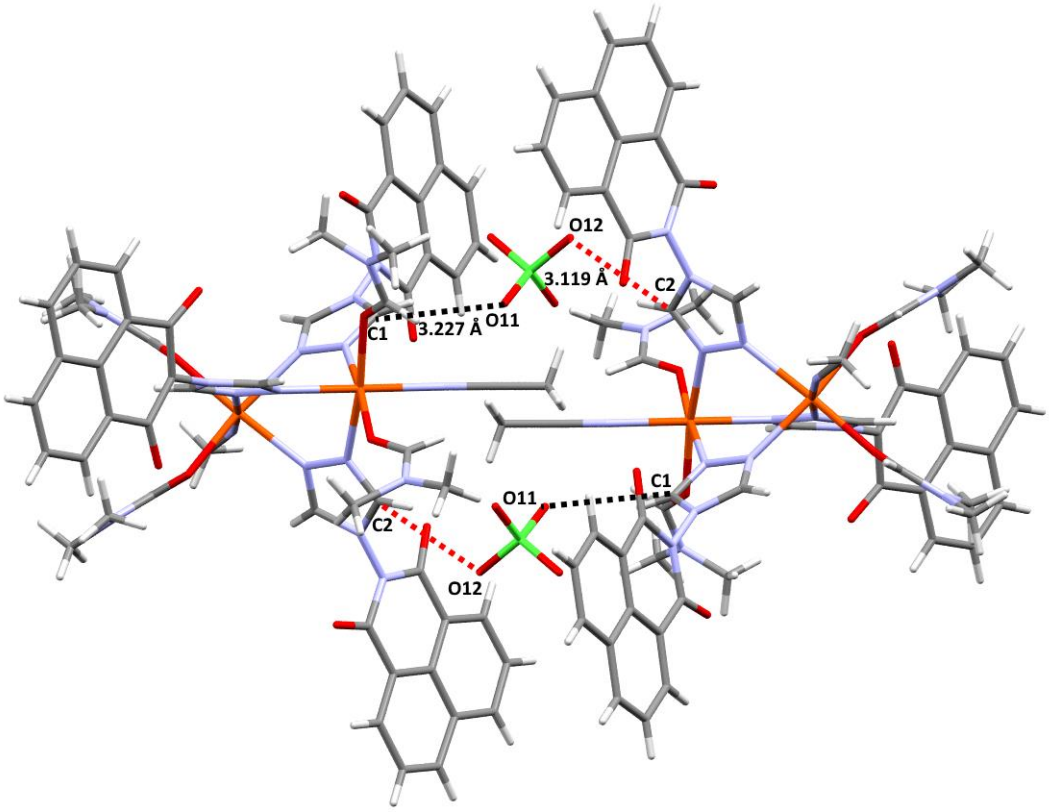

Figure 4-34 View of hydrogen-bonding interactions in **C_4**

C_4 has a similar molecular geometry to that of **C_1**, where packing interactions are controlled by weak hydrogen bonding, anion···π and π···π stacking. Much like the packing of **C_1**, in **C_4** a 2D sheet of molecules is formed through π···π stacking interactions between naphthalimide groups [centroid···centroid = 3.907 Å and 3.881 Å] (figure 4-37). These sheets are then linked together through non-classical CH hydrogen bonding and anion···π interactions. Molecules of **C_4** are linked through hydrogen bonding between the coordinated triazole CH group from neighbouring naphthalimide moieties and a ClO_4 molecule [C1···O11 = 3.227(6) Å, ∠(C1-H-O11 = 145(9)° and C2···O12 =3.119(3) Å, ∠(C2-H···O12= 126(6)°] (Figure 4-34).

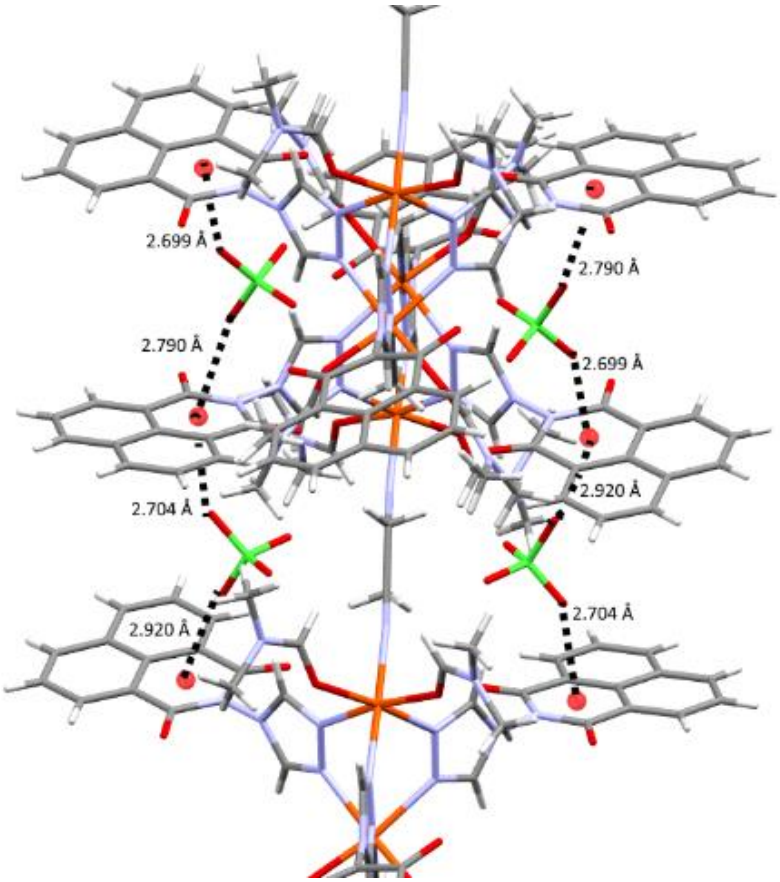

Figure 4-35 View of anion···π interactions in **C₄**

Further linking of **C₄** molecules occurs along the b axis direction, through anion···π interactions between naphthalimide rings and ClO_4 anions, with the distances ranging from 2.699 Å to 2.920 Å (Figure 4-35). Overall these interactions form a grid network, where the naphthalimide is, as expected, a key feature of the packing interactions (Figure 4-36).

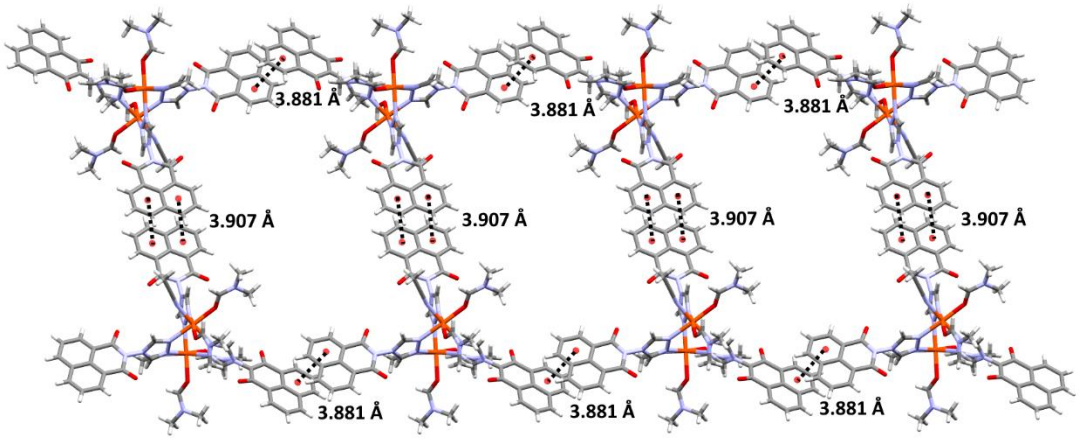

Figure 4-36 Packing interaction of **C₄** showing π···π stacking

4.4 Modification to Ligand – Synthesis and Characterisation of 4-Ethyl-1,2,4-trz)-Nap-H (L_6)

With the inability to achieve crystallographic characterisation for complexes of many of the aforementioned ligand systems, an attempt to alter the ligand structure was carried out as solubility was thought to play a role. The modifications of ligands were attempted to improve the solubility. With very rigid systems for $\mathbf{L_1}$ – $\mathbf{L_5}$ and little room for flexibility, it was decided to trial a system where the 1,2,4-triazole ring and the naphthalimide moiety were separated by an ethylene spacer as this has been used previously to impart better solubility on systems.[150-151] Using this design idea, 4-Ethyl-(1,2,4tz)-Nap-H ($\mathbf{L_6}$) was prepared via a multi-step synthesis.

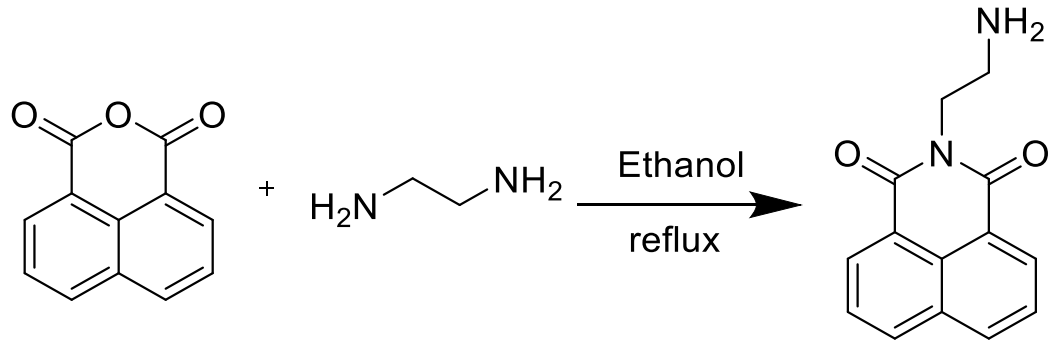

Figure 4-37 Synthesis of 2-aminoethyl-naphthalic anhydride

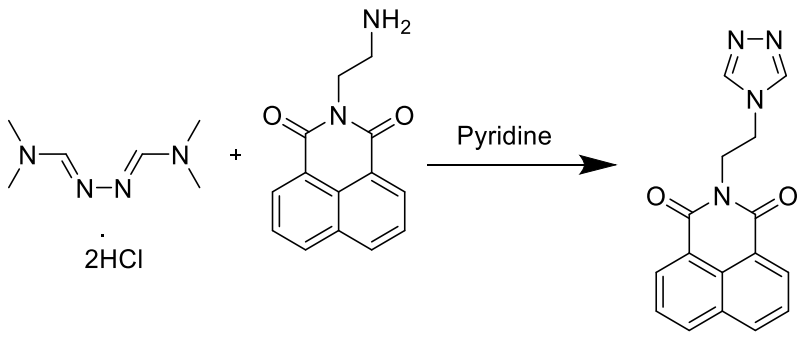

Figure 4-38 Synthesis of 4-ethyl-(1,2,4tz)-Nap-H($\mathbf{L_6}$))

Initially, an ethyl amino terminated naphthalimide (2-aminoethyl-naphthalimide) was prepared (figure 4-22) before it was reacted with N,N-dimethylformamide azine dihydrochloride (DMAZ). 2-Aminoethyl-naphthalic anhydride was prepared from 1,8-naphthalic anhydride and a large excess ethylenediamine in refluxing EtOH for 6 hrs. The solution was filtered under vacuum and filtrate was evaporated under reduce pressure. The residue was recrystallized from EtOH, producing white crystals of 2-aminoethyl-naphthalic anhydride.

DMAZ was synthesised from a large excess of thionyl chloride and aqueous hydrazine hydrate in DMF in an ice bath following a published procedure.[56] After the mixture was stirred for 24 hrs, the

white precipitate of DMAZ N,N-dimethylformamide azine dihydrochloride was collected by filtration followed by washing with ice cold DMF and Et_2O.

4-Ethyl-(1,2,4tz)-Nap-H was synthesised by refluxing DMAZ and 2-aminoethyl-naphthalic anhydride in pyridine overnight, the solution was then cooled and icecold water added. The resulting white precipitate was filtered and washed with ice cold water to give **L_6** in poor yield.

Small pale yellow block-like single crystals of **L_6** were obtained by slow evaporation from a DMF solution and the low temperature (100K) crystal structure determined. **L_6** crystallised in the tetragonal space group $I4_1/a$ and contained one complete molecule in the asymmetric unit (Figure 4-39a).

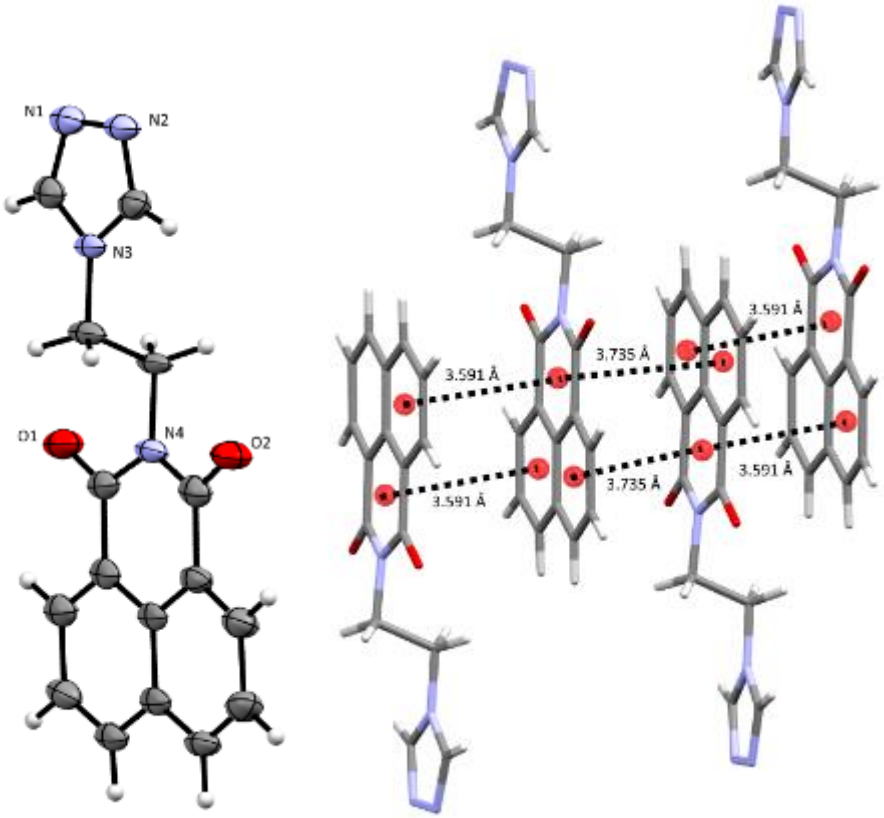

(a) (b)

Figure 4-39 (a) Molecular structure of **L_6** with ellipsoids at 50% probability level. (b) Packing of **L_6** showing $\pi\cdots\pi$ stacking between molecules.

The crystal packing interactions are still dominated by the quasi-planar geometry of the naphthalimide moieties, in which give rise to an anti-parallel head-to-tail arrangement directed by the $\pi\cdots\pi$ stacking of the aromatic rings. The centroid distances between the alternative naphthalimides are 3.591 Å and 3.735 Å respectively (Figure 4-39b). Additionally, weak non-classic hydrogen bonds from the triazole group and carbonyl oxygen atoms are also observed between

neighbouring molecules [C11···O1=3.253(2) Å and ∠(C-H···O)=130.72(6)°, C-H···O=3.352(3) Å and ∠(C-H···O)=166.14(5)°, C-H···N=3.361(5) Å and ∠(C-H···N)=133.33(9)°] (Figure 4-40). Along both the a and b axes, π stacking interactions organise the molecules into long supramolecular chains as shown in Figure 4-41.

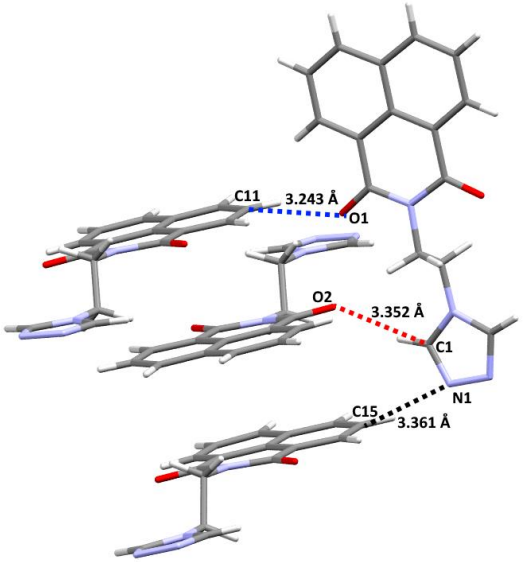

Figure 4-40 View of CH-based hydrogen-bonding interactions in **L_6**, weak non-classical hydrogen bonding shown in dashed line.

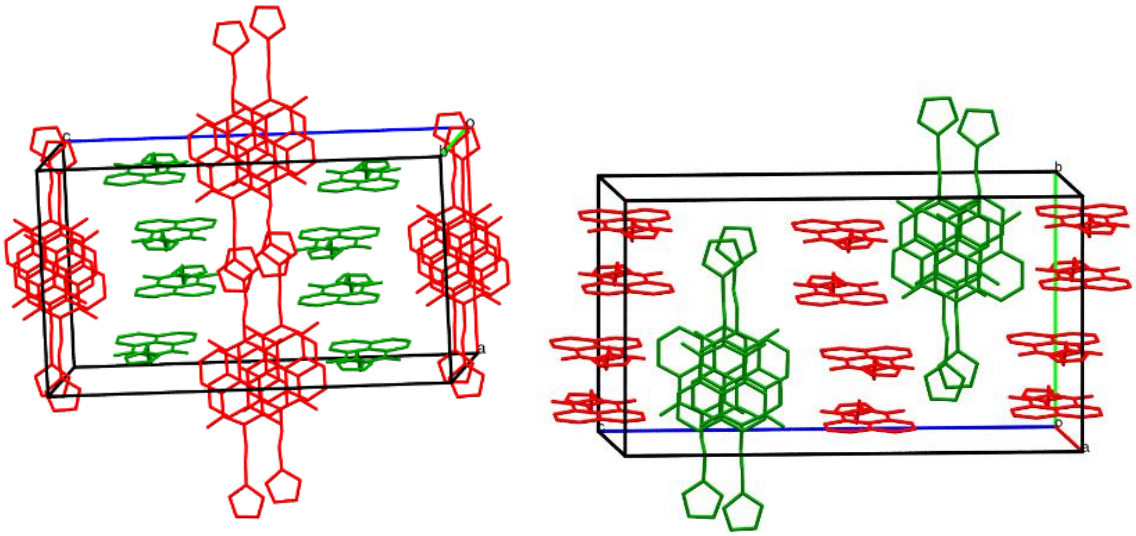

(a) (b)

Figure 4-41 (a) Packing of **L_6** showing π-stacking in the crystallographic *a* direction. (b) Packing of **L_6** showing π-stacking in the crystallographic *c* direction.

4.5 Attempted Complexation of L_6

Whilst it was expected that **L_6** might have better solubility, it only appeared appreciably soluble in DMF and DMSO. Complexation reactions with Fe(II) and Co(II) were attempted in DMF using sealed scintillation vials at elevated temperatures (>120° C), however despite multiple attempts no single crystals could be obtained and decomposition of the ligand appeared to occur in most cases (brown oils typically resulted). For this reason, and the low yielding multi-step procedure, no attempts were continued to access the substituted naphthalimide versions of these ligands as yields were expected to be even lower and solubility was not improved on inclusion of the ethyl linker.

4.6 Conclusions

A series of N-substituted-1,8-naphthalimide derivatives have been synthesised and crystallised. The crystal packing revealed significant π-based interactions. Varying the substituents provides extra hydrogen bonding functionality and the presence of electron donating/withdrawing groups can alter the nature of the packing. The synthesis of coordination complexes was attempted with different Co(II) and Fe(II) salts and ligands, however single crystals of the desired SCO polymer complexes were not produced due to solubility factors and limited space issues of naphthalimide ligands. As DMF was used to improve solubility, metal centres were both coordinated with ligands and DMF in **C_1**, **C_2**, **C_4**, resulting only in HS configuration complexes. In **C_3** it was not possible to prevent Fe(II) being oxidised to Fe(III), even when protected under a N_2 atmosphere in the presence of ascorbic acid. However, analysis of **C_1**-**C_4** structures shows π···π interactions continue to be dominant and enable functional networks to be constructed using supramolecular self-assembly. **C_4** formed clear π···π interactions in a range of directions due to the octahedral geometry imposed by the metal centre on an array of naphthalimide moieties.

Whilst some the complexes may have been produced as oils and gummy solids, given the nature of the study only reactions where single crystals were obtained were further investigated which led to a limited exploration of novel complexes. Crystallisation of polymeric systems, such as the previously mentioned polymeric complex first produced by Lavrenova in 1995[136], are notoriously difficult with this example not gaining structural analysis until 16 years after first being reported.

In this chapter a number of complexes were however successfully synthesised, and these exhibit a range of π-based interactions. The nature of the interactions merits further investigation, it is therefore proposed that the free ligands themselves are used to probe the energy of the π-based interactions. Therefore, a systematic experimental and theoretical electron density and

topological analysis on the ligands **L_1**-**L_4** presented in the next chapter. This study will analyse how the different properties of several 4-substituents influences the nature of intermolecular interactions and how they in-turn change the contribution of π···π interactions to the system.

4.7 Experimental

4.7.1 Synthesis of 4-(1,2,4trz)-Nap-H (L_1)

1,8-Naphthalic anhydride (1.570 g, 8.0 mmol) and 4-amino-4*H*-1,2,4-triazole (0.706 g, 8.0 mmol) were added to DMF (16 mL) to give a suspension. The off-white reaction mixture was stirred at 160 °C under nitrogen for 8 h. The resulting reaction mixture was then cooled and distilled water (20 mL) was added giving a voluminous white precipitate. The resulting solid was isolated by filtration and washed by distilled water (2 × 50 mL). The solid was recrystallized from hot methanol and dried to give an offwhite solid, 0.9 g (43%). Mass Spec. (HR, ESI+) *m/z*: 265.0715 ([**L_1** + H]$^+$, C14H9N4O2 requires 265.0720), 287.0532 ([**L_1** + Na]$^+$, C14H8N4O2Na requires 287.0539). ^{1}H NMR (DMSO-d6, 400 MHz) *δ* ppm: 7.98 (dd, 2H), 8.62 (d, 4H), 8.82 (s, 2H). ^{13}C NMR (DMSO-d6, 101 MHz) *δ* ppm: 122.0, 127.9, 128.0, 132.0, 132.3, 136.3, 143.7, 161.7.

X-ray quality colourless plate-like single crystals (0.17 × 0.06 × 0.16 mm) of **L_1** were grown by slow evaporation of DMF. Crystal Data for **L_1**: $C_{14}H_8N_4O_2$ (*M* = 264.25 g/mol): monoclinic, space group *P*21/*c* (No.14), *a* = 11.406(2) Å, *b* = 15.520(3) Å, *c* = 6.8292(14) Å, β = 103.97(3)°, V = 1173.2(4) Å^3, Z = 4, T = 100(2) K, *μ*(Mo-Kα) = 0.105 mm^{-1}, *Dcalc* = 1.4960 g cm^{-3}, 8158 reflections measured (5.24° ≤ 2Θ ≤ 50°), 2056 unique (*R*int = 0.1530, *R*σ = 0.2543) which were used in all calculations. The final *R*1 was 0.0584 ($I > 2\sigma(I)$) and *wR*2 was 0.1331 (all data).

4.7.2 Synthesis of 4-(1,2,4trz)-Nap-NO_2 (L_2)

4-nitro-1,8-naphthalic anhydride (0.972 g, 4 mmol), 4-Amino-4H-1,2,4-triazole (0.680 g, 8 mmol), and imidazole (6.02 g, 66 mmol) were added to chloroform (48 mL) and the suspension was stirred at reflux for eight hours. After cooling to room temperature, the solvent was removed *in* vacuum and distilled water (5 mL) was added to give an orange solid. The mixture was sonicated for 10 minutes in an ice cold sonicator and then filtered and washed with ice-cold ethanol (2x 10 mL) resulting in an orange solid (0.780 g, 63%). HRMS (ESI+): Calculated for [**L_2** + H]$^+$ m/z = 310.05, found m/z = 310.0563.^{1}H NMR (400 MHz, DMSO-d6) δ 8.86 (dd, J = 8.77, 1.11 Hz, 1H,), 8.80 (s, 2H,), 8.76 (m, 2H,), 8.64 (d, J = 7.99 Hz, 1H), 8.19 (dd, J = 8.72, 7.35 Hz). ^{13}C NMR (101 MHz, DMSO-d_6) δ 160.82, 160.13, 150.12, 143.08, 132.85, 130.85, 130.37, 130.20, 128.33, 125.98, 124.40, 123.06, 122.25.

X-ray quality, colourless, block-like single crystals (0.16 × 0.10 × 0.20 mm) of **L_2** were grown by slow evaporation of DMF. Crystal Data for **L_2**: $C_{14}H_7N_5O_4$ (*M* =309.25 g/mol): monoclinic, space group $P2_1/c$ (No. 14), *a* = 8.1554(5) Å, *b* = 20.5191(17) Å, *c* = 7.4425(5) Å, β = 95.693(7)°, *V* = 1239.30(15) Å^3, Z = 4, T = 100(2) K, μ(Mo Kα) = 0.127 mm^{-1}, D*calc* = 1.657 g/cm^3, 3967 reflections measured (3.97° ≤ 2Θ ≤ 49.99°), 2012 unique (R_{int} = 0.0412, R_σ = 0.0429) which were used in all calculations. The final R_1 was 0.0852 (I > 2σ(I)) and wR_2 was 0.2571 (all data).

4.7.3 Synthesis of 4-(1,2,4trz)-Nap-NH$_2$ (L_3)

4-(1,2,4tz)-Nap-NO$_2$ (70 mg, 0.4 mmol) was suspended in methanol (12 ml) with a 10% palladium on carbon catalyst (20 mg) and stirred under a hydrogen atmosphere for 12 h. Acetone (500 ml) was added to the suspension which was then was filtered through celite. Removal of solvent in vacuum gave a red solid. HRMS (ESI+): Calculated for [**L_3** + H]$^+$ m/z = 279.08, found m/z = 280.0829.^{1}H NMR (400 MHz, DMSO-d6) δ 8.80 (s, 2H), 8.72 (dd, 1 H, J=8.44, 0.98 Hz), 8.51 (dd, 1H, J=7.34, 0.98 Hz), 8.24 (d, 1H, J=8.56 Hz), 7.77 (s, 2 H), 7.73 (dd, 1H, J=8.31, 7.46 Hz), 6.91 (d, 1H, J=8.44 Hz). ^{13}C NMR (101 MHz, DMSO-d$_6$) δ 162.12, 160.81, 154.53, 143.99, 135.56, 132.68, 131.19, 130.55, 124.75, 121.51, 120.02, 109.13, 106.36.

X-ray quality, yellow, plate-like single crystals (0.03 × 0.02 × 0.03 mm) of **L_3** were grown by slow evaporation of DMF. Crystal Data for **L_3**: $C_{16}H_{11}N_3O_2$ (*M* =277.28 g/mol): orthorhombic, space group $Pna2_1$ (no. 33), *a* = 6.8114(3) Å, *b* = 14.6610(6) Å, *c* = 11.7894(5) Å, *V* = 1177.31(9) Å^3, *Z* = 4, *T* = 100(2) K, μ(MoKα) = 0.107 mm^{-1}, *Dcalc* = 1.564 g/cm^3, 4998 reflections measured (4.434° ≤ 2Θ ≤ 49.996°), 1906 unique (R_{int} = 0.0141, R_{sigma} = 0.0179) which were used in all calculations. The final R_1 was 0.0274 (I > 2σ(I)) and wR_2 was 0.0750 (all data).

4.7.4 Synthesis of 4-(1,2,4trz)-Nap-N(Me)$_2$ (L_4)

4-Dimethylamino-1,8-naphthalic anhydride (1.442 g, 6.0 mmol) and 4-amino-4*H*-1,2,4-triazole (1.040 g, 12.0 mmol) were added to DMF (16 mL) to give a suspension. The orange–brown reaction mixture was stirred at 160 °C under nitrogen for 8 h. The resulting reaction mixture was then cooled and distilled water (20 mL) was added. Removal of solvent *in* vacuum gave pure **L_2** as an orange solid, 0.490 g (30%). Mass Spec. (HR, ESI+) *m/z*: 308.1148 ([**L_4** + H]$^+$, $C_{16}H_{14}N_5O_2$ requires 308.1142). ^{1}H NMR (DMSO-d$_6$, 400 MHz) *δ* ppm: 3.19 (s, 6H), 7.27 (br d, 1H,), 7.82 (br dd, 1H), 8.41 (br d, 1H), 8.55 (br d, 1H), 8.65 (br d, 1H,), 8.80 (s, 2H,). ^{13}C NMR (DMSO-d6, 101 MHz) *δ* ppm: 44.9, 111.8, 113.2, 122.1, 124.4, 125.4, 130.6, 132.2, 133.7, 133.9, 158.1, 161.0, 161.9.

X-ray quality small orange plate-like single crystals (0.3 × 0.07 × 0.2 mm) of **L_4** were grown by slow evaporation of DMF. Crystal Data for **L_4**: Crystal data: C16H13N5O2 (*M* = 307.31 g/mol):

monoclinic, space group $P2_1/c$ (No. 14), a = 12.0954(4) A, b = 15.9987(4) A, c = 7.0636(2) A, β = 96.094(3)°, V = 1359.16(7) Å^3, Z = 4, T = 100 K, μ(Cu-Kα) = 0.859 mm^{-1}, D$calc$ = 1.502 g cm^{-3}, 4481 reflections measured (13.292° ≤ 2 Θ ≤ 133.984°), 4481 unique (Rint = 0.0397, $R\sigma$ = 0.0203) which were used in all calculations. The final $R1$ was 0.0380 ($I > 2\sigma(I)$) and $wR2$ was 0.1099 (all data).

4.7.5 Synthesis of 4-(1,2,4trz)-Nap-Troger's base (L_5)

4-Amino-1,8-nap-NH_2(70 mg, 0.25 mmole) and paraformaldehyde (15 mg, 0.5 mmol) were stirred in neat TFA (2 ml) for 12 hours at room temperature under a nitrogen atmosphere. Ethanol (500 ml) was added to the suspension which was then filtered through celite. Removal of solvent in vacuum gave a yellow solid. HRMS (ESI+): Calculated for [$\mathbf{L_2}$ + H]$^+$ m/z = 595.15, found m/z = 595.1580. ^{1}H NMR (400 MHz, DMSO-d_6) δ 8.88 (d, J = 8.4 Hz, 2H), 8.75 (d, J = 6.3 Hz, 4H), 8.60 (d, J = 7.2 Hz, 2H), 8.25 (d, J = 6.5 Hz, 2H), 8.07 (t, J = 7.9 Hz, 2H), 5.25 (d, J = 17.3 Hz, 2H), 4.81 – 4.72 (m, 4H). ^{13}C NMR (101 MHz, DMSO-d_6) δ 161.74, 161.06, 150.78, 143.70, 132.23, 131.79, 130.95, 128.06, 127.97, 127.45, 127.04, 122.41, 117.42, 66.47, 57.43.

X-ray quality yellow block-like single crystals (0.02 × 0.02 × 0.01 mm) of $\mathbf{L_5}$ were grown by slow evaporation of DMF. Crystal Data for $\mathbf{L_5}$ $C_{34}H_{25}N_{11}O_5$ (M =205.43 g/mol): monoclinic, space group $P2_1/c$ (no. 14), a = 11.4958(11) Å, b = 22.187(2) Å, c = 11.7544(7) Å, β = 91.924(7)°, V = 2996.4(4) Å^3, Z = 4, T = 100.15 K, μ(MoKα) = 0.105 mm^{-1}, D$calc$ = 1.480 g/cm^3, 23628 reflections measured (3.672° ≤ 2Θ ≤ 49.996°), 5270 unique (R_{int} = 0.0916, R_{sigma} = 0.0728) which were used in all calculations. The final R_1 was 0.1111 (I > 2σ(I)) and wR_2 was 0.3145 (all data).

4.7.6 4-Ethyl-(1,2,4trz)-Nap-H (L_6)

Thionyl chloride (7.15 ml, 0.1 mol) was added to DMF (3.75 ml) in an ice water bath and stirred for 6 h. Hydrazing hydrate (1.25 ml, 0.25 mol) in DMF (5 ml) was then added to the resulted solution. The mixture was stirred at room temperature for 24 h and the white precipitate of N,N-dimethylformamide azine dihydrochloride (DMAZ) was collected by filtration and washed with ice cold DMF (5 ml) and Et_2O (20 ml).

1, 8-naphthalic anhydride (2 g, 10.1 mmol) was added to a solution of ethylenediamine (4.5 ml, 68.68 mmol) in EtOH (100 mL) and the mixture was heated to reflux during 6 h. The mixture was filtered under vacuum and filtrate was evaporated under reduce pressure. The residue was recrystallized from EtOH to give a white solid (516 mg, 21.5%). MS (ESI+):241.2845 Calculated for (2-aminoethyl-naphthalic anhydride + H]$^+$ m/z = 241.09, found m/z = 241.3. ^{1}H NMR (400 MHz, DMSO-d_6) δ 8.48 (dd, J = 16.4, 7.6 Hz, 4H), 7.88 (t, J = 7.2 Hz, 2H), 4.12 – 4.05 (m, 2H), 2.85 – 2.78 (m, 2H).

N,N-Dimethylformamide azine dihydrochloride (350 mg, 2.5 mmol) and 2-aminoethyl-naphthalic anhydride (300 mg, 1.25 mmol) were refluxed in pyridine (3 ml) overnight. After cooling to room temperature, the solvent was removed in vacuum and distilled water (5 mL) was added to the pale orange solid. This was filtered to give a pale orange solid (300 mg, 82.2 %) MS (ESI+):293.3342 Calculated for [$\mathbf{L_6}$ + H]$^+$ *m/z* = 293.10, found m/z = 293.3. ^{1}H NMR (400 MHz, DMSO-d_6) δ 8.52 (s, 2H), 8.50 – 8.44 (m, 4H), 7.88 (dd, *J* = 8.2, 7.3 Hz, 2H), 4.42 (d, *J* = 1.5 Hz, 4H). ^{13}C NMR (101 MHz, DMSO) δ 163.88, 143.89, 134.96, 131.81, 131.33, 127.99, 127.69, 122.33, 43.10.

X-ray quality pale-yellow block-like single crystals (0.16 × 0.12 × 0.16 mm) of $\mathbf{L_6}$ were grown by slow evaporation of DMF. Crystal Data for $\mathbf{L_6}$: $C_{16}H_{12}N_4O_2$ (*M* =292.30 g/mol): tetragonal, space group $I4_1/a$ (no. 88), *a* = 14.1843(12) Å, *c* = 25.385(4) Å, *V* = 5107.3(11) Å^3, *Z* = 16, *T* = 100 K, μ(MoKα) = 0.105 mm^{-1}, *Dcalc* = 1.521 g/cm^3, 11859 reflections measured (6.42° ≤ 2Θ ≤ 49.976°), 2249 unique (R_{int} = 0.0746, R_{sigma} = 0.0437) which were used in all calculations. The final R_1 was 0.0896 (I > 2σ(I)) and wR_2 was 0.2299 (all data).

4.7.7 Synthesis of [$[Co_2(L_1)_3(DMF)_4(H_2O)_2](BF_4)_4 \cdot 4DMF \cdot H_2O$] ($C_1$)

$\mathbf{L_1}$ (0.0264 g, 0.1 mmol) and $Co(BF_4)_2$ (0.0341 g, 0.1 mmol) were dissolved in DMF (4 ml) in sealed vials and then heated to 135 °C for 24 hours. The resulting orange solutions were slowly cooled to room temperature and left to evaporate. After a few weeks, a small number of orange block-like crystals were obtained amongst an oily residue. Crystal Data for $\mathbf{C_1}$: $C_{66}H_{86}B_4Co_2F_{16}N_{20}O_{17}$ (*M* =1896.64 g/mol): triclinic, space group $P\bar{1}$ (No. 2), *a* = 15.2085(3) Å, *b* = 16.8311(3) Å, *c* = 17.9708(3) Å, α = 104.312(2)°, β = 101.708(2)°, γ = 103.837(2)°, *V* = 4156.71(14) Å^3, Z = 2, T = 100(2) K, *μ*(MoKα) = 0.511 mm^{-1}, D*calc* = 1.515 g/cm^3, 45578 reflections measured (3.244° ≤ 2Θ ≤ 50°), 14629 unique (R_{int} = 0.0385, $R_σ$ = 0.0404) which were used in all calculations. The final R_1 was 0.0677 (I > 2σ(I)) and wR_2 was 0.2045 (all data).

4.7.8 Synthesis of $[Co_2(L_1)_2(DMF)_3(H_2O)_2(\mu_2\text{-}HCO_2)Co_2(L_1)_2(DMF)_3(H2O)_2](NO_3)_7.4DMF$ (C_2)

$\mathbf{L_1}$ (0.0264 g, 0.1 mmol) and $Co(NO_3)_2$ (0.0291 g, 0.1 mmol) were dissolved in DMF (4 ml) in sealed vials and then heated to 135 °C for 24 hours. The resulting orange solution was left to evaporate for a few weeks resulting in a small number of orange block shaped crystals amongst a brown oil. Crystal Data for $\mathbf{C_2}$: $C_{58}H_{63}Co_2N_{21}O_{26}$ (*M* =1588.15 g/mol): triclinic, space group $P\bar{1}$ (No. 2), *a* = 15.0827(5) Å, *b* = 16.3826(6) Å, *c* = 16.4163(6) Å, α = 83.814(3)°, β = 63.343(4)°, γ = 82.939(3)°, V = 3591.4(2) Å^3, Z = 2, T = 100(2) K, *μ*(MoKα) = 0.556 mm^{-1}, D*calc* = 1.469 g/cm^3, 53264 reflections

measured (3.032° ≤ 2Θ ≤ 49.998°), 12641 unique (R_{int} = 0.0437, R_σ = 0.0422) which were used in all calculations. The final R_1 was 0.1073 (I > 2σ(I)) and wR_2 was 0.3527 (all data).

4.7.9 Synthesis of $[Fe(L_1)_6](ClO_4)_3$ (C_3)

L_1 (0.0264 g, 0.1 mmol) and $Fe(II)(ClO_4)_2$ (0.0254 g, 0.1 mmol) were stirred in MeOH (10 ml) at 60 ^oC for 3 hours. The solution was concentrated to give a light yellow solution that was subjected to vapour diffusion of diethyl ether. After three days, this resulted in yellow block-like crystals. Crystal Data for **C_3**: $C_{84}H_{48}Cl_2FeN_{24}O_{20}$ (M =183.61 g/mol): trigonal, space group $P\bar{3}$ (No. 147), a = 15.4078(4) Å, c = 9.1523(2) Å, V = 1881.66(11) $Å^3$, Z = 1, T = 100(2) K, μ(MoKα) = 0.300 mm^{-1}, $Dcalc$ = 1.296 g/cm^3, 10993 reflections measured (4.45° ≤ 2Θ ≤ 49.972°), 2225 unique (R_{int} = 0.0225, R_σ= 0.0151) which were used in all calculations. The final R_1 was 0.0331 (I > 2σ(I)) and wR_2 was 0.1059 (all data).

4.7.10 Synthesis of $[[Fe_2(L_1)_3(DMF)_4(MeCN)_2](ClO_4)_4]$ C_4

L_1 (0.0264 g, 0.1 mmol) and $Fe(II)(ClO_4)_2$ (0.0254 g, 0.1 mmol) were stirred in a solvent mixture of MeCN (20 ml) and DMF (0.5 ml) at 60 ^oC for 3 hours. The resulting yellow solution was subjected to vapour diffusion of diethyl ether resulting in the formation of yellow block-like crystals. Crystal Data for **C_4**: $C_{30}H_{30}Cl_2FeN_9O_{12}$ (M =1670.76 g/mol): triclinic, space group $P\bar{1}$ (No. 2), a = 15.2335(4) Å, b = 15.2713(4) Å, c = 18.7277(4) Å, α = 98.829(2)°, β = 100.334(2)°, γ = 105.517(2)°, V = 4035.47(18) $Å^3$, Z = 1, T = 100(2) K, μ(MoKα) = 0.573 mm^{-1}, $Dcalc$ = 1.375 g/cm^3, 72359 reflections measured (3.204° ≤ 2Θ ≤ 61.386°), 22697 unique (R_{int} = 0.0345, R_σ = 0.0396) which were used in all calculations. The final R_1 was 0.0987 (I > 2σ(I)) and wR_2 was 0.3461 (all data)

Chapter 5 Electron Density Studies of 1,2,4-Trz-Naphthalimide ligands

5.1 1,2,4-Trz-naphthalimide Ligand Family Selection

A series of 1,2,4- electron donating/withdrawing substituted naphthalimide-based ligands have been made and analysed using standard resolution crystallography, as described in Chapter 4. The packing interactions of **L_1**, **L_3**, **L_4**, are all dominated by $\pi\cdots\pi$ stacking between neighbouring molecules, where the naphthalimides are arranged in a head-to-head configuration through offset $\pi\cdots\pi$ stacking of the naphthalene ring. Unlike the π-based packing interactions in **L_1**, **L_3**, **L_4**, the structure of **L_2** does not show offset head-to-head $\pi\cdots\pi$ stacking, instead a head-to-tail stacking is observed. Additionally, the electron withdrawing nature of the nitro group results in a strong $NO_2\cdots\pi$ stacking in **L_2**. The packing is displayed in Figure 5-1, viewed along different axes.

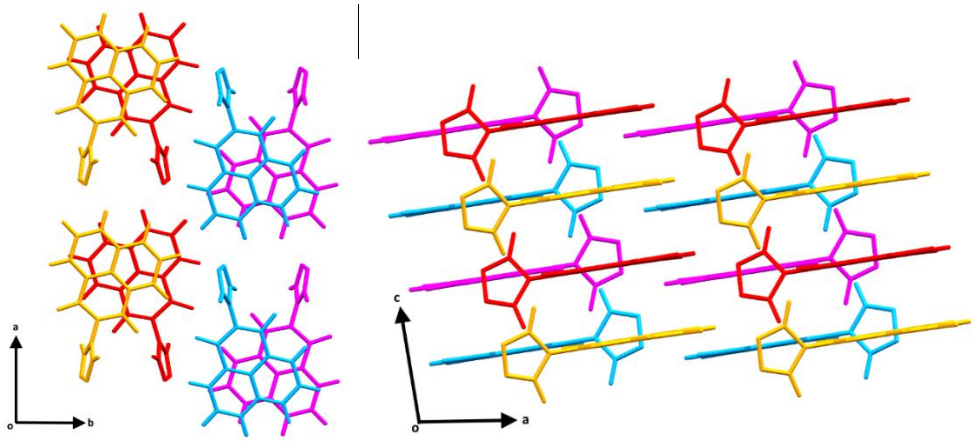

L_1(a) **L_1**(b)

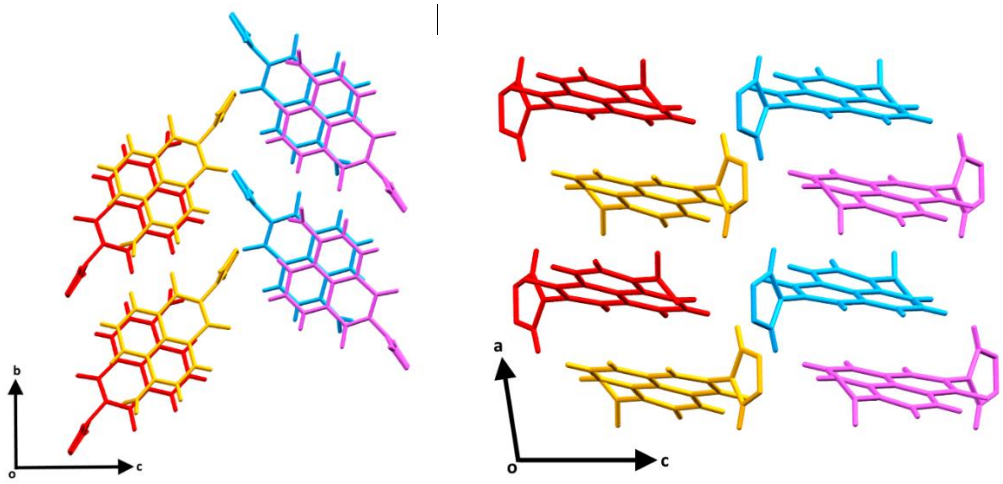

L_2(a) **L_2**(b)

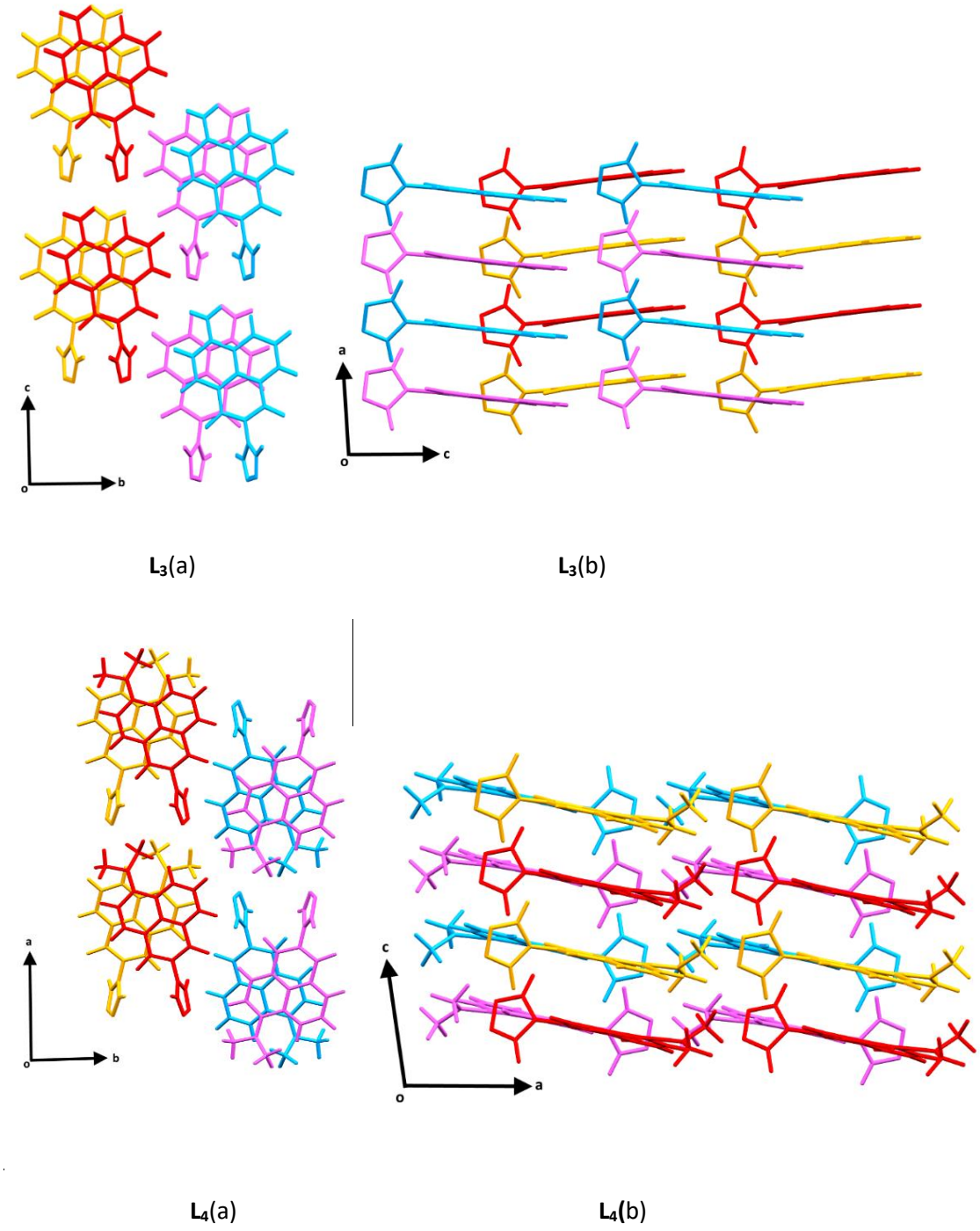

L₃(a) **L₃**(b)

L₄(a) **L₄**(b)

Figure 5-1 A comparison of the packing in L_1-L_4.

The structural analysis of the intermolecular interactions from low resolution data has been identified and described in Chapter 4. As introduced in 4.2, many interesting packing arrangements can be formed via π-based interactions and weak hydrogen bonds, presenting different conformations in the solid structure. In order to ascertain properties, such as the strength and nature of non-covalent interactions, experimental high-resolution X-ray diffraction data has been collected. This is complemented by theoretical energy calculations conducted with the approaches from both Crystal Explorer (C.E.) and PIXEL software packages. These methods

allow quantitative analysis of systems at the electronic level, and therefore intermolecular electron distribution can be investigated and non-covalent interactions between molecules can be assessed. The aim of the work presented in this chapter is to apply systematic charge density analysis to investigate the effect of altering naphthalimide ring substituents on the π-based interaction and associated weak hydrogen bonding in the crystal structure.

5.2 Theoretical Approaches to Analysis of Crystal Structure Assemblies

Theoretical methods have now become a recommended, reliable, and accessible approach to fully understand a molecular crystal system. As many interactions do manifest as particular atom···atom features they cannot be easily identified or quantified in experimental charge density analysis. Two available and appropriate methods used for this study are that of Spackman,[152] implemented in Crystal Explorer (C.E.)[153] and Gavezzotti,[154-155] in the PIXEL[156] package.

Interaction energies can be partitioned into different constituents, these contributions can further indicate characteristics of the non-covalent bonds, shown as Equation 5-1.

$$E_{tot} = E_{coul} + E_{pol} + E_{disp} + E_{rep}$$

Equation 5-1 Energy partitioning into four component terms, Coulombic energy, E_{coul}, polarisation energy, E_{pol}, dispersion energy, E_{disp}, and exchange-repulsion energy, E_{rep}.

5.2.1 The PIXEL Method

PIXEL[154, 156] is a semi-empirical method of molecule-molecule energy calculation, which uses electron density obtained from individual molecular orbital calculations. The electron densities are reduced to units called pixels and arranged as a three-dimensional array, where the distance between a pixel assigned to an atom and the related nuclei is less than the atomic radius. In this way, symmetry is applied to the positions of all pixels and nuclei, which produces a cluster molecule and accounts for a duplication of the original density. Intermolecular molecular energies can be calculated as a sum of pair-wise pixel-pixel interaction which are also partitioned to determine the different components as shown in Equation 5-1.

The Coulombic (electrostatic) term is the interaction between two molecules which is calculated from the sum of all pixel-pixel, pixel-nuclei, and nuclei-nuclei. It is described by Equation 5-2, where Q represents a charge and r is the distance between two charge entities. [154]

$$E_{coul} = \frac{Q_1 Q_2}{4\pi\varepsilon^0 r}$$

Equation 5-2 Calculation of Coulombic energy

The polarisation energy E_{pol} at a given pixel i, is calculated as Equation 5-3. ε_i is the total electric field exerted by surrounding molecules at pixel i; α_i is the polarisation at pixel i; μ_i is the dipole induced at pixel I; d_i, is a dampening to reduce physically unrealistic contributions.[155]

$$E_{pol,i} = -\frac{1}{2}\mu_i[\varepsilon_i d_i] = -\frac{1}{2}\alpha_i[\varepsilon_i d_i]^2$$

Equation 5-3 polarisation energy equation.

The polarisation of a molecule is the sum of that at all the pixels assigned to it, this is distinct from summing the polarisation terms from each molecule-molecule relationship.

The dispersion energy is based on the London formula,[157] which is calculated by summation of pixel-pixel terms as in Equation 5-4.

$$E_{disp} = -\frac{3}{4}\frac{(E_{ION} f(R)\alpha_i\alpha_j)}{[(4\pi\varepsilon^0)^2 R_{ij})^6]}$$

Equation 5-4 Dispersion energy calculation according to the London formulation between two molecules of polarizability α and ionization energy E_{ION}. ε denotes electric field, and a dampening fumction f(R) is included to avoid peculiarities due to short pixel-pixel distances, R_{ij}.

For a PIXEL calculation, the total dispersion energy is determined from half of the summation of all the two-body molecule-molecule interactions, as per Equation 5-5.[154, 156]

$$E_{disp,AB} = \frac{1}{2}\sum\sum E_{disp,AB}$$

Equation 5-5 Dispersion energy calculation in a crystal according to PIXEL

The repulsion energy calculation is determined from the overlap, S_{AB}, of electron densities of two molecules, A and B, from Equation 5-6.

$$E_{rep,AB} = (K_1 - K_2\Delta\chi_{AB})S_{AB}$$

Equation 5-6 The repulsion energy PIXEL calculation between two molecules A and B. $\Delta\chi_{AB}$ denotes the difference in Pauling electronegativity, K_1 and K_2 are disposable parameters.

$$S_{AB} = \sum_{i,A}\sum_{j,B}[\rho_i(A)\rho_j(B)]V$$

Equation 5-7 The calculation of electron density overlap S between molecule A and B comprised overlapping pixel electron densities, ρ over pixel volume, V.

Similar to the dispersion calculation for the crystal, E_{rep} is the sum of all two-body molecule-molecule interactions as in Equation 5-8.

$$E_{rep} = \frac{1}{2}\sum\sum E_{rep,AB}$$

Equation 5-8 Calculation for the total repulsion energy in a crystal.

5.2.2 The Crystal Explorer Method

A similar method to Gavezzotti's PIXEL calculation is used by Spackman *et al*. and implemented in Crystal Explorer (C.E.). The total interaction energy calculation in C.E. is constructed from the individual components. Each individual component has a scale factor, Equation 5-9.[76]

$$E_{tot} = k_{coul}E'_{coul} + k_{pol}E'_{pol} + k_{disp}E'_{disp} + k_{rep}E'_{rep}$$

Equation 5-9 The calculation of total interaction energy in Crystal Explorer.

The Coulombic (electrostatic) E_{coul} term is the attraction between two unperturbed charge distributions from the antisymmetric combination of the monomer orbitals.[158]

The polarisation energy, E_{pol}, is estimated from the sum of nuclei with $-(1/2)\alpha_{mean}|F|^2$, where α_{mean} are isotropic atomic polarizabilities and F is the electric field computed for each nucleus from charge distribution of other monomer. [159]

The dispersion energy E_{disp} is the sum of all the intermolecular pairs according to the Grimme's D2[160] dispersion correction.

Similar to E_{coul}, the repulsion energy E_{rep} is also calculated from two unperturbed charge distributions by the antisymmetric combination of the monomer orbitals.[158]

5.2.3 Hirshfeld Surface Analysis

The analysis of calculated Hirshfeld surfaces is one of the best ways to explore and visualise these intermolecular interactions. The Hirshfeld surface was developed from F.L. Hirshfeld's stockholder partitioning scheme[161] being applied as a definition of the space occupied by a molecule in a crystal. The Hirshfeld surface is defined according to the weight function in Equation 5 -10.[162]

$$w_A(\boldsymbol{r}) = \sum_{i \in molecule\ A} \rho_i^{at}(\boldsymbol{r}) \Big/ \sum_{\in crystal} \rho_i^{at}(\boldsymbol{r})$$

$$= \rho_{promolecule}(\boldsymbol{r}) / \rho_{procrystal}(\boldsymbol{r})$$

Equation 5-10 Weight function applied for defining a molecule in a crystal for Hirshfeld surface

In this equation, $\rho_{promolecule}(\boldsymbol{r})$ is the sum of electron density over the atoms in the molecule of interest (the promolecule), and $\rho_{procrystal}(\boldsymbol{r})$ is that over the crystal (the procrystal). The Hirshfeld surface is determined by both the molecule and its nearest neighbours, which not only envelops a molecule but also provides a way to probe intermolecular interactions and calculate their properties. Distances from the surface to the nearest nucleus inside and outside of the surface are denoted as d_i (internal distance) and d_e (external distance) respectively and these can be mapped to a 2D fingerprint plot.[163] These plots are useful to identify the differences in structures and to analyse and compare the different interactions. The parameter d_{norm} in a 2D fingerprint plot combines both d_i and d_e normalised by the van der Waals radii of the atoms. Hirshfeld surfaces and fingerprint plots for triazole-based-1,8 –naphthalimide ligands are presented in section 5.4.

5.3 Hirshfeld Analysis of Triazole-Based-1,8 –Naphthalimide Ligands

The nature of packing and interactions in each crystal structure are firstly analysed through the Hirshfeld surface, which can help to provide an overall insight into the intermolecular contacts. Figure 5-2a shows the Hirshfeld surfaces (left) of molecules **L_1-L_4**, where the contacts of hydrogen bonds and π-π interactions produce donor-acceptor features. Red regions indicate that the intermolecular distance between two atoms is shorter than the sum of their van der Waals radii. Fingerprint plots are generated (right) from the values of d_i and d_e at the Hirshfeld surface points. This enables different interaction types, such as hydrogen bonding, van der Waals contacts, C-H···π, N-O···π and π···π stacking to be identified. The fingerprint plots of the ligand crystal structures are depicted in Figure 5-2b. The shape of fingerprint plots for these ligands are relatively similar. The locations of different contact types are reported to aid the analysis. The colour gradient indicates the number of contacts, from dark blue to bright yellow-green as the areas of lowest to greatest density. The locations of π···π interactions and hydrogen bonding are highlighted in these fingerprint plots.

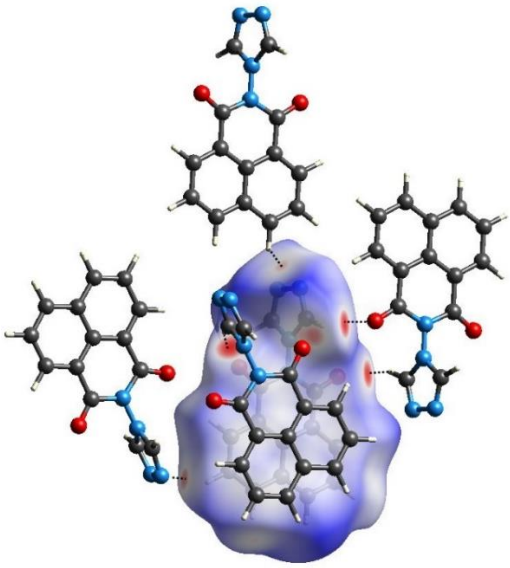

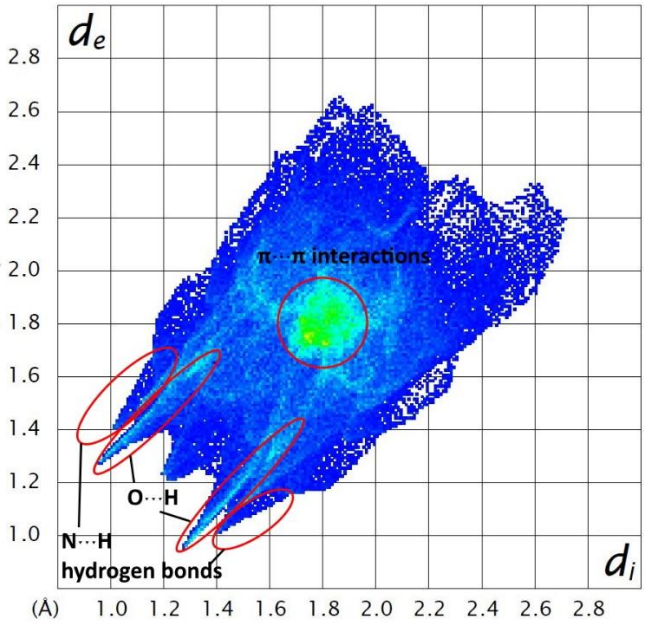

L_1-a

L_1-b

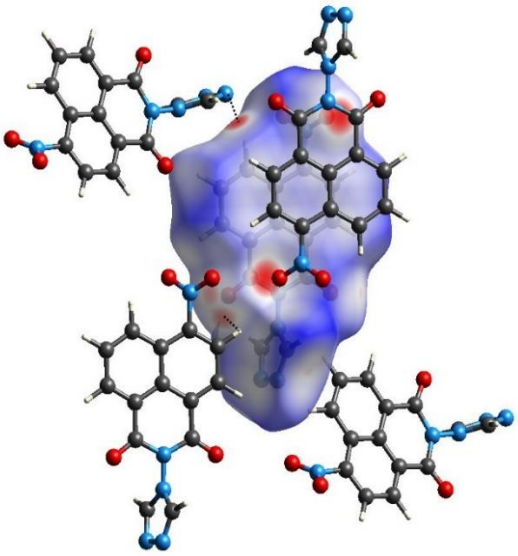

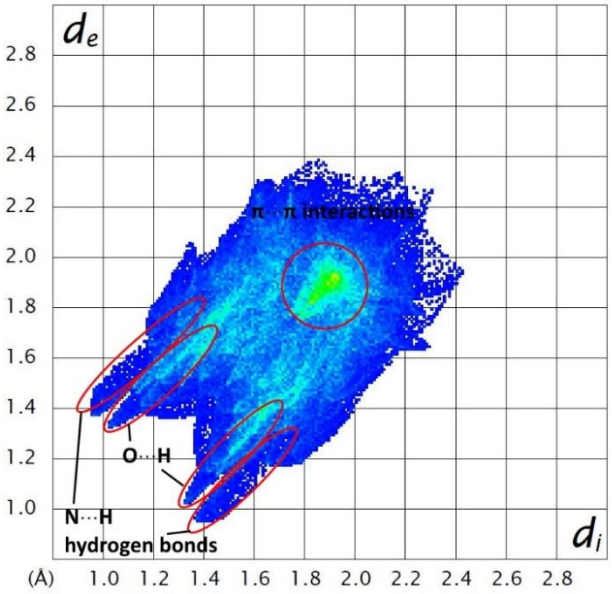

L_2-a

L_2-b

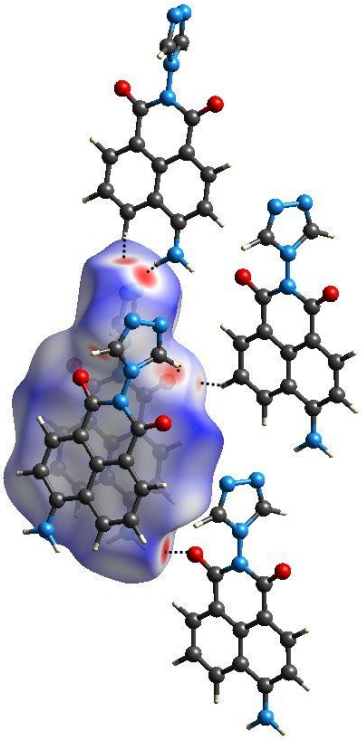

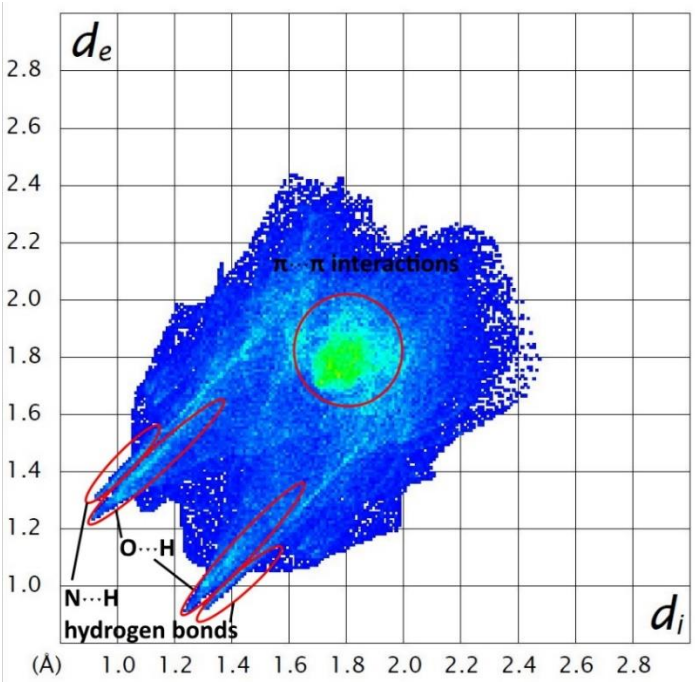

L_3-a **L_3-b**

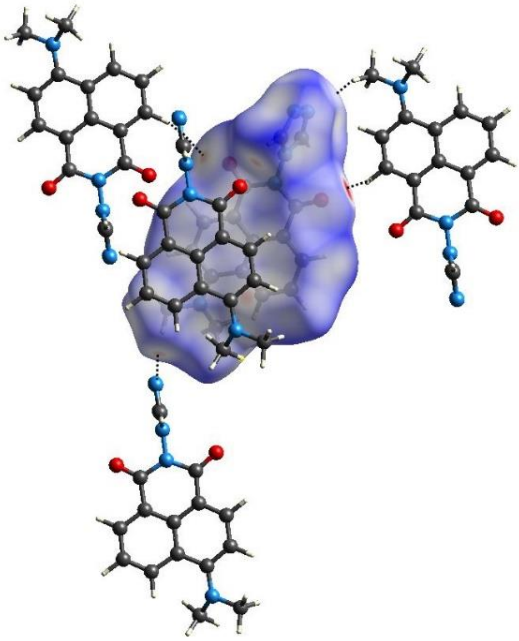

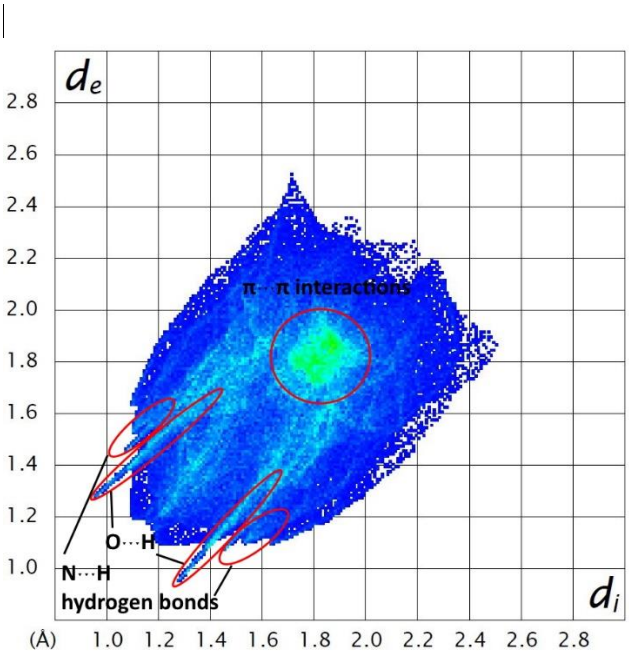

L_4-a **L_4-b**

Figure 5-2 (a) Hirshfeld surface of **L_1** to **L_4** molecules mapped with d_{norm}. The white colour describes the distance of two atoms equal to the sum of van der Waals radius of two atoms; red and blue are shorter and longer than the sum respectively. (b) Fingerprint plot for the single molecules **L_1** to **L_4**.

Figure 5-3 presents the distribution of individual intermolecular interactions based on the plots of the relative contributions of each contact from Hirshfeld surface analysis for **L_1-L_4**. Overall, H···H contacts dominate in the systems, while **L_2** exhibits a fairly dramatic loss of the H···H contacts relative to the other ligands as it has NO_2 functional substitution present, which partake in stronger and alternative O···H contacts (red region). Additional to these, the NO_2 group in **L_2** donates additional N-O···π interactions, resulting in a larger distribution of C···O contacts than the other three, as seen from the yellow region in Figure 5-3. Also due to the presence of different substituents, **L_1**, **L_3**, and **L_4** have more N···H contacts than **L_2**. The relative contribution of O···H and N···H contacts can be analysed by comparing the brick red and grey region in Figure 5-3.

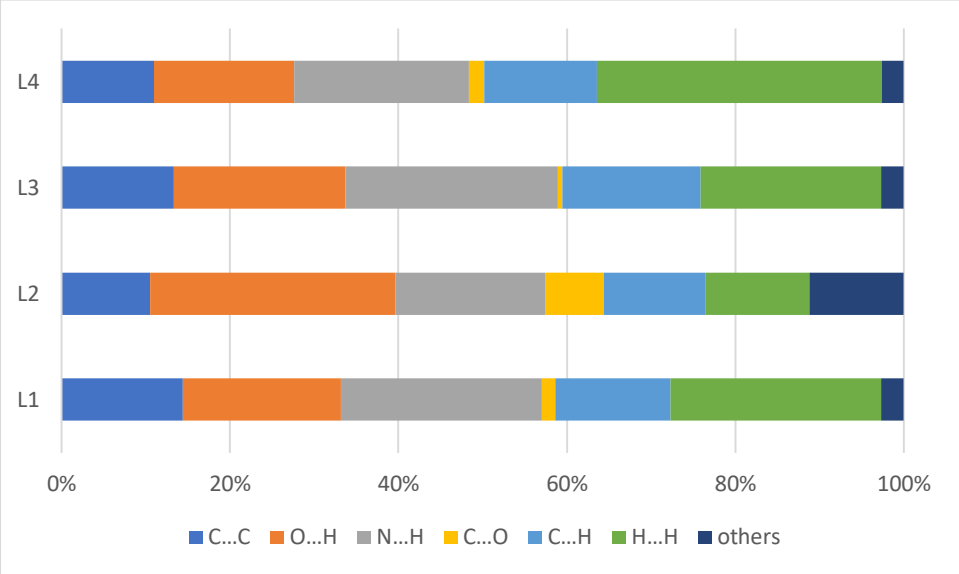

Figure 5-3 Distribution of individual interactions on the basis of Hirshfeld surface analysis of **L_1-L_4**.

5.4 Analysis of Intermolecular Interactions in Triazole-Based-1,8 – Naphthalimide Ligands

The theoretical approaches of Crystal Explorer and PIXEL produce molecular interaction energies. The calculation of intermolecular interaction energies by Crystal Explorer (Chapter 5.2.2) provides an overview of molecule···molecule interactions, applying Gaussian B3LYP/6-31G wavefunctions for calculation of interaction energies. Figure 5-4, as an example, displays the interaction energy calculation window in C.E., where molecular pairwise interactions associated to the central molecules are calculated and illustrated by the colour next to the energy's value. Gavezzotti's PIXEL approach (Chapter 5.2.1) is similar to C.E. calculation, however it provides further information about interaction types, particularly in two or more component systems. PIXEL calculates and separately displays the energies as A···A, A···B, and B···B, respectively. The interaction energies calculated from PIXEL can be compared to these from C.E. and together give

a comprehensive overview of interactions. These interactions can be broken down into their constituents, Coulombic, polarisation, dispersion and repulsion as Equation 5-1, allowing the chemical nature of an interaction to be inferred. Hydrogen bonds are generally the source of the Coulombic energy observed.[158] In aromatic rings the dispersion energy component is the main contributor to the attraction between stacked aromatic regions.[164-165] The following sections discuss and compare these ligands through the two methods.

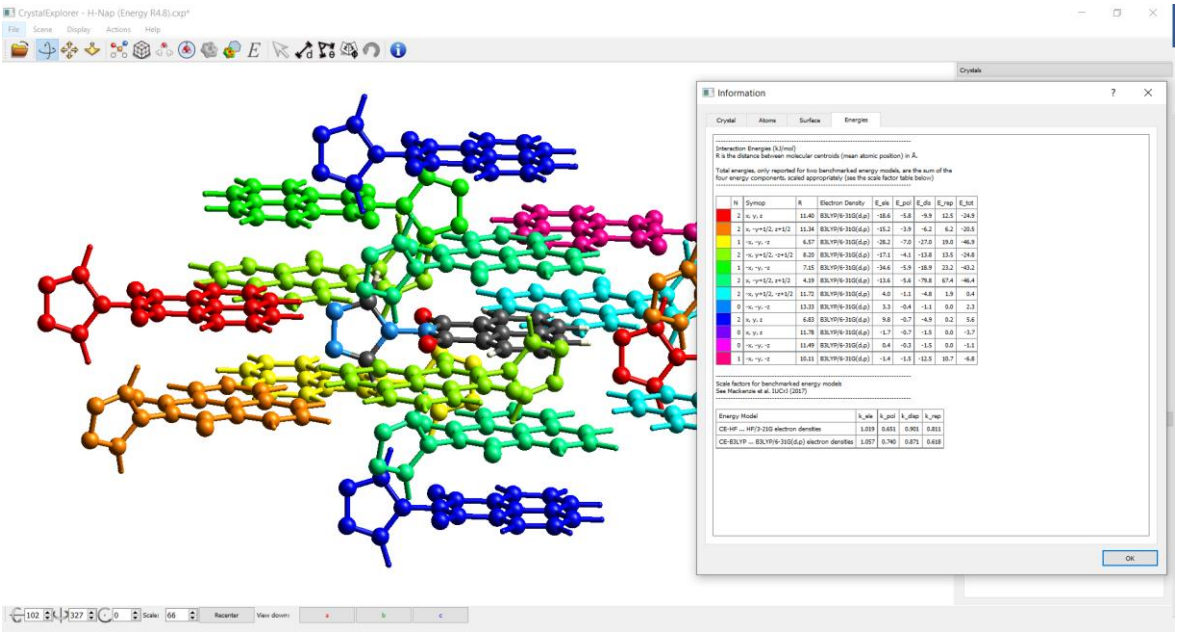

Figure 5-4 Main graphic display of Crystal Explorer 17.5 showing the pairwise molecular interaction energies identified and denoted by different colours.

5.4.1 Overview of 4-(1,2,4trz)-Nap-H (L_1) Interactions

L_1 has the simplest structure of the four ligands chosen for more detailed investigation. This molecule does not have any hydrogens replaced with other substituents and so exhibits no significant conventional interaction apart from the π-based effects and hydrogen bonding involving the triazole-based naphthalimide ring. Hence, this ligand is introduced first in this study and acts as a reference for the further substituted systems.

The interaction energies calculated by Crystal Explorer (C.E.) and PIXEL are plotted against the molecule···molecule centroid distances in Figure 5-5 (in which only interactions stronger than -5 kJ $mol^{-1}$are considered). The energy distributions observed for the C.E. and PIXEL methods are in good agreement.

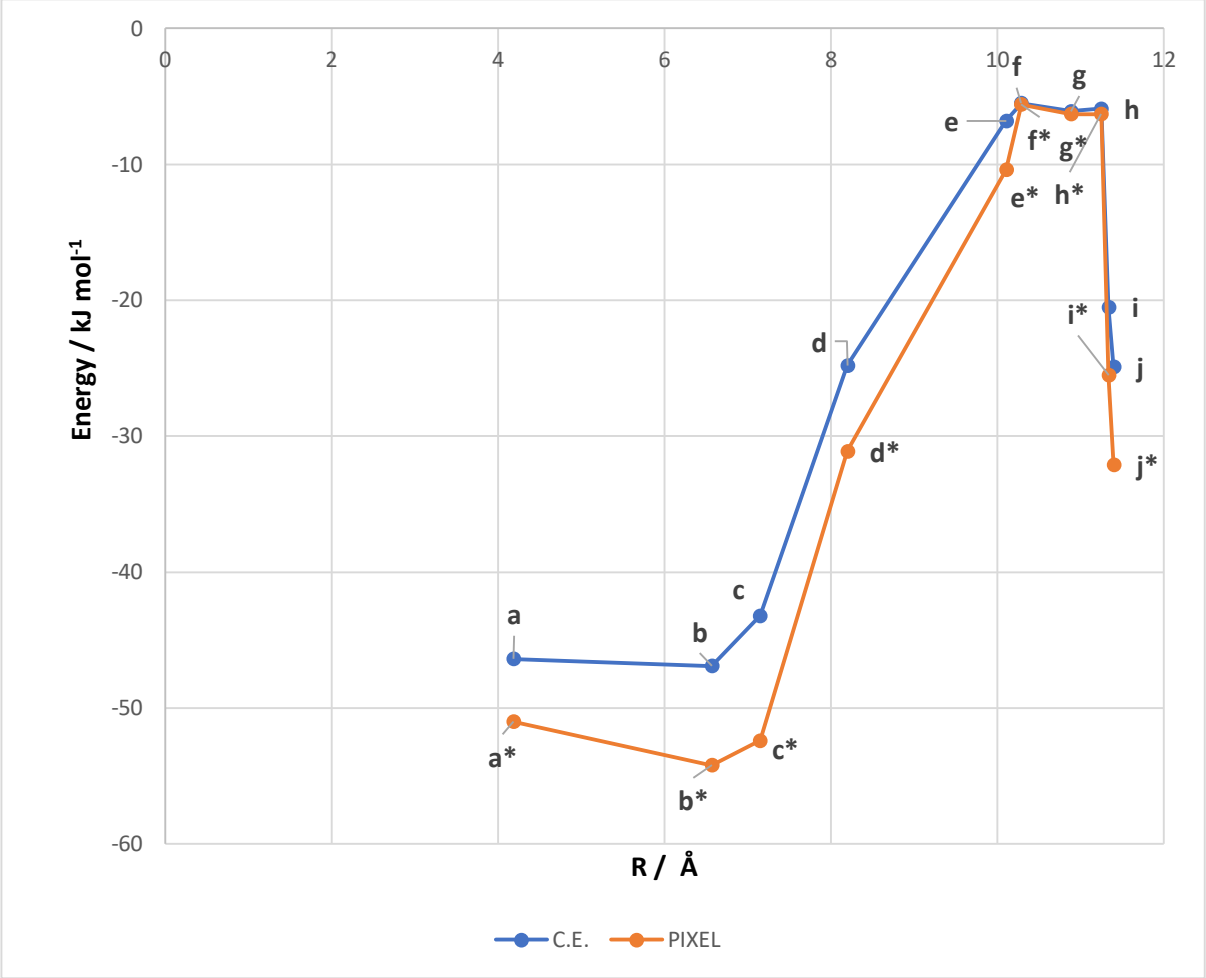

Figure 5-5 Interaction energies for L_1 determined from Crystal Explorer and PIXEL calculations, plotted against molecule···molecule centroid distances (R). Red represents PIXEL calculation, blue represents Crystal Explorer.

The strongest three interaction energies (a/a*, b/b*/ and c/c*) are in the range -40 to -60 kJ mol^{-1}. These interactions also exhibit short molecule···molecule centroid distances. Further details for these three strongest interactions are identified in Table 5-1 and Figure 5-6. a/a*, b/b* and c/c* have similar total interaction energies, while they are driven by dramatically different energy components contributions. For the closer aromatic stacking molecules, a/a*, the large dispersion energy (-79.8 kJ mol^{-1} calculated from C.E. and -73.7 kJ mol^{-1} calculated from PIXEL) observed indicates the large π···π interactions between the overlapped molecules. The b/b* and c/c* molecules have dispersion values about 70% and 80 % lower than a/a*. However, this isn't reflected in the total energy, as b/b* and c/c* have a stronger Coulombic energy component, most likely from the C-H···O hydrogen bonds between them.

Table 5-1 Energy components for a/a*, b/b*, and c/c* determined from Crystal Explorer and PIXEL calculations.

	No.	Symmetry	R /Å	Energies /kJ mol^{-1}									
				Crystal Explorer					**PIXEL**				
				E_{coul}	E_{pol}	E_{dis}	E_{rep}	E_{tot}	E_{coul}	E_{pol}	E_{dis}	E_{rep}	E_{tot}
	a/a*	x, -y+1/2, z+1/2 x, -y+1/2, z-1/2	4.19	-13.6	-5.6	-79.8	67.4	-46.4	-24	16.4	-73.7	63.2	-51
	b/b*	-x+1, -y+1, -z+1	6.57	-28.2	-7	-27	19	-46.9	-34.8	-9.7	-26.5	16.8	-54.2
	c/c*	-x+1, -y+1, -z+2	7.15	-34.6	-5.9	-18.9	23.2	-43.2	-42.8	11.2	-20.2	21.8	-52.4

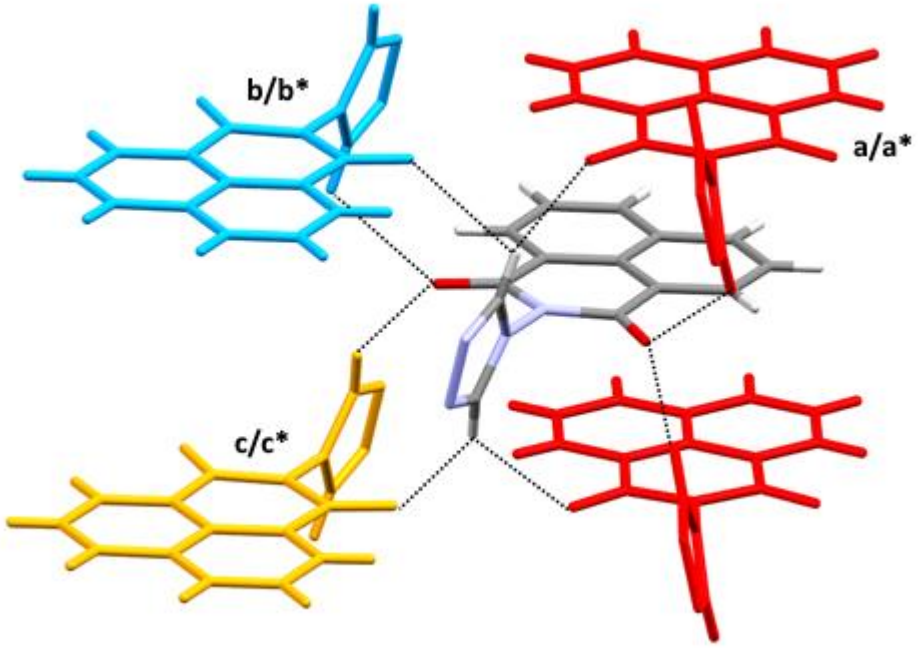

Figure 5-6 Location of the strongest interaction energies a/a*, b/b* and c/c*.

There are three further molecule-molecule relationships with moderate energies in the range -20 to 35 kJ mol^{-1}, and four with energies below -15 kJ mol^{-1}. Notably, h/h*, i/i* and j/j* have similar distances but large differences in interaction energies. The position of these three molecules and detailed energy information is shown in Table 5-2 and Figure 5-7. Although they have similar distances, the Coulombic forces in pairs i/i* (-15.2 kJ mol^{-1} calculated from C.E. and -18.5 kJ mol^{-1} calculated from PIXEL) and j/j* (-18.6 kJ mol^{-1} calculated from C.E. and -24.6 kJ mol^{-1} calculated from PIXEL) are significantly greater than the h/h* pair (-4.9 kJ mol^{-1} calculated from C.E. and -5.7 kJ mol^{-1} calculated from PIXEL), which is also reflected in the total energies. The large energy

difference can be explained as j/j* and h/h* have additional hydrogen bonding interactions that do not exist in i/i*.

Table 5-2 Energy components for h/h*,i/i* and j/j* determined from Crystal Explorer and PIXEL calculations.

	No.	Symmetry	R /Å	Energies /kJ mol^{-1}									
				Crystal Explorer					**PIXEL**				
				E_{coul}	E_{pol}	E_{dis}	E_{rep}	E_{tot}	E_{coul}	E_{pol}	E_{dis}	E_{rep}	E_{tot}
	h/h*	-x+1, -y, -z+2	11.25	-4.9	-0.2	-0.6	0	-5.9	-5.7	-0.2	-0.3	0	-6.3
	i/i*	x-1, -y+1/2, z-1/2	11.34	-15.2	-3.9	-6.2	6.2	-20.5	-18.5	-5.2	-7.4	5.6	-25.5
	j/j*	x-1, y, z	11.4	-18.6	-5.8	-9.9	12.5	-24.9	-24.6	-7.6	-12.8	13	-32.1

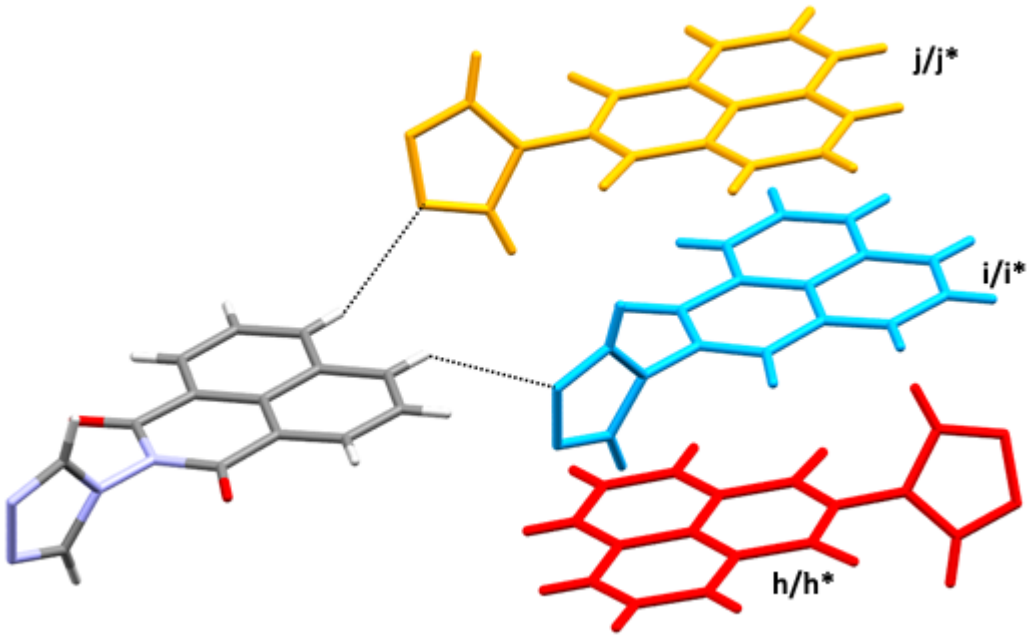

Figure 5-7 The location of weak molecule-molecule interaction energies h/h*,i/i* and j/j*.

5.4.2 Overview of 4-(1,2,4trz)-Nap-NO_2 (L_2) interactions

Compared to **L_1**, **L_2** has an electron withdrawing NO_2 substituent in the 4-position of the naphthalimide ring. The NO_2 group enables N-O···π interactions. This leads to head-to-tail stacking, which also gives additional N-O···H hydrogen bonds. The interaction energies of **L_2** have

been calculated by Crystal Explorer and PIXEL, and plotted against molecule···molecule centroid distances in Figure 5-8 (in which only interactions stronger than -5 kJ mol^{-1} are plotted).

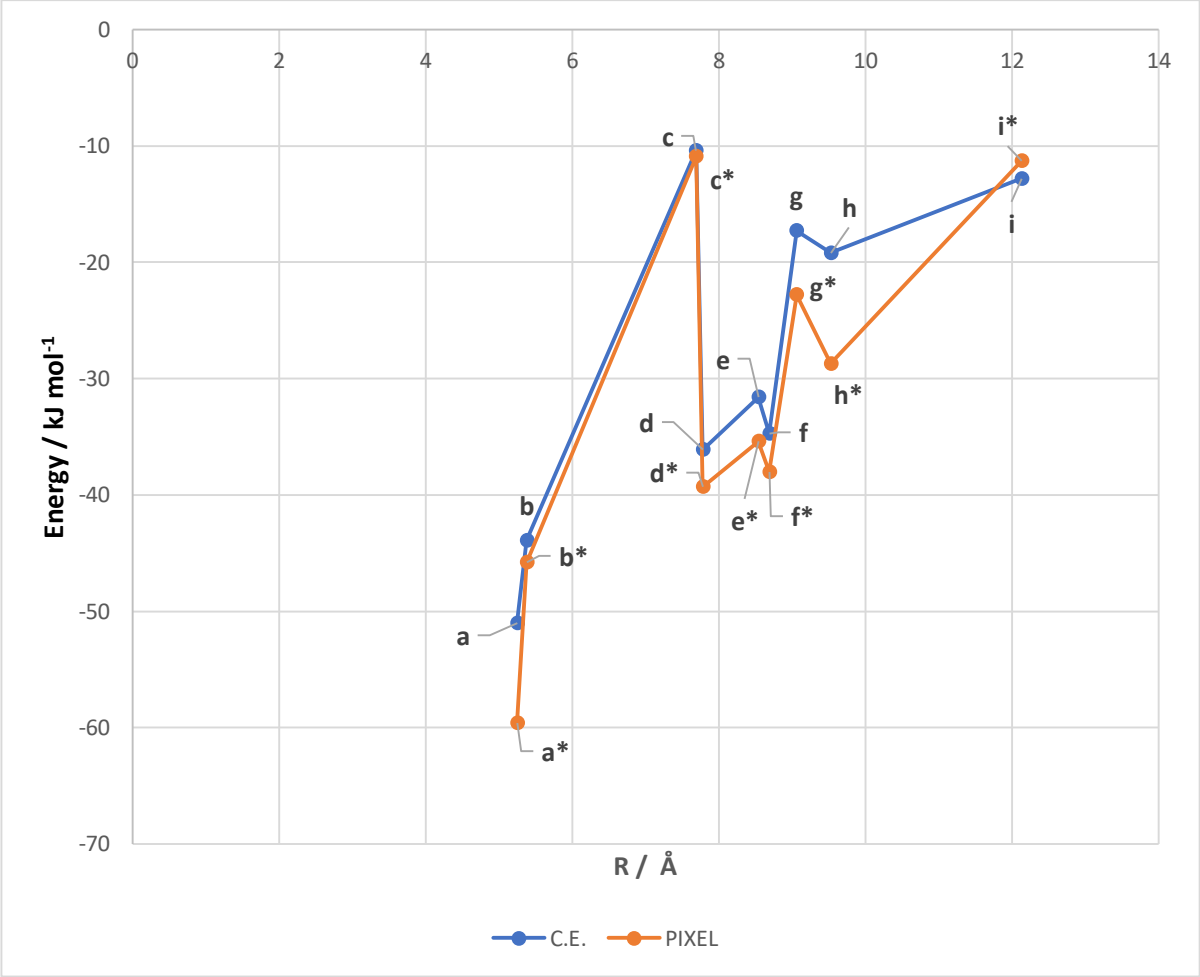

Figure 5-8 Interaction energies for L_2 determined from Crystal Explorer (blue) and PIXEL (red) calculations and plotted against molecule···molecule centroid distances (R).

The two strongest energy interactions, a/a* and b/b*, occur within the range -40 to -60 kJ mol^{-1} and exhibit the shortest molecule···molecule centroid distances, with details shown in Figure 5-9 and Table 5-3. Both a/a* and b/b* molecules are stacked through N-O···π and π···π interactions with large dispersion energies. In this structure the NO_2 functional group is twisted 39° from the mean plane of the naphthalimide ring, resulting in slightly different centroid distances between two stacked molecules. Interaction a/a*, with a smaller distance, is observed with a greater dispersion energy interaction as well as greater total energy than b/b*.

Table 5-3 Energy components for interactions a/a* and b/b* determined from Crystal Explorer and PIXEL calculations.

	No.	Symmetry	R /Å	Energies /kJ mol^{-1}									
				Crystal Explorer					**PIXEL**				
				E_{coul}	E_{pol}	E_{dis}	E_{rep}	E_{tot}	E_{coul}	E_{pol}	E_{dis}	E_{rep}	E_{tot}
	a/a*	-x+1, -y+1, -z+1	5.25	-14.2	-6.9	-75.5	56.6	-51.0	-29	-14	-71.7	55.6	-59.6
	b/b*	-x, -y+1, -z+1	5.38	-9.1	-5.1	-64.6	41.8	-43.9	-16.7	-8.2	-59.9	39.0	-45.8

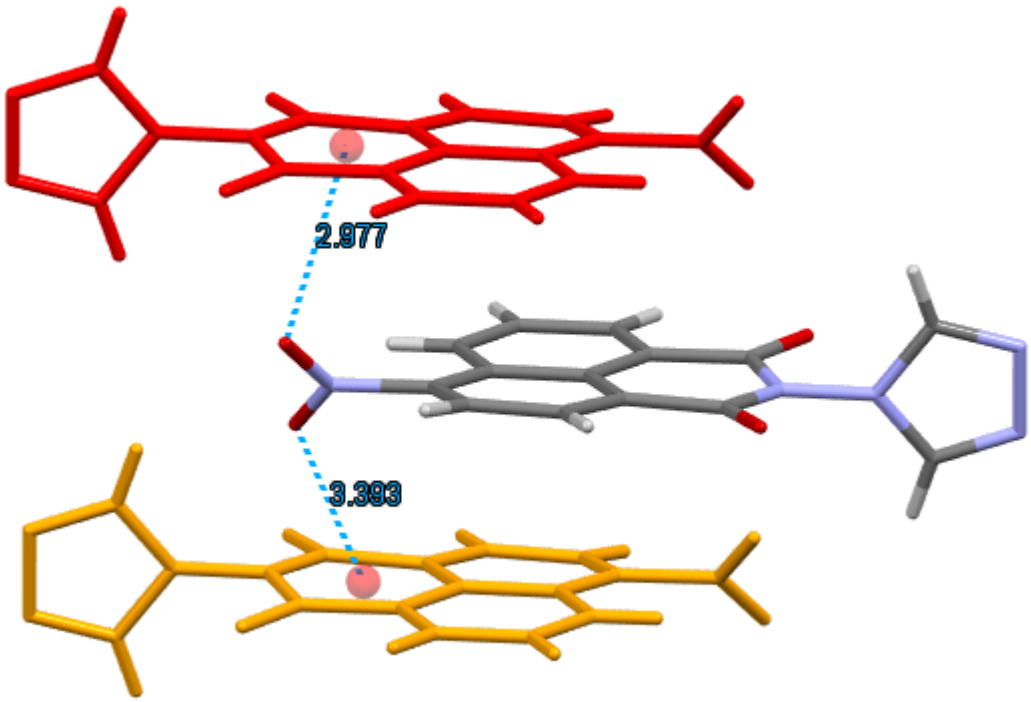

Figure 5-9 Positions of the strongest interaction energies a/a* and b/b*

The next five strongest interaction energies are in the range -15 to -40 kJ mol^{-1}. An additional two weaker interactions are observed at approximately -10 kJ mol^{-1}. Among them, d/d* has a slightly longer distance than c/c*. However, due to the non-classic C-H···O hydrogen present in d/d*, its Coulombic energy (-24.6 kJ mol^{-1} calculated from C.E. and -24.8 kJ mol^{-1} calculated from PIXEL) is almost four times greater than c/c* (-4.3 kJ mol^{-1} calculated from C.E. and -5.5 kJ mol^{-1} calculated from PIXEL). The molecular packing and energy information is shown in Table 5-4 and Figure 5-10.

Table 5-4 Energy components for energies c/c* and d/d* determined from Crystal Explorer and PIXEL calculations.

	No.	Symmetry	R /Å	Energies /kJ mol^{-1}									
				Crystal Explorer					**PIXEL**				
				E_{coul}	E_{pol}	E_{dis}	E_{rep}	E_{tot}	E_{coul}	E_{pol}	E_{dis}	E_{rep}	E_{tot}
	c/c*	-x+2, -y, -z+1	7.69	-4.3	-1.1	-5.8	0	-10.4	-5.5	-1.1	-4.4	0	-10.9
	d/d*	-x+1, -y, -z+1	7.78	-24.6	-6	-23.1	23.4	-36.1	-24.8	-6.6	-25.6	22	-39.3

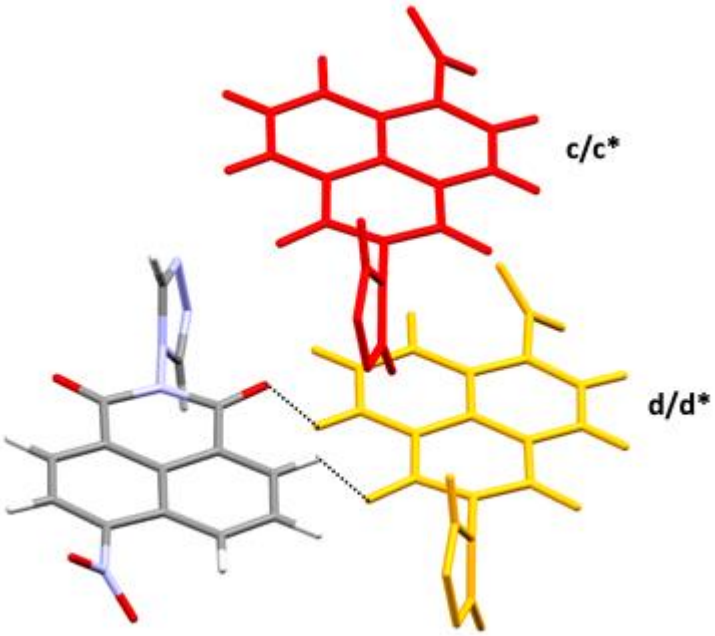

Figure 5-10 Molecule packing for c/c* and d/d* interactions.

5.4.3 Overview of 4-(1,2,4trz)-Nap-NH_2 (L_3) Interactions

L_3 has an electron donating NH_2 substituent in the 4-position of the naphthalimide ring. The NH_2 group was constrained to remain planar with respect to the aromatic ring's geometry and is therefore not involved in the π···π interaction (unlike the NO_2 group contribution in L_2, described in section 5.4.2 above), which leads to additional N-H hydrogen bond donor groups. The interaction energies of **L_3** have been calculated by Crystal Explorer and PIXEL and plotted against

the molecule···molecule centroid distances as shown in Figure 5-11 (in which only interactions stronger than -5 kJ mol^{-1} are included).

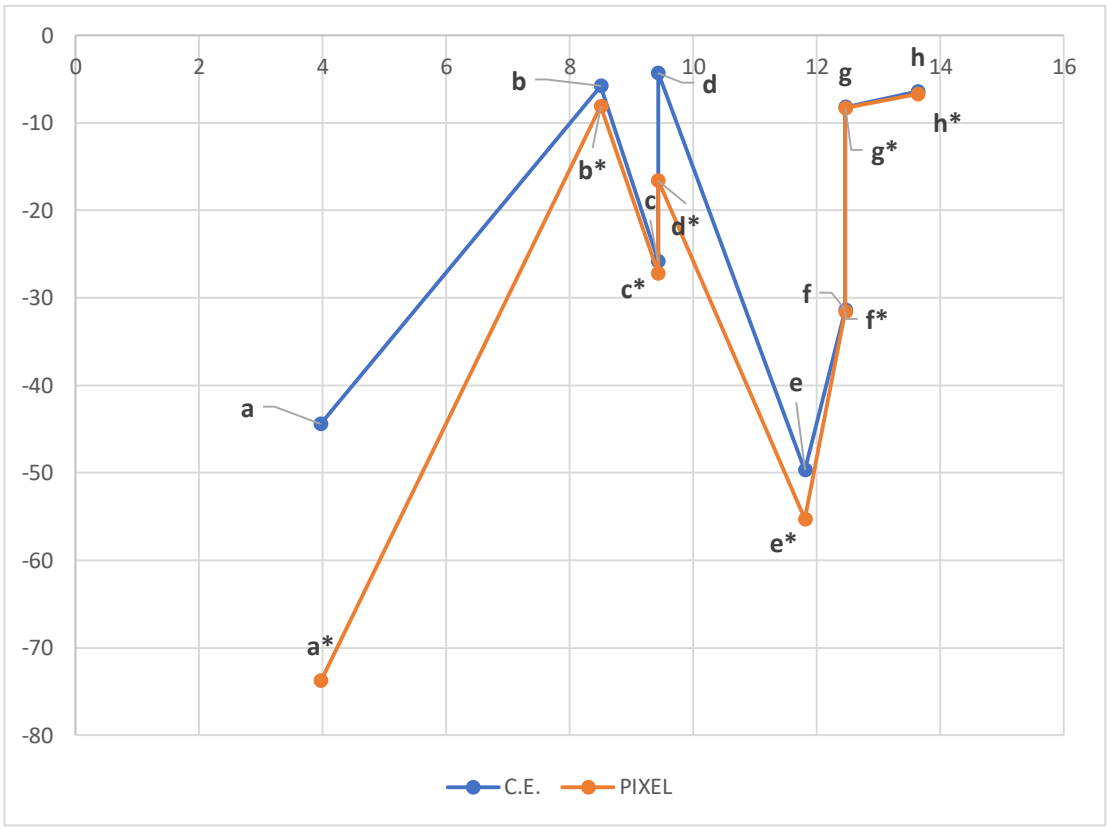

Figure 5-11 Interaction energies for L_3 determined from Crystal Explorer (blue) and PIXEL (red) calculations, plotted against molecule···molecule centroid distances (R).

From Figure 5-11, the two strongest interaction energies are observed between -40 and -80 kJ mol^{-1} and exhibit a large range in distance. The packing structure and energy components of these are presented in Table 5-5 and Figure 5-12. In these two molecule···molecule relationships, packing is driven by different interactions. Relationship a/a* has a strong dispersion energy contribution (-91.7 kJ mol^{-1} calculated from C.E. and -89.9 kJ mol^{-1} calculated from PIXEL) which indicates the overlapped stacking is dominated by π···π interactions; whilst b/b* interactions were mainly comprised of a large Coulombic energy (-46.3 kJ mol^{-1} calculated from C.E. and -50.7 kJ mol^{-1} calculated from PIXEL), which is provided by N-H···N hydrogen bonds between the NH_2 groups and adjacent triazole rings.

Table 5-5 Energy components for energies a/a* and b/b* determined from Crystal Explorer and PIXEL calculations.

	No.	Symmetry	R /Å	Energies /KJ mol^{-1}									
				Crystal Explorer					**PIXEL**				
				E_{coul}	E_{pol}	E_{dis}	E_{rep}	E_{tot}	E_{coul}	E_{pol}	E_{dis}	E_{rep}	E_{tot}
	a/a*	x-1/2, -y+3/2, z x+1/2, -y+3/2, z	3.97	-6.6	-7.5	-91.7	77.7	-44.4	-32.8	-26.6	-89.9	75.5	-73.8
	b/b*	x, y, z-1 x, y, z+1	11.81	-46.3	-12.3	-11.2	29.4	-49.7	-50.7	-17.7	-17.3	30.5	-55.3

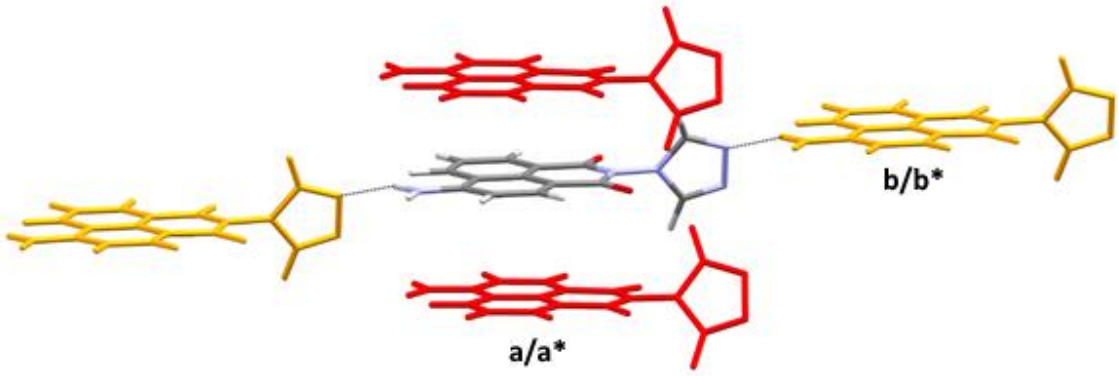

Figure 5-12 Location of the strongest interaction energies a/a* and b/b*.

5.4.4 4-(1,2,4trz)-nap-NMe_2 (L_4)

L_4 also has an electron donating substituent, NMe_2, in the 4-position of the naphthalimide ring. However, unlike the planar NH_2 group in **L_3**, the NMe_2 group and naphthalimide moiety intersect at 37.68 °. The NMe_2 substituent also provides additional hydrogen bonding functionality. The interaction energies of **L_4** have been calculated by Crystal Explorer and PIXEL and plotted against molecule···molecule centroid distances as shown in Figure 5-13 (in which only interactions stronger than -5 kJ mol^{-1} are considered).

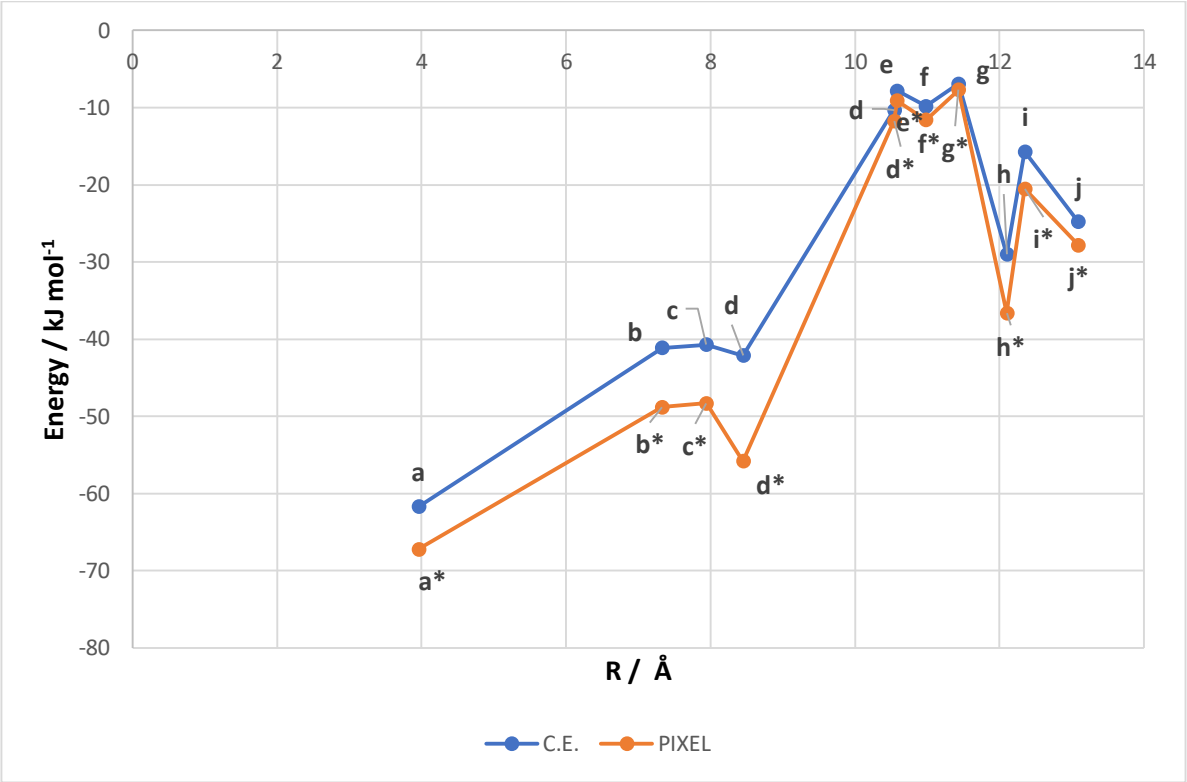

Figure 5-13 Interaction energies for L_4 determined from Crystal Explorer (blue) and PIXEL (orange) calculations, plotted against molecule···molecule centroid distances (R).

The strongest energy interaction, a/a*, occurs between -70 kJ mol^{-1} and -60 kJ mol^{-1} and exhibits the shortest distance. The structure and energy components are detailed in Table 5-6 and Figure 5-14. The large dispersion energy (-107.1 kJ mol^{-1} calculated from C.E. and -102.9 kJ mol^{-1} calculated from PIXEL) observed is due to the molecule···molecule interactions of a/a* related to the π···π interactions. However, the Coulombic and polarisation forces are significantly lower. This indicates the π···π contribution is greater than the other interactions in the aromatic stacking relationship.

Table 5-6 Energy components for energies a/a*

	No.	Symmetry	R /Å	Energies /kJ mol^{-1}									
				Crystal Explorer					**PIXEL**				
				E_{coul}	E_{pol}	E_{dis}	E_{rep}	E_{tot}	E_{coul}	E_{pol}	E_{dis}	E_{rep}	E_{tot}
	a/a*	x, -y+3/2, z-1/2 x, -y+3/2, z+1/2	3.96	-12.7	-8	-107.1	82.3	-61.7	-29	-23.9	-102.9	88.7	-67.2

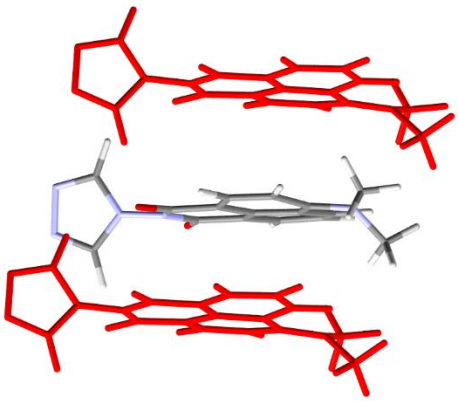

Figure 5-14 Location of the strongest interaction energy a/a*.

The next three strongest interaction energies are b/b*, c/c* and d/d* in the range -40 to -60 kJ mol^{-1}. These interactions are mainly driven by the different types of hydrogen bonds shown in Figure 5-15. In Table 5-7, d/d* has the strongest Coulombic energy (-31.4 kJ mol^{-1} calculated from C.E. and -43.7 kJ mol^{-1} calculated from PIXEL) indicating that stronger C-H···O and C-H ···N hydrogen bonds are present. c/c* has the next strongest Coulombic energy (-23.5 kJ mol^{-1} calculated from C.E. and -29.5 kJ mol^{-1} calculated from PIXEL) and is related to C-H···O type hydrogen bonds. b/b* has a slightly smaller Coulombic energy (-20.6 kJ mol^{-1} calculated from C.E. and -27.4 kJ mol^{-1} calculated from PIXEL) mainly arising from the non-classic C-H···C type hydrogen bonds.

Table 5-7 Energy components for b/b*,c/c* and d/d* determined from Crystal Explorer and PIXEL calculations.

	No.	Symmetry	R /Å	Energies /kJ mol^{-1}									
				Crystal Explorer					**PIXEL**				
				E_{coul}	E_{pol}	E_{dis}	E_{rep}	E_{tot}	E_{coul}	E_{pol}	E_{dis}	E_{rep}	E_{tot}
	b/b*	-x+1, -y+1, -z+2	7.33	-20.6	-6.2	-27	14.1	-41.1	-27.4	-9.7	-24.4	12.6	-48.8
	c/c*	-x+1, -y+1, -z+1	7.94	-23.5	-5.4	-21.4	10.9	-40.7	-29.5	-9	-19.8	10.1	-48.3
	d/d*	-x+1, y-1/2, -z+3/2 -x+1, y+1/2, -z+3/2	8.45	-31.4	-7.6	-18.8	21.2	-42.1	-43.7	-13	-22.2	23.1	-55.8

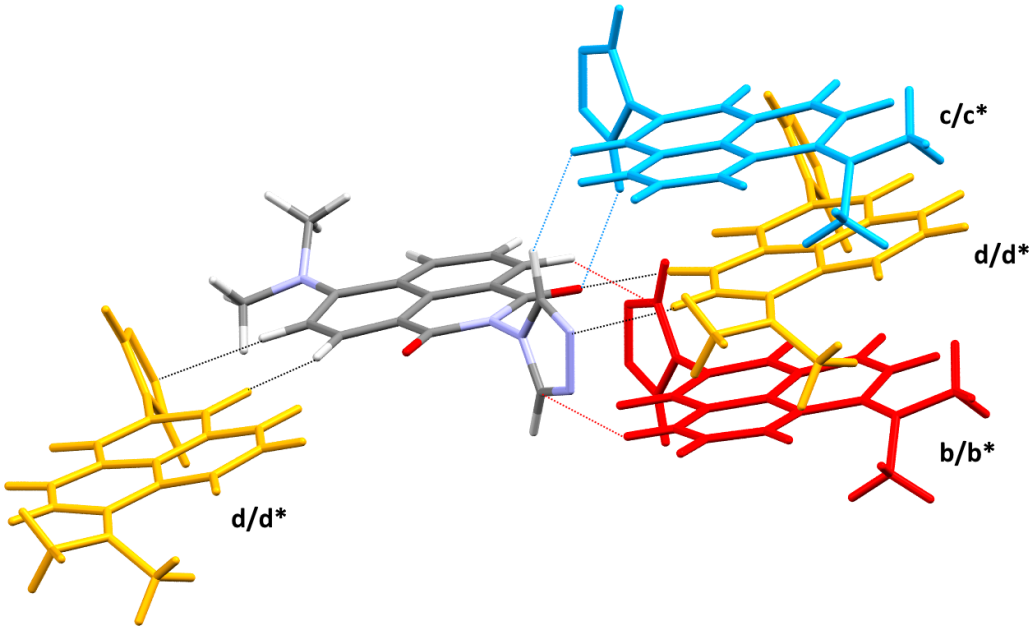

Figure 5-15 Location of the next strongest interaction energies b/b*, c/c*, and d/d*.

5.4.5 Contributions to the Total Energy

Table 5-8 presents the values of Coulombic (electrostatic), polarisation, dispersion and repulsion contributions to the lattice energy and the total lattice energy calculated by Crystal Explorer and PIXEL. A good agreement is observed between the two methods of energy determination.

It shows that the total energy appears to be dominated by dispersion contributions, as this component is by far the largest in this system. This strongly indicates that π···π interactions dominate in this ligand system. Relatively, the NMe_2 substituted **L_4** has the strongest dispersion contribution (-200 kJ mol^{-1} calculated from C.E. and -197 kJ mol^{-1} calculated from PIXEL), which is about 57% of the sum of E_{dis}, E_{pol}, and E_{dis}. The NH_2 and NO_2 have next stronger dispersion contribution contribution, which occupied 61% and 59 % of the sum of E_{dis}, E_{pol}, and E_{dis}. The non-substituted **L_1** ligand has a smaller dispersion energy component (-155.05 kJ mol^{-1} calculated from C.E. and -155.3 kJ mol^{-1} calculated from PIXEL) than the other substituted ligands occupied about 56 % of the sum of E_{dis}, E_{pol}, and E_{dis}. The Coulombic energy components of this system are similar in value, but the NMe_2 substituted **L_4** also has the strongest relative contribution (-106.1 kJ mol^{-1} calculated from C.E. and -134.1 kJ mol^{-1} calculated from PIXEL).

Table 5-8 Lattice energy components for L_1 to L_4 determined from Crystal Explorer and PIXEL calculations.

No.		Energies /kJ mol^{-1}								
	Crystal Explorer					**PIXEL**				
	E_{coul}	E_{pol}	E_{dis}	E_{rep}	E_{tot}	E_{coul}	E_{pol}	E_{dis}	E_{rep}	E_{tot}
L_1	-92.95	-30.95	-155.05	128.15	-177.3	-111.9	-39.9	-155.3	121.6	-185.6
L_2	-89.4	-32.05	-175.8	139.7	-185.2	-129.5	-42.5	-179.4	138.1	-213.3
L_3	-63.3	-47.6	-176.4	163.8	-154.9	-66.8	-82.8	-183.1	159.8	-172.9
L_4	-106.1	-41.3	-200	145.8	-226.85	-134.1	-46.5	-197	148.8	-228.8

5.5 Experimental Charge Density Analysis

The theoretical molecular interaction calculations in the previous sections indicate a number of potential non-covalent interactions. However, confirmation of the energetic strength of these non-covalent interactions can be provided by an analysis of charge distribution data. Experimental high resolution data of **L_1**-**L_4** were subject to multipolar refinement in the Mopro[166] software. Various 3D electron density maps derived from the multipole model total electron density are depicted in Appendix C. As explained in Chapter 1.4.4, critical points can be identified where the gradient vector of the electron density becomes zero and these can be used to describe the topology of the electron density. The highlighted aromatic stacking interactions and weak hydrogen bonds in the crystal packing discussed in Chapter 5.4 will be further evaluated and explained by critical point analysis in sections 5.5.1 and 5.5.2.

5.5.1 Evaluation of π···π interactions from CPs

Intermolecular interactions can be classified based on topological properties of the electron density. According to the values of $\nabla^2\rho(\boldsymbol{r}_{BCP})$, $G(\boldsymbol{r}_{BCP})$, $V(\boldsymbol{r}_{BCP})$, and $H(\boldsymbol{r}_{BCP})$ at critical points, there are three types of interactions. These are as follows: shared shell ($\nabla^2\rho(\boldsymbol{r}_{BCP}) < 0$, $H(\boldsymbol{r}_{BCP}) < 0$, $|V(\boldsymbol{r}_{BCP})|/G(\boldsymbol{r}_{BCP}) > 2$), closed shell ($\nabla^2\rho(\boldsymbol{r}_{BCP}) > 0$, $H(\boldsymbol{r}_{BCP}) < 0$, $1 < |V(\boldsymbol{r}_{BCP})|/G(\boldsymbol{r}_{BCP}) < 2$) and pure closed shell ($\nabla^2\rho(\boldsymbol{r}_{BCP}) > 0$, $H(\boldsymbol{r}_{BCP}) > 0$, $|V(\boldsymbol{r}_{BCP})|/G(\boldsymbol{r}_{BCP}) < 1$) interactions.[100] Accordingly, the π···π interactions discussed below can be classified as pure closed shell interactions. The results are similar to those reported for benzene and pyridine based

compounds.[100] Waller *et al.*[167] proposed a linear relationship between π-based binding energy, ΔE, and the sum of $\rho(\boldsymbol{r}_{BCP})$ values of intermolecular interactions, based on a study to estimate π···π interaction energies for benzene, pyridine and DNA/RNA based compounds. The relationship derived is shown in Equation 5-11.

$$\Delta E = 724.58 \sum \rho_{\pi} + 0.072$$

Equation 5-11 Calculation of the π···π interaction binding energy. $\rho(\boldsymbol{r}_{BCP})$ is shown in atomic units.

The π···π interaction binding energy given here is expressed as the energy to break the interaction and therefore it is positive, but it should be remembered that this is in fact an attractive force. Section 5.5.3 will use this equation to estimate and evaluate π···π interaction energies for the four ligands presented in this study. However the value of the binding energy from theoretical calculations is of course negative, so in order to enable a consistent comparison Equation 5-11 is modified so that the sign of the calculated binding energy is inverted so as to be negative.

5.5.1.1 CPs of π···π interactions in 4-(1,2,4trz)-Nap-H (L_1)

There are five CPs involved in π···π interactions for this ligand. In Figure 5-16, these CPs are found in region between the two stacked naphthalene rings. The properties of CPs in Table 5-9 indicate the presence of interactions, which obey pure closed shell ($\nabla^2\rho(\boldsymbol{r}_{BCP}) > 0$, $H(\boldsymbol{r}_{BCP}) > 0$, $|V(\boldsymbol{r}_{BCP})|/G(\boldsymbol{r}_{BCP}) < 1$) interactions. In total this gives more than 20 kJ mol^{-1} binding energy, which is approximately the same as that in benzene derivatives (19.251 kJ mol^{-1}), but twice as energetically stabilising as pure benzene (9.665 kJ mol^{-1}) or pure pyridine (12.04 kJ mol^{-1}) structures.[100]

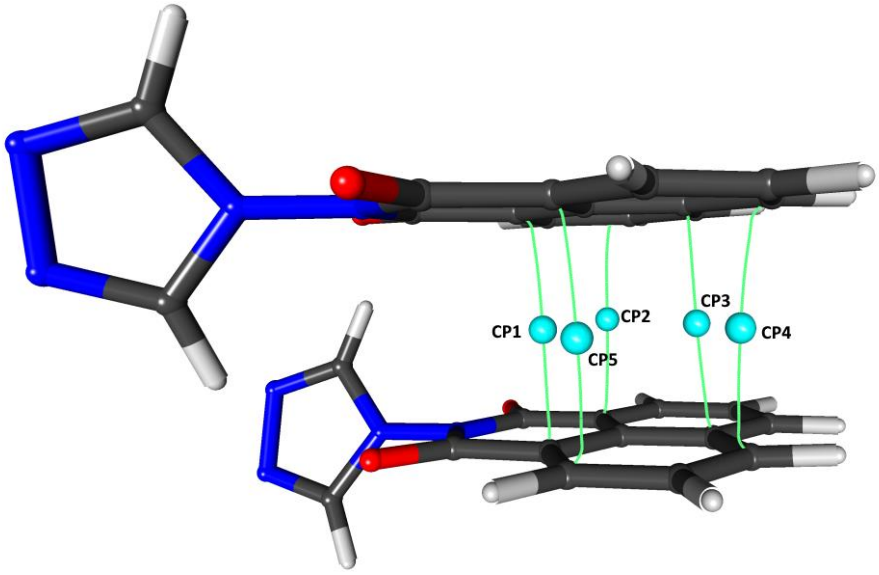

Figure 5-16 Selected critical points involved in the π···π interaction in L_1. Blue spheres and bond paths represent bond critical points (BCP).

Table 5-9 Properties for the L_1 π···π interaction critical points.

No.	Atomic Distance / Å	G_{BCP} / kJ mol^{-1} Bohr^{-3}	V_{BCP} / kJ mol^{-1} Bohr^{-3}	$\rho_{(BCP)}$ / e Å^{-3}	$\nabla^2 \rho_{(BCP)}$ / e Å^{-5}	$\sum \rho_{BCP}$	ΔE_π [a] / kJ mol^{-1}
CP1	3.4454	9.40	-6.99	0.04102	0.433	0.19199	-20.68731
CP2	3.4879	8.13	-5.19	0.03597	0.380		
CP3	3.4850	8.07	-5.82	0.03529	0.379		
CP4	3.3739	9.00	-6.64	0.03940	0.417		
CP5	3.4042	9.27	-6.86	0.04031	0.429		

5.5.1.2 CPs of π···π interactions in 4-(1,2,4trz)-Nap-NO_2 (L_2)

As discussed in **L_2** 5.3.2, this structure has the electron withdrawing NO_2 functional group twisted at an angle of 39° from the mean plane of the naphthalimide ring, resulting in a head-to-tail stacking which in-turn gives noticeably different centroid distances between two stacked molecules. In Figure 5-17, For the red molecule, 4 CPs (CP1, CP2, CP5, CP6) are distributed from NO_2···π, while for the yellow molecule there are only two CPs (CP7 and CP12) relevant to the NO_2···π interaction. A change in arrangement from the offset π···π stacking seen in **L_1** to NO_2···π stacking contacts is observed in **L_2** and this leads to a different and more compact packing. It can be seen in Table 5-10 that the red molecule with the shorter distance has a larger π···π binding energy. The red molecule has an associated energy of 22.827 kJ mol^{-1}, while the yellow molecule has an associated energy of only 15.027 kJ mol^{-1}. These results are also consistent with the intermolecular interaction energies determined from C.E. in section 5.4.2.

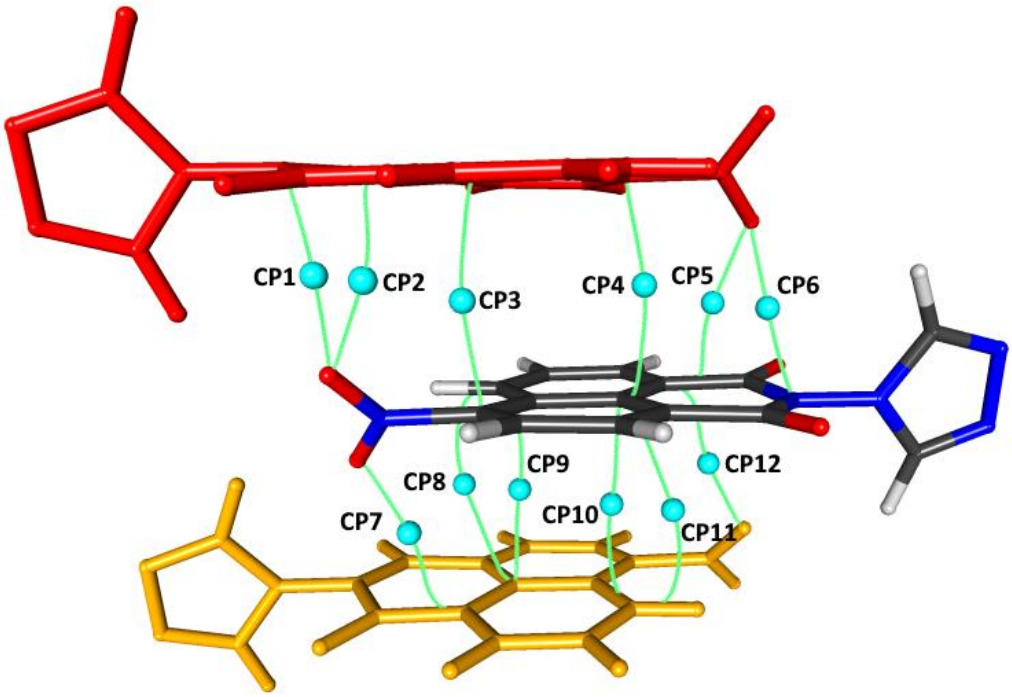

(a)

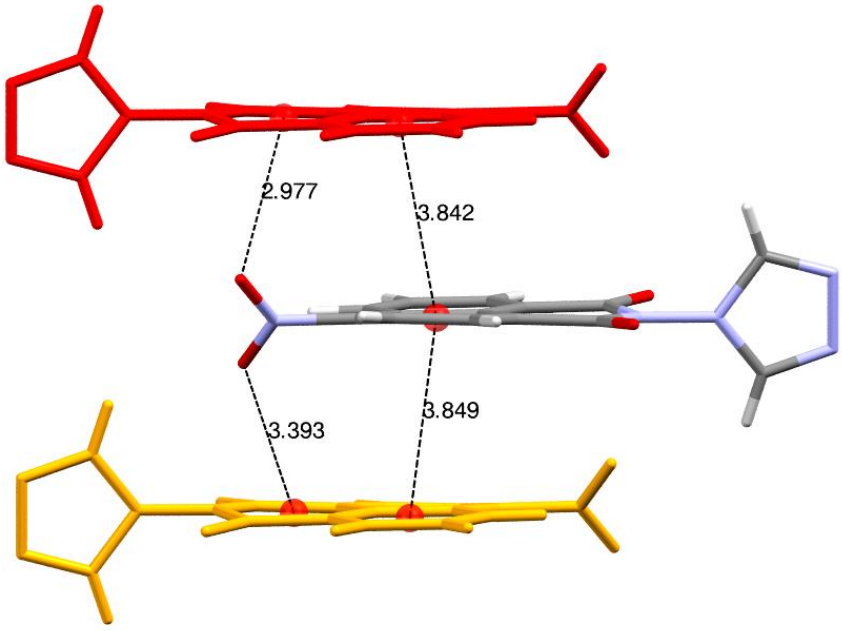

(b)

Figure 5-17 (a) Selected critical points involved in the π···π interaction in **L_2**. Blue spheres and bond paths represent bond critical points (BCP). (b) The separation distances between **L_2** molecules.

Table 5-10 Properties for the L_2 π···π interaction critical points.

No.	Atomic Distance / Å	G_{BCP} / kJ mol^{-1} Bohr^{-3}	V_{BCP} / kJ mol^{-1} Bohr^{-3}	$\rho_{(BCP)}$ / e Å^{-3}	$\nabla^2 \rho_{(BCP)}$ / e Å^{-5}	$\sum \rho_{BCP}$	ΔE_π [a] / kJ mol^{-1}	E_{tot}(C.E.) / kJ mol^{-1}
CP1	3.0087	16.93	-11.30	0.04660	0.828	0.21192	-22.827	-59.6
CP2	3.1874	13.37	-8.80	0.03905	0.659			
CP3	3.5644	3.08	-2.25	0.02031	0.144			
CP4	3.5644	3.08	-2.25	0.02032	0.144			
CP5	3.1874	13.37	-8.80	0.03905	0.659			
CP6	3.0087	16.93	-11.30	0.04662	0.828			
CP7	3.2180	11.37	-7.80	0.03908	0.549	0.13928	-15.027	-45.8
CP8	3.5518	1.82	-1.31	0.01431	0.086			
CP9	3.5518	3.11	-2.04	0.01625	0.153			
CP10	3.5518	3.11	-2.04	0.01625	0.153			
CP11	3.5518	1.82	-1.31	0.01431	0.086			
CP12	3.2180	11.37	-7.80	0.03908	0.549			

5.5.1.3 CPs of π···π interactions in 4-(1,2,4trz)-Nap-NH_2 (L_3)

Unlike L_1 and L_2, L_3 has an electron donating group which is in the same plane as the naphthalimide ring and causes a slightly larger repulsion between the two molecules. 6 CPs were found in the region between nanphthalimide rings again, Figure 5-18. In Table 5-11 Similar to the properties of CPs observed in L_1, which also belong to pure closed shell ($\nabla^2\rho(\boldsymbol{r}_{BCP}) > 0$, $H(\boldsymbol{r}_{BCP}) > 0$, $|V(\boldsymbol{r}_{BCP})|/G(\boldsymbol{r}_{BCP}) < 1$) interactions . From Table 5-11 it can be seen that six CPs provide about 19 kJ mol^{-1} binding energy, which is slightly smaller than L_1.

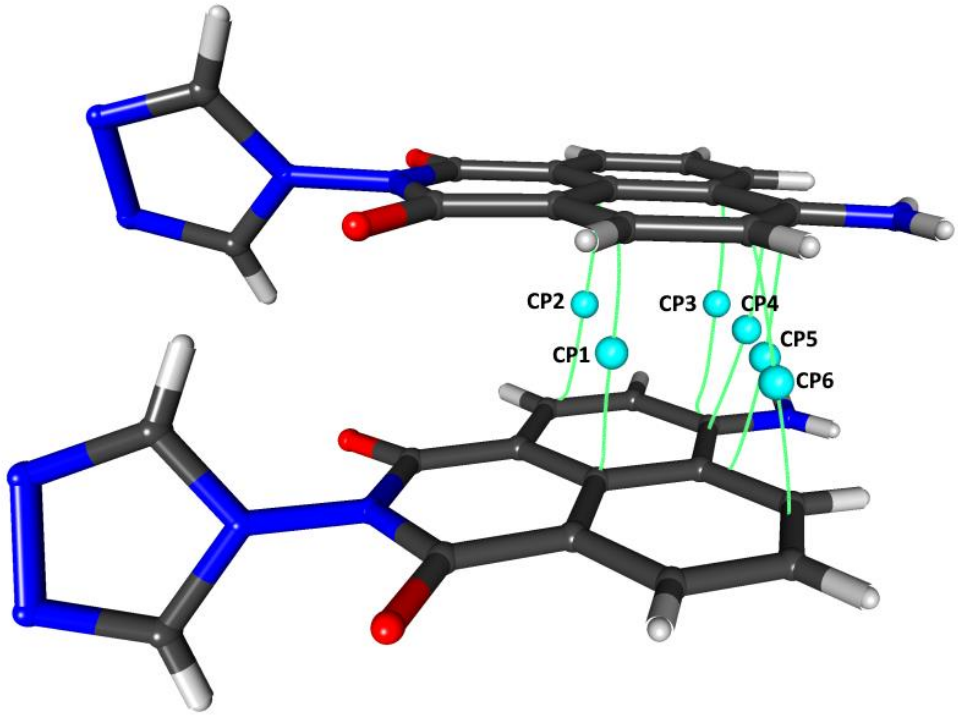

Figure 5-18 Selected critical points involved in the π···π interaction in **L₃**. Blue spheres and bond paths represent bond critical points (BCP).

Table 5-11 Properties for the **L₃** π···π interaction critical points.

No.	Atomic Distance / Å	G_{BCP} / kJ mol^{-1} Bohr^{-3}	V_{BCP} / kJ mol^{-1} Bohr^{-3}	$\rho_{(BCP)}$ / e Å^{-3}	$\nabla^2 \rho_{(BCP)}$ / e Å^{-5}	$\sum \rho_{BCP}$	ΔE_{π} [a] / kJ mol^{-1}
CP1	3.4267	8.21	-5.98	0.03636	0.383	0.18016	-19.41704
CP2	3.5287	7.36	-5.24	0.03261	0.348		
CP3	3.4100	5.95	-4.39	0.03079	0.0275		
CP4	3.6234	6.17	-4.25	0.02740	0.297		
CP5	3.4984	6.17	-4.41	0.02582	0.331		
CP6	3.4640	6.21	-4.26	0.02720	0.300		

5.5.1.4 CPs of π···π interactions in 4-(1,2,4trz)-Nap-NO_2 (L_4)

L_4 also has an electron donating NMe_2 substituent in the 4-position of the naphthalimide ring. However, unlike the planar NH_2 group in L_2, the NMe_2 group is twisted at an angle of 37.68° with respect to the mean plane of the naphthalimide. Additionally, due to the influence of the NMe_2 group, the naphthalimide ring system has a bent geometry where the substituted ring forms an angle of 6.63° with respect to the mean plane of the rest of the napthalimide in Figure 5-19. This causes two very different centroid···centroid distances between the two benzene rings. The CPs mainly occur in the region of the shorter centroid···centroid distance. From Table 5-12, this gives a 21.286 kJ mol^{-1} binding interaction, which is similar to the stronger L_2 interaction and larger than L_1 and L_3.

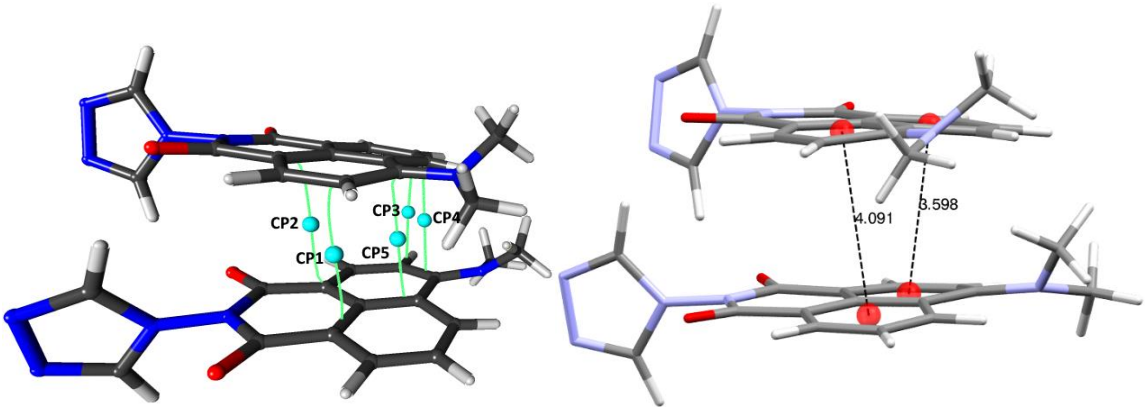

(a) (b)

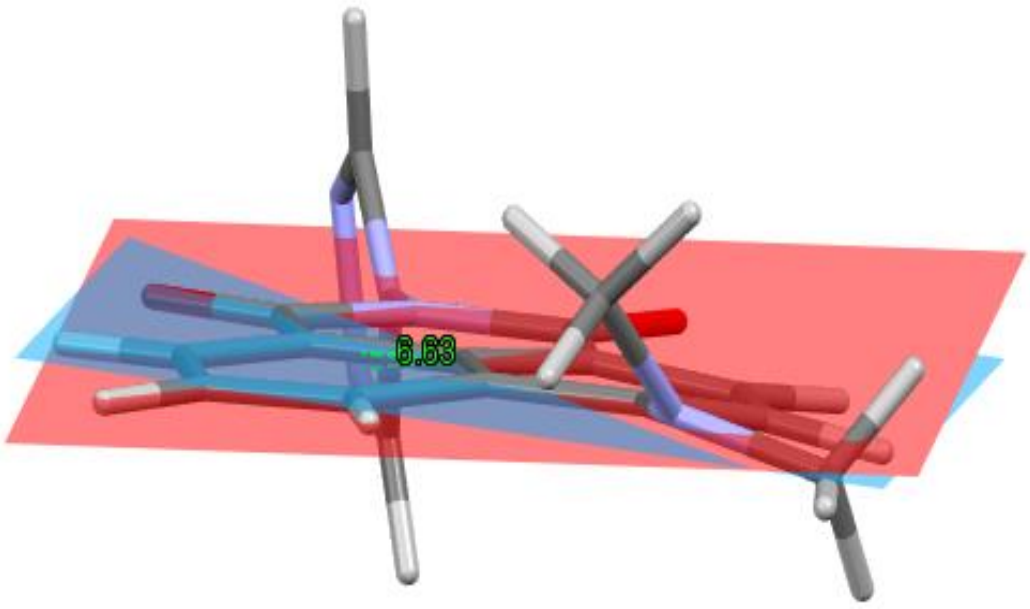

(c)

Figure 5-19 (a) Selected critical points involved in the π···π interaction in L_4. Blue spheres and bond paths represent bond critical points (BCP). (b) The separation distance between two

molecules. (c) Deformation from planarity in the naphthalimide ring, the substituted ring forms an angle of 6.63°.

Table 5-12 Properties for L_4 π···π interaction critical points.

No.	Atomic Distance / Å	G_{BCP} / kJ mol^{-1} Bohr^{-3}	V_{BCP} / kJ mol^{-1} Bohr^{-3}	$\rho_{(BCP)}$ / e Å^{-3}	$\nabla^2 \rho_{(BCP)}$ / e Å^{-5}	$\sum \rho_{BCP}$	ΔE_π [a] / kJ mol^{-1}
CP1	3.5072	7.07	-5.00	0.03141	0.335	0.19862	-21.2860
CP2	3.5423	9.45	-7.10	0.04193	0.433		
CP3	3.3694	9.62	-7.23	0.04237	0.441		
CP4	3.2920	10.51	-7.99	0.04566	0.478		
CP5	3.5347	8.20	-6.05	0.03725	0.380		

5.5.2 Hydrogen Bond Evaluation from CPs

The Laplacian, $\nabla^2\rho(\mathbf{r}_{BCP})$, and local electron density, H_{BCP}, of the hydrogen bond critical points are two important parameters that can be used to evaluate the strength of hydrogen bonds. Strong hydrogen bonds with $E_{HB} > 100$ kJ mol^{-1} have both $\nabla^2\rho(\mathbf{r}_{BCP})$ and $H_{BCP} < 0$; moderate hydrogen bonds with 50 kJmol^{-1} $\leq E_{HB} \leq$100 kJ mol^{-1} have both $\nabla^2\rho(\mathbf{r}_{BCP})>0$ and $H_{BCP} < 0$; weak hydrogen bonds with $E_{HB} < 50$ kJ mol^{-1} have both $\nabla^2\rho(\mathbf{r}_{BCP})$ and $H_{BCP} > 0$. Additionally, V_{BCP} and G_{BCP} terms provide further information indicating whether hydrogen bonds interactions are stabilised. If the V_{BCP}/G_{BCP} ratio > 1 this indicates an intermediate closed-shell interaction, while $V_{BCP}/G_{BCP} < 1$ indicates an electrostatic interaction.[168]

5.5.2.1 CPs of Hydrogen bonds in 4-(1,2,4trz)-Nap-H (L_1)

Three neighbouring molecules showing the strongest hydrogen bonds were chosen for analysis in Figure 5-20. The hydrogen bond energy, E_{HB}, estimated from the individual BCP properties indicates the strength of the atom-atom interaction. The sum of the estimated interaction energy, $\sum E_{HB}$, reflects the intermolecular interaction between two molecules. All the information of CPs properties for $\mathbf{L_1}$ hydrogen bond critical points presented in Table 5-13. The strongest interaction

in **L_1** involves 4 BCPs (CP1-4) giving a summed energy of -15.43 kJ mol^{-1}, which also corresponds to the strongest total intermolecular interaction calculated with C.E.. The second and third strongest interactions are also related to the triazole group and are -11.95 kJ $mol^{-1}$and -8.285 kJ mol^{-1} respectively. A good agreement is observed between the estimated interaction energy and calculated intermolecular energy from C.E. presented in Chapter 5.4.1.

Table 5-13 CPs properties for **L_1** hydrogen bond critical points.

	No.	D / Å	G_{BCP} / kJ mol^{-1} $Bohr^{-3}$	V_{BCP} / kJ mol^{-1} $Bohr^{-3}$	H_{BCP} / kJ mol^{-1} $Bohr^{-3}$	$\rho(r_{BCP})$ / e $Å^{-3}$	$\nabla^2 \rho(r_{BCP})$ / e $Å^{-5}$	E_{HB} / kJ mol^{-1}	$\sum E_{HB}$/ kJ mol^{-1}	E_{tot} (C.E.) / kJ mol^{-1}
	CP1	2.7880	11.35	-8.01	3.34	0.04149	0.540	-4.005	-15.43	-43.2
	CP2	2.2760	10.75	-7.43	3.32	0.03838	0.517	-3.715		
	CP3	2.2760	10.75	-7.41	3.34	0.03830	0.517	-3.705		
	CP4	2.7880	11.35	-8.01	3.34	0.04150	0.540	-4.005		
	CP5	2.7481	13.41	-9.39	4.02	0.04507	0.640	-4.695	-11.95	-24.9
	CP6	2.5317	19.17	-14.51	4.66	0.06494	0.875	-7.255		
	CP7	2.4236	19.33	-13.62	5.71	0.05697	0.919	-6.81	-8.285	-24.8
	CP8	2.8911	5.45	-2.95	2.5	0.01011	0.292	-1.475		

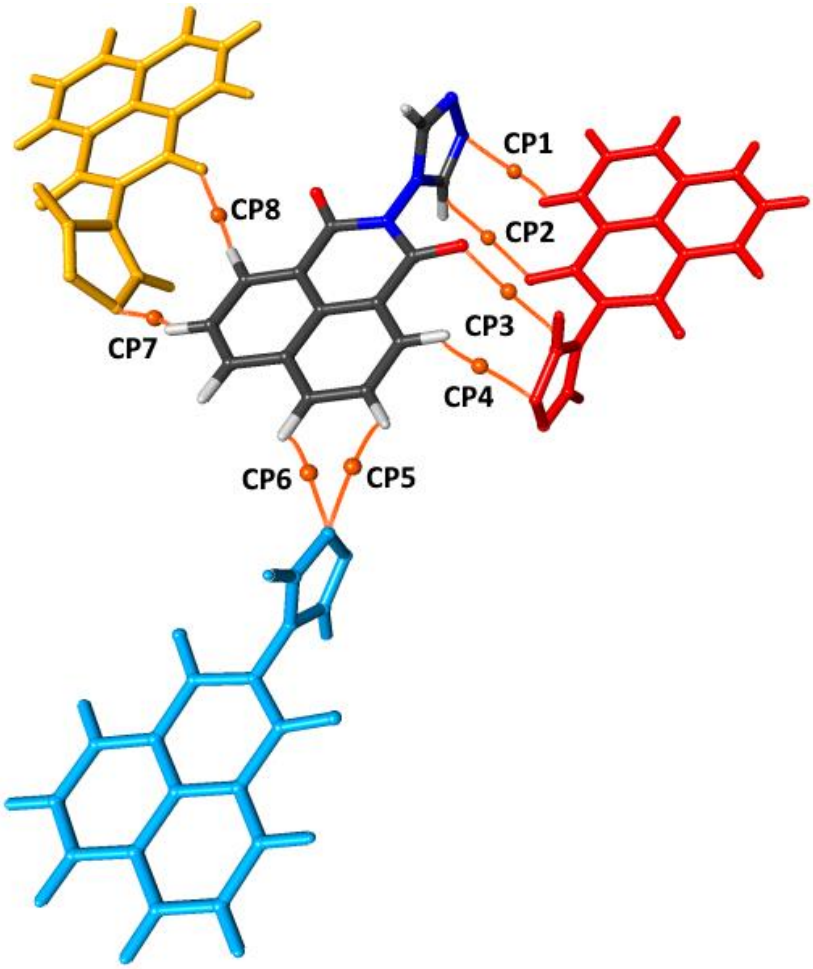

Figure 5-20 Selected critical points involved in hydrogen bond interactions in **L_1**. Orange spheres and bond paths represent bond critical points.

5.5.2.2 CPs of Hydrogen bonds in 4-(1,2,4trz)-Nap-NO_2 (L_2)

Unlike the π-based interactions discussed in section 5.5.1.2, NO_2 substitution does not generate strong hydrogen bonding interactions. All the information of CPs properties for **L_2** hydrogen bond critical points presented in Table 5-14. C-H···O interactions are observed in the crystal between neighbouring molecules (Figure 5-21). Due to symmetry they are arranged in pairs, which leads to stronger interaction energies in the red molecule the sum of the hydrogen bond energy is -11.285 kJ mol^{-1}. The next strongest molecular pair has a similar interaction energy, which is -9.71 kJ mol^{-1} split between C-H···O (CP3) and C-H···N (CP4). The weak hydrogen bonds through C-H···O (CP5) and C-H···N (CP6) interactions from the triazole group give a total of -5.93 kJ mol^{-1}. A correlation with the estimated energy strength is also observed in the intermolecular energy calculated from C.E. in Chapter 5.4.2.

Table 5-14 Properties for **L_2** hydrogen bond critical points.

	No.	D / Å	G_{BCP} / kJ mol^{-1} $Bohr^{-3}$	V_{BCP} / kJ mol^{-1} $Bohr^{-3}$	H_{BCP} / kJ mol^{-1} $Bohr^{-3}$	ρ(BCP) / e $Å^{-3}$	∇^2 ρ(BCP) / e $Å^{-5}$	E_{HB} / kJ mol^{-1}	$\sum E_{HB}$/ kJ mol^{-1}	E_{tot} (C.E.) / kJ mol^{-1}

	CP1	2.3659	19.15	-11.14	8.01	0.03261	0.997	-5.57	-11.285	-36.1
	CP2	2.3659	19.03	-11.43	7.6	0.03691	0.977	-5.715		
	CP3	2.5353	19.38	-11.20	8.18	0.03199	1.012	-5.6	-9.71	-34.7
	CP4	2.6670	13.67	-8.22	5.45	0.03035	0.702	-4.11		
	CP5	2.6896	13.51	-7.49	6.02	0.02064	0.717	-3.745	--5.93	-19.2
	CP6	3.0436	6.99	-4.37	2.62	0.02303	0.353	-2.185		

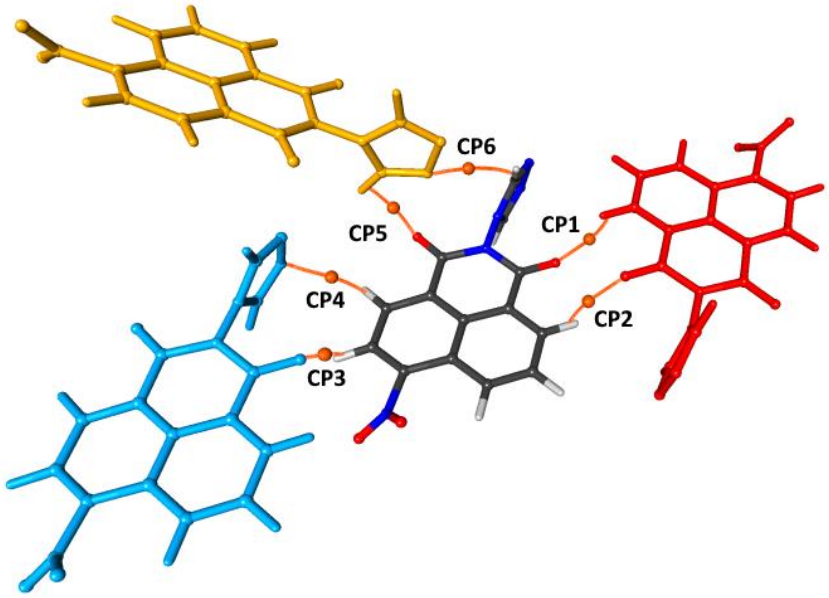

Figure 5-21 Selected critical points involved in hydrogen bond interactions in **L_2**. Orange spheres and bond paths represent bond critical points.

5.5.2.3 CPs of Hydrogen bonds in 4-(1,2,4trz)-Nap-NH_2 (L_3)

Unlike **L_1** and **L_2**, additional hydrogen bonds from the NH_2 substituent group are seen in the crystal packing of **L_3**. All the information of CPs properties for **L_3** hydrogen bond critical points presented in Table 5-15. Strong interaction energies are observed for CP1 and CP5, which are predominately from NH_2 groups and arise from C-H···O and C-H···N contacts respectively. In addition to these, weaker C-H···O hydrogen bonds in CP4 and CP6 are also observed, Figure 5-22. The sum of experimental hydrogen bonds for each molecular pair of red and blue molecules have similar calculated energies, -19.91 kJ mol^{-1} and -18.35 kJ mol^{-1} respectively. However, the total intermolecular energy calculated from C.E. gives a stronger interaction energy in the red molecular pair than the blue one, which indicates the presence of other interactions affecting the intermolecular interaction. The weaker C-H···O hydrogen bonds exist in the yellow molecular pair, giving a -5.78 kJ mol^{-1} interaction energy.

Table 5-15 Properties for L_3 hydrogen bond critical points.

	No.	D / Å	G_{BCP} / kJ mol^{-1} Bohr^{-3}	V_{BCP} / kJ mol^{-1} Bohr^{-3}	H_{BCP} / kJ mol^{-1} Bohr^{-3}	ρ(BCP) / e Å^{-3}	∇^2 ρ(BCP) / e Å^{-5}	E_{HB} / kJ mol^{-1}	$\sum E_{HB}$/ kJ mol^{-1}	E_{tot} (C.E.) / kJ mol^{-1}
	CP1	2.5161	21.40	-19.03	2.37	0.08904	0.873	-9.515	-19.91	-49.7
	CP2	2.4498	25.20	-20.79	4.41	0.08813	1.087	-10.395		
	CP3	2.7857	6.87	-4.22	2.65	0.02159	0.349	-2.11	-18.35	-31.4
	CP4	2.3252	19.31	-12.05	7.26	0.04220	0.975	-6.025		
	CP5	3.0526	27.26	-20.43	6.83	0.07886	1.251	-10.215		
	CP6	2.5914	16.35	-11.56	4.79	0.05182	0.777	-5.78	-5.78	-25.8

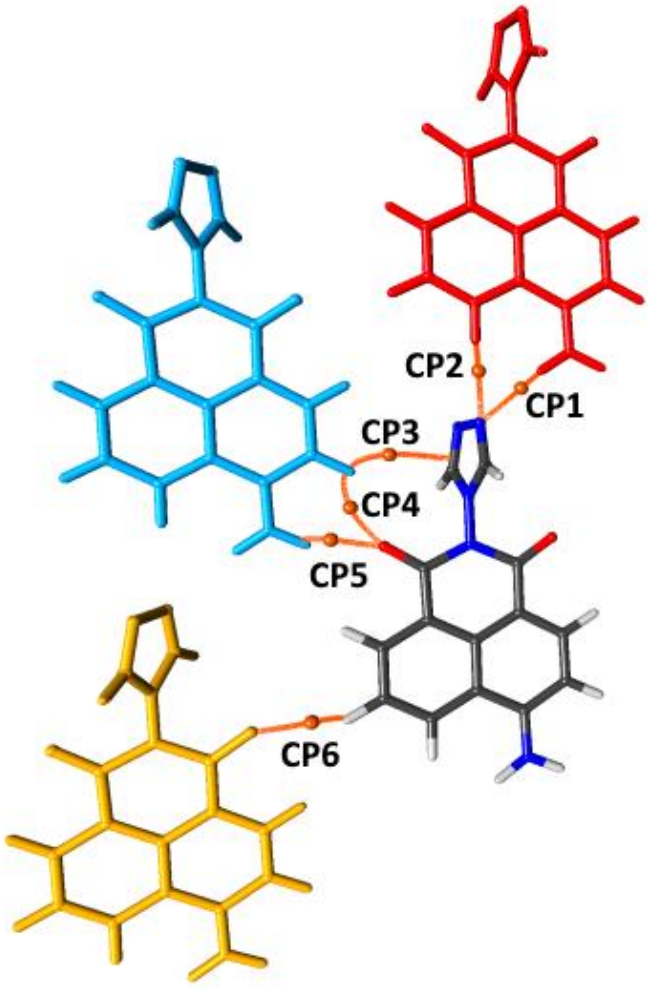

Figure 5-22 Selected critical points involved in hydrogen bond interactions in L_3. Orange spheres and bond paths represent bond critical points.

5.5.2.4 CPs of Hydrogen bonds in 4-(1,2,4trz)-Nap-NMe_2 (L_4)

The stronger interaction associated with the red molecule (CP1) is formed from the C=O group of the naphthalimide to C-H group of the other molecule and is -9.89 kJ mol^{-1}. All the information of

CPs properties for **L_4** hydrogen bond critical points presented in Table 5-16 and the relevant hydrogen interaction shown in Figure 5-23. The large total hydrogen bond energy, $\sum E_{HB}$, estimated from the BCP properties observed in the red and blue molecule pairs are -14.405 kJ mol^{-1} and -12.31 kJ mol^{-1} respectively. The total energies calculated by C.E. are also strong interactions with energies of -42.1 kJ mol^{-1} and -41.1 kJ mol^{-1} respectively. The interaction contacts of **L_4** are of a similar order to that seen in **L_1**, however the substitution of NMe_2 generates very weak hydrogen bonds in CP8 (-4.765 kJ mol^{-1}) and a weak C-H···N hydrogen bond (CP7) in the yellow molecular pair resulting in a total of -7.165 kJ mol^{-1}.

Table 5-16 Properties for **L_4** hydrogen bond critical points.

	No.	D / Å	G_{BCP} / kJ mol^{-1} Bohr^{-3}	V_{BCP} / kJ mol^{-1} Bohr^{-3}	H_{BCP} / kJ mol^{-1} Bohr^{-3}	ρ(BCP) / e Å^{-3}	∇^2 ρ(BCP) / e Å^{-5}	E_{HB} / kJ mol^{-1}	$\sum E_{HB}$/ kJ mol^{-1}	E_{tot} (C.E.) / kJ mol^{-1}
	CP1	2.2390	29.05	-19.78	9.27	0.06749	1.407	-9.89	-14.405	-42.1
	CP2	2.6489	13.35	-9.03	4.32	0.04165	0.649	-4.515		
	CP3	2.9710	7.46	-5.05	2.41	0.02944	0.362	-2.525	-12.31	-41.1
	CP4	2.8585	10.26	-7.26	3.00	0.03930	0.487	-3.63		
	CP5	2.8585	10.26	-7.26	3.00	0.03932	0.487	-3.63		
	CP6	2.9710	7.46	-5.05	2.41	0.02944	0.362	-2.525		
	CP7	2.9393	7.58	-4.80	2.78	0.02505	0.380	-2.40	-7.165	-29.0
	CP8	2.7219	13.12	-9.53	3.58	0.04791	0.614	-4.765		

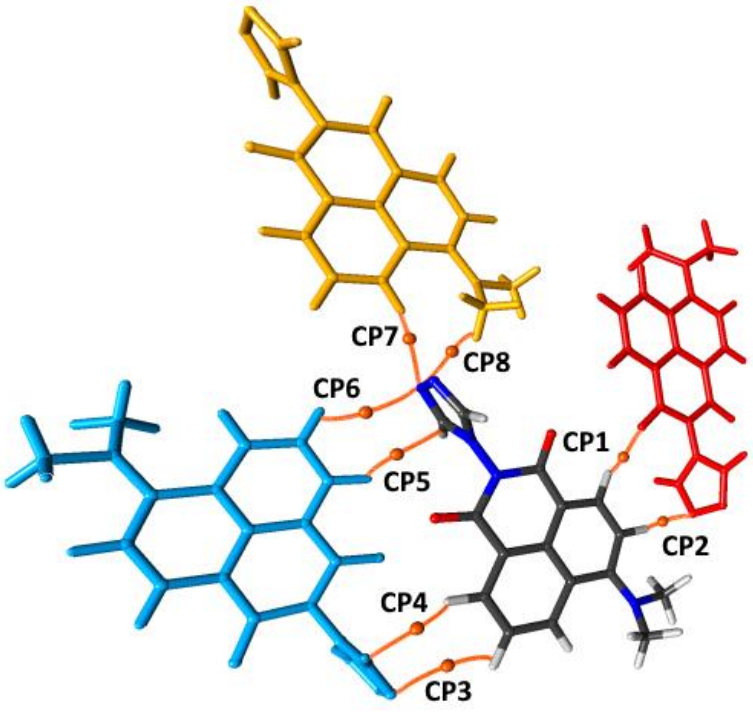

Figure 5-23 Selected critical points involved in hydrogen bond interactions in **L_4**. Orange spheres and bond paths represent bond critical points.

5.6 Comparisons

An overview of the number and type of short contacts in the crystals of this ligand system is readily provided by the Hirshfeld surface in Chapter 5.3. A deeper understanding of the intermolecular interactions of the **L_1**-**L_4** ligands has been provided by the combination of theoretical calculations from PIXEL and Crystal Explorer and experimental analysis of the electron density distribution. The analysis of π···π interactions and weak hydrogen bonds has been performed using topological properties of the electron density, which is also compared with the calculations from C.E. in Chapter 5.4. These comparisons have been made that the predominated dispersion and Coulombic contribution resulting the similar total molecule-molecule stabilisation.

A final comparison that can be made across this ligand system is an analysis of the significant strong π···π stacking between layers of the molecules (Table 5-17).

Table 5-17 π···π binding energies calculated from CPs and the total energies calculated from C.E. for the closest overlapped stacking .

No.	Atomic Distance / Å	ΔE_π [a] / kJ mol^{-1}	E_{dis} / kJ mol^{-1}	E_{rep} / kJ mol^{-1}	E_{tot} / kJ mol^{-1}
L_1	4.19	-20.687	-79.8	67.4	-46.4
L_2(a/a*)	5.25	-22.827	-75.5	56.6	-51.0
L_2(b/b*)	5.38	-15.027	-64.6	41.8	-43.9
L_3	3.97	-19.417	-91.7	77.7	-44.4
L_4	3.96	-21.296	-107.1	82.3	-61.7

From values of the π···π binding energy it can be seen in Table 5-17 that strong π···π interactions exist and are almost half of the total energies. In overlapped stacking structures, π···π interactions are influential in the crystal assembly and lead to directional aromatic interactions. The electron donating groups H (**L_1**), NH_2 (**L_3**), and NMe_2 (**L_4**) exhibit similar head-to-head π-stacking, however the NMe_2 substituent bends the naphthalimide ring and this results in different strength π interactions in two aromatic rings. The NO_2 (**L_4**) electron donating group alters the π-stacking from

head-to-head to head-to-tail and accordingly in addition to normal π···π interactions, strong NO_2···π interactions also exist. Notably, the head-to-tail packing type gives relatively smaller repulsion energies than the other head-to-head types.

In addition, relevant non-classical hydrogen bonds also exist in these molecules and are illustrated and demonstrated through the electron density distributions discussed in Chapter 5.5.2. The packing in these systems, especially π···π stacking, is dramatically affected by different ligand substituents however, the strength of intermolecular interactions do not have a direct relationship with the extent of electron donation or withdrawal in these groups. Notably, all the quantum analyse methodologies used in naphthalimide systems are also available to apply on the similar π-based systems.

Chapter 6 Conclusion and Future Works

6.1 Conclusions

The primary goal of this work was to design potential SCO Fe(II) complexes with a range of π-containing 1,8-naphthalimide systems and evaluate how π···π interactions affect the SCO phenomenon.

Firstly, Fe(II) complexes containing the bis-picolylamine ligand with simple anions were synthesised. A family of sulfonate containing 1,8-nanphthalimide anions with various electron donating/withdrawing substituents were successfully synthesised and fully characterised by nuclear magnetic resonance spectroscopy (NMR) and mass spectrometry (MS). These anion systems were then incorporated into Fe(II) systems in place of less complex anions. The aim of this work was to further develop the cooperativity between complexes to modify the SCO behaviour. Unfortunately, the magnetic susceptibility measurements showed most of complexes remained low spin across the temperature range measured (50 – 400 K). This is supported by NMR and single crystal X-ray studies, which also indicated the LS state at the temperatures measured. Only the complex with the 4-sulfanilic naphthalimide anion, H-Ar(4-SO_3)-Nap, showed potential for SCO modification. Given this promising result, the H-Ar(4-SO_3)-Nap family was chosen for further investigation with a more synthetically challenging SCO active cationic complex.

The following work introduced the Ar(4-SO3)-Nap anion family into 1,2,4-triazole based dinuclear complexes, as they have a long history of being SCO active compounds. Fe(II) complexes with PMAT and **PMBzT** ligands were synthesised and successfully characterised, including by single crystal X-ray diffraction. The incorporation of 1,8-naphthalimide anions with different substituents into the complexes drastically altered the magnetic properties of the systems. Magnetic measurements were conducted in the 320-20 K range. $[Fe_2(\mathbf{PMAT})_2](\mathbf{A_1})_4$ (**12**) and $[Fe_2(\mathbf{PMBzT})_2](\mathbf{A_1})_4$ (**14**) displayed gradual HS-HS to HS-LS half SCO transition, while $[Fe_2(\mathbf{PMBzT})_2](\mathbf{A_2})_4$ (**15**) remained HS-HS. Remarkably, $[Fe_2(\mathbf{PMAT})_2](\mathbf{A_2})_4$ (**13**) and $[Fe_2(\mathbf{PMBzT})_2](\mathbf{A_5})_4$ (**16**) were the first examples of a LS-LS configuration in these ligand systems, as confirmed by single crystal X-ray studies which indicated the LS state at the temperatures measured.

In the final synthetic work of this project, a series of triazole naphthalimide ligands were successfully synthesised and fully characterised by nuclear magnetic resonance spectroscopy (NMR), mass spectrometry (MS) and single crystal X-ray diffraction (SXRD). These ligands were

reacted with various metal salts and the resulting complexes were characterised by single crystal X-ray diffraction techniques. Analysis of the single crystal structure of these complexes confirmed the interactions between the 1,2,4-triazole functional group and metal ions with the naphthalimide groups π-stacking effectively to create supramolecular networks. Unfortunately, the magnetic properties of these complexes were not investigated within the time frame of this work.

High resolution charge density data sets were collected on a selection of triazole-ligands and the resulting distribution and properties data was analysed. These structures are categorised and the interactions were studied using a number of methods. Initial theoretical calculations used Crystal Explorer and PIXEL to systematically calculate the molecule-molecule interactions. Based on modern high resolution crystallography approaches, the experimental charge distribution and its topology were then calculated and used to fully characterise and quantify π-π interactions and other weak hydrogen bonds.

The results summarised above have been acquired and used to address the aims listed in Section 1.5.

Aim 1: Systematically design and modify a series of electron withdrawing/donating naphthalimide-based functional groups as the target for this project. These electron deficient 1,8-naphthalimide systems are then not only introduced into potential SCO complexes as non-coordinating anions, but also utilised as ligand scaffolds for metal complexes.

Aim 2: Initially, use standard resolution X-ray crystallography to characterise the compounds and then investigate their magnetic properties in order to begin to analyse the effect of altering chemical substituents on both the crystal structures and magnetic properties.

Firstly, sulfonated 1,8-naphthalimide anions were successfully incorporated into Fe(II) complexes which led to supramolecular control of the packing within the complexes. From the magnetic susceptibility measurements, it was demonstrated that the 4- sulfanilic nanphthalimide anions changed the spin state of $[Fe(\mathbf{bpa})_2]^{2+}$ at 300 K, which provides evidence of the performance of nanphthalmide anions in developing cooperativity between complexes. 4-Sulfanilic nanphthalimide anions introduced into $[Fe_2(\mathbf{PMBzT})_2]^{4+}$ gave even more interesting results. In the $[Fe_2(\mathbf{PMBzT})_2]^{4+}$ complexes the 4-sulfanilic nanphthalimide anions not only changed the ligand binding geometry around the metal centre but also drastically changed the SCO properties due to the altering substitutions of the naphthalimides. The H-substituted system improved the spin transition from a low temperature to more accessible temperature. The electron withdrawing NO_2-substituted naphthalimide allowed the spin state to remain HS-HS. The Tröger base anion

changed the ligands from a *cis*-bonded to *trans*-bonded configuration. This is notable, as it is both LS-LS and *trans* configuration, which to the best of our knowledge is a first. In $[Fe_2(\mathbf{PMBzT})_2](BF_4)_4 \cdot MeCN$ and $[Fe_2(\mathbf{PMAT})_2](\mathbf{A_5})_2 \cdot MeCN$ the distortion of the metal geometry was less pronounced with a reduced Σ value ranging from 99.4° (Both Fe1 & Fe2) to 69.9° (Fe1) and 66.9° (Fe2) respectively. All the supramolecular structures of these new complexes were driven by π-based interactions, which gave a similar layered packing in all cases. The results discussed above provide proof that π···π interactions dramatically affect SCO properties. Unfortunately, at this stage there are not enough magnetism results to determine and predict the relationships between π···π interactions and SCO properties.

Aim 3: In order to analyse the relationship between π interactions and magnetic properties, in the 1,8-based naphthalimide ligands system in particular, a deeper and more extensive analysis of intermolecular interactions and associated energies needs to be conducted using high resolution x-ray crystallography and quantum crystallographic methods.

Unfortunately, the other triazole-naphthalimide ligands family were not successfully complexed with Fe(II). The original purpose was to synthesise polymer complexes with triazole-nanphthalimide ligands in an attempt to increase cooperativity through π···π interaction from naphthalimide moieties and achieve hysteresis loops in the SCO. Unfortunately, the insoluble gel or powder complexes were hard to characterise and crystallise and so no data was collected. Further modification of the naphthalimide ligands needs to be improved and addressed in different ways. However, the ligands system with quantum crystallographic studies are still carried on to analyse the relationship with different substitutions and molecular interactions.

Aim 4: Electron density distribution analysis will be conducted to analyse the effects of different substituents on π···π interactions and hydrogen bonds strength in the system. Particularly, to understand how the π-stacking controls the cooperativity of the systems.

The final question to answer is how the electron withdrawing/donating substituents affect naphthalmide stacking and the strength of π···π interactions. From the standard X-ray structure geometric analysis, different aromatic overlap types were identified. Hydrogen and the two electron donating groups NH_2 and $N(Me)_2$, showed similar head-to-head packing type, while the election withdrawing NO_2 group gave head-to-tail type packing. There is evidence from PIXEL and C.E. energy calculations that the prevalence of these interactions for overlapping stacked packing is driven by dispersive forces. The electron donating groups NH_2 and $N(Me)_2$ have greater dispersion energies than H and NO_2 groups, which indicates large π···π interaction . The head-to-tail geometry in NO_2 leads to minimised repulsion energies in the ligands. Further characterisation and contribution to understanding these systems was provided by experimental charge density

analysis. The values of π···π binding energies were calculated individually. NO_2, NH_2 and $N(Me)_2$ substituted ligands all have greater π-based interactions than the ligand with the H group. However, the NO_2 has complicated π-based interactions, which can be classified to NO_2···π and π···π interactions from analysis of the CPs. If one considers only the pure π···π interactions in NO_2, this is lower than that of the other three ligands. For all of these ligands, the contribution of π-based interactions are around half of the total interactions in the system. Consequently, π-based interactions can be considered to have a strong structure directing effect in naphthalimide crystal assembly and therefore very likely to be of use in future studies investigating SCO systems.

6.2 Future Work

Further analysis is still needed for some aspects of this research, specifically the magnetic properties and elemental analysis of some complexes have yet to be obtained. In particular, $[Fe_2(\mathbf{PMAT})_2](\mathbf{A_2})_4$ (**13**) and $[Fe_2(\mathbf{PMBzT})_2](\mathbf{A_5})_4$ (**16**) would greatly benefit from Mössbauer analysis to fully confirm the presence of a completely LS-LS state. It would also be useful to investigate the magnetic properties of the triazole based naphthalimide complexes presented in chapter 4.

Given the success of the Tröger base anion at modulating the long range structure, additional advanced linking groups should be introduced to the 4-position of the naphthalimide in order to develop a series of bridged naphthalimide ligands and anions (Figure 6-1). Further complexation and crystallisation of these ligands could be performed and the resulting structures fully analysed.

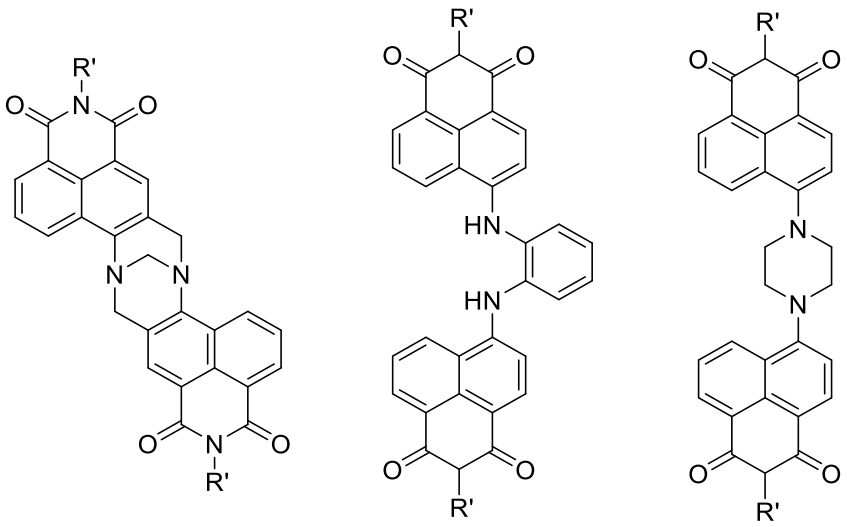

Figure 6-1 Examples of potential bridged ligand systems.

In Chapter 3, the **PMRT** system displayed interesting SCO properties with 1,8-naphthalimide anions incorporated. It is would be interesting to produce naphthalimide based **PMRT** ligands which should retain their potential to induce SCO in Fe(II) systems (Figure 6-2). Further

complexation and magnetic studies will provide insight into how the π···π interactions influence the SCO properties.

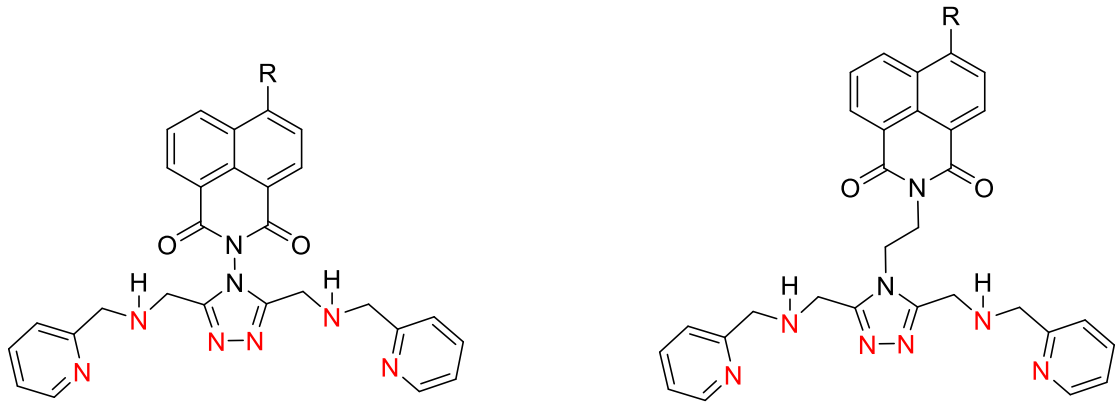

R= H, NO_2, NH_2, NMe_2

Figure 6-2 Examples of naphthalimide based **PMRT** ligands.

Currently, we only investigated detailed quantum properties for the naphthalimide based ligands. Attempts can be made to directly study the SCO complexes using quantum crystallography, which would further develop detailed structure function relationships and provide understanding and control over spin crossover materials.

.

Appendix A

A.1 NMR and MS data of Ar(4-SO_3)-Nap-H·PyH (A_1·PyH)

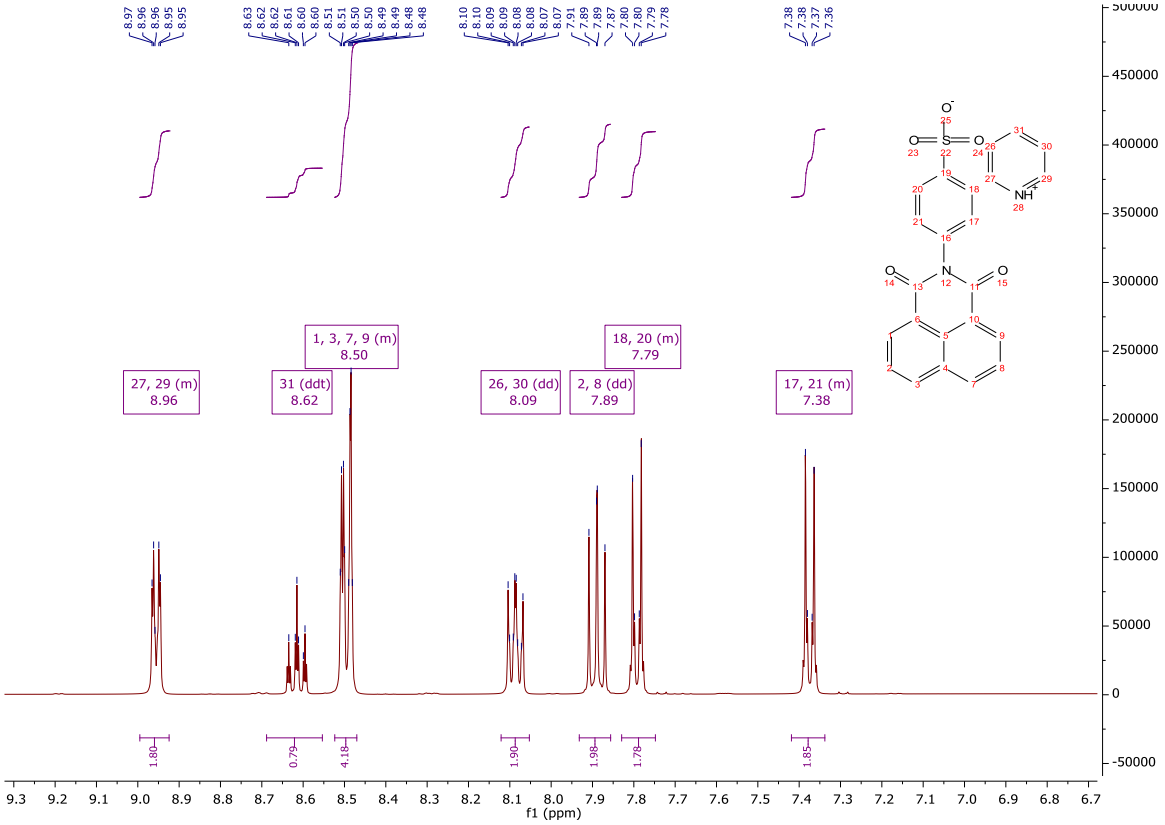

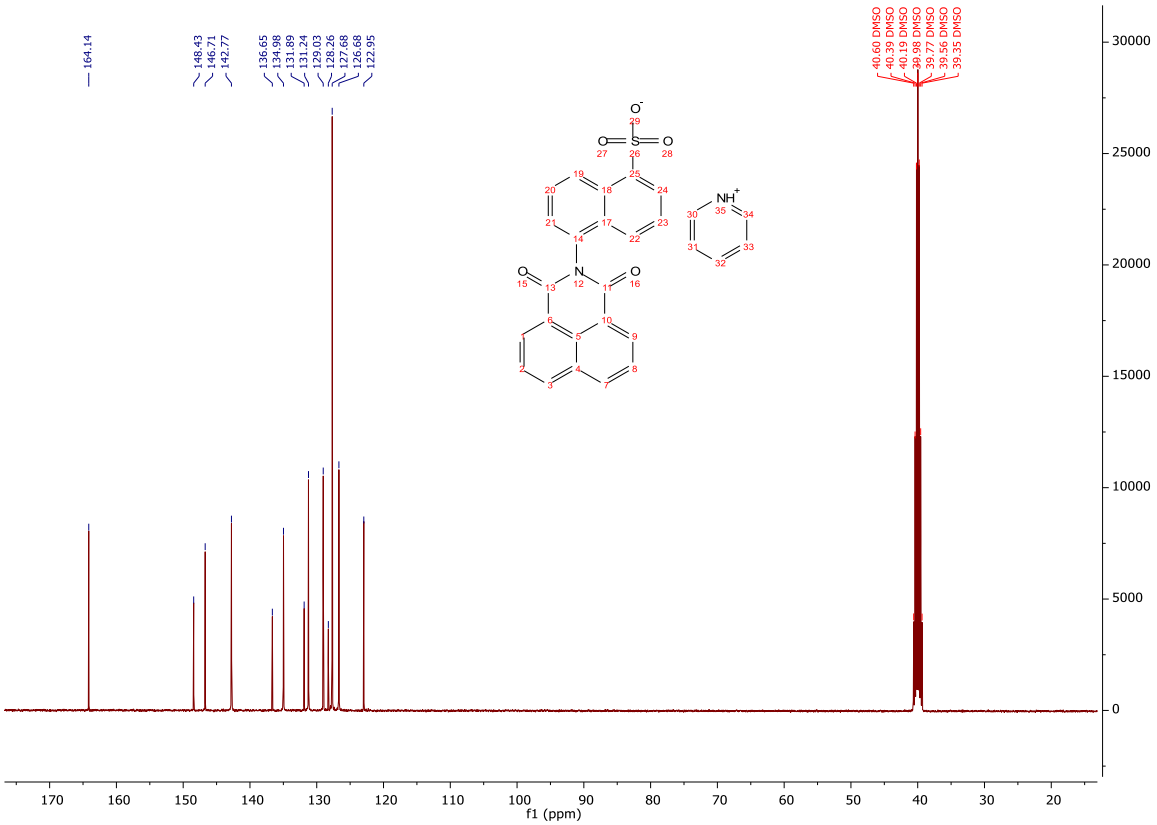

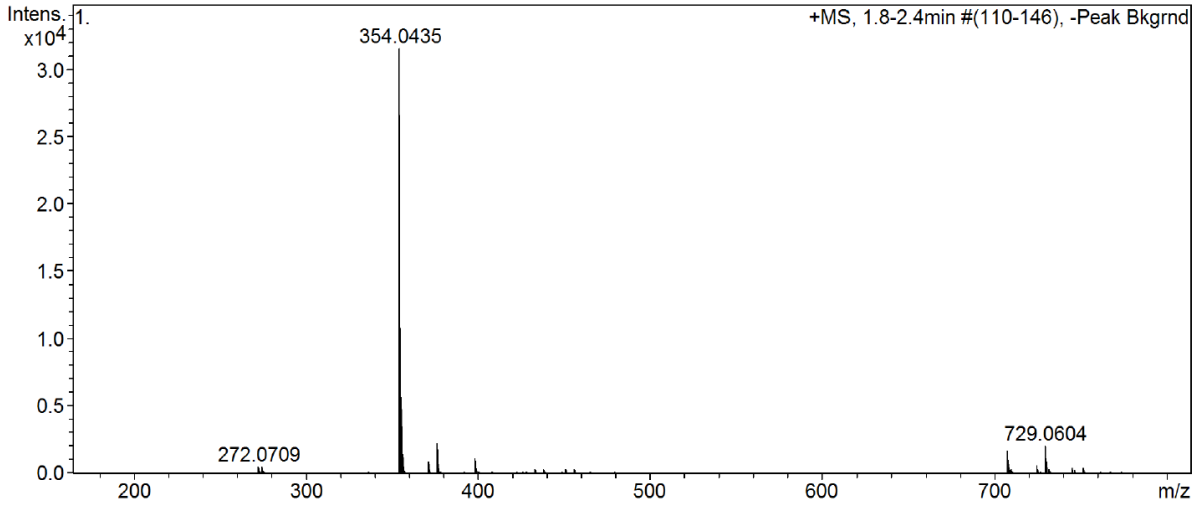

Meas. m/z	Formula	m/z	err [ppm]	err [mDa]	# Sigma	mSigma	rdb	e⁻ Conf	N-Rule
354.0435	C 18 H 12 N O 5 S	354.0431	-1.2	-0.4	1	18.4	13.5	even	ok

A.2 NMR and MS data of Ar(4-SO_3)-Nap-NO_2·ImdH (A_2·ImdH)

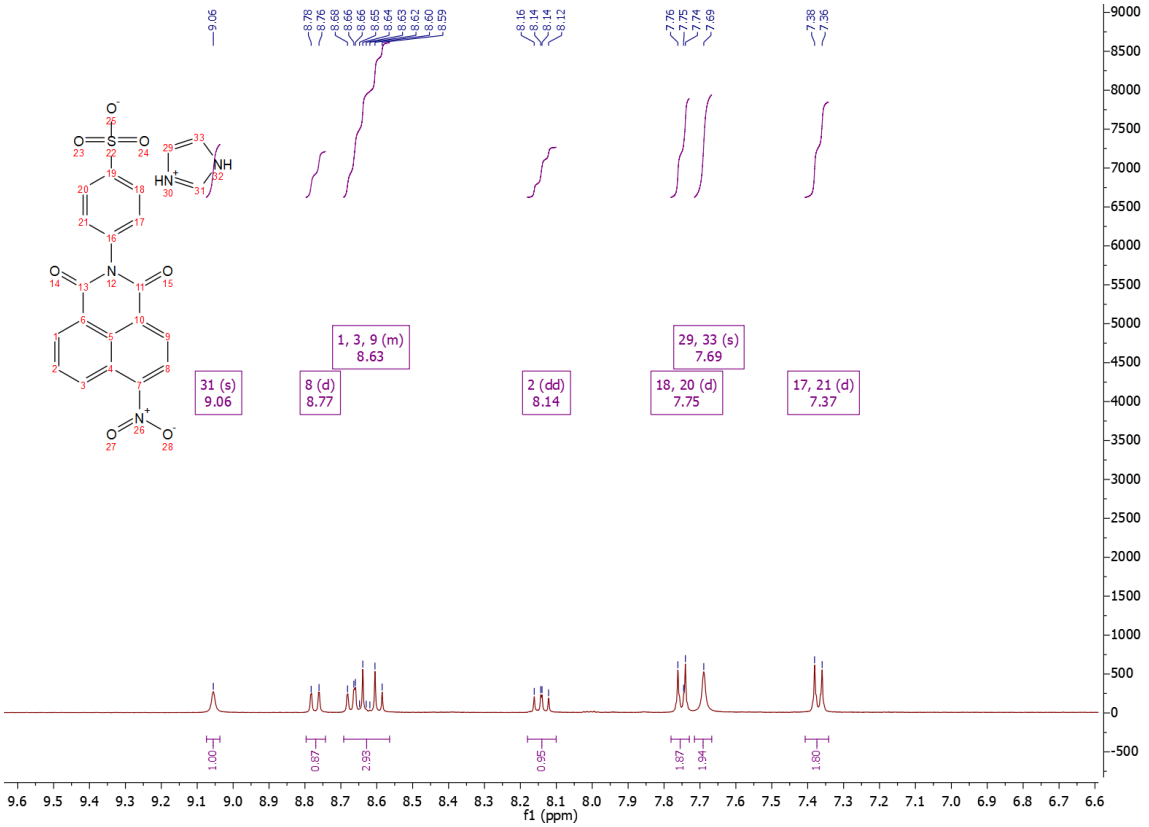

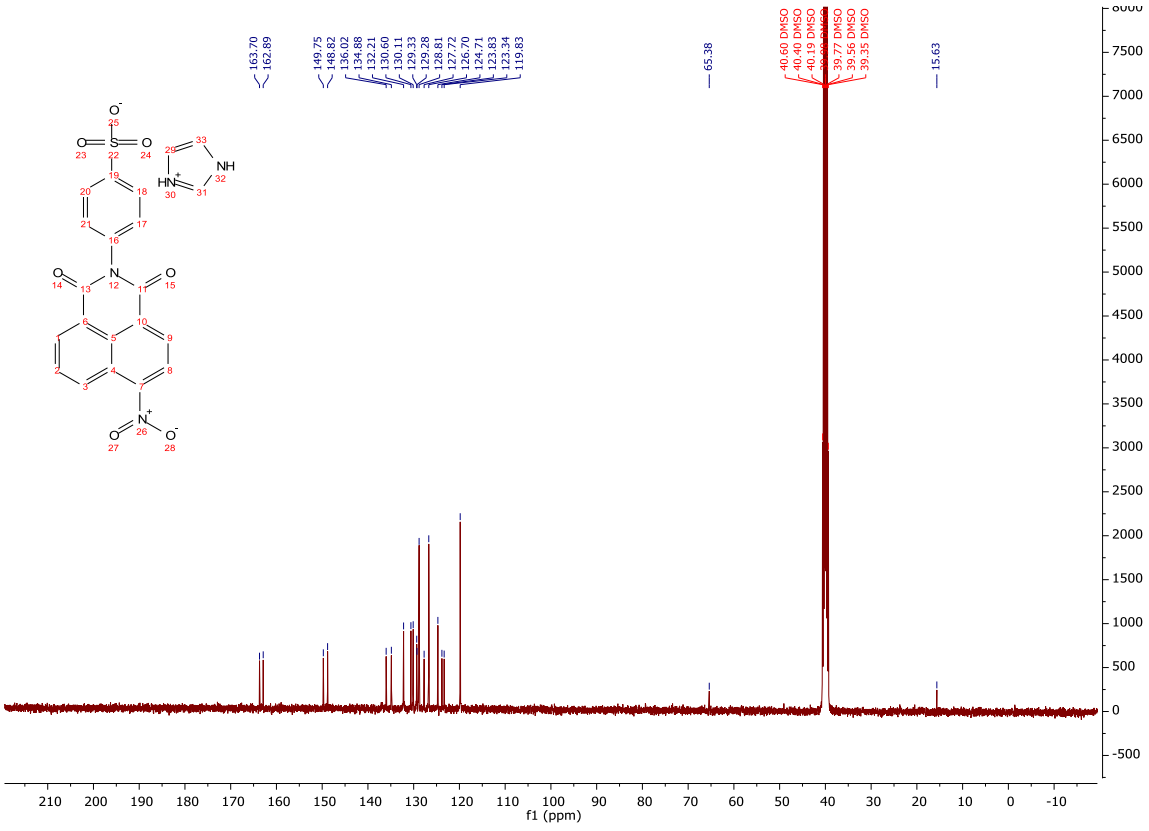

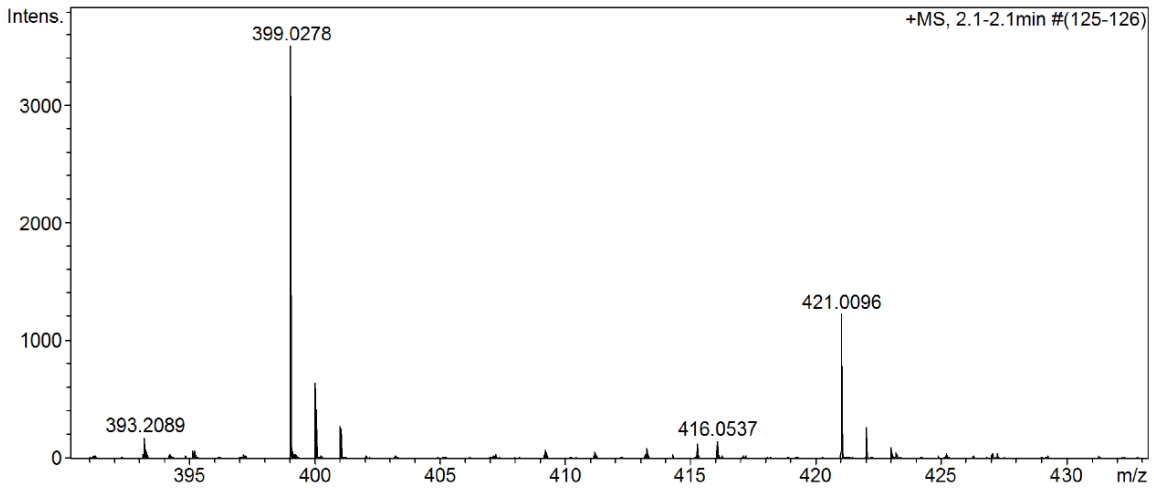

Meas. m/z	Formula	m/z	err [ppm]	err [mDa]	# Sigma	mSigma	rdb	e¯ Conf	N-Rule
399.0278	C 18 H 11 N 2 O 7 S	399.0281	0.9	0.4	1	15.5	14.5	even	ok

A.3 NMR and MS data of Ar(4-SO_3)-Nap-N(Me)$_2$·H (A_3·H)

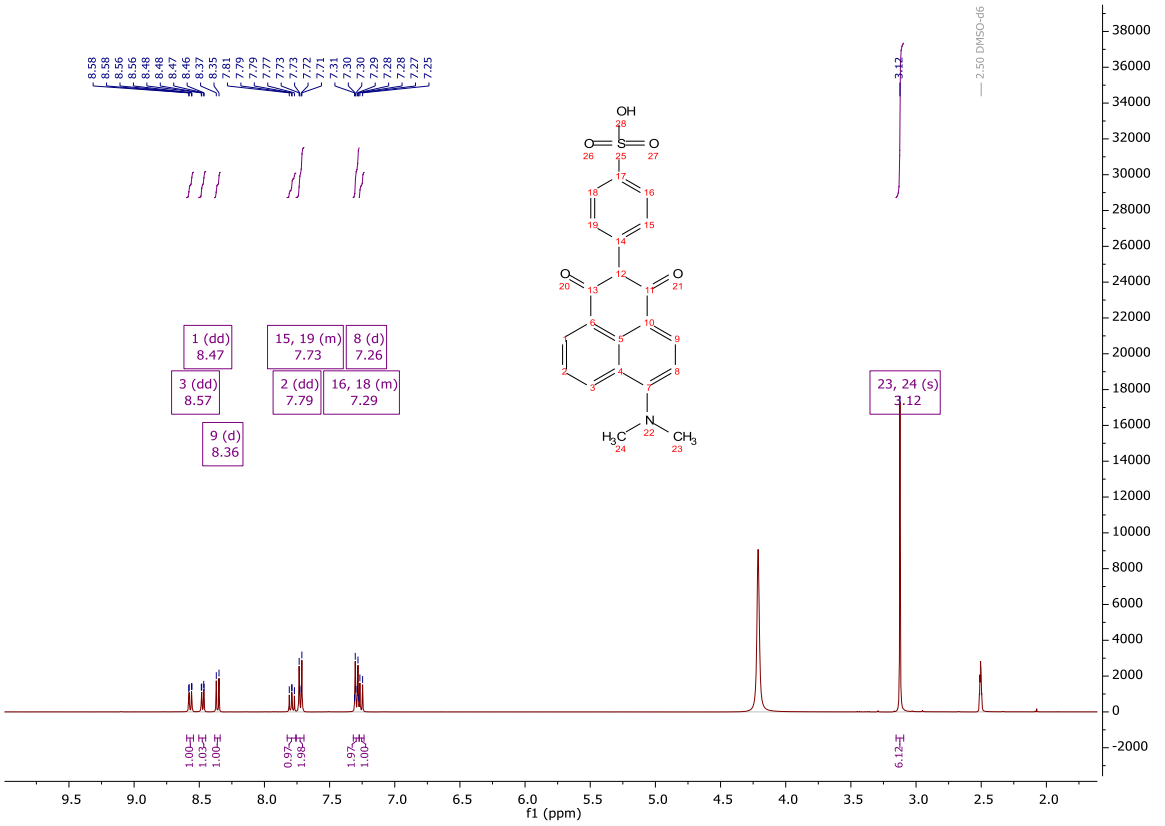

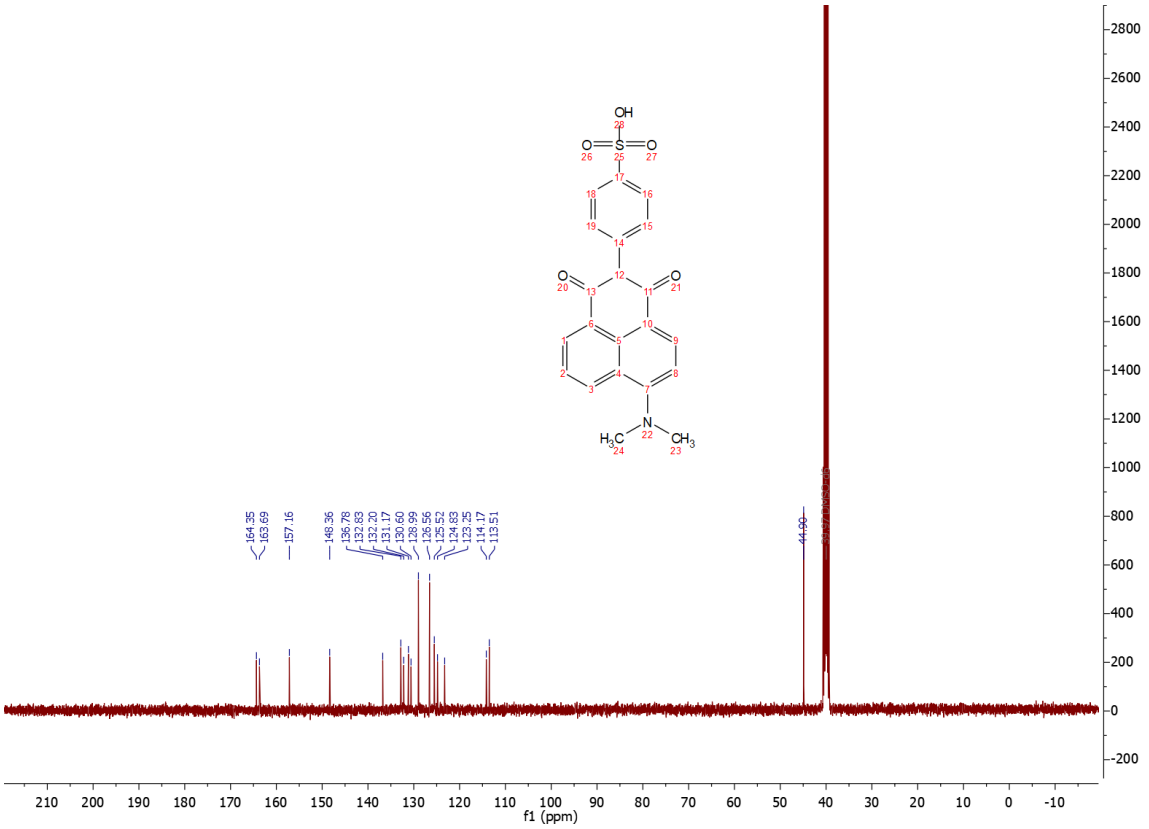

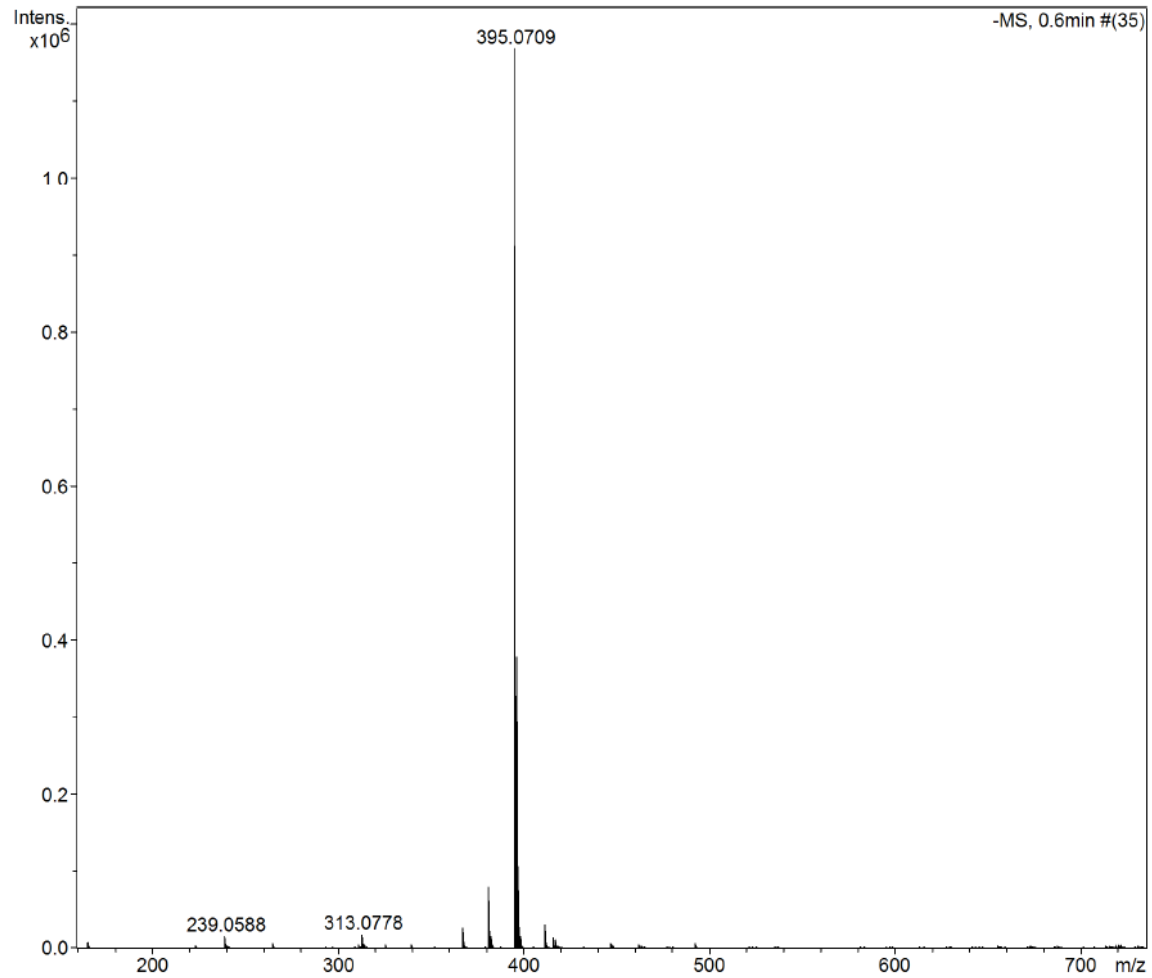

Meas. m/z	Formula	m/z	err [ppm]	err [mDa]	# Sigma	mSigma	rdb	e⁻ Conf	N-Rule
395.0709	C 20 H 15 N 2 O 5 S	395.0707	-0.4	-0.2	2	45.7	14.5	even	ok

A.4 NMR and MS data of Ar(4-SO_3)-Nap-NH_2·H (A_4·H)

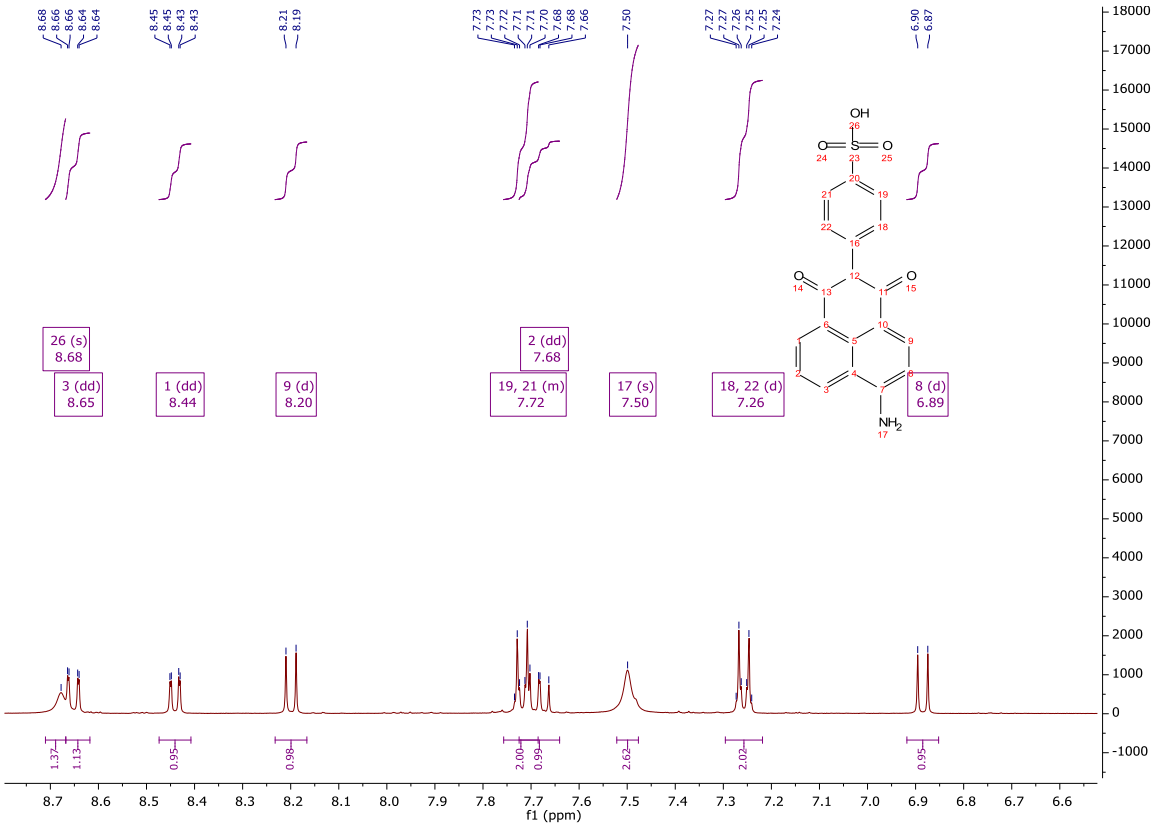

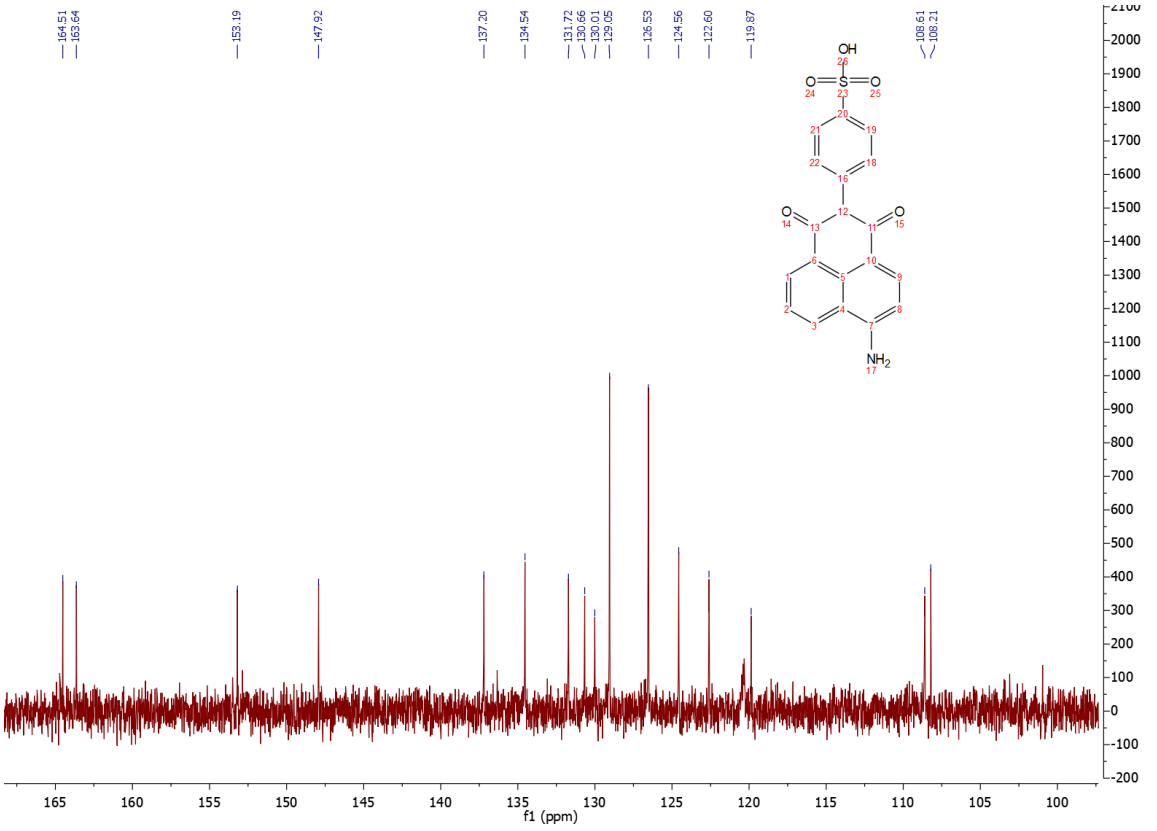

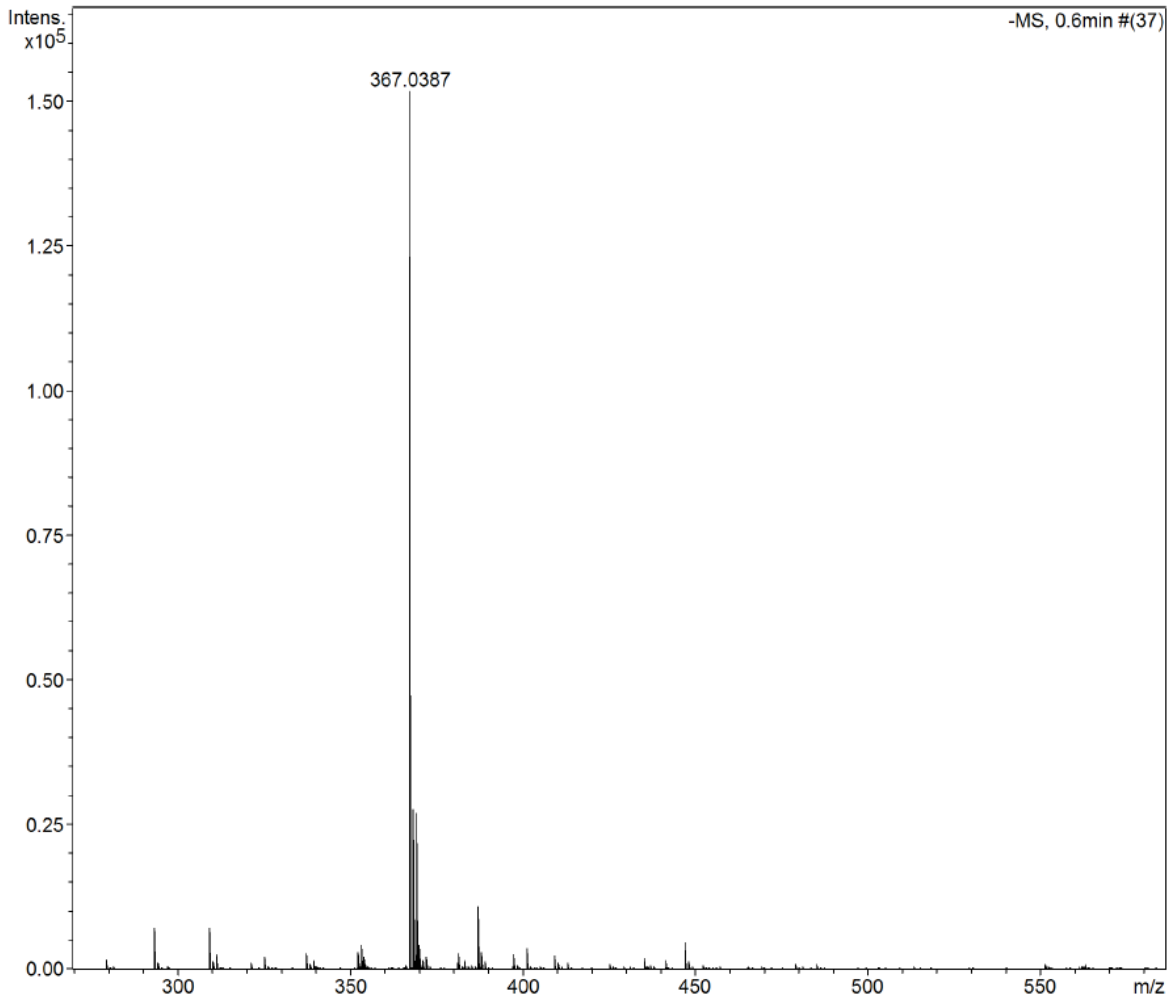

Meas. m/z	Formula	m/z	err [ppm]	err [mDa]	# Sigma	mSigma	rdb	e⁻ Conf	N-Rule
367.0387	C 18 H 11 N 2 O 5 S	367.0394	1.9	0.7	2	40.9	14.5	even	ok

A.5 MS data of Ar(4-SO_3)-Nap-Tröger's base·2H (A_5·2H)

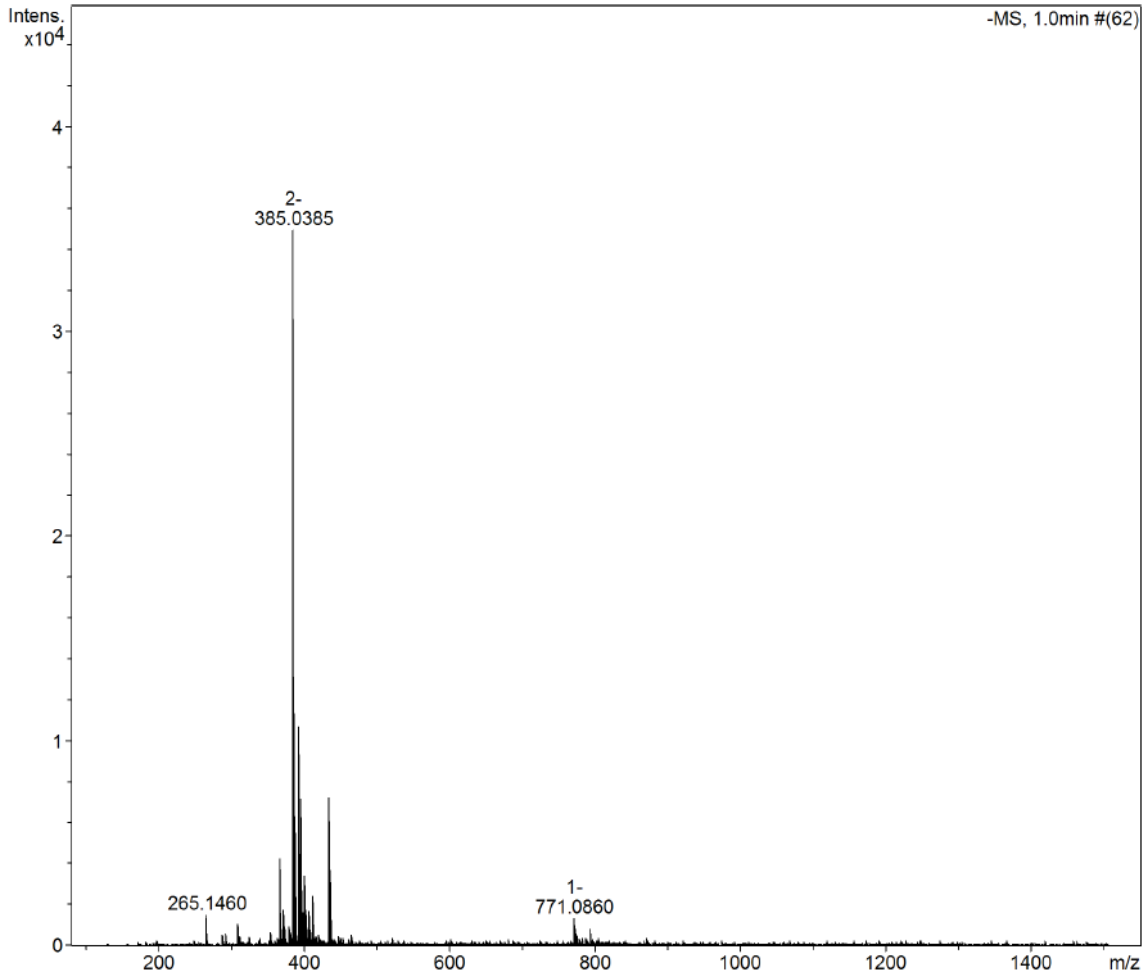

Meas. m/z	Formula	m/z	err [ppm]	err [mDa]	# Sigma	mSigma	rdb	e¯ Conf	N-Rule
771.0860	C 39 H 23 N 4 O 10 S 2	771.0861	0.1	0.1	8	185.2	30.5	even	ok

A.6 NMR and MS data of Ar(3-SO_3)-Nap-H·PyH (A_6·PyH)

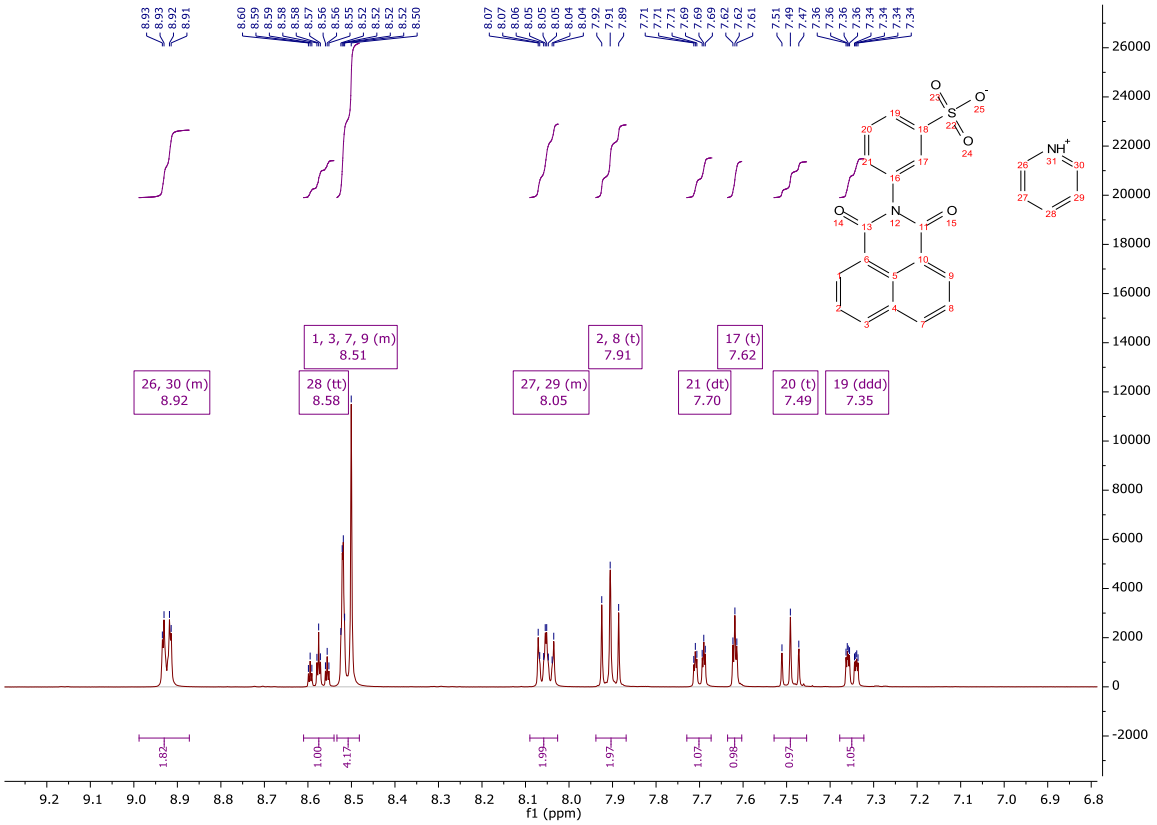

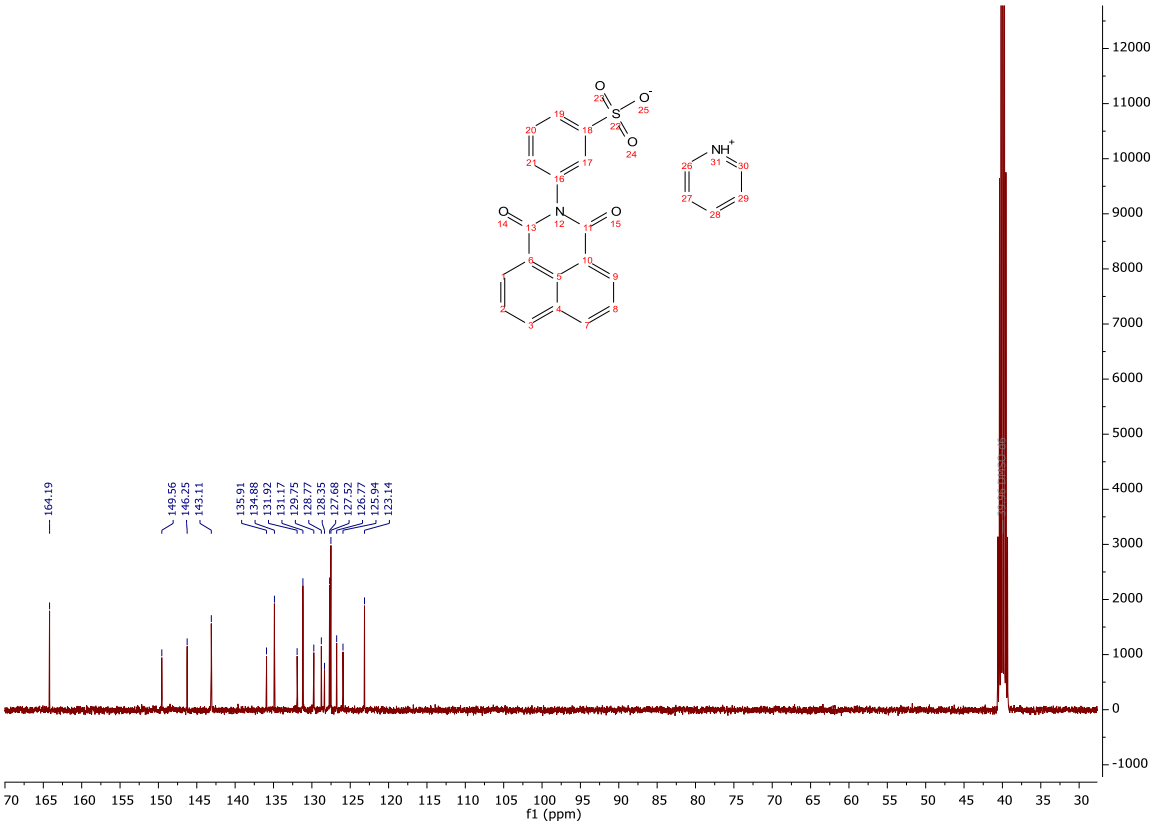

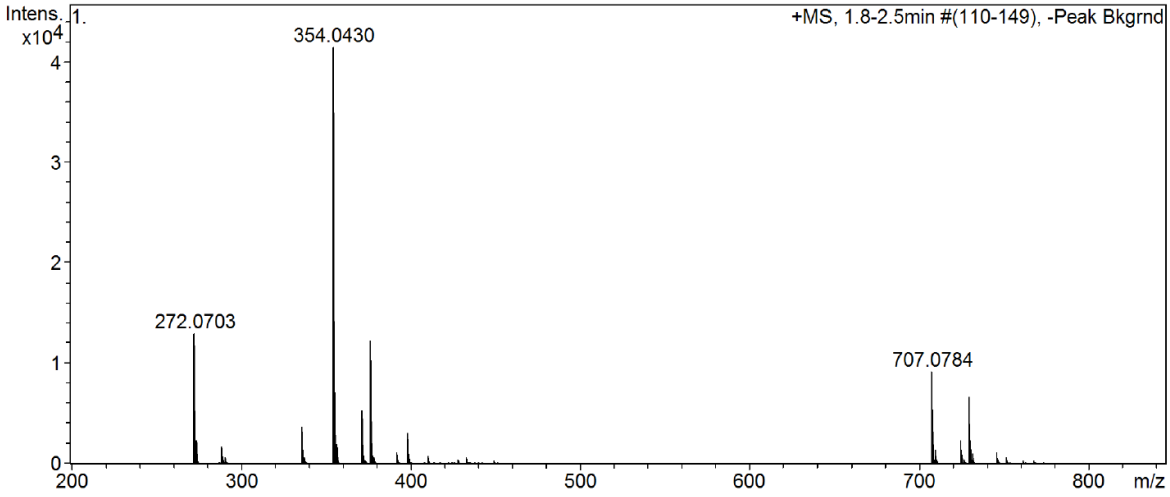

Meas. m/z	Formula	m/z	err [ppm]	err [mDa]	# Sigma	mSigma	rdb	e⁻ Conf	N-Rule
354.0430	C 18 H 12 N O 5 S	354.0431	0.2	0.1	1	14.3	13.5	even	ok

A.7 NMR and MS data of Ar(3-SO_3)-Nap-NO_2·ImdH (A_7 ·ImdH)

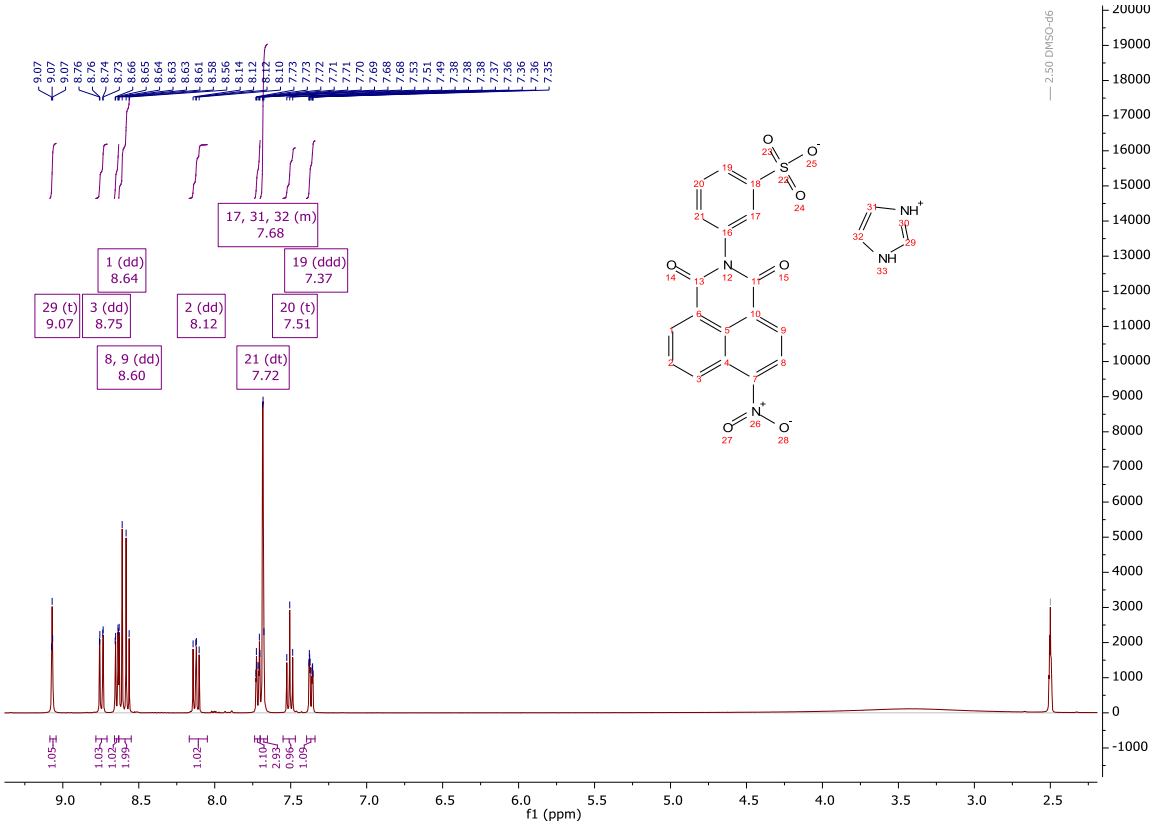

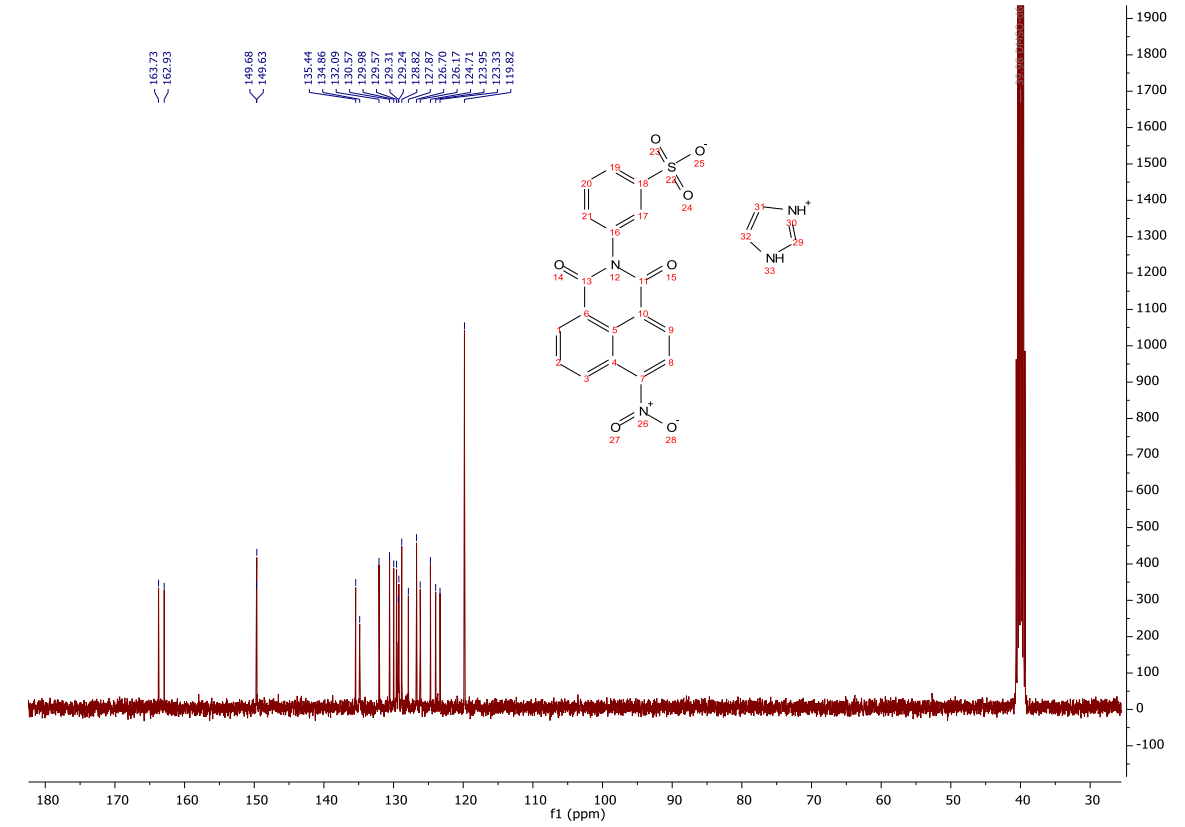

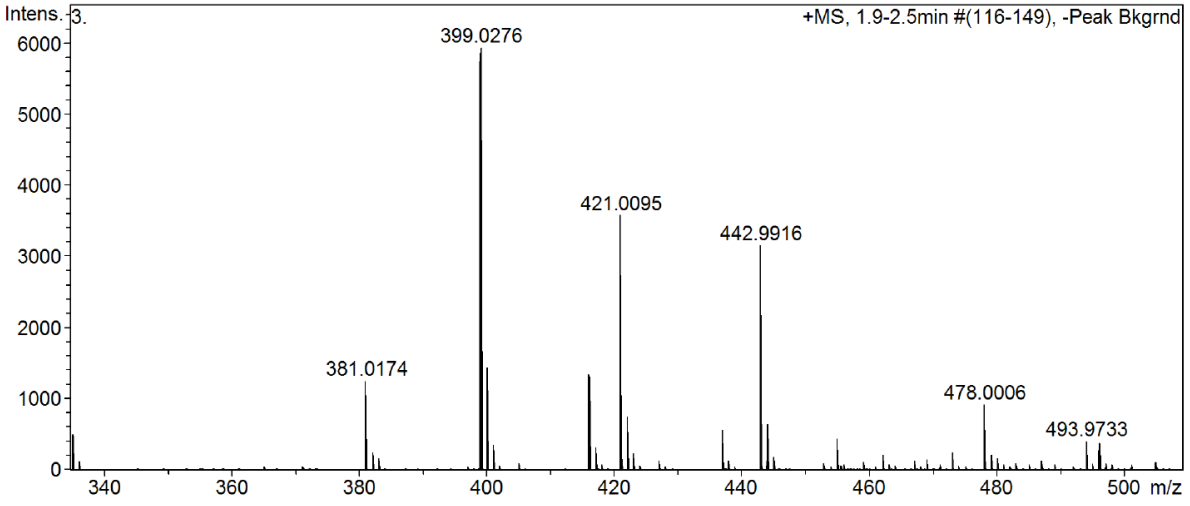

Meas. m/z	Formula	m/z	err [ppm]	err [mDa]	# Sigma	mSigma	rdb	e⁻ Conf	N-Rule
399.0276	C 18 H 11 N 2 O 7 S	399.0281	1.3	0.5	2	20.7	14.5	even	ok

A.8 NMR and MS data of Ar(3-SO_3)-Nap-N(Me)$_2$·H (A_8·H)

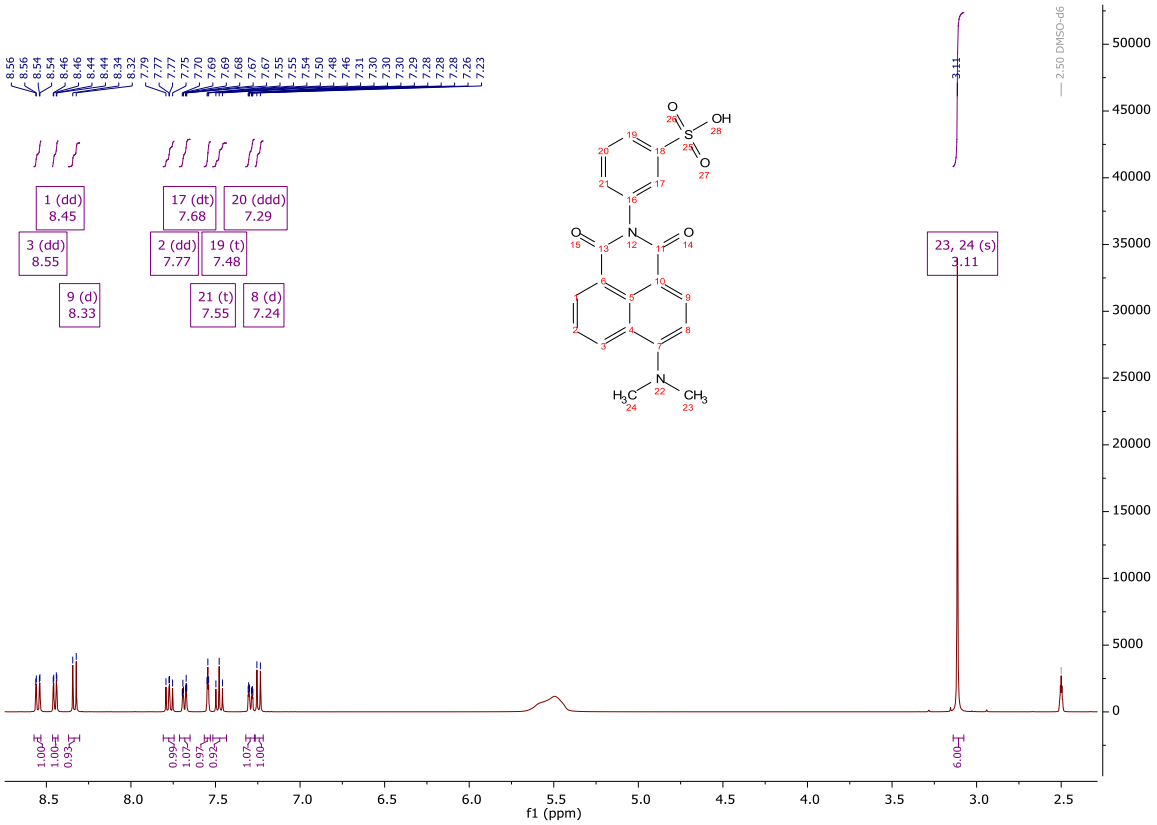

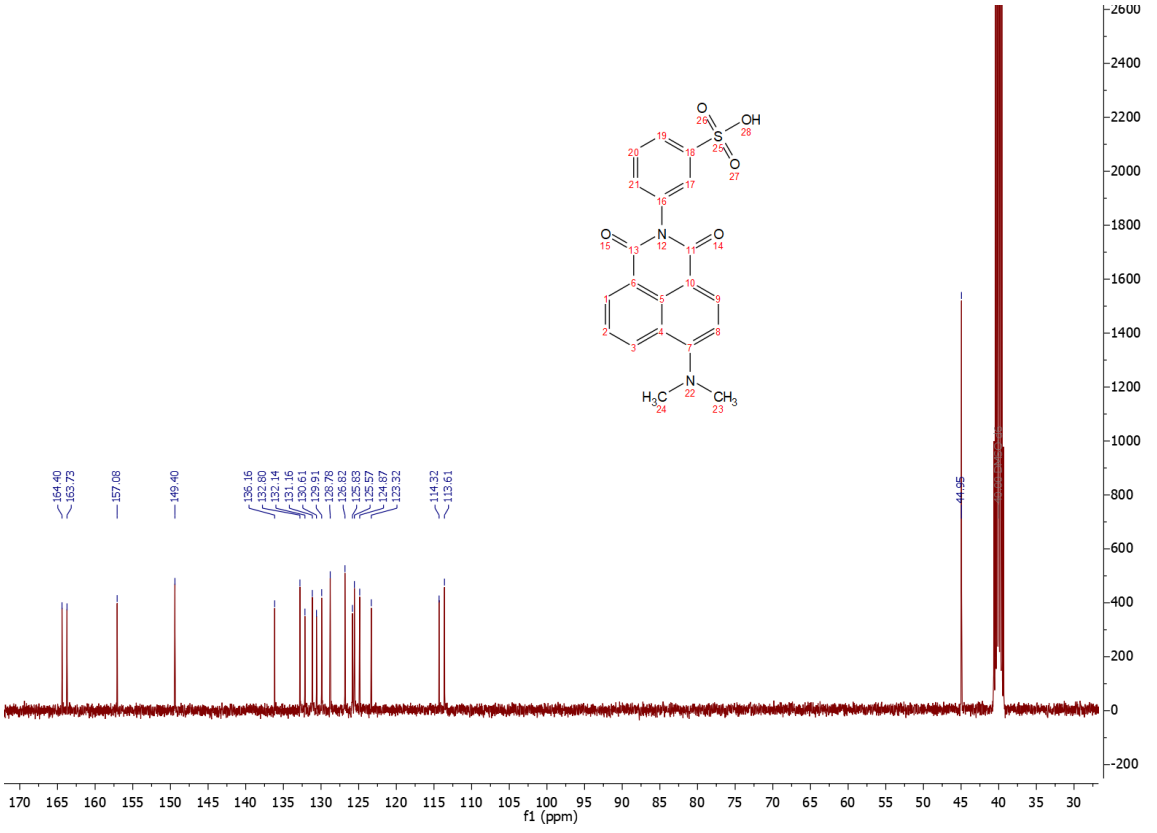

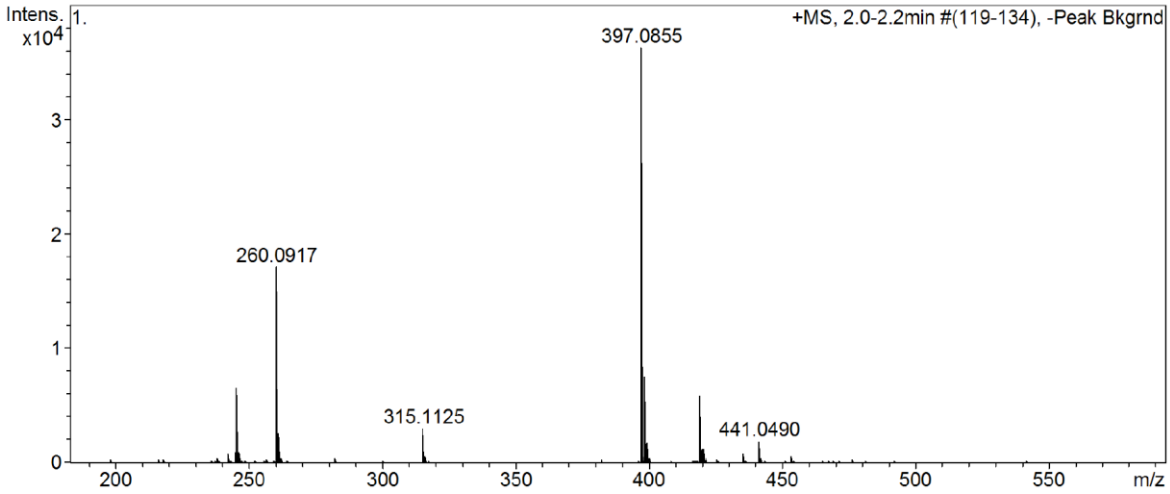

Meas. m/z	Formula	m/z	err [ppm]	err [mDa]	# Sigma	mSigma	rdb	e⁻ Conf	N-Rule
397.0855	C 20 H 17 N 2 O 5 S	397.0853	-0.6	-0.3	1	21.6	13.5	even	ok

A.9 NMR and MS data of 5-Naph(1-SO_3)-Nap-H·PyH (A_9·PyH)

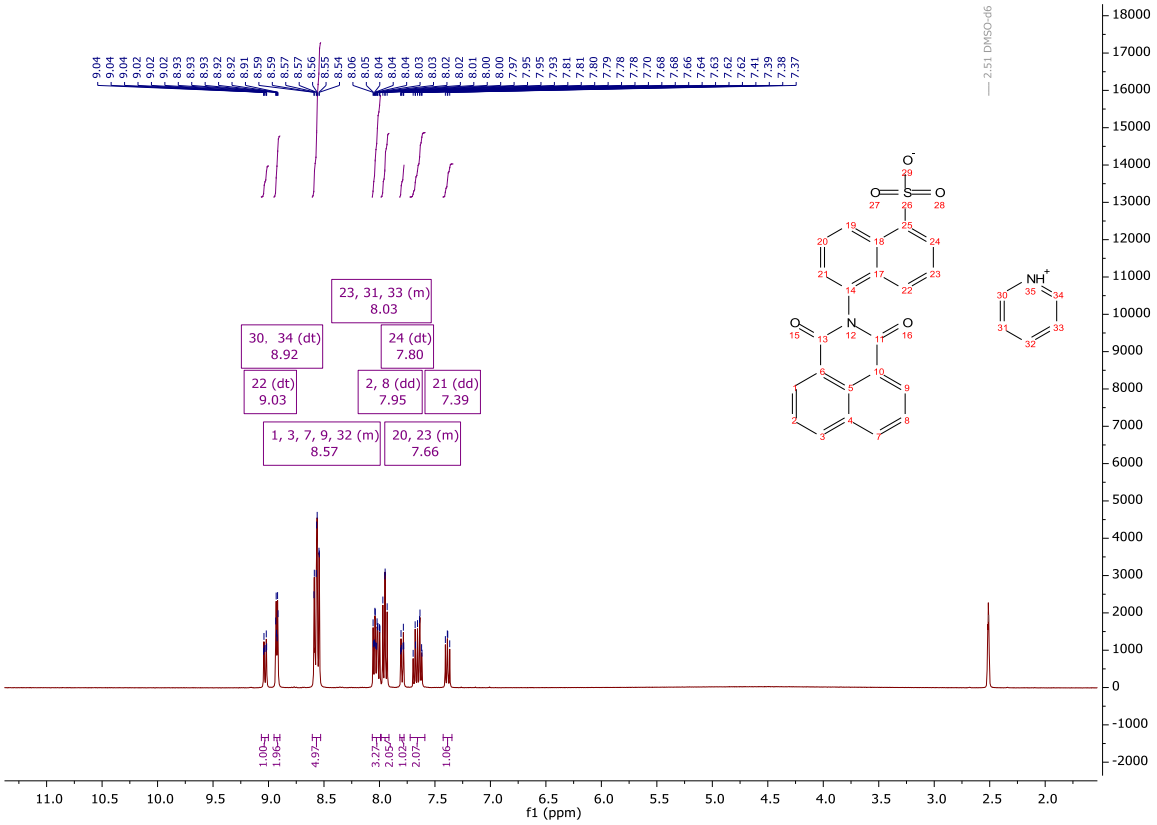

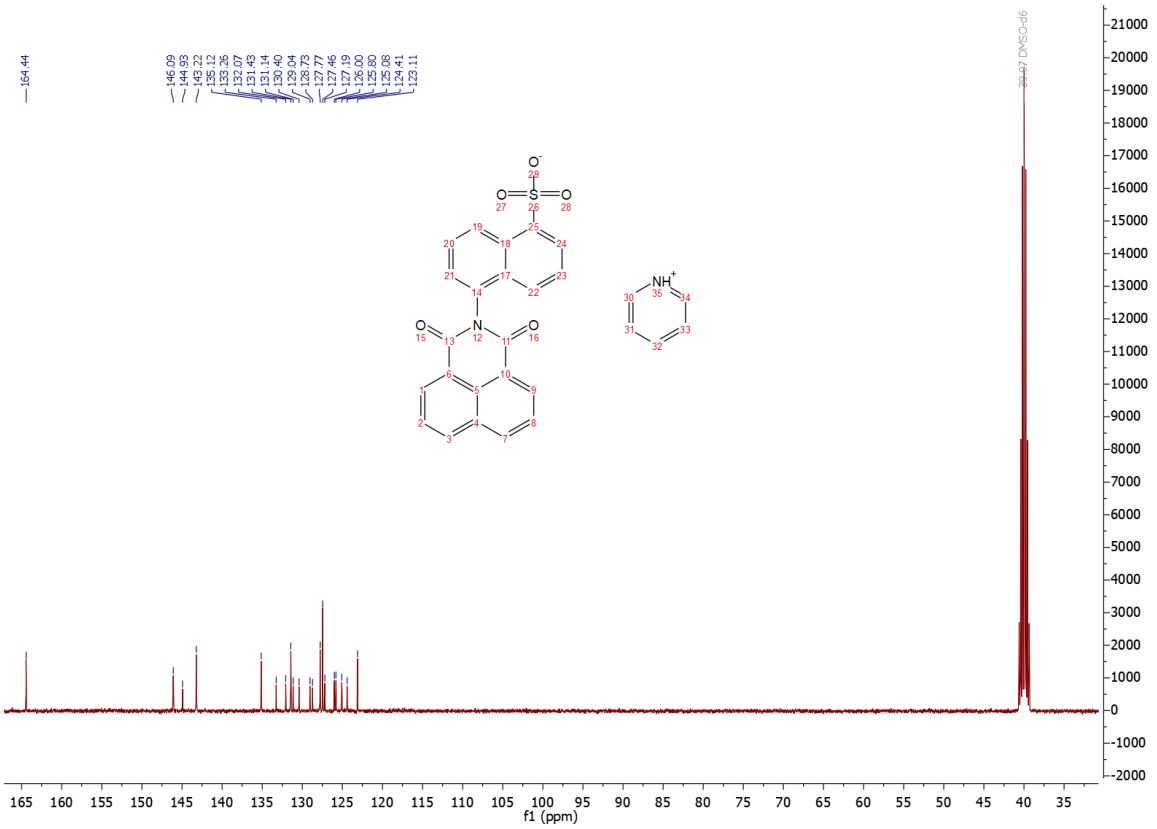

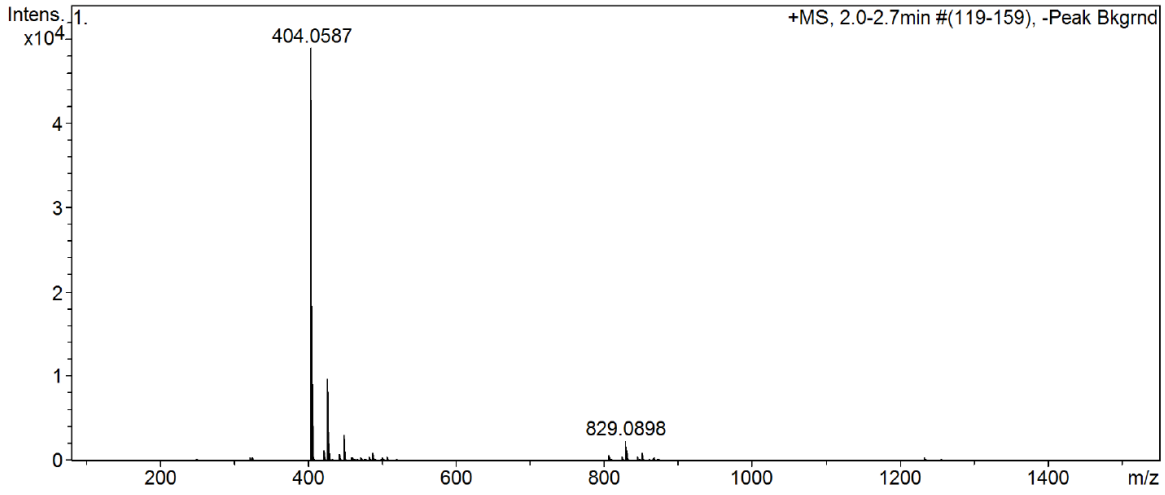

Meas. m/z	Formula	m/z	err [ppm]	err [mDa]	# Sigma	mSigma	rdb	e⁻ Conf	N-Rule
404.0587	C 22 H 14 N O 5 S	404.0587	0.1	0.1	4	26.4	16.5	even	ok

A.10 NMR and MS data of 5-Naph(1-SO_3)-Nap-NO_2·PyH (A_{10}·PyH)

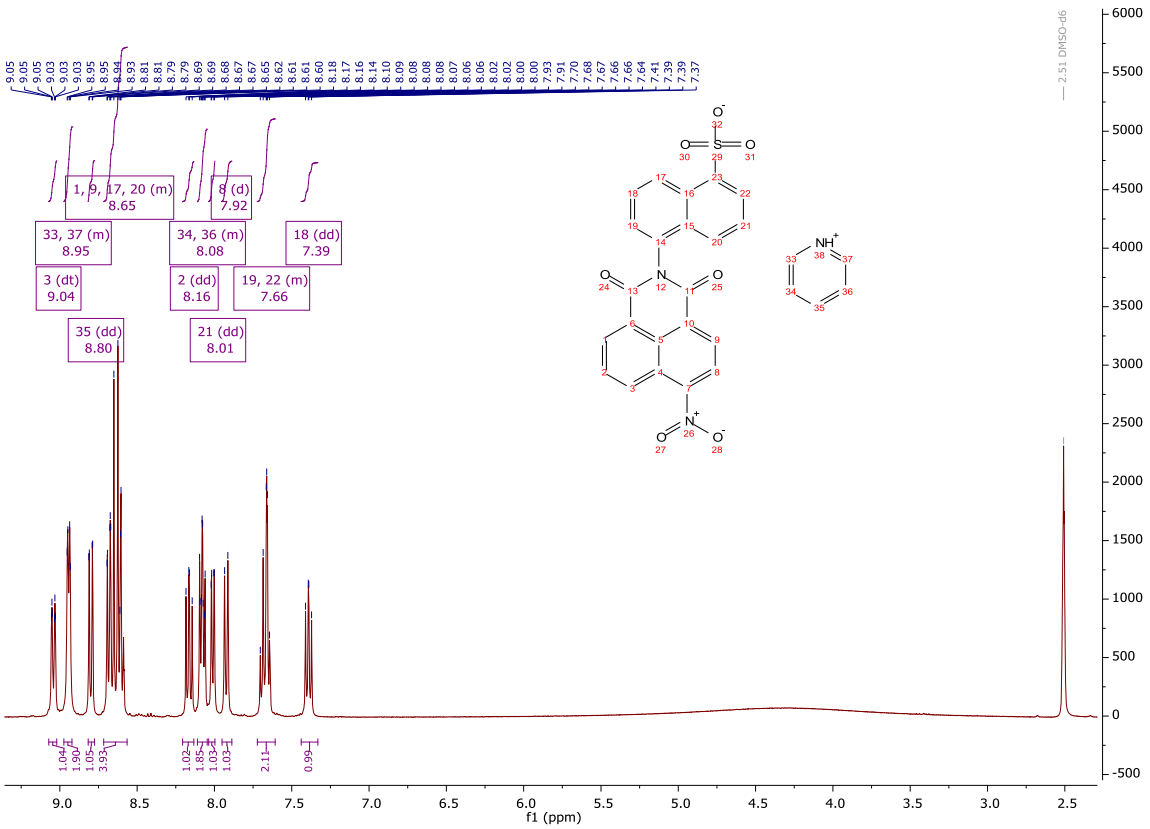

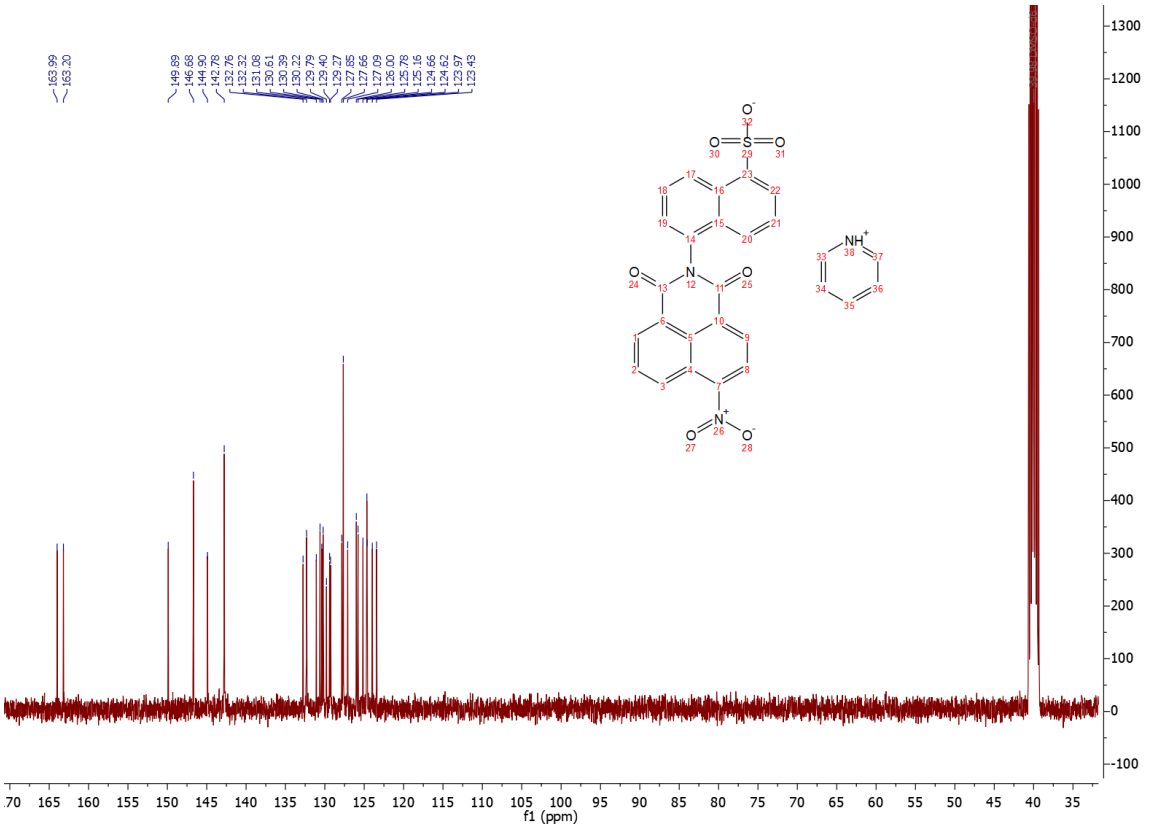

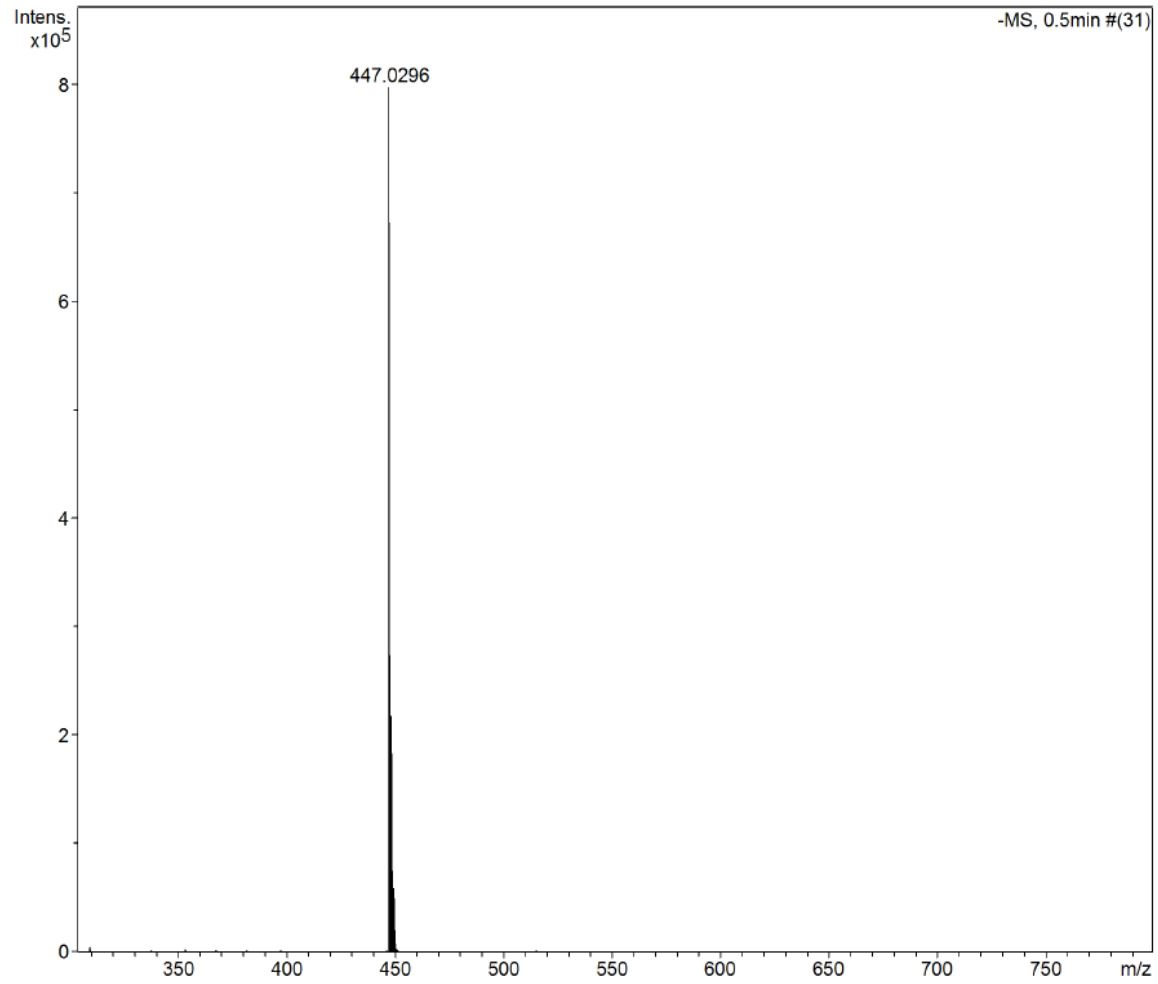

Meas. m/z	Formula	m/z	err [ppm]	err [mDa]	# Sigma	mSigma	rdb	e Conf	N-Rule
447.0296	C 22 H 11 N 2 O 7 S	447.0292	-0.8	-0.4	1	12.7	18.5	even	ok

A.11 NMR and MS data of 5-Naph(1-SO_3)-Nap-N(Me)$_2$·H (A_{11}·H)

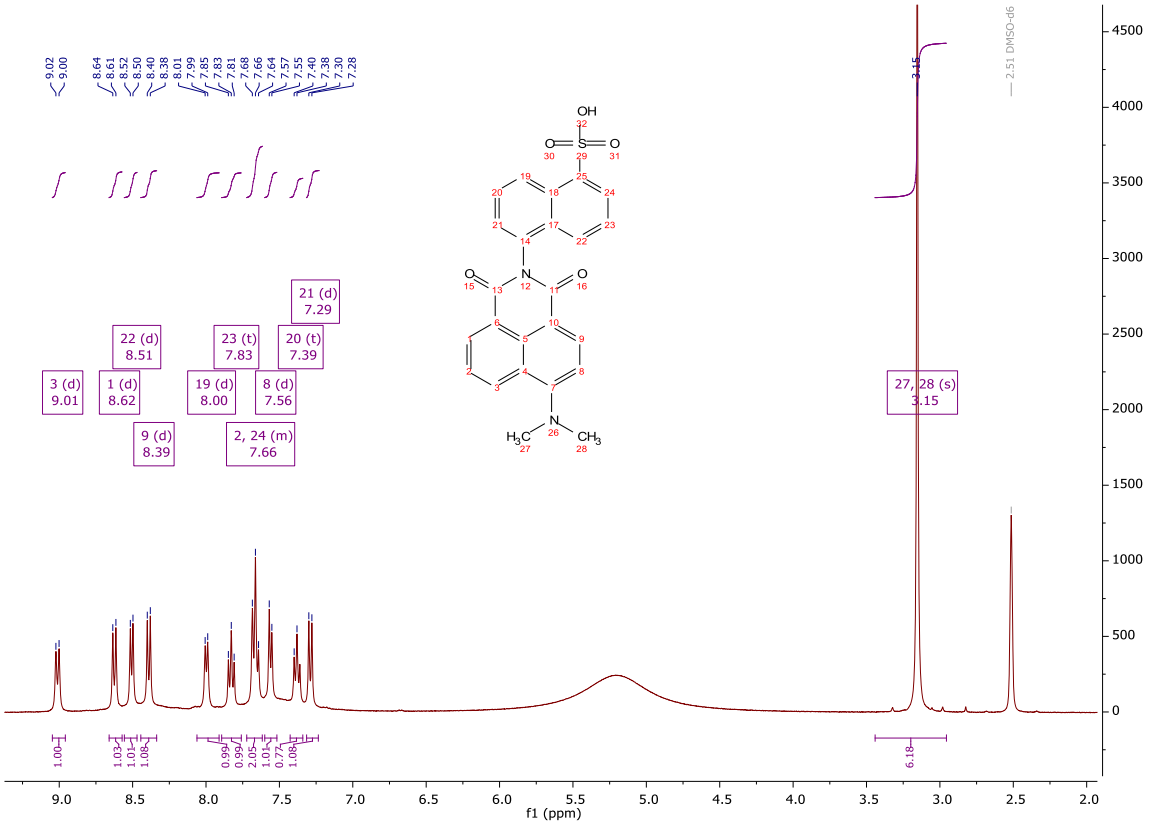

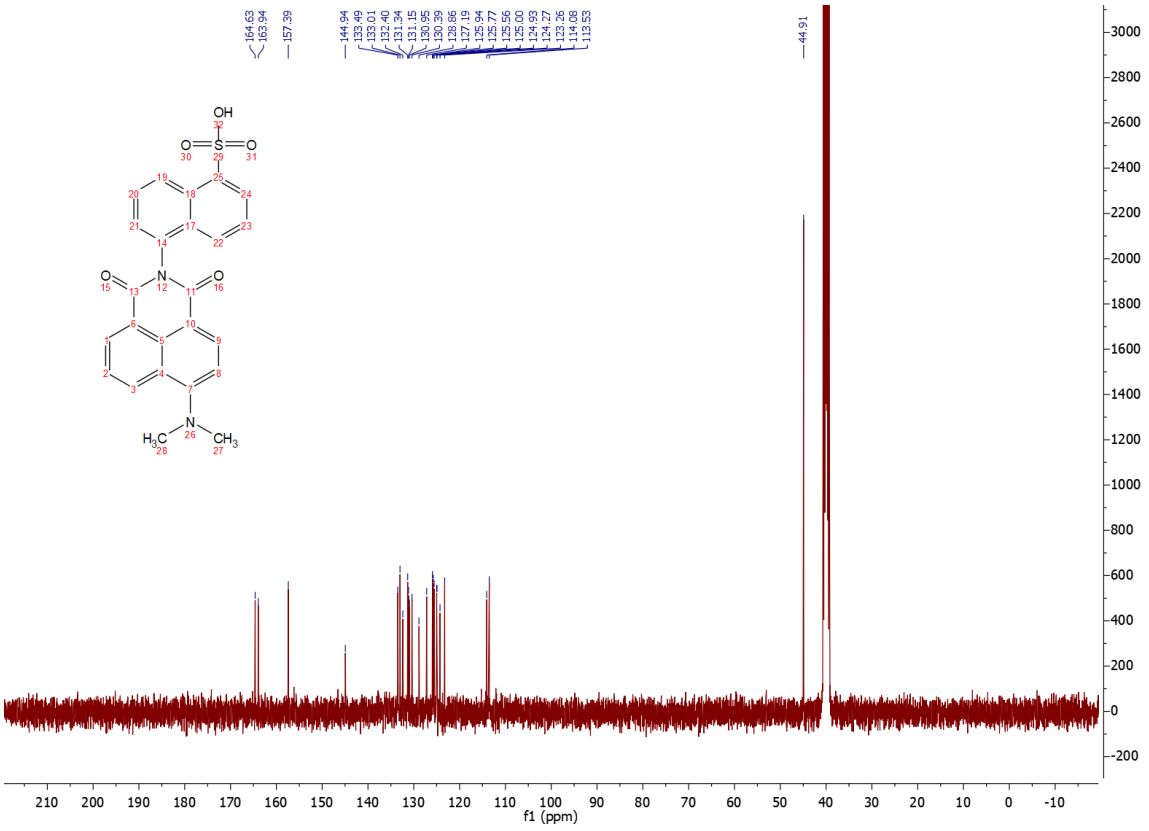

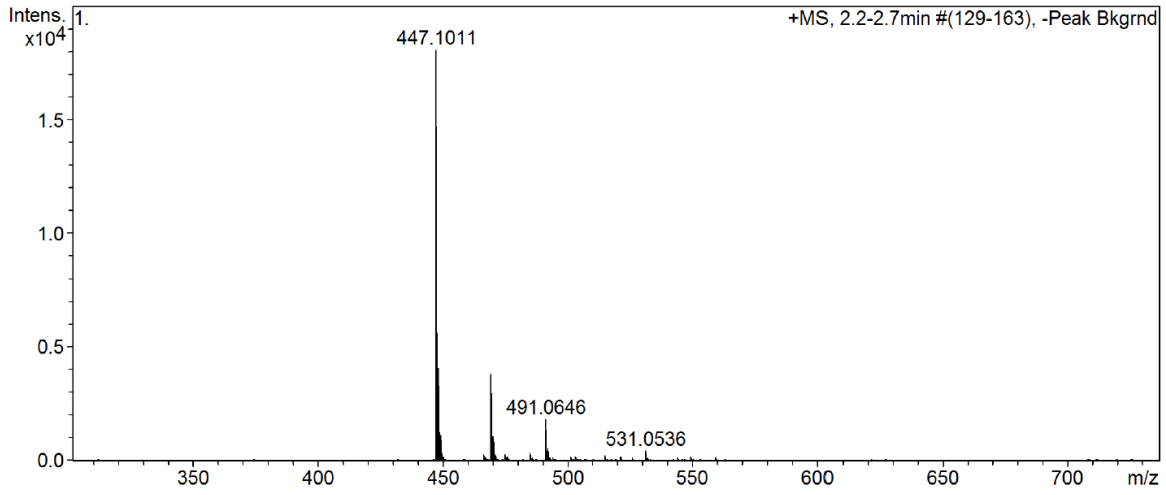

Meas. m/z	Formula	m/z	err [ppm]	err [mDa]	# Sigma	mSigma	rdb	e⁻ Conf	N-Rule
447.1011	C 24 H 19 N 2 O 5 S	447.1009	-0.4	-0.2	4	29.4	16.5	even	ok

A.12 NMR and MS data of 5-Naph(2-SO_3)-Nap-H·PyH (A_{12}·PyH)

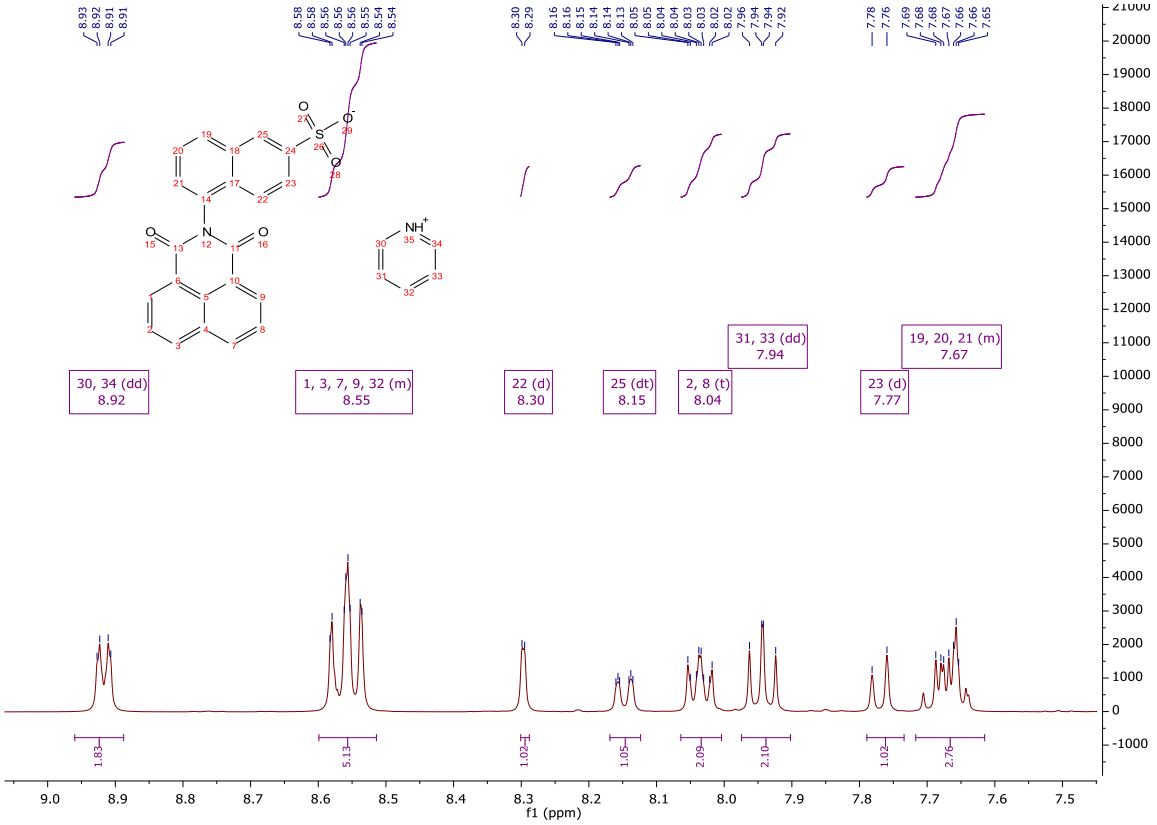

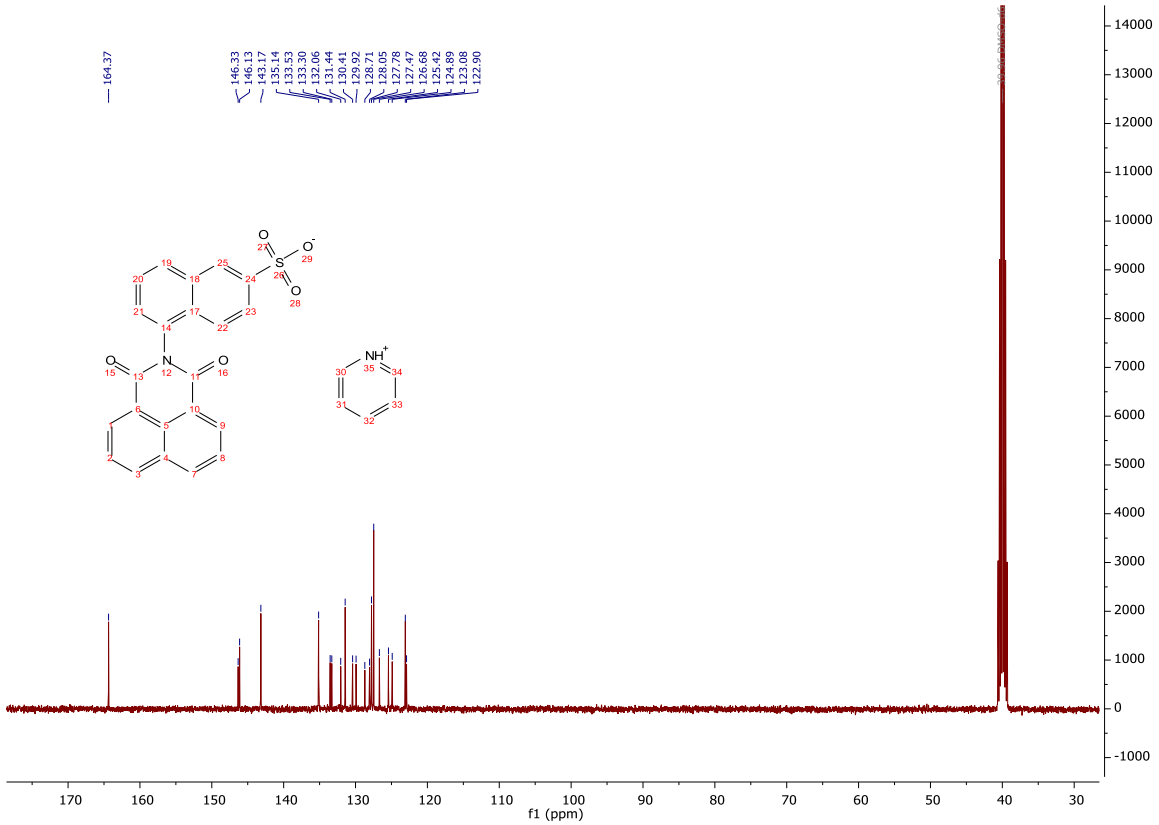

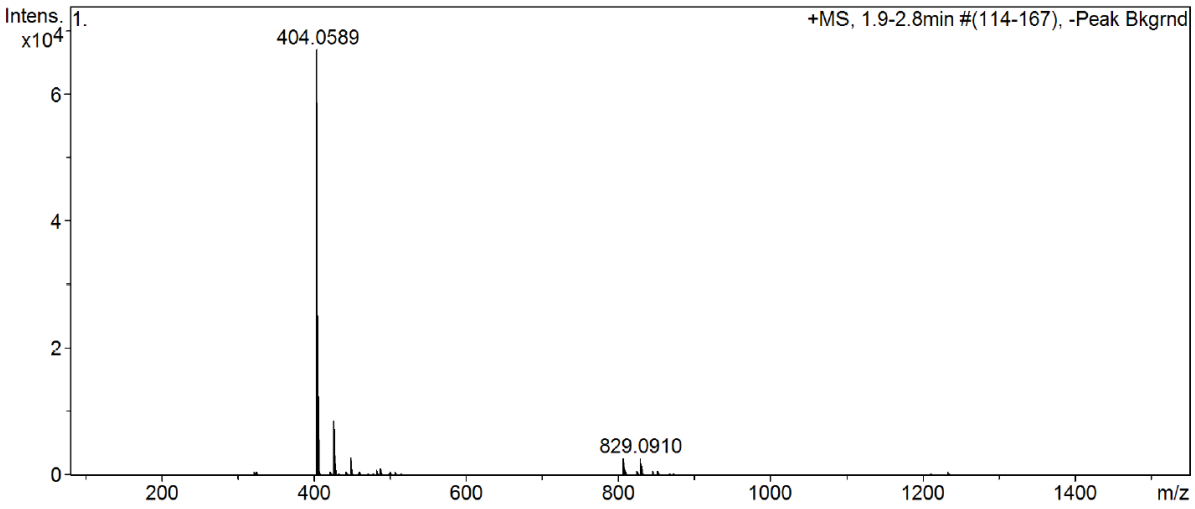

Meas. m/z	Formula	m/z	err [ppm]	err [mDa]	# Sigma	mSigma	rdb	e Conf	N-Rule
404.0589	C 22 H 14 N O 5 S	404.0587	-0.4	-0.1	4	27.3	16.5	even	ok

A.13 NMR and MS data of 5-Naph(2-SO_3)-Nap-NO_2·PyH (A_{13}·PyH)

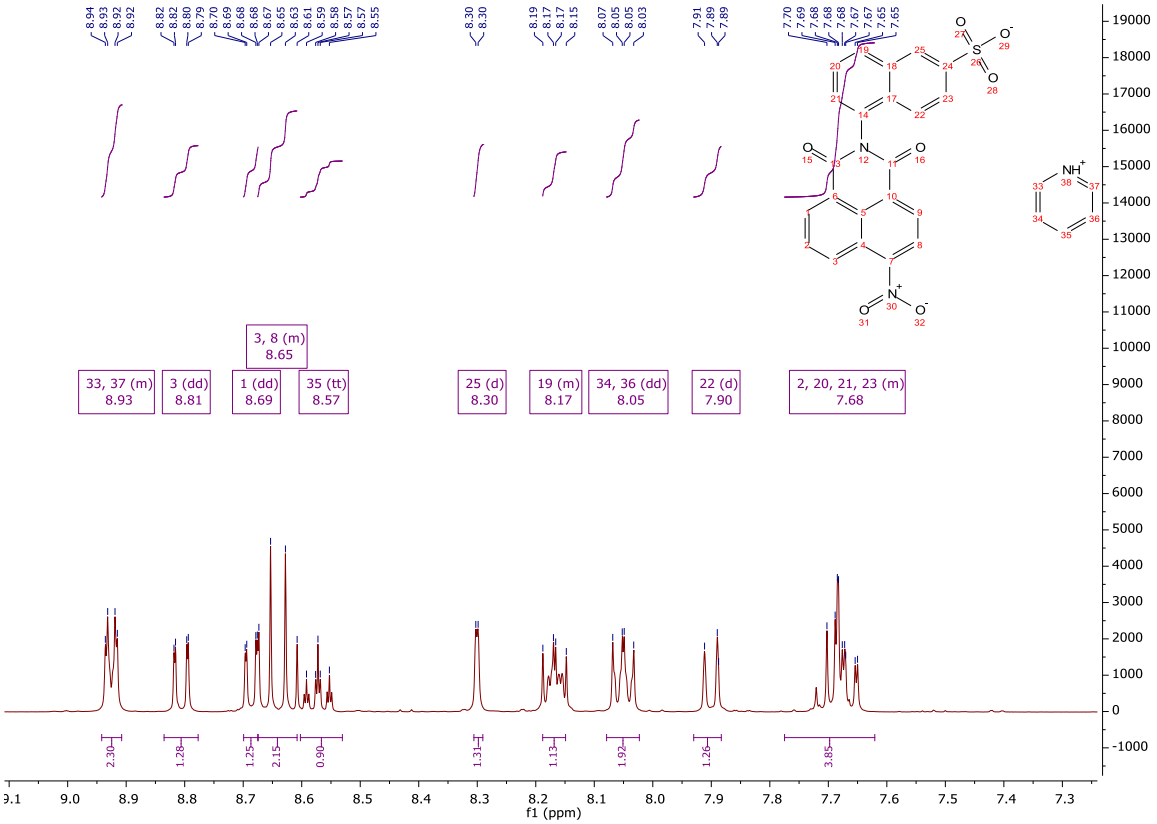

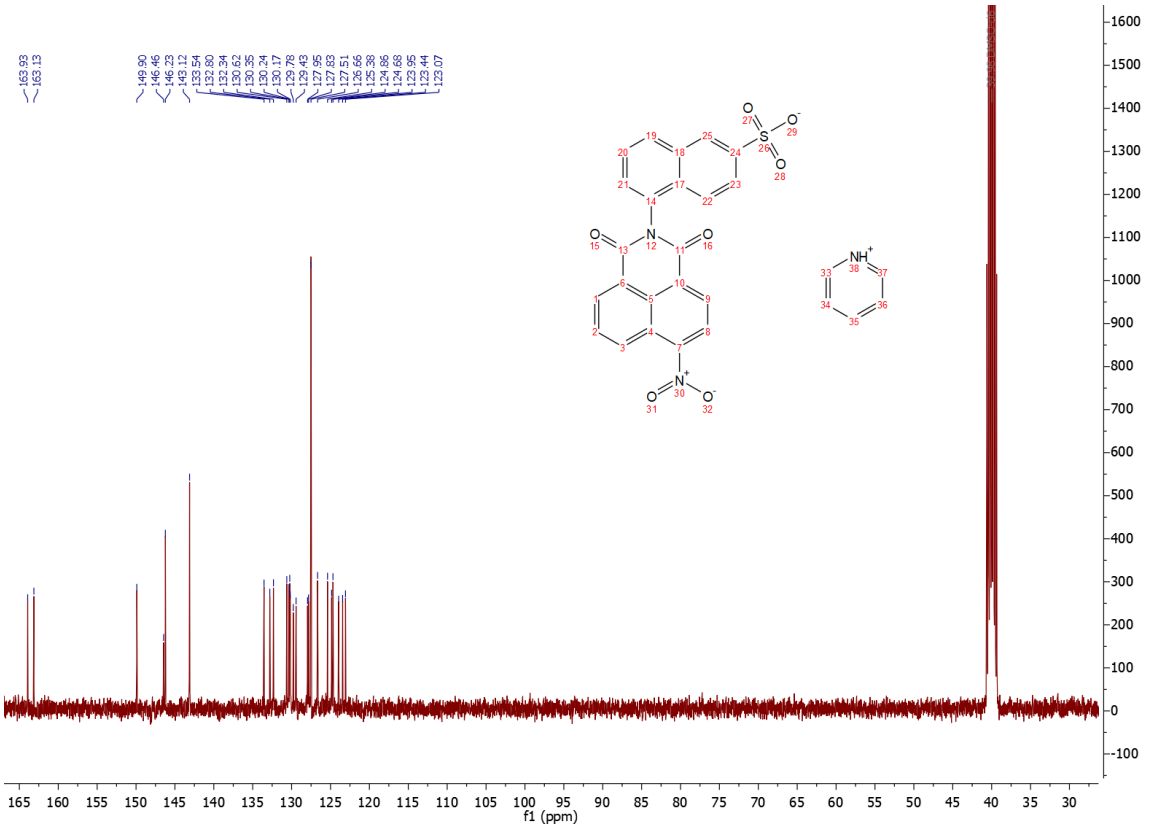

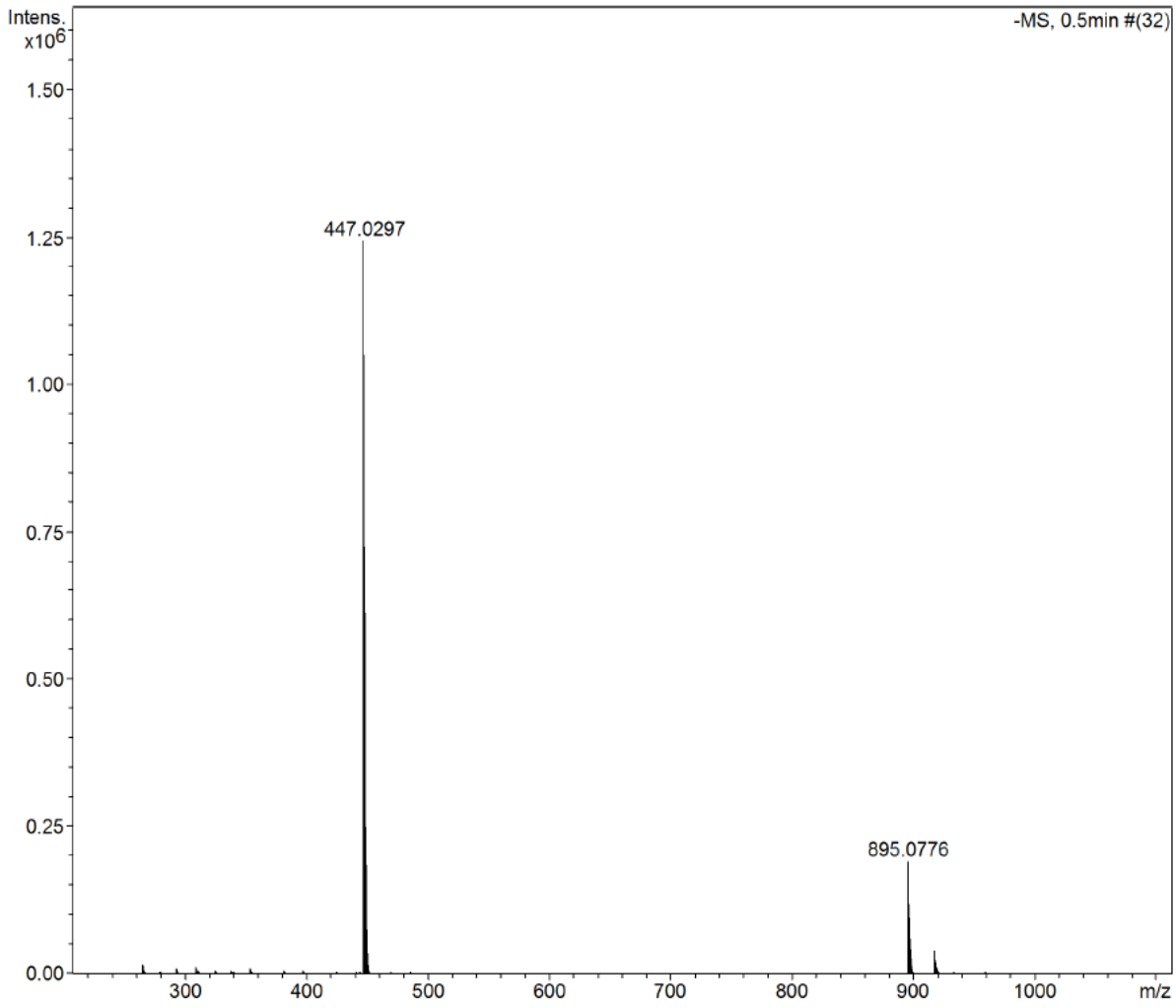

Meas. m/z	Formula	m/z	err [ppm]	err [mDa]	# Sigma	mSigma	rdb	e⁻ Conf	N-Rule
447.0297	C 22 H 11 N 2 O 7 S	447.0292	-1.1	-0.5	3	170.3	18.5	even	ok

A.14 NMR and MS data of 5-Naph(2-SO_3)-Nap-N(Me)$_2$·H (A_{14}·H)

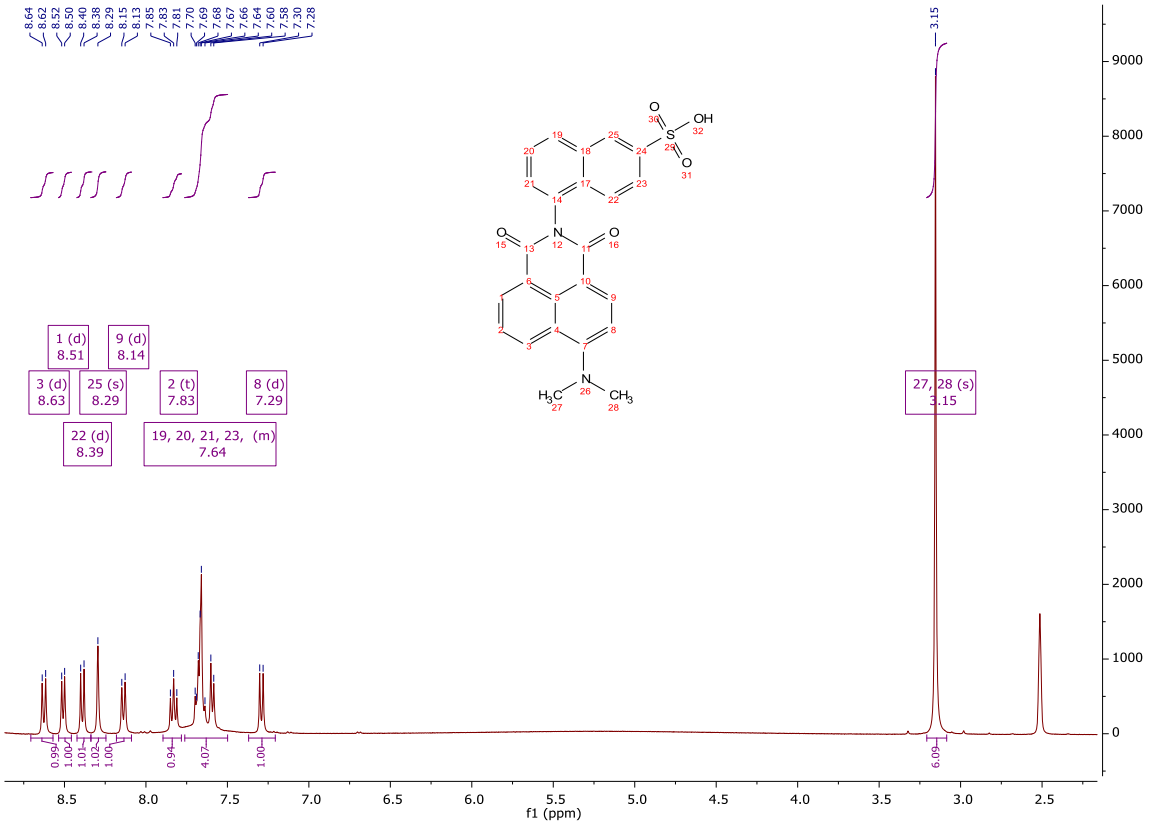

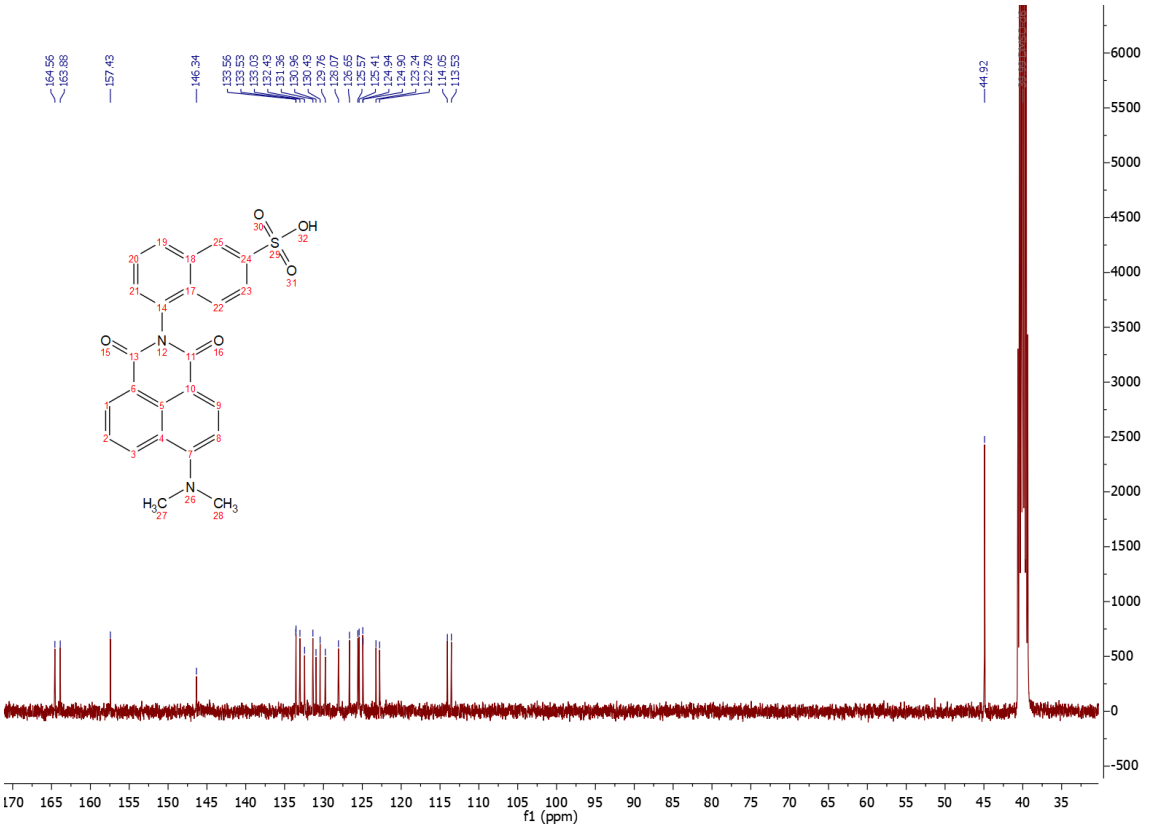

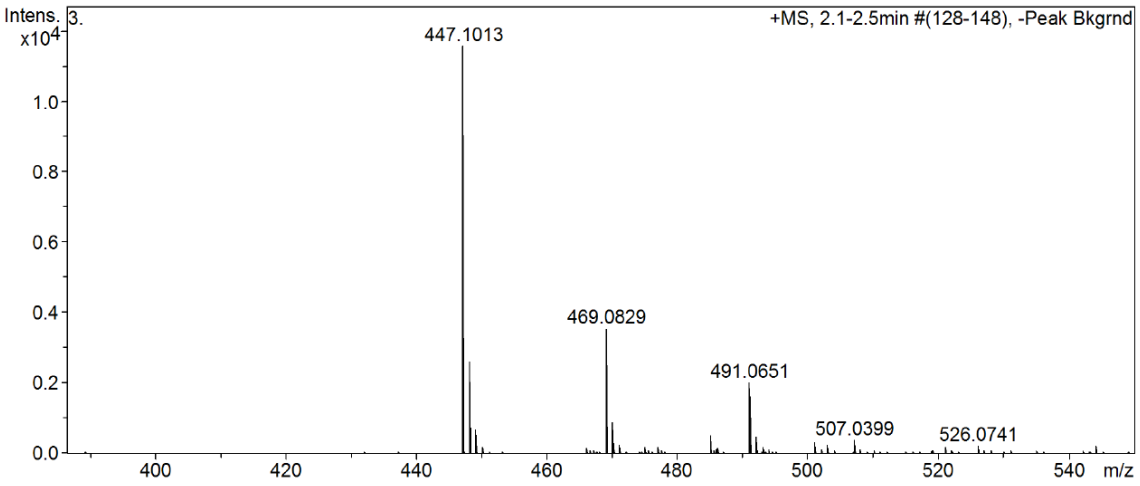

Meas. m/z	Formula	m/z	err [ppm]	err [mDa]	# Sigma	mSigma	rdb	e⁻ Conf	N-Rule
447.1013	C 24 H 19 N 2 O 5 S	447.1009	-0.9	-0.4	5	29.7	16.5	even	ok

A.15 NMR and MS data of 4-(1,2,4trz)-Nap-NO_2 (L_2)

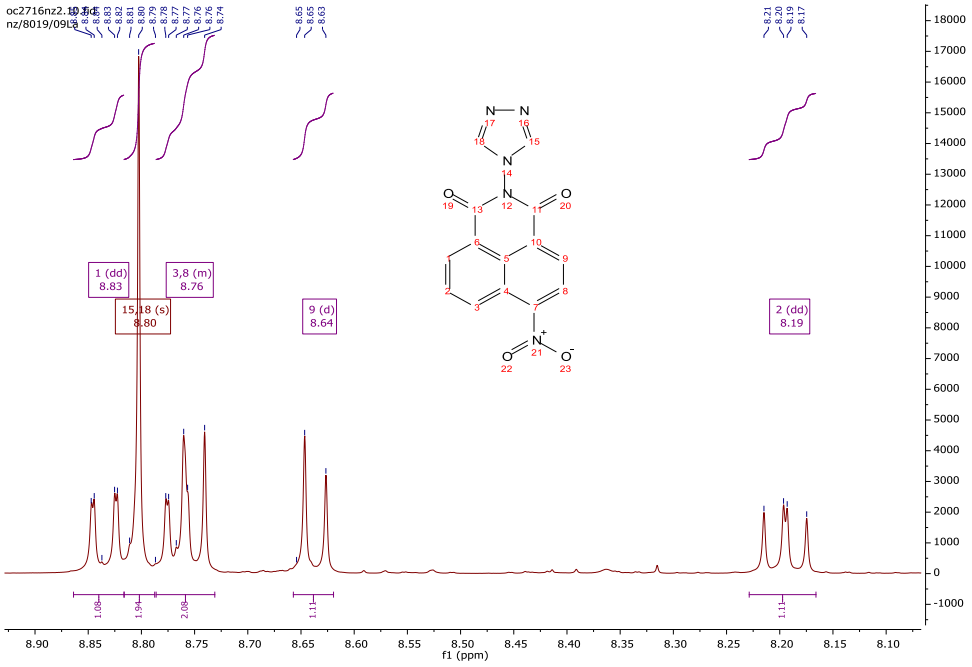

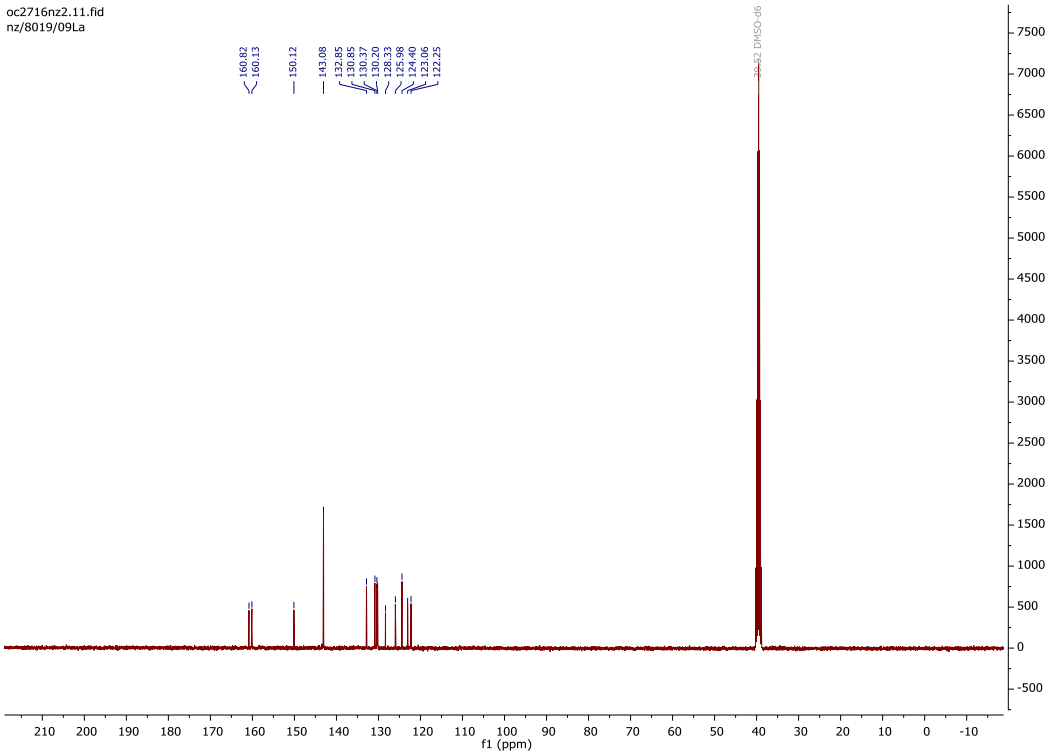

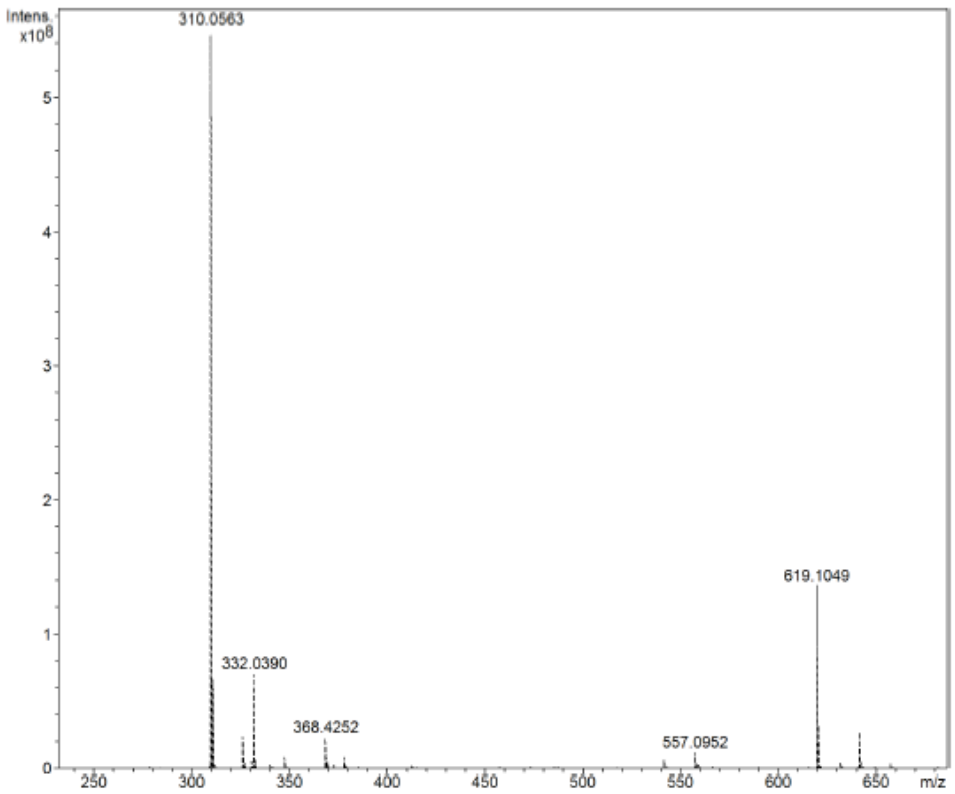

Meas. m/z	Formula	m/z	err [ppm]	err [mDa]	# Sigma	mSigma	rdb	e⁻ Conf	N-Rule
310.0563	C 14 H 8 N 5 O 4	310.0571	2.4	0.7	1	29.8	13.5	even	ok

A.16 NMR and MS data of 4-(1,2,4trz)-nap-NH_2 (L_3)

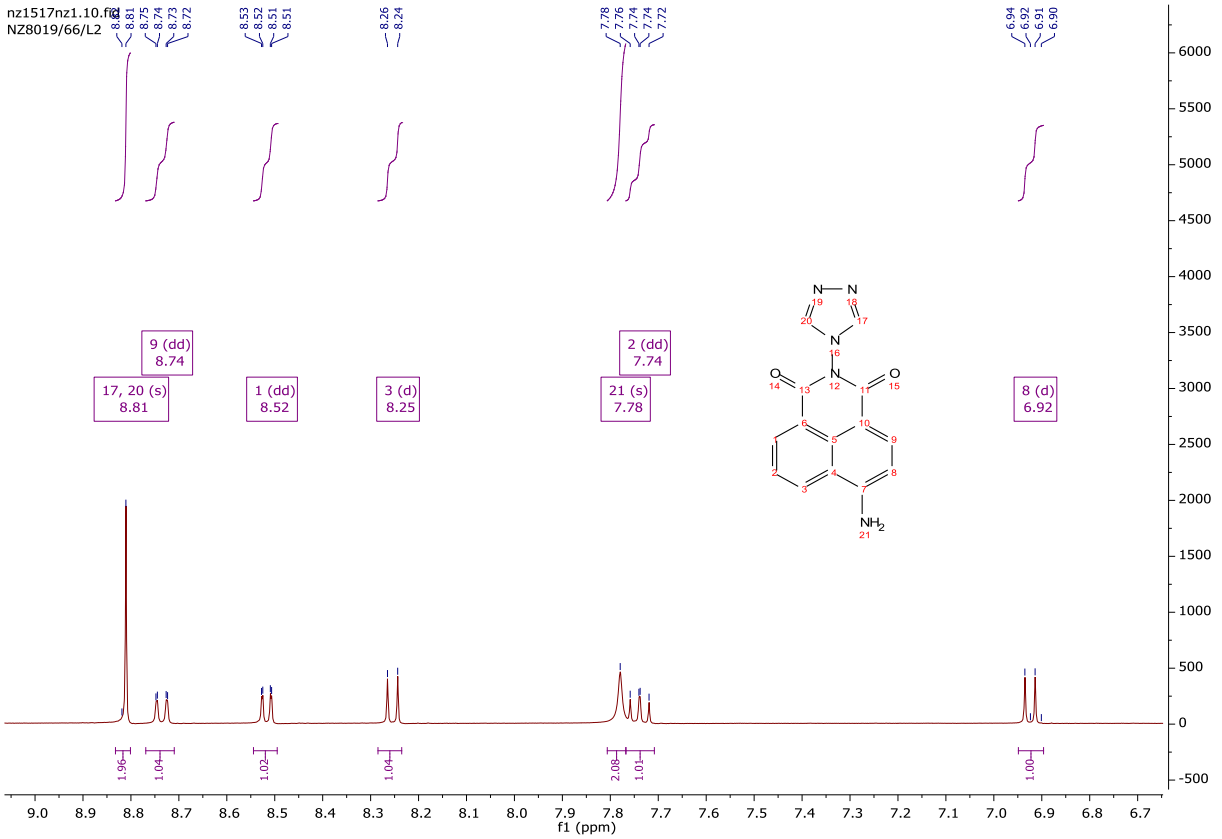

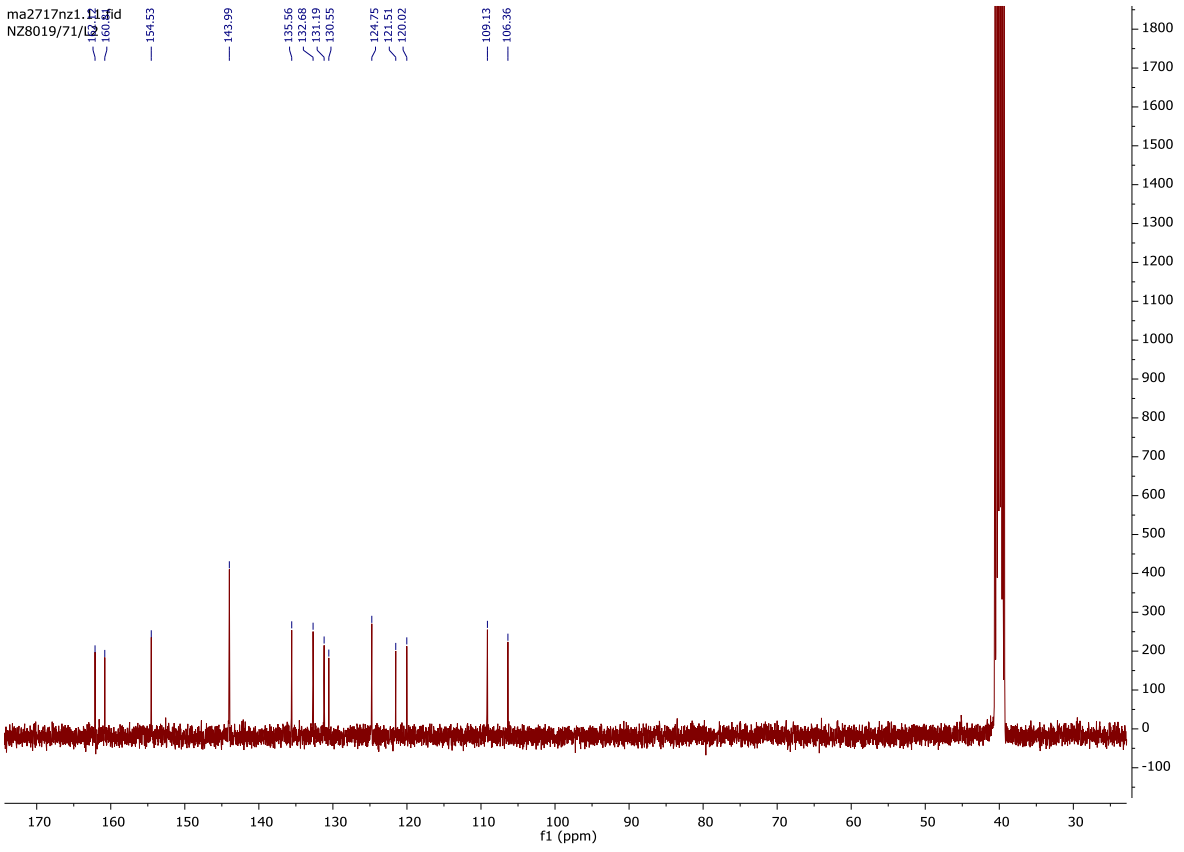

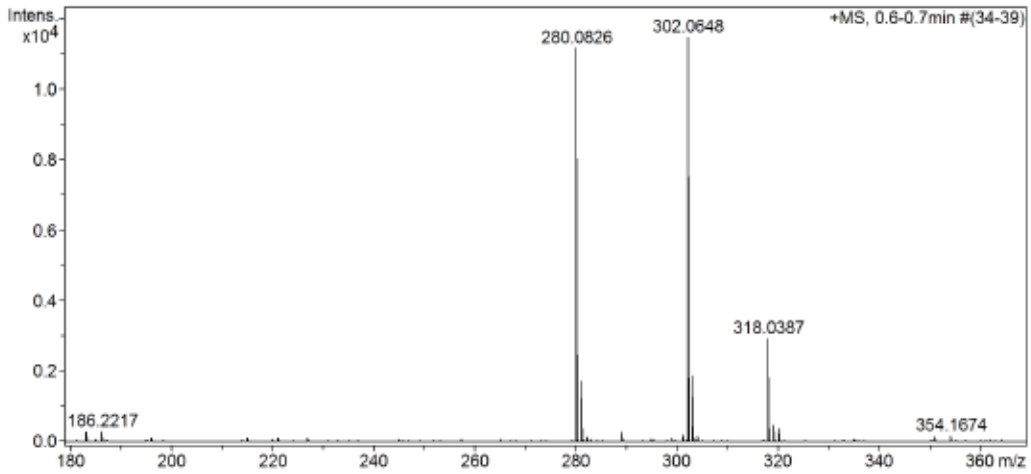

Meas. m/z	Formula	m/z	err [ppm]	err [mDa]	# Sigma	mSigma	rdb	e¯ Conf	N-Rule
280.0826	C 14 H 10 N 5 O 2	280.0829	1.0	0.3	1	8.9	12.5	even	ok

A.17 NMR and MS data of 4-(1,2,4trz)-nap-troger's base (L_5)

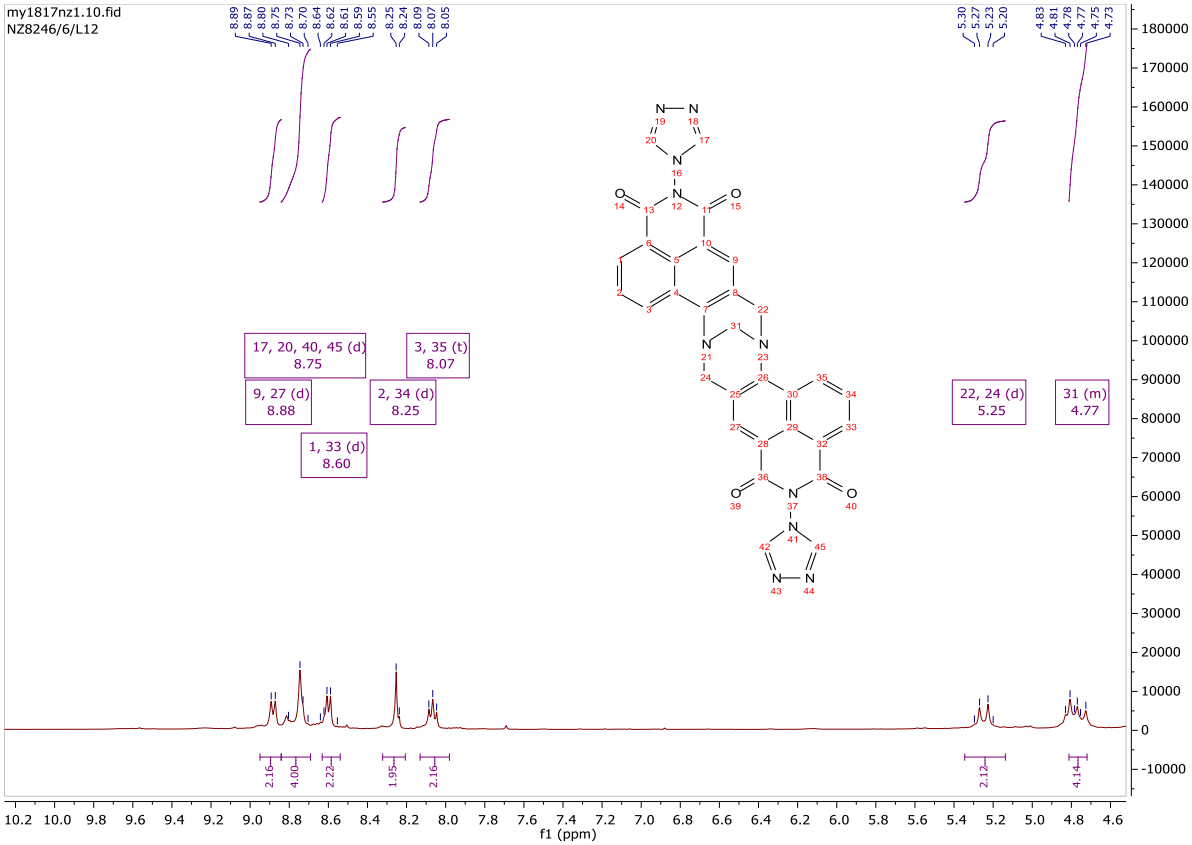

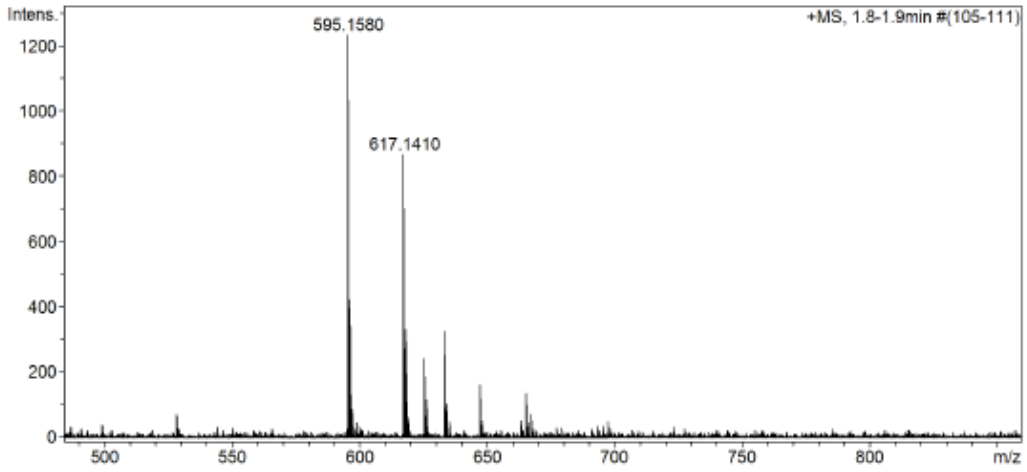

Meas. m/z	Formula	m/z	err [ppm]	err [mDa]	# Sigma	mSigma	rdb	e⁻ Conf	N-Rule
595.1580	C 31 H 19 N 10 O 4	595.1585	0.8	0.5	4	40.9	27.5	even	ok

A.18 NMR and MS data of 4-ethyl-(1,2,4trz)-Nap-H (L_6)

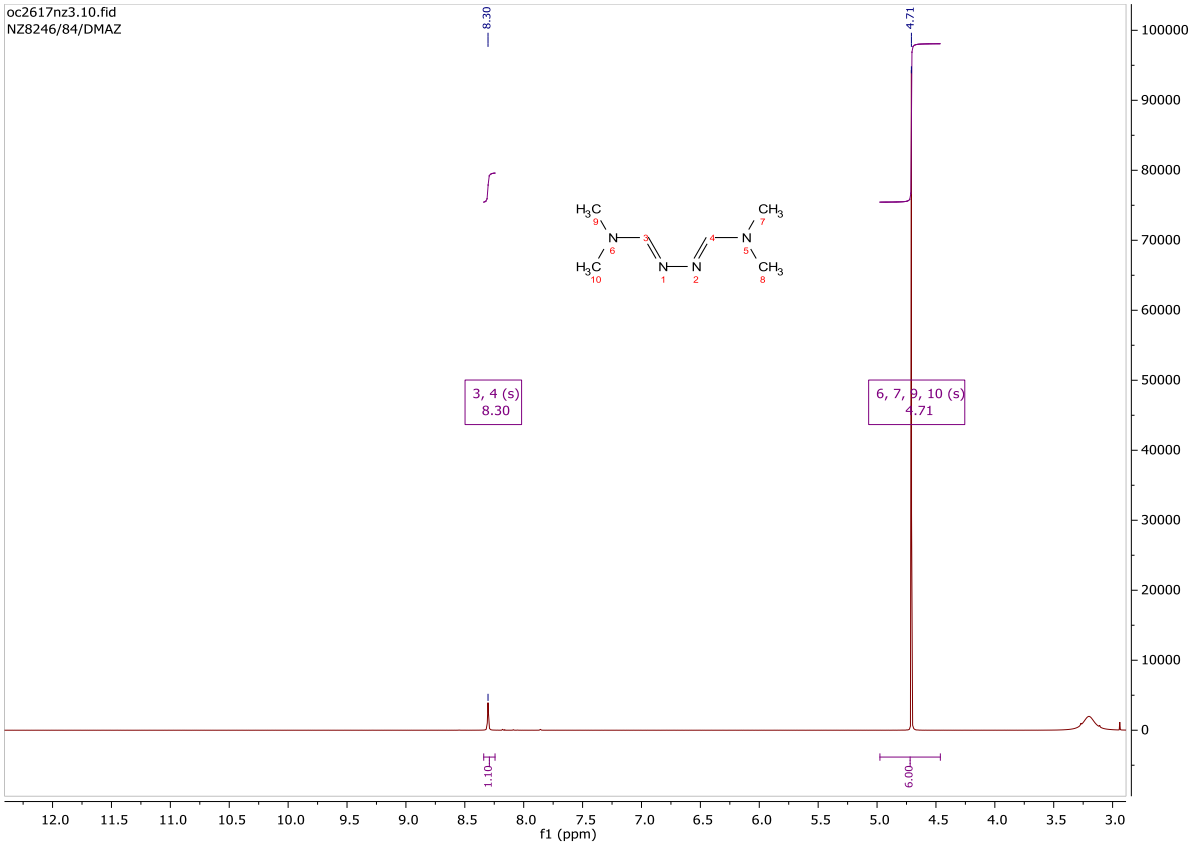

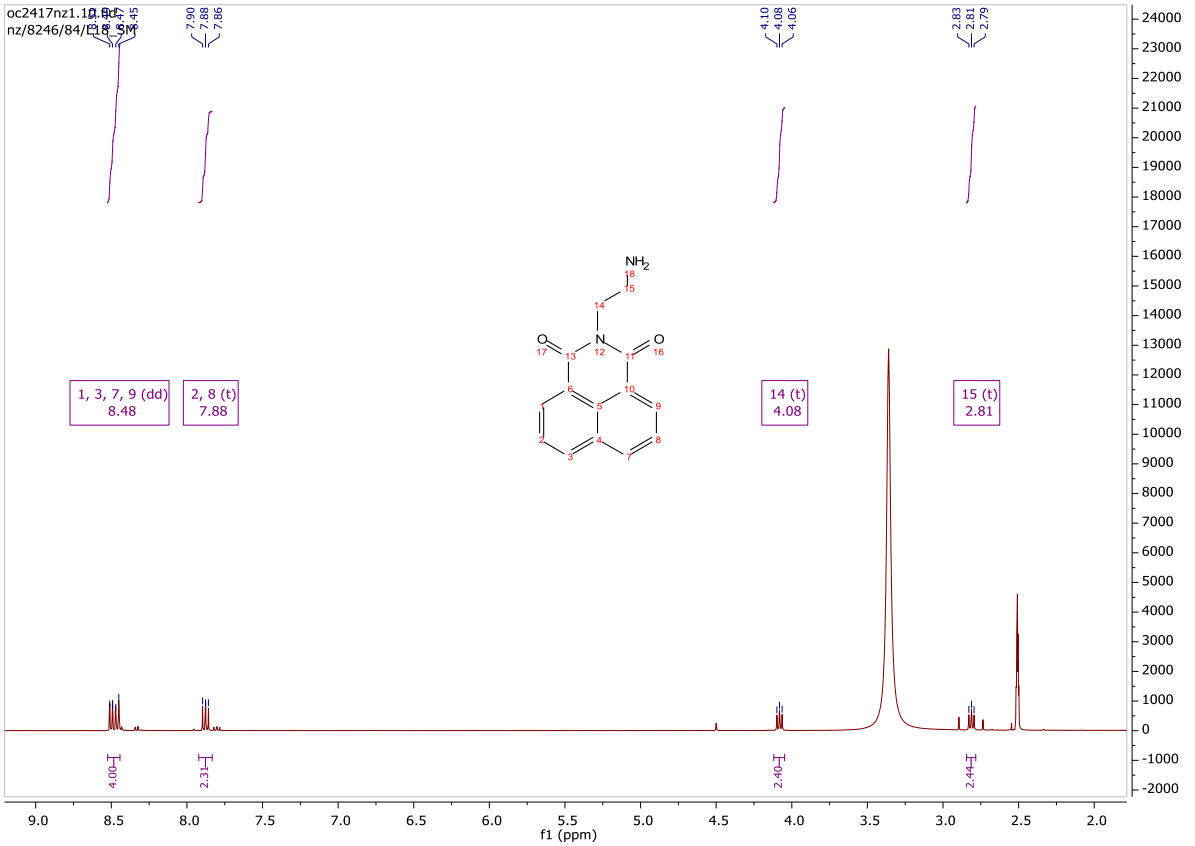

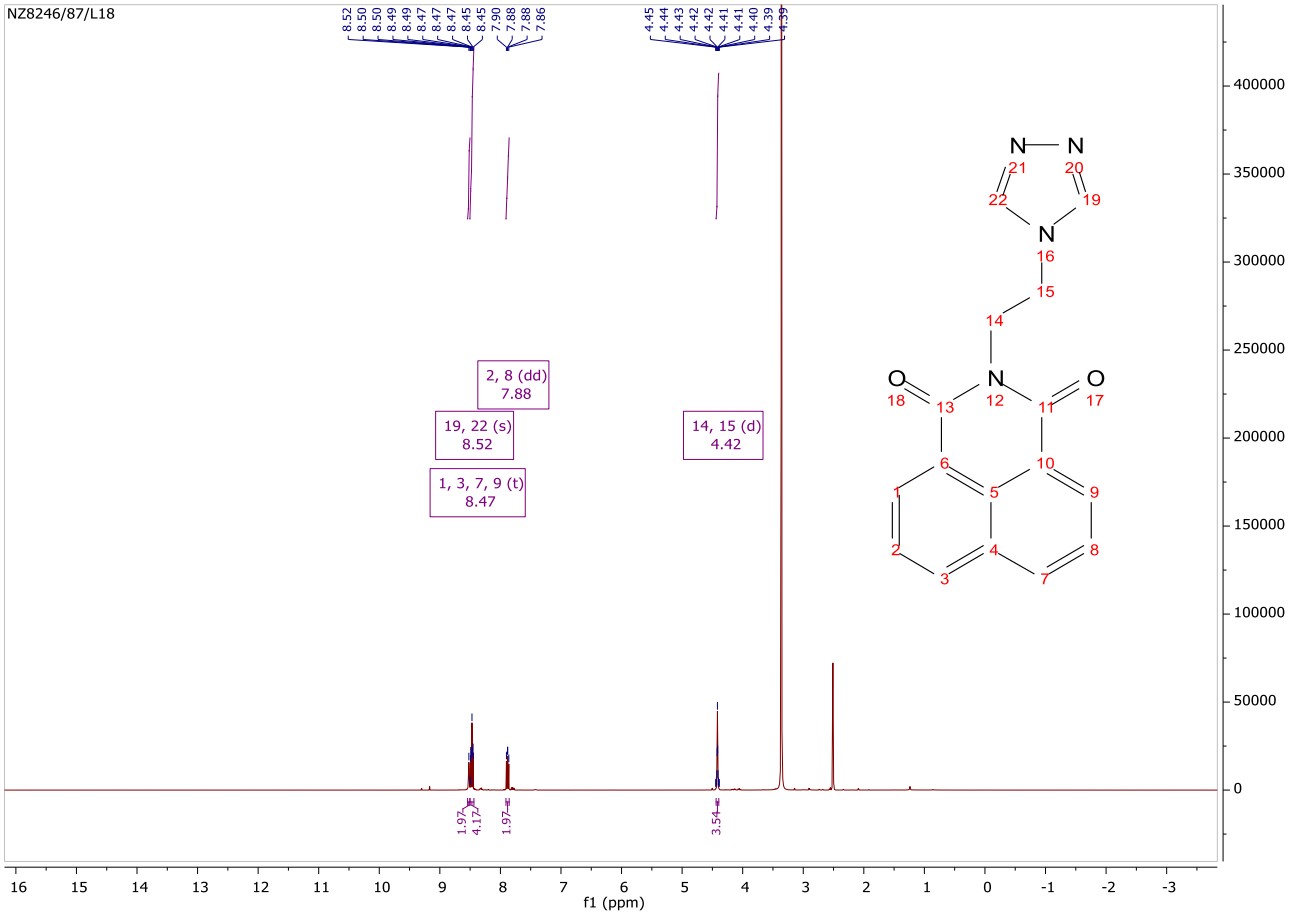
NZ8246/87/L18
8.52
8.50
8.50
8.49
8.49
8.47
8.47
8.47
8.45
8.45
7.90
7.88
7.88
7.86
4.45
4.44
4.43
4.42
4.42
4.41
4.41
4.40
4.39
4.39
2, 8 (dd)
7.88
19, 22 (s)
8.52
1, 3, 7, 9 (t)
8.47
14, 15 (d)
4.42
1.97
4.17
1.97
3.54
f1 (ppm)

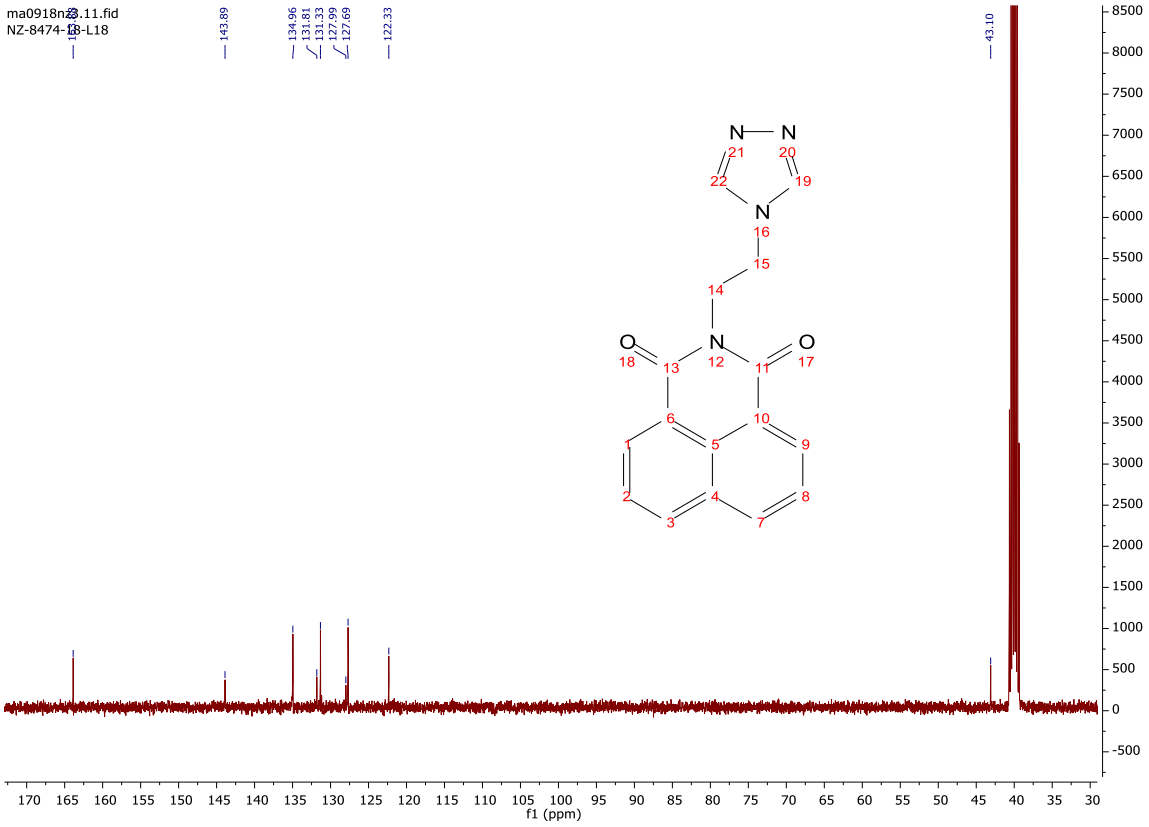
ma0918nz8.11.fid
NZ-8474-L18
143.89
134.96
131.81
131.33
127.99
127.69
122.33
43.10
f1 (ppm)

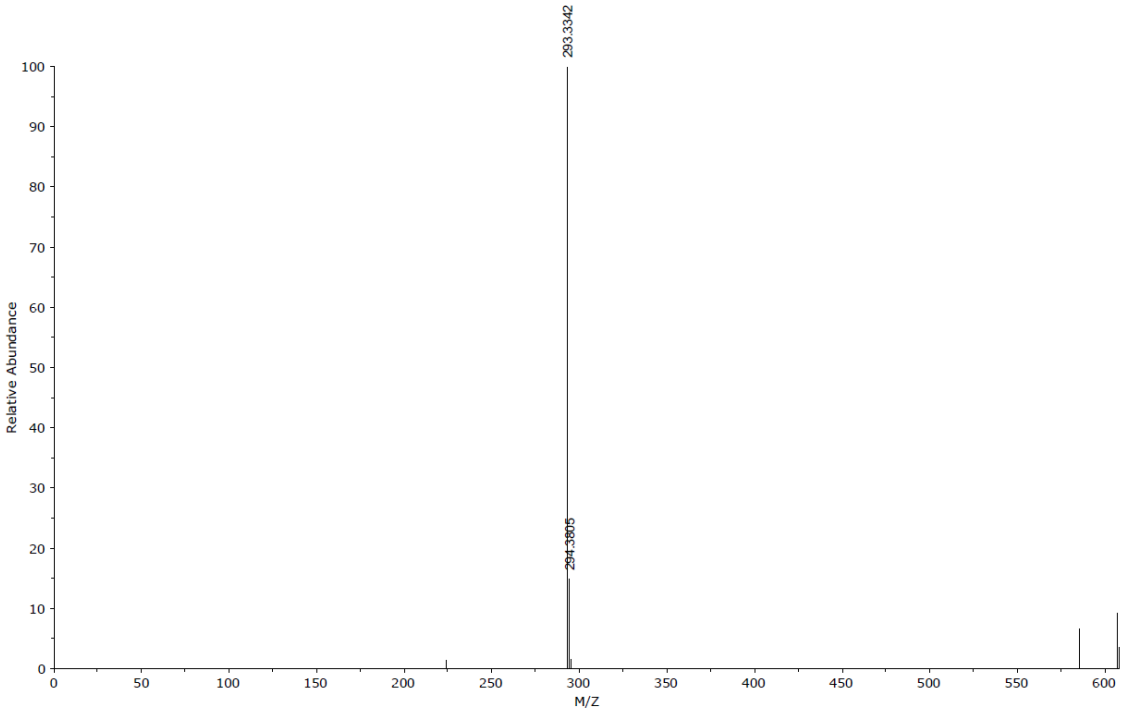
293.3342
294.3805
Relative Abundance
M/Z
0
10
20
30
40
50
60
70
80
90
100
0
50
100
150
200
250
300
350
400
450
500
550
600

Appendix B Crystallographic Details

B.1 $[Fe(bpa)_2](A_1)_2 \cdot CH_3OH$ (1)

Bond precision: C-C = 0.0030 A Wavelength=0.71073

Cell: a=11.2103(3) b=14.7235(3) c=17.8602(4)
alpha=90 beta=107.395(2) gamma=90
Temperature: 100 K

	Calculated	Reported
Volume	2813.10(12)	2813.09(12)
Space group	P 21/n	P 1 21/n 1
Hall group	-P 2yn	-P 2yn
Moiety formula	C24 H26 Fe N6, 2(C18 H10 N2 O5 S), 2(C H4 O)	2(C24 H26 Fe N6), 4(C18 H10 N O5 S), 4(C H4 O)
Sum formula	C62 H54 Fe N8 O12 S2	C124 H108 Fe2 N16 O24 S4
Mr	1223.10	2446.20
Dx,g cm-3	1.444	1.444
Z	2	1
Mu (mm-1)	0.416	0.416
F000	1272.0	1272.0
F000'	1273.73	
h,k,lmax	15,19,24	15,19,24
Nref	7272	7223
Tmin,Tmax	0.923,0.959	0.675,1.000
Tmin'	0.920	

Correction method= # Reported T Limits: Tmin=0.675 Tmax=1.000
AbsCorr = MULTI-SCAN

Data completeness= 0.993 Theta(max)= 28.699

R(reflections)= 0.0445(6521) wR2(reflections)= 0.1179(7223)

S = 1.048 Npar= 390

B.2 $[Fe(bpa)_2](A_2)_2 \cdot CH_3OH$ (2)

Bond precision: C-C = 0.0034 A Wavelength=0.71073

Cell: a=8.4691(4) b=10.9865(5) c=17.2843(9)
alpha=72.563(5) beta=79.889(4) gamma=68.649(4)
Temperature: 100 K

	Calculated	Reported
Volume	1425.02(13)	1425.02(13)
Space group	P -1	P -1
Hall group	-P 1	-P 1
Moiety formula	2(C18 H9 N2 O7 S), C24 H26 Fe N6, 2(C H4 O)	C24 H26 Fe N6, 2(C18 H9 N2 O7 S), 2(C H4 O)
Sum formula	C62 H52 Fe N10 O16 S2	C62 H52.43 Fe N10 O16 S2
Mr	1313.11	1313.54
Dx,g cm-3	1.530	1.531
Z	1	1
Mu (mm-1)	0.422	0.422
F000	680.0	680.0
F000'	680.91	
h,k,lmax	11,14,23	11,14,23
Nref	7363	6769
Tmin,Tmax	0.985,0.998	0.632,1.000
Tmin'	0.967	

Correction method= # Reported T Limits: Tmin=0.632 Tmax=1.000
AbsCorr = MULTI-SCAN

Data completeness= 0.919 Theta(max)= 28.698

R(reflections)= 0.0466(6013) wR2(reflections)= 0.1099(6769)

S = 1.079 Npar= 442

B.3 $[Fe(bpa)_2](A_3)_2 \cdot (CH_3)_2CO$ (3)

Bond precision: C-C = 0.0063 A Wavelength=0.71075

Cell: a=8.6396(7) b=9.5036(6) c=20.1911(14)
alpha=92.693(5) beta=95.523(6) gamma=96.876(6)
Temperature: 100 K

	Calculated	Reported
Volume	1635.4(2)	1635.4(2)
Space group	P -1	P -1
Hall group	-P 1	-P 1
Moiety formula	C24 H26 Fe N6, 2(C20 H15 N2 O5 S), 2(C3 H6 O) [+ solvent]	C24 H26 Fe N6, 2(C20 H15 N2 O5 S), 2(C3 H6 O)
Sum formula	C70 H68 Fe N10 O12 S2 [+ solvent]	C70 H76 Fe N10 O16 S2
Mr	1361.31	1433.37
Dx,g cm-3	1.382	1.455
Z	1	1
Mu (mm-1)	0.366	0.374
F000	712.0	752.0
F000'	712.89	
h,k,lmax	10,11,24	10,11,24
Nref	5791	5763
Tmin,Tmax	0.956,0.978	0.570,1.000
Tmin'	0.945	

Correction method= # Reported T Limits: Tmin=0.570 Tmax=1.000
AbsCorr = MULTI-SCAN

Data completeness= 0.995 Theta(max)= 25.028

R(reflections)= 0.0764(3868) wR2(reflections)= 0.2197(5763)

S = 1.050 Npar= 434

B.4 $[Fe(bpa)_2](A_5)\cdot DMF$ (4)

Bond precision: C-C = 0.0103 A Wavelength=1.54178

Cell: a=12.5603(8) b=14.1964(7) c=23.5545(12)
alpha=73.807(5) beta=77.945(5) gamma=68.824(5)
Temperature: 100 K

	Calculated	Reported
Volume	3733.5(4)	3733.5(4)
Space group	P -1	P -1
Hall group	-P 1	-P 1
Moiety formula	C39 H22 N4 O10 S2, C24 H26 Fe N6, C3 H7 N O [+ solvent]	2(C12 H13 Fe0.5 N3), C39 H22 N4 O10 S2, C3 H7 N O
Sum formula	C66 H55 Fe N11 O11 S2 [+ solvent]	C66 H49 Fe N11 O13.20 S2
Mr	1298.18	1327.33
Dx,g cm-3	1.155	1.181
Z	2	2
Mu (mm-1)	2.633	2.669
F000	1348.0	1371.0
F000'	1351.00	
h,k,lmax	14,16,28	14,16,28
Nref	13172	12969
Tmin,Tmax	0.894,0.974	0.792,1.000
Tmin'	0.852	

Correction method= # Reported T Limits: Tmin=0.792 Tmax=1.000
AbsCorr = MULTI-SCAN

Data completeness= 0.985 Theta(max)= 66.596

R(reflections)= 0.0952(6836) wR2(reflections)= 0.2749(12969)

S = 1.021 Npar= 825

B.5 $[Fe(bpa)_2](A_6)_2 \cdot CH_3OH$ (5)

Bond precision: C-C = 0.0046 A Wavelength=1.54184

Cell: a=8.4078(4) b=11.2222(5) c=15.5918(7)
alpha=84.554(4) beta=89.406(4) gamma=71.275(4)
Temperature: 100 K

	Calculated	Reported
Volume	1386.68(12)	1386.68(11)
Space group	P -1	P -1
Hall group	-P 1	-P 1
Moiety formula	2(C18 H10 N O5 S), C24 H26 Fe N6, 2(C H4 O) [+ solvent]	C24 H26 Fe N6, 2(C18 H10 N O5 S), 2(C H4 O)
Sum formula	C62 H54 Fe N8 O12 S2 [+ solvent]	C64 H58 Fe N8 O10 S2
Mr	1223.10	1219.15
Dx,g cm-3	1.465	1.460
Z	1	1
Mu (mm-1)	3.503	3.473
F000	636.0	636.0
F000'	637.40	
h,k,lmax	10,13,19	10,13,18
Nref	5289	5161
Tmin,Tmax	0.812,0.901	0.700,1.000
Tmin'	0.594	

Correction method= # Reported T Limits: Tmin=0.700 Tmax=1.000
AbsCorr = MULTI-SCAN

Data completeness= 0.976 Theta(max)= 70.156

R(reflections)= 0.0634(4819) wR2(reflections)= 0.1810(5161)

S = 1.075 Npar= 523

B.6 $[Fe(bpa)_2](A_8)_2$ (6)

Bond precision: C-C = 0.0047 A Wavelength=1.54184

Cell: a=9.6824(3) b=13.3534(5) c=14.7445(5)
alpha=109.541(3) beta=105.198(3) gamma=103.933(3)
Temperature: 100 K

	Calculated	Reported
Volume	1616.69(12)	1616.69(10)
Space group	P -1	P -1
Hall group	-P 1	-P 1
Moiety formula	2(C20 H15.53 N2 O5 S), C24 H26 Fe N6 [+ solvent]	C12 H13 Fe0.5 N3, C20 H15.53 N2 O5 S
Sum formula	C64 H57.06 Fe N10 O10 S2 [+ solvent]	C34 H33 Fe0.50 N5 O7 S
Mr	1246.22	683.64
Dx,g cm-3	1.280	1.404
Z	1	2
Mu (mm-1)	3.000	3.098
F000	649.1	714.0
F000'	650.45	
h,k,lmax	11,16,18	11,16,17
Nref	6173	5995
Tmin,Tmax	0.800,0.883	0.741,1.000
Tmin'	0.609	

Correction method= # Reported T Limits: Tmin=0.741 Tmax=1.000
AbsCorr = MULTI-SCAN

Data completeness= 0.971 Theta(max)= 70.407

R(reflections)= 0.0657(5389) wR2(reflections)= 0.1999(5995)

S = 1.082 Npar= 426

B.7 $[Fe(bpa)_2](A_9)_2 \cdot 5CH_3OH$ (7)

Bond precision: C-C = 0.0035 A Wavelength=1.54178

Cell: a=11.8611(1) b=13.9723(2) c=20.4738(2)
alpha=95.451(1) beta=105.032(1) gamma=95.614(1)
Temperature: 293 K

	Calculated	Reported
Volume	3235.56(7)	3235.56(6)
Space group	P -1	P -1
Hall group	-P 1	-P 1
Moiety formula	C24 H26 Fe N6, 2(C22 H12 N O5 S), 5(C H4 O)	C24 H26 Fe N6, 2(C22 H12 N O5 S), 5(C H4 O)
Sum formula	C73 H70 Fe N8 O15 S2	C73 H70 Fe N8 O15 S2
Mr	1419.34	1419.34
Dx,g cm-3	1.457	1.457
Z	2	2
Mu (mm-1)	3.121	3.121
F000	1484.0	1484.0
F000'	1487.48	
h,k,lmax	14,17,24	14,16,24
Nref	12345	12196
Tmin,Tmax		
Tmin'		

Correction method= Not given

Data completeness= 0.988 Theta(max)= 70.312

R(reflections)= 0.0486(11649) wR2(reflections)= 0.1389(12196)

S = 1.029 Npar= 900

B.8 $[Fe(bpa)_2](A_{11})_2 \cdot H2O \cdot CH_3OH$ (8)

Bond precision: C-C = 0.0064 A Wavelength=0.71075

Cell: a=8.1701(4) b=9.5689(4) c=21.1592(8)
alpha=100.522(3) beta=94.786(3) gamma=95.227(3)
Temperature: 100 K

	Calculated	Reported
Volume	1611.14(12)	1611.14(12)
Space group	P -1	P -1
Hall group	-P 1	-P 1
Moiety formula	C24 H26 Fe N6, 2(C24 H17 N2 O5 S), 2(C H4 O), 0.667(H2 O)	C12 H13 Fe0.5 N3, C24 H17 N2 O5 S, C H4 O, 0.33(H2 O)
Sum formula	C74 H69.33 Fe N10 O12.67 S2	C37 H35 Fe0.50 N5 O6.50 S
Mr	1421.36	713.68
Dx,g cm-3	1.465	1.471
Z	1	2
Mu (mm-1)	0.376	0.377
F000	742.7	746.0
F000'	743.57	
h,k,lmax	9,11,25	9,11,25
Nref	5706	5697
Tmin,Tmax	0.956,0.978	0.760,1.000
Tmin'	0.941	

Correction method= # Reported T Limits: Tmin=0.760 Tmax=1.000
AbsCorr = MULTI-SCAN

Data completeness= 0.998 Theta(max)= 25.027

R(reflections)= 0.0707(4437) wR2(reflections)= 0.2012(5697)

S = 1.075 Npar= 519

B.9 $[Fe(bpa)_2](A_{12})2{\cdot}0.66H_2O$ (9)

Bond precision: C-C = 0.0077 A Wavelength=1.54184

Cell: a=16.3311(3) b=9.2747(1) c=41.2768(7)
alpha=90 beta=90.571(2) gamma=90
Temperature: 100 K

	Calculated	Reported
Volume	6251.72(17)	6251.72(17)
Space group	P 2/c	P 1 2/c 1
Hall group	-P 2yc	-P 2yc
Moiety formula	2(C22 H12 N O5 S), C24 H26 Fe N6, 0.331(H2 O) [+ solvent]	2(C24 H26 Fe N6), 4(C22 H12 N O5 S), H1.32 O0.66
Sum formula	C68 H50.66 Fe N8 O10.33 S2 [+ solvent]	C136 H101.33 Fe2 N16 O20.66 S4
Mr	1265.08	2530.15
Dx,g cm-3	1.344	1.344
Z	4	2
Mu (mm-1)	3.110	3.110
F000	2621.2	2621.0
F000'	2626.93	
h,k,lmax	19,11,49	19,11,49
Nref	11045	11039
Tmin,Tmax	0.578,0.733	0.531,1.000
Tmin'	0.511	

Correction method= # Reported T Limits: Tmin=0.531 Tmax=1.000
AbsCorr = MULTI-SCAN

Data completeness= 0.999 Theta(max)= 66.579

R(reflections)= 0.0815(8922) wR2(reflections)= 0.2147(11039)

S = 1.052 Npar= 876

B.10 $[Fe(bpa)_2](A_{13})_2 \cdot H_2O \cdot CH_3OH$ (10)

```
Bond precision:  C-C = 0.0053 A          Wavelength=0.71075

Cell:          a=8.9362(2)       b=9.2403(3)       c=19.5603(4)
               alpha=81.641(2)   beta=85.433(2)    gamma=78.225(2)
Temperature:   100 K
```

	Calculated	Reported
Volume	1562.29(7)	1562.29(7)
Space group	P -1	P -1
Hall group	-P 1	-P 1
Moiety formula	2(C22 H11 N2 O7 S), C24 H26 Fe N6, 2(C H4 O), 2(H2 O)	0.33(C24 H26 Fe N6), 0.67(C22 H11 N2 O7 S), 0.67(C H4 O), 0.67(
Sum formula	C70 H60 Fe N10 O18 S2	C23.33 H20 Fe0.33 N3.33 O6 S0.67
Mr	1449.25	483.08
Dx,g cm-3	1.540	1.540
Z	1	3
Mu (mm-1)	0.395	0.395
F000	752.0	752.0
F000'	752.95	
h,k,lmax	11,11,24	11,11,24
Nref	6397	6394
Tmin,Tmax	0.927,0.961	0.688,1.000
Tmin'	0.924	

```
Correction method= # Reported T Limits: Tmin=0.688 Tmax=1.000
AbsCorr = MULTI-SCAN

Data completeness= 1.000          Theta(max)= 26.373

R(reflections)= 0.0672( 5754)     wR2(reflections)= 0.1731( 6394)

S = 1.082                 Npar= 481
```

B.11 $[Fe(bpa)_2]\cdot(A_{14})_2\cdot H_2O$ (11)

Bond precision: C-C = 0.0040 A Wavelength=1.54178

Cell: a=8.8437(2) b=9.0638(2) c=19.7303(3)
alpha=92.303(2) beta=90.827(1) gamma=95.388(2)
Temperature: 100 K

	Calculated	Reported
Volume	1573.01(6)	1573.01(6)
Space group	P -1	P -1
Hall group	-P 1	-P 1
Moiety formula	2(C24 H17 N2 O5 S), C24 H26 Fe N6, 2(H2 O)	C24 H26 Fe N6, 2(C24 H17 N2 O5 S), 2(H2 O)
Sum formula	C72 H64 Fe N10 O12 S2	C72 H64 Fe N10 O12 S2
Mr	1381.30	1381.30
Dx,g cm-3	1.458	1.458
Z	1	1
Mu (mm-1)	3.168	3.168
F000	720.0	720.0
F000'	721.63	
h,k,lmax	10,11,24	10,10,24
Nref	6005	5839
Tmin,Tmax	0.881,0.939	0.532,1.000
Tmin'	0.881	

Correction method= # Reported T Limits: Tmin=0.532 Tmax=1.000
AbsCorr = MULTI-SCAN

Data completeness= 0.972 Theta(max)= 70.369

R(reflections)= 0.0572(5321) wR2(reflections)= 0.1729(5839)

S = 1.070 Npar= 444

B.12 $[Fe_2(PMAT)_2](A_1)_4 \cdot MeOH$ (12)

Bond precision: C-C = 0.0045 A Wavelength=1.54184

Cell: a=10.9689(3) b=12.0883(3) c=22.0093(4)
alpha=75.835(2) beta=86.454(2) gamma=73.906(2)
Temperature: 100 K

	Calculated	Reported
Volume	2718.65(12)	2718.65(12)
Space group	P -1	P -1
Hall group	-P 1	-P 1
Moiety formula	C32 H40 Fe2 N16, 4(C18 H10 N O5 S), 2(C H4 O) [+ solvent]	C16 H20 Fe N8, 2(C18 H10 N O5 S), C H4 O
Sum formula	C106 H88 Fe2 N20 O22 S4 [+ solvent]	C62 H0.50 Cl3 Fe0.50 N8 O8 S0.50
Mr	2233.90	1135.51
Dx,g cm-3	1.365	1.387
Z	1	2
Mu (mm-1)	3.517	3.281
F000	1156.0	1129.0
F000'	1158.51	
h,k,lmax	13,14,26	13,14,26
Nref	10377	10129
Tmin,Tmax	0.790,0.906	0.851,1.000
Tmin'	0.769	

Correction method= # Reported T Limits: Tmin=0.851 Tmax=1.000
AbsCorr = MULTI-SCAN

Data completeness= 0.976 Theta(max)= 70.333

R(reflections)= 0.0531(9648) wR2(reflections)= 0.1433(10129)

S = 1.037 Npar= 771

B.13 $[Fe_2(PMAT)_2](A_2)_4$ (13)

```
Bond precision:  C-C = 0.0118 A          Wavelength=1.54184

Cell:          a=11.1788(3)       b=19.2268(9)     c=30.0855(13)
               alpha=106.525(4)   beta=90.498(3)   gamma=98.919(3)
Temperature:   100 K
```

	Calculated	Reported
Volume	6114.8(4)	6114.8(4)
Space group	P -1	P -1
Hall group	-P 1	-P 1
Moiety formula	C31 H40 Fe2 N17, 4(C18 H9 N2 O7 S) [+ solvent]	0.2(C31 H40 Fe2 N17), 0.8(C18 H9 N2 O7 S)
Sum formula	C103 H76 Fe2 N25 O28 S4 [+ solvent]	C20 H20 Fe N6 O6 S2
Mr	2351.83	560.39
Dx,g cm-3	1.277	1.522
Z	2	10
Mu (mm-1)	3.206	6.969
F000	2418.0	2880.0
F000'	2423.75	
h,k,lmax	13,22,35	13,22,35
Nref	21623	21449
Tmin,Tmax	0.636,0.757	0.538,1.000
Tmin'	0.312	

```
Correction method= # Reported T Limits: Tmin=0.538 Tmax=1.000
AbsCorr = MULTI-SCAN

Data completeness= 0.992          Theta(max)= 66.598

R(reflections)= 0.0933( 12784)    wR2(reflections)= 0.2494( 21449)

S = 1.030                 Npar= 1489
```

B.14 $[Fe_2(PMBzT)_2](A_1)_4 \cdot MeCN$ (14)

```
Bond precision:  C-C = 0.0044 A          Wavelength=0.71075

Cell:          a=11.8637(2)      b=12.3709(3)      c=19.5210(5)
               alpha=87.155(2)   beta=87.576(2)    gamma=78.282(2)
Temperature:   293 K

                Calculated                Reported
Volume          2800.31(11)               2800.31(11)
Space group     P -1                      P -1
Hall group      -P 1                      -P 1
                C48 H50 Fe2 N12, 2(C17 H10 C48 H50 Fe2 N12, 2(C17 H10
Moiety formula  N2 O5 S), 2(C18 H10 N O5  N2 O5 S), 2(C18 H10 N O5
                S), 4(C2 H3               S), 4(C2 H3
Sum formula     C126 H102 Fe2 N22 O20 S4  C126 H102 Fe2 N22 O20 S4
Mr              2484.24                   2484.23
Dx,g cm-3       1.473                     1.473
Z               1                         1
Mu (mm-1)       0.418                     0.418
F000            1288.0                    1288.0
F000'           1289.70
h,k,lmax        17,18,29                  17,18,28
Nref            19912                     16288
Tmin,Tmax       0.923,0.959               0.696,1.000
Tmin'           0.920

Correction method= # Reported T Limits: Tmin=0.696 Tmax=1.000
AbsCorr = MULTI-SCAN

Data completeness= 0.818          Theta(max)= 32.299

R(reflections)= 0.0675( 13195)    wR2(reflections)= 0.1800( 16288)

S = 1.025                 Npar= 786
```

B.15 $[Fe_2(PMBzT)_2](A_2)_4$ (15)

Bond precision: C-C = 0.0086 A Wavelength=1.54178

Cell: a=11.7521(3) b=14.0281(3) c=19.4654(3)
alpha=94.428(2) beta=96.013(2) gamma=97.583(2)
Temperature: 100 K

	Calculated	Reported
Volume	3149.98(12)	3149.98(12)
Space group	P -1	P -1
Hall group	-P 1	-P 1
Moiety formula	C44 Fe2 N16, 4(C18 N2 O7 S) [+ solvent]	0.13(C44 Fe2 N16), 0.5(C18 N2 O7 S)
Sum formula	C116 Fe2 N24 O28 S4 [+ solvent]	C15 H15 Fe N2 O2 S
Mr	2417.34	343.20
Dx,g cm-3	1.274	1.447
Z	1	8
Mu (mm-1)	3.142	8.961
F000	1204.0	1416.0
F000'	1207.08	
h,k,lmax	14,16,23	13,16,23
Nref	11537	11455
Tmin,Tmax	0.224,0.956	0.674,1.000
Tmin'	0.111	

Correction method= # Reported T Limits: Tmin=0.674 Tmax=1.000
AbsCorr = MULTI-SCAN

Data completeness= 0.993 Theta(max)= 68.243

R(reflections)= 0.0908(9094) wR2(reflections)= 0.2644(11455)

S = 1.041 Npar= 803

B.16 $[Fe_2(PMBzT)_2](A_5)_2 \cdot MeCN$ (16)

```
Bond precision:  C-C = 0.0118 A          Wavelength=1.54178

Cell:          a=18.4514(8)      b=18.5702(6)      c=22.9770(7)
               alpha=111.764(3)  beta=101.350(3)   gamma=101.707(3)
Temperature:   100 K
```

	Calculated	Reported
Volume	6831.8(5)	6831.8(5)
Space group	P -1	P -1
Hall group	-P 1	-P 1
Moiety formula	C46 H50 Fe2 N14, 2(C39 H22 N4 O10 S2) [+ solvent]	C46 H50 Fe2 N14, 2(C39 H22 N4 O10 S2)
Sum formula	C124 H94 Fe2 N22 O20 S4 [+ solvent]	C125 H94 Fe2 N21 O20 S4
Mr	2452.15	2450.15
Dx,g cm-3	1.192	1.191
Z	2	2
Mu (mm-1)	2.839	2.836
F000	2536.0	2534.0
F000'	2541.54	
h,k,lmax	21,22,27	21,22,27
Nref	24116	23838
Tmin,Tmax		0.482,1.000
Tmin'		

```
Correction method= # Reported T Limits: Tmin=0.482 Tmax=1.000
AbsCorr = MULTI-SCAN

Data completeness= 0.988          Theta(max)= 66.594

R(reflections)= 0.1059( 11936)    wR2(reflections)= 0.3236( 23838)

S = 1.026                 Npar= 1683
```

B.17 $[Co_2(L_1)_3(DMF)_4(H_2O)_2](BF_4)_4 \cdot 4DMF \cdot H_2O$ (C_1)

```
Bond precision:  C-C = 0.0076 A          Wavelength=0.71073

Cell:          a=15.2085(3)       b=16.8311(3)      c=17.9708(3)
               alpha=104.312(2)   beta=101.708(2)   gamma=103.837(2)
Temperature:   100 K
```

	Calculated	Reported
Volume	4156.71(16)	4156.71(14)
Space group	P -1	P -1
Hall group	-P 1	-P 1
Moiety formula	2(C53.77 H55.95 Co2 N16 O12), 8(B F4), 8(C3 H7 N O), O	C53.772 H55.952 Co2 N16 O12, 4(B F4), 4(C3 H7 N O), 0.5(O)
Sum formula	C131.54 H167.90 B8 Co4 F32 N40 O33	C65.61 H83.44 B4 Co2 F16 N20 O16.50
Mr	3767.70	1881.38
Dx,g cm-3	1.505	1.503
Z	1	2
Mu (mm-1)	0.510	0.510
F000	1937.2	1934.0
F000'	1939.73	
h,k,lmax	18,20,21	18,20,21
Nref	14634	14623
Tmin,Tmax	0.922,0.970	0.924,1.000
Tmin'	0.922	

```
Correction method= # Reported T Limits: Tmin=0.924 Tmax=1.000
AbsCorr = MULTI-SCAN

Data completeness= 0.999          Theta(max)= 25.000

R(reflections)= 0.0732( 11923)    wR2(reflections)= 0.2098( 14623)

S = 1.017                Npar= 1182
```

B.18 $[Co_2(L_1)_2(DMF)_3(H_2O)_2(\mu_2\text{-}HCO_2)Co_2(L_1)_2(DMF)_3(H_2O)_2](NO_3)_7.4DMF$ (C_2)

Bond precision: C-C = 0.0044 A Wavelength=0.71075

Cell: a=15.1141(4) b=16.4203(3) c=16.4671(3)
alpha=83.841(2) beta=63.220(2) gamma=82.953(2)
Temperature: 100 K

	Calculated	Reported
Volume	3614.63(15)	3614.63(15)
Space group	P -1	P -1
Hall group	-P 1	-P 1
Moiety formula	C103 H98 Co4 N30 O24, 4(N O3), 4(C3 H7 N O) [+ solvent]	C103 H98 Co4 N30 O24, 4(C3 H7 N O), 4(N O3)
Sum formula	C115 H126 Co4 N38 O40 [+ solvent]	C115 H126 Co4 N42 O52
Mr	2916.26	3164.29
Dx,g cm-3	1.340	1.454
Z	1	1
Mu (mm-1)	0.539	0.552
F000	1510.0	1634.0
F000'	1512.07	
h,k,lmax	21,23,23	21,23,23
Nref	22089	22069
Tmin,Tmax	0.957,0.994	0.888,1.000
Tmin'	0.957	

Correction method= # Reported T Limits: Tmin=0.888 Tmax=1.000
AbsCorr = MULTI-SCAN

Data completeness= 0.999 Theta(max)= 30.509

R(reflections)= 0.0501(17645) wR2(reflections)= 0.1408(22069)

S = 1.023 Npar= 1023

B.19 $[Fe(L_1)_6](ClO_4)_3$ (C_3)

Bond precision: C-C = 0.0025 A Wavelength=0.71073

Cell: a=15.4078(4) b=15.4078(4) c=9.1523(2)
alpha=90 beta=90 gamma=120
Temperature: 100 K

	Calculated	Reported
Volume	1881.66(11)	1881.66(11)
Space group	P -3	P -3
Hall group	-P 3	-P 3
Moiety formula	C84 H48 Fe N24 O12, 2(Cl O4)	C84 H48 Fe1 N24 O12, 2(Cl1 O4)
Sum formula	C84 H48 Cl2 Fe N24 O20	C84 H48 Cl2 Fe N24 O20
Mr	1840.21	1840.21
Dx,g cm-3	1.624	1.624
Z	1	1
Mu (mm-1)	0.370	0.370
F000	940.0	940.0
F000'	941.06	
h,k,lmax	21,21,12	21,21,12
Nref	3500	3232
Tmin,Tmax	0.931,0.957	0.886,1.000
Tmin'	0.929	

Correction method= # Reported T Limits: Tmin=0.886 Tmax=1.000
AbsCorr = MULTI-SCAN

Data completeness= 0.923 Theta(max)= 29.512

R(reflections)= 0.0389(2810) wR2(reflections)= 0.0988(3232)

S = 1.059 Npar= 198

B.20 $[Fe_2(L_1)_3(DMF)_4(MeCN)_2](ClO_4)_4$ (C_4)

```
Bond precision:  C-C = 0.0048 A          Wavelength=0.71073

Cell:          a=15.2335(4)      b=15.2713(4)      c=18.7277(4)
               alpha=98.829(2)   beta=100.334(2)   gamma=105.517(2)
Temperature:   293 K
```

	Calculated	Reported
Volume	4035.47(19)	4035.47(18)
Space group	P -1	P -1
Hall group	-P 1	-P 1
Moiety formula	C58 H56 Fe2 N18 O10, 4(Cl O4) [+ solvent]	C58 H56 Fe2 N18 O10, 4(Cl O4)
Sum formula	C58 H56 Cl4 Fe2 N18 O26 [+ solvent]	C60 H60 Cl4 Fe2 N18 O24
Mr	1674.71	1670.76
Dx,g cm-3	1.378	1.375
Z	2	2
Mu (mm-1)	0.574	0.573
F000	1716.0	1716.0
F000'	1719.38	
h,k,lmax	18,18,22	18,18,22
Nref	14193	14176
Tmin,Tmax	0.896,0.944	0.905,1.000
Tmin'	0.892	

```
Correction method= # Reported T Limits: Tmin=0.905 Tmax=1.000
AbsCorr = MULTI-SCAN

Data completeness= 0.999          Theta(max)= 24.999

R(reflections)= 0.0524( 12019)    wR2(reflections)= 0.1504( 14176)

S = 1.018                 Npar= 1023
```

B.21 Ar(4-SO_3)-Nap-Tröger's base·2H (A_5·2H)

```
Bond precision:  C-C = 0.0045 A          Wavelength=0.71073

Cell:          a=9.3292(5)       b=18.3198(7)      c=18.4859(8)
               alpha=70.885(4)   beta=84.102(4)    gamma=76.035(4)
Temperature:   293 K
```

	Calculated	Reported
Volume	2896.0(2)	2896.0(2)
Space group	P -1	P -1
Hall group	-P 1	-P 1
Moiety formula	2(C39 H22 N4 O10 S2), 2(C2 H8 N), H2 O [+ solvent]	C39 H23 N4 O10.5 S2, C2 H8 N
Sum formula	C82 H62 N10 O21 S4 [+ solvent]	C41 H31 N5 O10.50 S2
Mr	1651.66	825.83
Dx,g cm-3	0.947	0.947
Z	1	2
Mu (mm-1)	0.138	0.138
F000	856.0	856.0
F000'	856.92	
h,k,lmax	12,23,23	12,23,24
Nref	13266	12786
Tmin,Tmax	0.992,0.997	0.739,1.000
Tmin'	0.973	

```
Correction method= # Reported T Limits: Tmin=0.739 Tmax=1.000
AbsCorr = MULTI-SCAN

Data completeness= 0.964          Theta(max)= 27.484

R(reflections)= 0.0930( 8272)     wR2(reflections)= 0.3079( 12786)

S = 1.122                 Npar= 605
```

B.22 4-(1,2,4trz)-Nap-H (L_1)

```
Bond precision:  C-C = 0.0012 A          Wavelength=0.71075

Cell:            a=11.3968(1)     b=15.5442(1)         c=6.8280(1)
                 alpha=90         beta=104.066(1)      gamma=90
Temperature:     100 K

                 Calculated                Reported
Volume           1173.34(2)                1173.34(2)
Space group      P 21/c                    P 1 21/c 1
Hall group       -P 2ybc                   -P 2ybc
Moiety formula   C14 H8 N4 O2              C14 H8 N4 O2
Sum formula      C14 H8 N4 O2              C14 H8 N4 O2
Mr               264.24                    264.24
Dx,g cm-3        1.496                     1.496
Z                4                         4
Mu (mm-1)        0.105                     0.105
F000             544.0                     544.0
F000'            544.23
h,k,lmax         15,21,9                   15,21,9
Nref             3026                      3025
Tmin,Tmax                                  0.756,1.000
Tmin'

Correction method= # Reported T Limits: Tmin=0.756 Tmax=1.000
AbsCorr = MULTI-SCAN

Data completeness= 1.000          Theta(max)= 28.699

R(reflections)= 0.0354( 2944)     wR2(reflections)= 0.1017( 3025)

S = 1.086                 Npar= 181
```

B.23 4-(1,2,4trz)-Nap-NO_2 (L_2)

```
Bond precision:  C-C = 0.0018 A          Wavelength=0.71075

Cell:          a=7.60949(5)    b=8.69371(5)       c=18.71096(10)
               alpha=90        beta=94.2512(5)    gamma=90
Temperature:   100 K

               Calculated                Reported
Volume         1234.412(13)              1234.412(12)
Space group    P 21/c                    P 1 21/c 1
Hall group     -P 2ybc                   -P 2ybc
Moiety formula C14 H7 N5 O4              C14 H7 N5 O4
Sum formula    C14 H7 N5 O4              C14 H7 N5 O4
Mr             309.25                    309.25
Dx,g cm-3      1.664                     1.664
Z              4                         4
Mu (mm-1)      0.127                     0.127
F000           632.0                     632.0
F000'          632.31
h,k,lmax       9,11,24                   9,11,24
Nref           2825                      2825
Tmin,Tmax      0.970,0.987               0.396,1.000
Tmin'          0.968

Correction method= # Reported T Limits: Tmin=0.396 Tmax=1.000
AbsCorr = MULTI-SCAN

Data completeness= 1.000          Theta(max)= 27.481

R(reflections)= 0.0395( 2786)     wR2(reflections)= 0.1109( 2825)

S = 1.062                 Npar= 208
```

B.24 4-(1,2,4trz)-Nap-NH_2 (L_3)

Bond precision: C-C = 0.0023 A Wavelength=0.71075

Cell: a=6.8203(1) b=14.6723(2) c=11.8129(2)
alpha=90 beta=90 gamma=90
Temperature: 100 K

	Calculated	Reported
Volume	1182.11(3)	1182.11(3)
Space group	P n a 21	P n a 21
Hall group	P 2c -2n	P 2c -2n
Moiety formula	C14 H9 N5 O2	C14 H9 N5 O2
Sum formula	C14 H9 N5 O2	C14 H9 N5 O2
Mr	279.26	279.26
Dx,g cm-3	1.569	1.569
Z	4	4
Mu (mm-1)	0.112	0.112
F000	576.0	576.0
F000'	576.23	
h,k,lmax	9,19,15	9,19,15
Nref	3056[1599]	3049
Tmin,Tmax		0.535,1.000
Tmin'		

Correction method= # Reported T Limits: Tmin=0.535 Tmax=1.000
AbsCorr = MULTI-SCAN

Data completeness= 1.91/1.00 Theta(max)= 28.697

R(reflections)= 0.0350(3025) wR2(reflections)= 0.0973(3049)

S = 1.060 Npar= 190

B.25 4-(1,2,4trz)-Nap-N(Me)$_2$ (L$_4$)

```
Bond precision:  C-C = 0.0021 A          Wavelength=0.71075

Cell:            a=12.0958(1)     b=15.9850(2)       c=7.0609(1)
                 alpha=90         beta=96.305(1)     gamma=90
Temperature:     100 K

                 Calculated                Reported
Volume           1356.98(3)                1356.98(3)
Space group      P 21/c                    P 1 21/c 1
Hall group       -P 2ybc                   -P 2ybc
Moiety formula   C16 H13 N5 O2             C16 H13 N5 O2
Sum formula      C16 H13 N5 O2             C16 H13 N5 O2
Mr               307.31                    307.31
Dx,g cm-3        1.504                     1.504
Z                4                         4
Mu (mm-1)        0.105                     0.105
F000             640.0                     640.0
F000'            640.25
h,k,lmax         16,21,9                   16,21,9
Nref             3508                      3504
Tmin,Tmax        0.976,0.997               0.413,1.000
Tmin'            0.974

Correction method= # Reported T Limits: Tmin=0.413 Tmax=1.000
AbsCorr = GAUSSIAN

Data completeness= 0.999          Theta(max)= 28.700

R(reflections)= 0.0521( 3394)     wR2(reflections)= 0.1410( 3504)

S = 1.165                 Npar= 210
```

B.26 4-(1,2,4trz)-Nap-Tröger's base (L_5)

```
Bond precision:  C-C = 0.0090 A          Wavelength=0.71073

Cell:            a=11.4958(11)     b=22.187(2)        c=11.7544(7)
                 alpha=90          beta=91.924(7)     gamma=90
Temperature:     100 K

                 Calculated                Reported
Volume           2996.4(4)                 2996.4(4)
Space group      P 21/c                    P 1 21/c 1
Hall group       -P 2ybc                   -P 2ybc
Moiety formula   C31 H18 N10 O4, C3 H7 N O [+ solvent]  C31 H18 N10 O4, C3 H7 N O
Sum formula      C34 H25 N11 O5 [+ solvent] C34 H25 N11 O5
Mr               667.65                    667.65
Dx,g cm-3        1.480                     1.480
Z                4                         4
Mu (mm-1)        0.105                     0.105
F000             1384.0                    1384.0
F000'            1384.57
h,k,lmax         13,26,13                  13,26,13
Nref             5281                      5278
Tmin,Tmax        0.999,0.999               0.358,1.000
Tmin'            0.998

Correction method= # Reported T Limits: Tmin=0.358 Tmax=1.000
AbsCorr = MULTI-SCAN

Data completeness= 0.999          Theta(max)= 25.024

R(reflections)= 0.1124( 2732)     wR2(reflections)= 0.3163( 5278)

S = 1.063                 Npar= 453
```

B.27 4-ethyl-1,2,4-trz)-Nap-H (L_6)

```
Bond precision:  C-C = 0.0056 A          Wavelength=0.71073

Cell:            a=14.1843(12)     b=14.1843(12)     c=25.385(4)
                 alpha=90          beta=90           gamma=90
Temperature:     100 K

                 Calculated                Reported
Volume           5107.3(12)                5107.3(11)
Space group      I 41/a                    I 41/a
Hall group       -I 4ad                    -I 4ad
Moiety formula   C16 H12 N4 O2             C16 H12 N4 O2
Sum formula      C16 H12 N4 O2             C16 H12 N4 O2
Mr               292.30                    292.30
Dx,g cm-3        1.521                     1.521
Z                16                        16
Mu (mm-1)        0.105                     0.105
F000             2432.0                    2432.0
F000'            2433.00
h,k,lmax         16,16,30                  16,16,30
Nref             2252                      2249
Tmin,Tmax        0.995,0.995               0.412,1.000
Tmin'            0.995

Correction method= # Reported T Limits: Tmin=0.412 Tmax=1.000
AbsCorr = MULTI-SCAN

Data completeness= 0.999          Theta(max)= 24.988

R(reflections)= 0.0896( 1888)     wR2(reflections)= 0.2298( 2249)

S = 1.161                 Npar= 199
```

Appendix C

C.1 Molecular Electrostatic Potential

The molecular electrostatic potential maps derived from the Multipole Model total electron density is depicted in Appendic C 1. They appear at an electron donor site on the surface of N atoms of triazole groups and near the O atoms of imides; at an electron acceptor site on the surface near the C-H groups of triazole and the H atoms of naphthalimide rings. Accordingly, this gives an overview of interactions displayed in the crystal packing.

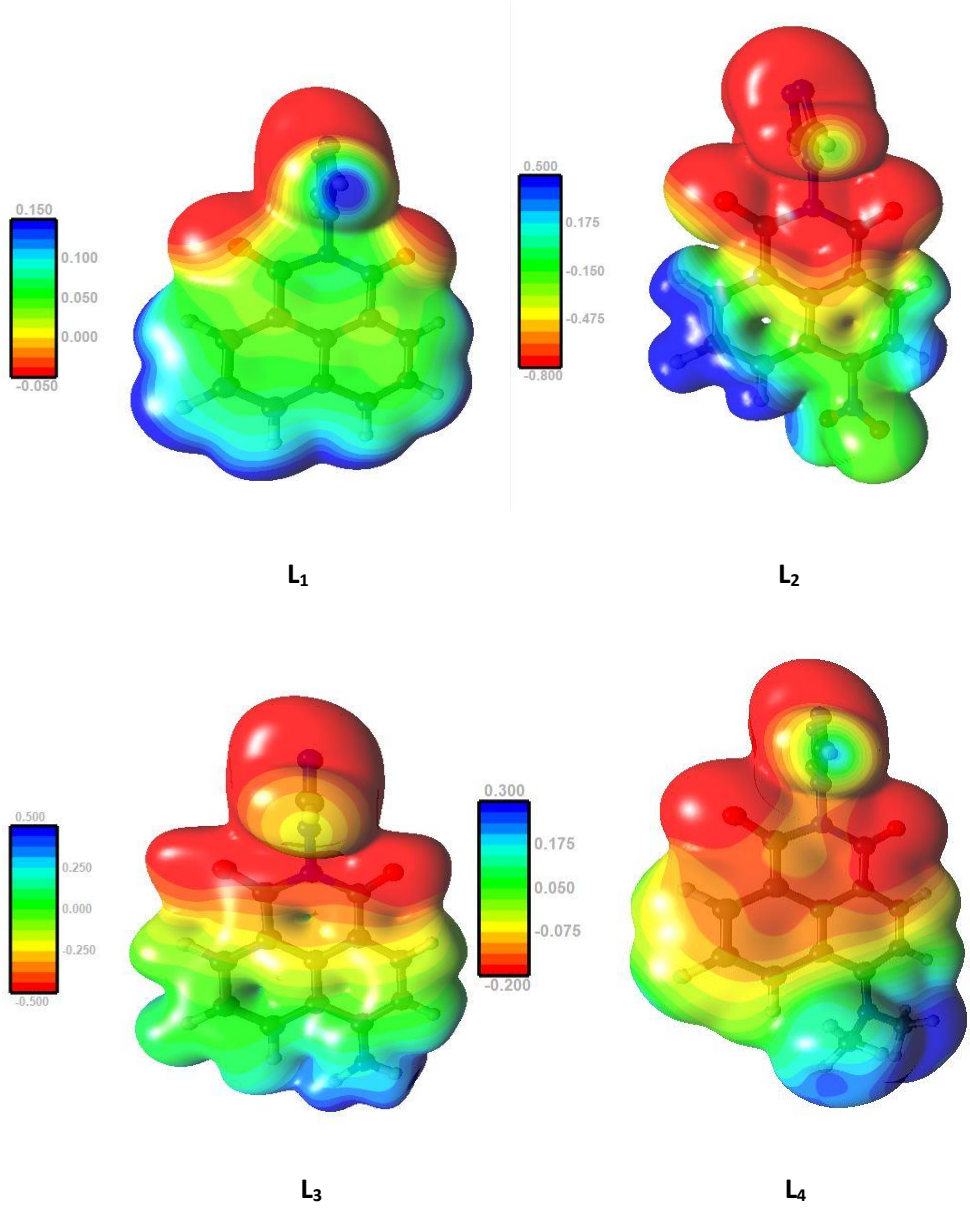

Appendix C 1 Molecular electrostatic potential of L_1-L_4 molecules based on Multipole Model

C.2 Experimental

Synthesis and crystallisation procedures are provided in chapter 4. Data collection for the high resolution studies were run exclusively on the rotating anode source diffractometer with the HyPix-600HE detector, which is the left-hand port on National Crystallography Service FR-E+ SuperBright Molybdenum X-Ray generator. This side has a highly focused beam (70μm) achieved with the VariMax VHF (Very High Flux) optics. The setup is completed with an AFC12 goniometer and a HyPix-600HE detector. Data is routinely collected at 100K with the aid of an Oxford Cryosystems Cobra. The high resolution data were collected under slightly different conditions for each crystal, but in all instances a full sphere of data was collected to a resolution of 0.38 A. Data reduction was completed using CrystalisPro software, each experiment treated separately.

The experimental parameters for all systems were in Appendix C 2

Appendix C 2 Experimental parameters for high resolution X-ray diffraction data collections for 4-(1,2,4trz)-Nap-H (L_1), 4-(1,2,4trz)-Nap-NO_2 (L_2), 4-(1,2,4trz)-Nap-NH_2 (L_3), 4-(1,2,4trz)-Nap-$N(Me)_2$ (L_4).

	L_1	L_2	L_3	L_4
Crystal system	Monoclinic	Monoclinic	Monoclinic	Monoclinic
2θ positions /°	-29/-87	-29/-87	-29/-87	-29/-87
Exposure /s	2/26	2/30	3/35	2/30
Scan width /°	0.5	0.5	0.5	0.5
Redundancy	6	7	8	7
Completeness /%	99.9	99.9	99.9	99.9

List of References

1. Gutlich, P.; Goodwin, H. A., *Spin crossover - An overall perspective*. 2004; Vol. 233, p 1-47.
2. Reger, D. L.; Debreczeni, A.; Smith, M. D.; Jezierska, J.; Ozarowski, A., Copper(II) Carboxylate Dimers Prepared from Ligands Designed to Form a Robust pi center dot center dot center dot pi Stacking Synthon: Supramolecular Structures and Molecular Properties. *Inorg Chem* **2012,** *51* (2), 1068-1083.
3. Czaja, A. U.; Trukhan, N.; Muller, U., Industrial applications of metal-organic frameworks. *Chem Soc Rev* **2009,** *38* (5), 1284-1293.
4. Licchelli, M.; Biroli, A. O.; Sangermani, C.; Zemab, M.; Poggi, A.; Donatella Sacchi, a., Excimer emission induced by metal ion coordination in 1,8-naphthalimide-tethered iminopyridine ligands. *Dalton Trans* **2003**, 4537-4545.
5. Reger, D. L.; Semeniuc, R. F.; Elgin, J. D.; Rassolov, V.; Smith, M. D., 1,8-Naphthalimide Synthon in Silver Coordination Chemistry: Control of Supramolecular Arrangement. *Cryst Growth Des* **2006,** *6* (12).
6. Cambi, L.; Szegö, L., Über die magnetische Susceptibilität der komplexen Verbindungen. *Ber deutsch chem Ges (A and B Series)* **1931,** *64* (10), 2591-2598.
7. Madeja, K.; Konig, E., Zur frage der bindungsverhaltnisse in komplexverbindindungen des Eisen(II) mit 1, 10-phenanthrolin. *J Inorg Nucl Chem* **1963,** *25*, 377-385.
8. Housecroft, C. E.; Sharpe, A. G., *Inorganic Chemistry*. Second edn. ed.; Pearson Education Limited: Essex, England, 2005.
9. Halcrow, M. A., *Spin-Crossover Materials: Properties and Applications*. 1st Ed. edn. ed.; John Wiley & Sons, Ltd: 2013.
10. Halcrow, M. A., Structure:function relationships in molecular spin-crossover complexes. *Chem Soc Rev* **2011,** *40* (7), 4119-42.
11. House, J. E., *Inorganic Chemistry*. Second edn. ed.; Academic Press, Elsevier,: 2008.
12. Gütlich, P.; Goodwin, H. A., *Spin crossover in transition metal compounds*. Springer: Berlin ; New York, 2004.
13. Nemec, I.; Herchel, R.; Travnicek, Z., The relationship between the strength of hydrogen bonding and spin crossover behaviour in a series of iron(III) Schiff base complexes. *Dalton Trans* **2015,** *44* (10), 4474-84.
14. Bonnet, S.; Siegler, M. A.; Costa, J. S.; Molnar, G.; Bousseksou, A.; Spek, A. L.; Gamez, P.; Reedijk, J., A two-step spin crossover mononuclear iron(II) complex with a [HS-LS-LS] intermediate phase. *Chem Commun (Camb)* **2008,** (43), 5619-21.
15. Fukuroi, K.; Takahashi, K.; Mochida, T.; Sakurai, T.; Ohta, H.; Yamamoto, T.; Einaga, Y.; Mori, H., Synergistic spin transition between spin crossover and spin-Peierls-like singlet formation in the halogen-bonded molecular hybrid system: $[Fe(Iqsal)_2][Ni(dmit)_2]CH_3CNH_2O$. *Angew Chem Int Ed Engl* **2014,** *53* (7), 1983-6.
16. Pavlov, A. A.; Denisov, G. L.; Kiskin, M. A.; Nelyubina, Y. V.; Novikov, V. V., Probing Spin Crossover in a Solution by Paramagnetic NMR Spectroscopy. *Inorg Chem* **2017,** *56* (24), 14759-14762.
17. Gutlich, P.; Gaspar, A. B.; Garcia, Y., Spin state switching in iron coordination compounds. *Beilstein J Org Chem* **2013,** *9*, 342-91.
18. Moliner, N.; Munoz, M. C.; Letard, S.; Letard, J. F.; Solans, X.; Burriel, R.; Castro, M.; Kahn, O.; Real, J. A., Spin-crossover in the $[Fe(abpt)_2(NCX)_2]$ (X = S, Se) system: structural, magnetic, calorimetric and photomagnetic studies. *Inorg Chim Acta* **1999,** *291* (1-2), 279-288.
19. Iwai, S.; Yoshinami, K.; Nakashima, S., Structure and Spin State of Iron(II) Assembled Complexes Using 9,10-Bis(4-pyridyl)anthracene as Bridging Ligand. *Inorg* **2017,** *5* (3).
20. Matouzenko, G. S.; Bousseksou, A.; Borshch, S. A.; Perrin, M.; Zein, S.; Salmon, L.; Molnar, G.; Lecocq, S., Cooperative spin crossover and order-disorder phenomena in a mononuclear compound $[Fe(DAPP)(abpt)](ClO_4)_2$ [DAPP = [bis(3-aminopropyl)(2-pyridylmethyl)amine], abpt = 4-amino-3,5-bis(pyridin-2-yl)-1,2,4-triazole]. *Inorg Chem* **2004,** *43* (1), 227-36.

21. Real, J. A.; Gaspar, A. B.; Niel, V.; Munoz, M. C., Communication between iron(II) building blocks in cooperative spin transition phenomena. *Coordin Chem Rev* **2003,** *236* (1-2), 121-141.
22. Janiak, C., A critical account on pi-pi stacking in metal complexes with aromatic nitrogen-containing ligands. *J Chem Soc Dalton* **2000,** (21), 3885-3896.
23. Renovitch, G. A.; Baker, W. A., Spin Equilibrium in Tris(2-aminomethylpyridine)iron(II) Halides. *J Am Chem Soc* **1967,** *86* (24), 2.
24. Gutlich, P.; Hauser, A.; Spiering, H., Thermal and Optical Switching of Iron(II) Complexes. *Angew Chem Int Ed Engl* **1994,** *33*, 30.
25. Zhao, X. H.; Zhang, S. L.; Shao, D.; Wang, X. Y., Spin Crossover in [Fe(2-Picolylamine)3](2+) Adjusted by Organosulfonate Anions. *Inorg Chem* **2015,** *54* (16), 7857-67.
26. Reger, D. L.; Debreczeni, A.; Reinecke, B.; Rassolov, V.; Smith, M. D., Highly Organized Structures and Unusual Magnetic Properties of Paddlewheel Copper(II) Carboxylate Dimers Containing the pi-pi Stacking, 1,8-Naphthalimide Synthon. *Inorg Chem* **2009,** *48* (18), 8911-8924.
27. Tsuzuki, S.; Honda, K.; Uchimaru, T.; Mikami, M.; Tanabe, K., Origin of Attraction and Directionality of the ππ Interaction Model Chemistry Calculations of Benzene Dimer Interaction. *J Am Chem Soc* **2001**.
28. Galet, A.; Gaspar, A. B.; Munoz, M. C.; Levchenko, G.; Real, J. A., Pressure effect and crystal structure reinvestigations on the spin crossover system: [Fe(bt)$_{(2)}$(NCS)$_{(2)}$] (bt=2,2'-bithiazoline) polymorphs A and B. *Inorg Chem* **2006,** *45* (24), 9670-9679.
29. Chen, B. L.; Xiang, S. C.; Qian, G. D., Metal-Organic Frameworks with Functional Pores for Recognition of Small Molecules. *Accounts Chem Res* **2010,** *43* (8), 1115-1124.
30. Lovitt, J. I.; Hawes, C. S.; Lynes, A. D.; Haffner, B.; Möbius, M. E.; Gunnlaugsson, T., Coordination chemistry of N-picolyl-1,8-naphthalimides: colourful low molecular weight metallo-gelators and unique chelation behaviours. *Inorg Chem Front* **2017,** *4* (2), 296-308.
31. Reger, D. L.; Horger, J. J.; Debreczeni, A.; Smith, M. D., Syntheses and Characterization of Copper(II) Carboxylate Dimers Formed from Enantiopure Ligands Containing a Strong pi center dot center dot center dot pi Stacking Synthon: Enantioselective Single-Crystal to Single-Crystal Gas/Solid-Mediated Transformations. *Inorg Chem* **2011,** *50* (20), 10225-10240.
32. Am J Dig DisAm J PhysiolReger, D. L.; Leitner, A.; Smith, M. D., Homochiral, Helical Coordination Complexes of Lanthanides(III) and Mixed-Metal Lanthanides(III): Impact of the 1,8-Naphthalimide Supramolecular Tecton on Structure, Magnetic Properties, and Luminescence. *Cryst Growth Des* **2015,** *15* (11), 5637-5644.
33. Phan, A.; Czaja, A. U.; Gandara, F.; Knobler, C. B.; Yaghi, O. M., Metal-Organic Frameworks of Vanadium as Catalysts for Conversion of Methane to Acetic Acid. *Inorg Chem* **2011,** *50* (16), 7388-7390.
34. Reger, D. L.; Leitner, A. P.; Smith, M. D., Supramolecular Metal–Organic Frameworks of s- and f-Block Metals: Impact of 1,8-Naphthalimide Functional Group. *Cryst Growth Des* **2015,** *16* (1), 527-536.
35. Wang, H.; Yang, L.; Zhang, W.; Zhou, Y.; Zhao, B.; Li, X., A colorimetric probe for copper(II) ion based on 4-amino-1,8-naphthalimide. *Inorg Chim Acta* **2012,** *381*, 111-116.
36. Mendiguchia, B. S.; Aiello, I.; Crispini, A., Zn(II) and Cu(II) complexes containing bioactive O,O-chelated ligands: homoleptic and heteroleptic metal-based biomolecules. *Dalton Trans* **2015,** *44* (20), 9321-9334.
37. Reger, D. L.; Leitner, A.; Smith, M. D., Cesium complexes of naphthalimide substituted carboxylate ligands: Unusual geometries and extensive cation-π interactions. *J Mol Struct* **2015,** *1091*, 31-36.
38. Rowsell, J. L. C.; Yaghi, O. M., Strategies for hydrogen storage in metal-organic frameworks. *Angew Chem Int Edit* **2005,** *44* (30), 4670-4679.
39. Reger, D. L.; Leitner, A.; Pellechia, P. J.; Smith, M. D., Framework complexes of group 2 metals organized by homochiral rods and pi...pi stacking forces: a breathing supramolecular MOF. *Inorg Chem* **2014,** *53* (18), 9932-45.

40. Tyagi, N.; Viji, M.; Karunakaran, S. C.; Varughese, S.; Ganesan, S.; Priya, S.; Saneesh Babu, P. S.; Nair, A. S.; Ramaiah, D., Enhancement in intramolecular interactions and in vitro biological activity of a tripodal tetradentate system upon complexation. *Dalton Trans* **2015,** *44* (35), 15591-601.
41. Grepioni, F.; d'Agostino, S.; Braga, D.; Bertocco, A.; Catalano, L.; Ventura, B., Fluorescent crystals and co-crystals of 1,8-naphthalimide derivatives: synthesis, structure determination and photophysical characterization. *J Mater Chem C* **2015,** *3* (36), 9425-9434.
42. Reger, D. L.; Elgin, J. D.; Semeniuc, R. F.; Pellechia, P. J.; Smith, M. D., Directional control of pi-stacked building blocks for crystal engineering: the 1,8-naphthalimide synthon. *Chem Commun* **2005,** (32), 4068-70.
43. Reger, D. L.; Debreczeni, A.; Smith, M. D., Rhodium paddlewheel dimers containing the π···π stacking, 1,8-naphthalimide supramolecular synthon. *Inorg Chim Acta* **2011,** *378* (1), 42-48.
44. Reger, D. L.; Derek Elgin, J.; Pellechia, P. J.; Smith, M. D.; Simpson, B. K., Structural organization of a {ruthenium[tris(bipyridyl)]}$^{2+}$ complex by strong π–π stacking of a tethered 1,8-naphthalimide synthon: Impact on electrochemical and spectral properties. *Polyhedron* **2009,** *28* (8), 1469-1474.
45. Reger, D. L.; Horger, J.; Smith, M. D.; Long, G. J., Homochiral, helical metal-organic framework structures organized by strong, non-covalent pi-pi stacking interactions. *Chem Commun* **2009,** (41), 6219-21.
46. Banerjee, S.; Bright, S. A.; Smith, J. A.; Burgeat, J.; Martinez-Calvo, M.; Williams, D. C.; Kelly, J. M.; Gunnlaugsson, T., Supramolecular approach to enantioselective DNA recognition using enantiomerically resolved cationic 4-amino-1,8-naphthalimide-based Troger's bases. *J Org Chem* **2014,** *79* (19), 9272-83.
47. Banerjee, S.; Kitchen, J. A.; Bright, S. A.; O'Brien, J. E.; Williams, D. C.; Kelly, J. M.; Gunnlaugsson, T., Synthesis, spectroscopic and biological studies of a fluorescent Pt(II) (terpy) based 1,8-naphthalimide conjugate as a DNA targeting agent. *Chem Commun* **2013,** *49* (76), 8522-4.
48. Murphy, S.; Bright, S. A.; Poynton, F. E.; McCabe, T.; Kitchen, J. A.; Veale, E. B.; Williams, D. C.; Gunnlaugsson, T., Synthesis, photophysical and cytotoxicity evaluations of DNA targeting agents based on 3-amino-1,8-naphthalimide derived Troger's bases. *Org Biomol Chem* **2014,** *12* (34), 6610-23.
49. Shanmugaraju, S.; Dabadie, C.; Byrne, K.; Savyasachi, A. J.; Umadevi, D.; Schmitt, W.; Kitchen, J. A.; Gunnlaugsson, T., A supramolecular Troger's base derived coordination zinc polymer for fluorescent sensing of phenolic-nitroaromatic explosives in water. *Chem Sci* **2017,** *8* (2), 1535-1546.
50. Veale, E. B.; Gunnlaugsson, T., Synthesis, photophysical, and DNA binding studies of fluorescent Troger's base derived 4-amino-1,8-naphthalimide supramolecular clefts. *J Org Chem* **2010,** *75* (16), 5513-25.
51. Veale, E. B.; Frimannsson, D. O.; Lawler, M.; Gunnlaugsson, T., 4-Amino-1,8-naphthalimide-Based Troger's Bases As High Affinity DNA Targeting Fluorescent Supramolecular Scaffolds. *Org Lett* **2009,** *11* (18).
52. Reger, D. L.; Debreczeni, A.; Horger, J. J.; Smith, M. D., Structures of Bifunctional Molecules Containing Two Very Different Supramolecular Synthons: Carboxylic Acid and Strong pi center dot center dot center dot pi Stacking 1,8-Naphthalimide Ring. *Cryst Growth Des* **2011,** *11* (9), 4068-4079.
53. Reger, D. L.; Leitner, A.; Smith, M. D.; Tran, T. T.; Halasyamani, P. S., Homochiral helical metal-organic frameworks of group 1 metals. *Inorg Chem* **2013,** *52* (17), 10041-51.
54. Reger, D. L.; Leitner, A. P.; Smith, M. D., Homochiral helical metal-organic frameworks of potassium. *Inorg Chem* **2012,** *51* (19), 10071-3.
55. Timothy G. Carter; Healey, E. R.; Melanie A. Pitt; Johnson, D. W., Secondary Bonding Interactions Observed in Two Arsenic Thiolate Complexes. *Inorg Chem Commun* **2015,** (44), 9634-9636.
56. Hardcastle, I. R.; Liu, J.; Valeur, E.; Watson, A.; Ahmed, S. U.; Blackburn, T. J.; Bennaceur, K.; Clegg, W.; Drummond, C.; Endicott, J. A.; Golding, B. T.; Griffin, R. J.; Gruber, J.; Haggerty, K.; Harrington, R. W.; Hutton, C.; Kemp, S.; Lu, X.; McDonnell, J. M.; Newell, D. R.; Noble, M. E.;

Payne, S. L.; Revill, C. H.; Riedinger, C.; Xu, Q.; Lunec, J., Isoindolinone inhibitors of the murine double minute 2 (MDM2)-p53 protein-protein interaction: structure-activity studies leading to improved potency. *J Med Chem* **2011,** *54* (5), 1233-43.

57. Zhang, J.; Li, H.; Chen, P.; Sun, W.; Gao, T.; Yan, P., A new strategy for achieving white-light emission of lanthanide complexes: effective control of energy transfer from blue-emissive fluorophore to Eu(iii) centres. *J Mater Chem C* **2015,** *3* (8), 1799-1806.
58. Grabowsky, S.; Genoni, A.; Burgi, H. B., Quantum crystallography. *Chem Sci* **2017,** *8* (6), 4159-4176.
59. Ghanem, A.; Gardiner, M. G.; Williamson, R. M.; Muller, P., First X-ray structure of a N-naphthaloyl-tethered chiral dirhodium(II) complex: structural basis for tether substitution improving asymmetric control in olefin cyclopropanation. *Chem Commun* **2010,** *16* (11).
60. Konovalova, I. S.; Nelyubina, Y. V.; Lyssenko, K. A.; Paponov, B. V.; Shishkin, O. V., Intra- and intermolecular interactions in the crystals of 3,4-diamino-1,2,4-triazole and its 5-methyl derivative. Experimental and theoretical investigations of charge density distribution. *J Phys Chem A* **2011,** *115* (30), 8550-62.
61. Hehre, W. J., *A Guide to Molecular Mechanics and Quantum Chemical Calculations*. United States of America, 2002.
62. Soman, R.; Sujatha, S.; Arunkumar, C., Quantitative crystal structure analysis of fluorinated porphyrins. *J Fluor Chem* **2014,** *163*, 16-22.
63. Stalke, D., Meaningful structural descriptors from charge density. *Chem-Eur J* **2011,** *17* (34), 9264-78.
64. J. Gillespie; A., P. L., *Popelier-Chemical Bonding and Molecular Geometry. From Lewis to Electron Densities*. Oxford University Press, USA, 2001.
65. Jacob Overgaard; Waller, M. P.; Ross Piltz; Platts, J. A.; Emseis, P.; Leverett, P.; Williams, P. A.; Hibbs, D. E., Experimental and Theoretical Charge Density Distribution in Two Ternary Cobalt(III) Complexes of Aromatic Amino Acids. *J Phys Chem A* **2007,** (111), 10123-10133.
66. McKinnon, J. J.; Jayatilaka, D.; Spackman, M. A., Towards quantitative analysis of intermolecular interactions with Hirshfeld surfaces. *Chem Commun* **2007**, 3814-3816.
67. Nguyen, T. H.; Groundwater, P. W.; Platts, J. A.; Hibbs, D. E., Experimental and theoretical charge density studies of 8-hydroxyquinoline cocrystallized with salicylic acid. *J Phys Chem A* **2012,** *116* (13), 3420-7.
68. Spackman, M. A.; McKinnon, J. J., Fingerprinting intermolecular interactions in molecular crystals. *CrystEngComm* **2002,** *4* (66), 378-392.
69. Tidey, J. P.; Zhurov, V. V.; Gianopoulos, C. G.; Zhurova, E. A.; Pinkerton, A. A., Experimental Charge-Density Study of the Intra- and Intermolecular Bonding in TKX-50. *J Phys Chem A* **2017,** *121* (46), 8962-8972.
70. Brock, C. P.; Dunitz, J. D., Towards a Grammar of Crystal Packing. *Chem Mater* **1994,** *6* (8), 1118-1127.
71. Müller-Dethlefs, K.; Hobza, P., Noncovalent Interactions: A Challenge for Experiment and Theory. *Chem Rev* **2000,** *100* (1), 143-168.
72. Hobza, P., Calculations on Noncovalent Interactions and Databases of Benchmark Interaction Energies. *Acc Chem Res* **2012,** *45* (4), 663-672.
73. Corpinot, M. K.; Bučar, D.-K., A Practical Guide to the Design of Molecular Crystals. *Cryst Growth Des* **2019,** *19* (2), 1426-1453.
74. Gavezzotti, A., The "sceptical chymist": intermolecular doubts and paradoxes. *CrystEngComm* **2013,** *15* (20), 4027-4035.
75. Bauzá, A.; Mooibroek, T. J.; Frontera, A., Towards design strategies for anion–π interactions in crystal engineering. *CrystEngComm* **2016,** *18* (1), 10-23.
76. Turner, M. J.; Grabowsky, S.; Jayatilaka, D.; Spackman, M. A., Accurate and Efficient Model Energies for Exploring Intermolecular Interactions in Molecular Crystals. *J Phy Chem Lett* **2014,** *5* (24), 4249-4255.
77. Dunitz, J. D.; Gavezzotti, A., Molecular Recognition in Organic Crystals: Directed Intermolecular Bonds or Nonlocalized Bonding? *Angew Chem Int Ed* **2005,** *44* (12), 1766-1787.

78. Martinez, C. R.; Iverson, B. L., Rethinking the term “pi-stacking”. *Chem Sci* **2012,** *3* (7), 2191-2201.
79. Yao, Z.-F.; Wang, J.-Y.; Pei, J., Control of π–π Stacking via Crystal Engineering in Organic Conjugated Small Molecule Crystals. *Cryst Growth Des* **2018,** *18* (1), 7-15.
80. Tsuzuki, S.; Honda, K.; Uchimaru, T.; Mikami, M.; Tanabe, K., Origin of Attraction and Directionality of the π/π Interaction: Model Chemistry Calculations of Benzene Dimer Interaction. *J Am Chem Soc* **2002,** *124* (1), 104-112.
81. Jennings, W. B.; Farrell, B. M.; Malone, J. F., Attractive Intramolecular Edge-to-Face Aromatic Interactions in Flexible Organic Molecules. *Acc Chem Res* **2001,** *34* (11), 885-894.
82. Hunter, C. A.; Sanders, J. K. M., The nature of .pi.-.pi. interactions. *J Am Chem Soc* **1990,** *112* (14), 5525-5534.
83. Elangannan, A.; Gautam, R. D.; Roger, A. K.; Joanna, S.; Steve, S.; Ibon, A.; David, C. C.; Robert, H. C.; Joseph, J. D.; Pavel, H.; Henrik, G. K.; Anthony, C. L.; Benedetta, M.; David, J. N., Defining the hydrogen bond: An account (IUPAC Technical Report). *Pure Appl Chem* **2011,** *83* (8), 1619-1636.
84. Steiner, T., The Hydrogen Bond in the Solid State. *Angew Chem Int Ed* **2002,** *41* (1), 48-76.
85. Taylor, R., Which intermolecular interactions have a significant influence on crystal packing? *CrystEngComm* **2014,** *16* (30), 6852-6865.
86. Perlstein, J., The Weak Hydrogen Bond In Structural Chemistry and Biology (International Union of Crystallography, Monographs on Crystallography. *J J Am Chem Soc* **2001,** *123* (1), 191-192.
87. Bragg, W. L.; Bragg, W. H., The structure of some crystals as indicated by their diffraction of X-rays. *Proceedings of the Royal Society of London Series A, Containing Papers of a Mathematical and Physical Character* **1913,** *89* (610), 248-277.
88. Koritsanszky, T. S.; Coppens, P., Chemical Applications of X-ray Charge-Density Analysis. *Chem Rev* **2001,** (101).
89. Macchi, P., Modern charge density studies: the entanglement of experiment and theory. *Crystallogr Rev* **2013,** *19* (2), 58-101.
90. Matta, C. F.; Boyd, R. J., *Atoms in Molecules A Quantum Theory International Series of Monographs on Chemistry*. WILEY-VCH: 2007.
91. Kohn, W.; Sham, L. J., Self-Consistent Equations Including Exchange and Correlation Effects. *Phys Rev A* **1965,** *140* (4A), A1133-A1138.
92. Hohenberg, P.; Kohn, W., Inhomogeneous Electron Gas. *Phys Rev A* **1964,** *136* (3B), B864-B871.
93. Chimpri, A. S.; Gryl, M.; Santos, L. H. R. D.; Krawczuk, A.; Macchi, P., Correlation between accurate electron density and linear optical properties in Amino acid derivatives. *Cryst Growth Des* **2013,** *13* (7), 2995-3010.
94. Dkhissi, A.; Ducere, J. M.; Blossey, R.; Pouchan, C., Can the hybrid meta GGA and DFT-D methods describe the stacking interactions in conjugated polymers? *J Comput Chem* **2009,** *30* (8), 1179-84.
95. Bader, R. F. W., A Quantum Theory (International Series of Monographs on Chemistry. *Oxford University Press, USA)* **1994**.
96. Coppens, P.; Baker, E. N., *x-ray-charge-densities-and-chemical-bonding*. 1997.
97. Armstrong, F. A.; Takano, M.; Day, l. P.; Duan, X.; Poeppelmeier, K. R., Electron Density and Chemical Bonding II. **2011**.
98. Gatti, C., The Source Function Descriptor as a Tool to Extract Chemical Information from Theoretical and Experimental Electron Densities. In *Electron Density and Chemical Bonding II*, University of Oxford, 2011; pp 193-285.
99. Meindl, K.; Henn, J., Residual Density Analysis. In *Electron Density and Chemical Bonding II*, pringer-Verlag Berlin Heidelberg: 2010; pp 143-192.
100. Wu, L. C.; Chung, W. C.; Wang, C. C.; Lee, G. H.; Lu, S. I.; Wang, Y., A charge density study of pi-delocalization and intermolecular interactions. *Phys Chem Chem Phys* **2015,** *17* (21), 14177-84.

101. Munshi, P.; Guru Row, T. N., Evaluation of weak intermolecular interactions in molecular crystalsvia experimental and theoretical charge densities. *Crystallogr Rev* **2005,** *11* (3), 199-241.
102. Johnson, C. K.; Burnett, M. N.; Dunbar, W. D., Crystallographic Topology and Its Applications. 1996.
103. Espinosa, E.; Molins, E.; Lecomte, C., Hydrogen bond strengths revealed by topological analyses of experimentally observed electron densities. *Chem Phy Lett* **1998,** *285* (3), 170-173.
104. Abramov, Y. A., On the Possibility of Kinetic Energy Density Evaluation from the Experimental Electron-Density Distribution. *Acta Crystallogr Section A* **1997,** *53* (3), 264-272.
105. Freedman, D. E.; Harman, W. H.; Harris, T. D.; Long, G. J.; Chang, C. J.; Long, J. R., Slow Magnetic Relaxation in a High-Spin Iron(II) Complex. *J Am Chem Soc* **2010,** *132* (4), 1224-1225.
106. Greenaway, A. M.; O'Connor, C. J.; Schrock, A.; Sinn, E., High- and low-spin interconversion in a series of (.alpha.-picolylamine)iron(II) complexes. *Inorg Chem* **1979,** *18* (10), 2692-2695.
107. Hostettler, M.; Törnroos, K. W.; Chernyshov, D.; Vangdal, B.; Bürgi, H.-B., Challenges in Engineering Spin Crossover: Structures and Magnetic Properties of Six Alcohol Solvates of Iron(II) Tris(2-picolylamine) Dichloride. *Angew Chem Int Ed* **2004,** *43* (35), 4589-4594.
108. Katz, B. A.; Strouse, C. E., Spin-state isomerism of tris(2-picolylamine)iron(II). The diiodide and the hydrated dichloride. *Inorg Chem* **1980,** *19* (3), 658-665.
109. Wiehl, L.; Kiel, G.; Koehler, C. P.; Spiering, H.; Guetlich, P., Structure determination and investigation of the high-spin .tautm. low-spin transition of tris[2-(aminomethyl)pyridine]iron(2+) dibromide.monoethanol. *Inorg Chem* **1986,** *25* (10), 1565-1571.
110. Langer, R.; Bönisch, F.; Maser, L.; Pietzonka, C.; Vondung, L.; Zimmermann, T. P., Substitutional Lability of Diphosphine Ligands in Tetrahedral Iron(II) Chloro Complexes. *Eur J Inorg Chem* **2015,** *2015* (1), 141-148.
111. Lenze, M.; Martin, E. T.; Rath, N. P.; Bauer, E. B., Iron(II) α-Aminopyridine Complexes and Their Catalytic Activity in Oxidation Reactions: A Comparative Study of Activity and Ligand Decomposition. *ChemPlusChem* **2013,** *78* (1), 101-116.
112. Chernyshov, D.; Vangdal, B.; Törnroos, K. W.; Bürgi, H.-B., Chemical disorder and spin crossover in a mixed ethanol–2-propanol solvate of FeII tris(2-picolylamine) dichloride. *New J Chem* **2009,** *33* (6), 1277-1282.
113. Zhu, Y.; Zhou, G.; Xu, Y.; Zhu, D.; Zheng, X., Solvothermal Synthesis, Crystal Structure and P roperties of a New Organic Templated Lanthanum Sulfate $[C_4N_3H_{16}][La(SO_4)_3(H_2O)]$. *Z Anorg Allg Chem***2008,** *634* (3), 545-548.
114. Butcher, R. J.; Addison, A. W., Structural aspects of the bis(2,2′-dipicolylamine)iron(II) cation. *Inorg Chim Acta* **1989,** *158* (2), 211-215.
115. Malassa, A.; Görls, H.; Buchholz, A.; Plass, W.; Westerhausen, M., Pyridylmethylamines as Ligands in Iron Halide Complexes – Coordination Behaviour Depending on the Halide, the Denticity of the Amino Ligand and the Oxidation State of Iron. *Z Anorg Allg Chem* **2006,** *632* (14), 2355-2362.
116. Davies, C. J.; Solan, G. A.; Fawcett, J., Synthesis and structural characterisation of cobalt(II) and iron(II) chloride complexes containing bis(2-pyridylmethyl)amine and tris(2-pyridylmethyl)amine ligands. *Polyhedron* **2004,** *23* (18), 3105-3114.
117. Malassa, A.; Agthe, C.; Görls, H.; Friedrich, M.; Westerhausen, M., Deprotonation and dehydrogenation of Di(2-pyridylmethyl)amine with $M[N(SiMe_3)_2]_2$ (M = Mn, Fe, Co, Zn) and $Fe(C6H2\text{-}2,4,6\text{-}Me_3)_2$. *Journal of Organometallic Chemistry* **2010,** *695* (12), 1641-1650.
118. Carter, A. B.; Laverick, R. J.; Wales, D. J.; Akponasa, S. O.; Scott, A. J.; Keene, T. D.; Kitchen, J. A., Investigating the Structure Directing Properties of Designer 1,8-Naphthalimide and Amphiphilic Sulfonate Anions and Their FeIII Thiosemicarbazone Complexes. *Cryst Growth Des* **2017,** *17* (10), 5129-5144.
119. Hübschle, C. B.; Sheldrick, G. M.; Dittrich, B., ShelXle: a Qt graphical user interface for SHELXL. *J appl crystallogr* **2011,** *44* (Pt 6), 1281-1284.

120. Dolomanov, O. V.; Bourhis, L. J.; Gildea, R. J.; Howard, J. A. K.; Puschmann, H., OLEX2: a complete structure solution, refinement and analysis program. *J appl crystallogr* **2009,** *42* (2), 339-341.
121. Kitchen, J. A.; Olguín, J.; Kulmaczewski, R.; White, N. G.; Milway, V. A.; Jameson, G. N. L.; Tallon, J. L.; Brooker, S., Effect of N4-Substituent Choice on Spin Crossover in Dinuclear Iron(II) Complexes of Bis-Terdentate 1,2,4-Triazole-Based Ligands. *Inorg Chem* **2013,** *52* (19), 11185-11199.
122. Klingele, M. H.; Moubaraki, B.; Murray, K. S.; Brooker, S., Synthesis and Some First-Row Transition-Metal Complexes of the 1,2,4-Triazole-Based Bis(terdentate) Ligands TsPMAT and PMAT. *Chemistry – Chem-Eur J* **2005,** *11* (23), 6962-6973.
123. Klingele, M. H.; Moubaraki, B.; Cashion, J. D.; Murray, K. S.; Brooker, S., The first X-ray crystal structure determination of a dinuclear complex trapped in the [low spin-high spin] state: $[Fe(II)_2(PMAT)_2](BF_4)_4 \cdot$DMF. *Chem Commun (Camb)* **2005,** (8), 987-9.
124. Spek, A. L., Single ‐ crystal structure validation with the program PLATON. *J appl crystallogr* **2003,** *36* (1).
125. Kitchen, J. A.; White, N. G.; Jameson, G. N.; Tallon, J. L.; Brooker, S., Effect of counteranion X on the spin crossover properties of a family of diiron(II) triazole complexes $[Fe(II)_2(PMAT)_2](X)_4$. *Inorg Chem* **2011,** *50* (10), 4586-97.
126. Klingele, M. H.; Brooker, S., The coordination chemistry of 4-substituted 3,5-di(2-pyridyl)-4H-1,2,4-triazoles and related ligands. *Coordin Chem Rev* **2003,** *241* (1-2), 119-132.
127. Scott, H. S.; Ross, T. M.; Moubaraki, B.; Murray, K. S.; Neville, S. M., Spin Crossover in Polymeric Materials Using Schiff Base Functionalized Triazole Ligands. *Eur J Inorg Chem* **2013,** *2013* (5-6), 803-812.
128. Roubeau, O., Triazole-Based One-Dimensional Spin-Crossover Coordination Polymers. *Chem-Eur J* **2012,** *18* (48), 15230-15244.
129. Haasnoot, J. G., Mononuclear, oligonuclear and polynuclear metal coordination compounds with 1,2,4-triazole derivatives as ligands. *Coordin Chem Rev* **2000,** *200*, 131-185.
130. Sheu, C.-F.; Pillet, S. b.; Lin, Y.-C.; Chen, S.-M.; Hsu, I.-J.; Lecomte, C.; Wang, Y., Magnetostructural Relationship in the Spin-Crossover Complex t-{Fe(abpt)2[N(CN)2]2}: Polymorphism and Disorder Phenomenon. *Inorg Chem* **2008**.
131. Lavrenova, L. G.; Shakirova, O. G., Spin Crossover and Thermochromism of Iron(II) Coordination Compounds with 1,2,4-Triazoles and Tris(pyrazol-1-yl)methanes. *Eur J Inorg Chem* **2013,** *2013* (5 ‐ 6), 670-682.
132. Kitchen, J. A.; White, N. G.; Boyd, M.; Moubaraki, B.; Murray, K. S.; Boyd, P. D. W.; Brooker, S., Iron(II) Tris-[N4-substituted-3,5-di(2-pyridyl)-1,2,4-triazole] Complexes: Structural, Magnetic, NMR, and Density Functional Theory Studies. *Inorg Chem* **2009,** *48* (14), 6670-6679.
133. Feltham, H. L. C.; Barltrop, A. S.; Brooker, S., Spin crossover in iron(II) complexes of 3,4,5-tri-substituted-1,2,4-triazole (Rdpt), 3,5-di-substituted-1,2,4-triazolate (dpt−), and related ligands. *Coordin Chem Rev* **2017,** *344*, 26-53.
134. Dirtu, M. M.; Neuhausen, C.; Naik, A. D.; Rotaru, A.; Spinu, L.; Garcia, Y., Insights into the origin of cooperative effects in the spin transition of $[Fe(NH_2trz)_3](NO_3)_2$: the role of supramolecular interactions evidenced in the crystal structure of $[Cu(NH_2trz)_3](NO_3)_2 \cdot H_2O$. *Inorg Chem* **2010,** *49* (12), 5723-36.
135. Martin, J.-P.; Zarembowitch, J.; Bousseksou, A.; Dworkin, A.; Haasnoot, J. G.; Varret, F., Solid State Effects on Spin Transitions: Magnetic, Calorimetric, and Moessbauer-Effect Properties of $[Fe_xCo_{1-x}(4,4'\text{-bis-}1,2,4\text{-triazole})_2(NCS)_2] \cdot H_2O$ Mixed-Crystal Compounds. *Inorg Chem* **1994,** *33* (26), 6325-6333.
136. Lavrenova, L. G.; Yudina, N. G.; Ikorskii, V. N.; Varnek, V. A.; Oglezneva, I. M.; Larionov, S. V., Spin-Crossover and Thermochromism in Complexes of Iron(Ii) Iodide and Thiocyanate with 4-Amino-1,2,4-Triazole. *Polyhedron* **1995,** *14* (10), 1333-1337.
137. Grosjean, A.; Daro, N.; Kauffmann, B.; Kaiba, A.; Letard, J. F.; Guionneau, P., The 1-D polymeric structure of the [Fe(NH(2)trz)(3)](NO3)(2)center dot nH(2)O (with n=2) spin crossover compound proven by single crystal investigations. *Chem Commun* **2011,** *47* (45), 12382-12384.

138. Lochenie, C.; Schötz, K.; Panzer, F.; Kurz, H.; Maier, B.; Puchtler, F.; Agarwal, S.; Köhler, A.; Weber, B., Spin-Crossover Iron(II) Coordination Polymer with Fluorescent Properties: Correlation between Emission Properties and Spin State. *J Am Chem Soc* **2018,** *140* (2), 700-709.
139. Wang, J.-L.; Liu, Q.; Lv, X.-J.; Wang, R.-L.; Duan, C.-Y.; Liu, T., Magnetic fluorescent bifunctional spin-crossover complexes. *Dalt Trans* **2016,** *45* (46), 18552-18558.
140. Kitchen, J. A.; Zhang, N.; Carter, A. B.; Fitzpatrick, A. J.; Morgan, G. G., Structural and magnetic properties of dinuclear Cu(II) complexes featuring triazolyl-naphthalimide ligands. *J Coord Chem* **2016,** *69* (11-13), 2024-2037.
141. Dolenský, B.; Elguero, J.; Král, V.; Pardo, C.; Valík, M., Current Tröger's Base Chemistry. In *Advances in Heterocyclic Chemistry*, Katritzky, A. R., Ed. Academic Press: 2007; Vol. 93, pp 1-56.
142. Banerjee, S.; Bright, S. A.; Smith, J. A.; Burgeat, J.; Martinez-Calvo, M.; Williams, D. C.; Kelly, J. M.; Gunnlaugsson, T., Supramolecular Approach to Enantioselective DNA Recognition Using Enantiomerically Resolved Cationic 4-Amino-1,8-naphthalimide-Based Tröger's Bases. *J Org Chem* **2014,** *79* (19), 9272-9283.
143. Veale, E. B.; Frimannsson, D. O.; Lawler, M.; Gunnlaugsson, T., 4-Amino-1,8-naphthalimide-Based Tröger's Bases As High Affinity DNA Targeting Fluorescent Supramolecular Scaffolds. *Org Lett* **2009,** *11* (18), 4040-4043.
144. Shanmugaraju, S.; Dabadie, C.; Byrne, K.; Savyasachi, A. J.; Umadevi, D.; Schmitt, W.; Kitchen, J. A.; Gunnlaugsson, T., A supramolecular Tröger's base derived coordination zinc polymer for fluorescent sensing of phenolic-nitroaromatic explosives in water. *Chem Sci* **2017,** *8* (2), 1535-1546.
145. Kitchen, J. A.; Zhang, N. J.; Carter, A. B.; Fitzpatrick, A. J.; Morgan, G. G., Structural and magnetic properties of dinuclear Cu(II) complexes featuring triazolyl-naphthalimide ligands. *J Coord Chem* **2016,** *69* (11-13), 2024-2037.
146. Muzart, J., N,N-Dimethylformamide: much more than a solvent. *Tetrahedron* **2009,** *65* (40), 8313-8323.
147. Forgan, R. S., Modulated self-assembly of metal–organic frameworks. *Chem Sci* **2020,** *11* (18), 4546-4562.
148. Heravi, Majid M.; Ghavidel, M.; Mohammadkhani, L., Beyond a solvent: triple roles of dimethylformamide in organic chemistry. *RSC Advances* **2018,** *8* (49), 27832-27862.
149. Benaicha, B.; Van Do, K.; Yangui, A.; Pittala, N.; Lusson, A.; Sy, M.; Bouchez, G.; Fourati, H.; Gomez-Garcia, C. J.; Triki, S.; Boukheddaden, K., Interplay between spin-crossover and luminescence in a multifunctional single crystal iron(ii) complex: towards a new generation of molecular sensors. *Chem Sci* **2019,** *10* (28), 6791-6798.
150. Tumiatti, V.; Milelli, A.; Minarini, A.; Micco, M.; Gasperi Campani, A.; Roncuzzi, L.; Baiocchi, D.; Marinello, J.; Capranico, G.; Zini, M.; Stefanelli, C.; Melchiorre, C., Design, synthesis, and biological evaluation of substituted naphthalene imides and diimides as anticancer agent. *J Med Chem* **2009,** *52* (23), 7873-7.
151. Wang, W.; Ling, Y.; Yang, L.-J.; Liu, Q.-L.; Luo, Y.-H.; Sun, B.-W., Crystals of 4-(2-benzimidazole)-1,2,4-triazole and its hydrate: preparations, crystal structure and Hirshfeld surfaces analysis. *Res Chem Inters* **2015,** *42* (4), 3157-3168.
152. Turner, M. J.; Thomas, S. P.; Shi, M. W.; Jayatilaka, D.; Spackman, M. A., Energy frameworks: insights into interaction anisotropy and the mechanical properties of molecular crystals. *Chem Commun* **2015,** *51* (18), 3735-3738.
153. Turner M. J., M. J. J., Wolff S. K., Grimwood D. J., Spackman P. R., Jayatilaka D. and Spackman M. A., CrystalExplorer17.5. University of Western Australia.
154. Gavezzotti, A., Calculation of Intermolecular Interaction Energies by Direct Numerical Integration over Electron Densities. I. Electrostatic and Polarization Energies in Molecular Crystals. *J Phy Chem B* **2002,** *106* (16), 4145-4154.
155. Gavezzotti, A., Computational Studies of Crystal Structure and Bonding. In *Advanced X-Ray Crystallography*, Rissanen, K., Ed. Springer Berlin Heidelberg: Berlin, Heidelberg, 2012; pp 1-32.

156. Gavezzotti, A., Calculation of Intermolecular Interaction Energies by Direct Numerical Integration over Electron Densities. 2. An Improved Polarization Model and the Evaluation of Dispersion and Repulsion Energies. *J Phy Chem B* **2003,** *107* (10), 2344-2353.
157. Maitland, G. C., *Intermolecular forces : their origin and determination*. Clarendon Press: Oxford, 1987.
158. Su, P.; Li, H., Energy decomposition analysis of covalent bonds and intermolecular interactions. *J Chem Phy* **2009,** *131* (1), 014102.
159. Maroulis, G., *Atoms, Molecules and Clusters in Electric Fields*.
160. Curutchet, C.; Orozco, M.; Luque, F. J.; Mennucci, B.; Tomasi, J., Dispersion and repulsion contributions to the solvation free energy: Comparison of quantum mechanical and classical approaches in the polarizable continuum model. *J Comput Chem* **2006,** *27* (15), 1769-1780.
161. Hirshfeld, F. L., Bonded-atom fragments for describing molecular charge densities. *Theoretica chimica acta* **1977,** *44* (2), 129-138.
162. Spackman, M. A.; Jayatilaka, D., Hirshfeld surface analysis. *CrystEngComm* **2009,** *11* (1), 19-32.
163. Spackman, M. A.; McKinnon, J. J., Fingerprinting intermolecular interactions in molecular crystals. *CrystEngComm* **2002,** *4* (66), 378-392.
164. Wheeler, S. E.; Bloom, J. W. G., Toward a More Complete Understanding of Noncovalent Interactions Involving Aromatic Rings. *J Phy Chem A* **2014,** *118* (32), 6133-6147.
165. Sinnokrot, M. O.; Sherrill, C. D., High-Accuracy Quantum Mechanical Studies of π−π Interactions in Benzene Dimers. *J Phy Chem A* **2006,** *110* (37), 10656-10668.
166. Guillot, B.; Lagoutte, A.; Lecomte, C.; Jelsch, C., Advances in protein and small-molecule charge-density refinement methods using MoPro. *J Appl Crystallogr* **2005,** *38* (1), 38-54.
167. Waller, M. P.; Robertazzi, A.; Platts, J. A.; Hibbs, D. E.; Williams, P. A., Hybrid density functional theory for π-stacking interactions: Application to benzenes, pyridines, and DNA bases. *J Comput Chem* **2006,** *27* (4), 491-504.
168. Rozas, I.; Alkorta, I.; Elguero, J., Behavior of Ylides Containing N, O, and C Atoms as Hydrogen Bond Acceptors. *J Am Cheml Soc* **2000,** *122* (45), 11154-11161.